The timescales of magmatic processes prior to a caldera-forming eruption

Gareth Nicholas Fabbro

N° d'Ordre : D.U. 2452

UNIVERSTÉ BLAISE PASCAL–CLERMONT-FERRAND II
U.F.R. Sciences et Technologies

ÉCOLE DOCTORALE DES SCIENCES FONDAMENTALES
N° 785

THÈSE

Présentée pour obtenir le grade de

DOCTEUR D'UNIVERSITÉ

Spécialité : Volcanologie

Par **Gareth N. FABBRO**

MSci BA (Cantab)

The timescales of magmatic processes prior to a caldera-forming eruption

Les échelles de temps des processus magmatiques avant d'un éruption caldierique

Soutenue publiquement le 24 avril 2014 devant la commission d'examen composée de :

Président :	
Bruno Scaillet	Université d'Orléans, France
Rapporteur :	
Luca Caricchi	Université de Genève, Suisse
Ralf Gertisser	Keele University, Royaume-Uni
Examinateur :	
Thierry Menand	Université Blaise Pascal, France
Directeur de thèse :	
Fidel Costa	Nanyang Technological University, Singapour
Tim Druitt	Université Blaise Pascal, France

Abstract

Large, explosive, caldera-forming eruptions are amongst the most destructive phenomena on the planet, but the processes that allow the large bodies of crystal-poor silicic magma that feed them to assemble in the shallow crust are still poorly understood. Of particular interest is the timescales over which these reservoirs exist prior to eruption. Long storage times—up to 10^5 y—have previously been estimated using the repose times between eruptions and radiometric dating of crystals found within the eruptive products. However, more recent work modelling diffusion within single crystals has been used to argue that the reservoirs that feed even the largest eruptions are assembled over much shorter periods—10^1–10^2 y.

In order to address this question, I studied the $>10\,km^3$, 22-ka, dacitic Cape Riva eruption of Santorini, Greece. Over the $\sim$18 ky preceding the Cape Riva eruption a series of dacitic lava dome and coulées were erupted, and these lavas are interspersed with occasional dacitic pumice fall deposits (the Therasia dome complex). These dacites have similar major element contents to the dacite that was erupted during the Cape Riva eruption, and have previously been described as "precursory leaks" from the growing Cape Riva magma reservoir. However, the Cape Riva magma is depleted in incompatible elements (such as K, Zr, La, Ce) relative to the Therasia magma, as are the plagioclase crystals in the respective magmas. This difference cannot be explained using shallow processes such as fractional crystallisation or crustal assimilation, which suggests that the Cape Riva and Therasia magmas are separate batches. Furthermore, there is evidence that the Therasia dacites were not fed from a long-lived,

melt-dominated reservoir. There are non-systematic variations in melt composition, plagioclase rim compositions, and plagioclase textures throughout the sequence. In addition, high-temperature residence times of plagioclase and orthopyroxene crystals from the Therasia dacites estimated using diffusion chronometry are 10^1–10^2 y. This is short compared to the average time between eruptions (∼1,500 y), which suggests the crystals in each lava grew only shortly before eruption. The different incompatible element contents of the Cape Riva and Therasia magmas and plagioclase crystals suggest that a new batch of incompatible-depleted silicic magma arrived in the shallow volcanic plumbing system shortly before the Cape Riva eruption. This influx must have taken place after the last Therasia eruption, which $^{40}Ar/^{39}Ar$ dates show occurred less than $2{,}800 \pm 1{,}400$ years before the Cape Riva eruption.

The rims of the plagioclase crystals found in the Cape Riva dacite are in equilibrium with a rhyodacite, with a similar composition to the Cape Riva glass. However, the major and trace element zoning patterns of the crystals record variations in the melt composition during their growth. The compositions at the centre of most crystals are the same as the rims; however, these crystals are often partially resorbed and overgrown by more calcic plagioclase. The plagioclase then grades normally back to rim compositions. This cycle is repeated up to three times. The tight relationships between the anorthite, Sr and Ti contents of the different zones suggests that the composition of the plagioclase crystals correlates with the composition of the melt from which they grew. The different plagioclase compositions correspond to dacitic and rhyodacitic melt compositions. The orthopyroxene crystals reveal a similar sequence, although they only record one cycle. These zoning patterns are interpreted to document the assembly of the Cape Riva reservoir in the shallow crust through the amalgamation of multiple batches of compositionally diverse magma. Models of magnesium diffusion in plagioclase and Fe–Mg interdiffusion in orthopyroxene suggest that this amalgamation took place within 10^1–10^2 y of the Cape Riva eruption.

Keywords: calderas, Santorini, diffusion, magma chambers, crystal residence times

Résumé

Les grandes éruptions calderiques sont parmi les phénomènes les plus destructeurs de la Terre, mais les processus à l'origine des grands réservoirs de magma siliceux et pauvre en cristaux qui alimentent ces éruptions ne sont pas bien compris. Le temps de stockage de ces réservoirs dans la croûte supérieure a un intérêt particulier. De longs temps de stockage—jusqu'à 10^5 ans—ont été estimés en utilisant les temps de repos entre les éruptions et les âges radiométriques des cristaux qui se trouvent dans les produits éruptifs. Par contre, des travaux récents sur la diffusion dans des cristaux suggèrent que les réservoirs qui alimentent même les plus grandes éruptions peuvent se mettre en place pendant une période beaucoup plus courte—10^1–10^2 ans.

Afin de répondre à cette question, j'ai étudié l'éruption dacitique de Cape Riva de Santorin, Grèce (>10 km^3, 22 ka). Pendant les ∼18.000 ans précédant cette éruption, une série de dômes et de coulées dacitiques a été émise, alternant avec des dépôts de ponce dacitique (le complexe de dômes de Therasia). Ces dacites ont des compositions similaires à celle qui a été émise pendant l'éruption de Cape Riva, et ont été décrites précédemment comme des « fuites » provenant du réservoir de Cape Riva pendant sa croissance. Cependant, le magma de Cape Riva est appauvri en éléments incompatibles (tels que K, Zr, La, Ce) par rapport au magma de Therasia, une différence qui apparaît également dans les cristaux de plagioclase. Cette différence ne peut pas être expliquée par des processus peu profonds, tels que la cristallisation fractionnée ou l'assimilation de la croûte, ce qui suggère que les magmas de Cape Riva et Therasia ont des origines différentes. En outre, il existe des arguments tendant à montrer que les dacites

de Therasia n'ont pas été alimentées par un réservoir majoritairement liquide ayant eu une longue durée de vie. Il y a des variations non systématiques dans la composition du magma, les compostions des bords ainsi que les caractéristiques des cristaux de plagioclase tout au long de la séquence. De plus, les temps de résidence à haute température des cristaux de plagioclase et d'orthopyroxène estimés par des modèles de diffusion sont 10^1–10^2 ans. Ces temps sont courts par rapport au temps moyen entre éruptions ($\sim$1.500 ans), ce qui suggère que les cristaux observés dans chaque coulée ne se sont formés que peu de temps avant l'éruption. Les différentes teneurs en éléments incompatibles indiquent qu'un nouveau magma s'est mis en place dans le système volcanique superficiel peu de temps avant l'éruption de Cape Riva. Cet apport de magma a eu lieu après la dernière éruption de Therasia, qui s'est produite $<2.800 \pm 1.400$ ans avant l'éruption de Cape Riva selon les âges $^{40}Ar/^{39}Ar$.

Les périphéries des cristaux de plagioclase présents dans la dacite de Cape Riva sont en équilibre avec une rhyodacite, avec une composition similaire à celui du verre de l'éruption. Cependant, les zonations dans les éléments majeurs et traces enregistrent des changements dans la composition du liquide magmatique pendant la croissance des cristaux. La composition du centre de la plupart des cristaux de plagioclase est la même que celle des bords ; toutefois ces cristaux sont souvent partiellement résorbés, et la croissance a repris avec du plagioclase plus calcique. Ces cycles se répètent jusqu'à trois fois. La relation étroite entre la teneur en anorthite, Sr et Ti des différentes zones suggère que la composition des plagioclases est corrélé avec la composition du liquide, allant de liquides dacitiques à rhyodacitiques. Des cristaux d'orthopyroxène révèlent une séquence similaire. Les motifs de zonation sont interprétés comme un témoin de la formation du réservoir de Cape Riva dans la croûte supérieure par le mélange de plusieurs magmas ayant des compositions diverses. Des modèles de diffusion de Mg dans le plagioclase et de Fe–Mg dans l'orthopyroxène suggèrent que ce mélange a eu lieu 10^1–10^2 ans avant l'éruption.

Mots clés : caldeira, Santorin, diffusion, chambres magmatiques, temps de résidence de cristaux

Acknowledgements

I would like to thank my supervisors, Tim Druitt and Fidel Costa, for all their support and advice over the past three and a half years.

Stéphane Scaillet (ISTO, Université de Orléans) is thanked for providing $^{40}Ar/^{39}Ar$ ages for the Therasia lavas; Mhammed Benbakkar (LMV, Université Blaise Pascal, Clermont-Ferrand) and Cathérine Chauvel (ISTerre, Grenoble) for the for running the AES and ICP-MS analyses of the whole rock and groundmass samples. Thanks also go to Jean-Luc Devidal (LMV) for aiding me with the EMP and LA ICP-MS analyses, and to Jean-Marc Henot (LMV) for help with the SEM.

Financial support was provided by the Auvergne Region, as well as the French Agence Nationale de la Recherche (ANR) and Centre National de la Recherche Scientifique (CNRS).

Finally, I would like to thank all my friends, who welcomed me to a new country and made my stay thoroughly enjoyable. I would also like to thank my family, without whom I would not be where I am today.

For Engielle

Contents

List of Figures

List of Tables

Introduction

Silicic eruptions can be highly explosive, and can erupt over 1,000 km^3 of magma (Mason et al., 2004; Miller and Wark, 2008). The magma that feeds these eruptions is generally believed to be stored in a single, large body of magma prior to eruption (Bachmann and Bergantz, 2008a; Hildreth, 1981; Smith, 1979). There is, however, considerable debate over the form these magma bodies take, the processes that produce them, and importantly, the timescales over which they are active. On the one hand, individual volcanoes can remain active for up to several million years, and there is a loose relationship between repose time and eruption size (Reid, 2008). This suggests that magma may accumulate over long periods before being erupted, up to a million years in extreme cases. However, there is increasing evidence that large, melt-dominated bodies of eruptible magma are ephemeral, and may exist for less than a few centuries before their eruption (e.g. Allan et al., 2013; Druitt et al., 2012; Sutton et al., 2000; Wilson and Charlier, 2009).

There is often a distinction made between crystal-rich and crystal-poor ignimbrites, and the processes that bring about their eruption (Bachmann and Bergantz, 2004; Hildreth, 1981). Crystal-rich ignimbrites are believed to be re-mobilised crystal mushes, that can be stored for long periods in the crust in a partially crystalline state. The assembly of large bodies of melt-dominated, crystal-poor silicic magmas, on the other hand, requires that the melt is segregated from its crystals prior to eruption. Understanding the processes that assemble large reservoirs of eruptible magma and the timescales over which they occur is of crucial importance for monitoring restless caldera

systems.

Thesis objectives

In this thesis I explore the formation of large bodies of crystal-poor silicic magma in the shallow crust. In particular, I focus on the following three questions:

1. How are large, shallow crustal bodies of volatile-rich, crystal-poor magma assembled?

2. How and where do the crystals in these eruptions form, and what do the zoning patterns of the crystals record?

3. What are the associated timescales of these processes?

Approach and thesis outline

I chose to focus on the 22-ka, caldera-forming Cape Riva eruption of Santorini, Greece. Santorini currently is the most active volcano in the Aegean, and has a history of large, explosive eruptions. One of the advantages of the Cape Riva eruption is that in was preceded by about 17 ky of dacitic extrusion, the lavas from which are exposed in the cliffs of the caldera. This allows us to track the evolution of the magma reservoir in the build-up to a large silicic eruption. This study aims to integrate the results from multiple different techniques used on the same sequence, in order to build up a more complete picture of the assembly of a crystal poor magma reservoir in the shallow crust.

Chapter 1 is a review of the literature relating to the storage of large, silicic bodies of eruptible magma. It looks at evidence gathered from silicic plutons; radiometric residence times of crystals with high closure temperatures, such as zircon; effusive eruptions of magma chemically similar to the magma erupted during the climactic

events, often interpreted to be "precursory leaks" from a growing magma reservoir; and numerical models of magma chamber stability.

The geological setting of the study is presented in **Chapter 2**. This includes the wider tectonic context of the Hellenic Arc, as well as the volcanic history of Santorini. Particular attention is paid to the history since ∼67 ka, which includes the Cape Riva and Therasia eruptions.

Chapter 3 looks at diffusion chronometry, a technique I use extensively in this thesis. I discuss the theory behind it, as well as the practical considerations required to apply it to magmatic systems. I review the experimental determinations of the diffusion coefficients that I use later in this thesis, and provide an overview of previous studies that have used diffusion chronometry to investigate volcanic systems.

I then go on, in **Chapter 4**, to present the results of my field study. In particular, I present the detailed stratigraphy of the Therasia dome complex. This is combined with $^{40}Ar/^{39}Ar$ dates provided by Dr Stéphane Scaillet (Institut des Sciences de la Terre d'Orléans), in order to provide a tight chronological framework in which to place the results of the following work.

Chapter 5 describes the chemistry and mineralogy of the Therasia lavas and the products of the Cape Riva eruption. Whole rock analyses are supplemented with analyses of groundmass separates. The groundmass represents the liquid portion of the magma immediately before eruption. Major element compositions and textural features of the different minerals present are also discussed. Combined with the stratigraphy from Chapter 4, this allows me to track the evolution of the volcanic plumbing system at Santorini through time.

Chapter 6 looks in more detail at the zoning patterns of the plagioclase phenocrysts in the Therasia and Cape Riva dacites. Plagioclases are imaged using the scanning electron microscope (SEM), and major elements are measured by electron microprobe. Trace elements are measured using the laser ablation ion coupled plasma mas spectrometer (LA ICP-MS). Melt compositions are deduced from the concentrations of

slowly diffusing elements, which allows zoning patterns to be matched up to magmatic processes. The timing of these processes is the estimated by modelling the diffusion of Mg. This timescale is compared to those found from the fieldwork and $^{40}Ar/^{39}Ar$ dates presented in Chapter 4.

Orthopyroxene phenocrysts are studied in detail in **Chapter 7**, in a similar fashion to the plagioclase crystals in Chapter 6. Back-scattered electron (BSE) images of the orthopyroxenes from the Cape Riva eruption were made using the SEM and semi-quantitative maps of the Mg, Fe, Ca and Al distributions are made on the electron microprobe. The zoning patterns of the different elements are used to deduce the crystals' histories, and these are compared to the histories inferred for the plagioclase phenocrysts in Chapter 6. Mg–Fe diffusion is modelled to estimate timescales, and these are compared to those found for the plagioclases in Chapter 6 and from the $^{40}Ar/^{39}Ar$ dates and fieldwork in Chapter 4.

All these results are then summarised in **Chapter 8**, and an integrated model for the evolution of the plumbing system of Santorini during the build-up to the Cape Riva is proposed.

Chapter 1

Large, silicic magma reservoirs

1.1 Introduction

Petrological studies of the deposits from large, explosive eruptions show that silicic magma is usually stored in the shallow crust immediately prior to eruption, generally at less than ∼15 km depth (e.g. Arce et al., 2012; Cadoux et al., 2014; Gertisser et al., 2012; Hildreth and Wilson, 2007; Liu et al., 2005; Scaillet and Evans, 1999). However, the magma is not necessarily produced at these depths. Silicic magma could be produced in the lower crustal hot zones by fractional crystallisation and partial melting of the lower crust, before being transferred to shallow crustal storage reservoirs (Allan et al., 2013; Andújar et al., 2010; Annen et al., 2006; Cadoux et al., 2014; Solano et al., 2012).

Investigations into the processes and timescales of the assembly of large, silicic magma reservoirs have principally followed three main avenues: the study of plutons, the study of the products of large silicic eruptions, and theoretical modelling of the thermal and mechanical properties of magma reservoirs. Recent discussions of the timescales of large, silicic magma bodies have been given by Costa (2008) and Reid (2008), although in the intervening years many additional studies have been published. The timescales revealed vary from 10^1 to 10^6 yr, with a lot of variation caused by the different magmatic processes that different techniques relate to. The following section

focuses on the timescales related to the assembly of a large, eruptible body of silicic magma in the shallow crust.

1.2 Terminology

There are many terms in igneous petrology that mean subtly different things to different people. For clarity, I have defined below the sense in which I use the terms in bold throughout this thesis.

Magma may be stored in a variety of different forms, either as completely crystal-free melt or as a rigid framework of crystals with a small amount of melt in the pores, or anywhere between these two endmembers. The viscosity of silicic magma increases dramatically if it contains more than 40–60 vol% crystals (Lejeune and Richet, 1995), making it difficult for crystal-rich magmas to convect or erupt. A single body of magma may have different properties in different volumes: for example, a liquid-dominated cap above a crystal-rich mush. It is therefore important to distinguish **magma reservoirs**, bodies of eruptible magma, from the wider **plumbing system** of the volcano, which includes any crystalline mush or plutons as well as any magma reservoirs present beneath the volcano.

When looking at the crystals found in these magmas, the **rim** is defined as the outermost part of the crystal to have grown within the magma chamber. These are distinguished from the thin (typically 10–10^2 µm **overgrowths** that grew during the ascent to the surface and eruption of the magma, and which are compositionally identical to the groundmass microlites.

Phenocrysts (*sensu stricto*) are those crystals which grew from the magma in which they are found. These should be differentiated from **antecrysts**, crystals that grew in a different, but but genetically related, magma and **xenocrysts**, crystals that grew from an unrelated melt. However, in practice it is often difficult to discriminate between true phenocrysts and antecrysts, as they often have very similar chemistry

and appearance. Individual crystals also often have complex histories, and can be transferred between different magmas before their eruption. In this study, the term "**Phenocryst**", therefore, is defined as any crystal with rims that are in chemical equilibrium with their host melt. This definition includes any antecrysts that grew from a compositionally similar melt to their host, as well as crystals that have a xenocrystic core, as long as the rims are in equilibrium with their host melt.

1.3 Evidence of storage timescales of silicic magma from plutons

We cannot directly observe the plumbing systems of active volcanoes. Plutons, however, can sometimes be matched to contemporaneously erupted tuffs, suggesting that they represent the exhumed plumbing systems of extinct volcanoes (e.g. Barth et al., 2012; Lipman, 2007; Zimmerer and McIntosh, 2012, 2013). Plutons can, therefore, be used to gain insight into the processes that occur prior to large, silicic eruptions.

Early work often assumed that individual plutons were emplaced in single events (e.g. Bowen, 1915; Daly, 1914), however recent work is changing this view. Large age ranges, up to 12 My, are reported for the crystallisation of individual plutons (Barth et al., 2012; Bolhar et al., 2010; Coleman et al., 2004; Davis et al., 2011; Glazner et al., 2004; Lipman, 2007; Miller et al., 2007). It is unlikely that magma could remain molten in the shallow crust for this length of time, which suggests that the construction of large plutons requires repeated injections of magma. This is supported by field evidence and analogue modelling that suggests that plutons are constructed by the incremental stacking of sills (Brown et al., 2000; Coleman et al., 2004; Menand, 2008; Wiebe, 1993; Wiebe and Collins, 1998). Detailed work on the San Juan Volcanic Region, Colorado, shows intrusion rates of between 10^{-4}–$10^{-2}\,km^3\,y$ (Lipman, 2007). These intrusion rates are of a similar magnitude to the long-term eruptive rates for other large silicic provinces (Mason et al., 2004).

These long durations reflect, however, the lifetime of the overall volcanic system. The low intrusion rates are time-averaged rates, and do not necessarily reflect the transient intrusion rate during the construction of large magma reservoirs.

1.4 Radiometric crystal residence times

Magmatic residence times are often estimated by dating crystals radiometrically. Radiometric dating relies on comparing the ratio of parent to daughter isotopes. At high temperatures, diffusion can act to reset this ratio. Below a certain temperature, referred to as the closure temperature T_c, diffusion is slow enough that it does not affect the calculated age. Radiometric ages are, therefore, the time since the crystal temperature dropped below the its closure value. A commonly used equation to estimate the closure temperature is that formulated by Dodson (1973):

$$\frac{E}{RT_c} = \ln\left(-\frac{AD_0RT_c^2}{x_c^2Es}\right) \tag{1.1}$$

where R is the molar gas constant, A is a constant relating to the shape of the crystal and the decay of the parent isotope, x_c is the characteristic distance over which diffusion acts, s is the cooling rate, and E and D_0 are, respectively, the activation energy and pre-exponential factor from the Arrhenius equation for the diffusion coefficient (discussed in more detail in Chapter 3):

$$D = D_0 \exp\left(-\frac{E}{RT}\right) \tag{1.2}$$

Different radiometric systems have diverse closure temperatures, and therefore will give varying ages. The radiometric clock in systems with low closure temperatures will only start after eruption. This contrasts with systems with higher closure temperatures, which will give ages that reflect crystallisation rather than eruption. Comparing eruption ages to crystallisation ages gives an estimate of the residence time of the

crystals. K–Ar in feldspars and micas can be used to estimate eruption ages, as they have low closure temperatures; Rb–Sr in feldspar and U–Pb in zircon have higher closure temperatures, and are suitable for evaluating crystallisation ages (Cherniak and Watson, 1992, 2001; Foland, 1994; Giletti and Casserly, 1994; Grove and Harrison, 1996).

Some of the earliest attempts to estimate residence times of crystals in large silicic magma reservoirs focused on Long Valley, and the >600 km^3, ~770 ka Bishop Tuff eruption (Hildreth, 1979, 1981). Rb–Sr isochrons from the pre-caldera Glass Mountain rhyolites gave ages of up to 360 ky older than K–Ar ages (Davies and Halliday, 1998; Davies et al., 1994; Halliday et al., 1989). Rb–Sr isochrons were also used to suggest the sanidine crystals in the Bishop Tuff itself started growing 300–500 ky before their eruption (Christensen and DePaolo, 1993). Ar–Ar isochrons from glass inclusions in quartz crystals suggested even longer residence times (up to 1.1 My; van den Bogaard and Schirnick, 1995), although this apparent age has since been attributed to excess ^{40}Ar in the melt inclusions (Winick et al., 2001).

An issue arises, however, with interpreting apparent isochrons as crystallisation ages. True isochrons are produced by the radioactive decay of the parent isotope in a closed system, but mixing between magmas with different isotopic ratios can produce similar variations in isotopic ratios. If mixing lines are interpreted as isochrons, then spurious ages are calculated. In addition to Rb and Sr isotopes, Wolff and Ramos (2003) looked at Pb isotope ratios in the Otowi member of the Bandelier Tuff, Valles Caldera, New Mexico (1.6 Ma, ~350 km^3). The range of $^{206}Pb/^{204}Pb$ ratios observed in the sanidine crystals cannot be produced by radioactive decay on a geologically reasonable timescale, and therefore must instead indicate that mixing occurred. This suggests that apparent Rb-Sr isochrons in the Bandelier Tuff are also due to mixing, rather than radioactive decay. If this is also true of the Bishop Tuff, then the apparent ages from Rb–Sr isochrons would be not reflect the residence times of the Bishop magma.

More recently, secondary high resolution ion mass spectrometry (SHRIMP) has allowed multiple ages to be determined from different zones of single crystals. Zircon is commonly used, as its high U content makes it an ideal target for U–Pb dating. Although dating single crystals leads to less precise ages than dating bulk separates, the extra petrological context that can be gained makes single crystal (and especially single zone) ages less ambiguous. U–Pb ages indicate that zircon crystallisation began in the Bishop Tuff less than 80 ky before eruption, which is much later than the estimates for sanidine crystallisation using Rb–Sr isochrons (Chamberlain et al., 2014; Reid and Coath, 2000; Simon and Reid, 2005). This suggests that the apparent Rb–Sr isochrons are caused by open system processes, rather than reflecting the residence time of the Bishop magma.

In general, residence times of accessory minerals from large silicic eruptions are of the order of 10^4–10^5 years (e.g. Brown and Fletcher, 1999; Folkes et al., 2011; Vazquez and Reid, 2004; Wilson and Charlier, 2009; Wotzlaw et al., 2013). These crystal residence times only relate to the amount of time that the zircons have been stored in the crust, however, as opposed to the amount of time that the zircons were stored in an eruptible body of magma. The zircons could be stored in a rigid crystal mush for much of their life, for example, in which case the time over which an eruptible body of magma exists is much shorter than the residence times of the crystals within it.

1.5 Crystal mushes

The crystal mush model was first proposed to explain the apparent longevity of the Bishop Tuff magma chamber (Mahood, 1990; Sparks et al., 1990), and has more recently been used to explain the high crystallinity of crystal-rich ignimbrites (the monotonous ignimbrites of Hildreth, 1981; e.g. Bachmann and Bergantz, 2008b). Latent heat buffering could keep magmas above their solidus but with low melt fractions for long periods with little heat input (Huber et al., 2009). High crystal contents will also pre-

vent convection, which would slow the loss of heat from the magma reservoir to the surrounding crust (Koyaguchi and Kaneko, 1999, 2000).

Some of the longest zircon residence times are, in fact, found in crystal-rich ignimbrites. For example, zircons up to 440 ky older than the age of the eruption are found in the Cerro Galán ignimbrite, and up to 600 ky older than the age of the eruption in the Fish Canyon Tuff (Bachmann et al., 2007b; Folkes et al., 2011; Wotzlaw et al., 2013). These ignimbrites appear to have spent large periods of time close to their solidus, and show signs of being rejuvenated only shortly before eruption. High Yb/Dy ratios in some of the zircons found in the Fish Canyon Tuff suggest that during their growth the crystallinity of the magma reached 75–80 % (Wotzlaw et al., 2013). Many of the crystals in the Fish Canyon Tuff show resorption textures or reverse zoning, suggesting a late-stage heating event reduced the crystallinity to ∼45 % (Bachmann et al., 2002).

A similar story is found in the crystal-rich Kos Plateau Tuff (25–35 % crystals), where a highly crystalline intrusion was remelted before eruption. The Kos Plateau Tuff contains crystal-rich pumices alongside highly crystalline granitic clasts. These granitic clasts have a range of textures; some are holocrystalline but most show varying degrees of remelting (Keller, 1969). The chemical and mineralogical similarities for all the clasts suggests that they have a shared origin. Zircons from both the granitic clasts and the crystal rich pumices have the similar, continuous age spectra (from 340 ka to eruption age, 160 ka, with one older zircon dated at ∼500 ka), which show both the granite and the pumice crystallised over the same period (Bachmann et al., 2007a). Partially resorbed crystals in the pumice and the textures of the granite clast show that the entire reservoir was reheated shortly before eruption.

Evidence for the prolonged storage of magma in a crystal mush is not restricted to crystal-rich ignimbrites; many crystal-poor silicic eruptions also exhibit features suggestive of storage in a crystal mush. For example, at Tarawera volcano, within the Okatania Volcanic Centre (New Zealand), 30 km^3 of rhyolitic magma has been erupted in four episodes over the last 22 ky. Zircons from these deposits have residence times

of over ∼100 ky, and often show discontinuous growth histories with hiatuses of up to ∼40 ky (Storm et al., 2011). Some zircons have high U and Th, suggesting that they grew during periods of high crystallinity. There are also zircons that have different ages on different crystal faces, and some that have crystal faces significantly older than the eruption age. These zircons could represent crystals that were partially or wholly enclosed as inclusions in other minerals but were released shortly before eruption.

Even relatively small-volume silicic eruptions can contain zircons with long residence times. Claiborne et al. (2010) sampled different units spanning the entire known eruptive history of Mount St. Helens and consistently found that the oldest zircons were at least 150 ky older than their eruption ages. Zircons from the Devils Kitchen record residence times of up to ∼200 ky, and some have high Th and U that require crystallinities of over 95 % (Miller and Wooden, 2004). Crystalline mushes appear to be common features of silicic volcanoes.

1.6 "Precursory leaks"

Before many large, explosive silicic eruptions there are often series of smaller, usually effusive eruptions of magma that has a similar composition to the magma from the climactic event. These smaller eruptions are frequently interpreted as leaks from a growing body of melt-dominated, eruptible magma (e.g. Bacon, 1985; Bacon and Druitt, 1988; Druitt, 1985; Metz and Mahood, 1991). The diffuse vent patterns that many of these "leaks" have has been used to argue that locally the stress field is dominated by the presence of a magma chamber rather than regional tectonics (Bacon, 1985). Regardless of the genetic relationship that any particular set of precursory leaks have with their climactic event, their close temporal and spacial relationships means that they should provide information on the evolution of the plumbing system in the build-up to a large, explosive eruption.

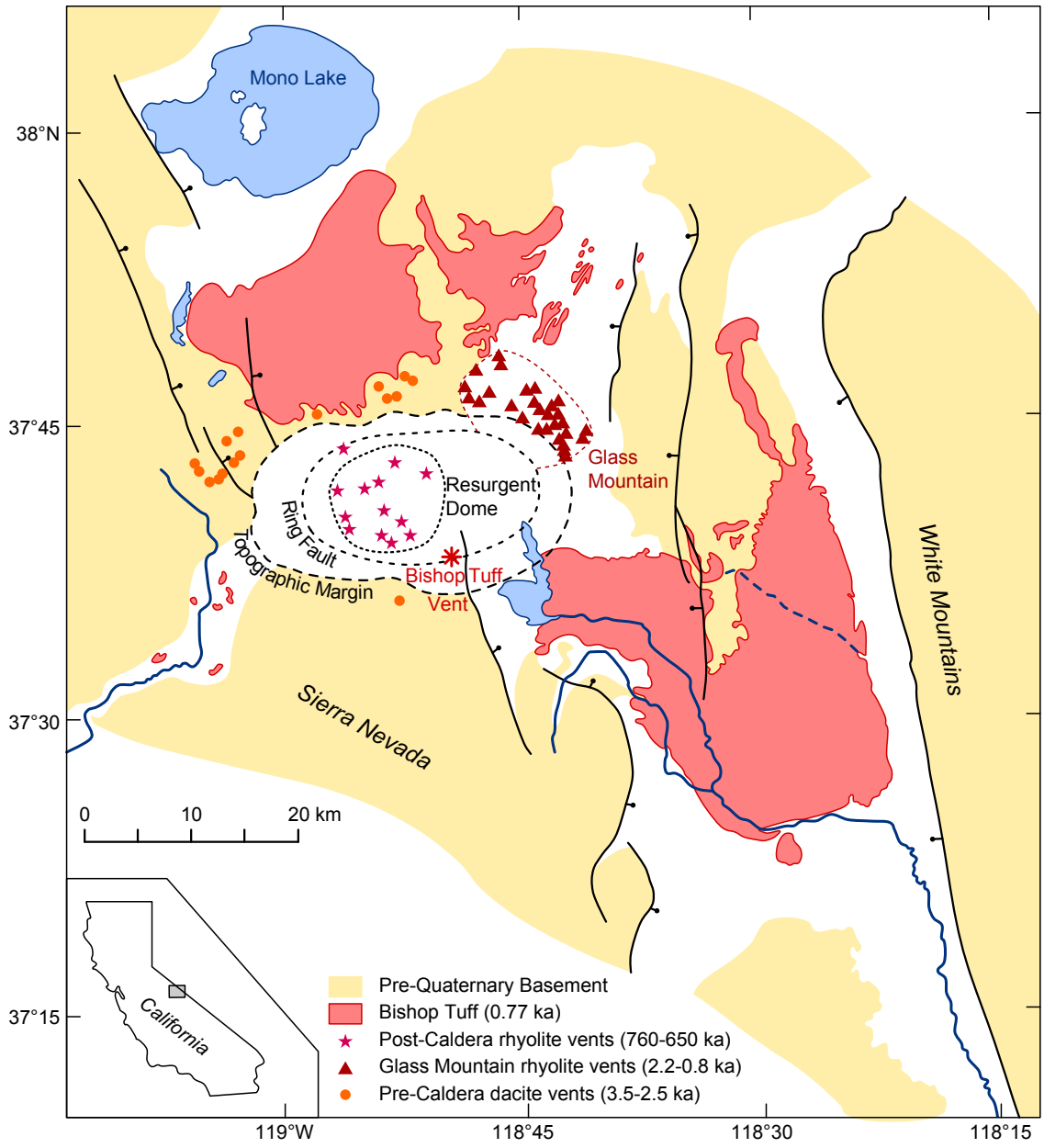

Figure 1.1: Simplified geological map of Long Valley, after Hildreth and Wilson (2007). The Bishop Tuff vent labelled on the map is that inferred for the first phase of the eruption from isopach maps

1.6.1 Glass Mountain and the Bishop Tuff, Long Valley, California

A classic example of a series of precursory leaks is the Glass Mountain rhyolites, which were erupted before the Bishop Tuff eruption of Long Valley, California (Figure 1.1). Between 2.1 Ma and the eruption of the Bishop Tuff 0.77 My ago, >50 km^3 of rhyolite

erupted as a series of domes and intercalated pyroclastic units (Metz and Mahood, 1985, 1991). It was the preservation of Rb–Sr isochrons in lavas erupted over up to 700 ky that first led to the suggestion that a long-lived melt reservoir existed under Long Valley in the run up to the Bishop Tuff eruption (Davies and Halliday, 1998; Davies et al., 1994; Halliday et al., 1989).

It was also noted that the younger lavas from Glass Mountain have a restricted range of chemical compositions and of Sr, Nd and Pb isotopic ratios. These chemical and isotopic compositions are similar to those of the Bishop Tuff rhyolite, which implies that the younger Glass Mountain rhyolites were tapping the growing Bishop Tuff magma reservoir (Halliday et al., 1989; Hildreth, 2004; Hildreth and Wilson, 2007; Metz and Mahood, 1985, 1991). The older Glass Mountain rhyolites, however, have a greater range of trace element and isotopic compositions.

The model that Hildreth and Wilson (2007) proposed for the growth of the Bishop Tuff magma chamber is shown in Figure 1.2. In this model, much of the plumbing system beneath Long Valley consisted of crystalline mush. During the early Glass Mountain phase, there was not a single, integrated magma reservoir. Instead, each eruption tapped a discrete lens of crystal-poor melt from within the mushy zone. Different magma reservoirs for each eruption would explain the chemical variability of the older Glass Mountain rhyolites. Mafic magma ascending from depth would have supplied heat, but the dense recharge magmas would have been trapped beneath the growing mush body. Fractional crystallisation of these mafic magmas would have produced rhyolitic melt, which could have segregated and risen in to the upper, more crystal-poor portions of the plumbing system. Starting at about 1.1 Ma, however, these lenses began to coalesce into a single, large body of melt. A unified melt reservoir would lead to less chemical variation between the products of eruptions, and was eventually expelled during the Bishop Tuff eruption.

Despite the chemical similarities between the Glass Mountain rhyolites and the Bishop Tuff, the zircons found in the Bishop Tuff are different to those found in both

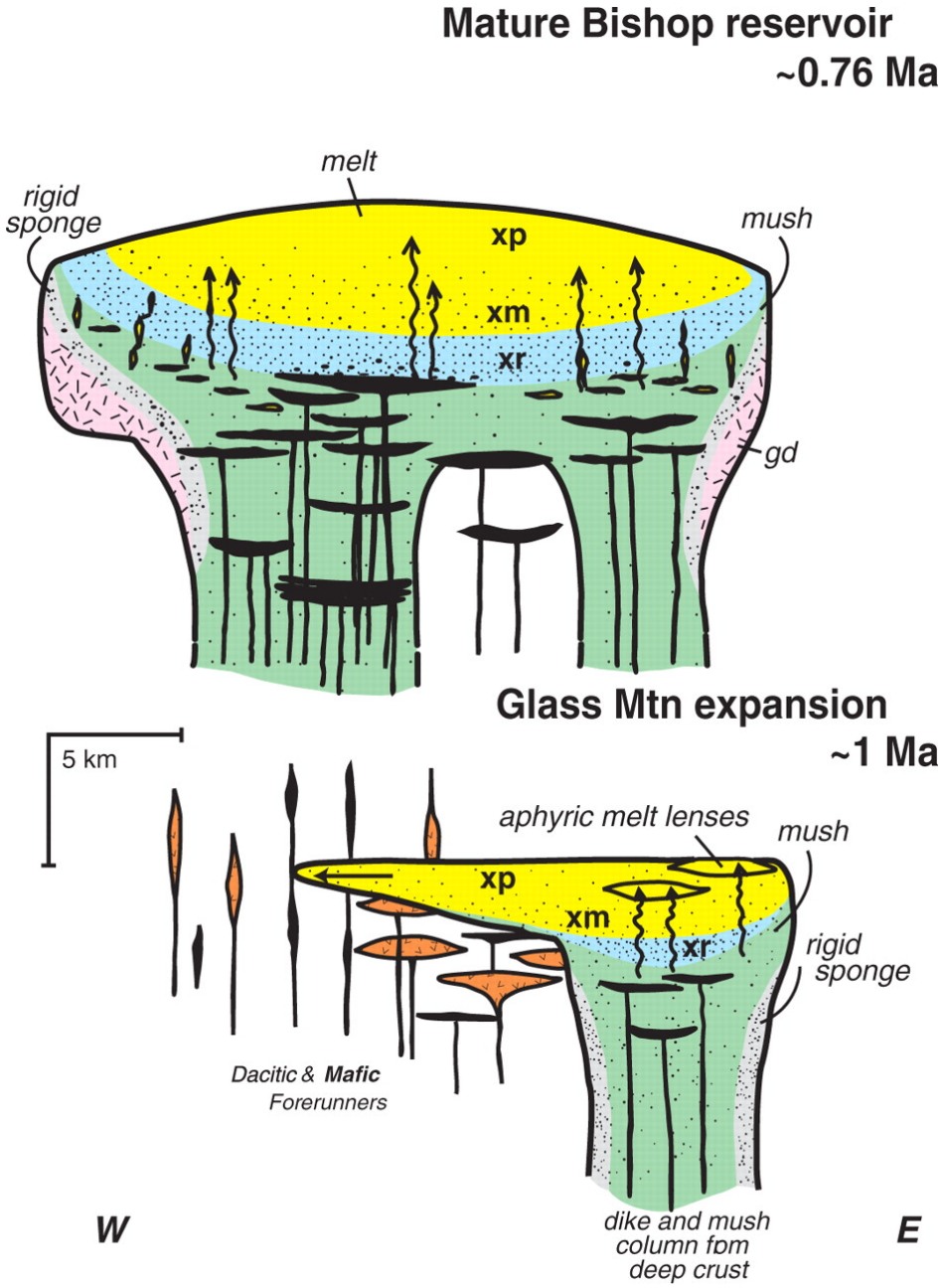

Figure 1.2: Conceptual schematic illustrations of mush model of rhyolite melt extraction from plutonic crystal mush of intermediate to silicic hybrid composition, from Hildreth and Wilson (2007). Scaled roughly to late Glass Mountain (below) and mature Bishop (above) evolutionary stages. Phenocryst contents of zoned mobile magma are proportional to stipple density: xp, crystal-poor (0–6 %); xm, intermediate crystal content; xr, crystal-rich (12–25 %; mush = 25–55 %).

the early and late Glass Mountain rhyolites. The Glass Mountain zircons can be distinguished from the Bishop Tuff zircons both texturally, and in terms of their U–Pb ages (Chamberlain et al., 2014; Reid and Coath, 2000; Simon and Reid, 2005). If the Glass Mountain rhyolites tapped the same reservoir as the Bishop Tuff, then earlier crystals must have been completely resorbed before the Bishop Tuff zircons first started crystallising (∼850 ka). There is also uncertainty in dating the end of the Glass Mountain eruptive activity. The K–Ar age for the youngest Glass Mountain dome (YA) determined by Metz and Mahood (1985) is 790 ± 20 ka, close to the 767.4 ± 2.2 ka Ar–Ar eruption age of the Bishop Tuff (Rivera et al., 2011). However, Chamberlain et al. (2014) found that the youngest zircons from this dome dated from 862 ± 23 ka, which they suggested meant that Glass Mountain activity ceased before the large Bishop Tuff magma reservoir began to form.

1.6.2 Mount Mazama, Crater Lake, Oregon

Another well-studied series of precursory leaks occurs at Crater Lake, Oregon. An andesitic to dacitic stratovolcano, Mount Mazama, was constructed at the present location of Crater lake between 420 and 35 ka (Bacon and Lanphere, 2006). Then, starting at about 27 ka, rhyodacite started to be erupted from diffuse vents across the edifice (Figure 1.3). This activity culminated with the eruption of ∼50 km^3 of rhyodacite at ∼7.7 ka, and the collapse of Mount Mazama to form the present-day caldera. The similar chemistry and petrology of the pre-climactic and climactic rhyolites suggests that they were erupted from the same magma reservoir (Bacon and Druitt, 1988; Druitt and Bacon, 1989).

An early pre-climactic rhyodacite lava, erupted ∼27 ka, was studied by Bacon and Lowenstern (2005). Comparison of the plagioclases with those found in the plutonic granodiorite blocks found in the climactic deposit shows that at least 80 % of the plagioclases in this dome were recycled from the plutonic rocks that underlay Mount Mazama (Bacon et al., 1989). Other crystals in the pre-climactic rhyodacite are also probably

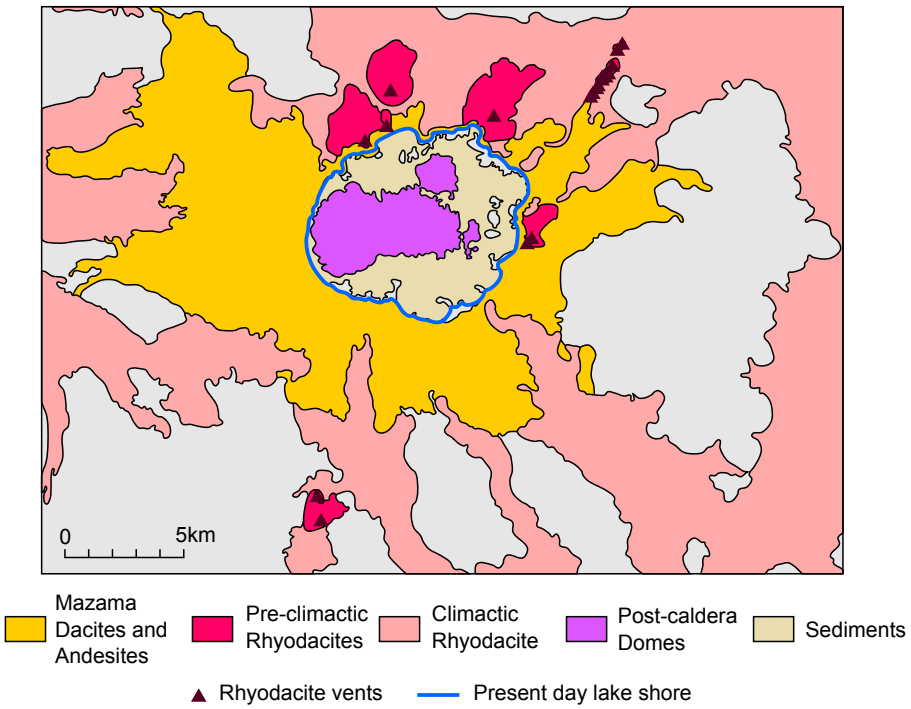

Figure 1.3: Simplified geologic map of Crater Lake, Oregon, after Bacon and Lanphere (2006)

derived from the granodiorite blocks, including zircon. The zircon ages from both the pre-climactic rhyodacite and the granodiorite blocks show that they crystallised between ∼20 ka and ≥300 ka, and record pulses of growth 50–70, ∼110 and ∼200 ka which coincide with periods of dacitic volcanism (Bacon and Lowenstern, 2005; Bacon et al., 2000).

The model that emerges for the climactic reservoir at Crater Lake is similar to that proposed for the Bishop Tuff. The climactic reservoir is inferred to have started growing shortly before the first eruption of rhyodacitic magma at Mount Mazama, at ∼27 ka (Bacon and Druitt, 1988; Druitt and Bacon, 1989). The growth of a long-lived, melt-dominated magma reservoir at Mount Mazama coincided with a pulse of increased mafic volcanism that affected the whole region and that would have supplied increased melt and heat to Mount Mazama (Bacon and Lowenstern, 2005). Prolonged magmatic activity prior to this had built up a large volume of plutonic mush. This plutonic material started to defrost and liberate crystals, including plagioclase and zircon into the rhyodacite (Bacon and Lowenstern, 2005). Zircon is undersaturated in

the pre-climactic rhyodacite, and the survival of zircons in this magma suggest that they could only have been incorporated a few tens of years before eruption. The magma reservoir continued to grow, mainly through fractional crystallisation of mafic magma supplied from depth, but incorporating up to 25 % partial melt from plutonic rocks (Bacon and Druitt, 1988; Bacon and Lowenstern, 2005; Druitt and Bacon, 1989). The climactic rhyodacite lacks zircon, despite containing the partially molten granodiorite blocks that are inferred to have supplied zircon to the pre-climactic rhyodacites. This implies that the residence time of the climactic rhyolite was long enough to resorb the zircons released from the plutonic mush (Bacon and Lowenstern, 2005).

1.6.3 The Oruanui eruption, Taupo Volcano, New Zealand

The 26.5 ka Oruanui eruption from Taupo Volcano, New Zealand, discharged ∼530 km^3 of crystal-poor (8–13 % crystallinity) rhyolite (Lowe et al., 2008; Sutton et al., 1995; Wilson, 2001). In the ∼20 ky that preceded the Oruanui eruption, several small volume (<1.5 km^3) magmatic and phreatomagmatic explosive rhyolitic eruptions occurred, along with the emplacement of rhyolitic domes from widespread vents. Many of these, including the ∼45 ka Tihoi and ∼30 ka Okaia eruptions, are chemically very similar to the Oruanui rhyolite (the "Oruanui-type" of Sutton et al., 1995).

However, when the ages of the zircons from the different units are examined, the Oruanui is found to lack some of the zircons found in the Tihoi and Okaia eruptions. All three eruption deposits have zircon population with a peak at 86–95 ka, alongside and another, younger population with a peak age that varies between eruptions (Charlier et al., 2005; Wilson and Charlier, 2009). The lack of Tihoi and Okaia zircons in the Oruanui cannot be explained by dissolution, because if that was the case then the older population should also have been resorbed. The Tihoi and Okaia cannot be leaks from the growing Oruanui magma reservoir. The similar ages of the older zircons in all of the Oruanui-type rhyolites does, however suggest a genetic link between them. The different eruptions probably represent different batches of melt that were extracted

from the same long-lived deep crystal mush (along with the 86–95 ka zircons), and then stored separately in the shallow crust in a holding reservoir for a shorter period of time before their eruption (Charlier et al., 2005; Wilson and Charlier, 2009).

There is also evidence that many post Oruanui rhyolite and dacite eruptions have short residence times in a shallow holding reservoir. Sutton et al. (1995, 2000) found sudden jumps in chemical and isotopic compositions between different groups of eruptions, which they interpreted as the arrival of a new batch of magma into the shallow reservoir. The time gaps between different magma batches range from 600 to 6 000 years, with the 1.77 ka, 15–35 km^3 eruption Y inferred to have resided in its holding reservoir for less than ∼1,000 years.

1.7 Diffusion chronometry

When there is disequilibrium between a crystal and its host melt, or between two different zones of the same crystal, the crystal will try to re-equilibrate by diffusion. This will set up compositional gradients within the crystal. The rate at which diffusion occurs is strongly dependent on temperature, therefore when the crystal cools these compositional gradients can become "frozen in". We can measure these compositional gradients, and model to diffusion in order to estimate the high-temperature residence times of the crystals after disequilibrium was established. The practical details of this technique are discussed in detail in the next section; here I discuss how the results of diffusion chronometry studies impact our understanding of the longevity of large, silicic magma reservoirs.

An early study by Hervig and Dunbar (1992) found zoning in Sr concentrations in two sanidine crystals, one from the Bishop Tuff and one from the Bandelier Tuff. They argued that the zoning was caused by pre-eruptive mixing between different rhyolites, and used diffusion modelling to estimate high-temperature residence times of $\sim 10^4$ years for the two crystals in their respective reservoirs after the mixing event. Sr

diffusion in another sanidine crystal modelled by Anderson et al. (2000) and Morgan and Blake (2005) gave a high-temperature residence time of 114–136 ky at 800 °C. These timescales are similar to the duration of zircon crystallisation in the Bishop Tuff estimated by radiometric dating (∼80 ky). However, more recent work has suggested shorter high-temperature residence times for crystals in the Bishop Tuff. Wark et al. (2007) used Ti diffusion in quartz, and found that the growth of the rims occurred less than ∼100 years before eruption. Gualda et al. (2012b) used Ti diffusion and melt inclusion faceting in quartz crystals, and calculated that all the quartz crystals they studied had residence times of less than 10,000 years: typically 500–3,000 years.

If we assume that the longer residence times calculated by radiometric dating are a better reflection of the true residence times of the magma, then there are two possible explanations for the shorter diffusion timescales. The first is that the diffusion models are not measuring the residence times of the whole crystal. This is clearly the case for the quartz crystals of Wark et al., which actually date the growth of the rims. These rims are richer in Ti, and similar rims are also seen in the Bishop Tuff zircons. The high-Ti rims are more common and thicker in the middle- and late-erupted pumice interpreted to have come from deep in the magma reservoir. This all suggests that the high-Ti rims grew as a hotter magma invaded the Bishop Tuff reservoir from below (Chamberlain et al., 2014; Roberge et al., 2013; Wark et al., 2007). The diffusion results of Wark et al., therefore, tell us that this magma arrived less than 100 y before the Bishop Tuff eruption, but they do not tell us how long the quartz resided in the Bishop Tuff magma reservoir before that. Similar Ti-rich rims are found on quartz crystals from the ∼1,000 km^3 Whakamaru eruption in the Taupo Volcanic Zone and the ∼2,000 km^3 Younger Toba Tuff in Sumatra, as well as in other, smaller (10–120 km^3) ignimbrite eruptions from the Taupo Volcanic zone (Matthews et al., 2012a,b; Saunders et al., 2010; Smith et al., 2010). Diffusion modelling of Ti across the boundaries of these rims gives similarly short ages, less than a few hundred years. Slightly longer timescales of 1,000–7,000 y are found for Ti-rich rims on quartz crystals from the Bandelier Tuff

(Wilcock et al., 2012).

The other way that short diffusion timescales can be consistent with long radiometric residence times is if the crystals spent significant time at low temperature. Because the rate of diffusion is strongly dependent on the temperature, crystals can sit at low temperatures for long periods without diffusion significantly modifying their zoning profiles. For example, plagioclase crystals from two andesitic eruptions of Mount Hood were found to have a minimum residence time of 21,000 y, based on U–Th and Th–Ra ages (Eppich et al., 2012). When these same crystals are dated using Sr diffusion at 750 °C, they have apparent ages of only 140–2,800 y (Cooper and Kent, 2014). These apparent ages drop to only a few decades at 900 °C. The only way the two different residence times are consistent is if plagioclase crystals spent at least 88 % of their time (and probably much more) at low temperature. Although this result is for an andesitic eruption, there are no studies that have directly compared radiometric and diffusion based residence times for the same minerals in a silicic system. However, similar arguments should apply to silicic systems. If the Bishop Tuff magma was stored as a low-temperature mush for most of its lifetime, then it would explain both the apparent long residence times of the zircons and the apparent short residence times of the quartz crystals. The up to 80 ky U–Pb residence times of the zircons would date their crystallisation, as the Bishop Tuff magma reservoir was forming, while the <10 ky diffusive residence times of the quartz would measure only the time spent at high temperature.

Magma mixing is a common way of creating disequilibrium between crystals and their melt, therefore most diffusion chronometry studies estimate the timing of these mixing events. Often the mixing events are interpreted as late-stage recharge, which triggered the eruption. These recharge events are estimated to have occurred within a few decades of eruption, often as short as a few months before (e.g. Coombs et al., 2000; Costa and Chakraborty, 2004; Costa et al., 2009; Gioncada et al., 2005; Martí et al., 2013; Martin et al., 2008; Morgan et al., 2006; Nakamura, 1995; Ruprecht and Cooper, 2012; Saito et al., 2010). Sometimes, however, these mixing events can include

the addition of a significant proportion of the magma that is eventually erupted at the surface. For example, Druitt et al. (2012) found that prior to the Minoan eruption of Santorini a dacitic and rhyolitic magma mixed to produce a hybrid rhyodacite, and that the injected dacite must have made up at least 15 % of the ∼60 km^3 that was erupted. Diffusion modelling of Mg in plagioclase demonstrated that this mixing must have started a few decades before the eruption, and continued up to at least a few months before eruption. This implies recharge rates of $>5 \times 10^{-2}\,km^3\,y^{-1}$

The zoning patterns of phenocrysts in the Oruanui are also thought to record a large influx of magma into the shallow magma reservoir shortly before eruption (Allan et al., 2013). The amphibole crystals from the Oruanui are interpreted to record a drop in pressure during their growth. Coexisting orthopyroxene crystals underwent a period of dissolution, followed by renewed growth. This is consistent with a transfer from a deep source region to a shallow holding chamber. Modelling Fe–Mg diffusion in the orthopyroxenes suggests that this transfer happened less than 3,000 y before erpution, with most of the crystals recording timescales of less than 1,000 y. This is consistent with the the zircon age spectra discussed above, which demonstrate that the Oruanui could not have resided in the shallow crust during the Okaia eruption, ∼3,000 y earlier (Charlier et al., 2005; Wilson, 2001). These ages give accumulation rates of $>0.33\,km^3\,y^{-1}$, possibly reaching $>1\,km^3\,y^{-1}$.

Not all chemical disequilibrium is interpreted as resulting from mixing between different magmas. Disequilibrium in oxygen isotopes, either between crystals and the melt or between different minerals, is often thought to be produced by assimilation or remelting of hydrothermally altered plutonic rocks. Zonation in oxygen isotopes in zircons from the Ammonia Tanks Tuff gives crystal residence times of $\sim 10^4$ years (Bindeman and Valley, 2003), while in zircons from Yellowstone, residence times of $\sim 10^3$ are found (Bindeman and Valley, 2001). Disequilibrium between oxygen isotope ratios in quartz and feldspars from the Bandelier Tuff and Cerro Toledo rhyolite could not be maintained without diffusive re-equilibration for more than 10^2–10^3 y (Wolff

et al., 2002). Individual quartz crystals from the Bishop Tuff often show large variations in $\delta^{18}O$ that could not have persisted for more than 10^2–10^4 years (Bindeman and Valley, 2002). In this interpretation, the diffusion models do not reveal the total residence time of the crystals in the crust, but rather their residence in the magma at high temperature after the assimilation or remelting of the pluton.

In summary, crystal residence times estimated from diffusion modelling are shorter than those measured using radiometric dating. However, these two techniques often measure different things. Radiometric ages of minerals with high closure temperatures, such as zircon, give residence times of these crystals. These radiometric ages are generally unaffected by the thermal histories of the crystals. In the other hand, diffusion chronometry only measures the residence of the crystals at high-temperature. Diffusion models also do not measure the total time between the growth of a crystal and its eruption. Instead, the diffusion clock is initiated when the crystals are placed in an environment where they are in disequilibrium with their melt, or an environment where they grow rims that are not in equilibrium with their cores. Typical magmatic processes that can create this disequilibrium include magma mixing, crustal assimilation, heating or changing the pressure.

1.8 Modelling magma chamber stability

Various attempts have been made to integrate the evidence for magma reservoir longevity discussed above with theoretical models. These models generally assume that large magma reservoirs are constructed incrementally, by the repeated injection of hot, fresh magma. Producing a large magma reservoir requires preventing both the freezing of the magma before it has the chance to erupt, and the eruption of the magma before the chamber has a chance to grow large. A key parameter determining the fate of magma chambers is the magma supply rate. If the supply rate is below a certain threshold, then each intrusion freezes before the next one arrives (Gelman et al., 2013; Schöpa and

Annen, 2013). However, too high a supply rate is likely to lead to high overpressure and trigger eruption (Caricchi et al., 2014; Karlstrom et al., 2010).

Annen (2009) modelled the evolution of a pluton as the intrusion of a series of sills at 5 to 15 km depth in the continental crust. She found that in order to produce a growing reservoir of liquid-dominated magma, sill accretion rates need to be above $10^{-2}\,\mathrm{m\,y^{-1}}$ and magma fluxes needed to exceed $10^{-2}\,\mathrm{km^3\,y^{-1}}$. Schöpa and Annen (2013) refined this model, to show that high transitory fluxes also could produce large, shallow-crustal magma chambers, although this transitory flux still has to be higher than $10^{-2}\,\mathrm{km^3\,y^{-1}}$. When Gelman et al. (2013) included the effects of a non-linear crystallisation–temperature relationship and temperature-dependent thermal conductivity they found that liquid-dominated magma reservoirs larger than $500\,\mathrm{km^3}$ could be maintained in the shallow crust at injection rates as low as $5 \times 10^{-3}\,\mathrm{km^3\,y^{-1}}$.

On the other hand, high magma flux into the reservoir will lead to high overpressures, which increases the chance of dyke propagation and eruption (Rubin, 1995). The viscosity of the country rock into which the magma reservoir is emplaced has an effect on the overpressure that is produced by magmatic input. More ductile country rock can relax faster, dissipating overpressure and making eruption less likely (Jellinek and DePaolo, 2003; Karlstrom et al., 2010). Warmer crust is less viscous than colder crust, which has two consequences. Firstly, deeper magma reservoirs tend to be more stable than shallow reservoirs. Secondly, a period of thermal preparation, through repeated magmatic intrusion, is probably necessary before large magma reservoirs can develop in the shallow crust. Warmer crust will also make the injected magma less likely to freeze before it has the chance to be erupted. Magmatic injection is also less likely to trigger the eruption of large magma reservoirs (Gregg et al., 2013). The eruption of large magma reservoirs may be triggered by buoyancy, or may be triggered tectonically (Allan et al., 2012; Caricchi et al., 2014).

1.9 Possible mechanisms for rapid generation of large silicic melt reservoirs in the shallow crust

If silicic magmas spend much of their time stored in crystal mushes, and these crystal mushes are too viscous to erupt, then some process is needed to reactivate the magma and allow its eruption. Two broad mechanisms have been proposed: rejuvenation and remelting of the mush, or segregation of melt into crystal-poor magma reservoirs.

Crystal-rich ignimbrites are thought to be remobilised crystal mushes. Their crystals often record long residence times (e.g. up to 600 ky in the Fish Canyon Tuff; Bachmann et al., 2007b), often show evidence of growth in a highly crystalline state (e.g. Wotzlaw et al., 2013), and often have resorption textures and reverse zoning typical of late-stage reheating (e.g. Bachmann et al., 2002). The remobilisation of a mush could be triggered by the influx of hotter magma, that is typically assumed to be mafic (e.g. Bachmann et al., 2002), although examples of recharge by silicic magma have also been found (e.g. Eichelberger and Izbekov, 2000; Smith et al., 2004). This would underplate the mush, and heat would then be transferred upwards into the overlying crystal mush. Conduction of heat would be slow, but heat could also be advected by volatiles released by the crystallising mafic magma ("gas sparging"; Bachmann and Bergantz, 2006). Other mechanisms have been suggested to remobilise magma mushes more rapidly, such as "unzipping" by convection (Burgisser and Bergantz, 2011) or by melt-induced over-pressurisation (Huber et al., 2011). The presence of gas bubbles would also reduce the viscosity of the magma, and might aid remobilisation of the mush (Pistone et al., 2013). Once the magma is remobilised, it can be homogenised by convection prior to eruption (Huber et al., 2012).

Mush remobilisation has been suggested as the trigger for several recent, well constrained eruptions. These include andesitic eruptions such as Soufrière Hills, Montserrat and Eyjafjallajökull, Iceland, as well as the dacitic 1991 eruption of Pinatubo, the Philippines. At Soufrière Hills, long radiometric residence times coupled with short

diffusive residence times suggest long-term storage of magmas in a cool crystal mush (Zellmer et al., 2003), and thermal models of a mushy storage region can be compared to seismic velocity anomalies measured in surveys of the volcano (Annen et al., 2014; Paulatto et al., 2012). At Eyjafjallajökull, geodetic and seismic monitoring, as well as high temporal resolution sampling of the eruptive products of the 2010 summit eruption revealed it was triggered when ascending basalt intersected a partially crystalline intrusion left over from previous eruptions (Sigmarsson et al., 2011; Sigmundsson et al., 2010). Similarly, geophysical monitoring and comparison of the products of the preclimactic extrusive eruptions with those of the Plinian phase of the 1991 Pinatubo eruption suggest it was also a rejuvenated mush (Pallister et al., 1992).

Melt segregation is the other mechanism that can produce large bodies of eruptible magma in the shallow crust, and it is generally though to be responsible for the formation of large bodies of crystal-poor silicic magma. The rate at which silicic melt can separate from crystals is limited by its high viscosity (Bachmann and Bergantz, 2008a; McKenzie, 1985). Possible processes include gravitational separation through hindered settling of individual crystals, or compaction of a porous crystal network (Figure 1.4; Bachmann and Bergantz, 2004). Melt migration driven by shear or gas filter pressing may generate small, local segregations (Brown and Solar, 1998; Pistone et al., 2013; Sisson and Bacon, 1999; Stevenson, 1989) that are subsequently concentrated into large melt lenses. This melt then accumulates at a particular crustal level — either in situ within the mush (e.g. Bachmann and Bergantz, 2004), or at higher levels in the plumbing system (e.g. Allan et al., 2013). Fast transfer of silicic magma from deep mush zone to shallow crustal magma chambers may also be triggered by tectonic stresses (Rowland et al., 2010).

These two mechanisms are not mutually exclusive. Indeed, sometimes crystal-poor rhyolite caps are erupted alongside more crystal-rich mush zones. The Ammonia Tanks Tuff is chemically zoned from trachyandesite to high-silica rhyolite (59 to 78 wt% SiO_2; Deering et al., 2011). The rhyolite end-member is crystal poor (<10 vol%), and is

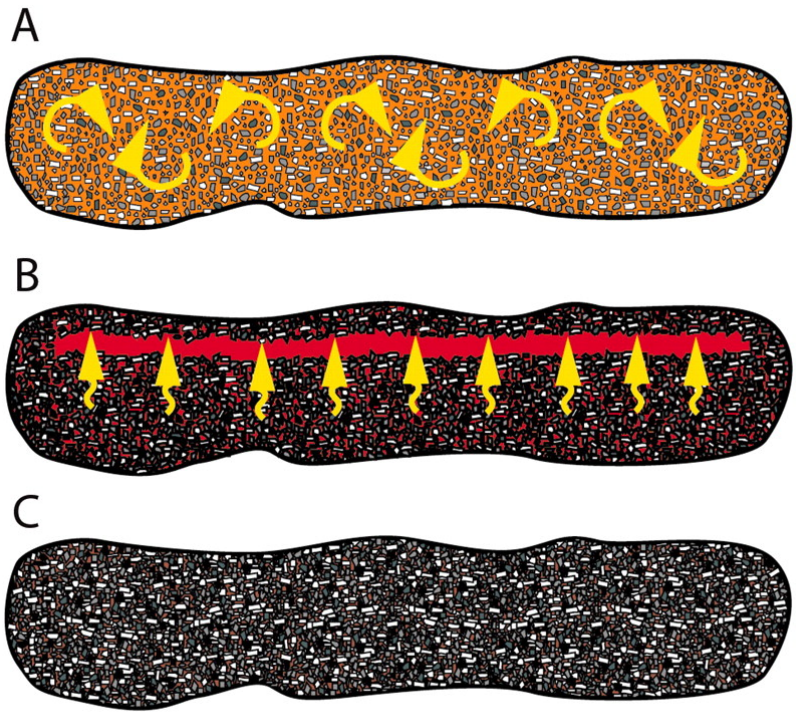

Figure 1.4: Schematic illustration of the evolution of a mushy magma reservoir and the extraction of silicic melt through hindered settling, from Bachmann and Bergantz (2008a). (A) Low-crystallinity stage (<45 vol% crystals): most crystals are kept in suspension by convection currents. (B) Medium-crystallinity stage (∼45-60 vol% crystals): the absence of convection and the high permeability provide a favourable window for crystal-melt separation through hindered settling. (C) High-crystallinity stage (>60 vol% crystals): the permeability is too low for high-viscosity melt to be extracted efficiently by compaction.

thought to represent the liquid extracted from a crystallising trachydacite magma. The trachyandesite is thought to represent the cumulate, although the relatively low crystal content (15–25 vol%) requires it to have been reheated before eruption. Abundant glomerocrysts suggest that the trachyandesite once contained a touching framework of crystals, while partially resorbed crystals support the idea that the trachyandesite was reheated. At La Pacana, in Chile, there is also evidence for the eruption of both an evolved cap and the residual mush, although in two separate eruptions (Lindsay et al., 2001). The Toconao ignimbrite is crystal poor and rhyolitic (76–77 wt% SiO_2), and it is overlain by the dacitic Atana ignimbrite (66–70 wt% SiO_2). The Atana ignimbrite is crystal-rich (30–40 % crystals), and the interstitial glass in the Atana pumices has a

similar composition to the Toconao pumices. This suggests that the Toconao ignimbrite segregated from an underlying body of Atana-like magma, which was itself evacuated in the Atana eruption.

Chapter 2

Geological setting

2.1 Regional Tectonics of the Aegean and the Hellenic subduction zone

Santorini is part of the Hellenic volcanic arc, stretching between Greece and Turkey through the Aegean (Figure 2.1). The cause of the volcanism is the subduction of Ionian oceanic lithosphere. The subducted slab dips at a shallow angle of about 10–20° from the Mediterranean Ridge towards the north, as shown by seismic tomography and the focal mechanisms of the earthquakes between the slab and the overriding Aegean lithosphere (Papazachos and Nolet, 1997; Pearce et al., 2012; Piromallo and Morelli, 2003; Shaw and Jackson, 2010). The steeper faults at the Hellenic Trench form part of the accretionary wedge. There is a well defined Benioff zone, which shows that the upper surface of the descending slab lies about 110 km beneath Santorini (Papazachos et al., 2000).

The current dynamics of the collision between Africa and Eurasia in the Eastern Mediterranean is somewhat complex. It is usually described using a series of rigid blocks, or micro-plates (Jackson, 1994; McKenzie, 1970; Nyst and Thatcher, 2004), however the fact that some deformation occurs within these blocks shows that this model is not strictly valid (Benetatos et al., 2004; Floyd et al., 2010). Deformation in

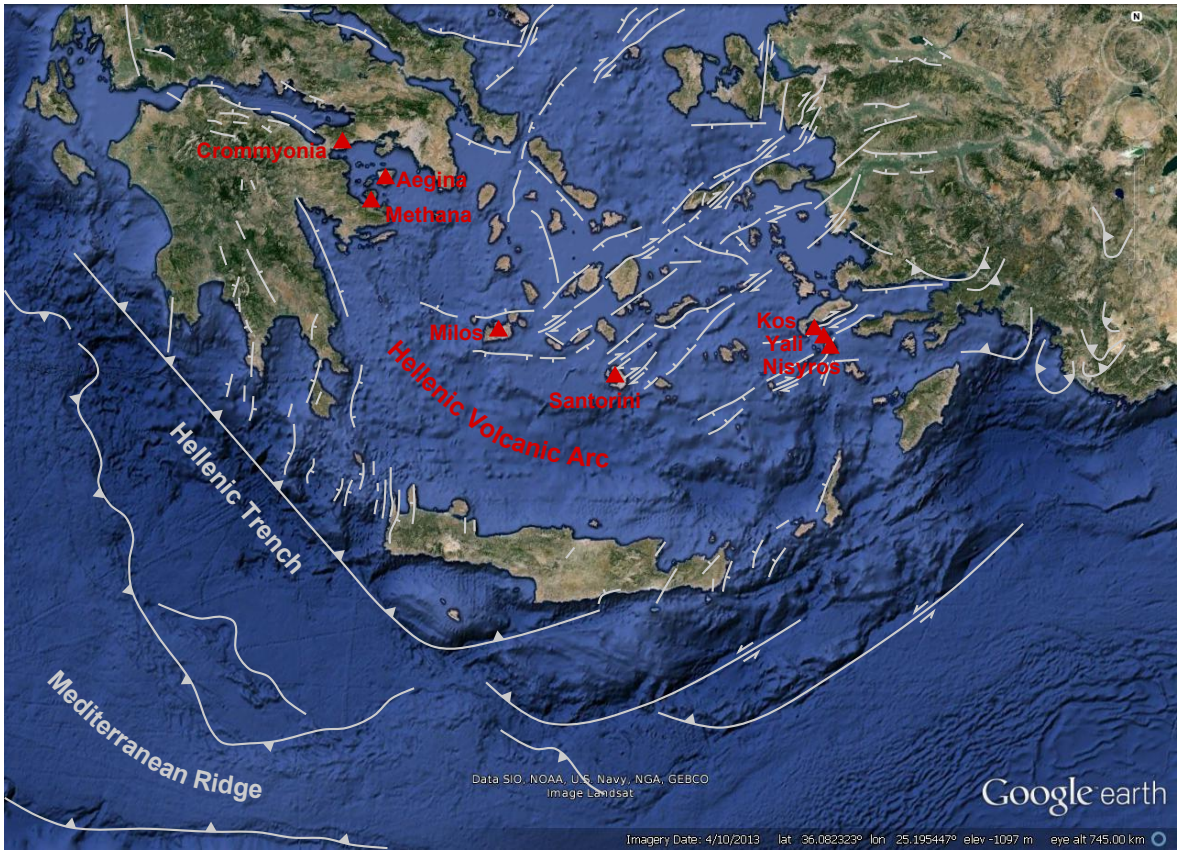

Figure 2.1: Map of the southern Aegean Sea. Volcanoes of the Hellenic arc are shown in red. Major faults compiled from Jackson (1994), Jolivet and Brun (2010) and Kokkalas and Aydin (2013).

the Aegean is principally driven by two forces: the westwards extrusion of Anatolia along the North Anatolian Fault (McKenzie, 1972), and the southward retreat of the subduction zone by slab roll-back (Le Pichon and Angelier, 1979). Although Africa is currently only converging with Eurasia at about 5 mm/yr, slab roll-back means that there is 35 mm/yr of convergence at the Hellenic trench (Nocquet, 2012; Reilinger et al., 2010, 2006).

Figure 2.2 shows the velocity field for the eastern Mediterranean calculated by Nocquet (2012) using GPS measurements. This motion leads to deformation along three dominant trends (Benetatos et al., 2004): (1) north-south extension of the Aegean caused by slab roll-back; (2) trench-parallel extension close to the subduction zone, due to the curvature of the trench; (3) right-lateral strike-slip motion, due to the motion of Anatolia and the Aegean relative to the Eurasian plate. The principal faults

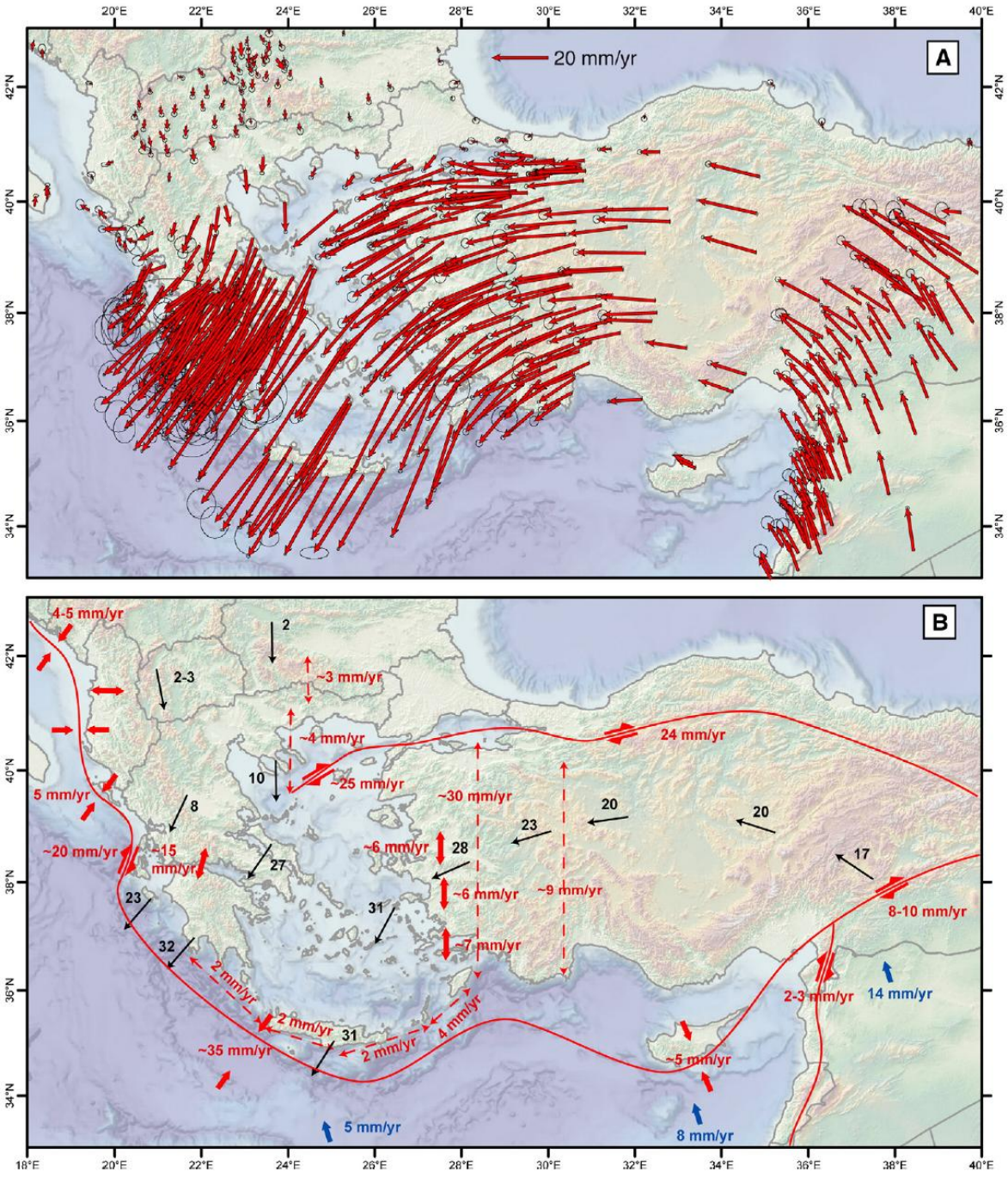

Figure 2.2: (A) Velocity field in a Eurasia fixed reference frame. (B) Kinematics sketch. Dashed double-arrow lines show integrated relative motion over a given area. Thin black arrows are velocities at selected locations. Taken from Nocquet (2012).

accommodating this deformation are shown in Figure 2.1. Large earthquakes can occur on these faults, such as the 1956 M_s 7.4 Amorgos earthquake that devastated much of Santorini (Okal et al., 2009; Papadopoulos and Pavlides, 1992).

The locations of the volcanoes of the Hellenic arc are controlled by the tectonic structure of the Aegean, lying on lines of weakness in the Aegean crust (Papazachos and Panagiotopoulos, 1993). Milos, Santorini and Nisyros all lie within pull-apart basin along major strike-slip faults (Kokkalas and Aydin, 2013). These same faults are interpreted to have played an important role in controlling the location of plutons from the Middle Miocene, by provided an easy path for their emplacement. The tectonic control on the spatial distribution of volcanoes is further shown by the way most vents on Santorini fall along two lines: the Coloumbo line in the north of Thera, and the Kameni line that runs through the Kameni islands in the centre of the caldera (discussed in more detail below)

The extension of the Aegean started ∼36–25 Ma, and slowed after a tectonic reorganisation that took place in the Pliocene (Jackson, 1994; Jolivet and Faccenna, 2000; Walcott and White, 1998). There was another, short pulse of extension that occurred along the Hellenic Arc between 5.0-4.4 Ma, which lead to rapid subsidence of 900 m at Milos, and similar subsidence at Aegina (van Hinsbergen et al., 2004). The continental crust of the Aegean has been thinned from about 50 km to 20–30 km as a result of this extension, and is now roughly 25 km thick under Santorini (Figure 2.3; Karagianni et al., 2005; Tirel et al., 2004).

The rocks revealed by this extension record two metamorphic events. There is a first stage of high-pressure–low-temperature metamorphism, related to convergence at the subduction zone. This is followed by a stage of low-pressure–high-temperature metamorphism, as the lithosphere is stretched due to slab roll-back (Avigad and Garfunkel, 1991; Jolivet et al., 2013; Lister et al., 1984; Trotet et al., 2001). The age of these two metamorphic events gets younger as you travel south through the Aegean, as a result of the progressive retreat of the subduction zone. In the Cycladic isles

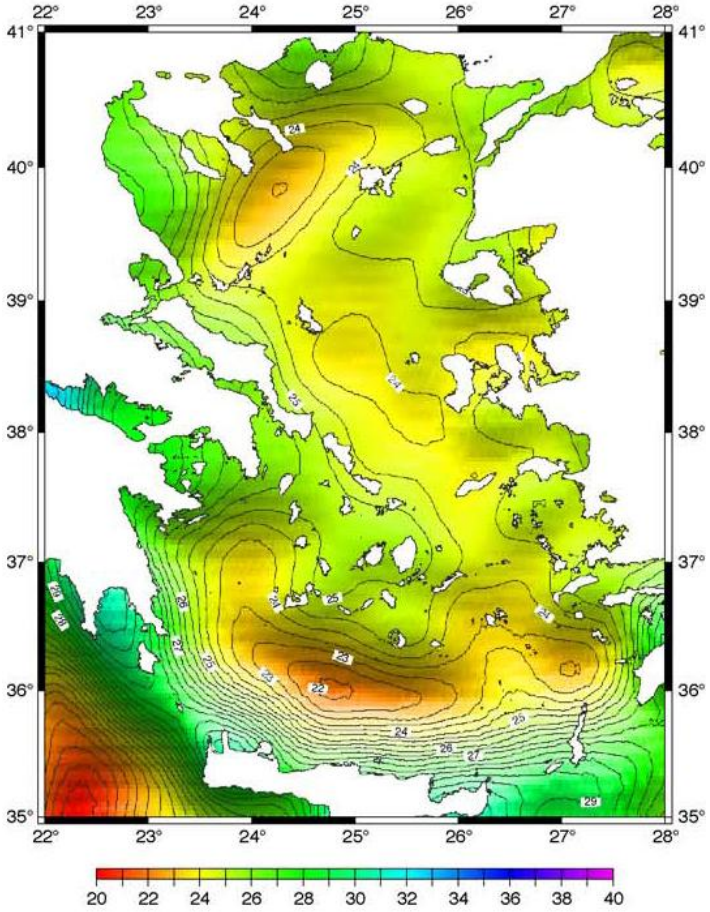

Figure 2.3: Crustal thickness in km from gravity measurements, isolines every 0.5 km, taken from Tirel et al. (2004).

just north of Santorini, the high-pressure–low-temperature metamorphism took place during the Eocene. The low-pressure–high-temperature metamorphism here occurred during the Oligocene and the Miocene. The metamorphic rocks in the Cycladic isles can reach into the blueschist and eclogite facies, as well as containing granites from crustal melting.

2.2 Volcanism along the Hellenic Arc

Volcanic activity in the Aegean started in the Oligocene, and occurred in two main phases with volumetrically smaller volcanism in between (Fytikas et al., 1984). The first phase ran from the Oligocene until the Middle Miocene, and the second began in the Middle Pliocene and continues today. Volcanism has migrated to the south with time, due to the retreat of the subduction zone (Jolivet and Brun, 2010; Jolivet et al.,

2013).

The type of volcanism along the Hellenic arc varies. The western volcanoes are dominantly andesitic to rhyolitic dome swarms, while central and eastern volcanoes are composites, often with large calderas. This, along with lower Eu/Eu* values for western volcanoes, suggests that shallow magma chambers play a larger role in the evolution of the western volcanoes (Innocenti et al., 1981). Crustal thickness ranges from 34 km under the western end of the arc to 24 km under the eastern end (Tirel et al., 2004), showing extension has been greater in the east. This may go some way to explaining these differences (Innocenti et al., 1981). Below are descriptions of the volcanoes that make up the currently active volcanic arc. Their locations are shown on Figure 2.1.

2.2.1 Crommyonia

Crommyonia is the westernmost volcano of the Hellenic arc, and is one of the oldest volcanic centres in the Hellenic arc, active between 3.9–2.7 Ma (Fytikas et al., 1984). The volcanic rocks consist of scattered dacitic flows and domes, and is far less voluminous than the volcanoes further east along the arc (Pe-Piper and Hatzipanagiotou, 1997). Their geochemistry falls within the volcanic arc field. Currently there is still low-level geothermal activity taking place around Sousaki, with water temperatures at depth only 50-80 °C (D'Alessandro et al., 2006). There is diffuse and focused CO_2 flux, at a rate of about 0.63 $kg\,s^{-1}$.

2.2.2 Aegina

Aegina was active contemporaneously with Crommyonia, between 4.4 Ma and 2.1 Ma (Pe-Piper et al., 1983). With the possible exception of the earliest, hydrothermally altered volcanic rocks there is no evidence for submarine volcanism. The volcanic rocks mostly form endogenous domes and lava flows, and can be split into at least four differentiation series, ranging from basaltic andesite to rhyodacite (Pe, 1973).

2.2.3 Methana

Methana is a basaltic to rhyodacitic lava dome complex (Simkin and Baker, 2014). The older part of the volcano has been dated with K-Ar at 900–550 ka, and the most recent confirmed eruption was a lava flow and explosive activity in 258 ±18 B.C.E.

There are currently only low levels of unrest, in the shape of thermal springs and CO_2 emissions. The low temperature of the thermal springs (less than 40 °C) and geochemical modelling of the fluid compositions suggests only a cool geothermal reservoir at about 150 °C, with a contribution of 23 % from arc-type magmatic water (Dotsika et al., 2010). The CO_2 output is also an order of magnitude lower than other volcanoes in the Hellenic such as Santorini and Nisyros, at 0.03 kg s^{-1} (D'Alessandro et al., 2008). $\delta^{13}C$ values suggest that 90 % of this CO_2 is from the decomposition of limestone, and although the isotopic composition of the He emitted indicates that up to 40 % of it comes from a mantle source, it is clear that there is little current magmatic activity under Methana.

2.2.4 Milos

Milos and some of the surrounding small islands are a collection of stratovolcanoes (Simkin and Baker, 2014). Four main cycles of activity were recognised by Fytikas et al. (1986), starting about 3 My ago (Stewart and McPhie, 2006). Initial submarine and subaerial volcanism was dominantly andesitic and basaltic, but more recent subaerial volcanism is more evolved and, is predominantly rhyolitic.

The earliest sequence mainly contains products of submarine eruptions, including pyroclastic flows and submarine tuffs with subordinate pillow lavas and breccias (Fytikas et al., 1986; Stewart and McPhie, 2006). The second cycle was subaerial, producing domes and flows with small explosive episodes producing local pyroclastic flows. After about 2 Ma activity shifted eastwards, and produced a submarine pyroclastic sequence associated with rhyolitic domes. The final cycle was concentrated in two centres, one on the north and one on the south of Milos. In both centres this final

phase is characterised by eruptions that begin phreaticly, then are phreatomagmatic and finally end end with the extrusion of lavas. The youngest known magmatic activity took place about 90 ky ago, however phreatic activity has continued since then. The last known phreatic explosion produced a lahar which destroyed a town or harbour on the island, and has been dated with ^{14}C at between 80–205 C.E (Traineau and Dalabakis, 1989). There is currently a hydrothermal system on the island, releasing fluids at temperatures of up to 115 °C (Valsami-Jones et al., 2005).

Early erupted products are found to be compatible with a model of deep fractionation, while modelling the more recent, more evolved products suggests a large plagioclase contribution to the fractionation Fytikas et al. (1986). This suggests the more recent eruptions were fed from shallow magma chambers.

2.2.5 Kos-Yali-Nisyros

Kos, Yali and Nisyros sit on the eastern end of the Hellenic Arc. Although they form distinct centres, they have similar geochemistry and mineralogy suggesting they form a single petrogenetic system (Pe-Piper and Moulton, 2008). While most of the island of Kos is non-volcanic, there are the remains of at least two calderas (Simkin and Baker, 2014). The older of the two is younger than the Zini lava dome, which has been dated at 1.0–0.55 Ma. The younger is associated with the 160 ka Kos Plateau Tuff. Both Nisyros and Yali are younger than, and situated in or on the edge of, the 160 ka Kos Plateau Tuff caldera, and none of the products of the Kos Plateau Tuff have been found on them (Allen and Cas, 1998). The caldera may be as wide as 20 km, and stretch from present-day Kos across to Nisyros, with Yali sitting at its centre.

The earliest volcanism on Kos were rhyolitic domes (Pe-Piper and Moulton, 2008). This was followed by the growth of an andesitic stratocone, which was destroyed by the Kos Plateau Tuff, and whose existence is known only form fragments found in the deposits of that eruption. The distribution of products from for the Kos Plateau Tuff eruption suggests it was erupted from a vent near the present location of Yali

(Allen et al., 1999). It was one of the largest eruption to take place in the Hellenic arc during the Quaternary, erupting a minimum of 90 km^3 of magma (Allen and Cas, 1998). Ignimbrite deposits form this eruption have been found 40 km away on the islands and peninsulas of Turkey surrounding Kos. The eruption commenced in a phreatoplinian style, and changed to a 'dry' style as it progressed. U–Pb and U–Th ages, along with isotopic data, on zircon crystals suggest that the magma was stored for a period of ∼200 ky with little crustal contamination, perhaps as a crustal mush (Bachmann et al., 2007a; Keller, 1969). Recent activity on Kos itself is restricted to fumerolic fields (Simkin and Baker, 2014).

Yali is a collection of rhyolitic obsidian domes and pumice deposits. While no historical eruptions are known from Yali, rhyolitic pumice deposits overlie pottery and Neolithic obsidian artefacts dated at about 30-35 ka. This would make these pumice deposits the youngest magmatic products from the Kos-Yali-Nisyros system (Buettner et al., 2005).

Nisyros, on the south-east edge of the possible Kos Plateau Tuff caldera, is a stratovolcano. It was constructed during the last 150 ky, with recent phreatic eruptions in 1422, 1871-1873 and 1888 C.E. and continuing intense hydrothermal activity. It has its own small, 3–4 km caldera which has been dated by different authors at either <24 ka or >44 ka (Simkin and Baker, 2014). As with most volcanoes of the Hellenic arc, activity started below the sea, before building up a subaerial edifice (Di Paola, 1974). The early pillow lavas and hyaloclastites, along with early subaerial lava flows, are basaltic andesite. The transition from submarine to subaerial is gradual, with alternating hyaloclastites and lavas (Francalanci et al., 1995). The subaerial pre-caldera sequence continues with andesitic to rhyolitic lavas flows and domes, and several major explosive events, with at least one erupting 2-3 km^3 and a column heigh of 15-20 km (Limburg and Varekamp, 1991). This lead to the formation of an earlier, now-buried caldera. The present caldera is associated with a a pumice fall, surge and flow sequence, erupting 6-7 km^3 of magma.

Post-caldera activity on Nisyros is fairly homogeneous. Much of the caldera has been filled up with large, dacitic lava domes of similar composition (Di Paola, 1974). There are no pyroclastic deposits. The locations of the recent domes and hydrothermal craters are strongly controlled by by north-east–south-west striking oblique-slip faults (Caliro et al., 2004). These faults are a response to east-west extension. There is an active hydrothermal system at present, with isotopic chemistry suggesting that fumerolic gases containing a mantle-derived component (Brombach et al., 2003). Temperatures of up to 340 °C were recorded in geothermal wells at a depth of 1,800 m. Between 1995-2000 a period of inflation and increased seismicity was observed (Sachpazi et al., 2002), which Lagios et al. (2005) found could not be explained sufficiently using only the tectonic faults found on the island. Their preferred model used two inflating Mogi point sources which they interpreted as magma chambers, one under the western edge of Nisyros, and the other close to Yali.

2.3 The local tectonic setting of Santorini

Santorini is located in the middle of a north-east–south-west trending chain of volcanoes (Figure 2.4). To the south-west lie the Christiana islands. Deposits on Santorini and Anafi have been correlated with a large, explosive eruption from the Christiana islands (Keller et al., 2012). The volcanic activity on the Christiana islands is thought to predate most of the activity on Santorini.

To the north-east lies a chain of 19 submarine volcanoes (Nomikou et al., 2013a, 2012b, 2013b). The largest of these, Coloumbo, has a small caldera, formed during an eruption that took place in 1650 C.E. Most of the remaining cones in the chain are covered in sediment, and show no signs of recent volcanic activity.

The 1650 C.E. eruption of Coloumbo was rhyolitic, large, and was accompanied by a tsunami and the release of toxic gasses that killed many of the inhabitants of Santorini and their livestock (Cantner et al., 2014; Dominey-Howes et al., 2000; Fouqué, 1879;

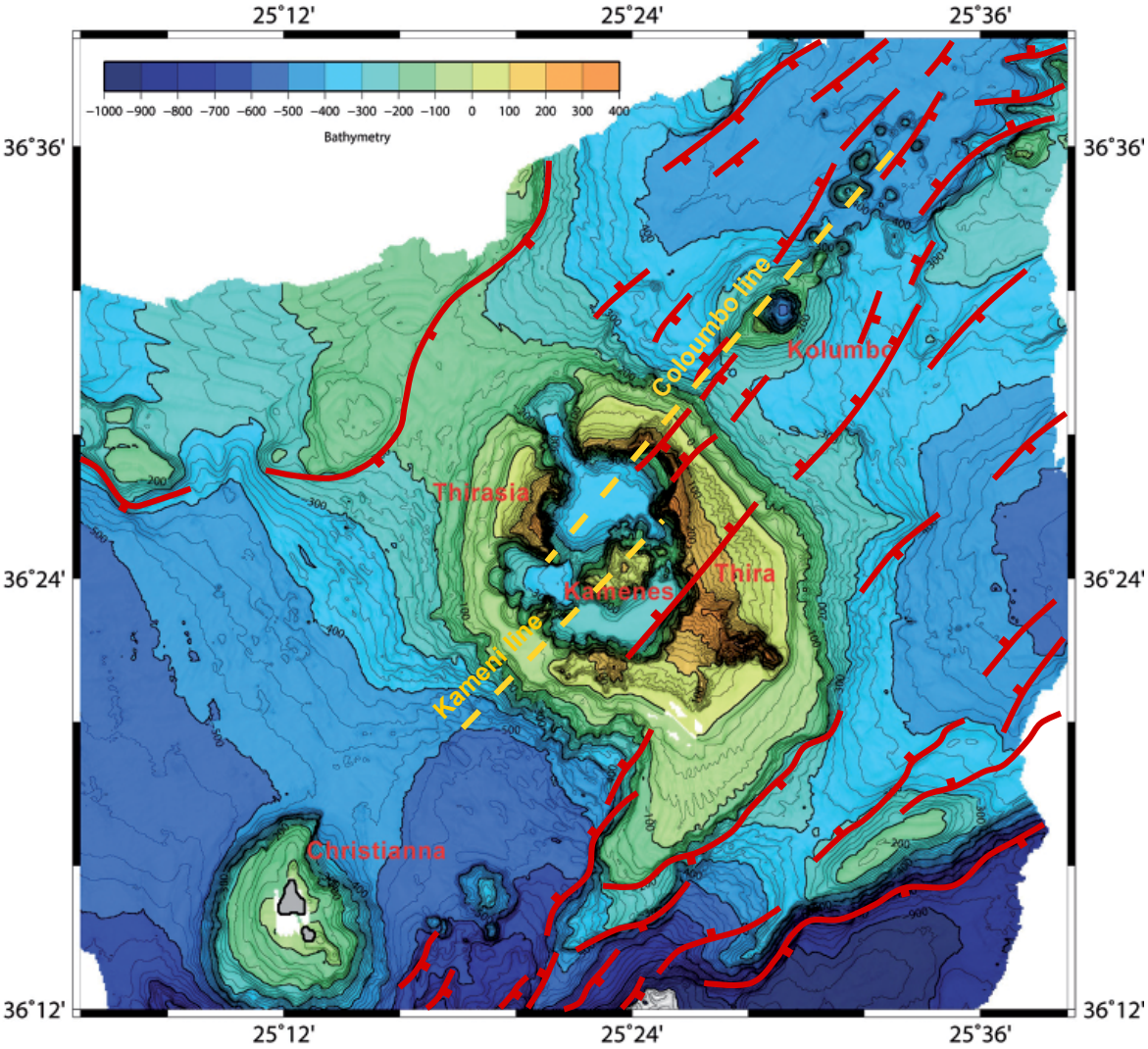

Figure 2.4: Bathymetry of the Christiana–Santorini–Coloumbo volcanic zone, from Nomikou et al. (2013a). Faults drawn from Sakellariou et al. (2010) and Feuillet (2013)

Nomikou et al., 2012a; Ulvrová et al., 2013). It is currently more hydrothermally active than Santorini. Hydrothermal vents up of to 220 °C can be found in the crater of Coloumbo, compared to vent temperatures of 15-17 °C found in Santorini's caldera (Carey et al., 2013; Kilias et al., 2013; Sigurdsson et al., 2006). There is a 3 km wide column of micro-seismicity extends from the surface to about 15 km depth beneath the north-eastern flank of the volcano (Dimitriadis et al., 2009). Dimitriadis et al. (2010) imaged a low seismic velocity zone possibly connecting Santorini with Coloumbo at depth.

Santorini lies at end of the Santorini–Amorgos rupture zone, a region of oblique

extensional faulting (Feuillet, 2013; Sakellariou et al., 2010). It corresponds to a vertical region of increased earthquake activity trending north-east, from Santorini through and Coloumbo to Amorgos (Bohnhoff et al., 2006). This zone is 30-40 km wide, and extends to a depth of 45 km. The Santorini Amorgos rupture zone is probably a pull-apart basins, and part of a larger strike-slip system (Kokkalas and Aydin, 2013).

The oblique extension is accommodated on north-east–south-west trending faults. These faults control the location of volcanic vents, which fall along two tectonic "lines": the Coloumbo line and the Kameni line (Figure 2.4). In the north of Santorini, many of the dykes that fed the Peristeria volcano (see below) are orientated north-east–south-west, parallel to the Coloumbo line (Heiken and McCoy, 1984). To the north-east the Coloumbo line is seen to continue, in the orientation of the offshore volcanic cones. To the south, the vents of the Kameni Isles fall along a roughly parallel line: the Kameni line (Nomikou et al., 2014; Pyle and Elliott, 2006).

2.4 The volcanic history of Santorini

A simplified map of the geology of Santorini is shown in Figure 2.5, and its eruptive history is summarised in Table 2.1. In this section I will briefly discuss the early volcanism, before looking at the sequence from 67 ka up to the 22 ka Cape Riva eruption in more detail. It is this period that the rest of this thesis is chiefly concerned with. I finish by presenting the most recent volcanism on Santorini. The chemistry and petrology is covered in more detail in the next section.

2.4.1 Early activity: Akrotiri and Peristeria centres (650–340 ka)

Before volcanism commenced on Santorini, an island already existed, consisting of the schists and marbles that make up the south-east of the present-day island (Figure 2.5). The earliest volcanism on the island dates back 650–550 ky (Druitt et al., 1999), and

Table 2.1: Summary of the volcanic history of Santorini, updated from Druitt et al. (1999)

Age	Eruption/Eruptive sequence	Description
3.6 ka–Present	Kameni islands	Dacitic shield-building
3.6 ka[a]	Minoan eruption	Plinian eruption and caldera collapse
22 ka[b]	Cape Riva eruption	Plinian eruption and caldera collapse
	Therasia shield	Predominantly dacitic shield building
54 ± 3 ka[c]	Upper Scoria 2 eruption	Dominantly andesitic plinian eruption
67 ± 9–54 ± 3 ka[c]	Skaros shield	Basaltic andesite–dacitic shield building
	Caldera collapse	Possibly linked to Upper Scoria 1, or incremental collapse
80 ka[d,e,f]	Upper Scoria 1 eruption	Scoria fall and spatter agglomerate
100 ka[d,e,f]	Vourvoulos eruption	Scoria fall, pumice fall and ignimbrite
76 ± 28; 54 ± 23[c]	Megalo Vouno; Columbus tuff ring	Spatter and cinder cones; tuff ring
145 ka[d,e,f]	Middle Pumice eruption	Plinian eruption
	Cape Thera eruption	Pumice fall and ignimbrite
172 ± 4 ka	Simandiri shield	basaltic to andesitic shield building
172 ka[d,e,g]	Lower Pumice 2 eruption	Plinian eruption and caldera collapse
184 ka[d,e,g]	Lower Pumice 1 eruption	Plinian eruption
196 ka[d]	Cape Therma 3 eruption	Andesitic pumice fall and ignimbrite
224 ± 5 ka	Cape Alonaki and NE Thera	Rhyodacitic lavas
	Cape Therma 2 eruption	Rhyodacitic pumice fall
	Cape Therma 1 eruption	Andesitic ignimbrite
∼360 ka	Cape Alai	Andesitic lavas
450–340 ka	Akrotiri cinder cones	Andesitic and basaltic spatter and cinder cones
530–430 ka	Peristeria stratovolcano	Predominantly basaltic to andesitic lavas and tuffs
650–550 ka	Early Akrotiri centres	Amphibole bearing silicic lavas and tuffs

[a] Friedrich et al. (2006) [b] See Chapter 4 [c] Druitt et al. (1999) [d] Keller et al. (2000) [e] Schwarz (2000)
[f] Vespa et al. (2006) [g] Gertisser et al. (2009)

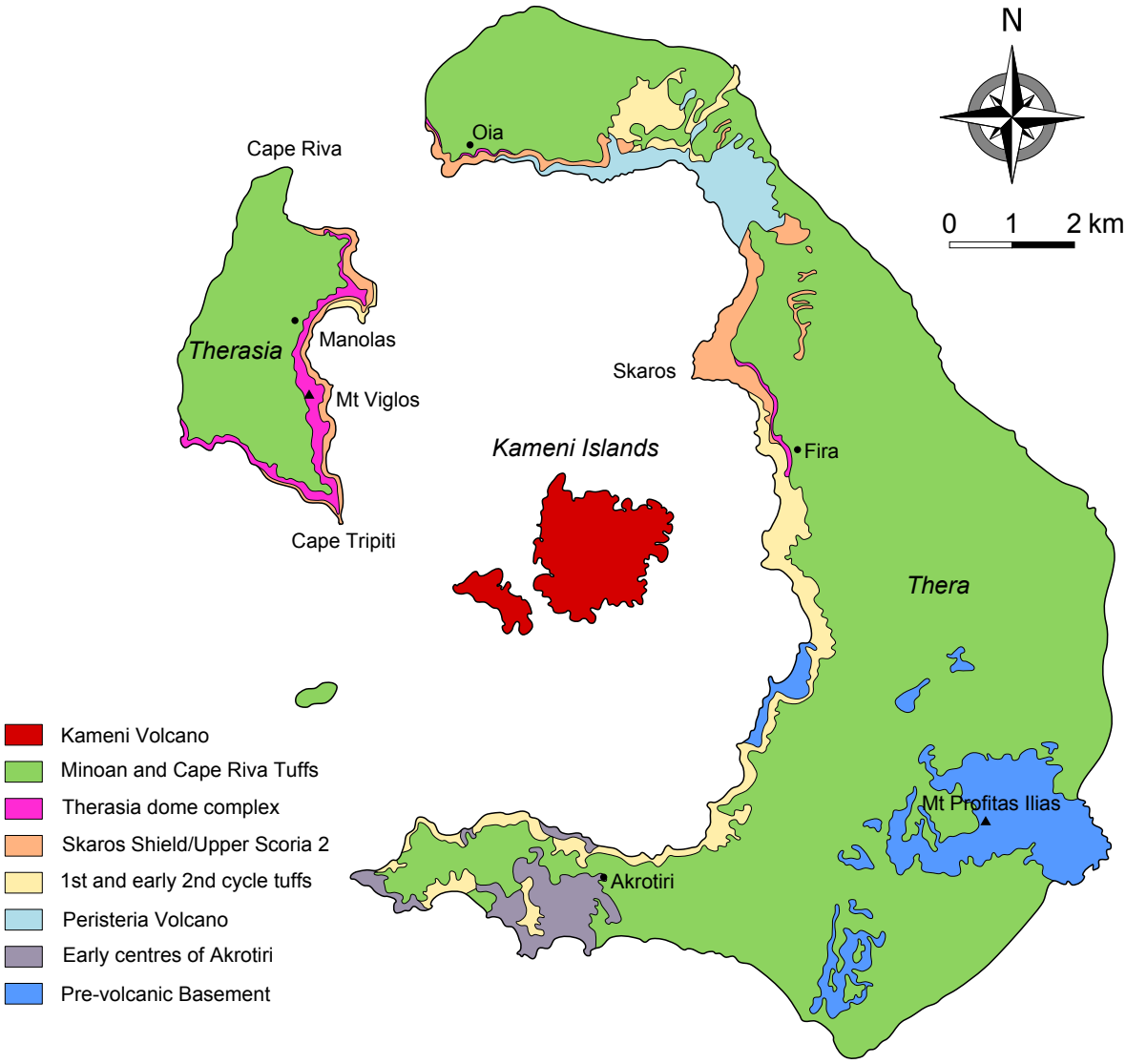

Figure 2.5: Sketch geological map of Santorini, adapted from Druitt et al. (1999).

is confined to the Akrotiri peninsula in the south of the island (Figure 2.5). The early activity consists predominantly of dacitic-rhyodacitic submarine domes, coulées, and hyloclastite aprons. These are intercalated with the products of more explosive submarine eruptions and marine sediments containing benthic and planktonic forams. Towards the end of activity on the Akrotiri peninsula some eruptions were probably subaerial.

The stratigraphical relationships between the various units are complex, and in places faulted. The presence of unambiguous marine sediments at elevations of over 100 m above the present sea level show that they have been uplifted. Two separate fault

blocks exist on the peninsula. The Akrotiri volcanics are geochemically distinct from the main volcanic series that followed, and are the only volcanic rocks from Santorini that have been found to contain significant amounts of amphibole. The silicic members are richer in Ba and Sr and poorer in K, Rb, and Zr compared to the Thera volcanics.

Activity started in the north of the island with the Peristeria stratovolcano (530–430 ka), that makes up Mt. Micro Profitas Ilias. It has been split into three sequences: a core of andesitic lavas, tuffs and hyloclastites; massive silicic andesite lava flows; and a succession of thin andesitic and basaltic lavas with subordinate dacites. About 50 dykes are revealed in the caldera cliff, the majority of which trend north to north-west. In total, the subaerial volume was at least 2 km^3.

Towards the end of the construction of Peristeria cinder and spatter cones were formed at three centres on the Akrotiri peninsula. These have been dated using K–Ar and Ar–Ar methods at between 450–340 ka, and lie above the early Akrotiri centres but beneath the Thera pyroclastics.

2.4.2 Thera pyroclastics (<360 ka)

The current sequence of explosive volcanism started 360 ky ago, and consists of at least twelve plinian eruptions. These have been split into two cycles, and in each cycle there is a general trend towards more silicic compositions. Both cycles end with a pair of large dacitic to rhyolitic eruptions; Lower Pumice 1 and 2 in the first cycle and the Cape Riva and Minoan eruption in the second. Lower Pumice 2, Cape Riva and Minoan eruptions are associated with caldera collapse. Vents for the Thera pyroclastics are concentrated in the northern half of Santorini, and most lie (or are inferred to lie) on either the Kameni or Coloumbo lines. In between the plinian eruptions there are numerous effusive and smaller explosive eruptions.

First eruptive cycle (360–180 ka)

The first eruptive cycle consisted of five large, explosive eruptions and numerous smaller effusive and explosive events. Cape Therma 1, 2 and 3 were all dominantly intermediate in composition. Cape Therma 1 is and andesitic ignimbrite, up to 60 m thick. Cape Therma 2 is a rhyodacitic pumice fall deposit. Cape Therma 3 is andesitic, with pyroclastic flow deposits overlying a stratified pumice fall, rich in obsidian fragments. Between Cape Therma 2 and 3 several rhyodacitic lava flows are preserved in the caldera cliffs.

The first cycle came to an end with the Lower Pumice 1 and 2 eruptions. Both were rhyodacitic, and Lower Pumice 2 resulted in the earliest known caldera collapse on Santorini. Lower Pumice 1 commenced with a Plinian phase, leaving deposits up to 5 m thick, whose isopachs are consistent with a vent somewhere near the present-day Kameni isles. Bomb sags are common at the top of this Plinian deposit, implying a strong ballistic component to the second phase of the eruption. This second phase deposited a coarse-grained lithic lag breccia up to 14 m thick. This phase is compositionally zoned, with the vesicular component changing from rhyodacite at the bottom to andesite at the top. Lenses of welded and non-welded ignimbrite occur in places under the breccia.

Lower Pumice 2 is separated from Lower Pumice 1 by only a single palaeosol. Initial Plinian deposits are up to 25 m thick, consisting of an initial thin, white basal unit overlain by an inversely graded main fall unit. Deposits are uniformly rhyodacitic, except for this Plinian deposit which also contains a small amount of of basaltic to andesitic scoria. Isopach maps suggest a vent near the present-day Kameni isles. Phreatomagmatic explosions the produced a series of dune cross-bedded surge deposits followed by a thick, massive and poorly sorted pumiceous deposit.

Second eruptive cycle (180–3.6 ka)

After the eruption of Lower Pumice 2, effusive activity began to fill the caldera. The Simandiri shield is exposed near sea-level in the cliffs of Therasia, just to the north of Manolas. At the base are stratified phreatomagmatic tuffs and conglomerates. These are overlain by thin basaltic lavas and thick andesitic domes and coulées. These dip west, away from the present caldera. This was followed by the Middle Tuff sequence, four of which discharged several km^3 of magma.

The Cape Thera Tuff lies at the same stratigraphic height as the Simandiri lavas, separated from Lower Pumice 2 below by a palaeosol up to 13 m thick. This probably represents a period of hundreds to thousands of years of only minor activity following the collapse of the first caldera. The Cape Therma Tuff consists of a thin pumice fall, up to 85 cm thick, and an ignimbrite deposit.

After the Cape Thera eruption, 5 m of minor pyroclastics and palaeosols are preserved. Above this lies the Middle Pumice deposits, which begin with a Plinian pumice fall deposit, which is densely welded beneath Fira. Isopachs, and the location of the welded deposit imply a vent to the west of Fira. Above the pumice fall deposit lie lithic lag breccias, and the top of the pumice fall contains deep impact sags, demonstrating a violent ballistic event at the onset of pyroclastic flow production. The eruption ended with a second Plinian phase, from the same vent as the first.

Up to 9 m of minor pyroclastics and palaeosols lie between the Middle Pumice deposits and the Vourvoulos deposits. At the base of this eruption's deposits lie a scoria fall, which may correlate with the two cinder cones by Kokkino Vouno that erupted at about the same time. The Vourvoulos deposits only reach a maximum of a few metres, but they are widespread. They consist of a pumice fall deposit, followed by cross-bedded surge deposits and an ignimbrite.

Above the Vourvoulos deposits lies the deposits from the Upper Scoria 1 eruption. This commenced with a black scoria fall, within which lies a pair of ash beds. The ash beds are less than a metre thick, and contain accretionary lapilli and climbing-

ripples, suggesting a phreatomagmatic base surge origin. An isopach map for the scoria fall, along with the flow directions recorded by the base surge units, imply a vent near the present-day Kameni isles. Above the scoria deposits is a distinctive spatter agglomerate, formed by a pyroclastic flow containing rags of fluid andesite. Lithic clasts are also common. A caldera was present after the Upper Scoria 1 eruption (the Skaros caldera, Figure 2.6a), but its formation cannot be connected unambiguously to the eruption itself.

2.4.3 The build-up to the Cape Riva eruption (67–22 ka)

Skaros shield (67–54 ka)

A period of effusive volcanism filled up the caldera with a series of mainly basaltic and andesic lavas — the Skaros shield (Figure 2.6b). A lava flow at sea-level has an Ar–Ar age of 67 ± 9 ka (Druitt et al., 1999). The Skaros sequence has been described in detail by Huijsmans (1985) and Huijsmans and Barton (1989). It consists mainly of basaltic and andesitic lavas; all the flows have less than 64 wt % SiO_2 and most have less than 55 wt %. The most silicic lavas are at the base of the sequence, erupted shortly after the Upper Scoria 1 eruption. Interspersed between the lavas are the occasional deposits from explosive eruptions, and these have higher SiO_2 than the lavas above and below.

Huijsmans and Barton described several cycles of volcanism, starting with a silicic eruption and with subsequent eruptions having progressively lower SiO_2 contents. These trends were repeated in other elements, for example there are increases in MgO and CaO and decreases in Na_2O and K_2O with stratigraphic height within each cycle. They explained this as repeated tapping of a zoned magma reservoir, each eruption reaching a deeper and more mafic level. Before each cycle the system begins to stagnate, building up a silicic cap. Before dacite can be produced, however, an explosive eruption occurs.

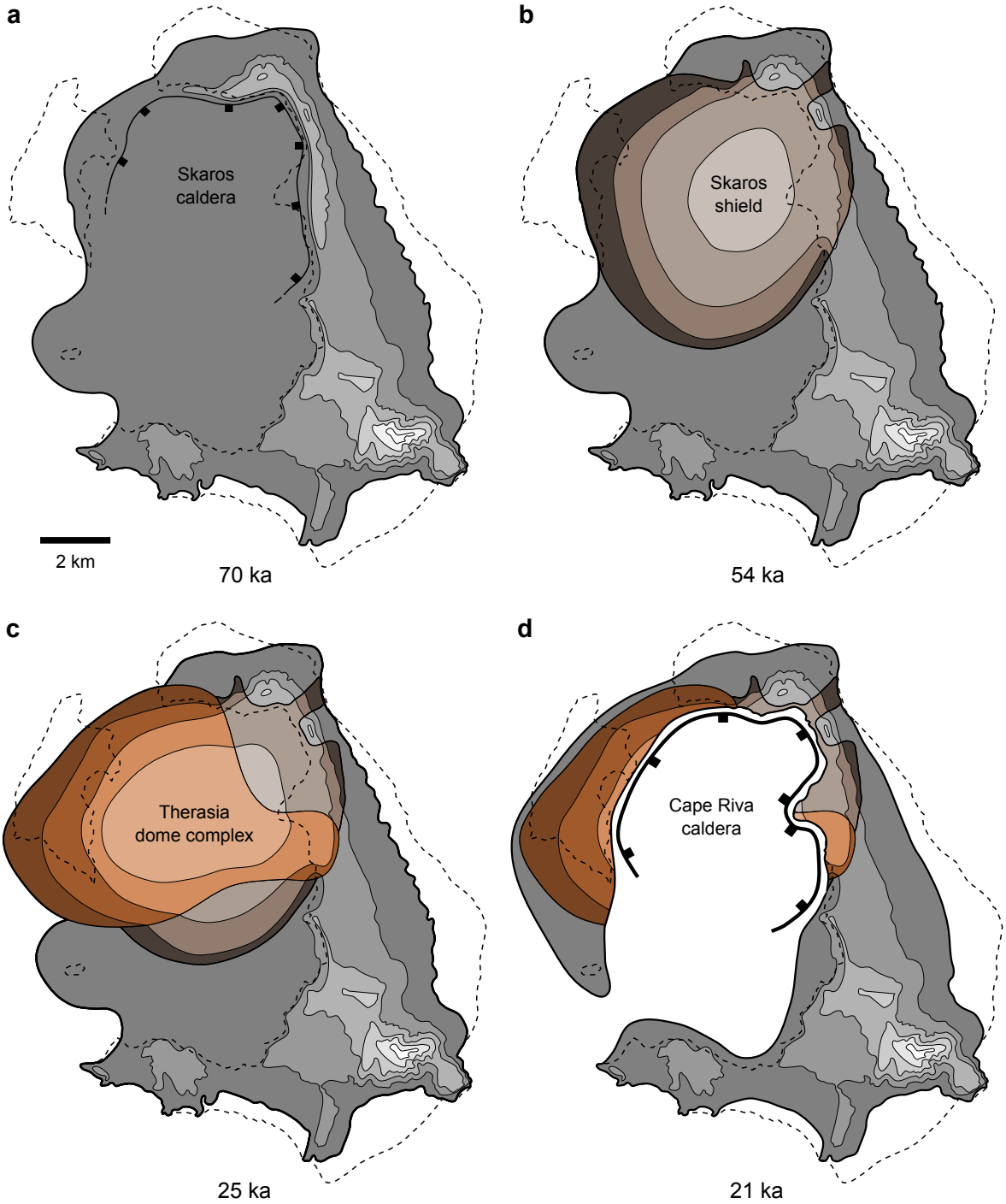

Figure 2.6: Morphological evolution of Santorini between 70 and 21 ka, after Druitt et al. (1999). The dashed line is the present-day outline of the islands. Contours are at 100-m intervals. (a) The volcano after collapse of the Skaros caldera, which happened some time before the first Skaros lava was erupted at 67 ± 9 ka. (b) The maximum extent of the Skaros shield, which culminated with the 54 ± 3 ka Upper Scoria 2 eruption. (c) The maximum extent of Therasia dome complex at ∼25 ka. (d) The island shortly after the ∼22 ka Cape Riva eruption

Upper Scoria 2 eruption (54 ka)

The cycles of partial stagnation then eruption continue until the Upper Scoria 2 eruption. Upper Scoria 2 is a dominantly andesitic explosive eruption, that deposited several km^3 of magma over much of Santorini. Its distinctive red colour and widespread distribution make it an excellent stratigraphic marker. It also represents a change in behaviour for the volcanic system.

Shortly before — perhaps immediately before — a small dacitic pumice fall is deposited from a vent near the Kameni isles. While the volume represented by this pumice fall is much smaller than the andesite erupted during the Upper Scoria 2 eruption this is the first time dacite was erupted since Upper Scoria 1. Afterwards, during the Therasia Sequence, dacite becomes the dominant composition. Upper Scoria 2 can therefore be thought of as the last failed stagnation, where an initial build-up of silicic magma is interrupted by an eruption. Its position at the peak of the TiO_2 variation diagram rules out large-scale mixing, however the Sr isotopic signature of some of the crystals shows that they have been incorporated from a previous magma batch (Martin et al., 2010). The main phase of the eruption began with the emplacement of andesitic pyroclastic surge deposits. This was followed by scoria flows, with spatter rags similar to the ones found in the Upper Scoria 1 deposits.

Mellors and Sparks (1991) reported two ^{14}C dates of $38.9^{+2.2}_{-1.8}$ and $36.9^{+1.9}_{-1.4}$ ka, while Druitt et al. (1999) present a K–Ar age of 79 ± 8 and a more precise, Ar–Ar age of 54 ± 3 ka. The Ar–Ar age is the only one that is consistent with both the ages of Skaros lavas and the Megalo Vouno cinder cone which predate Upper Scoria 2 (Druitt et al., 1999), and the youngest Therasia lava which postdates it. As the dates of Mellors and Sparks are at the limit of conventional ^{14}C dating, the Ar–Ar date of 54 ka is assumed to be the most accurate.

Therasia dome complex (54–22 ka)

The Therasia dome complex is a series of mainly dacitic domes and coulées that covered the summit and western flank of the Skaros shield (Figure 2.6c). Interspersed between the lavas are several pumice fall deposits and soils. The sequence is capped by a crystal-rich andesite, here named the upper Therasia andesite. The lavas are well-exposed in the cliffs of the western side of the present-day caldera, on Therasia, and lavas are also found at Oia and Fira on Thera (Figure 2.5). The well-exposed stratigraphy of the Therasia dome complex makes it an ideal opportunity to study the changes in the plumbing system of a volcano in the build-up to a caldera-forming eruption.

The Therasia dacites are chemically and petrologically similar to the Cape Riva dacite, which led Druitt (1985) to propose that they were "precursory leaks" from the growing Cape Riva magma reservoir (see Chapter 1). In this thesis, however, I shall argue that the Therasia dacites are not precursory leaks, and are a distinct batch of magma.

2.4.4 Cape Riva eruption (22 ka)

While the exact amount of magma erupted during the Cape Riva is unknown, it is at least several km^3, and is associated with a caldera collapse (Figure 2.6d). It has been correlated with the Y-2 ash layer in Mediterranean sediments, and is found as far away as the Marmara Sea (Figure 2.7).

The eruption has been split into four phases (Figure 2.8). It commenced with the mainly dacitic Plinian phase Cape Riva A , that left pumice fall deposits up to 7 m thick (corrected for compaction; Druitt, 1985). The Plinian deposits also contain ~5 % andesitic scoria, that is not found in the later phases. This andesite is also a hybrid, with a similar SiO_2 content to the upper Therasia andesite. The deposits of phase A are found only in the north of Santorini, around Cape Riva and Oia (Figure 2.5), and the deposits on Cape Riva are densely welded. This suggests that the vent for the first phase of the Cape Riva eruption was located nearby.

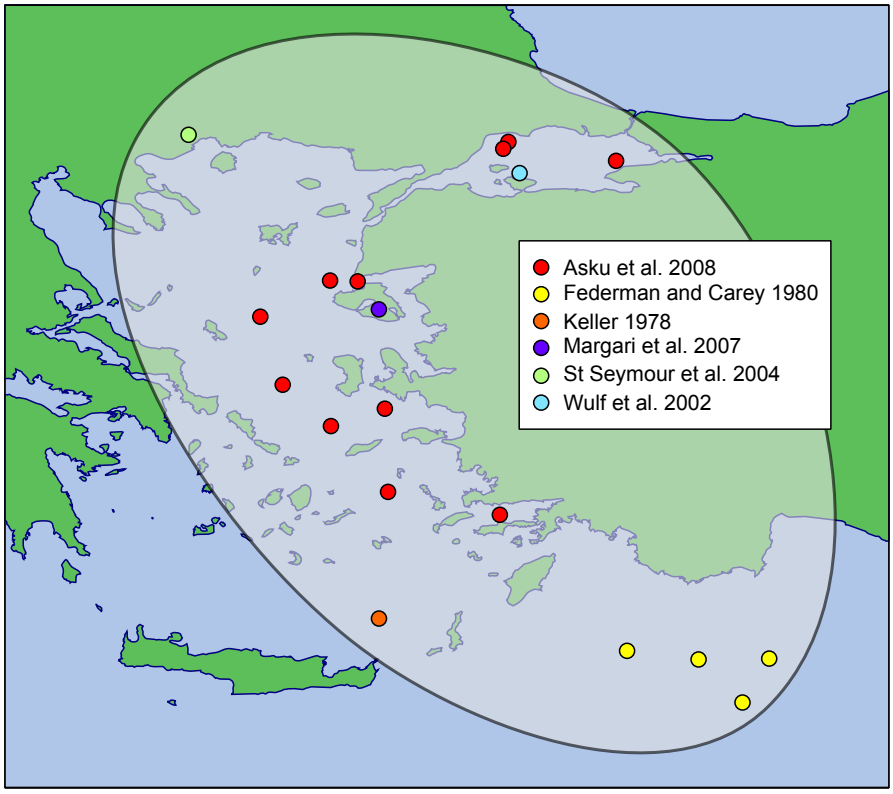

Figure 2.7: Distribution of the Cape Riva ash in marine and lake-bed sediment cores. Data from Asku et al. (2008), Federman and Carey (1980), Keller et al. (1978), Margari et al. (2007), St Seymour et al. (2004), Wulf et al. (2002).

The second phase (Cape Riva B) of the eruption produced welded ignimbrite deposits which underlie lithic lag breccias. These breccias grade laterally and vertically into non-welded and pumiceous ignimbrites. Deposits from phase B are widely distributed around Santorini, and form veneers up to 4 m thick that drape the pre-existing topography. The deposits from phase B are particularly thick to the east of Akrotiri where they fill a pre-existing channel and reach up to 12 m in thickness.

Cape Riva C was the most voluminous phase, and the deposits are the thickest (reaching up to 25 m) and most widespread of the Cape Riva deposits found on Santorini. The most conspicuous deposits of this phase are the coarse co-ignimbrite lithic lag breccias, interpreted to have formed by strong gas fluidisation and the segregation of large and dense blocks from the flows (Druitt and Sparks, 1982). There is little systematic spacial variation in the grain size of the breccias across Santorini, and lithic blocks 1–2 m in diameter are common wherever the lag breccia is found. These

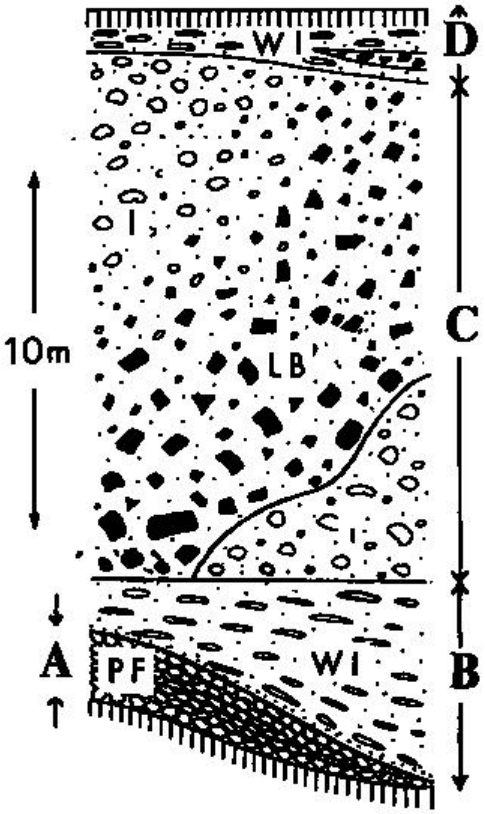

Figure 2.8: Schematic section through the Cape Riva deposits, from Druitt (1985). PF: pumice fall; WI: welded ignimbrite; I: non-welded ignimbrite; LB: lithic breccias. Letters refer to the different phases of the eruption, discussed in the text.

lag breccias grade horizontally and vertically into pumiceous ignimbrite, and repeated flow units are often seen. The large increase in the lithic content of these deposits probably signals the onset of caldera collapse Druitt (1985).

The deposits from final phase of the eruption, Cape Riva D, is similar in appearance to Cape Riva B. They consist of surface-draping veneers of welded ignimbrite up to 2 m thick, that outcrop on the north of Thera.

2.4.5 Post-Cape Riva activity

The Cape Riva eruption was accompanied by caldera collapse, as demonstrated by the existence of a water-filled caldera prior to the Minoan eruption (Druitt and Francaviglia, 1992; Eriksen et al., 1990; Friedrich et al., 1988). There are few volcanic deposits found dating from the period between the Cape Riva and the Minoan, with the notable exception of a basaltic scoria fall (Vaggelli et al., 2009; Vespa et al., 2006). The existence of an andesitic to rhyodacitic cone in the caldera can be inferred from the

presence of blocks of lava in the deposits of the Minoan eruption (Druitt, 2014).

Minoan eruption (3.6 ka)

The Minoan eruption has been dated at 1600–1627 B.C.E. (Friedrich et al., 2006; Manning et al., 2006). Although it has previously been suggested that this eruption was responsible for the collapse of the Minoan civilisation on Crete (hence the name), current evidence suggests that the Minoan civilisation lasted for over a generation afterwards. It was, however, responsible for the destruction of the flourishing trading port of Akrotiri on the island (Cioni et al., 2000). Deposits at Palaikastro suggest that a 9 m high tsunami reached Crete (Bruins et al., 2008)

This eruption produced 30-60 km^3 of magmatic products, with deposits up to 60 m thick on the island and ash from the eruption is found across the eastern Mediterranean (Asku et al., 2008; Federman and Carey, 1980; Keller et al., 1978). The products are dominantly rhyodacitic, apart from subordinate andesitic scoria found in the first, Plinian phase of the eruption. This activity was interrupted by the access of sea-water into the vent. This lead to violent phreatomagmatic explosions, and base surge deposits with dune cross-bedding and impact sags. Interstratified within the base surges are pumice fall deposits, showing Plinian fallout continued during this time. Massive tuffs above the surge deposits are interpreted to have been deposited by hot ($\leq$300 °C) debris flows and low temperature pyroclastic flows. The final phase of the eruption involved hot (300–350 °C) pyroclastic flows spreading across the whole island, leaving deposits up to 40 m thick (Druitt et al., 1999).

The Minoan eruption is associated with caldera collapse, and is responsible for most of the islands present distinctive topography.

Post-Minoan activity (<3.6 ka)

Since the Minoan eruption, the volcano has returned to constructive volcanism. Historical documentation of eruptions in the centre of the Minoan caldera date back to

197 B.C.E, when an island first broke the surface. Since then a series of eruptions have produced the ∼10 km^3 of lava that make up the present-day Kameni islands, along with small explosive eruptions (Fouqué, 1879; Nomikou et al., 2014; Pyle and Elliott, 2006). The 20th century has seen eruptions in 1925-6, 1928, 1939-41 and 1950. These produced small plumes and thick lava flows. Chemically, the dacitic lavas have remained very similar over the 2,200 years of flows exposed today (Barton and Huijsmans, 1986). Numerous mafic enclaves showing that recharge is ongoing (Holness et al., 2005; Martin, 2005; Martin et al., 2006).

2.5 Chemistry and petrology

2.5.1 Major and trace element chemistry

The variations of major element concentrations as a function of SiO_2 content is shown in Figure 2.9, and the variations of selected trace elements is shown in Figure 2.10. The field for all of the Thera volcanics is shown in grey, and the products of the eruptions since 67 ka are plotted as individual points. Also shown is the field of Peristeria lavas, for comparison. Not shown are the early centres of the Akrotiri peninsula, as these form a chemically and petrologically distinct series.

Most of the elements fall along fairly tight fractional crystallisation trends. Some of these trends are strongly curved. For example, TiO_2 behaves incompatibly in Santorini magmas up to about 55–60 wt% SiO_2. In more evolved melts Fe–Ti oxides start to crystallise, lowering the amount of TiO_2 in the residual melt. This leads to the curved trend seen in Figure 2.9. Strongly compatible trace elements, such as Cr and Ni (Figure 2.10a,b), become rapidly depleted with small amounts of fractional crystallisation. Magmas formed by mixing will tend to plot between the two arms of these curved trends. This can be seen clearly on Figure 2.9f for Cape Riva, Therasia and Minoan andesites with about 60 wt% SiO_2. Magma mixing in the Cape Riva and Therasia andesites is discussed in more detail in Chapter 5.

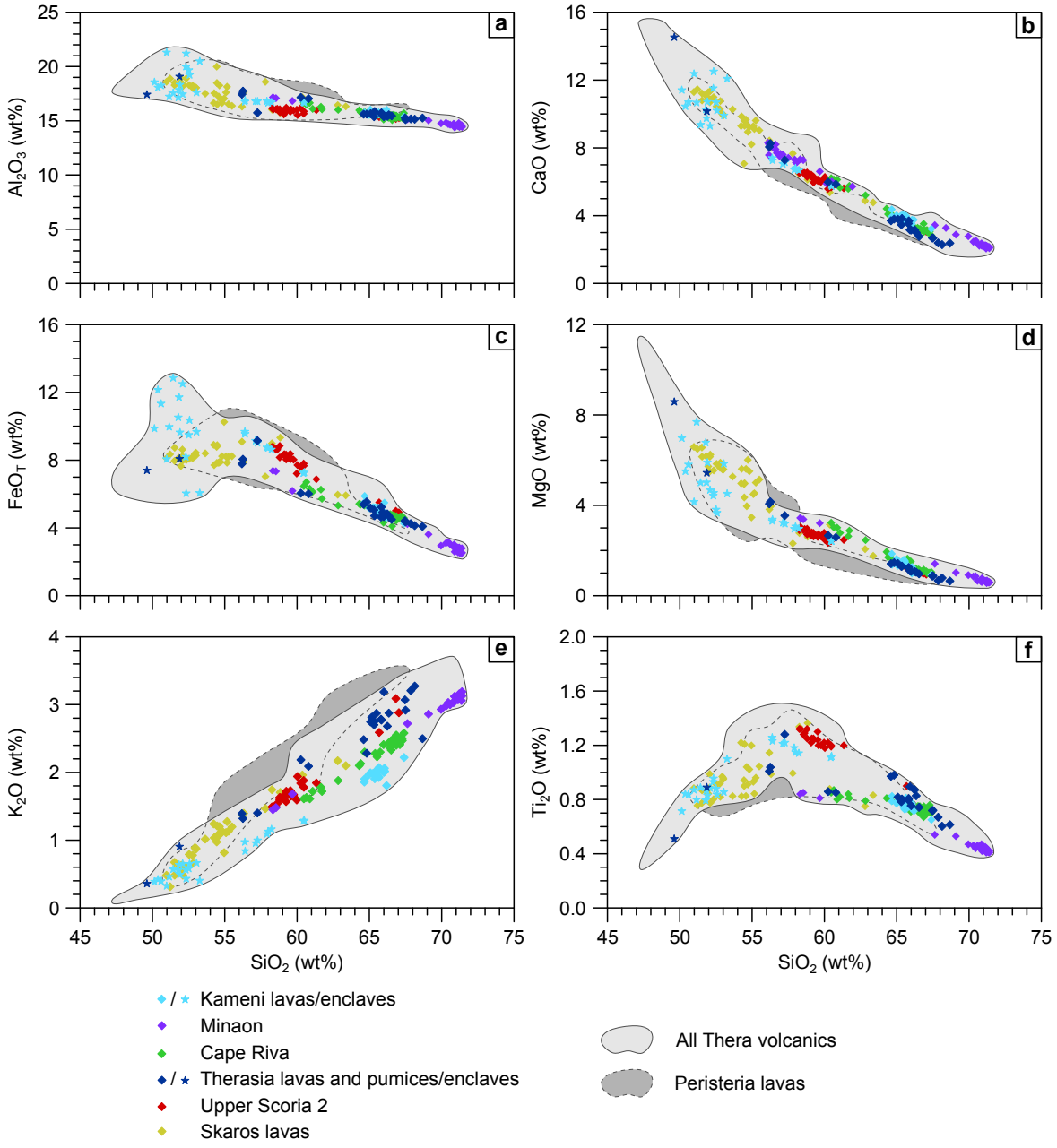

Figure 2.9: Variation diagrams for major elements in Santorini magmas. Kameni lava, Skaros and Peristeria data from Huijsmans (1985); Kameni enclave data from Martin (2005); Therasia data from this work; all other data from Druitt et al. (1999). FeO_T is the total FeO and Fe_2O_3 plotted as FeO.

The Peristeria volcanics follow the same trends as the later Thera volcanics, for the most part. They do have slightly higher incompatible element concentrations; this is part of a long-term trend on Santorini towards more depleted compositions, discussed below. A major distinguishing feature, however, is the high Sr content of some of the Peristeria basalts and andesites compared to later basalts and andesites (Figure 2.10c).

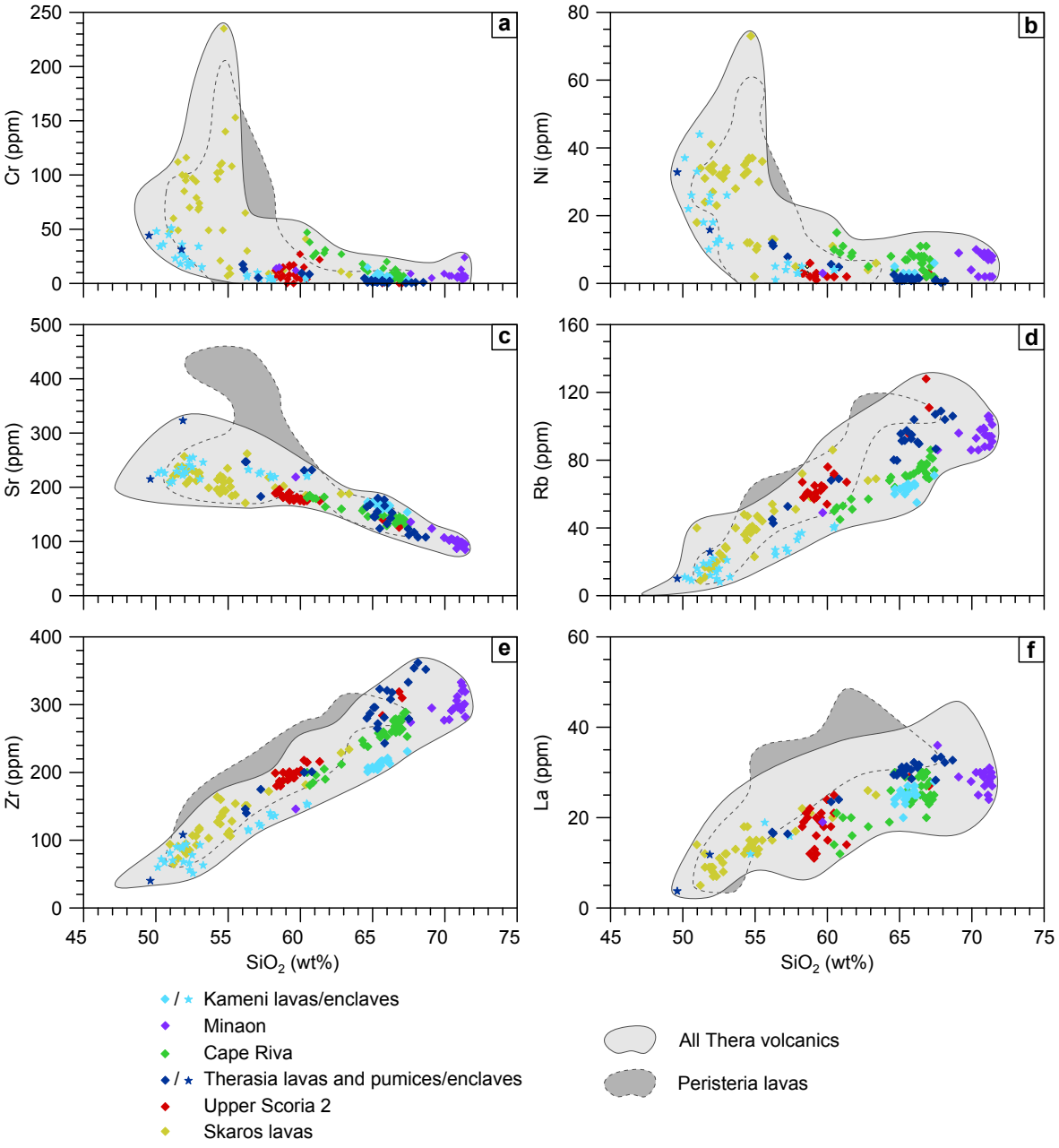

Figure 2.10: Variation diagrams for trace elements in Santorini magmas. Kameni lava, Skaros and Peristeria data from Huijsmans (1985); Kameni enclave data from Martin (2005); Therasia data from this work; all other data from Druitt et al. (1999).

2.5.2 Isotopic variation

The $^{87}Sr/^{86}Sr$ and $^{143}Nd/^{144}Nd$ variations of Santorini pumices are shown in Figure 2.11. Pumices from Santorini are seen to form a trend away from the mantle correlation line, towards more radiogenic compositions. This is consistent with contamination by upper crustal rocks. The degree of contamination is found to correlate

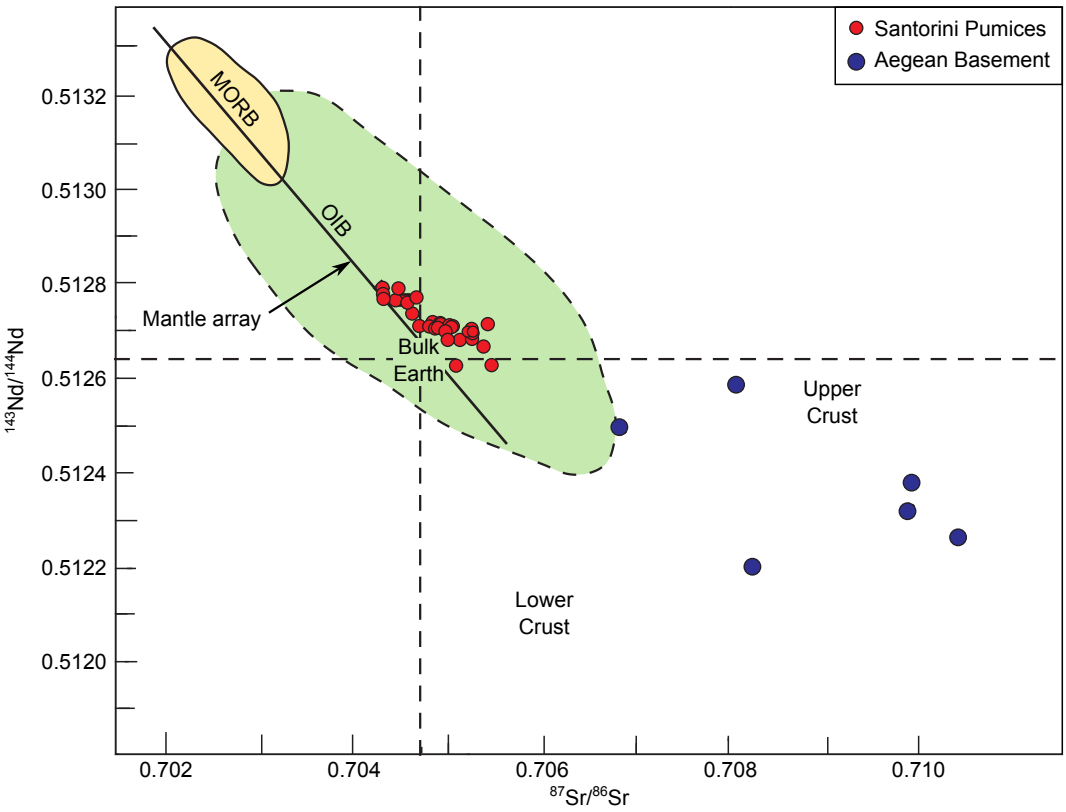

Figure 2.11: $^{87}Sr/^{86}Sr$ and $^{143}Nd/^{144}Nd$ variation for Santorini pumices and Aegean basement, after Druitt et al. (1999)

with SiO_2 content, suggesting the contamination occurs during fractional crystallisation (Druitt et al., 1999). Assimilation and fractional crystallisation (AFC) models suggest the ratio of mass assimilated to mass crystallised is between 0.1–0.2.

Figure 2.12 shows the variation in $^{87}Sr/^{86}Sr$ and $^{143}Nd/^{144}Nd$ ratios with stratigraphic height. It shows that there is no simple trend in the isotopic composition of Santorini magmas with time. $^{87}Sr/^{86}Sr$ ratio first decreases with time, up until the Upper Scoria 1 eruption. It then increases, up until the Minoan eruption. The $^{143}Nd/^{144}Nd$ ratio shows a mirror image of the $^{87}Sr/^{86}Sr$ variations. Martin et al. (2010) show that there are isotopic variations even within the products of a single eruption.

2.5.3 Decrease in incompatibles with time

Since volcanism commenced in the north of the island, there has been a progressive decrease in the concentration of incompatible trace elements such as K, Nb, Rb and Zr

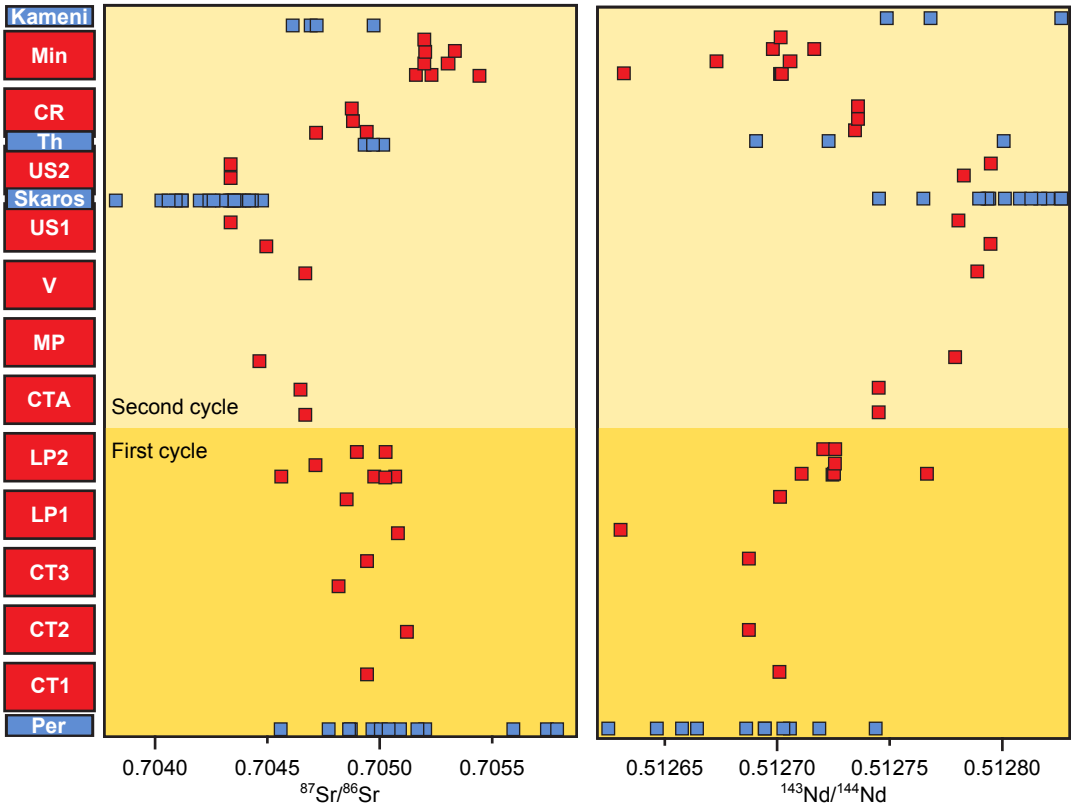

Figure 2.12: $^{87}Sr/^{86}Sr$ and $^{143}Nd/^{144}Nd$ variation with stratigraphic height for Santorini pumices and lavas, after Druitt et al. (1999). Pumices in red, lavas in blue. Min: Minoan, CR: Cape Riva, Th: Therasia, US1/2: Upper Scoria 1/2, v: Vourvoulos, MP: Middle Pumice, CTA: Cape Thera, LP1/2: Lower Pumice 1/2, CT1/2/3: Cape Therma 1/2/3, Per: Peristeria.

(Figure 2.13). There have been several different explanations proposed to account for this observation. Druitt et al. (1999) attributed these decreases as a result of growing isolation of the magma chamber from the crust due to an increasing amount of plutonic rocks intruded under Santorini. This would decrease the amount of assimilation and hence lower the concentration of incompatibles in the most evolved erupted magmas. However, there is no evidence for a decrease in the $^{87}Sr/^{86}Sr$ ratio with time at Santorini (Figure 2.12). Isotopic signatures fluctuate with time, and some young melts are amongst the most radiogenic in the history of the volcano (Martin et al., 2010; Vaggelli et al., 2009).

Incompatible trace element contents and isotopic signatures at Santorini are decoupled, ruling out a simple common origin. A more likely explanation for the observed trends lies in the nature of the mantle sources of the parental basalts feeding the vol-

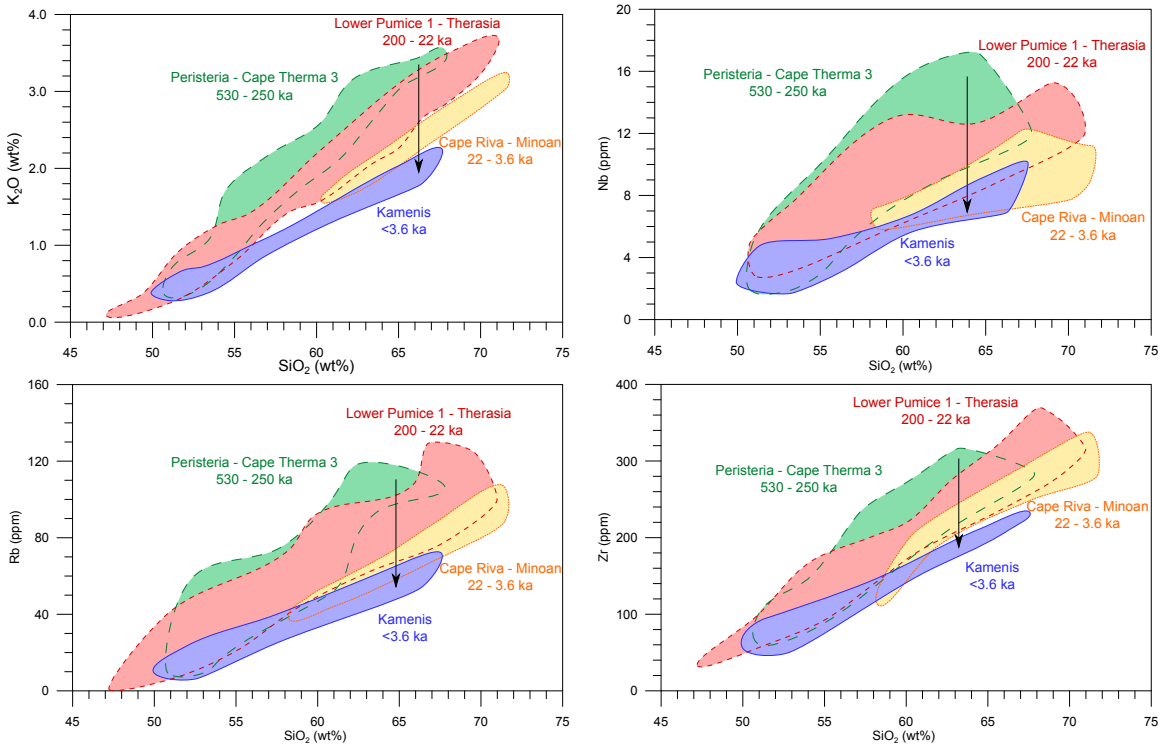

Figure 2.13: Selected variation diagrams showing the decrease in incompatible element concentrations throughout the volcanic history of Santorini, since the commencement of volcanism in the north of the island. Normalised to dry compositions. Whole rock data taken form Druitt et al. (1999) and Huijsmans (1985), Kameni enclave data from Martin (2005)

canic system. Recent studies have found that multiple basalt series with differing trace element and isotopic ratios are contemporaneously active in the volcanic plumbing system (Bailey et al., 2009; Vaggelli et al., 2009). The different trace element contents of these series requires their mantle source underwent varying degrees of metasomatism by sediment-derived fluids or melts. Variations in Nd suggest the involvement of small amounts of sedimentary melts, as it is fluid-immobile (Bailey et al., 2009; Vaggelli et al., 2009). Aqueous fluids may also play a role in controlling the trace element chemistry, as has been proposed for the Kameni Isles (Zellmer et al., 2000).

Another possible explanation for the variation in incompatible element concentrations with time is varaitions in the degree of partial melting. Incompatible elements are the first elements to go into any melt, and are therefore enriched at small melt fractions. An increase in the melt fraction of the mantle source would lead to a decrease

in incompatible element concentrations. This could explain the progressive depletion in incompatibles on Santorini, while the variations in isotopic ratios would be due to changes in AFC processes in shallow magma reservoirs or sediment contamination from the descending slab (Francalanci et al., 2005).

Chapter 3

Diffusion chronometry

3.1 Introduction

Diffusion dating is becoming an increasingly exploited way of accessing the timescales of magmatic processes. Because of the different speeds at which various elements diffuse in crystals, events lasting from hours (e.g. Coogan et al., 2005) to millions of years (e.g. Faryad and Chakraborty, 2005) can be timed. Unlike radiometric dating, this technique is not restricted to young rocks. Because diffusion slows to an effective stop at low temperatures, the timescales recorded by diffusion profiles can be calculated long after the event (e.g. the cooling rate of chondrules in meteorites during the formation of the solar system; Béjina et al., 2009).

Another advantage of diffusion chronometry is the way it can be carried out on single crystals, in situ, using well-established micro-sampling techniques. Diffusion profiles can be measured using secondary ion mass spectrometry (SIMS), the electron probe or laser ablation mass spectrometry (LA ICP MS). In some cases two dimensional images of crystals can be used, such as from backscattered electron images (BSE) for Mg-Fe inter-diffusion in olivine (Martin et al., 2008; Morgan et al., 2006, 2004) or cathodoluminescence images for Ti diffusion in quartz (Girard and Stix, 2010; Saunders et al., 2010; Smith et al., 2010). This allows petrological information to be combined

with the timescales recovered, and allows timescales from many crystals in the same sample to be recovered individually.

This chapter discusses the theory behind diffusion chronometry. I also review the data on the different diffusion coefficients, and the factors that influence them. I focus in this chapter mainly on plagioclase and orthopyroxene, as these are the minerals I use later in this thesis. However, various other minerals have also been used to estimate the timescales of magmatic and volcanic processes. These include olivine, clinopyroxene, magnetite, quartz and alkali feldspars (e.g. Costa and Chakraborty, 2004; Girard and Stix, 2010; Morgan et al., 2006, 2004; Nakamura, 1995). Diffusion chronometry is also regularly applied to metamorphic systems (e.g. Ague and Baxter, 2007; Faryad and Chakraborty, 2005).

3.2 Diffusion theory

3.2.1 Basic Theory

Diffusion occurs in crystalline solids due to the random jumps of individual atoms, either to nearby vacancies or to interstitial sites. Diffusion normally occurs in all directions with equal probability, leading to no overall change in composition. However, if there is some driving force making jumps in a particular direction more energetically favourable, such as a chemical potential gradient, it will lead to a flow of atoms in that direction. The flux of those atoms per unit area, J, can be written as a function of the chemical potential μ:

$$J = -L\frac{\partial \mu}{\partial x} \tag{3.1}$$

where L is the phenomenological constant for the element or isotope of interest.

Chemical potentials are not easy to measure. However, for ideal solutions or diluted components the concentration gradient, $\partial C/\partial x$, can be used instead (Costa et al., 2008). Elemental concentrations can be measured directly, unlike chemical potential,

and hence most diffusion chronometry studies model concentrations. Replacing the chemical potential gradient by the concentration gradient, and the phenomenological constant L with the diffusion coefficient D, leads to Fick's first law:

$$J = -D\frac{\partial C}{\partial x} \tag{3.2}$$

We can then look at the case of one dimensional flow through an infinitesimally small volume $\mathrm{d}x.\mathrm{d}y.\mathrm{d}z$. The flow of atoms into this volume by diffusion is $J\left(x\right).\mathrm{d}y.\mathrm{d}z$ and the flow out of this volume is $J\left(x+\mathrm{d}x\right).\mathrm{d}y.\mathrm{d}z$. The rate of change of the number of atoms $\partial N/\partial t$ in this volume over an infinitesimally small time $\mathrm{d}t$ is, therefore:

$$\begin{aligned}\frac{\partial N}{\partial t} &= J\left(x\right).\mathrm{d}y.\mathrm{d}z - J\left(x+\mathrm{d}x\right).\mathrm{d}y.\mathrm{d}z \\ &= -\frac{\partial J}{\partial x}.\mathrm{d}x.\mathrm{d}y.\mathrm{d}z\end{aligned} \tag{3.3}$$

Dividing through by the volume in order to give concentration, we get:

$$\frac{\partial C\left(x,t\right)}{\partial t} = -\frac{\partial J}{\partial x} \tag{3.4}$$

Equation 3.2 can then be substituted in for J, to give (Fick, 1855):

$$\frac{\partial C\left(x,t\right)}{\partial t} = \frac{\partial D}{\partial x}\frac{\partial C\left(x,t\right)}{\partial x} + D\frac{\partial^2 C\left(x,t\right)}{\partial x^2} \tag{3.5}$$

If D is independent of x this can be simplified to Fick's second law:

$$\frac{\partial C\left(x,t\right)}{\partial t} = D\frac{\partial^2 C\left(x,t\right)}{\partial x^2} \tag{3.6}$$

This equation can be solved analytically for simple systems. One of these is diffusion in an infinite slab, which is a useful approximation to diffusion in the centre of a large, flat crystal face. In this case, diffusion is mostly parallel to the crystal face, and can

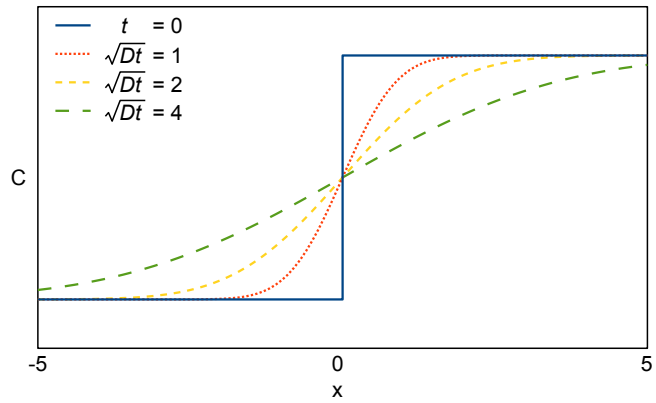

Figure 3.1: The evolution of an initial step function in an infinite slab by diffusion (Equation 3.7).

be modelled in one dimension. Starting with an initial step function, the following equation satisfies Fick's second law (Lasaga, 1998):

$$C\left(x,t\right) = C^{\text{left}} + \frac{C^{\text{left}} - C^{\text{right}}}{2}\left[1 + \text{erf}\left(\frac{x}{\sqrt{tD}}\right)\right] \tag{3.7}$$

where C^{left} and C^{right} are the initial concentration the left and the right of the step function, respectively; x is the distance, centred on the initial step function; t is the time; and $\text{erf}\left(u\right)$ is the error function, shown below:

$$\text{erf}(u) = \frac{2}{\sqrt{\pi}}\int_0^u e^{-k^2}\text{d}k \tag{3.8}$$

where k is a dummy variable.

3.2.2 Trace element diffusion in plagioclase

Modelling trace element diffusion in plagioclase is not as simple as the analytical solution above. The partition coefficients of many trace elements are strongly dependent on plagioclase composition (Bindeman et al., 1998; Blundy and Wood, 1991), which means that concentration cannot be used directly as a proxy for chemical potential (Costa et al., 2003; Zellmer et al., 1999, 2003). The diffusion coefficients of trace elements are also often strongly dependent on plagioclase composition (e.g. Giletti and Casserly,

1994; Van Orman et al., 2014), which means the simplification shown in Equation 3.6 cannot be applied either.

Costa et al. (2003) formulated an equation for the diffusion of a trace element i in plagioclase starting from Equation 3.1 above:

$$J_i = -L_i \frac{\partial \mu_i}{\partial x} \tag{3.9}$$

The chemical potential can be expanded to give:

$$\mu_i = \mu_i^0 + RT \ln C_i + RT \ln \gamma_i \tag{3.10}$$

where μ_i^0 is the standard-state potential of i, R is the molar gas constant ($8.31\,\mathrm{J\,K^{-1}\,mol^{-1}}$), T is the temperature in kelvin, C_i is the concentration of i in units of mass per unit mass and γ_i is the activity coefficient for i.

The activity coefficient for element i in plagioclase in equilibrium with a given liquid can be estimated using the expressions of Blundy and Wood (1991) and Bindeman et al. (1998) that relate trace element partitioning to the composition of the host plagioclase:

$$RT \ln \frac{C_i^{\mathrm{xl}}}{C_i^{\mathrm{liq}}} = AX_{\mathrm{An}} + B \tag{3.11}$$

where C_i^{xl} and C_i^{liq} are the concentration of i in the plagioclase crystal and liquid, respectively; X_{An} is the molar fraction of anorthite in the plagioclase; and A and B are experimentally determined constants. At equilibrium, the chemical potential of i in the crystals is by definition equal to that of the liquid, which gives us the following relationship:

$$\begin{aligned} \mu_i^{0,\mathrm{xl}} + RT \ln C_i^{\mathrm{xl}} + RT \ln \gamma_i^{\mathrm{xl}} &= \mu_i^{0,\mathrm{liq}} + RT \ln C_i^{\mathrm{liq}} + RT \ln \gamma_i^{\mathrm{liq}} \\ RT \ln \frac{C_i^{\mathrm{xl}}}{C_i^{\mathrm{liq}}} &= \mu_i^{0,\mathrm{liq}} - \mu_i^{0,\mathrm{xl}} + RT \ln \gamma_i^{\mathrm{liq}} - RT \ln \gamma_i^{\mathrm{xl}} \end{aligned} \tag{3.12}$$

This can be substituted into Equation 3.11 to get:

$$RT \ln \gamma_i^{\mathrm{xl}} = \mu_i^{0,\mathrm{liq}} - \mu_i^{0,\mathrm{xl}} + RT \ln \gamma_i^{\mathrm{liq}} - AX_{\mathrm{An}} - B \tag{3.13}$$

which can be combined with the equation for chemical potential (Equation 3.10), and substituted into the equation for flux (Equation 3.9) to give:

$$J_i = -L_i \frac{\partial}{\partial x} \left(RT \ln C_i + \mu_i^{0,\mathrm{liq}} + RT \ln \gamma_i^{\mathrm{liq}} - AX_{\mathrm{An}} - B \right) \tag{3.14}$$

Differentiating and cancelling out the terms that do not vary with distance we are left with:

$$J_i = \frac{-RTL_i}{C_i} \frac{\partial C_i}{\partial x} + L_i A \frac{\partial X_{\mathrm{An}}}{\partial x} \tag{3.15}$$

Finally, the change in concentration due to time can be calculated using the relationship:

$$\begin{aligned} \frac{\partial C_i}{\partial t} = -\frac{\partial J_i}{\partial x} &= \frac{\partial}{\partial x} \left(\frac{RTL_i}{C_i} \frac{\partial C_i}{\partial x} - L_i A \frac{\partial X_{\mathrm{An}}}{\partial x} \right) \\ &= \frac{\partial}{\partial x} \left(D_i \frac{\partial C_i}{\partial x} - D_i C_i \frac{A}{RT} \frac{\partial X_{\mathrm{An}}}{\partial x} \right) \end{aligned} \tag{3.16}$$

3.3 Application to magmatic systems

Figure 3.2 shows an example of how diffusion can modify the initial concentration of a crystal. In Figure 3.2a a crystal grows in equilibrium with its melt. The concentration of some element in the crystal along the profile marked with a blue line is shown in Figure 3.2b. The environment that this crystal resides in then changes (Figure 3.2c). This could occur in several different ways. The resident magma could evolve by fractional crystallisation, for example, changing its composition. A recharge magma could underplate the magma reservoir, raising the temperature, or it could enter the reservoir and entrain crystals. Other processes could also occur; what is required for diffusion

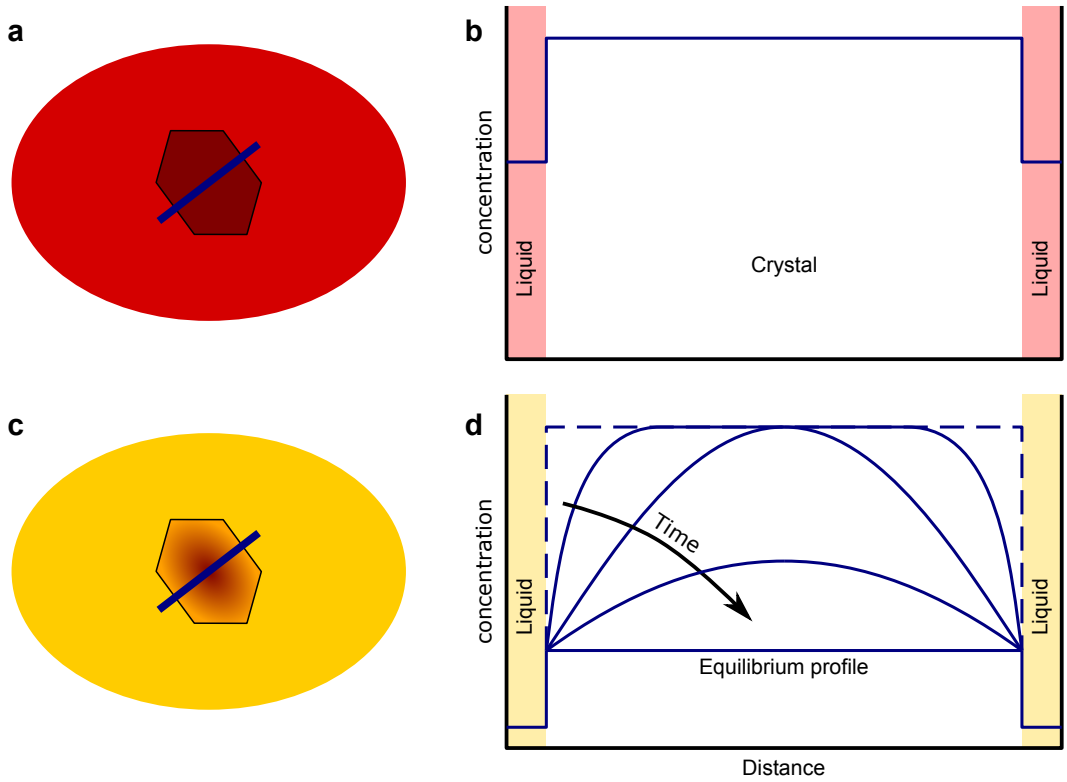

Figure 3.2: A schematic example of the progressive modification of the zoning patterns of a crystal by diffusion. (a) A crystal grows in equilibrium with its melt. (b) The concentration of some element along the profile shown by the thick blue line across the crystal in (a). (c) This crystal is transferred to a new melt, where it is no longer in equilibrium. (d) The evolution of the compositional profile with time.

chronometry to work is that this processes places the crystal out of equilibrium with its surroundings. In our schematic example, the crystal is transferred to a melt with lower trace element concentrations. Figure 3.2d shows how the composition of the crystal will evolve with time, as the crystal tries to re-equilibrate. In this example, the element shown in Figure 3.2d diffuses out of the crystal until its concentration is in equilibrium with the new melt.

The rate of diffusion is strongly dependent on the temperature. When the crystal is erupted, it cools rapidly and its composition becomes "frozen in". If the crystal is erupted before it completely re-equilibrates, then compositional profiles intermediate between the initial and equilibrium profiles can be preserved. We can use these profiles to estimate how much diffusion has taken place. If we know the rate at which diffusion occurs, then we can then calculate timescales from these profiles.

Below is a a more detailed discussion of the practical issues that need to be considered in order to extract timescales from diffusive gradients recorded in crystals.

3.3.1 Initial conditions

In order to model diffusion in a crystal, we first need a starting point. The example shown in Figure 3.2 is obviously very simple, and modelling real crystals can be much more complicated. Common initial conditions that are assumed include:

Homogeneous crystals

The simplest assumption that can be made for the initial conditions of a crystal is to presume that it was initially homogeneous. If the crystal grew in a stable environment, where storage conditions did not vary significantly during growth, then it would be homogeneous. However, diffusion can also produce homogeneous crystals. If diffusion is allowed to proceed for long enough, it will erase any zoning patterns that formed during crystal growth. This means that unzoned crystals that are in equilibrium with their host melts could be young (they grew from their host melt), or could be old (they re-equilibrated with their host melt). If a process such as recharge occurs repeatedly, the crystals may only record the last of these events. Diffusion can erase all trace of earlier episodes.

Unzoned crystals in equilibrium with their surroundings will not change their composition, and therefore cannot be used to estimate residence times. In order to set up compositional gradients, some processes must occur to set up disequilibrium between the crystal and its environment. Common processes include magma mixing, crustal assimilation and magma ascent (e.g. Bindeman and Valley, 2003; Charlier et al., 2012; Demouchy et al., 2006; Klügel, 1998; Martin et al., 2008; Pan and Batiza, 2002; Wolff et al., 2002). The range of processes that have previously been studied by diffusion chronometry is discussed in more detail in Section 3.5 below. Once disequilibrium is established, diffusion will begin. The timescales calculated in these diffusion models

will be estimates of the time that these crystals resided at high temperatures after whatever event created the disequilibrium.

Even if we can assume that the crystals were initially homogeneous, we still need to estimate their original composition. If diffusion is arrested early enough, the centre of the crystals will still preserve their original composition. Flat plateaus in the centres of compositional profiles are evidence that this is the case, and the plateau composition can be used as the initial composition of the entire crystal. Where the initial compositions cannot be estimated directly from the profiles, for example where diffusion has progressed to the point where the entire crystal has been affected, the most extreme possible variation between the initial and equilibrium composition can be chosen. This will give the maximum time that those crystals could have resided at high temperature (Zellmer et al., 1999, 2011). Rather than use the maximum possible variation in their crystals as the initial conditions, Zellmer et al. (2012) used the maximum observed variation. This gave residence times relative to the youngest crystal, that they argued had only resided in the magma for a short period based on independent evidence.

Sharp zone boundaries

Zones of different compositions can grown in crystals as a response to changing storage conditions, and these zones will not be in equilibrium with each other. Diffusion will act to smooth these zones. In diffusion chronometry, it is often assumed that the boundaries between these zones was initially sharp, and that any gradient is due diffusion. Models of diffusion between two zones will estimate the time that that crystal has resided at high temperature after the growth of the outer zone.

Like for homogeneous crystals above, if diffusion is arrested early enough then the original compositions of the two zones will be preserved far from the zone boundary. These compositions can then be used in analytical models with an initial step function for one-dimensional profiles (Figure 3.1), as well as simple two- and three-dimensional shapes. More complicated shapes can be modelled numerically.

In practice, the boundaries between two zones will be sharp if the storage conditions change fast compared to crystal growth, or if new storage conditions first trigger a period of partial dissolution before growth recommences. If the storage conditions change slowly, then the composition of the crystals will change gradually. This will lead to a compositional gradient rather than a sharp zone boundary. It is often difficult to tell the difference between gradients created by crystal growth from those created by diffusion. Growth gradients can sometimes be distinguished from diffusive gradients by their shape (Costa et al., 2008), or different isotopes of the same element can also sometimes be used to distinguish growth from diffusion (Sio et al., 2013). Some components, such as NaSi–CaAl in plagioclase and Al in orthopyroxene, diffuse so slowly that their concentrations are unlikely to have been modified over the lifetimes of the crystals (Section 3.4). Their zoning patterns can therefore be used to reconstruct the initial zoning patterns of elements that diffuse more quickly (e.g. Allan et al., 2013). However, even if it is not possible to rule out growth as the cause of compositional gradients, diffusion models can still give useful information. Assuming that the zone boundary was initially a step function will give maximum residence times.

Comparison with slowly diffusing elements

As well as using the qualitative zoning patterns of slowly diffusing elements to estimate the initial zoning patterns of fast-diffusing elements, some studies have used the concentrations of slowly diffusing elements to quantitatively calculate the initial concentrations of fast-diffusing elements.

Druitt et al. (2012) used the slower diffusion of Sr in plagioclase relative to Mg to recreate the original Mg concentrations of plagioclase crystals from Santorini. Sr and Mg are correlated with each other in whole rock data from Santorini, so they should also be correlated in plagioclase crystals. The initial Mg concentrations of the plagioclase crystals could then be estimated using their Sr concentrations, assuming that Sr had not diffused significantly, and any difference in the measured Mg concentrations was

then assumed to be due to diffusion of Mg.

Morgan and Blake (2005) started with the assumption that two different elements with different diffusion coefficients, such as Ba and Sr in feldspar, are often correlated in a crystal as it grows. This would occur if their liquid/crystal partition coefficients remain in a constant ratio, and if the concentration of the elements in the melt is not altered by magma mixing. If the diffusivities of the two elements are different, and neither element is in equilibrium across the crystal, then diffusion will act to reduce the correlation between them. Morgan and Blake (2005) fixed the profile of the fast-diffusing element, and modelled the diffusion of the slowly diffusing element. They showed that the time their models required to bring the composition of the back into correlation of the fast-diffusing element was simply related to the residence time of the crystals at high temperature.

Fractional crystallisation models

Where there is enough information on the magmatic system, then petrologic models can be employed to estimate the initial compositions of the crystals. For example, Zellmer et al. (2003) modelled crystallisation at Montserrat to estimate the initial Sr concentrations of their plagioclase. They found that crystallisation would increase the Sr concentration in the melt, but they argued that changes in the plagioclase/liquid partition coefficient would roughly cancel out this increase in the Sr concentrations of the plagioclase crystals. Zellmer et al. (2003) therefore used an initially uniform Sr concentration, and diffusion was then driven by the chemical potential gradient set up by the differing anorthite content of the adjacent plagioclase zones. Cooper and Kent (2014) also studied Sr diffusion in plagioclase. They used the rhyolite-MELTS fractional crystallisation model of Gualda et al. (2012a) in order to estimate the initial Sr concentration of their crystals.

3.3.2 Boundary conditions

The boundary conditions are the conditions at the edge of the system under study, usually the crystal face. Boundary conditions are said to be either "open" or "closed", depending on whether material can diffuse across them. This makes little difference to the form of the diffusion profile, but does affect the timescale calculated. Using a closed boundary when an open boundary should have been used can lead to underestimates of the timescale of more than one order of magnitude (Costa et al., 2008).

Closed boundaries can be applied if the crystal is surrounded by another phase in which either the diffusion of the element in question is much slower or it does not partition significantly into. In this case the external mineral quickly either becomes depleted or builds up an excess close to the boundary in the element in question, depending on which way diffusion across the boundary occurs. The greater the excess or depletion, the greater the reduction in diffusion across the boundary.

Diffusion of most elements in silicic melts, however, is generally much faster than in crystals (Zhang et al., 2010). This means that any element that diffuses out of a crystal into the melt can rapidly be transported away into and mixed into the rest of the melt. Similarly, any element that gets depleted close to the crystal/melt interface can swiftly be replaced. In some circumstances this can lead to fixed boundary conditions, for example if the melt volume in the chamber is large compared to the total volume of the crystals. However, if the melt volume is limited, diffusion into or out of the crystal can significantly change the concentrations in the melt. The melt composition can also change for other reasons, for example by fractional crystallisation or mafic recharge.

3.3.3 Picking a diffusion coefficient

Diffusion coefficients are measured experimentally using a variety of different techniques, reviewed recently by Cherniak et al. (2010). These methods usually involve placing a mineral grain or powder into a reservoir either enriched in the element in question or with an isotopic tracer, annealing the mineral under know conditions, and

then measuring how much diffusion has taken place. This is repeated under different experimental conditions to see how the diffusion coefficient varies, allowing empirical relationships between the diffusion coefficient and different variables to be formulated. A few studies use natural samples. These match two (or more) elements, one with known diffusion coefficients and one without. By comparing the compositional profiles of the two elements, the unknown diffusion coefficient can be calculated (e.g. Klügel, 2001; Qian et al., 2010).

In order to calculate timescales from diffusion profiles, it is important to pick a diffusion coefficient that is applicable to the system you are studying. Below is a discussion of how different factors can affect diffusion coefficients; the diffusion coefficients of the systems modelled in this thesis are reviewed in Section 3.4. All diffusion coefficients presented in the text are in $\mathrm{m^2\,s^{-1}}$.

Temperature

In order for an atom to jump from one site in the crystal lattice to an adjacent one, as is required for diffusion to occur, it must overcome an energy barrier Q ($\mathrm{J\,mol^{-1}}$). This leads to an Arrhenius equation linking diffusivity D exponentially to temperature T:

$$D = D_0 \exp\left(\frac{-Q}{RT}\right) \tag{3.17}$$

where D_0 is a constant. Most diffusion experiments span a range of temperatures, and the results are usually presented as fits to an Arrhenius equation.

Arrhenius plots (plots of $\log(D)$ against $1/T$) should form a straight line, with a gradient proportional to Q. However, at higher temperatures different mechanisms of diffusion can become active, leading to different activation energies (Chakraborty, 2008). These show up as kinks in an Arrhenius plot. For this reason, extrapolation outside the range of temperatures covered by experimental work is highly uncertain. The effects of other parameters, such as those discussed below, are incorporated into

D_0.

Anisotropy

Crystallographic direction can have a strong influence on diffusivity, with diffusion along fast directions up to an order of magnitude faster than along slow directions (e.g. Cherniak and Watson, 1994, 2012; Mackwell and Kohlstedt, 1990). However, even when the crystal structure of a mineral is anisotropic, such as feldspar, diffusion can still be isotropic (e.g. Behrens et al., 1990). The anisotropy of the systems modelled in this thesis are discussed below.

If the crystallographic orientation of a given sample is known, then the anisotropy of the system can be incorporated into diffusion models. If the orientation of the crystals being modelled is not known, the effects of anisotropy can be assessed by measuring diffusion profiles along different crystallographic directions.

Composition

The composition of a mineral can have an effect on the prevalence of defects in the crystal structure, and as diffusion often occurs via defects this can affect the diffusion coefficient. For example, in Fe-rich minerals such as pyroxene and olivine, the molar fraction of Fe (X_{Fe}) plays a large role in the formation of vacancies. When removing an atom from the crystalline structure to create a vacancy, charge balance must be maintained. Fe in the structure can change its valency from Fe^{2+} to Fe^{3+}, and this can balance the effective charge of a vacancy. This means that vacancy creation is more energetically favourable in Fe-rich compositions, increasing the diffusion rate for any element that diffuses through vacancies (Dohmen and Chakraborty, 2007; Ganguly and Tazzoli, 1994; Jaoul and Raterron, 1994).

Similar effects can be seen in plagioclase. Diffusion for elements such as Mg, K, Sr and Pb is fastest for Na-rich plagioclase and slowest for Ca-rich (Giletti and Casserly, 1994; Giletti and Shanahan, 1997; Van Orman et al., 2014). Again it is suggested

that this is due to the fact that the enthalpy of formation of vacancies depends on the composition, and is lower for the removal of Na^+ than Ca^{2+}. Vacancies would, therefore, be more common in more Na rich crystals, increasing the diffusion rate for those elements that diffuse through a vacancies. Elements that diffuse by jumping between interstitial sites rather than between vacancies, such as Li, do not show a compositional dependence on their diffusion coefficients because the number of available interstitial sites is unaffected by the composition (Giletti and Shanahan, 1997).

The effect of composition on the diffusion coefficient takes the form:

$$D_0 \propto \exp(\alpha X_i) \tag{3.18}$$

where α is a constant and X_i is either the molar fraction of Fe or anorthite, depending on the mineral. The specific compositional dependence of the systems studied in this thesis are presented in the next section.

Oxygen fugacity

Oxygen fugacity is found to have a strong influence on diffusion in Fe-rich minerals such as pyroxene and olivine. Diffusion is faster at higher oxygen fugacities, and this is again thought to be due to vacancies (Buening and Buseck, 1973; Dimanov and Wiedenbeck, 2006; Dohmen et al., 2007; Hermeling and Schmalzried, 1984). The more oxidising the conditions, the more Fe^{3+} there will be in the olivine, and hence the greater densities of vacancies.

Little work has been done on the effect of oxygen fugacity on diffusion in plagioclase. Cherniak (2003) found that Si diffusion in anorthite was slightly slower under reducing conditions (NNO buffer) than in samples annealed in air, but Giletti and Casserly (1994) found that Sr diffusion was within experimental error the same for annealing in air and with a graphite buffer.

The relationship between the diffusion coefficient is usually modelled using the

following relationship:

$$D_0 \propto (f\mathrm{O}_2)^m \tag{3.19}$$

where the exponent, m is based either on experimental data or on theoretical modelling of the physics of diffusion.

Water or hydrogen fugacity

A lot of the work on the effect of water fugacity on diffusion rates has been done in olivine, where it has important implications for diffusion-controlled deformation processes. The presence of small amounts of water is found to greatly increase the rates of Si, O and Fe–Mg diffusion in olivine (Costa and Chakraborty, 2008; Hier-Majumder et al., 2005; Wang et al., 2004). A similar effect is seen for Al–Si and O diffusion in feldspars (Farver and Yund, 1990; Graham and Elphick, 1990), as well as NaSi–CaAl interdiffusion in plagioclase (discussed below). The suggested mechanism for this effect is again through the creation of vacancies. H^+ can be accommodated in interstitial sites, providing charge balance for vacancies.

The form of water fugacity dependence is the same as for oxygen fugacity:

$$D_0 \propto (f\mathrm{H}_2\mathrm{O})^n \tag{3.20}$$

Pressure

Pressure also affects the diffusivity of elements. Pressure dependence is usually incorporated into the equation for the diffusion coefficient using an activation volume, V^*, in an analogous way to the activation energy, Q. This leads to the following relationship:

$$D_0 \propto \exp\left(\frac{PV^*}{RT}\right) \tag{3.21}$$

Diffusion experiments are often carried out at atmospheric pressure. Where high-pressure work has been done, it is often done on elements involved in diffusion creep

in minerals that are found in the mantle (e.g. Béjina et al., 2003). Activation volumes generally lie between 10^{-5} and 10^{-6} m^3 mol^{-1}, which is too small to have a large impact on diffusion coefficients at the pressures found in upper-crustal magma reservoirs (e.g. Béjina et al., 2003, and references therein). However, Yund and Snow (1989) found NaSi–CaAl diffusion in plagioclase could be significantly affected at upper-crustal pressures. The pressure dependence of individual diffusion coefficients, where that data exists, is discussed below.

Summary

A complete equation for the diffusion coefficient of an element, taking into account all the variables discussed above, takes the form:

$$D = D_0 \exp\left(\alpha X_i + \frac{-Q + PV^*}{RT}\right) \times (f\mathrm{O}_2)^m \times (f\mathrm{H}_2\mathrm{O})^n \tag{3.22}$$

However, most diffusion coefficients have not been studied in enough detail to fully quantify the relationships between all these different parameters. These diffusion coefficients will only be valid under the experimental conditions at which they were determined, and care must be taken in extrapolating them to other conditions.

3.4 Diffusion coefficients used in this thesis

Recent reviews of the experimental data on diffusion coefficients in plagioclase and orthopyroxene have been written by Cherniak (2010) and Cherniak and Dimanov (2010), respectively. Below is a summary of the data for the elements I have used in this thesis.

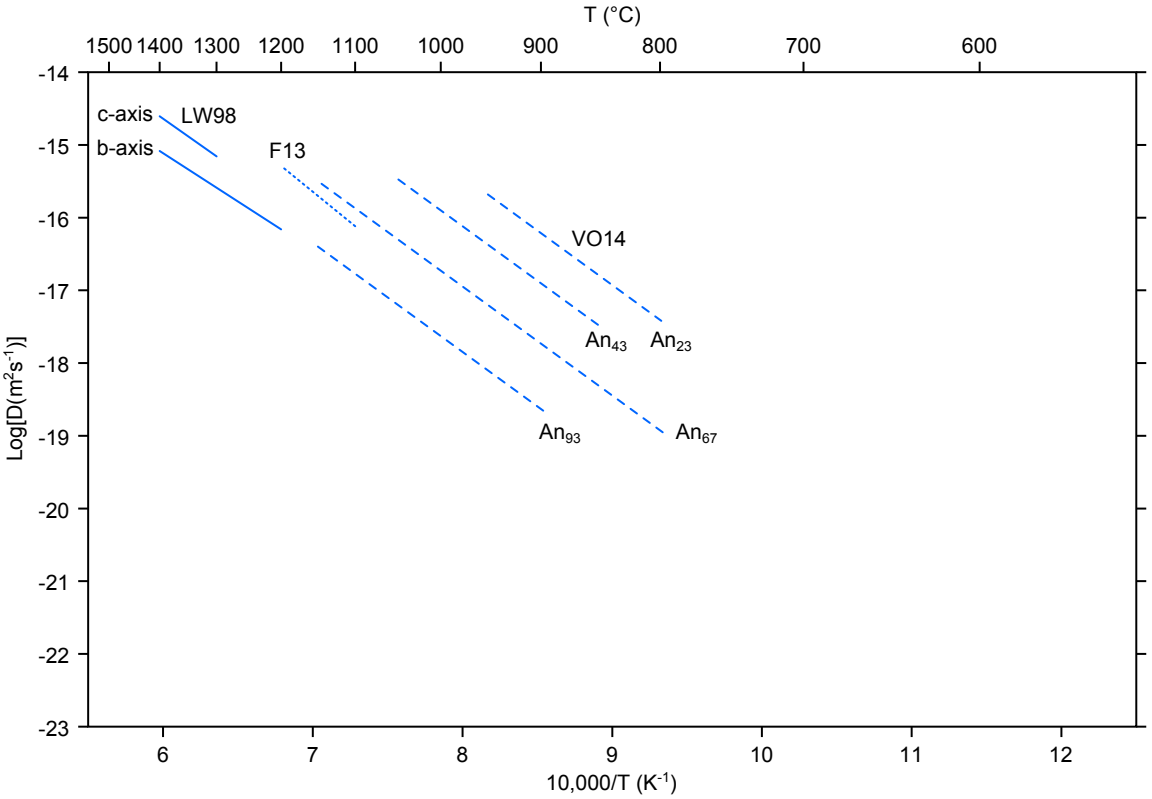

Figure 3.3: Diffusion coefficients for Mg in plagioclase. References: LW98 (solid lines): LaTourrette and Wasserburg (1998); F13 (dotted line): Faak et al. (2013), silica saturated; VO14 (dashed lines): Van Orman et al. (2014).

3.4.1 Plagioclase

Magnesium

Three studies have systematically investigated the diffusion coefficient of Mg in plagioclase, and these are shown in Figure 3.3. LaTourrette and Wasserburg (1998) carried out their experiments in crystals of An_{95} at high temperature, while Faak et al. (2013) used plagioclase crystals of An_{50} to An_{67}, and Van Orman et al. (2014) used plagioclase crystals with compositions between An_{23} and An_{93}.

All three studies report similar activation energies: LaTourrette and Wasserburg (1998) give 254 ± 43 and $278 \pm 43\,\mathrm{kJ\,mol^{-1}}$ for diffusion parallel to the b and c axes, respectively; Faak et al. (2013) give $321\,\mathrm{kJ\,mol^{-1}}$; and Van Orman et al. (2014) give $287 \pm 10\,\mathrm{kJ\,mol^{-1}}$. Both LaTourrette and Wasserburg (1998) and Van Orman et al. (2014) find slight anisotropy for Mg diffusion, with diffusion parallel to the c axis

up to 2–3 times as fast as diffusion parallel to the b axis. Van Orman et al. (2014) find a large compositional (i.e. X_{An}) dependence, similar to that reported for Sr, Pb, Ba, Nd and Ca (Behrens et al., 1990; Cherniak, 1995, 2002a,b; Cherniak and Watson, 1994; LaTourrette and Wasserburg, 1998). However, Faak et al. (2013) do not find this compositional dependence over the range of plagioclase compositions that they studied (An_{50-67}). Faak et al. (2013) report a dependence on the activity of silica, with $D_{\mathrm{Mg}}^{\mathrm{plag}} \propto (a_{\mathrm{SiO_2}})^{2.6}$.

In this thesis I choose to use the data of Van Orman et al. (2014), as their experiments cover the largest range of temperatures and plagioclase compositions. Importantly, their temperature range includes the temperatures of Santorini dacites and rhyodacites (Chapter 5), therefore extrapolation to lower temperatures is not required. Their complete equation for the diffusion of Mg as a function of temperature and plagioclase composition is:

$$D_{\mathrm{Mg}}^{\mathrm{plag}} = \exp\left[(-6.06 \pm 1.10) - (7.96 \pm 0.42)\, X_{\mathrm{An}} - \frac{287,000 \pm 10,000}{RT}\right] \tag{3.23}$$

Strontium

Three major studies have systematically looked at Sr diffusion in plagioclase, and these are shown in Figure 3.4. Not shown are the results of LaTourrette and Wasserburg (1998), who also compared Sr diffusion to Mg diffusion in An_{95}. They did not get enough data on Sr diffusion to calculate an Arrhenius relationship, but found it to be a factor of 100 slower than Mg diffusion at the same temperature (consistent with the data of Giletti and Casserly (1994) and Cherniak and Watson (1992) shown in Figure 3.4).

All three studies found that Sr has similar activation energies to Mg. Giletti and Casserly (1994) found an activation energy of $276\,\mathrm{kJ\,mol^{-1}}$ fit all their data, regardless of composition; Cherniak and Watson (1994) present activation energies of 273 ± 13, 265 ± 8, and $268 \pm 8\,\mathrm{kJ\,mol^{-1}}$ for An_{23}, An_{43}, and An_{67}, respectively; and Cherniak

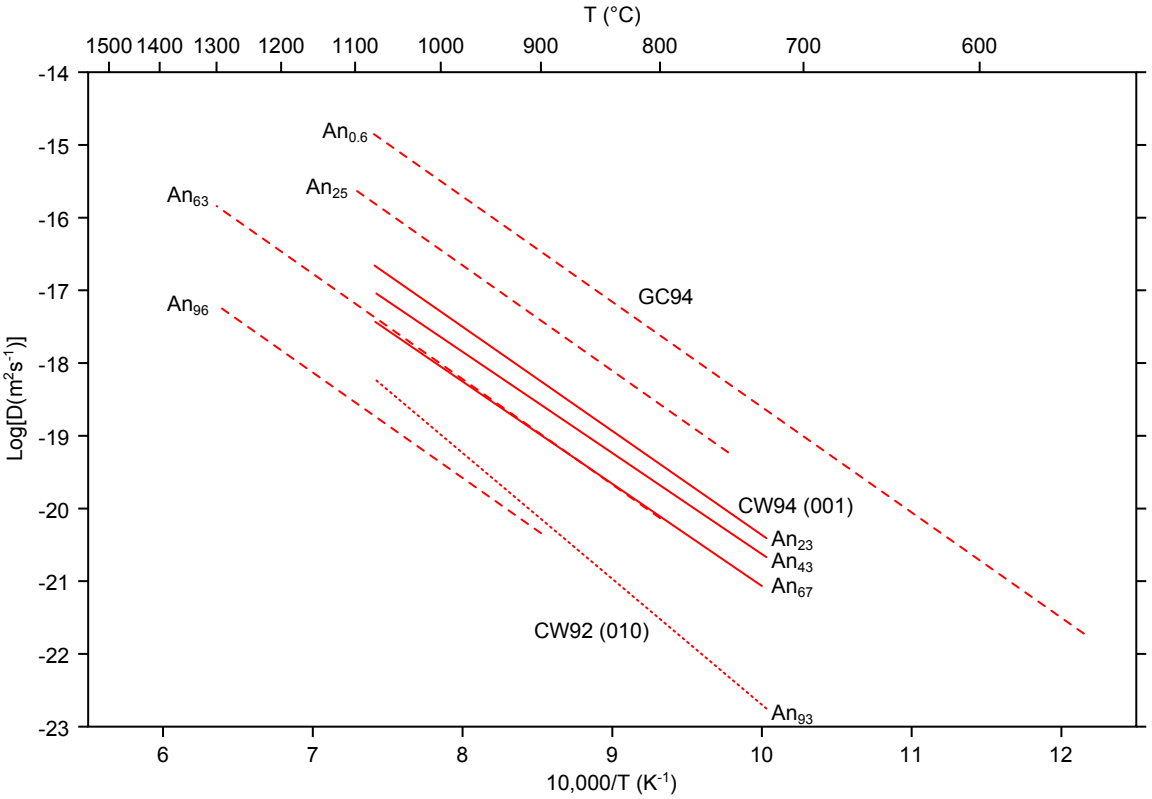

Figure 3.4: Diffusion coefficients for Sr in plagioclase. References: CW92 (dotted line): Cherniak and Watson (1992); CW94 (solid line): Cherniak and Watson (1994); GC94 (dashed line); Giletti and Casserly (1994).

and Watson (1992) present a slightly higher value of $330 \pm 23\,\mathrm{kJ\,mol^{-1}}$ for An_{93}.

Both Giletti and Casserly (1994) and Cherniak and Watson (1994) found that the diffusion rate increases with a decrease in the anorthite content of the plagioclase. There is good agreement on the diffusion coefficient of Sr in An_{95} and An_{65}, however, Giletti and Casserly (1994) find higher diffusion coefficients than Cherniak and Watson (1994) in more sodic plagioclase (Figure 3.4).

The complete function for the diffusion coefficient of Sr calculated by Giletti and Casserly (1994) is:

$$D_{\mathrm{Sr}}^{\mathrm{plag}} = \exp\left(-18.8 + 9.4 X_{\mathrm{Ab}} + \frac{276,000}{RT}\right) \tag{3.24}$$

where X_{Ab} is the molar fraction of albite.

Cherniak and Watson (1994) found that diffusion normal to (010) was about 0.7 log

units slower that normal to (001), but that this anisotropy was less pronounced in their more sodic samples. Giletti and Casserly (1994) compared their data to that of Giletti (1991), and found that Sr diffusion in albite ($An_{0.6}$) was isotropic, unaffected by oxygen and water fugacity, and unaffected by pressure up to at least 100 MPa.

Potassium

The diffusion of K in plagioclase was measured by Giletti and Shanahan (1997), and their results are shown in Figure 3.5. Giletti and Shanahan (1997) compared their results for K diffusion in albite ($An_{0.6}$) to those of Kasper (1975), reported in Brady (1995), and found that their results were slower than Kasper (1975)'s by about an order of magnitude. The bulk diffusion method used by Kasper (1975) tends to overestimate diffusion coefficients; calculating diffusion coefficients from compositional profiles, as was done by Giletti and Shanahan (1997), should be more accurate.

In An_{67}, the diffusion coefficient of K is similar to that of Mg found by Van Orman et al. (2014). Like Mg and Sr, K diffusion is faster in more sodic plagioclase. However, the compositional dependence of K diffusion is not as strong as that found for Mg by Van Orman et al. (2014), or as strong as that found for Sr by Giletti and Casserly (1994). Giletti and Shanahan (1997) report no dependence on water pressure between 0.004 and 100 MPa.

The Arrhenius relationships for K diffusion Giletti and Shanahan (1997) found for K are, for An_{67}:

$$D_{\mathrm{K}}^{\mathrm{plag}} = 10^{-5.5\pm3.8} \exp\left(\frac{-278,000 \pm 82,000}{RT}\right) \tag{3.25}$$

and, for An_{27}:

$$D_{\mathrm{K}}^{\mathrm{plag}} = 10^{-5.2\pm2.5} \exp\left(\frac{-264,000 \pm 53,000}{RT}\right) \tag{3.26}$$

Lanthanum

The diffusion coefficient of four REE (La, Nd, Dy and Yb) in plagioclase were measured by Cherniak (2002b), and the results for La are shown in Figure 3.5. The Arrhenius

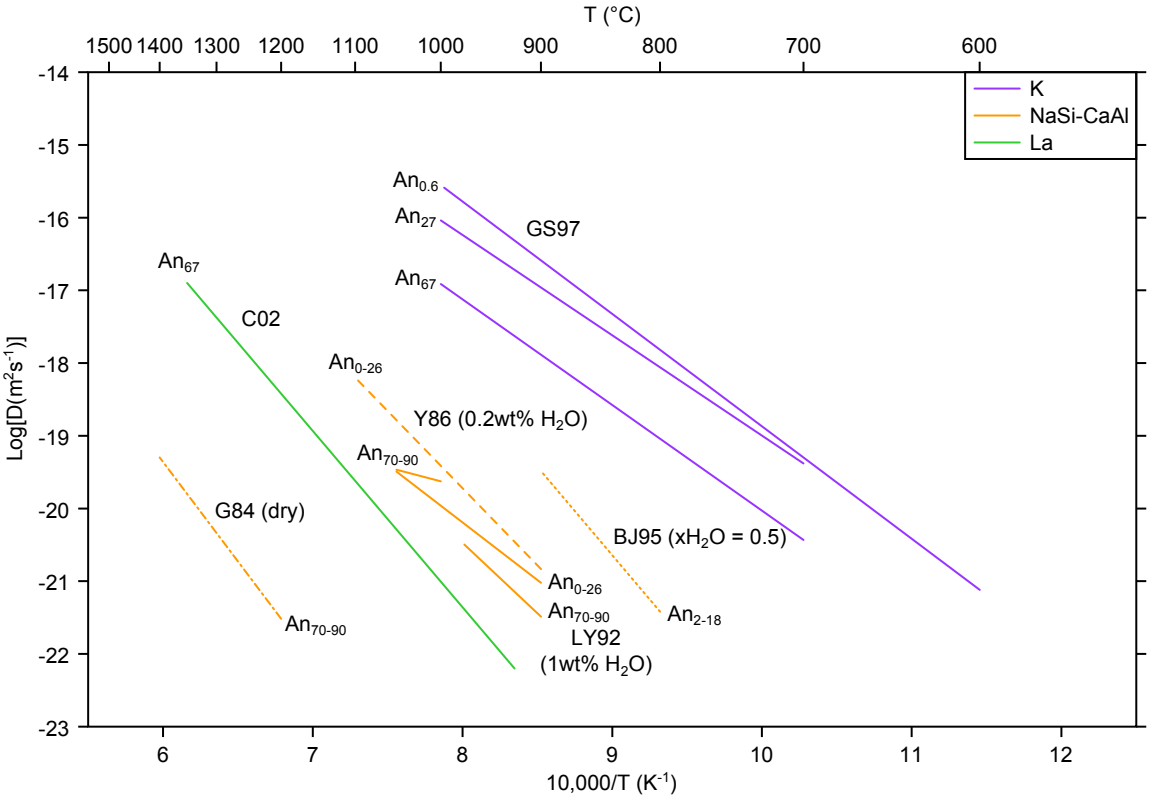

Figure 3.5: Diffusion coefficients for K (purple), NaSi–CaAl (orange) and La (green) in plagioclase. References: BJ95 (dotted line): Baschek and Johannes (1995); C02 (solid green line): Cherniak (2002b); GS97 (solid purple lines): Giletti and Shanahan (1997); G84 (dot-dashed line): Grove et al. (1984); LY92 (solid orange lines): Liu and Yund (1992); Y86 (dashed line): Yund (1986).

relationship for La calculated by Cherniak (2002b) is:

$$D_{\mathrm{La}}^{\mathrm{plag}} = 1.1 \times 10^{-2} \exp\left(\frac{-464,000}{RT}\right) \tag{3.27}$$

The diffusion coefficients for the four REE measured by Cherniak (2002b) are almost identical in An_{67}. Cherniak (2002b) also measured the diffusion coefficient of Nd in An_{23} and An_{93}, and found that Nd diffused faster in more sodic plagioclase. This is consistent with the results for Mg, Sr and K discussed above, and it is likely that La will also diffuse more quickly in more sodic plagioclase.

NaSi–CaAl interdiffusion

The experimental data for NaSi–CaAl interdiffusion is also shown in Figure 3.5. Most of the experiments on NaSi–CaAl interdiffusion use the homogenisation of exsolution lamellae in plagioclase, which is assumed to occur by diffusion. The diffusion coefficient may vary across the lamellae, for example due to compositional differences; this method calculates the average diffusion coefficient.

There is a large range of diffusion coefficients for NaSi–CaAl interdiffusion; this is partly down to the different experimental conditions. Grove et al. (1984) found the slowest diffusion coefficients, in An_{70-90} annealed in air at atmospheric pressure. Their Arrhenius relationship is:

$$D^{\text{plag}}_{\text{NaSi–CaAl}} = 1.01 \times 10^{-3} \exp\left(\frac{-516,000}{RT}\right) \tag{3.28}$$

Yund (1986) carried out experiments in An_{0-26}. One experiment annealed in air gave a maximum diffusion coefficient consistent with the experiments of Grove et al. (1984) in An_{70-90}. However, in Yund (1986)'s experiments at 1.5 GPa with 0.2 wt% water added, NaSi–CaAl interdiffusion was several orders of magnitude faster. The Arrhenius relationship they presented for their wet data is:

$$D^{\text{plag}}_{\text{NaSi–CaAl}} = 1.8^{+10.8}_{-1.5} \times 10^{-3} \exp\left(\frac{-406,000 \pm 20,000}{RT}\right) \tag{3.29}$$

Liu and Yund (1992) carried out similar experiments to Yund (1986), with An_{0-26} and An_{70-90} at 1.5 GPa wit 1 wt% water. All of these experiments give similar diffusion coefficients for NaSi–CaAl interdiffusion, which suggests that there is little dependence on plagioclase composition. Liu and Yund (1992) did find a discontinuity in their data for An_{70-90} between 975 and 1000 °C, which they attributed to a change in the microstructure of the lamellae between these temperatures.

The effects of hydrogen fugacity and confining pressure on NaSi–CaAl interdiffusion

were investigated by Yund and Snow (1989). The hydrogen fugacity was varied by using three different buffers: wüstite–magnetite (WM), magnetite–haematite (MH), and Mn_3O_4–Mn_2O_3 (MO). Yund and Snow (1989) concluded that while hydrogen fugacity does effect $D^{\text{plag}}_{\text{NaSi–CaAl}}$, the range of hydrogen fugacities found in igneous rocks will not change $D^{\text{plag}}_{\text{NaSi–CaAl}}$ by more than about a factor of 2.

The effect of confining pressure found by Yund and Snow (1989) is much greater. At a constant hydrogen fugacity, $D^{\text{plag}}_{\text{NaSi–CaAl}}$ increases by a factor of about 18 between 0.1 and 500 MPa. The rate of change of $D^{\text{plag}}_{\text{NaSi–CaAl}}$ with pressure decreases above 500 MPa: between 500 and 1,500 MPa $D^{\text{plag}}_{\text{NaSi–CaAl}}$ only increases by a factor of about 3.

The effect of water on NaSi–CaAl interdiffusion was also studied by Baschek and Johannes (1995), who used different N_2–H_2O fluids to vary X_{H_2O} between 0 and 0.5. They found that $D_{\text{NaSi–CaAl}}$ increased by a factor of 2.2 with a 0.1 increase in X_{H_2O}. Their diffusion coefficients were faster than those found by Yund (1986), Yund and Snow (1989) and Liu and Yund (1992), a difference Baschek and Johannes (1995) attributed to differences in the vapour phase present.

3.4.2 Orthopyroxene

Fe–Mg

The available experimental data for Fe-Mg and Al diffusion in orthopyroxene are shown in Figure 3.6.

Ganguly and Tazzoli (1994) used crystal ordering processes to calculate the average diffusion coefficient for Fe–Mg in orthopyroxene along the b and c directions. Their theoretical work suggested that diffusion should be fastest along the c direction and slowest parallel to the a direction. The diffusion coefficient along the c direction that they calculated is:

$$D^{\text{opx}}_{\text{Fe–Mg}} = \exp\left(-6.77 - 5.99X_{\text{Mg}} - \frac{240,000}{RT}\right) \tag{3.30}$$

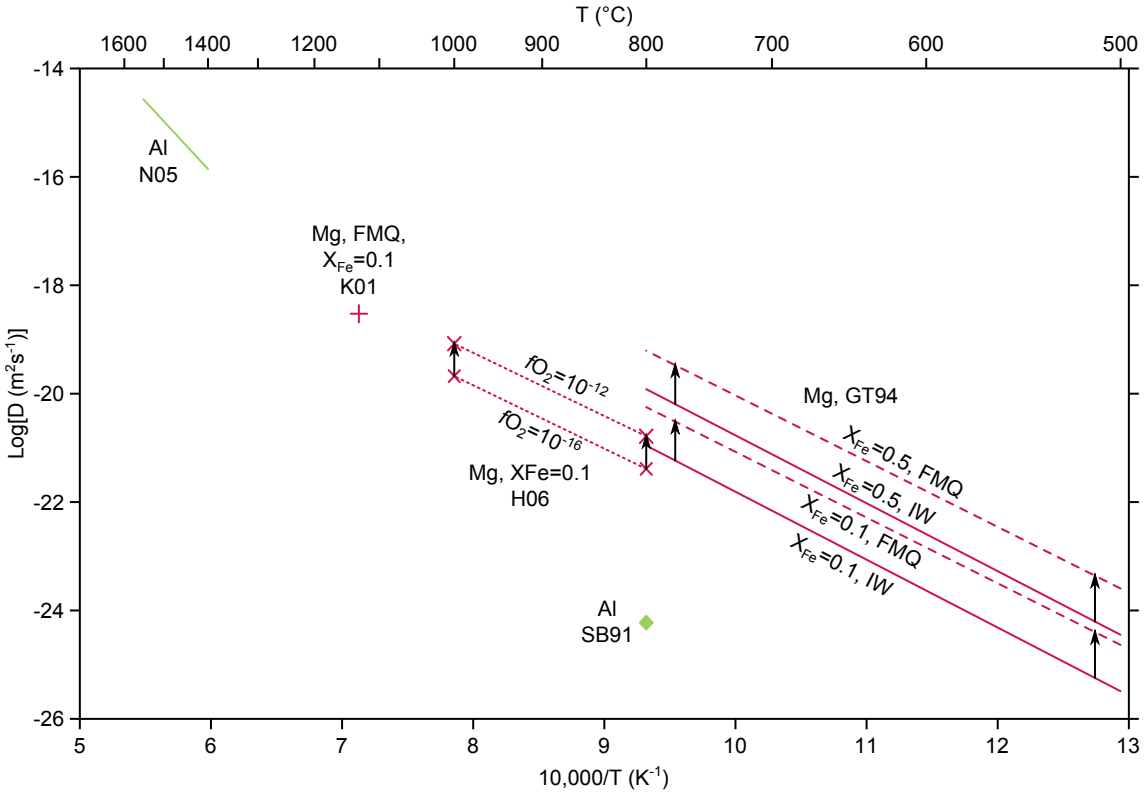

Figure 3.6: Diffusion coefficients of Fe–Mg (pink) and Al (green) in orthopyroxene. Fe–Mg data: GT94: original data of Ganguly and Tazzoli (1994) calculated for orthopyroxene with $X_{\mathrm{Fe}} = 0.1$ and $X_{\mathrm{Fe}} = 0.5$ IW buffer shown with solid lines, dashed lines are re-calculated for the FMQ buffer as discussed in the text; H06: ter Heege et al. (2006); K01: Klügel (2001). Al data: SB91: the minimum diffusion coefficient of Smith and Barron (1991); N05: Nakagawa et al. (2005).

Klügel (2001) found zoned olivine and orthopyroxene crystals in a harzburgite xenolith. They used the well-constrained diffusion coefficient of Fe–Mg in olivine to calculate the diffusion coefficient of $3 \times 10^{-19}\,\mathrm{m^2\,s^{-1}}$ for Fe–Mg diffusion in orthopyroxene at 1,130 °C. This is consistent with the data of Ganguly and Tazzoli (1994) extrapolated to high temperatures, and similar to the diffusion coefficient of (Fe,Mn)–Mg in clinopyroxene (Dimanov and Sautter, 2000; Müller et al., 2013). A small amount of data is presented in the abstract of ter Heege et al. (2006), and their diffusion coefficients are consistent with those of Ganguly and Tazzoli (1994) and Klügel (2001).

The diffusion coefficient calculated by Ganguly and Tazzoli (1994) was calibrated at the IW oxygen buffer, which is significantly more reduced than most magmatic systems (Frost, 1991). This can be corrected using the relationship $D \propto (fO_2)^m$.

Data on Fe–Mg ordering processes in orthopyroxene suggest that the exponent should be between 1/5.5 and 1/6.5 ($m \approx 0.17$; Stimpfl et al., 2005). This is similar to the exponent estimated for (Fe,Mn)–Mg diffusion in clinopyroxene (0.22 ± 0.02; Dimanov and Wiedenbeck, 2006). Ter Heege et al. (2006) state that in their experiments $D^{\text{opx}}_{\text{Fe–Mg}}$ increases by a factor of ∼4 when oxygen fugacity increases from 10^{-12} to 10^{-16} bar; this gives an exponent of ∼0.15. The diffusion coefficient of Ganguly and Tazzoli (1994) can be corrected for oxygen fugacity to give the following equation, which is used throughout this thesis:

$$D^{\text{opx}}_{\text{Fe–Mg}} = \exp\left(-6.77 - 5.99X_{\text{Mg}} - \frac{240,000}{RT}\right) \times \left(\frac{f\text{O}_2\,(\text{sample})}{f\text{O}_2\,(\text{IW buffer})}\right)^{\frac{1}{6}} \tag{3.31}$$

where $f\text{O}_2\,(\text{sample})$ is the oxygen fugacity of the sample for which we want to calculate $D^{\text{opx}}_{\text{Fe–Mg}}$, and $f\text{O}_2\,(\text{IW buffer})$ is the oxygen fugacity of the IW buffer at the temperature and pressure of interest.

Aluminium

Very little experimental work has been done on the diffusion coefficient of Al in orthopyroxene, but the available constraints are shown in Figure 3.6. A minimum diffusion coefficient of $6 \times 10^{-25}\,\text{m}^2\,\text{s}^{-1}$ was calculated by Smith and Barron (1991) using zoned orthopyroxene and garnet crystals in mantle xenoliths. Nakagawa et al. (2005) present (in abstract form) the results from high-temperature experiments that are consistent with the minimum diffusion coefficient of Smith and Barron (1991), and calculate the following equation for diffusion parallel to the c axis:

$$D^{\text{opx}}_{\text{Al}} = 0.621^{+5.35}_{-0.576} \exp\left(\frac{501,000 \pm 35,000}{RT}\right) \tag{3.32}$$

Nakagawa et al. (2005) also find that diffusion parallel to the a axis is about one order of magnitude slower than that parallel to the c axis.

3.5 Previous studies

The following discussion is not meant as an exhaustive review of all diffusion chronometry studies done to date, but instead is intended as an introduction to the range of magmatic processes that have been studied using this technique.

3.5.1 Magmatic recharge

Magma mixing is often thought to have triggered eruptions, and diffusion chronometry has been used to estimate the time between mixing and eruption. This has been done for many different types of eruptions, including: mid-ocean ridge basalts (Pan and Batiza, 2002; Zellmer et al., 2012, 2011), flood basalts (Ramos et al., 2005), arc basalts (Kahl et al., 2011; Parkinson et al., 2007; Saito et al., 2010), effusive andesitic eruptions (Coombs et al., 2000; Davidson et al., 2001), explosive andesitic eruptions (Andrews et al., 2008), effusive silicic eruptions (Costa and Chakraborty, 2004; Martin et al., 2008; Nakamura, 1995), explosive silicic eruptions (Druitt et al., 2012; Finney et al., 2008; Martí et al., 2013; Morgan et al., 2006; Ruprecht and Cooper, 2012; Tomiya and Takahashi, 2005). The composition and volume of the magma intruded varies between studies, but they all suggest that a recharge event occurred anywhere from a few days to a few decades before eruption. Diffusion chronometry suggests that even the largest eruptions — such as the Bishop Tuff, Bandelier Tuff, Cerro Galán ignimbrite, and Whakamaru eruption — can be triggered by magmatic recharge less than a few thousand years, and possibly just a few years, before eruption (Boyce and Hervig, 2008; Gualda et al., 2012b; Hervig and Dunbar, 1992; Saunders et al., 2010; Wark et al., 2007; Wilcock et al., 2012).

3.5.2 Mush rejuvenation

While most of the studies above assume that the recharge magma is intruded in to a melt-dominated reservoirs, other studies have looked at the remobilisation of crys-

tal mushes by magmatic recharge. For mafic magmas, the estimated times between intrusion and eruption are only a few days to a few years (Costa et al., 2009; Suzuki et al., 2013). In andesitic systems, the times found are decades to centuries (Cooper and Kent, 2014; Zellmer et al., 1999, 2003). Longer remobilisation times are found for large silicic systems, of a few centuries to a few thousand years (Girard and Stix, 2010; Smith et al., 2010). However, even in these systems, the final, triggering input can occur within a few decades of eruption (Matthews et al., 2012a,b).

3.5.3 Vapour fluxing

As well as the input of fresh magma, the input of vapour can be timed by diffusion chronometry. Plagioclase phenocrysts from the 2004 dome-forming eruption of Mount St. Helens are enriched in Li relative to plagioclase in gabbroic inclusions in the same lava. Kent et al. (2007) assumed that the Li enrichment in the phenocrysts was due to the transfer of a Li-rich vapour phase into the magma reservoir before eruption. The lower Li content in the gabbroic inclusions would be due to their larger size, and the longer time it would take for them to re-equilibrate diffusively. Kent et al. (2007) calculated that the gabbroic inclusions would not be able to preserve their low Li contents for more than about a year. Kent et al. (2007) also found Li concentration gradients in the plagioclase phenocrysts, with Li contents decreasing towards the rim. They explained this through late-stage degassing of the magma, and diffusion models of the Li gradients suggest that this degassing occurred at most one or two weeks before eruption.

3.5.4 Crustal assimilation

Crystals will inherit their isotopic ratios from their host melt during growth. If the isotopic ratio of the melt subsequently changes, then diffusion will act to re-equilibrate the crystals' isotopic ratios. Diffusion chronometry can be used to time the input of magma from different sources, based upon different isotopic ratios. The low spatial

resolution of techniques capable of determining isotopic ratios does somewhat limit the precision of the timescales estimates that are possible using this method, however.

Several studies have found that crystals record an input of low $^{87}Sr/^{86}Sr$ magmas at most a few thousand years (and down to only a few years) before eruption (Davidson et al., 2001; Ramos et al., 2005). The low $^{87}Sr/^{86}Sr$ magmas are interpreted to be primitive recharge magmas intruded into a crustally contaminated magma reservoir. While the $^{87}Sr/^{86}Sr$ variations of the crystals reveal that crustal contamination is implicated in the generation of these magmas, the timescales estimated from diffusion chronometry relate only to the timescales of mafic recharge.

Bindeman and Valley (2001, 2003) found that the cores of some zircon and quartz crystals in rhyolites from Yellowstone and the Southwestern Nevada Volcanic Field had higher $\delta^{18}O$ than their host melt. The lower $\delta^{18}O$ of the host melt is thought to result from the melting of hydrothermally altered plutonic rocks. The high $\delta^{18}O$ quartz and zircon crystals are interpreted to have remained unaltered in the pluton, before being incorporated into the melt. Once in the melt, they began to exchange O isotopes diffusively. The gradients in O isotopes at the edge of the crystals were modelled to show that these crystals were incorporated into the melt only 10^3–10^4 y before eruption. Slightly shorter timescales of crustal assimilation were found in the Bandelier Tuff by Wolff et al. (2002), who used the fact that quartz and feldspar would equilibrate diffusively at different speeds. Wolff et al. (2002) estimated assimilation occurred $\sim 10^2$ y before the eruption of the Bandelier Tuff.

O isotopes have also been used to time crustal assimilation in basaltic systems. Bindeman et al. (2006) found that olivine and plagioclase crystal from the Laki fissure eruption recorded assimilation of altered basaltic hyloclastites. Diffusion modelling estimated that this occurred less than a few thousand years before eruption.

3.5.5 Magma ascent

Mantle xenoliths have been used to calculate magma ascent rates via diffusion chronometry. Klügel (1998) studied a series of fractures in peridotite xenoliths in a basanite lava from La Palma in the Canary Islands. Fe–Mg gradients extend from the fracture surfaces into the xenoliths, and these are interpreted to be the result of diffusion. The timescales estimated by the modelling of these diffusive gradients fall into two populations. The older population has ages of between 6 and 83 y, and this is thought to represent the time during which the xenoliths were incorporated into their host melt at depth, transported to a shallow magma reservoir, and then stored before eruption. The younger population has ages of less than a few days; Klügel (1998) suggested that this is the time it took for the xenoliths to be transported from the shallow magma reservoir to the surface. Ruprecht and Plank (2013) also looked at the rise of melts from the mantle, by modelling Ni diffusion in olivine crystals from an andesitic eruption of Irazú volcano, Costa Rica. They found that olivine crystals from primitive mantle melts had magmatic residence times of a few months to a few years, suggesting that those mantle melts ascended only a short time before eruption.

Other studies have shown even faster ascent rates from the mantle all the way to the surface. Kelley and Wartho (2000) used Ar diffusion in phlogopite grains in mantle xenoliths to estimate rise times of a few hours to a few days. Demouchy et al. (2006) used hydrogen gradients in olivine crystals from peridotite xenoliths to estimate ascent times of a few hours for the Pali-Aike alkali basalt in Chile. Fe–Mg gradients in olivine crystals found in lherzolite xenoliths from the Hangay dome in Mongolia were modelled by Harris et al. (2009), who found rise times of about four days.

Many orthopyroxene crystals from the rhyolitic Oruanui eruption have internal resorption surfaces that Allan et al. (2013) suggest was caused by decompression. Allan et al. (2013) interpret this as recording the transfer of the Oruanui magma from a deep source mush to a shallower holding reservoir. Diffusion models across these resorption surfaces give the residence times of these crystals after orthopyroxene growth

recommenced in the shallow reservoir. Allan et al. (2013) found that these residence times were less than 1,600 y, and most of the crystals had residence times of less than 500 y. The final ascent of the Oruanui magma from the shallow holding reservoir to the surface has also been estimated, by Charlier et al. (2012), using Li gradients in quartz and feldspar crystals. Li diffusion was driven by a change in partitioning behaviour during decompression. Because Li diffuses rapidly in quartz and feldspar at magmatic temperatures, ascent times of only 125 to 720 s (equivalent to ascent speeds of 4–21 $\mathrm{m\,s^{-1}}$) could be recorded by the Li gradients.

Chapter 4

Fieldwork and age constraints

4.1 Introduction

The Therasia dome complex is $\sim$2 km^3 of mainly dacitic domes and coulées that underlies the explosive 22-ka Cape Riva eruption (Druitt, 1985; Druitt et al., 1999). The caldera collapse that accompanied the Cape Riva eruption cut the Therasia dome complex, and exposed a series of lava flows that should record the build-up to a Plinian eruption. Previous studies have noted the similarity in the chemistry and petrology of the Therasia dacites with the dacite erupted during the Cape Riva eruption. This led to the suggestion that the Therasia dacites were leaks from a growing Cape Riva magma chamber, similar to models proposed for Mt Mazama at Crater Lake (Oregon) and Glass Mountain in Long Valley (California) (Bacon, 1985; Bacon and Druitt, 1988; Druitt, 1985; Druitt and Bacon, 1989; Hildreth and Wilson, 2007).

In order to investigate the processes involved in the build-up to the Cape Riva eruption, and the timescales associated with those processes, it is first important to establish the stratigraphy of the lavas. The stratigraphy provides a framework which allows us to see how the chemistry and petrology of the system evolves with time (Chapter 5).

4.2 Methods

Lavas of the Therasia dome complex cropping out in the caldera cliffs were photographed from a boat, and the photos were merged using computer software and interpreted to produce synthetic sections detailing the relationships and lateral extents of individual lavas. Correlations were checked by on-land observations, and stratigraphic relationships were mapped out. Pumice layers and palaeosols between the lavas were also mapped.

Lavas from four key stratigraphic levels were dated by Dr Stépahane Scaillet using the $^{40}Ar/^{39}Ar$ technique (Fabbro et al., 2013). The groundmass of each sample was separated, hand-picked, and cleaned in an ultrasonic bath of dilute nitric acid prior to irradiation in the Cd-lined fast neutron slot $\beta 1$ of the Osiris reactor (CEA, Saclay) with sanidine ACR (1.206 ± 0.002 Ma, Renne et al., 2011, 2010). Upon receipt from the nuclear reactor, the samples were analysed by multiple laser fusion using a high-sensitivity MM5400 mass spectrometer operated in pulse-counting mode following the experimental and correction procedures of Scaillet et al. (2011, 2008). More than 25 individual ages were extracted from each sample via a two-step fusion of $\sim$10 mg of groundmass replicates (see procedural details in Scaillet et al., 2011).

4.3 Results

4.3.1 Field and stratigraphic relationships

Photographs and sketches of the Therasia cliffs are shown in Figure 4.1 and of the cliffs at Oia and Fira in Figure 4.2. Schematic diagrams summarising the architecture of the lavas are shown in Figure 4.3 with individual lavas numbered for reference, and Figure 4.4 shows the locations of the pumice falls and soil horizons between the lava flows. Lavas of the Therasia dome complex overlie Upper Scoria 2, separated by a palaeosol. They make up much of the present-day cliffs of Therasia (flows 1–24), and

one lava crops out at the top of the caldera wall north of Fira town (flow 25). Thin lava flows occupying the same stratigraphic position (between Upper Scoria and Cape Riva) occur beneath the town of Oia (flow 26; Andesite of Oia of Druitt et al., 1999).

The lava succession on Therasia consists of many individual lava flows, coulées and domes (termed flows for short). Individual flows range in thickness up to 60 m (Figure 4.5a,b); thin flows tend to be dark grey and glassy, whereas thicker ones are pale grey and de-vitrified. Many exhibit flow banding that is most evident in the thicker, de-vitrified flows. The greatest accumulated thicknesses occur near Cape Tripiti (∼150 m) and Mount Viglos (∼200 m), where, at each location, nine flows are stacked. Correlations of individual flows between the Tripiti and Viglos sections is difficult, as only two flows (3 and 4) are continuous between them. Flows 1 and 24 are compositionally very similar, and are probably the same flow. This is also true of flows 11 and 22.

Most of the lava flows on Therasia are dacitic to rhyodacitic, with two exceptions. First, the basal flows 1 and 24 are andesitic, and we refer to them jointly as the lower Therasia andesite. Second, the topmost flow on Mount Viglos (flow 22) is also andesitic, and we refer to this (and the compositionally similar flow 11) as the upper Therasia andesite. Enclaves of quenched basaltic magma with crenulated margins occur in some of the lowest lavas (flows 1 and 3; Figure 4.5c) and towards the top of the succession (flows 22 and 25); rare gabbroic enclaves also occur. The chemistry of the different units is discussed in more detail in Chapter 5. The widespread distribution of the Therasia lavas show that they were fed from vents extending from the summit to the western flank of the Skaros shield. The feeder dyke of flow 3 is preserved at Cape Tripiti (Figure 4.1b, c). The dyke is oriented NE-SW, parallel to the main dyke trend in northern Thera and the alignment of the recent vents on the Kameni Islands (Druitt et al., 1999; Heiken and McCoy, 1984).

At least five dacitic pumice fall units and a phreatomagmatic tuff occur intercalated within the Therasia succession (Figure 4.4). The pyroclastic units are concentrated towards the top of the succession (younger than flow 7 at Tripiti and younger than

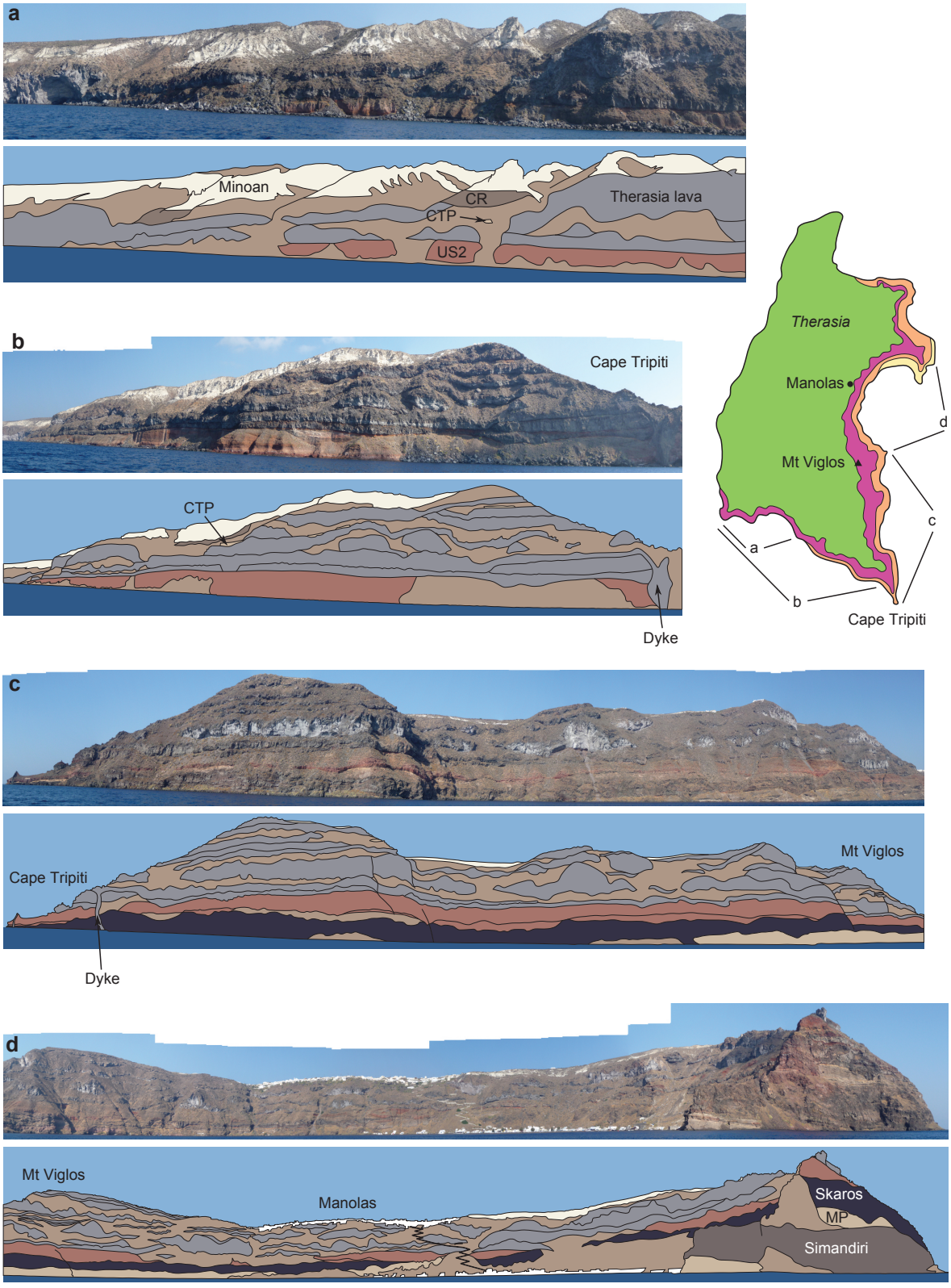

Figure 4.1: Photos of the cliffs of Therasia, and the sketches drawn from them. Inset is a map of Therasia, showing where the photos of the cliffs were taken from. CR = Cape Riva, CTP = Cape Tripiti Pumice, US2 = Upper Scoria 2, MP = Middle Pumice

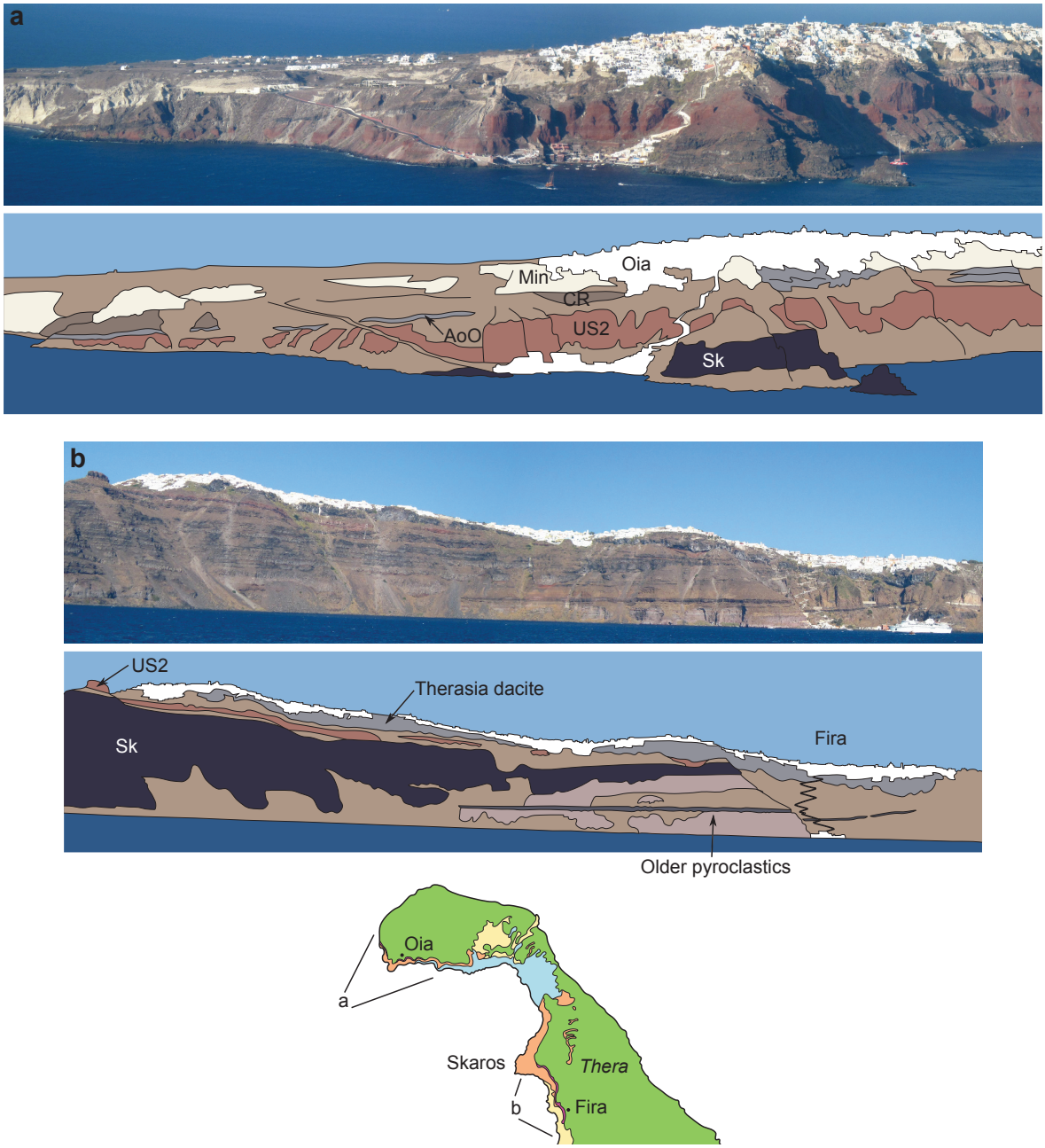

Figure 4.2: Photos of the cliffs at (a) Oia and (b) Fira, and the sketches drawn from them. Inset is a map of the north of Thera, showing where the photos of the cliffs were taken from. Min = Minoan, CR = Cape Riva, Sk = Skaros, US2 = Upper Scoria 2

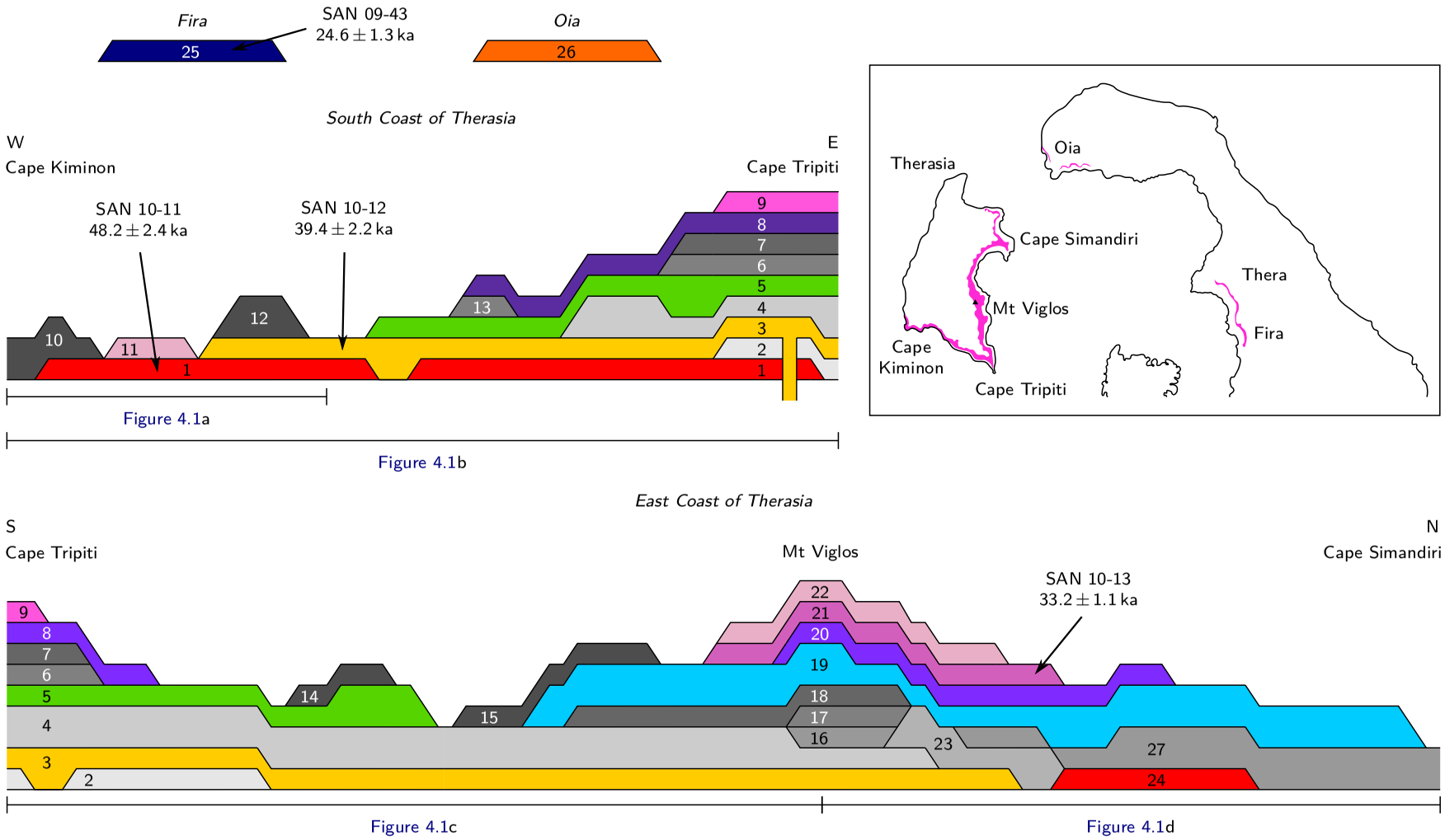

Figure 4.3: Schematic representation of the different lava flows from the Therasia dome complex. Individual flow numbers are referred to in the text. Flows that were sampled and analysed are coloured, while unsampled flows are in grey. Where a correlation of two flows is made based on their chemistry, they are drawn in the same colour. Flows that have been $^{40}Ar/^{39}Ar$ dated are labelled with arrows; $^{40}Ar/^{39}Ar$ ages are weighted mean ages. The inset map has outcrops of the Therasia dome complex in pink

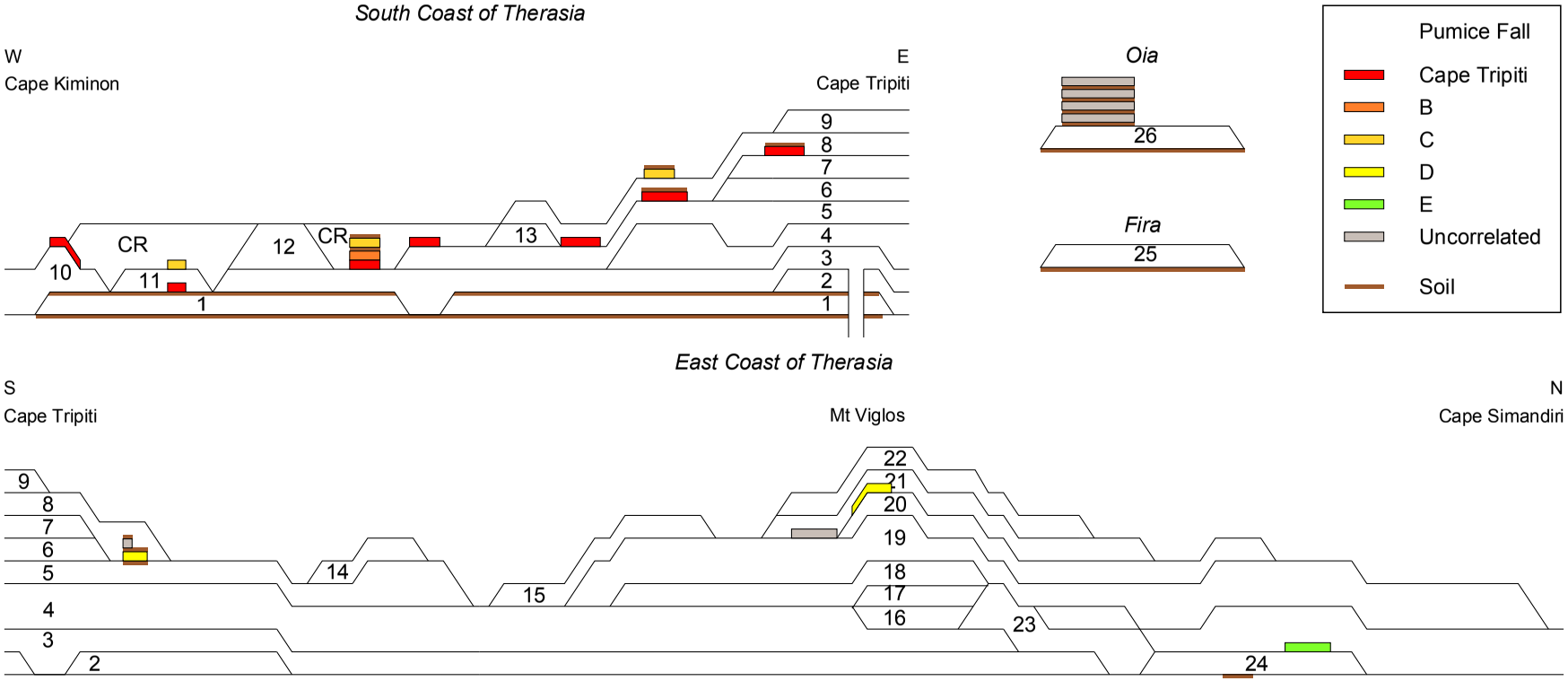

Figure 4.4: Schematic representation of the pumice fall deposits. Lava flows numbered as in Figure 4.3.

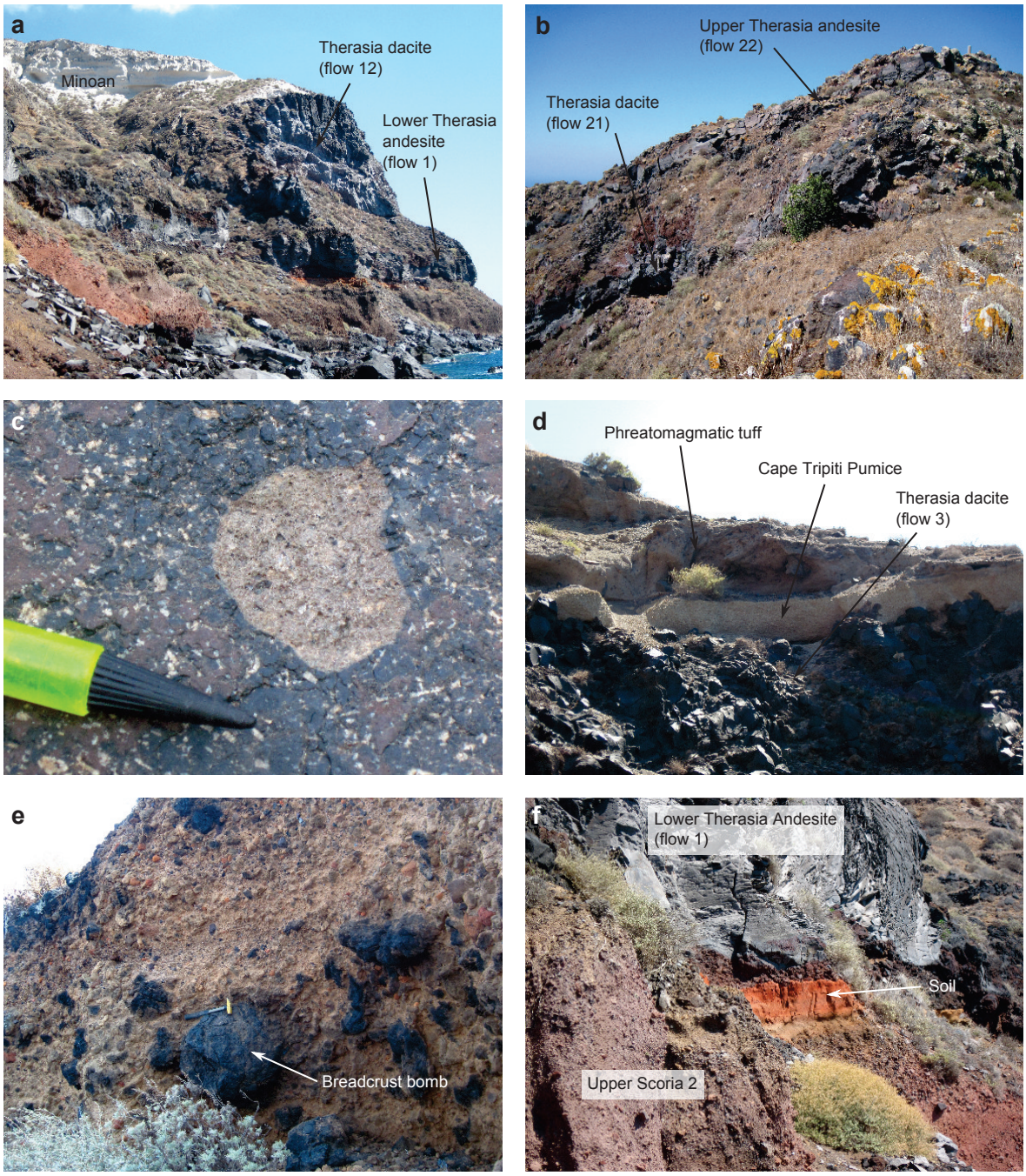

Figure 4.5: Photos of the Therasia dome complex. (a) A thick dacitic dome above the lower Therasia andesite. (b) The upper Therasia andesite on top of Mt Viglos (c) A basaltic enclave in a dacitic flow (flow 3) (d) The Cape Tripiti pumice fall and an overlying phreatomagmatic tuff (Pumice fall B) above lava flow 3 on the south coast of Therasia. (e) Pumice fall D (f) The thick, orange soil between Upper Scoria 2 and the lower Therasia andesite

flow 20 at Viglos; Figure 4.4), showing an increasing tendency for explosive activity with time during eruption of the Therasia dome complex. A single pumice fall deposit crops out between flows 24 and 27 below Manolas.

The most prominent fall deposit is up to a metre thick and widespread in the cliffs of southern Therasia (Figure 4.5d), but thickens considerably into paleotopography along the southern side of Therasia. It occurs stratigraphically between lava flows 7 and 8, is well sorted, and contains sparsely phyric grey to beige pumices. It is the product of a Plinian not recognised in previous studies. I named this unit the Cape Tripiti pumice fall deposit.

Pumice fall B consists of thinly laminated surge deposits overlain by a pumice fall containing angular shards of obsidian, characteristic of phreatomagmatic activity. Pumice fall C is a well sorted, grey pumice fall, overlain in places by a laminated surge deposit and then an ashy layer containing accretionary lapilli. Pumice fall C is only exposed on the southern cliffs of the island, and is always above every lava. The Cape Riva lies above. Pumice fall D has two magmatic components: a pale pumice, which has blackened thermally in some of the larger pumices, and a red pumice. There were also banded pumices, showing mixing continued up until eruption. In the exposure at Cape Tripiti there was a breadcrust bomb ∼1 m in diameter, although most of the pumices were $\sim 10^1$ cm at most (Figure 4.5e). Pumice fall E is only found beneath Manolas; it consists of well sorted, light-coloured pumice.

Palaeosols occur at several levels in the Therasia succession. A thick one separates the entire Therasia succession from Upper Scoria 2 (Figure 4.5f). Another separates the lower Therasia andesite from overlying dacitic flows, showing that eruption of the lower Therasia andesite was both preceded, and followed, by significant time breaks. Local palaeosols also occur between some of the pyroclastic layers.

The andesite of Oia is both underlain and overlain by thick palaeosols. Long periods therefore separated its eruption from both the preceding Upper Scoria 2 eruption and the subsequent Cape Riva eruption. Four thin pumice fall layers (5–25 cm thick) occur

within the palaeosol overlying the lava (sequence M11 of Vespa et al., 2006); they may correlate with the pumice layers intercalated within the lavas on Therasia, but this has not been checked chemically.

Products of the Cape Riva eruption are observed to overlie all lavas of the Therasia dome complex. They have been described in detail by Druitt and Sparks (1982), Druitt (1985), and Druitt et al. (1999). The products of the eruption are predominantly dacitic, but minor amounts of andesitic scoria were erupted during the initial Plinian phase.

4.3.2 Age constraints

Radiometric dating of the Therasia lavas

The ages of flows 1, 3, 21 and 25, as calculated by Dr Stéphane Scaillet, are reported as probability density plots in Figure 4.6. Also plotted are the corresponding Gauss plots that reflect the statistical distribution of individual ages for each sample. Complete $^{40}Ar/^{39}Ar$ analytical data are reported in Fabbro et al. (2013) and are summarized in Table 4.1, along with 2σ errors. All four samples exhibit relatively well behaved $^{40}Ar/^{39}Ar$ systematics in the form of unimodal density plots, with no (or only slightly) pronounced tails on either side of the mode. The homogeneity of the samples is reflected by the linear arrays formed by individual ages on the Gauss plots, indicating that they follow the distribution expected from the propagated Gaussian experimental errors. One exception is flow 3, which exhibits an age spread in excess of the variance expected from the analytical errors (i.e., excess-error scatter). This sample is, along with flow 1, the least glassy of the four, and both are characterized by slightly higher errors and some excess-error scatter. This suggests that flows 1 and 3 may have been affected by post-cooling alteration close to sea level near the base of the sequence, resulting in higher apparent ages (presumably due to K loss). In contrast, flows 21 and 25 are very glassy and pristine, with unusually tight error bars; especially flow 21.

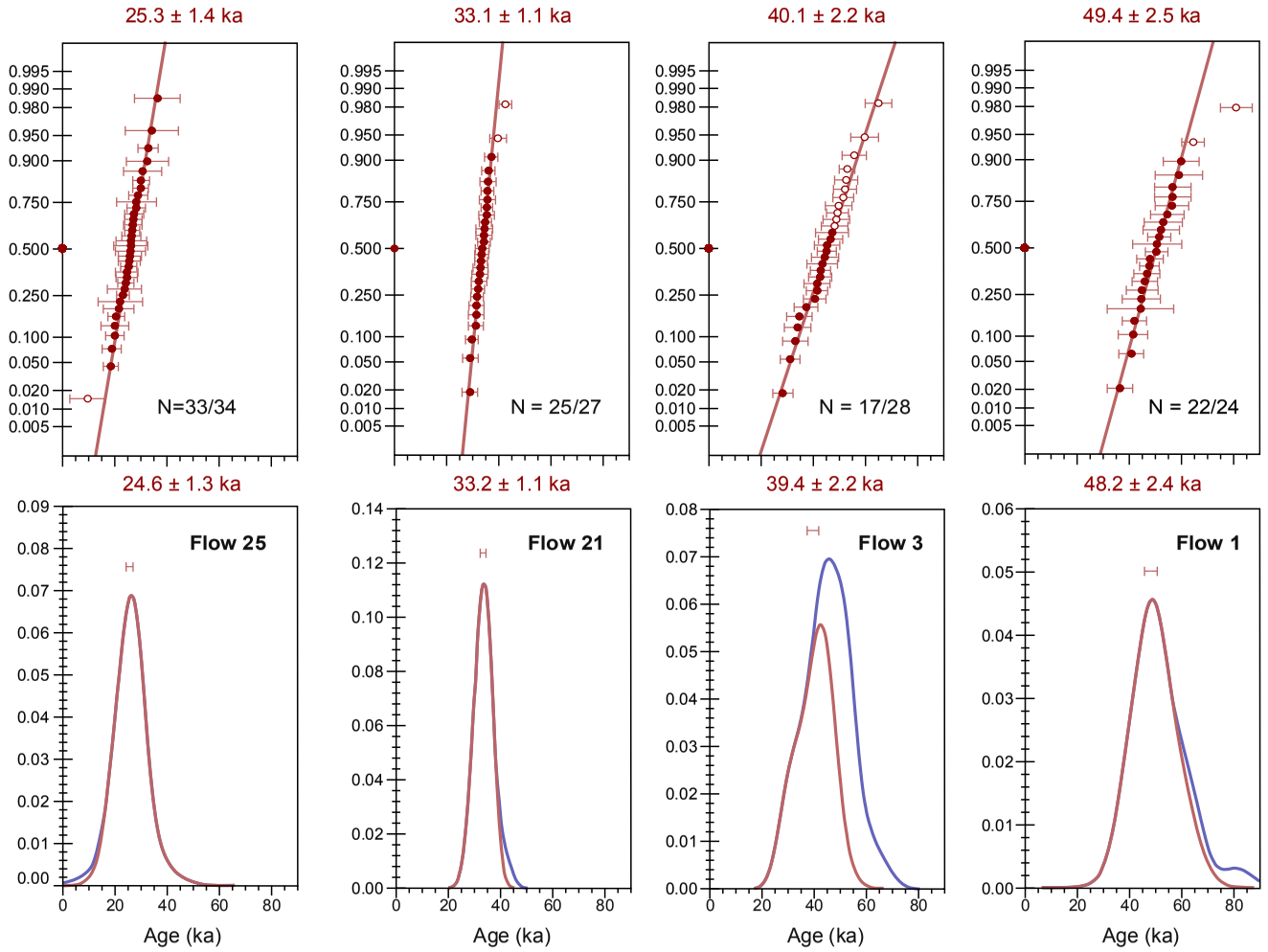

Figure 4.6: Probability density plots (below) and Gauss plots (above) of $^{40}Ar/^{39}Ar$ data obtained on the four lava flows dated in the Therasia sequence, taken from Fabbro et al. (2013). Ages reported above each plot are $\pm 2\sigma$ and represent inverse variance weighted mean ages (density plots) or best-fit apparent ages through the linear array (Gauss-plot). Empty symbols on Gauss-plots: data excluded from the fit. Red curve on density plots: density distribution with outlier removed; blue curve: density distribution of complete dataset. N: number of data points included in the fit over total number of runs for each sample.

Table 4.1: $^{40}Ar/^{39}Ar$-ages for the Therasia dacites, from Fabbro et al. (2013)

Sample	Unit	Gauss-plot age (ka)	Weighted mean age (ka)
SAN 09-43	Flow 25	25.3 ± 1.4	24.6 ± 1.3
SAN 10-13	Flow 21	33.1 ± 1.1	33.2 ± 1.1
SAN 10-12	Flow 3	40.1 ± 2.2	39.4 ± 2.2
SAN 10-11	Flow 1	49.4 ± 2.5	48.2 ± 2.4

To account for secondary alteration effects, the data from flows 1 and 3 were statistically screened by computing a weighted mean age using a MSWD cut-off value. This includes only the youngest sub-population conforming to a Gaussian distribution within each sample (see procedure in Gansecki et al., 1996; Scaillet et al., 2011). In every instance, the weighted mean age agrees with the age derived from the best-fit line through the corresponding Gauss-plot array (Figure 4.6). In what follows we cite the weighted mean ages.

The ages all are consistent with observed field stratigraphic constraints, as summarized in Figure 4.7. The age of the basal flow (flow 1; 48.2 ± 2.4 ka) is consistent with the presence of a palaeosol separating it from the underlying Upper Scoria 2 (previously dated by $^{40}Ar/^{39}Ar$ at 54 ± 3 ka by Druitt et al., 1999), and with another palaeosol separating it from the overlying flow 3 (39.4 ± 2.2 ka). Flow 21 yields an age of 33.2 ± 1.1 ka, and flow 25 (at Fira) gives an age of 24.6 ± 1.3 ka. Taken as a whole, our $^{40}Ar/^{39}Ar$ data between the base (48.2 ka) and the top (24.6 ka) of the lava sequence define a ~24 ky duration for the construction of the Therasia dome complex.

Correlation of the Cape Tripiti Pumice with the Y-4 deep-sea ash layer

The Cape Tripiti pumice is the most prominent pyroclastic layer in the Therasia sequence, and we have explored the possibility that, like most Plinian eruptions of Santorini, (Asku et al., 2008; Federman and Carey, 1980; Keller et al., 1978; Schwarz, 2000; Vinci, 1985; Wulf et al., 2002), the Cape Tripiti eruption left a recognisable ash layer in deep-sea sediments of the Aegean area. Previous studies have recognized a 2-7 cm-thick ash layer (Y-4 ash) preserved to the SE of Santorini; this ash lies stratigraphically be-

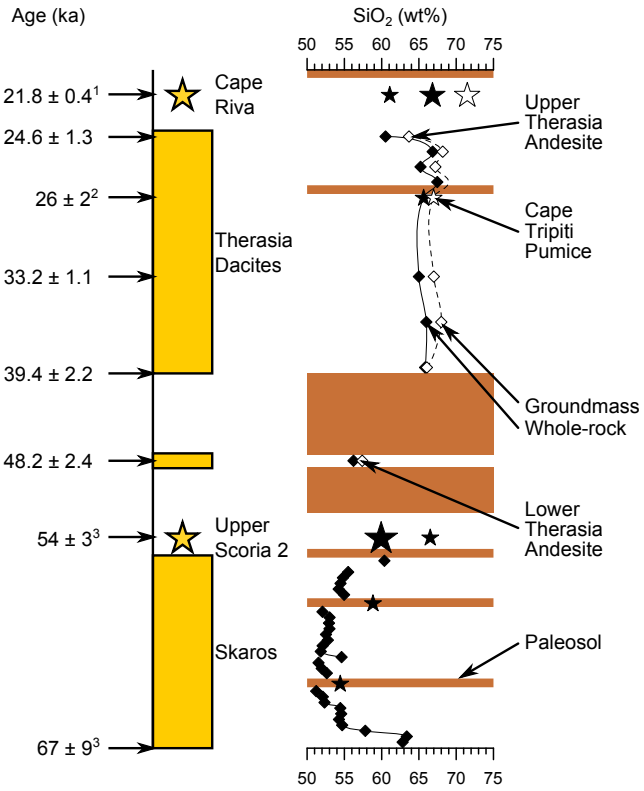

Figure 4.7: Summary of magma compositions and ages between 70 and 20 ka. Major explosive eruptions are represented by stars, with periods of edifice construction coloured in yellow. Periods of little or no preserved eruptive activity are left blank. The SiO_2 content of the eruptive products is shown on the right. Black symbols are whole rock compositions, and white symbols are groundmass composition. Skaros data is taken from Huijsmans (1985). [1] Data and citations in Table 4.2; [2] date taken from Schwarz (2000); [3] date taken from Druitt et al. (1999)

neath the Cape Riva Y-2 ash layer, and has an age of 25.8 ka estimated by interpolation in the sedimentary sequence of one core (Schwarz, 2000). The uncertainty on this age could be ±2 ka (J Keller, pers. comm). The mineralogy of the Y-4 ash (plag, opx, cpx) pinpoints its source to Santorini (Vinci, 1985). Schwarz (2000) explored the possibility that the Y-4 correlates with the rhyodacitic Plinian phase of Upper Scoria 2; however, the $^{40}Ar/^{39}Ar$ age data described above rule out this correlation, and show that the Y-4 lies chronologically in the period of the Therasia dome complex. I analysed the interstitial glass of three pumice lumps from the Cape Tripiti deposit, and find excellent agreement with glass composition of the Y-4 (Figure 4.8). A 26 ka age for the Cape Tripiti is consistent with all other age constraints (Figure 4.7).

Synthesis of published dates for the Cape Riva eruption

The Cape Riva eruption has been dated previously by radiocarbon on charcoal from beneath the ignimbrite and via $\delta^{18}O$ wiggle matching in deep-sea sequences hosting the distal equivalent Y-2 tephra layer (data and sources in Table 4.2). Calibration of the

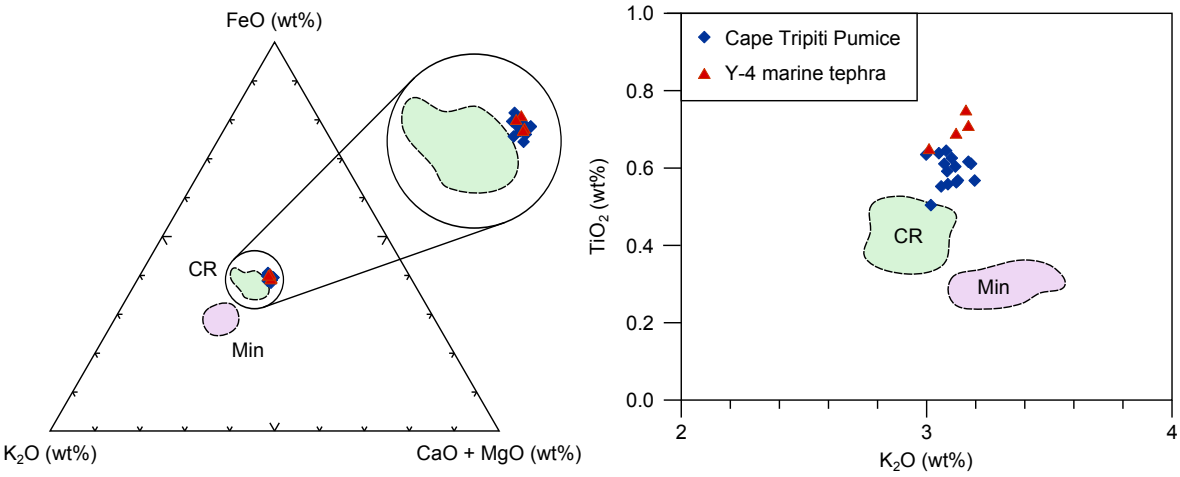

Figure 4.8: Chemical discrimination plots for the Cape Tripiti pumice and Y-4 ash layer, after Wulf et al. (2002). The Y-4 data is taken from Vinci (1985)and Schwarz (2000)

raw radiocarbon data against the curve of Fairbanks et al. (2005) returns a mean age of 21.8 ± 0.4 ka for Cape Riva (Table 4.2). This yields an interval of $2,800 \pm 1,400$ (2σ) years between the youngest dated Therasia lava (flow 25) and the Cape Riva eruption. This is a maximum estimate for the interval separating the Cape Riva eruption from the Therasia lavas, since some of the undated flows on Therasia may be younger than flow 25, or a younger flow could have been erupted and not preserved.

4.4 Discussion

4.4.1 Reconstruction of events leading up to the Cape Riva eruption

Construction of the $\sim$12 km^3 basaltic-to-andesitic Skaros shield between 67 and 54 ka represented a period where the eruption rate was close to the average for Santorini ($\sim$1 km^3 ky^{-1}; Druitt et al., 1999). The Skaros period culminated at 54 ka in the Upper Scoria 2 explosive eruption. Following Upper Scoria 2, the system stagnated and entered a $\sim$15 ky-long period of near-repose until effusive activity resumed at about 39 ka. Only two lava flows are preserved in the cliffs of Therasia from this

Table 4.2: Published ages for the Cape Riva eruption. The average of these ages is 21.8 ± 0.4 ka (2σ)

Uncalibrated ^{14}C age (ka)[a]	Calibrated age (ka)	Method	Sample dated	Reference
18.05 ± 0.34 18.17 ± 0.21 18.05 ± 0.34	21.46 ± 0.49[b] 21.63 ± 0.33[b] 22.47 ± 0.24[b]	^{14}C	Charred trees from ignimbrite	Pichler and Friedrich (1976)
18.15 ± 0.20	21.60 ± 0.32[b]	^{14}C	Charcoal from ignimbrite	Eriksen et al. (1990)
17.38 ± 0.23 18.53 ± 0.15 18.24 ± 0.14	20.53 ± 0.26[b] 21.75 ± 0.24[b] 22.14 ± 0.17[b]	^{14}C	Peat below Y-2 tephra, Philippi basin, Greece	St Seymour et al. (2004)
–	21.62	Interpolation between sapropels dated using ^{14}C		Asku et al. (2008)
–	19[c]	Interpolation between isotopic stages dated by ^{231}Pa/^{230}Th		Thunell et al. (1979)

[a] Published uncalibrated ^{14}C age
[b] Calibrated using the curve of Fairbanks et al. (2005)
[c] Not included in the average

period: the ∼48 ka lower Therasia andesite (flows 1 and 24) and an inaccessible flow (flow 2) immediately above it. The andesite of Oia could also belong to this period; it is chemically very similar to Upper Scoria 2 and could be residual magma from that eruption. This period of reduced activity, during which the apparent eruption rate based on preserved products was very low ($<0.1\,km^3\,ky^{-1}$), is marked by the development of thick palaeosols.

Any mantle-derived basalt injected into the crust during this period must have been trapped at depth, perhaps due to the stress imposed by the high Skaros edifice (Pinel and Jaupart, 2000). Accumulation of heat from prolonged, deep intrusion probably generated silicic melt by a combination of fractional crystallisation, partial melting of crustal rocks and defrosting of extant mushy intrusions (Barton et al., 1983; Druitt et al., 1999; Huijsmans, 1985; Huijsmans and Barton, 1989; Mann, 1983). Then, between 39 and 25 ka, a chemically monotonous series of dacites (the Therasia dome complex) was extruded from the summit of Skaros and from dykes on its western flank. The lack of any systematic variation of whole rock or groundmass (i.e., melt) composition with time during this period (Figure 4.7) suggests thermal buffering of the crustal storage region by an approximate balance of heat input, heat output and latent heat of crystallisation. The mean eruption rate during construction of the Therasia dome complex was very approximately 0.1–0.2 $km^3\,ky^{-1}$: lower than the long-term average on Santorini (∼1 $km^3\,ky^{-1}$), but higher than that during the preceding repose period. Towards the end of the Therasia activity, lava extrusion became increasingly punctuated by explosive activity. Any basaltic magma intruded beneath the summit region over the 15 ky was unable to reach the surface, except as rare quenched enclaves of dacite-contaminated olivine basalt. Towards the end of the period, basalt mixed with dacite in approximately equal proportions, forming the upper Therasia hybrid andesite.

Following extrusion of the last Therasia lava, no more than $2,800 \pm 1,400$ years elapsed before the 21.8 ± 0.4 ka Cape Riva eruption took place. At least 10 km^3 of 880 °C Cape Riva dacite, poorer in incompatible elements, was then erupted as Plinian

fallout and pyroclastic flows. The eruption also discharged a small quantity ($\ll 1\,\mathrm{km}^3$) of hybrid andesite formed by the mixing of olivine basalt and incompatible-depleted dacite in sub-equal proportions, and the Skaros-Therasia edifice collapsed (Druitt et al., 1999).

4.5 Summary

- The Therasia dome complex is made up of at least 11 different domes and coulées, with at least five pyroclastic deposits. The earliest dated flow is the lower Therasia andesite, which was erupted at $48.2 \pm 2.4\,\mathrm{ka}$. Dacite eruption had begun by $39.4 \pm 2.2\,\mathrm{ka}$, and most of the Therasia dome complex was emplaced after this date.

- The most prominent pyroclastic unit is the product of a previously unrecognised Plinian eruption, named here the Cape Tripiti pumice. This pumice fall correlates with the deep sea Y-4 ash layer. The Y-4 ash layer has been dated at $\sim 26\,\mathrm{ka}$, which is consistent with the $^{40}\mathrm{Ar}/^{39}\mathrm{Ar}$ ages of the lavas.

- The youngest dated lava flow was erupted at $24.6 \pm 1.3\,\mathrm{ka}$; this is $2,800 \pm 1,400$ years before the Cape Riva. This is a maximum estimate of the time between the end of the Therasia eruptions and the onset of the Cape Riva eruption: some of the undated flows of the Therasia dome complex may be younger, or younger flows may have been buried by the caldera collapse that accompanied the Cape Riva eruption.

Chapter 5

Chemistry and petrology

5.1 Introduction

Because the Therasia dome complex directly underlies the deposits from the Cape Riva eruption, it can be used to trace the evolution of the volcanic system in the build-up to the Cape Riva eruption. The stratigraphic relations discussed in Chapter 4 provide a framework which allows us to track the changes in magma chemistry and petrology with time. The radiometric ages of the different Therasia units, and of the Cape Riva eruption, constrain the timescales of these changes. From these ages we know that the eruption of dacite commenced ∼18 ky before the Cape Riva eruption, and the last Therasia lava was erupted at most $2\,800 \pm 1\,400$ years before the Cape Riva.

The petrology and chemistry of the Cape Riva products has already been studied in some detail (Druitt, 1983, 1985; Druitt et al., 1999). The majority of the Cape Riva deposits are dacitic, with 15–20 wt% of crystals of plagioclase, two pyroxenes and Fe–Ti oxides. The Cape Riva also has a minor hybrid andesite component. There is no systematic variation of the composition of the dacitic component with stratigraphic height, which suggests that a large body of homogeneous dacite existed in the crust before the onset of eruption. The collapse of the Skaros-Therasia edifice during the Cape Riva eruption suggests that this magma body was located beneath Skaros-Therasia.

Phase equilibria experiments constrain the depth of dacite storage before the eruption to 8 ± 2 km (Cadoux et al., 2014). The hybrid andesite either underlain the dacite, or was introduced shortly before eruption.

The Therasia lavas have not been studied in as much detail. Druitt (1983, 1985) reported that the whole-rock major element compositions and petrology of the Therasia dome complex are very similar to that of the Cape Riva. The majority of the lava flows and pumice fall deposits that make up the Therasia dome complex are dacitic, like the Cape Riva, and they have a similar phenocryst assemblage. Capping the Therasia sequence is a hybrid andesite, that closely resembles the one found in the Cape Riva deposits. These similarities, along with the fact that the vents for the Therasia dome complex were located in the area that subsequently collapsed to form the Cape Riva caldera, led to the Therasia dacites being interpreted as leaks from the growing Cape Riva magma chamber.

Before the crystal zoning patterns — and the ages recovered from diffusion modelling — can be interpreted, the wider context needs to be understood. This chapter looks at what the chemistry and petrology can tell us about the processes that occurred in Santorini's plumbing system prior to the Cape Riva eruption.

5.2 Methodology

Representative samples of lava and pumice from the Therasia complex, and pumice and scoria from the Cape Riva deposits, were collected for chemical analysis. All samples were chosen to be as fresh and glassy as possible. Groundmass separates of selected lavas were obtained in order to analyse the compositions of the melt phases of the magmas. This was done using a magnetic separator, and interstitial glasses of pumice samples were concentrated by flotation in water. Remaining crystals were then removed by hand picking under an optical microscope.

Major elements were analysed using inductively coupled plasma atomic emission

spectroscopy (ICP AES) at the Laboratoire Magmas et Volcans, Université Blaise Pascal, Clermont-Ferrand. Measurements were calibrated using three standards: a blank ($LiBO_2$), basalt (BR) and granite (GH). The DR-N and BHVO-2 standards were then passed as unknowns. Trace elements were analysed using inductively coupled plasma mass spectroscopy (ICP MS) at the Institut des Sciences de la Terre, Université de Grenoble. The ICP MS analyses were calibrated using the BR standard, and the BVHO-2 and AGV-1 standards were passed as unknowns. Some previous Cape Riva samples of Druitt et al. (1999) were re-analysed for comparison with the data of those authors. These comparisons showed good agreement between the two datasets for the elements used in the present paper.

Phenocryst contents were calculated by mass balance from incompatible element concentrations in the whole rock and groundmasses (Y, Zr, Nb, La, Ce, Pr, Nd, Sm, Eu, Gd, Tb, Dy, Ho, Er, Yb, Lu, Hf, Ta, Tl, Pb). The concentrations of these elements in the groundmass separates was plotted against their concentration in the whole rock analyses, and they were fit using a linear regression through the origin. By assuming the concentrations of these elements is negligible in the crystals, it is possible to calculate the total crystal content.

Mineral compositions were analysed using the Cameca SX 100 electron microprobe at the Laboratoire Magmas et Volcans, Université Blaise Pascal, Clermont-Ferrand, using a beam current of 15 nA. Glasses were analysed with a beam current of 4 nA and a defocussed beam (10–15 µm) in order to limit Na loss. Fe-Ti oxide compositions were analysed either in touching pairs or in pairs (that would have been in contact with the same melt) adhering to the outside of the same pyroxene crystal. Magmatic temperatures and oxygen fugacities were calculated with the ILMAT software package (Lepage, 2003) using the formulation of Andersen and Lindsley (1985) and Stormer (1983). This formulation has been found to give good agreement with data from phase-equilibria experiments within the 850–950 °C temperature range (Blundy and Cashman, 2008; Cottrell et al., 1999). These were compared to the temperatures

calculated using the method of Ghiorso and Evans (2008), obtained from the calculator on the authors' website (http://ctserver.ofm-research.org/webcalculators.html).

5.3 Results

5.3.1 Mineral chemistry and assemblages

In this section I focus on the petrology and chemistry of Therasia lavas and pumices younger than ∼39 ka (i.e., flow 3), as well as the products of the Cape Riva eruption (Figure 5.1). The lower Therasia andesite, and the andesite found at Oia are only discussed briefly, as they are significantly older than the bulk of the Therasia dome complex. In so doing we focus on the effusive leaks of dacite during the build-up to the Cape Riva eruption. The zoning patterns of plagioclase and orthopyroxene crystals from the dacites are discussed in more detail in Chapters 6 and 7, respectively.

Andesite of Oia

The andesite of Oia is found only underneath Oia. Its precise stratigraphic position relative to the lavas on Therasia is unknown, however as it sits above the Upper Scoria 2 deposits and below four Therasia pumice falls, it likely was erupted near the beginning of the Therasia sequence. It has a whole rock SiO_2 of 57.3 wt% and an MgO content of 3.5 wt%. It is crystal-poor, with 7.8 vol% crystals of plagioclase and pyroxene. It has a glassy groundmass with 58 wt% SiO_2 and 3.5 wt% MgO.

Figure 5.1 ***(facing page)*****:** Mineral compositions from the different rock units. Filled symbols are crystal cores or undifferentiated measurements, open symbols are crystal rims. Plagioclase populations are coloured according to their origin: orange symbols are groundmass crystals, blue symbols are populations that originated in a silicic magma and green symbols are populations that originated in a mafic magma. Some Cape Riva data taken from Druitt et al. (1999). The fields of pyroxene compositions in the dacites (a, d) are shown on the other figures, for comparison

a Therasia dacites

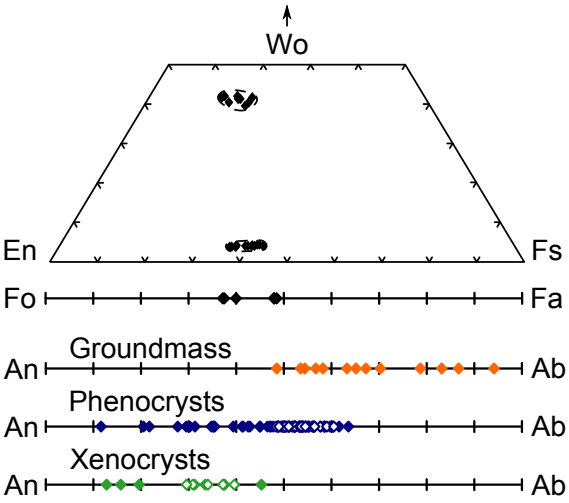

b Therasia Mafic enclave

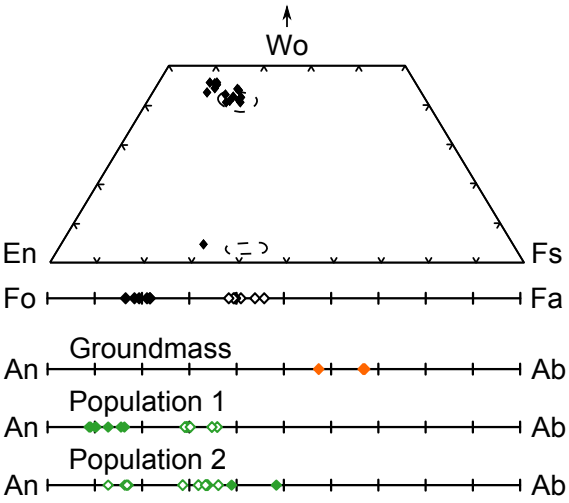

c Upper Therasia hybrid andesite

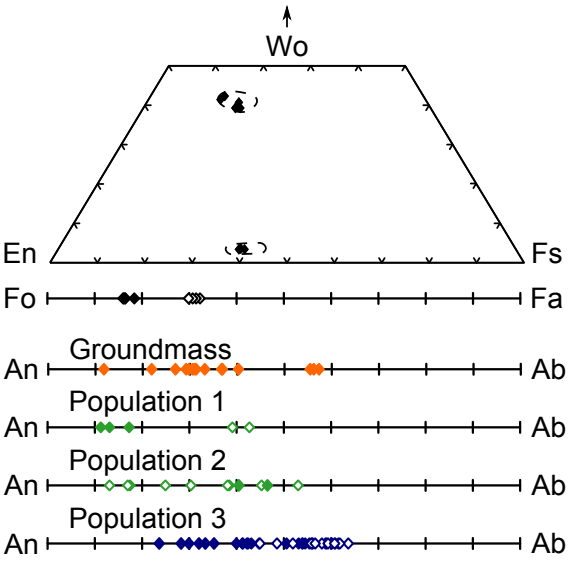

d Cape Riva dacite

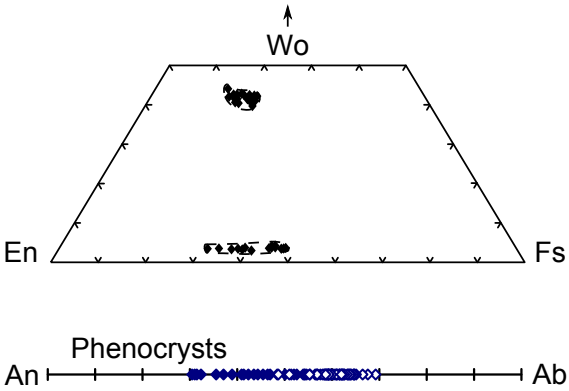

e Cape Riva mafic blebs

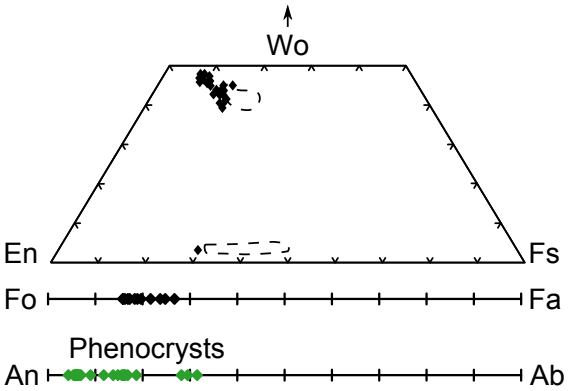

f Cape Riva hybrid andesite

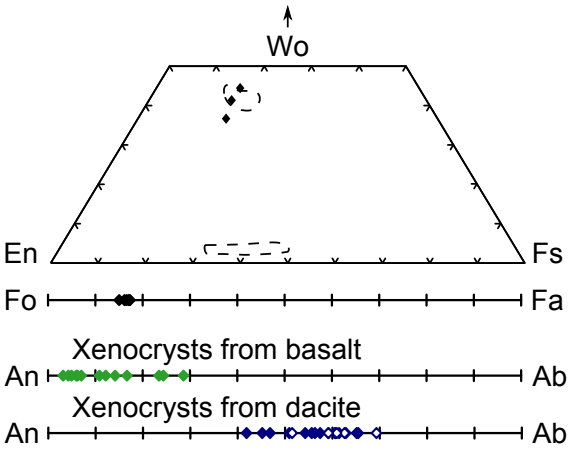

Lower Therasia andesite

The lower Therasia andesite has 56.2 wt% SiO_2 and 4.1 wt% MgO. It has 23.6 wt% crystals of plagioclase, pyroxene and olivine, set in a highly crystalline groundmass of acicular plagioclase, pyroxene and Fe-Ti oxides with 57.4 wt% SiO_2.

Therasia dacites

The Therasia dacites have whole rock SiO_2 contents of 64.6–68.7 wt% and MgO contents of 0.7–1.5 wt%, with groundmass (i.e. melt) SiO_2 contents of 64.7–69.1 wt%. No systematic evolution of either whole rock or groundmass composition is observed with height in the lava succession. The dacites contain 1–17 wt% phenocrysts (with a smallest dimension >0.5 mm) of plagioclase (75–85 vol%), two pyroxenes (10–20 %, with opx > cpx), Fe–Ti oxides (5–8 %) and trace amounts of olivine (Table 5.1). Apatite occurs as inclusions in orthopyroxene crystals. The glassy groundmass contains microlites of feldspar and Fe–Ti oxides. The petrology of flows 3 (GS10-27a), 5 (GS10-17), 8 (GS10-14) and 9 (GS10-16) were studied in detail.

The free-floating crystals can be split into three groups: phenocrysts, xenocrysts, and groundmass microlites. Some of the crystals are grouped into clusters, and these clusters can be split into two groups: glass-bearing clusters and subsolidus nodules.

Phenocrysts: Plagioclase phenocrysts are normally zoned, with cores of An_{50-89} and rims of An_{39-51}, and commonly contain multiple internal dissolution surfaces and sawtooth zoning. The rims are euhedral, and are compositionally similar to plagioclase microlites in the groundmass. The anorthite content of the mode of the phenocryst population varies slightly between flows. The some unzoned plagioclases, and the cores of some sawtooth-zoned plagioclases, in flow 5 have large, brown glass inclusions. These glass inclusions were not seen in the other flows. Orthopyroxene phenocrysts are euhedral and have compositions of $Wo_{3-4}En_{53-60}Fs_{37-43}$. Most of the orthopyroxenes have a #Mg of 58–64 and are unzoned, however a few crystals have either

Table 5.1: Total and modal crystal contents for the Therasia dome complex. Modal mineral compositions given as a percentage of the total crystal content.

Sample	Unit[1]	Flow	Total crystal content	Plagioclase	Pyroxene	Opaques	Olivine[2]
GS10-50	AO	26	7.8%				
GS10-44b	LTA	1	23.6%	79.0%	18.7%	2.0%	0.3%
GS10-27a	TD	3	8.6%	74.2%	18.6%	7.3%	n.d.
GS10-17	TD	5	4.0%	72.9%	20.3%	6.8%	n.d.
GS10-14	TD	8	5.2%	80.1%	13.5%	6.4%	n.d.
GS10-16	TD	9	6.9%				
GS10-30a	TD	19	2.3%	79.3%	12.9%	7.9%	n.d.
GS10-20	TD	20	5.1%	75.5%	15.8%	8.5%	0.3%
GS10-48	TD	21	2.3%	84.9%	9.8%	5.4%	n.d.
GS10-40	TD	25	4.6%				
GS10-27d	CTP	A	16.7%				
GS10-27h	TP	C	4.7%	93.3%	3.6%	3.0%	n.d.
GS10-28c	TP	D	0.6%				
GS10-28f	TP	D	1.3%				
GS10-28d	TP	D	0.3%				
GS10-22	UTA	22	25.4%	75.9%	18.5%	5.5%	0.1%

Total crystal contents are in wt%, mineral modes are in vol%

[1] AO: andesite of Oia, LTA: lower Therasia andesite, TD: Therasia dacite (lavas), CTP: Cape Tripiti pumice, TP: Therasia pumice fall, UTA: upper Therasia andesite.

[2] n.d.: none detected

cores or mantles with a #Mg of 65–71. Clinopyroxenes are also euhedral and poorly zoned, and their compositions are $Wo_{40-42}En_{42-43}Fs_{15-17}$.

Xenocrysts: Xenocrysts of calcic plagioclase (An_{60-89}) occur frequently in the dacites, along with more calcic clinopyroxenes ($Wo_{47-50}En_{30-44}Fs_{8-20}$).

Groundmass microlites: Acicular plagioclase is the dominant groundmass phase. Most crystal have compositions of An_{30-51}, although flow 9 contains some ternary feldspars which contain up to 47 mol% orthoclase ($KAlSi_3O_8$).

Glass-bearing clusters: These clusters were found in all the lavas studied except flow 5, and contain euhedral crystals of plagioclase, orthopyroxene and clinopyroxene. Plagioclases in these clusters are similar to those found freely floating in the magma; their composition varies in a similar fashion to the

phenocrysts, with cores of An_{44-70} and rims of An_{40-51}. However, they lack melt inclusions or saw-tooth zoning sometimes found in the free-floating phenocrysts. Both orthopyroxene and clinopyroxene crystals in the clusters have the same composition as those found individually in the magma, with compositions of $Wo_{3-4}En_{54-60}Fs_{36-42}$ and $Wo_{40-42}En_{39-42}Fs_{16-22}$, respectively. Between the crystals are pockets of brown glass, and electron microprobe analyses (with the beam opened to 10–20 µm) show these glass pockets to have similar composition to the groundmass (Table 5.2).

Subsolidus nodules: Alongside the glass-bearing clusters, there are holocrystalline nodules of plagioclase, pyroxene and sometimes olivine. The plagioclases in these clusters vary from flow to flow. In flow 3 they are highly calcic (An_{89}) and unzoned apart from a small syn-eruptive overgrowth on crystal faces exposed to the melt. The sub-solidus plagioclase crystals in flows 5 and 9 are similar to each other. They have variably calcic cores (An_{50-84}), but their rims are roughly in equilibrium with their host magma (An_{41-43} in flow 5, An_{48} in flow 8). Most of the orthopyroxenes from sub-solidus clusters have similar compositions to the phenocrysts, however there are a small number of more magnesian crystals (up to En_{69}). Clinopyroxenes that resemble those free-floating in the lavas are found in these clusters, along with another group of more calcic pyroxenes. These match the composition of the clinopyroxenes found in the mafic blebs ($Wo_{47-50}En_{30-44}Fs_{8-20}$, discussed below). Olivines are only found in the holocrystalline clusters, and have not been observed as individual crystals. They often show textures characteristic of sub-solidus reactions, such as olivines breaking down to form magnetite–pyroxene symplectites. They are unzoned, and have a range of compositions from Fo_{51} to Fo_{62}.

The similarity between phenocryst rims and groundmass microlite compositions suggests an equilibrium phenocryst rim assemblage in these lavas. The zoning patterns

Table 5.2: Average glass compositions inside glass-bearing clusters and groundmass compositions, measured using a defocused electron microprobe beam

		Flow 3		Flow 8		Flow 9	
		Cluster n = 2	Groundmass n = 2	Cluster n = 1	Groundmass n = 2	Cluster n = 3	Groundmass n = 4
Oxide (wt%)	SiO_2	69.97	67.12	68.48	69.67	68.73	69.74
	K_2O	3.00	2.96	5.05	3.22	5.38	3.46
	CaO	1.84	3.16	1.58	2.39	1.15	2.20
	FeO	3.39	3.71	3.35	2.89	3.70	3.08
	Na_2O	5.35	5.08	4.01	5.21	3.48	5.15
	Al_2O_3	13.34	15.61	14.11	14.99	12.21	14.88
	MgO	0.29	0.52	0.31	0.37	0.43	0.40
	TiO_2	0.81	0.49	0.67	0.65	0.73	0.59
	MnO	0.09	0.10	0.08	0.10	0.09	0.09
	Cr_2O_3	0.00	0.03	0.03	0.00	0.01	0.00
	P_2O_5	0.15	0.14	0.16	0.13	0.14	0.05
	Total	98.22	98.92	97.82	99.61	96.07	99.64

of the plagioclase and orthopyroxene are interpreted as recording varying melt composition during phenocryst growth, and are discussed in more detail in Chapters 6 and 7.

The glass-bearing clusters are interpreted as growing alongside the free-floating phenocrysts, but in a mush zone on the reservoir margins. This is supported by the textural and compositional similarity between the plagioclase, orthopyroxene and clinopyroxene found in these clusters and the phenocrysts, along with the fact that the glass within these clusters has the same composition as the glass outside. The euhedral shape of the crystals also suggests that these crystals have a simple growth history and they are not, for example, remelted plutonic mush.

The subsolidus nodules are interpreted as fragments of gabbro derived from plutonic material related to previous intrusions. Their holocrystalline nature is evidence that they represent magma that has fully solidified. The presence of symplectites in some of these clusters implies prolonged storage at elevated—but subsolidus—temperatures. Variations in the crystals in holocrystalline clusters in different flows suggest that the plutonic material they are derived from is heterogeneous.

Therasia mafic enclaves

Quenched basaltic (49.6–51.8 wt% SiO_2; 5.4–8.6 wt% MgO) enclaves 1–10 cm in diameter are found in flows 3 and 11, where they make up <1 % of the erupted volume. They contain phenocrysts of plagioclase (∼55 vol%), pyroxenes (∼35 vol%, with cpx ≫ opx) and olivine (∼10 vol%) set in a glassy, diktytaxitic groundmass. Two populations of plagioclase phenocrysts with different core compositions, but similar rim compositions, are observed: (1) normally zoned crystals with cores of An_{83-91} and rims of An_{64-71}; (2) reversely zoned crystals with cores of An_{51-61}, separated by a sieve-textured zone from rims normally zoned from An_{82-86} to An_{64-71}. Plagioclase in the groundmass is An_{32-42}. Olivines are normally zoned from cores of Fo_{77-82} to rims of Fo_{53-60}. Two clinopyroxene populations are found, although their textural relationships with the plagioclase populations are ambiguous. Both cpx populations are euhedral and unzoned, with compositions of (1) $Wo_{43-46}En_{42-46}Fs_{10-12}$ and (2) $Wo_{41-44}En_{39-43}Fs_{15-20}$. Rare orthopyroxenes with compositions of $Wo_3En_{67}Fs_{30}$ also occur.

The occurrence of two plagioclase populations with different core compositions, but similar, intermediate rim compositions is indicative of magma mixing. Plagioclases of population 1 are interpreted as derived from a basaltic melt, and those of population 2 from a more evolved melt. The cores of olivine crystals (molar Mg/Fe = 3.37–4.64) are in equilibrium with the whole rock (i.e., basaltic) composition (Mg/Fe = 1.20), assuming a crystal-melt partition coefficient of between 0.26 and 0.36 (Roeder and Emslie, 1970). The composition of population-2 clinopyroxenes is similar to that of the clinopyroxene phenocrysts in the dacite. The enclaves are interpreted as having formed by the in-mixing of a small proportion of more evolved magma (possibly dacitic, containing population-2 plagioclase cores + population-2 cpx) into a basalt (containing population-1 plagioclase cores + olivine + population-1 cpx; Figure 5.2). Mixing occurred long enough prior to eruption for plagioclase from the evolved component to partially melt (generating sieve texture), followed by overgrowth of equilibrium rim

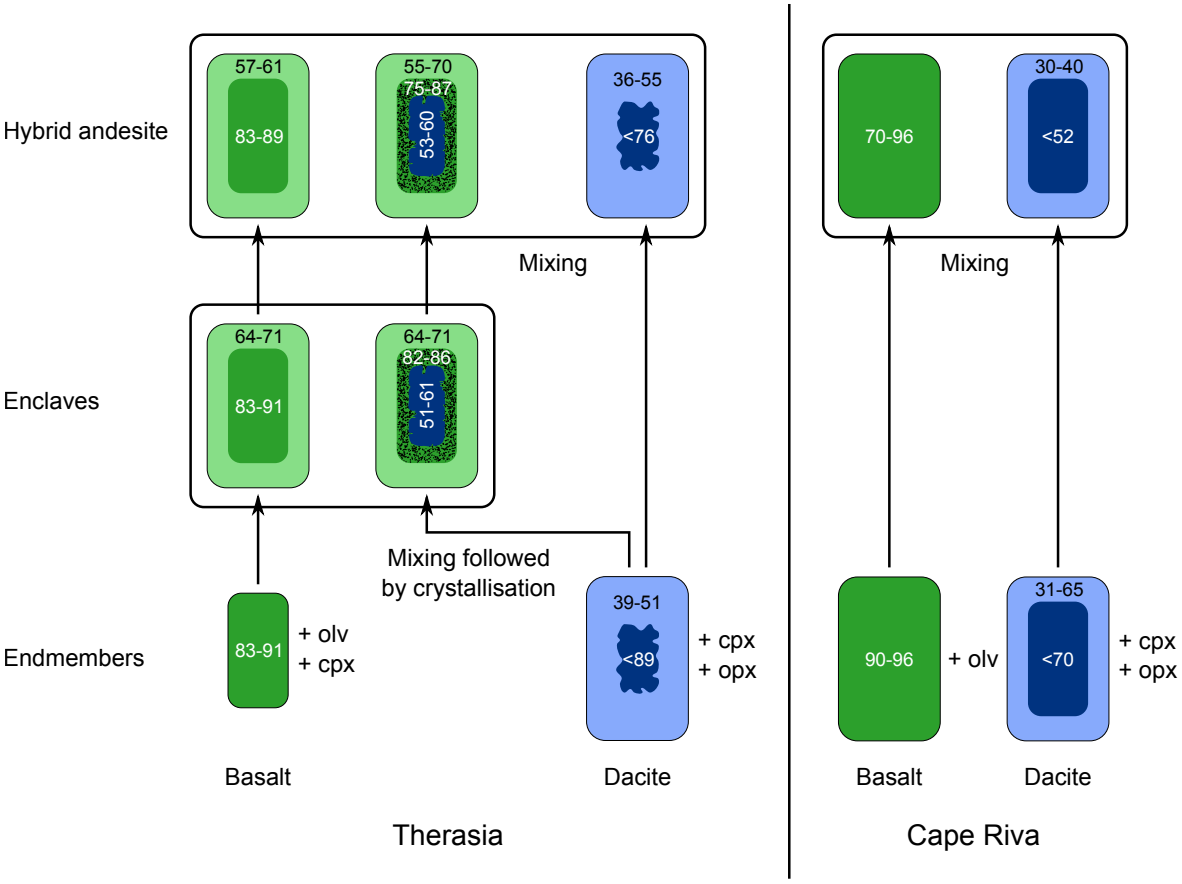

Figure 5.2: Summary of plagioclase populations in the Cape Riva and Therasia rocks. The numbers are the molar per cent anorthite content of the plagioclase

compositions on plagioclases from both populations.

Upper Therasia andesite

The upper Therasia andesite (60.5 wt% SiO_2, 2.6 wt% MgO) contains 26 wt% macroscopic crystals: plagioclase (75 vol%), pyroxenes (20 %, with opx ≈ cpx), Fe–Ti oxides (5 %) and trace amounts of olivine set in a glassy, 64 wt% SiO_2 groundmass containing microlites of plagioclase and magnetite (Table 5.1). Three distinct populations of plagioclase are observed: (1) normally zoned crystals with cores of An_{83-89}, and euhedral rims of An_{57-61}; (2) crystals with cores of An_{53-60} separated by a sieve-textured zone from rims normally zoned from An_{75-87} to An_{55-70}; (3) normally zoned crystals with cores as calcic as An_{76} and rims of An_{36-55}. Rare olivines have cores of Fo_{80-83}, and rims of Fo_{67-69}. Orthopyroxenes have compositions of $Wo_3En_{57-59}Fs_{38-39}$, and

clinopyroxenes have compositions of $Wo_{39-42}En_{40-43}Fs_{15-20}$.

Plagioclase populations 1 and 2 texturally and compositionally resemble plagioclase populations 1 and 2 (respectively) in the basaltic enclaves; population 3 resembles plagioclase phenocrysts in the dacites. The olivine rims have a molar Mg/Fe ratio of 1.99–2.22, which is in, or close to, equilibrium with the groundmass (Mg/Fe = 0.76), assuming a partition coefficient of between 0.26 and 0.36 (Roeder and Emslie, 1970); the cores have an Mg/Fe ratio of 4.11–4.81 and grew in equilibrium with a basaltic melt. The two pyroxenes are indistinguishable from the same phases in the dacites. The upper Therasia andesite is interpreted as a hybrid magma formed by the mixing of the basalt (containing plagioclase of populations 1 and 2 + olivine) represented by the enclaves, with typical Therasia dacite (containing population-3 plagioclase + opx + cpx; Figure 5.2). Mixing occurred long enough prior to eruption to permit physical homogenization of the resulting hybrid melt, but not long enough for crystals to grow rims in equilibrium with that melt, or for those from the dacite to be resorbed.

Cape Riva dacite

Dacitic pumices of the Cape Riva eruption have whole rock compositions of 64–67 wt% SiO_2 and 1.0–1.9 wt% MgO, and interstitial glasses with 70–72 wt% SiO_2. Phenocryst phases and proportions are the same as in the Therasia dacites, with total contents ranging from 15 to 20 wt%. Plagioclase phenocrysts are euhedral, with rims of An_{36-40}, and cores as calcic as An_{60}. As in the Therasia dacites, plagioclase phenocrysts in the Cape Riva dacite contain complex dissolution surfaces and saw tooth zoning. Rare xenocrysts of An_{70-96} also occur. Orthopyroxene phenocrysts have compositions of $Wo_3En_{52-68}Fs_{45-29}$, and clinopyroxenes from $Wo_{44}En_{41}Fs_{15}$ to $Wo_{40}En_{36}Fs_{24}$.

Cape Riva mafic enclaves

Millimetre-sized quenched blebs of basaltic magma occur dispersed ($\ll$1 %) through the Cape Riva dacite, and in banded pumices containing the dacite and andesite mingled

together. They contain An_{90-96} plagioclase, Fo_{72-84} olivine, $Wo_{41-44}En_{36-41}Fs_{15-23}$ cpx and rare $Wo_3En_{68}Fs_{29}$ opx. The enclaves have micro-crenulated surface textures, and many have a single crystal or xenocrystic fragment at their centres. They are interpreted as small fragments of chilled basaltic magma.

Cape Riva andesite

The Cape Riva andesitic scoria has 60–62 wt% SiO_2 and 3.2–2.5 wt% MgO; it contains ∼12 wt% macroscopic crystals of plagioclase, olivine, clinopyroxene and magnetite set in brown dacitic glass with 63.5 wt% SiO_2. The pure andesitic component (free of any in-mingled streaks of dacite) contains two populations of plagioclase: (1) a calcic population of An_{70-96}, with a discrete population of euhedral, unzoned grains of An_{90-96}, and (2) a less abundant population with cores up to An_{52} and rims of An_{30-40}. Olivines are compositionally uniform (Fo_{84}). Augites occur sparsely as microphenocrysts of $Wo_{40-41}En_{41-43}Fs_{19}$. No orthopyroxene has been observed.

The olivines and population-1 plagioclases in the andesite resemble phenocrysts present in the basaltic enclaves, whereas population-2 plagioclase resembles phenocrysts in the dacites. Genesis of the Cape Riva andesite is inferred to have involved the mixing of basaltic and dacitic magmas (Figure 5.2). Eruption occurred long after mixing for the hybrid glass to become homogeneous at the scale of the electron beam (∼10 µm).

5.3.2 Whole rock chemistry and mixing systematics

Whole rock analyses of representative samples of each unit are shown in Table 5.3, and representative groundmass analyses in Table 5.4. The complete dataset is presented in Appendix B. We have used a series of variation diagrams showing the whole rock compositions of the Therasia and Cape Riva magmas, plus those of the lavas of the Skaros shield (from Huijsmans, 1985) to gain insight into the petrogenesis of the dif-

ferent magmas (Figs 11 and 12). Typical fractionation trends for Santorini magmas are also shown (Mann 1983; Huijsmans 1985; Druitt et al. 1999).

Figure 5.3 shows the variations of five key major oxides (CaO, MgO, FeO, TiO_2, P_2O_5) and two strongly compatible trace elements (Cr and Ni). On the plots of CaO and MgO (also Na_2O, Al_2O_3, V and Sc) on which typical fractionation trends are weakly curved, all the Therasia and Cape Riva magmas fall on, or close to, the fractionation trend. However, on the plots of FeO, TiO_2, P_2O_5, Cr and Ni, on which the fractionation trends are strongly curved, the Cape Riva hybrid andesite falls systematically off the fractionation trend. This is what we would expect to see if it was generated by the mixing of mafic and silicic end-members. The upper Therasia hybrid andesite also falls off the fractionation trend on plots of FeO and TiO_2, it does not on the other plots because mixing occurred along the fractionation trend, not across it. The lower Therasia andesite has slightly lower FeO_{tot} and TiO_2, suggesting it may also be a hybrid. The andesite of Oia, however, sits near the top of the TiO_2 peak (Figure 5.3), showing that it is the product of fractionation and not mixing. Geochemically it is similar to the Upper Scoria 2, with slightly lower Al_2O_3 and Sr than the other Therasia andesites. This may mean that the andesite of Oia is left over magma from the Upper Scoria 2 eruption, or that it was produced by the same processes.

Mixing models using the 'PetroGraph' software (Petrelli et al., 2005) successfully reproduce the compositions of the upper Therasia and Cape Riva hybrid andesites (Table 5.5). In the case of the upper Therasia andesite, low Cr and Ni require the mafic end-member to also have low Cr and Ni. The relatively high P_2O_5, close to the fractionation trend, requires the silicic end-member to have a high P_2O_5 content, limiting it to a silica content of 64–67 wt%. The upper Therasia andesite can be successfully reproduced by mixing ∼60 wt% of a typical Therasia dacite with ∼40 wt% of mafic magma with the same composition as a basaltic enclave (GS10-43) collected from the same flow (sum of the squares of the residuals of 0.16). The Cape Riva andesite has higher Cr and Ni than the upper Therasia andesite, requiring that the

Table 5.3: Representative whole rock analyses of the Therasia and Cape Riva products

	Therasia mafic enclave	Upper Therasia andesite	Therasia dacite	Cape Riva andesite	Cape Riva dacite
Sample	GS10-43	GS10-22	GS10-17	S09-41	S09-40
Unit	Flow 22	Flow 22	Flow 5	Cape Riva A	Cape Riva A
Major elements (ICP-AES, wt% dry)					
SiO_2	51.87	60.26	66.00	60.19	65.84
Al_2O_3	19.07	17.16	15.38	16.43	15.40
TiO_2	0.89	0.86	0.75	0.88	0.76
FeO_T[1]	8.08	6.05	4.66	6.58	4.88
MgO	5.44	2.66	1.08	3.17	1.16
CaO	10.16	5.98	3.15	6.20	3.28
Na_2O	3.30	4.52	5.48	4.63	5.84
K_2O	0.90	2.18	3.19	1.56	2.45
MnO	0.16	0.14	0.13	0.16	0.16
P_2O_5	0.14	0.19	0.18	0.19	0.22
Trace elements (ICP-MS, ppm)					
Li	16.2	18.1	25.5	16.4	17.4
Sc	25.9	17.4	13.9	23.4	13.8
V	193.0	109.0	30.1	139.0	30.2
Cr	31.30	9.52	1.17	27.10	0.60
Ni	15.80	5.65	0.86	14.20	2.57
Rb	25.8	68.1	104.0	50.0	71.7
Sr	323	231	133	185	127
Y	23.8	37.9	50.8	38.5	45.9
Zr	108	200	321	175	250
Nb	4.71	9.47	12.90	7.12	9.44
Ba	251	391	513	297	375
La	11.9	23.5	32.2	19.0	23.7
Ce	26.9	49.5	66.5	40.7	50.5
Pr	3.37	5.93	7.70	4.98	6.09
Nd	14.2	23.4	30.1	20.4	24.6
Sm	3.43	5.40	6.91	5.14	5.77
Eu	0.97	1.29	1.43	1.29	1.34
Gd	3.67	5.57	7.14	5.56	6.44
Tb	0.62	0.92	1.20	0.95	1.07
Dy	3.92	5.96	7.94	6.16	7.06
Ho	0.84	1.27	1.68	1.33	1.54
Er	2.53	3.89	5.20	4.11	4.77
Yb	2.42	3.94	5.30	4.08	4.92
Lu	0.37	0.59	0.81	0.62	0.75
Hf	2.78	5.27	7.51	4.69	6.22
Ta	0.29	0.63	0.92	0.50	0.64

[1] FeO_T is the total FeO and Fe_2O_3 content calculated as FeO

Table 5.4: Representative groundmass analyses of the Therasia and Cape Riva products

	Upper Therasia andesite	Therasia dacite	Cape Riva andesite	Cape Riva dacite
Sample	GS10-22	GS10-17	S09-41	S09-40
Unit	Flow 22	Flow 5	Cape Riva A	Cape Riva A
Major elements (ICP-AES, wt% dry)				
SiO_2	63.67	67.99	61.53	69.88
Al_2O_3	15.44	14.70	16.98	15.05
TiO_2	0.79	0.63	0.74	0.48
FeO_T[1]	5.60	4.03	5.96	3.31
MgO	2.39	0.85	2.62	0.53
CaO	4.62	2.34	5.86	2.14
Na_2O	4.55	5.91	4.92	5.86
K_2O	2.60	3.25	1.82	2.95
MnO	0.14	0.12	0.15	0.12
P_2O_5	0.20	0.19	0.17	0.16
Trace elements (ICP-MS, ppm)				
Li	20.3	26.9	17.7	20.4
Sc	18.5	14.2	24.6	14.8
V	80.8	14.5	126.0	8.3
Cr	8.41	0.76	21.20	4.33
Ni	4.62	0.75	14.60	5.48
Rb	89.0	105.0	60.2	101.0
Sr	176	108	197	105
Y	44.9	53.6	44.2	61.1
Zr	271	334	214	341
Nb	11.40	13.30	7.58	11.60
Ba	455	542	323	460
La	27.9	33.9	20.5	28.9
Ce	63.2	70.2	43.6	61.6
Pr	7.07	8.22	5.41	7.40
Nd	27.9	31.9	21.6	29.5
Sm	6.31	7.16	5.28	7.09
Eu	1.20	1.33	1.27	1.28
Gd	6.40	7.35	5.68	7.50
Tb	1.09	1.27	0.97	1.29
Dy	7.12	8.43	6.58	8.58
Ho	1.51	1.80	1.41	1.87
Er	4.64	5.53	4.32	5.81
Yb	4.69	5.74	4.37	6.09
Lu	0.72	0.87	0.66	0.94
Hf	6.73	8.38	5.14	8.07
Ta	0.81	0.98	0.52	0.82

[1] FeO_T is the total FeO and Fe_2O_3 content calculated as FeO

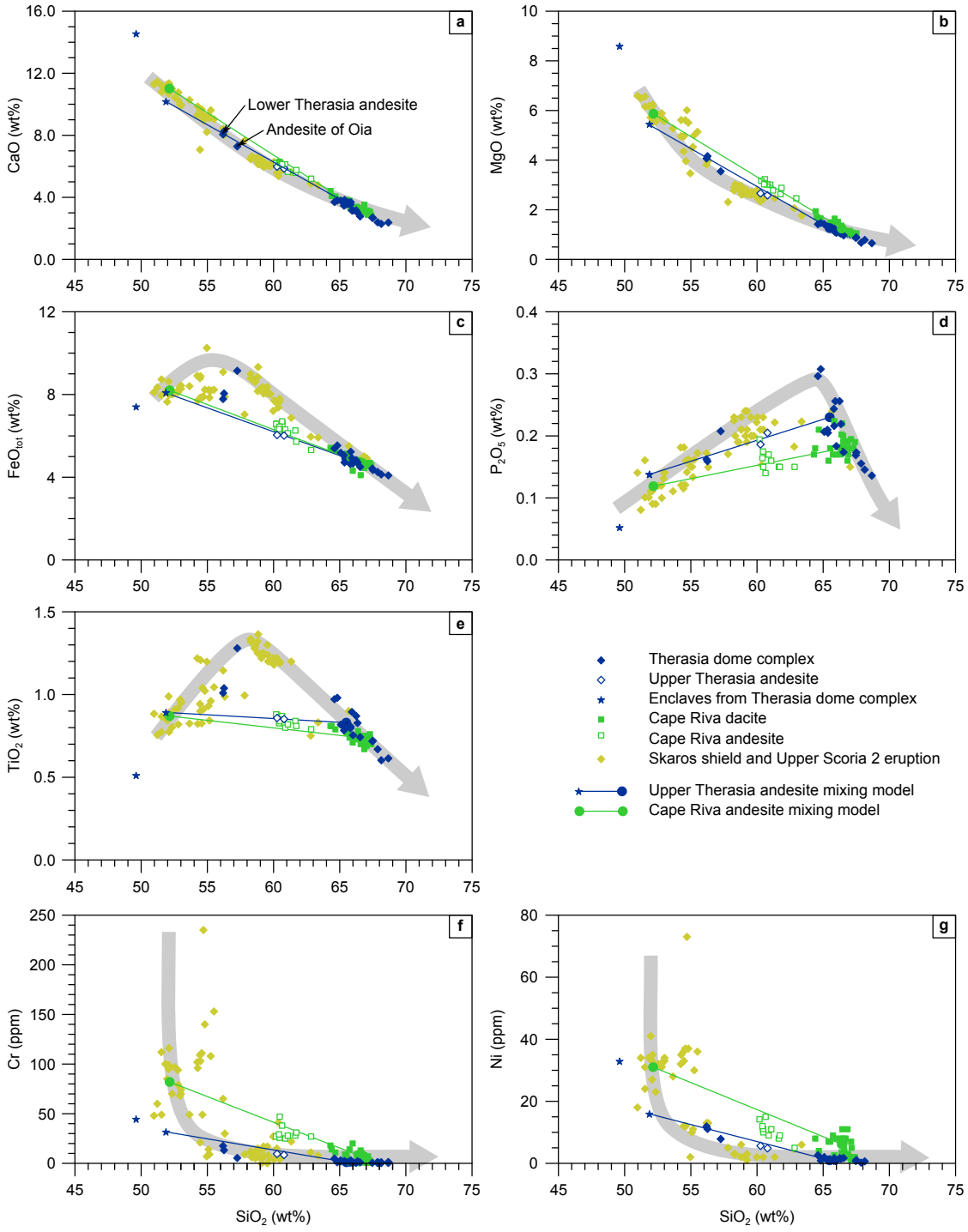

Figure 5.3: Variation diagrams of major elements and selected highly compatible trace elements. Mixing models for the upper Therasia andesite and the Cape Riva andesite are shown as blue and green lines, respectively. The mixing calculations are presented in Table 4. The typical fractionation trend for Santorini magmas discussed by (Nicholls, 1971), Mann (1983) and Druitt et al. (1999)is shown on the diagrams as a grey arrow. Composition of the Skaros lavas are also plotted for reference (Huijsmans, 1985) as are scoria from the Upper Scoria 2 eruption (Druitt et al., 1999)

mafic end-member also has higher contents of these elements. The composition of the Cape Riva andesite can be modelled by mixing ∼60 wt% of Cape Riva dacite with ∼40 wt% of an average Skaros basalt (sum of the squares of the residuals of 0.14). However, the calculated Ni content is higher than that measured in the Cape Riva andesite, suggesting that the mafic endmember had lower Ni than the average Skaros basalt.

Despite their broadly similar compositions in terms of silica content and many other major and trace elements, most of the Therasia dacites are enriched in incompatible elements such as K, Rb and Zr (also Nb, Ta, Th, Hf and LREE) compared to the Cape Riva dacite (Figure 5.4). LREE are also more enriched in the Therasia dacites relative to the HREE. For example, the Therasia dacites have an average La/Yb ratio of 5.91 ± 0.16 (2σ), while the Cape Riva dacite has a ratio of 4.85 ± 0.04. Amongst the HFSE, Nb and Ta are more enriched than Zr and Hf. The 23 analysed samples of Cape Riva pumice form a tight linear cluster on Figure 5.4, showing that the magma was well mixed. All of the 11 analysed Therasia lavas younger than ∼39 ka, and most of the intercalated pumice horizons, similarly form a tight linear cluster (at higher incompatible contents than the Cape Riva, for a given SiO_2 content). However, some of the Therasia pumices overlap with the Cape Riva field for some elements. Most prominent of these is the Cape Tripiti pumice, which lies in, or close to, the Cape Riva field for most incompatible elements except K, suggesting that the magma that fed the Cape Tripiti eruption had some chemical characteristics intermediate between the two groups of dacite.

The differences between the Therasia and Cape Riva dacites are also seen between the corresponding hybrid andesites of these two series. Despite having a similar SiO_2 content, the upper Therasia hybrid andesite is enriched in incompatible elements compared to the Cape Riva hybrid andesite (e.g. 2.1 wt% K_2O compared to 1.7 wt%, respectively). Like the Therasia dacites, the Therasia andesite is also enriched in LREE relative to HREE, and enriched in Nb and Ta relative to Zr and Hf compared top the

Table 5.5: Calculation for the mixing of (1) Therasia dacite plus Therasia basalt (mafic enclave) to produce the upper Therasia hybrid andesite, and (2) Cape Riva dacite plus Skaros basalt to produce the Cape Riva hybrid andesite.

			Upper Therasia Hybrid Andesite					Cape Riva Hybrid Andesite		
	Mean Therasia Dacite	Mafic Enclave (GS10-43)	Calculated	Measured (GS10-22)	Residual	Mean Cape Riva Dacite	Mean Skaros Basalt	Calculated	Mean Measured	Residual
Major Elements (wt%)										
SiO_2	65.50	51.86	60.28	60.26	0.02	66.41	52.16	61.22	61.14	0.08
TiO_2	0.83	0.89	0.85	0.86	−0.01	0.74	0.87	0.79	0.83	−0.04
Al_2O_3	15.51	19.07	16.87	17.16	−0.29	15.46	18.38	16.52	16.39	0.13
FeO_T[1]	4.93	8.08	6.13	6.05	0.08	4.75	8.20	6.01	6.27	−0.26
MnO	0.14	0.16	0.15	0.14	0.01	0.15	0.17	0.16	0.15	0.01
MgO	1.21	5.44	2.83	2.66	0.17	1.23	5.96	2.95	2.93	0.02
CaO	3.41	10.16	5.99	5.98	0.01	3.35	10.78	6.06	5.92	0.14
Na_2O	5.50	3.30	4.66	4.52	0.14	5.33	2.72	4.38	4.53	−0.15
K_2O	2.74	0.90	2.04	2.18	−0.14	2.40	0.64	1.76	1.68	0.08
P_2O_5	0.23	0.14	0.2	0.19	0.01	0.18	0.12	0.16	0.15	0.01
Total	100.00	100.00	100.00	100.00	0.00	100.00	100.00	100.01	99.99	0.02
			Sum of the Squares:		0.16			**Sum of the Squares:**		0.14
Trace Elements (ppm)										
Cr	2	31	13	10	3	8	82	35	33	2
Ni	1	16	7	6	1	6	31	15	10	5
Nb	12	5	9	9	0	10	4	8	8	0
Rb	92	26	66	68	−2	74	21	55	51	4
Zr	291	108	221	200	21	266	94	203	193	10
Sr	155	323	219	231	−12	143	226	173	179	−6

For the upper Therasia andesite, the mixing proportions are 38:62 mafic:silicic. For the Cape Riva andesite, the proportions are 36:64. Calculated using the PetroGraph software of Petrelli et al. (2005).

[1] FeO_T is the total FeO and Fe_2O_3 content calculated as FeO

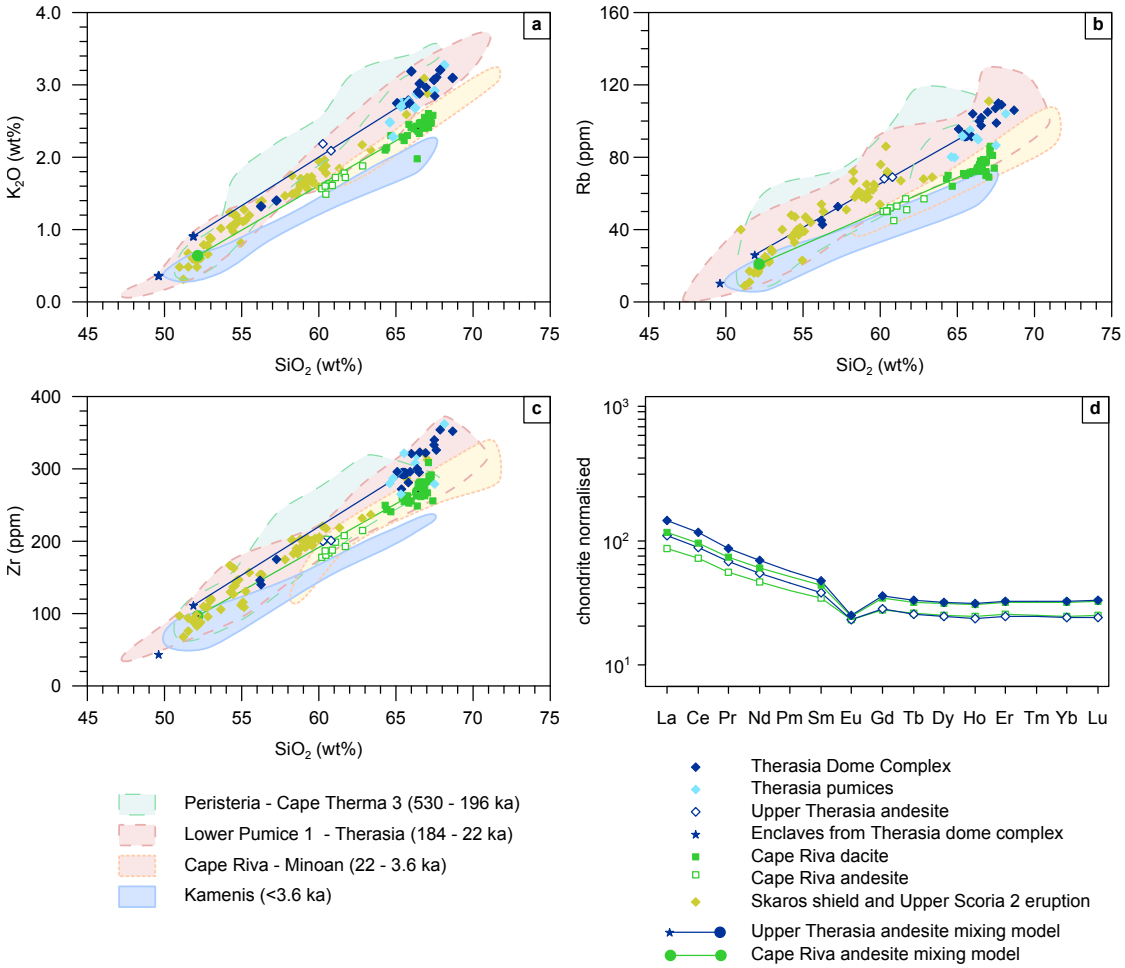

Figure 5.4: Incompatible element variation diagrams. (a–c) Therasia and Cape Riva data are plotted as points, along with the Skaros data of Huijsmans (1985) and Upper Scoria 2 data of Druitt et al. (1999). Mixing models for the upper Therasia andesite and the Cape Riva andesite are plotted, as in Figure 5.3. Fields of Santorini magma during the volcanic history since 530 ka are plotted, showing the long-term decrease in incompatible element concentration at Santorini Druitt et al. (1999); Huijsmans (1985); Martin (2005). (d) REE diagram showing the Therasia and Cape Riva magmas. The Therasia dacite is an average of 14 flows with 65–68 wt% SiO_2, and the Cape Riva dacite is an average of four analyses with SiO_2 contents of 66–67 wt% (mean: 66.5 wt%). The upper Therasia andesite is an average of flows 11 and 22 (mean: SiO_2 60.5 wt%), and the Cape Riva andesite is an average of three analyses with SiO_2 contents between 60.2 and 60.4 wt% (mean: 60.4 wt%)

Table 5.6: Temperatures, T, and oxygen fugacities, fO_2, of the three Therasia pumice fall units analysed, calculated using Fe–Ti oxide compositions using the two formulations discussed in the text.

Unit	Andersen and Lindsley (1985) with Stormer (1983)		Ghiorso and Evans (2008)	
	T (°C)	$\log(fO_2)$	T (°C)	$\log(fO_2)$
Therasia:				
Cape Tripiti	896 ± 12	-12.7 ± 0.3	901 ± 14	-12.7 ± 0.4
Pumice fall B	926 ± 9	-11.4 ± 0.2	956 ± 12	-10.9 ± 0.3
Pumice fall C	875 ± 5	-13.4 ± 0.1	876 ± 9	-13.4 ± 0.2
Cape Riva[1]	879 ± 11	-12.9 ± 0.2	891 ± 12	-12.6 ± 0.3

Errors are 2σ, where σ is the standard error of the mean.
[1] Data from Cadoux et al. (2014)

Cape Riva andesite. This is also reflected in the calculated mafic mixing end-members of the two hybrid andesites shown on Figure 5.4, although the difference is subtle.

5.3.3 Magmatic temperatures

Magmatic temperatures calculated from Fe–Ti oxide compositions from three pumice falls from the Therasia dome complex are reported in Table 5.6. Using the formulation of Andersen and Lindsley (1985) and Stormer (1983), temperatures for the Cape Tripiti pumice and pumice fall C range from about 875 °C to 895 °C, and $\log(fO_2)$ from −12.7 to −13.4 (at, or slightly below the FMQ oxygen buffer; Figure 5.5). These conditions are close to what Cadoux et al. (2014) found for the Cape Riva (879 ± 15 °C and $\log[fO_2] = -12.9 \pm 4$). Pumice fall B is hotter and more oxidised, with a temperature of about 925 °C and an oxygen fugacity on the NNO buffer. The temperatures and oxygen fugacities of the Cape Tripiti pumice and pumice fall C calculated using Ghiorso and Evans (2008) are in excellent agreement. However, the temperatures of pumice fall B calculated using Ghiorso and Evans's formulation are about 20 °C hotter, and the oxygen fugacities are about 0.5 log units higher.

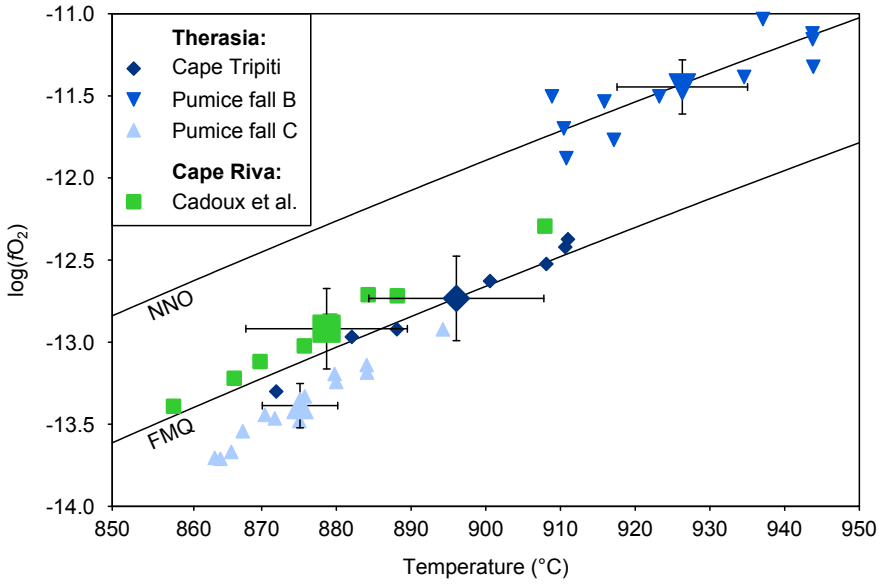

Figure 5.5: Temperature and oxygen fugacities of the three Therasia pumice fall units analysed, calculated using Fe–Ti oxide compositions using the formulation of Andersen and Lindsley (1985) and Stormer (1983). Large symbols with error bars are averages, errors are 2σ, where σ is the standard error of the mean. Cape Riva data from Cadoux et al. (2014) shown for comparison. NNO and FMQ oxygen buffers are calculated at 2 kbar, and are taken from Huebner and Sato (1970) and Frost (1991), respectively.

5.4 Discussion

5.4.1 Origin of the magma series

The Therasia and Cape Riva dacites have similar whole rock major element compositions (for all major elements except K), phenocryst assemblages, phenocryst rim compositions and Fe–Ti oxide temperatures, although the Cape Riva dacite has slightly more evolved interstitial melt. The main difference between the two magmas is that the Cape Riva dacite is depleted in incompatible elements compared to the Therasia dacite. The Cape Riva hybrid andesite is also incompatible-depleted relative to the upper Therasia hybrid andesite, and there are indications that the basaltic mixing end-members were similarly different. Throughout most of the 15 ky over which the Therasia dome complex was constructed, the eruptions tapped typical Therasia-type dacite. However, the 26 ka Cape Tripiti eruption tapped dacite with some incompatible trace element contents intermediate between those of Therasia and Cape Riva.

Since the Therasia and Cape Riva magma series form parallel trends on incompatible element variation diagrams (Figure 5.4), and have different LREE/HREE ratios, they cannot be related to each other simply by closed-system crystal fractionation schemes like those explored in previously published papers (Druitt et al., 1999; Mann, 1983; Nicholls, 1971). Neither can the Cape Riva dacite be generated by simple back-mixing of Therasia dacite with an incompatible-depleted basalt, since mixing would displace the silicic compositions almost parallel to the compositional trends rather than perpendicular to them. Crustal contamination of Therasia dacite to produce Cape Riva dacite is also unlikely, as this would be expected to increase incompatible element concentrations, not decrease them (Barton et al., 1983; Druitt et al., 1999). Moreover, the two dacite types have very similar whole-rock $^{87}Sr/^{86}Sr$ ratios (0.7050 and 0.7049 respectively; Briqueu et al., 1986; Druitt et al., 1999; Zellmer et al., 2000), ruling out a significant difference in the extent of upper crustal contamination. The Therasia and Cape Riva magma series (basalt, dacite and hybrid andesite in each case) represent two fundamentally distinct magma batches that cannot be related to each other in any simple way by shallow-level processes.

This conclusion is supported by comparison of the two magma series with longer-term geochemical trends at Santorini (Druitt et al., 1999; Huijsmans, 1985; Huijsmans et al., 1988). The same incompatible elements have decreased progressively in Santorini magmas over the last 530 ka, such that the lavas of the historical Kameni Volcano are the most incompatible-depleted (Figure 5.4). The difference between the (older) Therasia and (younger) Cape Riva series represents one step in this longer-term evolution. The magnitude of the decrease is similar for most incompatible elements, so that the ratios between them (e.g. K/Zr, Rb/Zr, Rb/La) have remained approximately constant with time. However, the LREE have become depleted relative to HREE, a change that is also apparent between Cape Riva and Therasia (Figure 5.4d). Similar changes also occur between different high field strength elements: Nb and Ta concentrations drop faster than those of Zr and Hf. Progressive depletion in K and other incompatible

elements with time has also occurred at other centres in the Aegean region (Francalanci et al., 2005).

A decrease in the extent of crustal contamination with time, as might be expected from the progressive sealing-off of ascending magmas from the crust, is not tenable; there is no evidence for a consistent decrease in the $^{87}Sr/^{86}Sr$ ratio with time at Santorini (Figure 2.12). Isotopic signatures fluctuate with time (Barton et al., 1983; Briqueu et al., 1986; Druitt et al., 1999; Martin et al., 2010), and some young melts are amongst the most radiogenic in the history of the volcano (Martin et al., 2010; Vaggelli et al., 2009).

Incompatible trace element contents and isotopic signatures at Santorini are decoupled, ruling out a simple common origin. A more likely explanation for the observed trends lies in the nature of the mantle sources of the parental basalts feeding the volcanic system. Possibilities include an increase with time in the degree of source depletion, an increase of source melt fraction, or a decrease in degree of source metasomatism by slab-derived fluids or melts. All of these mechanisms could potentially account for basaltic parents with decreasing incompatible element contents with time (Bailey et al., 2009; Clift and Blusztajn, 1999; Francalanci et al., 2005; Huijsmans et al., 1988; Zellmer et al., 2000).

A mantle origin is supported by the recent discovery at Santorini of multiple coexisting basalt types with different trace element and isotopic signatures (Bailey et al., 2009; Vaggelli et al., 2009). Changing proportions of different parental basalts that ascend into the crust, where they mix and differentiate at between 4 and 2 kb to intermediate and silicic compositions (Andújar et al., 2010; Cadoux et al., 2014), may account for the observed temporal variations of trace element chemistry. Irrespective of the exact explanation, our results demonstrate the availability of chemically distinct batches of silicic magma within the crustal plumbing system beneath Santorini, as has been demonstrated previously for basalts (Bailey et al., 2009).

5.5 Summary

From the chemistry and the petrology of the Therasia and Cape Riva deposits we can conclude:

- Between 39 ka and 25 ka, the $\sim$2 km^3 of magma erupted as lavas and pumice falls was compositionally (65–68 wt% SiO_2) and thermally (895–925 °C) monotonous.
- The Therasia and Cape Riva dacites are similar in most major elements, but the Cape Riva dacite has lower contents of K and incompatible trace elements (e.g., Rb, Zr, Th, LREE) than the Therasia dacites at a given silica content. This decrease in incompatibles that took place at 21.8 ka is one step in the well-documented longer-term decrease in incompatible elements with time observed at Santorini over the last 530 ky. The Therasia and Cape Riva dacites represent distinct magma batches that are unrelated by shallow-level processes
- Discharge of basaltic magma during this time period is limited to $\ll$1% quenched enclaves of olivine basalt in some Therasia lavas and in Cape Riva pumice. However, hybrid andesite magmas formed by the mixing of olivine basalt and dacite in approximately equal proportions were erupted as lava towards the end of the Therasia, and as scoria in the Cape Riva eruption. These hybrids may record an increased influx of basalt into the upper crust over the several thousands of years leading up to the Cape Riva eruption. Increased basaltic flux may have played a role in the rapid accumulation of incompatible-depleted Cape Riva magma beneath the summit of Skaros Volcano prior to its 21.8 ka eruption.

Chapter 6

Plagioclase

6.1 Introduction

There is a lot of information that can be gleaned by examining the crystals in volcanic rocks. Some of this has been described already in Chapter 5, such as how the different mineral assemblages in the upper Therasia and Cape Riva andesites reveal that they were formed by magma mixing.

In this chapter, I look in more detail at the zoning patterns of major and trace elements in plagioclase. I focus on the phenocrysts, as these provide the best record of the events that took place within the magma reservoir, and I focus mostly on phenocrysts in the dacites, as the dacites make up the majority of the erupted material during the both the Cape Riva eruption and the construction of the Therasia dome complex (Chapter 4).

The concentrations of a wide range of different elements were measured in the plagioclase crystals (Si, Al, Na, Ca, Li, Mg, K, Ti, Fe, Sr, Ba, La, Ce, Pb), as elements with different diffusivities can provide different insights into magmatic processes (Chapter 3). The concentrations of fast-diffusing elements can be used to estimate timescales of magmatic processes through the modelling of diffusive gradients. On the other hand, slowly-diffusing elements can be used to track growth conditions of crys-

tals, as such elements require long times to re-equilibrate with their host magma. Their concentrations in crystals should therefore reflect the magma composition at the time of growth, and they should be unaffected by any subsequent changes to its chemistry. Which elements can be considered 'fast-' and which can be considered 'slow-diffusing' depends the time- and length-scales of interest, as well as the temperature and plagioclase composition. This is discussed later in the chapter, after the zoning patterns are presented.

Of particular interest are the changes that occurred in the magma reservoir in the build-up to the Cape Riva eruption. In Chapter 5 we saw that a change in the concentration of incompatible elements between the Therasia and Cape Riva eruptions suggested that there was a large influx of new silicic magma shortly before the Cape Riva eruption. The field and chemical evidence constrains the timing of this influx to within $2{,}800 \pm 1{,}400$ y before the Cape Riva eruption (Chapter 4). We can look for evidence of this influx in the composition of the plagioclase crystals, using slowly-diffusing trace elements to track changes in the composition of the melt. Also of interest are the longevities of the Therasia and Cape Riva magma reservoirs, and the plagioclase crystals can be useful here as well. Diffusion modelling can provide estimates of the high-temperature residence times of the plagioclase crystals, which can then be related to magma reservoir longevity.

6.2 Methods

6.2.1 Analytical techniques

Thin sections from three dacitic lavas from the Therasia dome complex (flows 5, 8 and 9; samples GS10-17, GS10-14 and GS10-16, respectively) were studied in detail. Six pumices from the Cape Riva eruption were selected, covering all four phases of the eruption (phase A: GS11-34a and GS11-34f; phase B: S12-06; phase C: GS11-30b and S12-05; phase D: GS11-39b). These were hand-crushed, and plagioclase crystals were

hand-picked, set in resin and polished. Crystals with adhering melt were preferred, as adhering melt demonstrates that those crystal faces are original rather than fracture surfaces caused by crushing. Most of the plagioclase crystals are tabular, and these were orientated so that their shortest dimension would be within the plane of the polished surface. Trace element concentrations of plagioclase crystals in one thin section from the upper Therasia andesite (flow 22; GS10-22) were also analysed.

Mineral major element compositions were analysed using the Cameca SX 100 electron microprobe at the Laboratoire Magmas et Volcans, Université Blaise Pascal, Clermont-Ferrand, using a beam current of 15 nA.

Backscattered electron (BSE) images of selected plagioclase crystals were produced on the scanning electron microscope (SEM), and then calibrated for anorthite content using the analyses made with the electron microprobe. Five points on each crystal were analysed using the electron microprobe for their anorthite content, and the greyscale values of these same points was measured on the SEM images using the image analysis software package ImageJ (Rasband, 2012). The relationship between the greyscale value and composition was then calculated using a linear least-squares regression for each image. A typical example is shown in Figure 6.1. Correlation between greyscale value and anorthite content of the plagioclases was high, with correlation coefficients $r^2 > 0.97$ for most (and $r^2 > 0.90$ for all) the images used. This corresponds to a standard error in the calculated anorthite content of ± 1–2 mol%, estimated from the regression parameters. With this relationship, the anorthite content of any spot on the image could be calculated. This allowed me to quickly plot profiles of anorthite against distance at much greater spatial resolution than would otherwise be practical (pixel size was 0.5–1.5 µm depending on the image).

Before plotting anorthite profiles from the BSE images, the images were smoothed using a two pixel radius median filter. The advantage of a median filter over a moving average is that it removes noise while leaving any sudden changes in composition unchanged. This meant that sharp boundaries between the rim and core were not softened

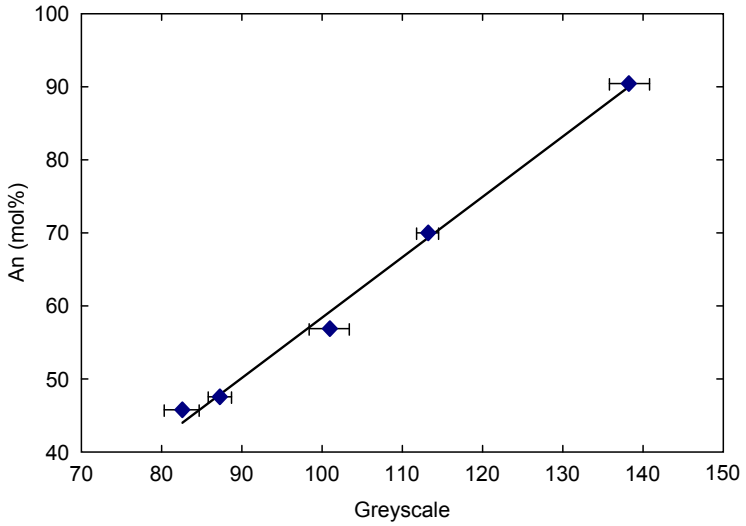

Figure 6.1: Typical calibration curve for a BSE image of a plagioclase crystal (GS10-14 XL66)

by the smoothing process. Each point on the profiles was the average of a strip 10×1 pixels perpendicular to the direction of the profile for each point. The distance from the rim for each point was corrected for profiles that were not perpendicular to the crystal rim, although this correction was usually minor.

Trace elements in the plagioclase crystals (Li, Mg, K, Ti, Fe, Sr, Ba, La, Ce, Pb) were measured at the Laboratoire Magmas et Volcans, Université Blaise Pascal, Clermont-Ferrand, France using a Resonetics M-50-E 193 nm laser ablation system connected to an Agilent 7500cs ICP MS. The beam size was 10–15 µm in diameter, and laser pulses were fired at a rate of 2 Hz.

Calcium was used as the internal standard for the LA ICP-MS analyses. For most of the analyses, Ca values were measured by electron microprobe before LA ICP-MS analysis. In the analyses from the profiles for diffusion modelling, Ca was again used as the internal standard, but the Ca was measured from calibrated BSE images. The grey scale of the BSE images of the selected plagioclases was calibrated for An content using the electron microprobe, as discussed above. Photomicrographs of the analysed crystals, with the laser pits visible, were then superimposed onto the calibrated BSE images. The anorthite content of the spots analysed by LA ICP-MS could then be calculated from the calibrated BSE images.

For diffusion modelling, 13 representative crystals were selected. In these crystals one or two profiles were measured perpendicular to the crystal edges by locating successive laser analyses as close as possible to each other. In crystals where two profiles were measured, these were placed perpendicular to each other. In crystals with only one profile, the location of that profile was chosen to cover the shortest possible distance between the core and the rim. This is the part of the crystal where trace element concentrations should change the fastest in response to diffusive exchange with the liquid (Costa et al., 2008).

6.2.2 Partition coefficients

Because the partitioning of trace elements between silicic melts and plagioclase is strongly dependent on the anorthite content of the plagioclase (Bédard, 2006; Bindeman et al., 1998; Blundy and Wood, 1991), the trace element concentrations in plagioclase tell us little on their own about the composition of the melt. The partition coefficients of Bindeman et al. (1998) were therefore used to calculate the compositions of melts that are in equilibrium with the measured plagioclase compositions; these are referred to as "liquid-equivalent compositions" in the following text.

The partition coefficients take the form (using K instead of the traditional D, in order to avoid confusion with the diffusion coefficient):

$$K = \exp\left(\frac{AX_{\mathrm{An}} + B}{RT}\right) \tag{6.1}$$

where A and B are empirically determined coefficients, X_{An} is the molar fraction of anorthite, R is the molar gas constant and T is the temperature (in K). Because the partition coefficients depend on temperature, we assumed that temperature was related to anorthite content as follows (Druitt et al., 2012):

$$T = 1\,128 + 200 \times \frac{X_{\mathrm{An}} - 0.4}{0.4} \tag{6.2}$$

This equation implies that plagioclase of An_{40} is equilibrium with a melt at 855 °C and An_{80} is in equilibrium at 1 055 °C, matching the temperatures of Santorini rhyodacites and basaltic andesites, respectively (Michaud et al., 2000).

The error in the liquid equivalent trace element concentrations, $\sigma_{C_{\text{melt}}}$, due to independent errors on the parameters in Equation 6.1 was estimated by error propagation:

$$\sigma^2_{C_{\text{melt}}} = \sigma^2_{C_{\text{plag}}} \left(\frac{\partial C_{\text{plag}}}{\partial C_{\text{melt}}}\right)^2 + \sigma^2_A \left(\frac{\partial A}{\partial C_{\text{melt}}}\right)^2 + \sigma^2_B \left(\frac{\partial B}{\partial C_{\text{melt}}}\right)^2 + \sigma^2_{X_{\text{An}}} \left(\frac{\partial X_{\text{An}}}{\partial C_{\text{melt}}}\right)^2 \quad (6.3)$$

where the errors on the trace element and anorthite contents of the plagioclase, $\sigma_{C_{\text{plag}}}$ and $\sigma_{X_{\text{An}}}$, were estimated from ICP-MS and EMP counting statistics, and the estimated errors in the coefficients of the partition coefficient equation, σ_A and σ_B were taken from Bindeman et al. (1998). This does not, however, take into account any error in the temperature.

6.3 Zoning patterns

6.3.1 Anorthite zoning

The focus of this section is on the phenocrysts from the Therasia and Cape Riva dacites. Xenocrysts and the plagioclase crystals found in the sub-solidus gabbro nodules in the Therasia dacites are not considered here. Only those crystals whose rims appear to be in equilibrium with the melt are discussed (Chapter 5).

Figure 6.2 ***(facing page)*:** Sketches of plagioclase crystals from the Therasia dacites, showing the characteristic features of the phenocrysts. Anorthite spot values from EMP analyses marked on the diagrams. On the right are the corresponding calibrated BSE images (a) A weakly zoned phenocryst (GS10-16 XL105) (b) a phenocryst without a calcic core, but with an internal resorption surface and a normally zoned, "sawtooth" outer zone (GS10-27a XL49) (c) a phenocryst with a glass inclusion-rich inner zone, overgrown by a normally zoned, "sawtooth" outer zone (GS10-17 XL57) (d) a phenocryst with a simply zoned calcic core (GS10-14 XL66) (e) a phenocryst with a partially resorbed, complexly zoned core, overgrown by an oscillatory zoned outer zone (GS10-17 XL60)

Representative plagioclase phenocrysts in the Therasia dacites

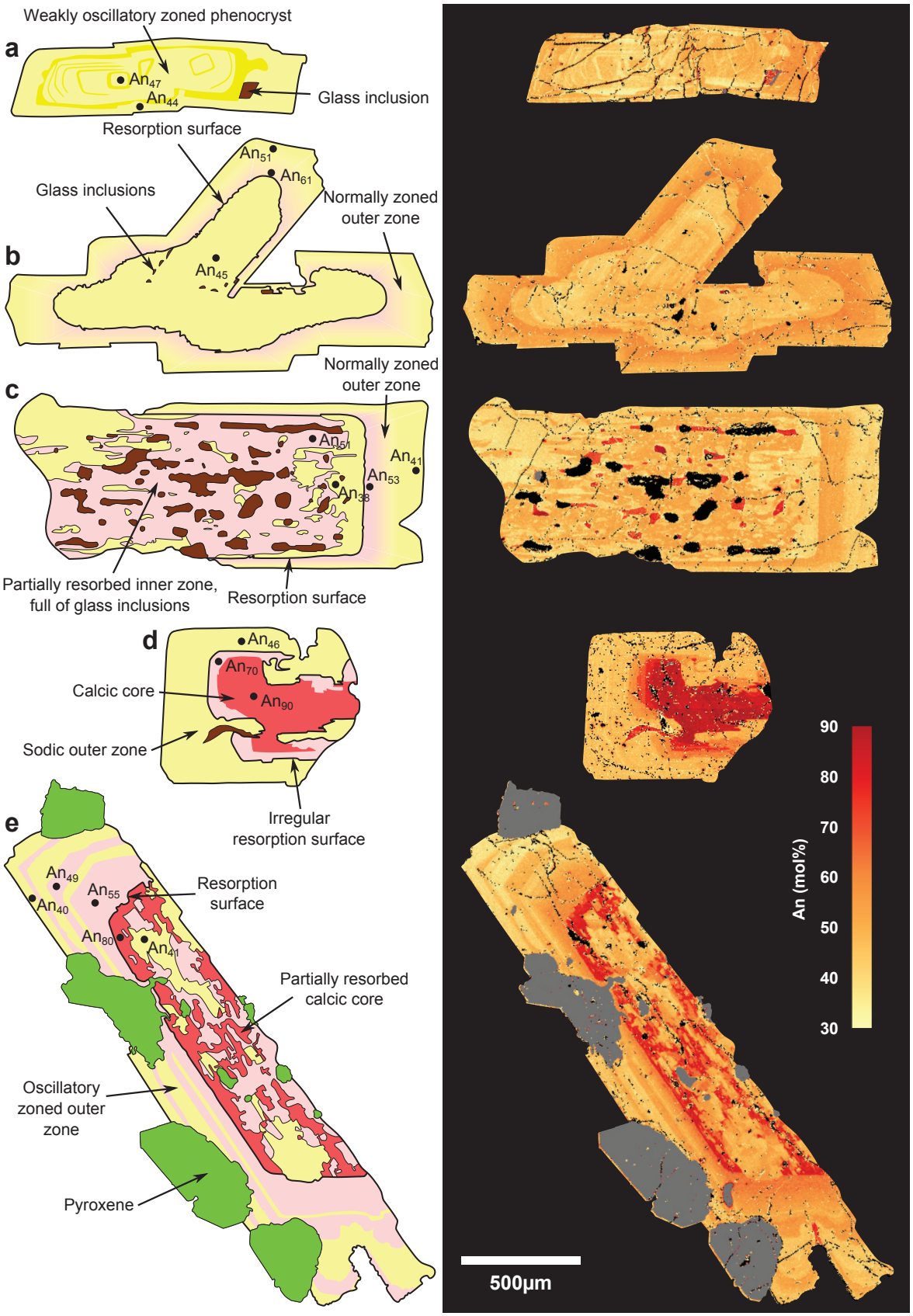

Therasia dacites

The majority of the plagioclase phenocrysts in the Therasia dacites are unzoned, or have weak oscillatory zonation (Figure 6.2a). The anorthite content of these crystals varies between An_{39} and An_{51}, depending on the lava flow, but the anorthite content of individual weakly zoned phenocrysts varies by less than about 5 mol%.

The rest can be split into two broad groups: those with sawtooth zoning, and those with calcic cores. I use the term "calcic core" to refer to a texturally well-defined entity at the centre of a crystal that has a much higher anorthite content than the outer zone. "Rim" is used to refer to the outermost part of the crystal to have grown within the magma chamber.

Sawtooth zoned phenocrysts: Some of the phenocrysts in the Therasia dacites have a single sawtooth, separating the crystal into two zones. The innermost zones of these crystals usually have a similar composition to the unzoned phenocrysts (An_{39} to An_{51}). Sometimes these inner zones are unzoned (Figure 6.2b), but sometimes they show signs of partial dissolution and have lots of large, brown glass inclusions (Figure 6.2c). The inner zones are separated from the outer zones by a resorption surface which is sometimes smooth, but can often have an irregular shape. The resorption surfaces are then overgrown by more calcic plagioclase (An_{59} to An_{72}). The crystals then gradually become more sodic towards the rims, eventually reaching the same compositions as the unzoned phenocrysts. An anorthite profile across a sawtooth zone from a similarly zoned crystal in the Cape Riva is shown in Figure 6.3.

Calcic cores: Some phenocrysts have distinct calcic cores, with anorthite contents between An_{50} and An_{91}. These calcic cores are sometimes simply zoned (Figure 6.2d), but sometimes show complex zoning indicative of partial dissolution (Figure 6.2e). The cores are separated from the rest of the crystal by an irregular resorption surface. Some calcic cores are overgrown by un-

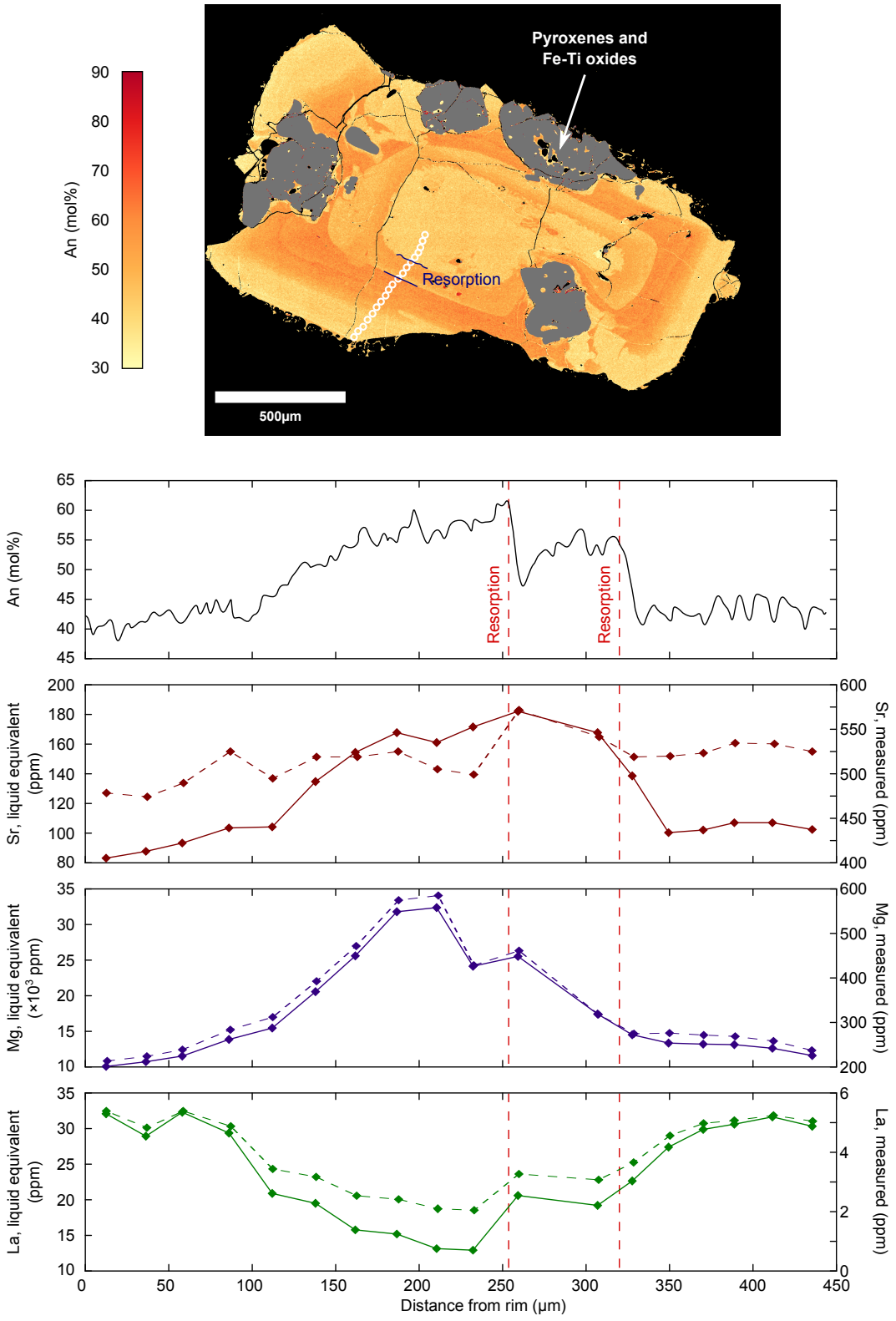

Figure 6.3: A calibrated BSE image of a plagioclase from the Cape Riva dacite (GS11-34a XL14) with sawtooth zoning. White circles indicate laser spots. The anorthite profile is measured from the calibrated BSE image, trace elements profiles were measured by LA ICP-MS. Solid lines: liquid equivalent concentrations; dashed lines: measured concentrations

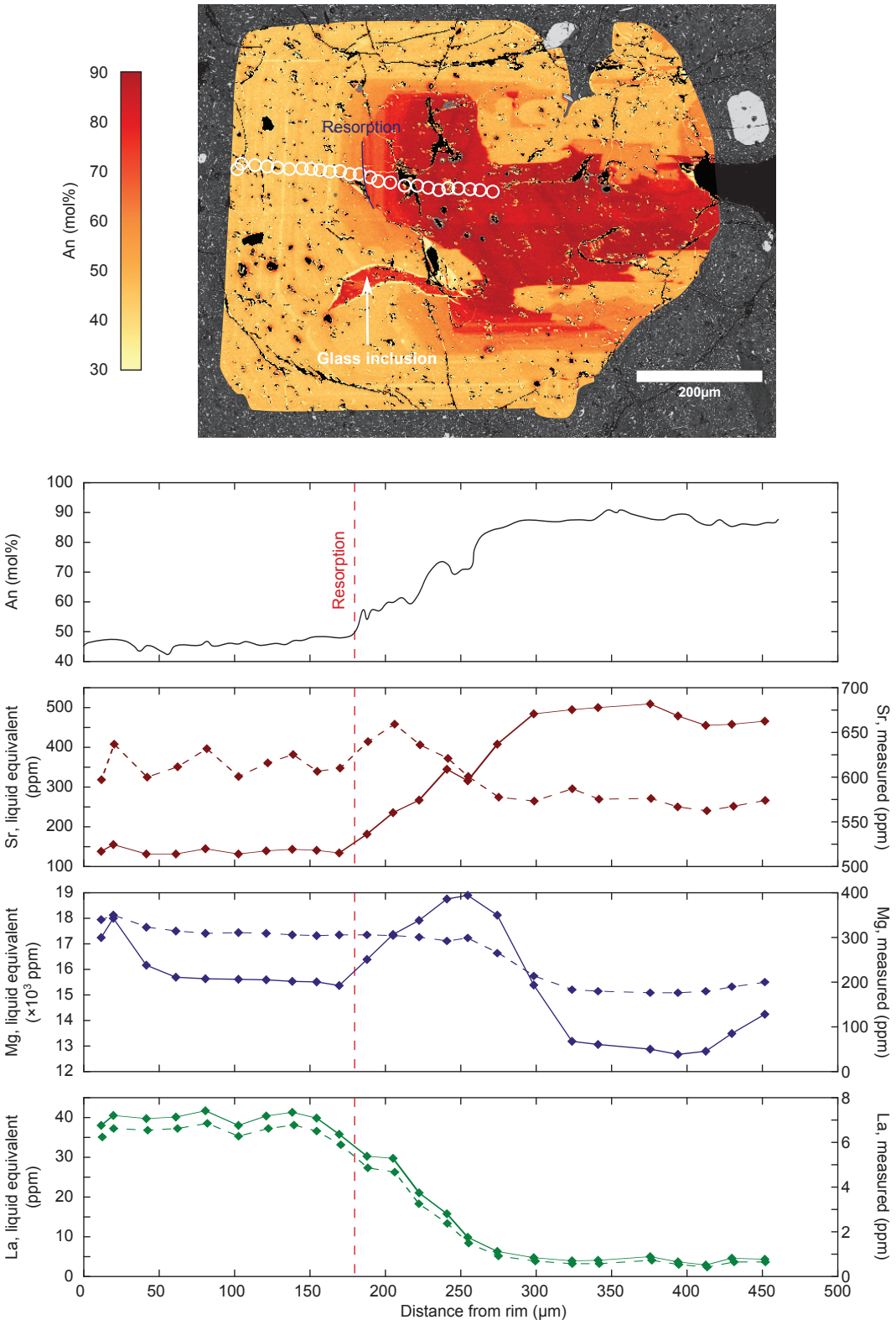

Figure 6.4: A calibrated BSE image of a plagioclase from the a Therasia dacite (GS10-14 XL66) with a calcic core. White circles indicate laser spots. The anorthite profile is measured from the calibrated BSE image, trace elements profiles were measured by LA ICP-MS. Solid lines: liquid equivalent concentrations; dashed lines: measured concentrations

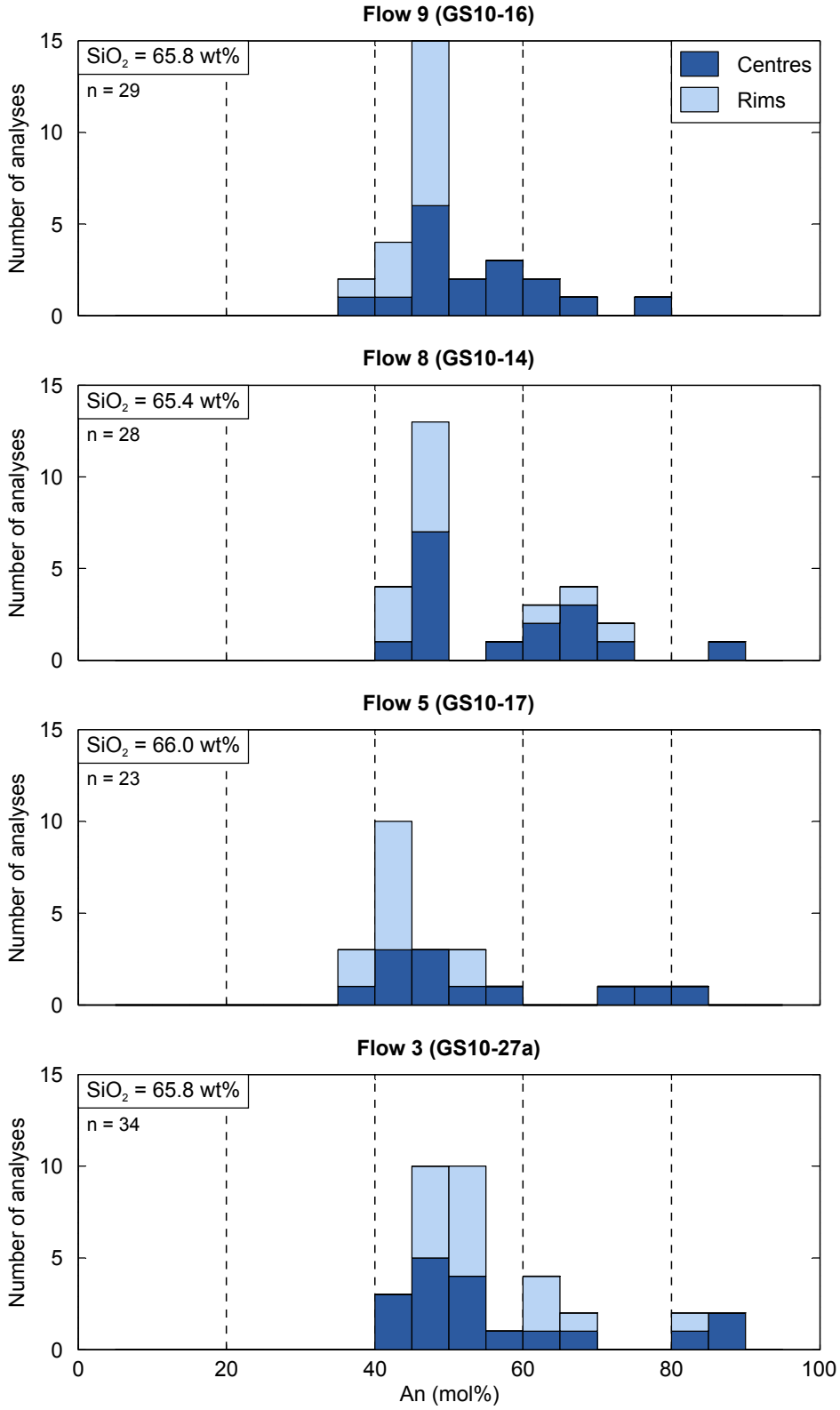

Figure 6.5: Histograms of the compositions of plagioclase crystals in the Therasia dacites. SiO_2 contents in the labels refers to whole rock compositions.

Table 6.1: Plagioclase compositions in different Therasia dacite lavas

Flow		Whole rock SiO_2 (wt%)	Phenocryst rims	Calcic cores
9	(GS10-16)	65.8	An_{44-48}	An_{53-78}
8	(GS10-14)	65.4	An_{45-46}	An_{65-91}
5	(GS10-17)	66.0	An_{41-43}	An_{50-80}
3	(GS10-27a)	65.8	An_{49-51}	—

zoned or weakly oscillatory zoned (e.g. Figure 6.2d), and these have the same compositions as the weakly zoned phenocrysts (An_{39-51}). Other calcic cores are overgrown by plagioclase that is normally zoned (e.g. Figure 6.2e), and these outer zones resemble the outer zones of the sawtooth-zoned crystals. An anorthite profile from a crystal with a calcic core is shown in Figure 6.4.

There are slight textural variations between the plagioclase found in the different dacitic lava flows of the Therasia dome complex. Sawtooth-zoned crystals were found in flows 3 and 5, but not in flows 8 and 9. Large, rounded, brown glass inclusions are found in many of the unzoned phenocrysts and the inner zones of the sawtooth-zoned phenocrysts in flow 5, but these glass inclusions are rare in the other flows. The composition of the rims and the calcic cores also vary slightly between the different flows (Table 6.1; Figure 6.5). These observations suggest that the phenocrysts in each flow are specific to that flow, and are not inherited from previous magma batches.

Figure 6.6 ***(facing page)*:** Sketches of plagioclase crystals from the Cape Riva dacites, showing the characteristic features of the phenocrysts. Anorthite spot values from EMP analyses marked on the diagrams. (a) a phenocryst with a simply zoned calcic core and an unzoned sodic rim (GS11-34a XL09) (b) a phenocryst with a partially resorbed calcic core, surrounded by a sodic rim with weak oscillatory zonation (GS11-39b XL29) (c) a phenocryst without a calcic core, but with two internal resorption surfaces, both overgrown by a normally zoned "sawtooth" (GS11-34a XL14) (d) a phenocryst with complexly zoned, partially resorbed core and a normally zoned, "sawtooth" rim (GS11-30b XL08)

Representative plagioclase phenocrysts from the Cape Riva dacite

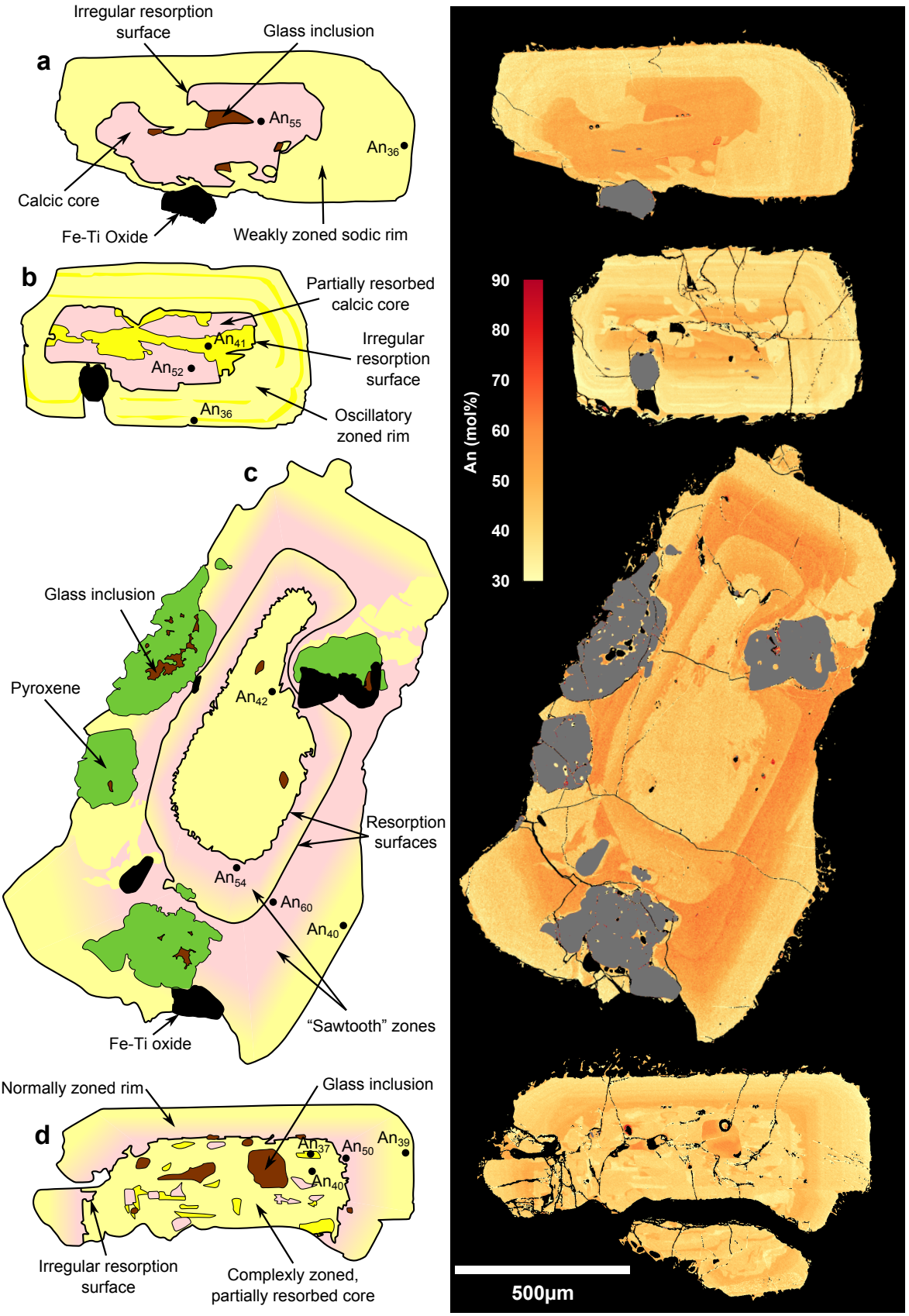

Cape Riva dacite

The plagioclases in the Cape Riva are texturally quite similar to those found in the Therasia dacites. Many of the Cape Riva plagioclases phenocrysts are unzoned or only weakly zoned, but like the Therasia dacites there are also crystals with sawtooth zoning. Most of the rims of the Cape Riva phenocrysts have a narrow range of anorthite content (An_{36-40}; Druitt, 1983; Druitt et al., 1999), suggesting the Cape Riva magma reservoir was better mixed than the Therasia magma reservoir.

Sawtooth zones: The sawtooth zoned crystals have either plain centres, with compositions similar to the unzoned phenocrysts (Figure 6.6c), or can be complexly zoned (Figure 6.6d). The complex zonation appears to be the result of partial dissolution, and these centres frequently contain large, brown glass inclusions. While parts of these centres can be quite calcic (up to An_{58}), the dominant portions of the complexly zoned cores have composition similar to those of the unzoned phenocrysts (An_{30} to An_{41}). These centres are then separated from their rims by a resorption surface. This surface is overgrown by calcic plagioclase of An_{46} to An_{60}, which gradually changes outwards towards more sodic compositions. This pattern is sometimes repeated up to three times, but the rim compositions always match those of the unzoned phenocrysts.

Although some Cape Riva plagioclases appear to have calcic cores (e.g. Figure 6.6a,b), these have similar compositions to the calcic parts of the sawtooth zones (An_{48-59}). These are therefore better described as the inner zone of a sawtooth-zoned crystal. The inner zones can be simply zoned (Figure 6.6a), however many of them show signs or partial resorption and regrowth (Figure 6.6b). Both types of inner zone are separated from the outer zone by an irregular resorption surface. The rims resemble the weakly zoned phenocrysts: they have compositions of An_{30} to An_{41}, and are either

Figure 6.7: Schematic sketches of the plagioclase crystals found in the Therasia and Cape Riva dacites.

unzoned or have subtle oscillatory zoning.

Interpretation

Figure 6.7 summarises the textures found in the Therasia and Cape Riva plagioclase phenocrysts. Most phenocrysts are unzoned or have multiple sawtooth zones (Figure 6.7a). The unzoned phenocrysts have the same composition as the rims of the crystals with sawtooth zoning. The unzoned phenocrysts can, therefore, be considered as equivalent to the rims of the sawtooth-zoned crystals. Either the unzoned crystals do not have the calcic part of the sawteeth, or the calcic part is not exposed in the section that was imaged. Some phenocrysts in the Therasia dacites have calcic cores (e.g. Figure 6.2d,e). The cores of these crystals are more calcic than the sawtooth zones, and the boundaries between them are sharp, rather than gradational as in the sawtooth zones.

6.3.2 Trace element zoning

Trace element profiles were measured in selected crystals using the LA ICP-MS. Two profiles are shown in Figures 6.3 and 6.4.

Figure 6.4 shows an example of a plagioclase with a calcic core. The core has higher liquid equivalent Sr contents, and lower liquid equivalent La contents, than the rims. This would be expected from their behaviour in Santorini magmas—there is more Sr in mafic melts and more La in evolved melts (Chapter 2)—and suggests that their concentrations reflect the compositions of the melts from which they grew. The Mg profile, on the other hand, is more complicated. Traced from the rim inwards, the liquid-equivalent Mg concentrations start off correlated with the anorthite content. However, the inner part of the core is in equilibrium with a melt with a lower Mg concentration than that with which the outer part of the core is in equilibrium. This is despite the fact that the inner part of the core has a higher anorthite content than the outer part. This suggests that the Mg concentrations in this crystal have partially re-equilibrated.

A similar pattern is seen in the crystals with sawtooth zoning (Figure 6.3). The Sr liquid equivalents are positively correlated with, and the La liquid equivalents are negatively correlated with, anorthite content. In this crystal, the shape of the Mg liquid equivalent profile also resembles that of the anorthite profile. This suggests that less diffusion has taken place in this crystal compared to Figure 6.4.

6.4 Using fast and slow diffusing elements to elucidate magmatic processes

As stated in the chapter's introduction, slow-diffusing elements can be used to estimate melt compositions, while fast-diffusing elements can be modelled to get timescales (Chapter 3). Which elements can be considered fast-diffusing and which can be considered slow-diffusing, however, depends on the distances and times in which we are

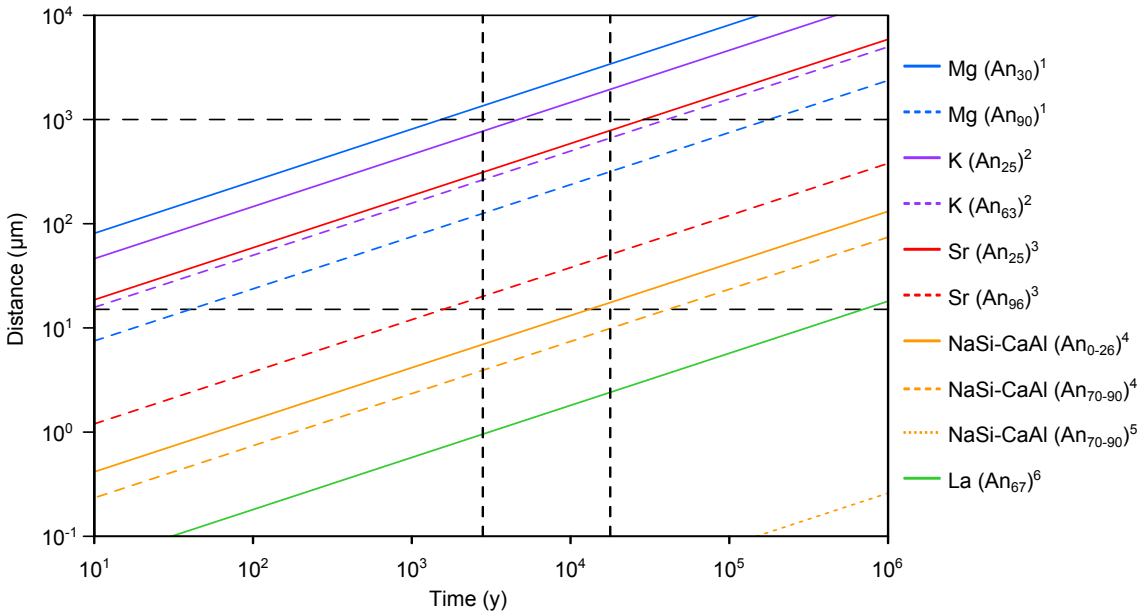

Figure 6.8: Characteristic diffusion distance against time, calculated using Equation 6.4 at 880 °C. The upper and lower horizontal dashed lines represent the typical plagioclase size (1 mm) and the size of the laser pits (10–15 µm), respectively. The left and right vertical dashed lines are the time between the youngest dated Therasia lava and the onset of the Cape Riva eruption (2,800 y), and the time between the first dacitic eruption of the Therasia dome complex and the onset of the Cape Riva eruption (18,000 y), respectively. References: 1: Van Orman et al. (2014); 2: Giletti and Shanahan (1997); 3: Giletti and Casserly (1994); 4: NaSi–CaAl interdiffusion at 1,500 MPa with 1 % H_2O, Liu and Yund (1992); 5: NaSi–CaAl interdiffusion at atmospheric pressure and dry, Grove et al. (1984); 6: Cherniak (2002b)

interested. The influence of diffusion on zoning patterns can be estimated using a back-of-the-envelope calculation for a characteristic length scale of diffusion, x:

$$x \approx \sqrt{Dt} \tag{6.4}$$

where D is the diffusion coefficient and t is the timescale in which we are interested. The diffusion coefficient is strongly dependent on the temperature, which for the Cape Riva dacite and two of the three analysed Therasia dacites is about 880 ± 25 °C (Chapter 5). The variation of characteristic distance with time for the elements discussed here at 880 °C is shown in Figure 6.8, along with the timescales and distances of interest in this study.

The plagioclases typically reach about 1 mm in length, so any element with a char-

acteristic distance longer than this will have mostly re-equilibrated at the scale of whole crystals. These elements will not, therefore, record original melt compositions. On the other hand, elements with characteristic distances smaller than the size of the laser pits (10–15 µm) will remain close to their initial concentration, and can also be used to study the compositions of the melt from which each crystal zone grew. In between these two limits are the elements that will have partially re-equilibrated—these are the elements that can be modelled to best estimate high-temperature crystal residence times.

For the Therasia–Cape Riva series, we are chiefly interested in processes that occurred on timescales shorter than the ∼18 ky of dacitic eruption (the time between the oldest Therasia dacite and the Cape Riva eruption; Chapter 4). Elements that remain immobile over this length of time have been used below (Section 6.5) to reconstruct melt compositions from plagioclase compositions. We are also particularly interested in the processes that occurred between the end of the construction of the Therasia dome complex and the onset of the Cape Riva eruption (∼2,800 y; Chapter 4). The diffusion of elements that are expected to partially re-equilibrate over this period have been modelled in Section 6.6 to estimate high-temperature crystal residence times.

From Figure 6.8, La and NaSi–CaAl can be considered immobile over 18 ky. Over 18 ky La has a characteristic distance of about 2 µm (Figure 6.8).

NaSi–CaAl exchange is a little more complicated, as a wide range of diffusion coefficients have been found for NaSi–CaAl interdiffusion (Chapter 3). The diffusion coefficient for NaSi–CaAl interdiffusion found by Liu and Yund (1992) at 1,500 MPa and 1 % H_2O is several orders of magnitude faster than that of Grove et al. (1984) under dry conditions at atmospheric pressure. However, NaSi and CaAl can be considered immobile whichever diffusion coefficient is used: using the diffusion coefficient of Liu and Yund (1992), the characteristic diffusion distance over 18 ky is 10–15 µm (depending

on the anorthite content), while using the diffusion coefficient of Grove et al. (1984) this distance is only 35 nm.

The diffusivity of Ti has not been measured, but the high charge of Ti^{4+} ions implies that it will be slow (Cherniak, 2010). The diffusion coefficient of Ce is also not known, however the low diffusivity of La and other REE suggest that Ce will also diffuse slowly (Cherniak, 2002b). The anorthite content of the plagioclases zones, along with their La, Ce and Ti concentrations, can therefore be used to estimate the composition of the melt from which each zone grew.

Sr has a slightly higher diffusion coefficient than the elements discussed above, and has a characteristic diffusion length of 50–800 µm over 18 ky (Chapter 3). However, Figure 6.8 shows that if the high-temperature residence times for the crystals are significantly less than the 2,800 y between the Therasia dome complex and the Cape Riva eruption, then the Sr concentrations should be close to original. The tightness of the relationship between Sr and anorthite in Figure 6.9a (see below) strongly suggests this is the case, since any diffusive partial re-equilibration of Sr following crystal growth would blur the Sr-anorthite relationship.

The fastest diffusing elements considered here, Mg and K, will almost completely re-equilibrate over 18 ky (Chapter 3). Mg has a characteristic diffusion distance of 300–3,000 µm over this time, while K has a characteristic diffusion distance of 600–2,000 µm (Giletti and Shanahan, 1997; Van Orman et al., 2014). This distance drops to 25–250 µm for Mg and 50–150 µm for K over 100 years. This means that if high-temperature crystal residence times are less than a few thousand years, Mg and K will only be partially re-equilibrated. This makes Mg and K ideal targets for estimating high-temperature crystal residence times by diffusion modelling. Mg was chosen over K because K is a major element in the ternary anorthite–albite–orthoclase system, which would complicate the diffusion modelling.

6.5 Reconstructing melt compositions from plagioclase compositions

The results of the LA ICP-MS analyses of the plagioclase crystals are shown in Figure 6.9, with concentrations converted to represent liquid compositions that are in equilibrium with those found in the plagioclases. For Sr and Ti, there is a tight relationship between their concentration and the anorthite content of the host crystal (Figure 6.9a,b). These relationships mirror those found in the whole rock data, with Sr decreasing with increasing degrees of melt evolution (i.e. decreasing An content), and Ti showing a peak at around An_{65} (Chapter 2).

La and Ce show greater scatter than Sr and Ti. Some of this spread is due to greater analytical uncertainty as a result of their very low concentrations. Although there is a small amount of overlap, the Therasia and Cape Riva plagioclases form two distinct trends (Figure 6.9c,d). For any given An content, the Therasia plagioclase contain more La and Ce. This difference is significant, as it reflects the two separate trends seen in the whole rock data (Chapter 5).

Although there is a general trend towards more Mg-rich compositions with increasing anorthite content, there is a broad spread of Mg concentrations (Figure 6.9e). This is particularly true for the calcic plagioclases. There are two possible interpretations for this spread: either the spread reflects a spread of magma compositions from which the plagioclases grew, or the Mg concentration has been modified by diffusion after growth.

The relationship between K and anorthite resembles that of La and Ce, with a general trend towards higher K concentrations with decreasing anorthite content, and with the Therasia plagioclases containing more K than the Cape Riva plagioclases at any given anorthite content(Figure 6.9f).

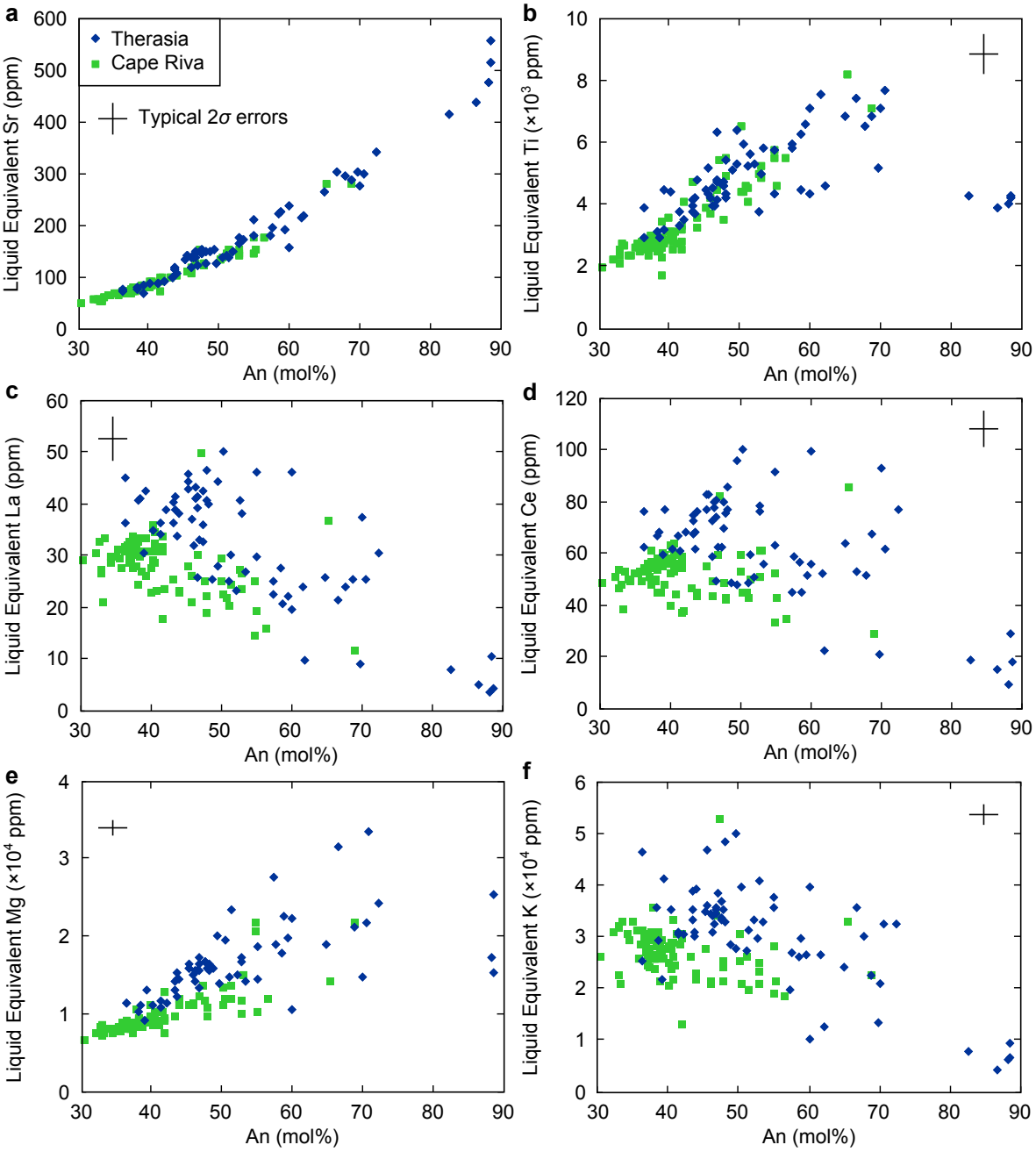

Figure 6.9: Liquid equivalent compositions for plagioclase crystals from the Therasia and Cape Riva eruptions. Typical anorthite error bars calculated from electron microprobe counting statistics, typical trace element error bars calculated using Equation 6.3.

6.5.1 Major element composition of the melt

In order to interpret the zoning patterns of the plagioclase, it is important to understand what is causing the changes in the anorthite content. There are three potential ways of changing the anorthite content of plagioclase:

1. Changing the temperature, e.g. by underplating the magma reservoir with hotter magma

2. Changing the water content of the melt, e.g. by degassing or volatile fluxing

3. Changing the melt composition through magma mixing (which would also change the temperature, and possibly P_{H_2O} as well)

The concentrations of slowly diffusing trace elements in plagioclase crystals can be used to distinguish between these different processes, as they will behave differently in each case.

Assuming that the total pressure and the melt composition remain constant, then the temperature and water pressure changes needed to produce the changes in anorthite content can be estimated using the the plagioclase–liquid thermometer and hygrometer equations of Putirka (2008). For example, the Cape Riva crystals have anorthite contents that vary between An_{36-40} and An_{55-60}. Assuming that the melt composition remains constant, this change can be produced by modest increases in the temperature ($\sim$20 °C) or H_2O concentration in the melt ($\sim$0.3 wt%).

However, there is a tight relationships between the anorthite content of the plagioclase and the apparent Sr concentration of the melt that it is in equilibrium with (Figure 6.9a). If the anorthite content of the plagioclase phenocrysts is controlled purely by temperature or P_{H_2O}, then this relationship must be an artefact of the partition coefficients chosen. While the temperature does affect the partitioning of Sr between plagioclase and silicic melts, this effect is not large enough to explain the apparent relationship. Changing the temperature by 100 °C (from 880 to 980 °C) using the partition coefficients of Bindeman et al. (1998) changes the estimated Sr concentrations in the melt by 10–15 ppm, while a differences of >100 ppm are seen in the liquid equivalent compositions of Cape Riva plagioclase phenocrysts (e.g. Figure 6.3) — and an even larger range is seen in the Therasia plagioclase phenocrysts (e.g. Figure 6.4).

The effects of water concentration in the melt on the partition coefficient are less well constrained. The global regression of all partition coefficient data carried out by Bédard (2006) suggest that a change of 1–2 wt% H_2O in the melt could produce a ∼100 ppm variation in Sr melt concentrations. However, Blundy and Wood (1991) found little difference between the partition coefficients of Sr from experiments both under hydrothermal conditions and with silicate melts, implying that P_{H_2O} has little effect on the partition coefficients of Sr. In either case, the total range of Sr melt concentrations shown in Figure 6.9a is too large to be explained by changes in the water content. Total pressure too has only a weak influence on the partition coefficient of Sr (Bédard, 2006; Blundy and Wood, 1991). The zoning patterns in the plagioclase crystals, therefore, must correlate principally with changes in the melt chemistry. These changes in the melt chemistry may well be accompanied by changes the temperature and P_{H_2O} of the melt — indeed studies of glass inclusions show that melt composition, temperature and volatile contents correlate well in Santorini magmas (Mercier et al., 2013) — the important point is that the compositions of the plagioclase crystals can be used to estimate the compositions of the melts from which they grew.

Plotted on Figure 6.10 are the liquid equivalent Sr and Ti concentrations estimated from the compositions of the plagioclase crystals, along with whole rock and groundmass compositions of different units from Santorini. Figure 6.10 shows that the Sr and Ti contents of the melt compositions estimated from plagioclase analyses do, in fact, match the whole rock compositions. For silicic magmas and sodic plagioclases there is a tight fractionation trend towards low-Sr and low-Ti melts, seen in both the whole rock plagioclase data. Most of the Cape Riva phenocrysts appear more evolved than the whole rock compositions, however this is also true for the Cape Riva glass. The Cape Riva plagioclases are therefore in equilibrium with compositions similar to — slightly more evolved than — the Cape Riva glass, and not whole rock compositions. The difference between Therasia whole rock and glass compositions is less significant, as the Therasia dacites have lower crystallinity then the Cape Riva dacite.

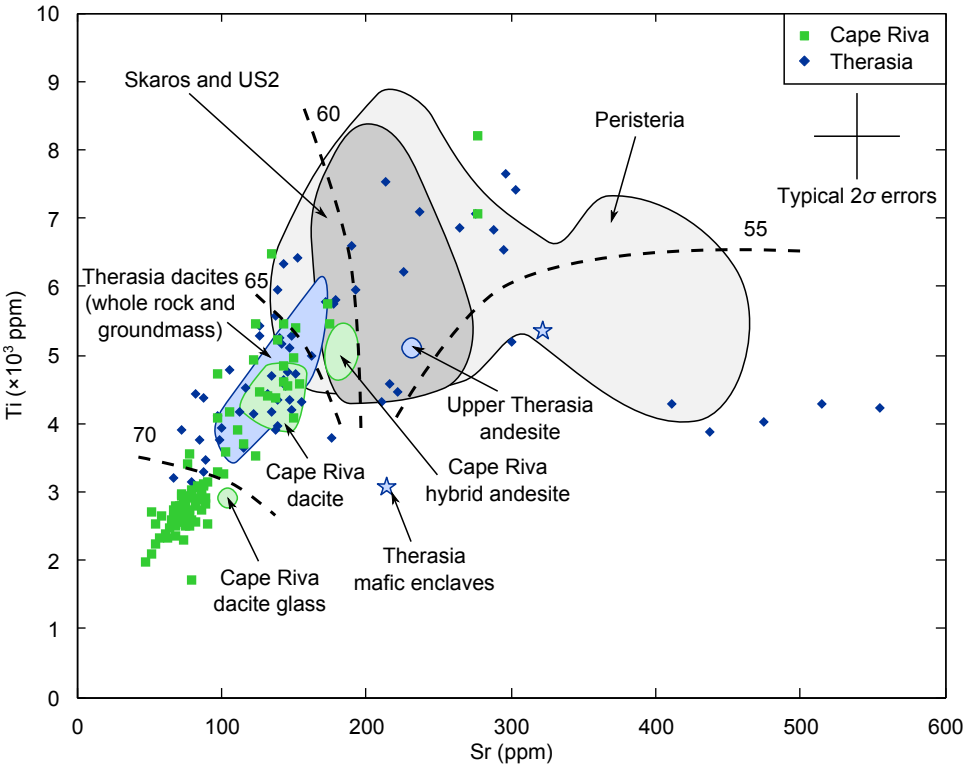

Figure 6.10: Sr and Ti liquid compositions calculated to be in equilibrium with plagioclase compositions. Fields are whole rock data for different Santorini units. Therasia whole rock, groundmass and mafic enclaves are from this work, and the Cape Riva dacite glass is one analysis from this work. Contours roughly match melt SiO_2 concentrations, in wt%. Cape Riva dacite and andesite, and Upper Scoria 2 (US2) data from Druitt et al. (1999). Skaros and Peristeria data from Huijsmans (1985).

However, for more mafic magmas and more calcic plagioclases there is far less of a trend. The plagioclase compositions still agree with whole rock compositions, however there is quite a large range of Sr contents in Santorini basalts, even between those with similar major element concentrations. In Skaros basalts and Therasia basaltic enclaves at about 54 wt% SiO_2, there is between 200 and 300 ppm Sr. Some Peristeria basalts have up to 450 ppm Sr, despite similar SiO_2 contents (Huijsmans, 1985; Huijsmans et al., 1988). The concentration of Sr in the whole rock can also change quite rapidly with some indicators of melt evolution, such as MgO content. This means that small amounts of uncertainty in the Sr concentration of the plagioclase crystal can lead to large uncertainties in the calculated melt composition. This is particularly important when we estimate initial Mg contents of the plagioclase crystals in order to model its diffusion in Section 6.6. I therefore decided instead to use Ti concentrations to match

up plagioclase compositions with whole rock compositions.

The differences in Sr concentrations between the different groups of Santorini basalts do, however, cast light on the origin of the calcic cores in the plagioclases found in the Therasia dacites. The most calcic crystal cores (with anorthite higher than An_{80}) have very high Sr, equivalent to up to 554 ppm in the melt (Figure 6.10). None of the Skaros basalts or Therasia basaltic enclaves have Sr that high (Chapter 2); the only magmas on Santorini with more than 350 ppm Sr are lavas from the Peristeria centre that was active between 530 and 430 ka (Druitt et al., 1999; Huijsmans, 1985; Huijsmans et al., 1988). This suggests that these cores were recycled from plutonic rock or mush from the Peristeria period. The Peristeria vents were located in the north of the island, and probably overlapped geographically with the locations of the Therasia vents. The crystals with An<80 , however, are all in equilibrium with melts with less than 350 ppm Sr. The Sr contents of these crystals cannot, therefore, distinguish between plutonic mush or mafic recharge as their source.

We can use the Ti and Sr liquid-equivalent values to estimate the compositions from which each plagioclase zone crystallised. Figure 6.11 shows how the Ti content was used to match plagioclase composition to the SiO_2 content of the melt in which it grew, and Table 6.2 summarises the results for the different zones of the Therasia and Cape Riva plagioclases. From Figure 6.11 we can see that plagioclase with a composition of between An_{30} and An_{40}, similar to that of the majority of the rims of the plagioclase crystals found in the Cape Riva pumice, probably grew from a liquid with between 69 and 72 wt% SiO_2: similar to the composition of the Cape Riva glass. The Therasia plagioclase rims are slightly more calcic (between An_{40} and An_{50}), and these compositions correspond to whole rock compositions of between 65 and 69 wt% SiO_2; this matches the whole rock and groundmass compositions observed in the Therasia dacites. The most calcic plagioclases ($\sim An_{90}$) would have crystallised from a basalt with about 50 wt% SiO_2.

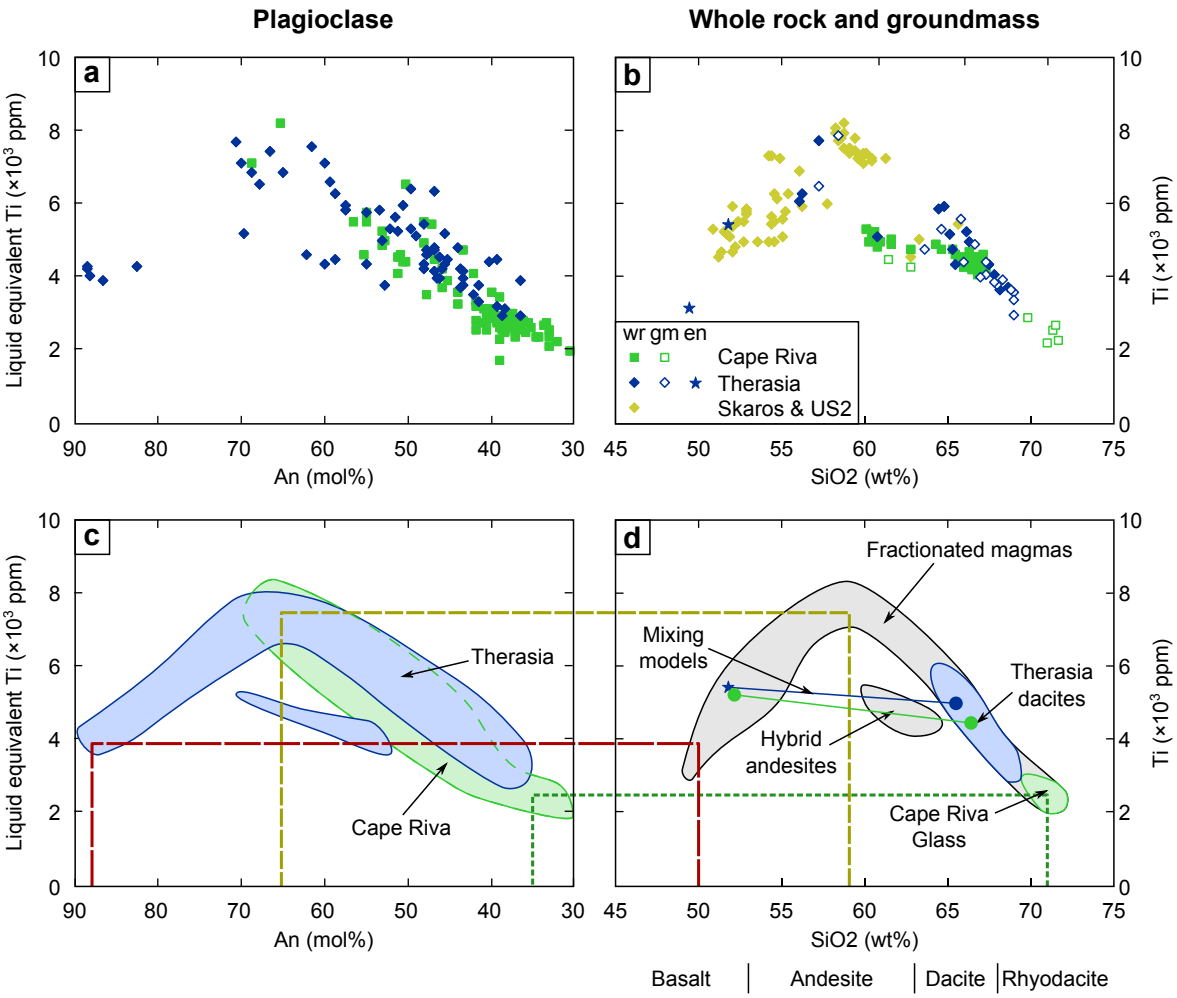

Figure 6.11: (a) Ti concentrations in melts in equilibrium with the composition of plagioclase crystals in lavas from the Therasia dome complex and pumices from the Cape Riva eruption. (b) Ti concentrations in whole rock (wr), groundmass separates (gm), and mafic enclaves (en) from the Skaros (Huijsmans, 1985), Upper Scoria 2 (US2; Druitt et al., 1999), Cape Riva and Therasia dome complex (Druitt et al., 1999; this study) (c) and (d) interpretive sketches of (a) and (b), respectively, with dashed lines showing how plagioclase and whole rock data can be matched up. Mixing models in (d) are those discussed in Chapter 5.

6.5.2 Distinguishing fractionated melts from hybrid melts

The Ti concentration also allows us to distinguish between crystals that grew in hybrid andesites and those that grew from andesites formed by fractionation (Chapter 5). Figure 6.11 shows that most plagioclases lie on a curved band that mirrors the fractionation trend seen in the whole rock data. Mixing between basalts and dacites and rhyolites produces hybrid melts that fall below this trend (Figure 6.11d), and any crystals that grow from these hybrid melts should fall below the equivalent trend in the

Table 6.2: Estimated melt compositions in equilibrium with the different plagioclase zones

	Plagioclase composition (An, mol%)	Melt composition (SiO_2, wt%)	
Therasia dacites			
Calcic cores	62–91	50–60	(basalt–andesite)
Peak of sawtooth zones	59–72	56–64	(andesite–dacite)
Rims	39–51	61–66	(dacite)
Cape Riva dacite			
Peak of sawtooth zones	46–60	61–67	(dacite)
Rims	36–40	68–72	(rhyodacite)

composition of the plagioclases (Figure 6.11c).

The melt evolution paths determined from two plagioclase crystals from the Therasia dacites are shown in Figure 6.12. Most of the crystals lie along the fraction trend, including GS10-17 XL57 (Figure 6.12a). The centre (point 1) and the rim (point 3) of GS10-17 XL57 both have low anorthite and liquid equivalent Ti contents. Where the crystal becomes more calcic (point 2) it also has an increased liquid equivalent Ti content, following melt fractionation trends again. This means that mixing with a basalt cannot produce the calcic plagioclase at point 2.

GS10-17 XL71 is an example of a crystal that lies below the fractionation trends (Figure 6.12a). Going from the centre of GS10-17 XL71 (point 1) towards the rim (point 7), the plagioclases becomes less calcic. The first four points are in the calcic core of the crystal, with compositions of An_{67-84}. There is then a jump in anorthite content, and the three points in the outer zone have compositions of An_{39-42}. At the same time, the liquid equivalent Ti content first increases, and reaches a peak at point 4, after which it falls. Most of the points lie along the fractionation trends, apart from point 4 which lies slightly below. This suggest that point 4 might have grown from a hybrid melt.

In total, six analysed crystals from the Therasia dome complex have zones that appear to have precipitated from hybrid melts (Figure 6.11); three of these are from

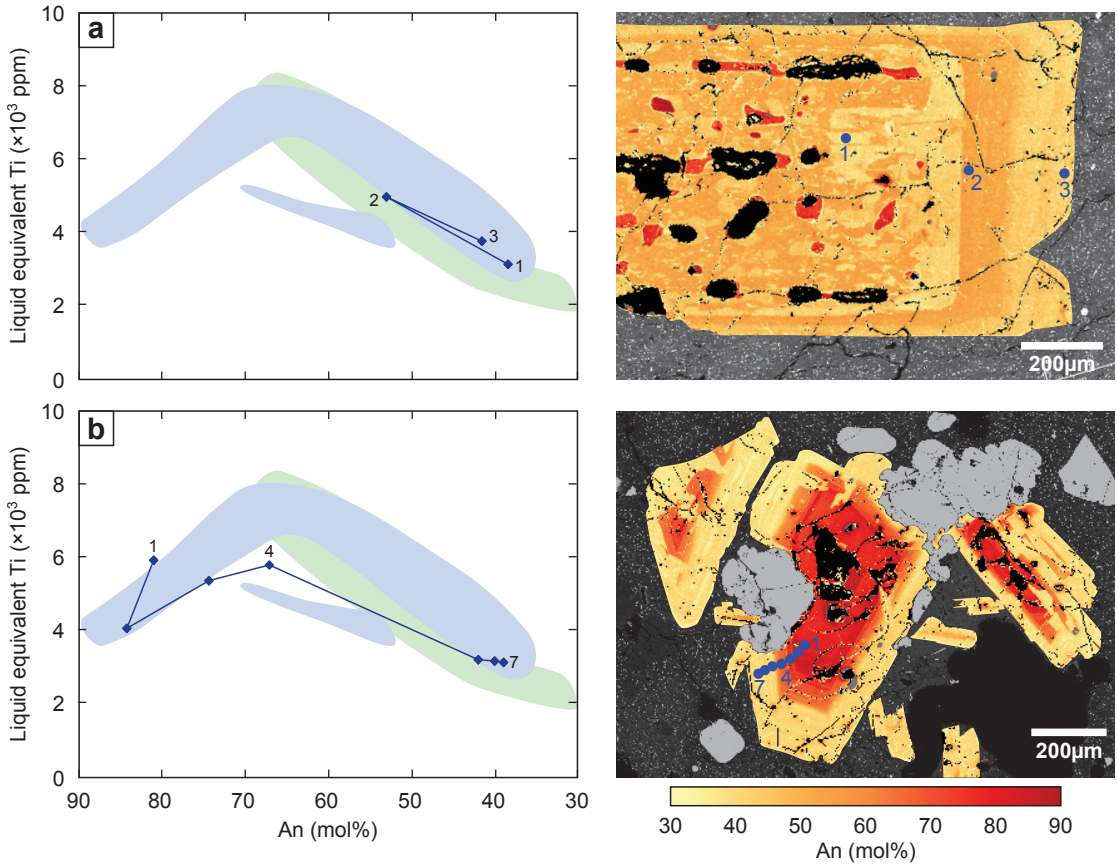

Figure 6.12: Melt evolution paths determined from Ti contents of plagioclase crystals from the Therasia dacites. The blue and green fields are the fields of Therasia and Cape Riva plagioclases from Figure 6.11. (a) GS10-17 XL57, (b) GS10-17 XL71.

the upper Therasia andesite that has already been shown to be hybrid (Chapter 5). The other three hybrid-derived plagioclase crystals, however, come from the uppermost flow on Cape Tripiti, the dacitic flow 9 (GS10-16). One of these analyses is of a resorbed inner zone; it could have emanated from the plutonic mush, and therefore it could be much older than the Therasia dome complex. The other two, however, are in the centres of crystals that grade normally into rims typical of the dacites and show no signs of dissolution. This suggests that there was an input of hybrid andesite into the magma reservoir before flow 9 was erupted.

The plagioclases from the Cape Riva dacite, on the other hand, all give liquid equivalent Ti values that lie along the trend defined by the fractionated magmas. This can be seen for four individual crystals in Figure 6.13. Above, it was argued that the Cape Riva plagioclases grew in equilibrium with melts ranging from dacite to

rhyodacite in composition. If the dacite was produced by magma mixing, then we can place constraints on the mafic endmember. A basaltic or basaltic-andesite melt would have low Ti, and would drive the plagioclase compositions between the two arms of the fractionation trend (as in the mixing models in Figure 6.11d). Because the Cape Riva plagioclases all lie along the right-hand arm of the fractionation trend, all the incoming magmas must have at least ∼57 wt% SiO_2. The sawtooth zoning in the Cape Riva plagioclases, therefore, records the mixing of melts that range from silicic andesite to rhyodacite.

6.5.3 Incompatible element concentrations of the melt

The difference in incompatible element concentrations in the Therasia and Cape Riva dacites provides a means of distinguishing crystals that grew in a Cape Riva-like magma from those that grew in a Therasia-like magma. The Cape Riva dacite is depleted in incompatible elements (such as La and Ce) relative to Therasia dacites, and this can be explained if a significant proportion of the Cape Riva dacite was a new silicic magma batch introduced into the sub-volcanic plumbing system less than $2{,}800 \pm 1{,}400$ y before the Cape Riva eruption (Chapter 5).

The lower La and Ce concentrations in the Cape Riva plagioclase, coupled with the very slow diffusion rates of La and Ce (Figure 6.8), indicate that the majority of the Cape Riva plagioclase grew from a Cape Riva-like magma. K also is depleted in the Cape Riva magma, however it diffuses much more rapidly (Chapter 3; Brady, 1995; Giletti and Shanahan, 1997). This means that K concentrations may not reflect the original growth conditions of the plagioclase, because the crystals may have re-equilibrated with their host magma. However, the low K values in Cape Riva plagioclases relative to Therasia plagioclases are consistent with a Cape Riva source for

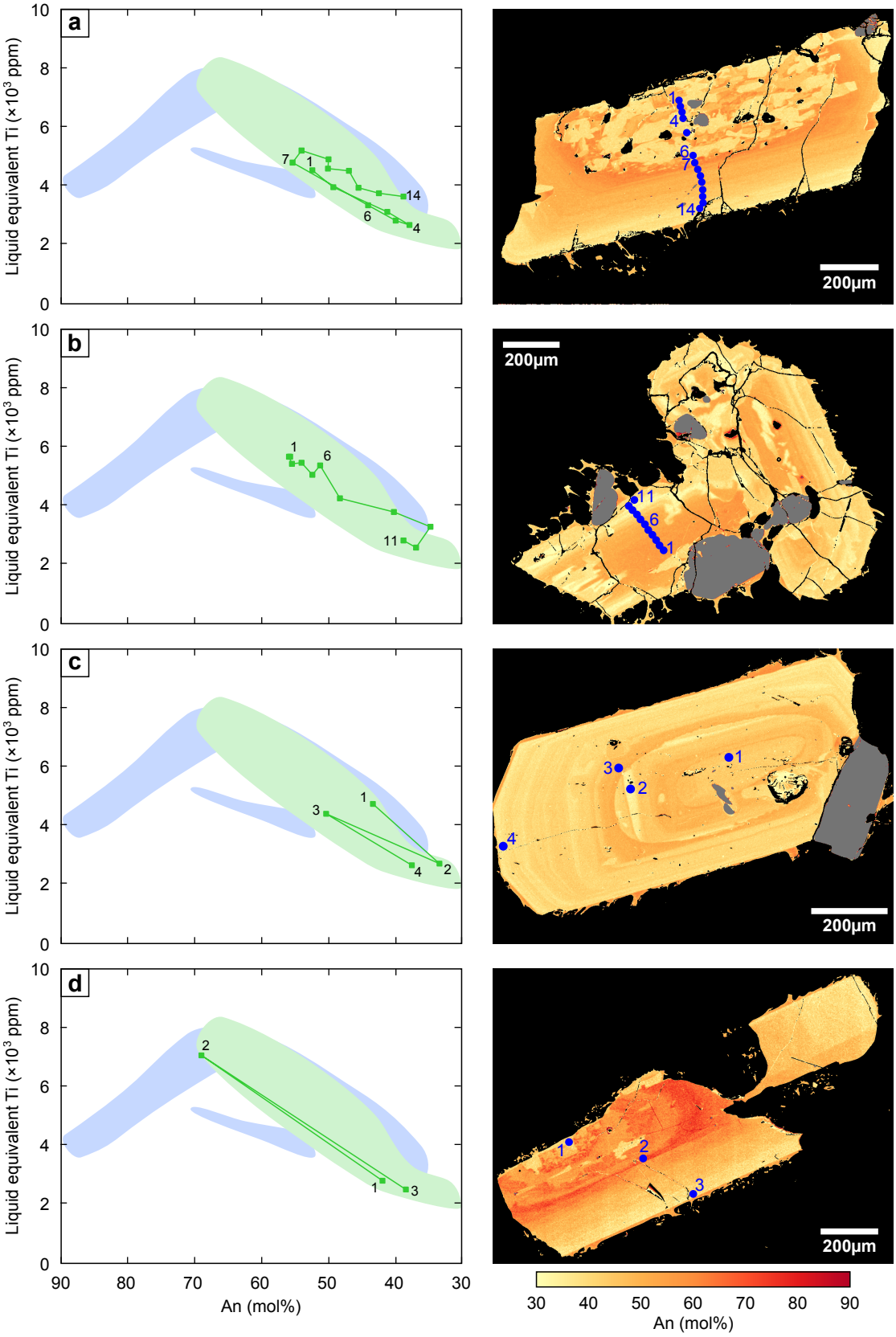

Figure 6.13: Melt evolution paths determined from Ti contents of plagioclase crystals from the Cape Riva dacite. The blue and green fields are from Figure 6.11. (a) GS11-30b XL18, (b) S12-06 XL24, (c) S12-05 XL08, (d) GS11-34f XL13.

most of the Cape Riva plagioclase (Figure 6.9f).

Only two out of the 90 analyses preformed on 37 different Cape Riva plagioclases have high La and Ce (Figure 6.9c,d). One of these analyses is from the inner zone of a crystal, and shows signs of resorption; this inner zone could be xenocrystic, and therefore tells us little about evolution of the Cape Riva melt. The other, however, is from the calcic part of a sawtooth zone of a crystal (S12-06 XL08). The centre of this crystal has low La and Ce, suggesting that it started growing in a Cape Riva-like magma. This crystal could then have been transferred to a Therasia-like magma, where it was partially resorbed and overgrown by more calcic plagioclase. S12-06 XL08 was then transferred back into Cape Riva-like magma, or the Therasia-like magma was possibly mixed into a much larger body of Cape Riva-like magma, as the rim of this crystal has the low La and Ce typical of the Cape Riva dacite. This interpretation implies that there was still at least a small amount of Therasia-like melt stored beneath Santorini when the Cape Riva magma was transferred to the shallow storage region, although interpretations based on only one data point are obviously rather speculative.

It is clear, however, that few (if any) Cape Riva plagioclases are antecrysts derived from the Therasia magmas. This has important implications for the residence time of the Cape Riva magma in the shallow crust. From the whole-rock data we know that a large volume of incompatible melt arrived in the shallow plumbing system less than ~2,800 years before the Cape Riva eruption. However, the chemistry did not allow us to rule out that up to half of the Cape Riva magma was actually residual Therasia magma. The lack of plagioclase crystals recycled from the Therasia period suggests that there was very limited mixing with residual magma, although it is still possible that the Therasia plagioclases were resorbed before the Cape Riva plagioclases grew. An important implication of this observation is that the high-temperature residence times for the Cape Riva crystals estimated from diffusion modelling below relate only to processes occurring in the Cape Riva magma.

6.6 Estimating timescales with diffusion modelling

6.6.1 Initial Mg concentration of the plagioclase crystals

Given the rate of diffusion of Mg in plagioclase (Figure 6.8), we might expect to find that Mg has diffused. The relationship between Mg and anorthite shown in Figure 6.9e suggests that this is indeed the case. In order to model the diffusion of Mg in plagioclase, it is first necessary to estimate the initial Mg concentration of the crystals. This was done in two steps. First, a equation relating the Ti and Mg concentrations in the whole rock data was constructed. Then, a similar relationship between Ti and An was found, and the two equations were combined to create the final equation for the initial Mg content in terms of An. The lines of best fit and the amount variation were estimated by eye.

The relationship between Ti and Mg in the whole-rock data can be fit by two exponential functions: one for the rocks produced by Fe-Ti oxide–absent fractional crystallisation (where Ti increases with the degree of fractionation), and one for where Fe-Ti oxides are present during fractionation (where Ti decreases with the degree of fractionation). Both of these equations have the form (Figure 6.14a):

$$C_{\mathrm{Mg}}^{\mathrm{liq}} = a_1 \exp\left(a_2 C_{\mathrm{Ti}}^{\mathrm{liq}}\right) \tag{6.5}$$

where a_1 and a_2 are coefficients to be determined. These can be combined with linear functions for Ti against An, where Ti concentrations are those in a liquid in equilibrium with the plagioclase (Figure 6.14b):

$$C_{\mathrm{Ti}}^{\mathrm{liq}} = b_1 X_{\mathrm{An}} + b_2 \tag{6.6}$$

where b_1 and b_2 are also coefficients to be determined.

Combining Equations 6.5 and 6.6 we get the concentration of Mg in the liquids that

crystallised plagioclase of a particular anorthite content:

$$C_{\mathrm{Mg}}^{\mathrm{liq}} = a_1 \exp\left[a_2 \left(b_1 X_{\mathrm{An}} + b_2\right)\right] \tag{6.7}$$

Using the partition coefficients of Bindeman et al. (1998), we can calculate the concentration of Mg in the plagioclase that would be in equilibrium with these liquids:

$$\begin{aligned} C_{\mathrm{Mg}}^{\mathrm{xl}} &= a_1 \exp\left(a_2 b_1 X_{\mathrm{An}} + a_2 b_2\right) \exp\left(\frac{A X_{\mathrm{An}} + B}{RT}\right) \\ &= a_1 \exp\left[a_2 b_2 + \left(a_2 b_1 + \frac{A}{RT}\right) X_{\mathrm{An}} + \frac{B}{RT}\right] \end{aligned} \tag{6.8}$$

Plugging the numbers in, this equation does not quite fit the data: the calculated initial concentrations are lower than those measured in the rims of the plagioclases. This may be a problem with the partition coefficients; Bindeman et al. (1998) measured theirs in basalt whereas our plagioclases grew from a dacite, and melt composition has been shown to effect trace element partitioning (Blundy and Wood, 2003). The same issue was also noted by Druitt et al. (2012). Multiplying the equation by a constant fixes this, however. The final equation used to predict the initial concentration of Mg in the plagioclases is (Figure 6.15):

$$C_{\mathrm{Mg}}^{\mathrm{init}} = \begin{cases} 310 \exp\left[\left(6.13 + \dfrac{A}{RT}\right) X_{\mathrm{An}} + \dfrac{B}{RT}\right] & \text{for An} < 69 \\ 2130 \exp\left[\left(3.33 + \dfrac{A}{RT}\right) X_{\mathrm{An}} + \dfrac{B}{RT}\right] & \text{for An} \geq 69 \end{cases} \tag{6.9}$$

The uncertainty in this estimate is given by the following bounds:

$$C_{\mathrm{Mg}}^{\text{init-low}} = \begin{cases} 340 \exp\left[\left(5.62 + \dfrac{A}{RT}\right) X_{\mathrm{An}} + \dfrac{B}{RT}\right] & \text{for An} < 72 \\ 1316 \exp\left[\left(3.73 + \dfrac{A}{RT}\right) X_{\mathrm{An}} + \dfrac{B}{RT}\right] & \text{for An} \geq 72 \end{cases} \tag{6.10}$$

$$C_{\mathrm{Mg}}^{\text{init-high}} = \begin{cases} 276 \exp\left[\left(6.72 + \dfrac{A}{RT}\right) X_{\mathrm{An}} + \dfrac{B}{RT}\right] & \text{for An} < 66 \\ 3150 \exp\left[\left(3.03 + \dfrac{A}{RT}\right) X_{\mathrm{An}} + \dfrac{B}{RT}\right] & \text{for An} \geq 66 \end{cases} \tag{6.11}$$

6.6.2 Equilibrium profiles

Final, equilibrium profiles for the plagioclase crystals can also be calculated using the plagioclase–liquid partition coefficients of Bindeman et al. (1998). As the plagioclase–liquid partition coefficient of element i is defined as:

$$K_i^{\text{plag/liq}} = \frac{C_i^{\text{plag}}}{C_i^{\text{liq}}} \tag{6.12}$$

we can combine the partition coefficients for two different plagioclase compositions (plag-1 and plag-2) as follows:

$$\frac{K_i^{\text{plag-1/liq}}}{K_i^{\text{plag-2/liq}}} = \frac{C_i^{\text{plag-1}}/C_i^{\text{liq}}}{C_i^{\text{plag-2}}/C_i^{\text{liq}}} = \frac{C_i^{\text{plag-1}}}{C_i^{\text{plag-2}}} \quad \left(= K_i^{\text{plag-1/plag-2}}\right) \tag{6.13}$$

If the rim is assumed to be in equilibrium with the melt, then the equilibrium profile can be constructed by working inwards. We can use Equation 6.13 to calculate the concentration of i in each part of the crystal that is in equilibrium with the part of the crystal immediately outside of it. Diffusion will tend to drive the composition of the plagioclase towards this equilibrium profile (Costa et al., 2003; Zellmer et al., 1999).

6.6.3 Numerical modelling

The diffusion of Mg in plagioclase can modelled numerically using the method of Costa et al. (2003) as used by Druitt et al. (2012). The changes in concentration due to diffusion of a trace element in plagioclase such as Mg, C_{Mg}, the following equation can

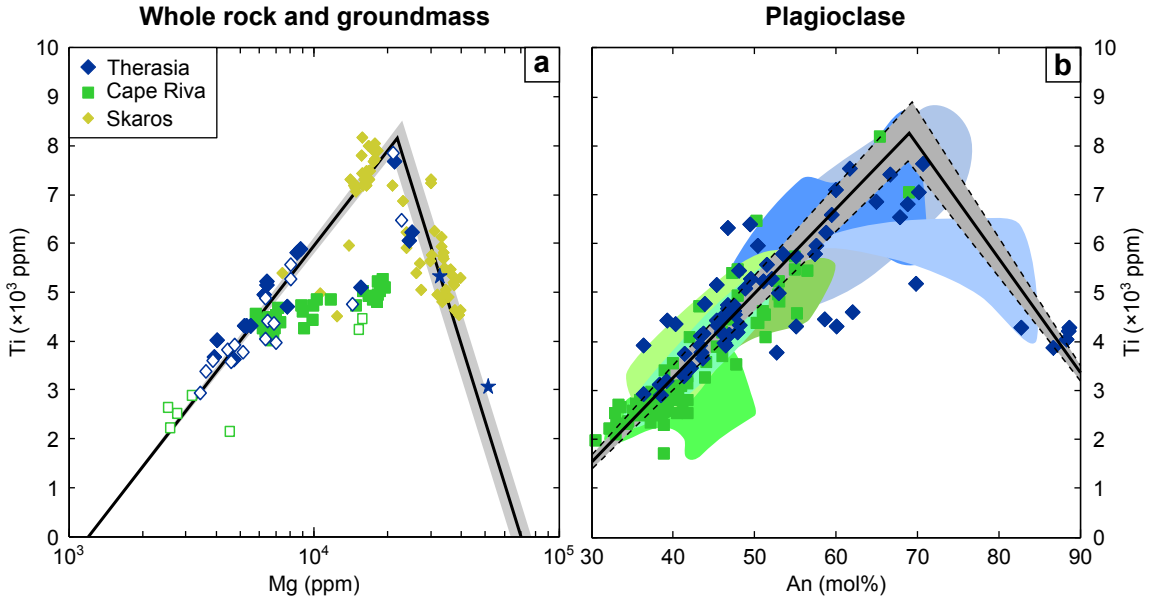

Figure 6.14: (a) Whole rock (filled symbols) and groundmass (open symbols) compositions of the Therasia, Cape Riva, Skaros and Upper Scoria 2 eruptions (b) Liquid equivalent compositions for plagioclases from the Cape Riva and Therasia eruptions. Solid black line is the equation used to estimate the initial Mg concentration of the plagioclase, dashed lines are an estimate of the uncertainty, covering ∼2/3 of the data. Each blue field in (b) contains all the analyses from the profiles in an individual crystal in the Therasia dacites, and the green fields are individual crystals from the Cape Riva dacite.

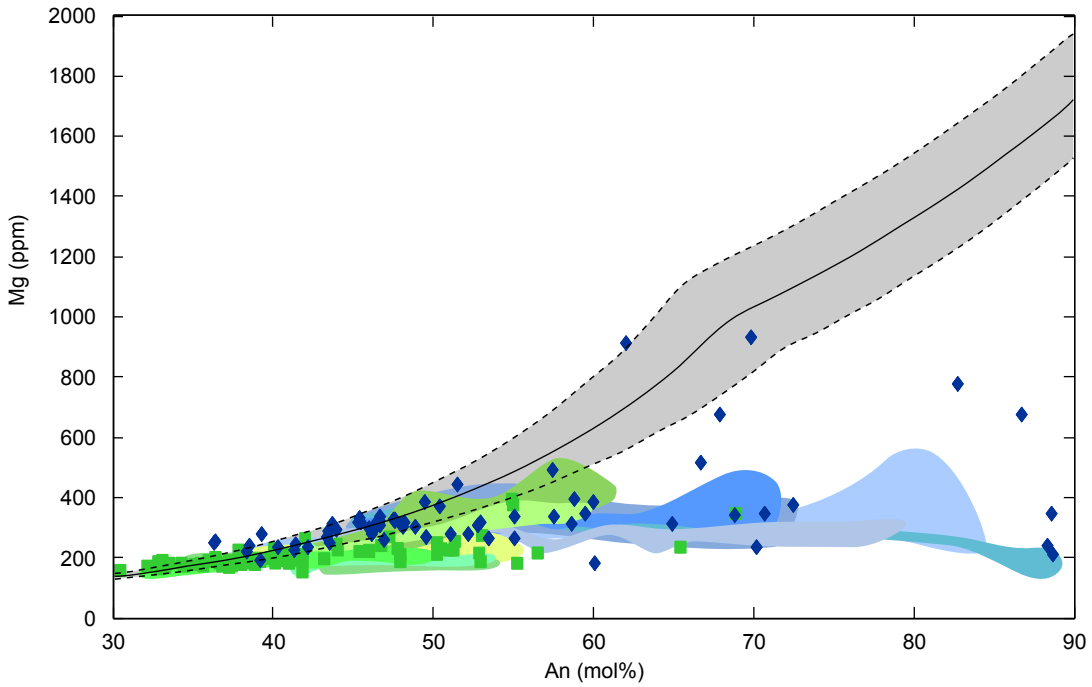

Figure 6.15: The estimate of the initial Mg concentration of the crystals, shown by the solid black line, from Equation 6.9. The uncertainty, from Equations 6.10 and 6.11 is shown by the dashed lines. Each blue field contains all the analyses from the profiles in an individual crystal in the Therasia dacites, and the green fields are individual crystals from the Cape Riva dacite.

be used (Equation 3.16 in Chapter 3):

$$\frac{\partial C_{\mathrm{Mg}}}{\partial t} = \frac{\partial}{\partial x}\left(D_{\mathrm{Mg}}\frac{\partial C_{\mathrm{Mg}}}{\partial x} - D_{\mathrm{Mg}}C_{\mathrm{Mg}}\frac{A}{RT}\frac{\partial X_{\mathrm{An}}}{\partial x}\right) \tag{6.14}$$

where D_{Mg} is the diffusion coefficient of Mg in plagioclase, A is the parameter that describes the variation of the partition coefficient of Mg with anorthite content in Equation 6.1 above.

In order to model the diffusion of Mg in plagioclase numerically, Equation 6.14 is expanded and converted to a finite difference scheme. The subscripts i and j refer to a discrete spacial and temporal step, respectively, with widths or durations of Δx and Δt:

$$\begin{aligned}\frac{\partial C_{\mathrm{Mg}}}{\partial t} =& D_{\mathrm{Mg}}\frac{\partial^2 C_{\mathrm{Mg}}}{\partial x^2} + \frac{\partial C_{\mathrm{Mg}}}{\partial x}\frac{\partial D_{\mathrm{Mg}}}{\partial x} \\ &- \frac{A}{RT}\left(D_{\mathrm{Mg}}\frac{\partial C_{\mathrm{Mg}}}{\partial x}\frac{\partial X_{\mathrm{An}}}{\partial x} + C_{\mathrm{Mg}}\frac{\partial D_{\mathrm{Mg}}}{\partial x}\frac{\partial X_{\mathrm{An}}}{\partial x} + D_{\mathrm{Mg}}C_{\mathrm{Mg}}\frac{\partial^2 X_{\mathrm{An}}}{\partial x^2}\right)\end{aligned} \tag{6.15}$$

$$\begin{aligned}\frac{C_{i,j+1} - C_{i,j}}{\Delta t} =& D_{i,j}\frac{C_{i+1,j} - 2C_{i,j} + C_{i-1,j}}{\Delta x^2} + \frac{\left(C_{i+1,j} - C_{i,j}\right)\left(D_{i+1,j} - D_{i,j}\right)}{\Delta x^2} \\ &- \frac{A}{RT}\left(D_{i,j}\frac{\left(C_{i+1,j} - C_{i,j}\right)\left(X_{\mathrm{An},i+1,j} - X_{\mathrm{An},i,j}\right)}{\Delta x^2}\right. \\ &+ C_{i,j}\frac{\left(D_{i+1,j} - D_{i,j}\right)\left(X_{\mathrm{An},i+1,j} - X_{\mathrm{An},i,j}\right)}{\Delta x^2} \\ &\left.+ D_{i,j}C_{i,j}\frac{X_{\mathrm{An},i+1,j} - 2X_{\mathrm{An},i,j} + X_{\mathrm{An},i-1,j}}{\Delta x^2}\right)\end{aligned} \tag{6.16}$$

Equation 6.16 allows $C_{i,j+1}$ to be calculated explicitly given $C_{i-1,j}$, $C_{i,j}$ and $C_{i+1,j}$, and was implemented using Matlab scripts (Appendix D).

The outside end of the profile was fixed assuming the first measured point was in equilibrium with the melt it resided in. The profile was assumed to be symmetrical

by implicitly mirroring it around the innermost point, except where the profile was significantly longer than half the crystal. Where the profile spanned the entire crystal, both ends of the profile were assumed to be in equilibrium with the liquid.

The diffusion times of all the profiles were first estimated using one-stage models: the whole crystal was assumed to have grown instantaneously, with no diffusion, and then allowed the re-equilibrate with the melt at 880 °C. The time taken for the calculated profile to match the measured profile is then assumed to be the high-temperature residence time of the crystal. Some of the profiles could, however, be better fit by a two-stage model. The two-stage models were run as follows:

1. First, the inner zone was assumed to grow instantaneously.

2. The inner zone was then allowed to partially re-equilibrate. The outer-most part of the inner zone was assumed to still have its initial Mg concentration, and to be in equilibrium with the melt. Diffusion is modelled at temperatures between 880 and 930 °C, depending on the anorthite content of the outside edge of the inner zone (estimated using Equation 6.2).

3. The outer zone was then assumed to grow instantaneously, with no diffusion taking place during growth.

4. The whole crystal was then allowed to re-equilibrate diffusively with the melt, as in the single-stage models.

Although this approach is still a simplification of the processes of concurrent growth and diffusion, it is closer approximation to reality than one stage models. This method allows two times to be calculated: the total high-temperature residence times of the inner zones, and the high-temperature residence times of the crystals following outer zone growth.

6.6.4 Diffusion coefficient

The different experimental calibrations of the diffusion coefficient of Mg in plagioclase are discussed in Chapter 3. I chose to used the diffusion coefficient of Van Orman et al. (2014), whose experiments were carried out between 800 and 1150 °C (which includes the temperatures of interest to this study). Their equation for the diffusion coefficient as a function of temperature and plagioclase composition is:

$$D_{\mathrm{Mg}}^{\mathrm{plag}} = \exp\left[(-6.06 \pm 1.10) - (7.96 \pm 0.42)\, X_{\mathrm{An}} - \frac{287,000 \pm 10,000}{RT}\right] \tag{6.17}$$

6.6.5 Results

The results of one-stage diffusion models of plagioclase crystals from the Therasia dacites are shown in Figure 6.16, and the results of two-stage diffusion models are shown in Figure 6.17. The results of one-stage and two-stage diffusion models for plagioclase crystals from the Cape Riva dacite are shown in Figures 6.18 and 6.19, respectively. Also shown on the graphs are the predicted initial Mg concentrations and uncertainties, calculated using Equations 6.9–6.11; and the Mg concentrations calculated to be in equilibrium with the edges of the crystals (and hence the melt), using Equation 6.13. The calibrated BSE images and anorthite profiles for all the crystals modelled are presented in Appendix E.

Most of the Mg concentrations of the analysed points (especially those in the centres of the crystals) sit somewhere between the estimated initial Mg concentrations and the estimated equilibrium concentrations. This confirms that the Mg has partially re-equilibrated by diffusion, and allows us to estimate high-temperature residence times for the crystal using diffusion modelling. Two crystals from the Cape Riva dacite (GS11-34a XL14 and XL23, Figures 6.18e-h and 6.20), however, have Mg concentrations within, or close, to the range of uncertainty of the initial Mg concentrations. The lack of Mg diffusion within these crystals suggest that they grew very shortly before eruption.

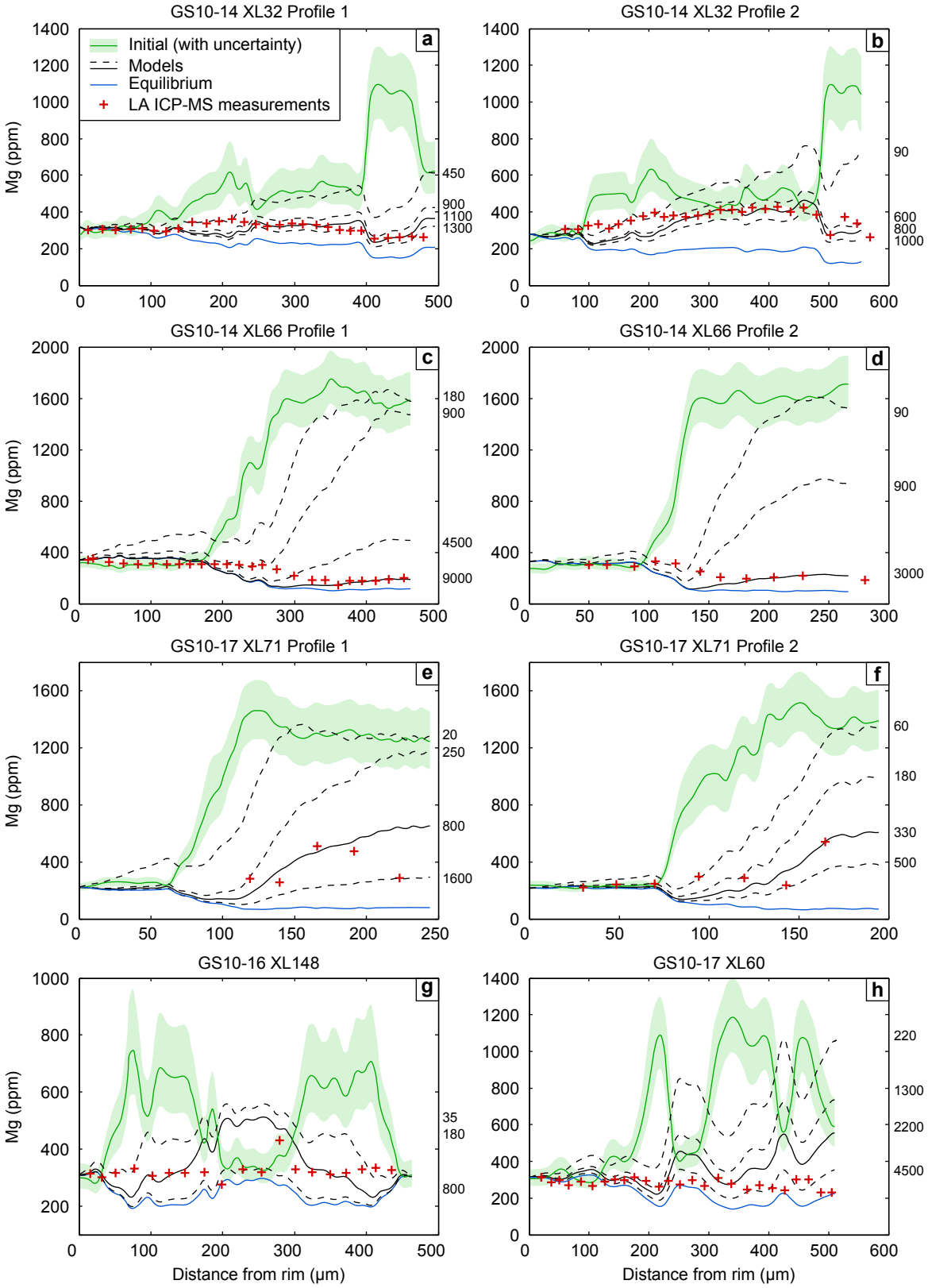

Figure 6.16: The results of one-stage diffusion models of plagioclase crystals from the Therasia dacites. Solid black lines are best fit models, while dashed lines show how the Mg profile evolves with time. Labels on the right of each figure are the time in years for each of the models shown. The results are summarised in Table 6.3.

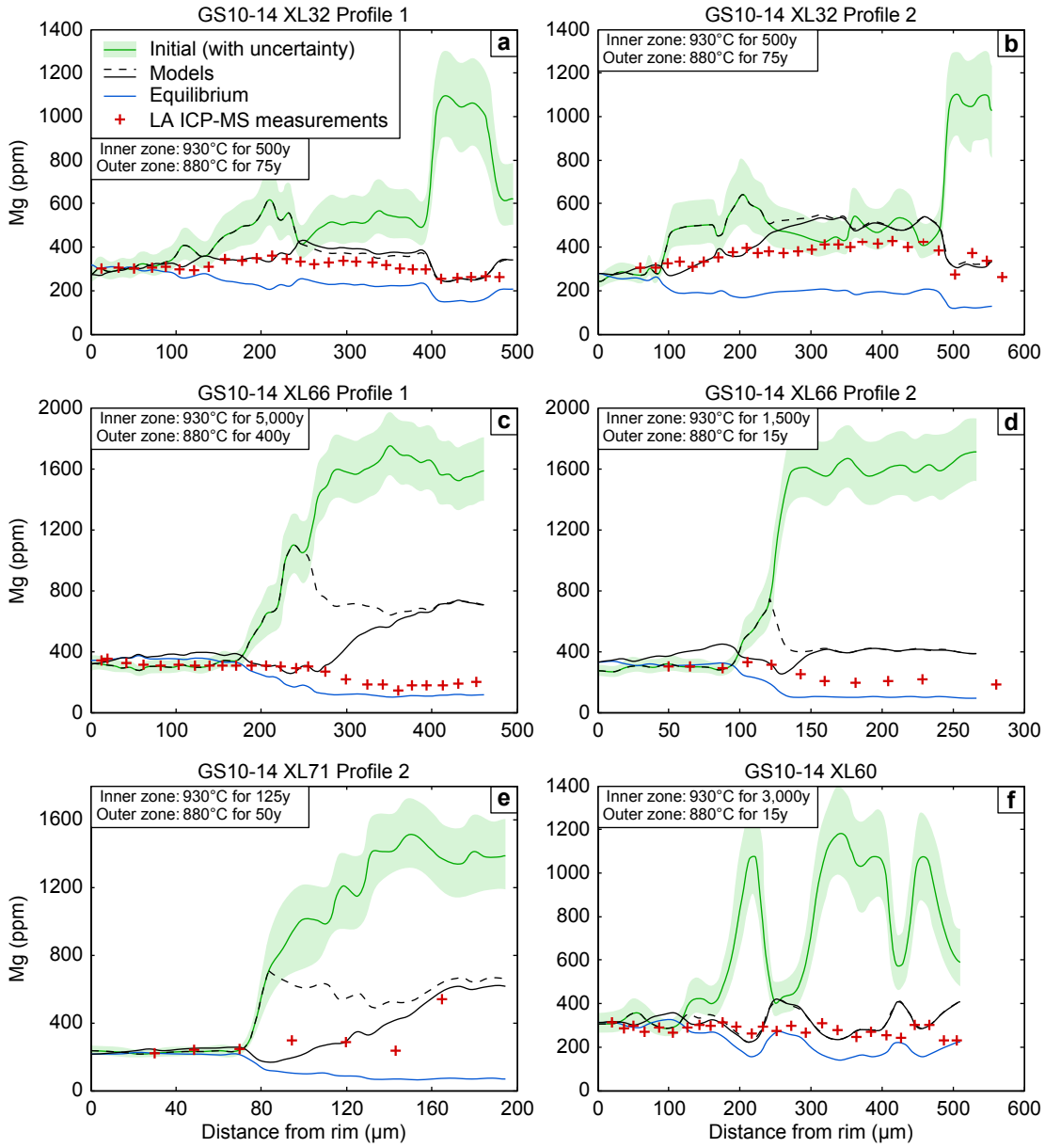

Figure 6.17: The results of two-stage diffusion models of plagioclase crystals from the Therasia dacites. Dashed black line is the modelled result after the first stage (inner zone only), solid black line is the result after both stages. The inner zone and outer zone times stated on the diagram are the times for each stage only; the total high-temperature residence times of the crystals is the inner zone residence time + outer zone residence time. The results are summarised in Table 6.3.

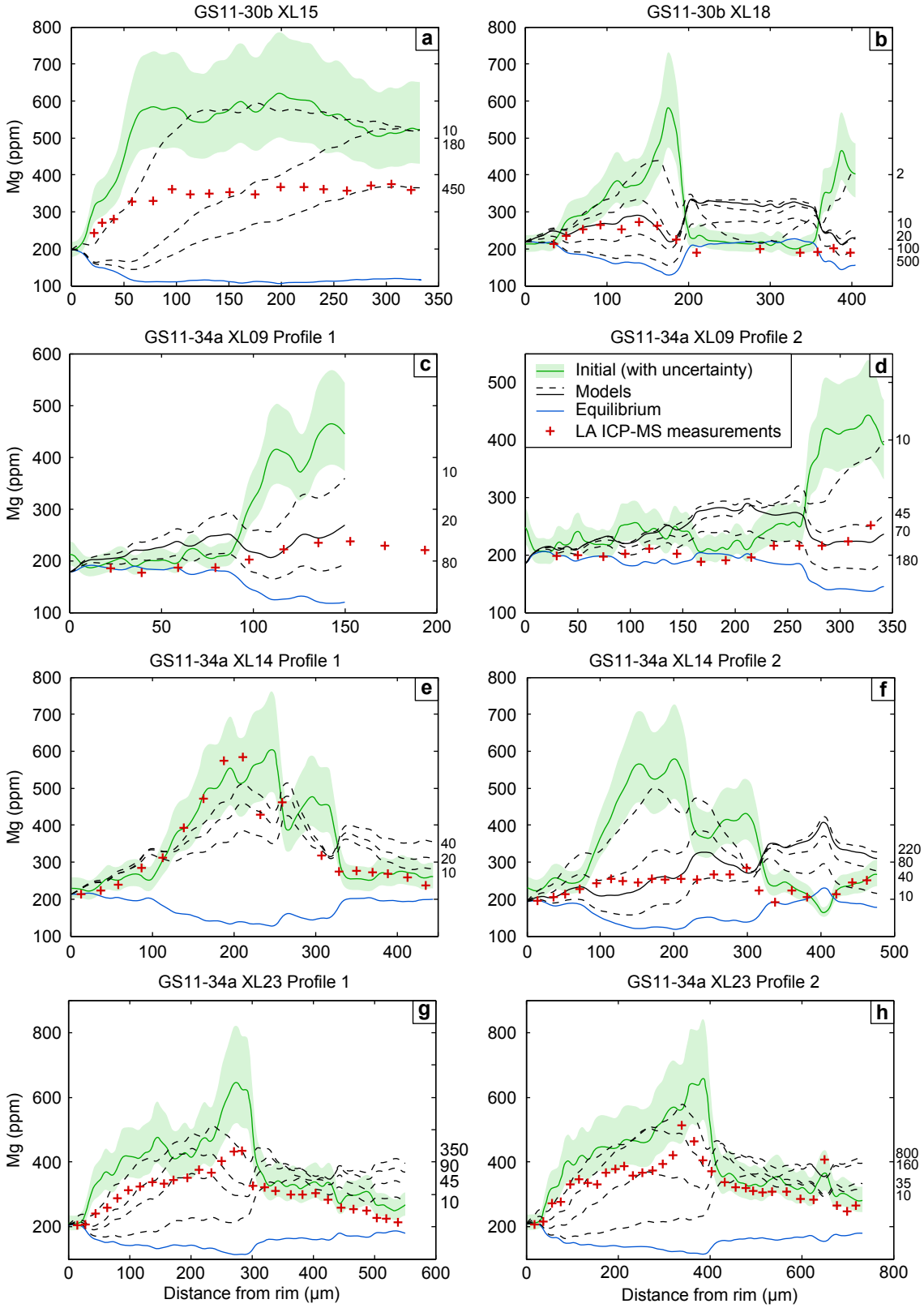

Figure 6.18: The results of one-stage diffusion models of plagioclase crystals from the Cape Riva dacite. Solid black lines are best fit models, while dashed lines show how the Mg profile evolves with time. Labels on the right of each figure are the time in years for each of the models shown. The results are summarised in Table 6.3.

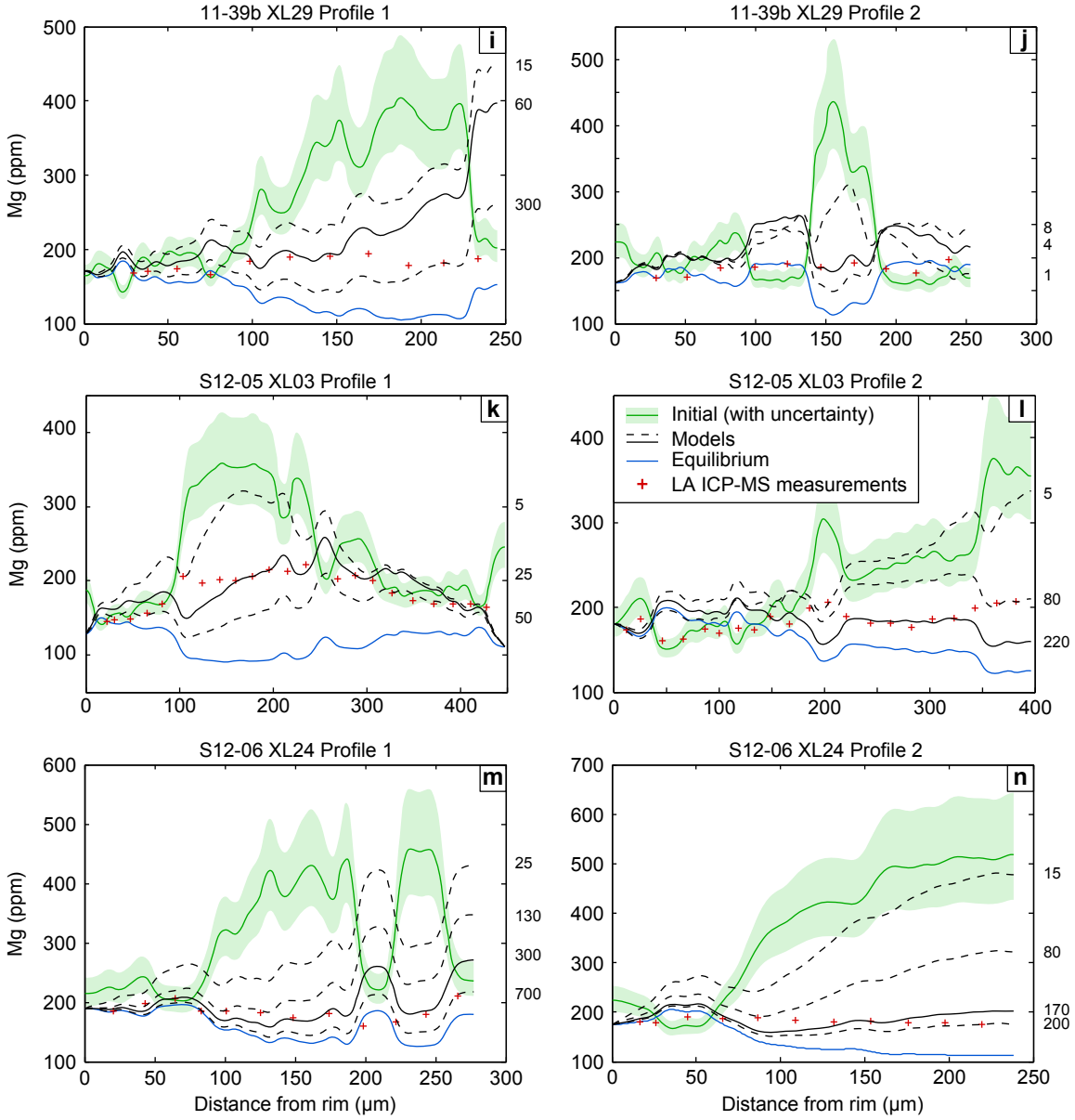

Figure 6.18 continued: The results of one-stage diffusion models of plagioclase crystals from the Cape Riva dacite.

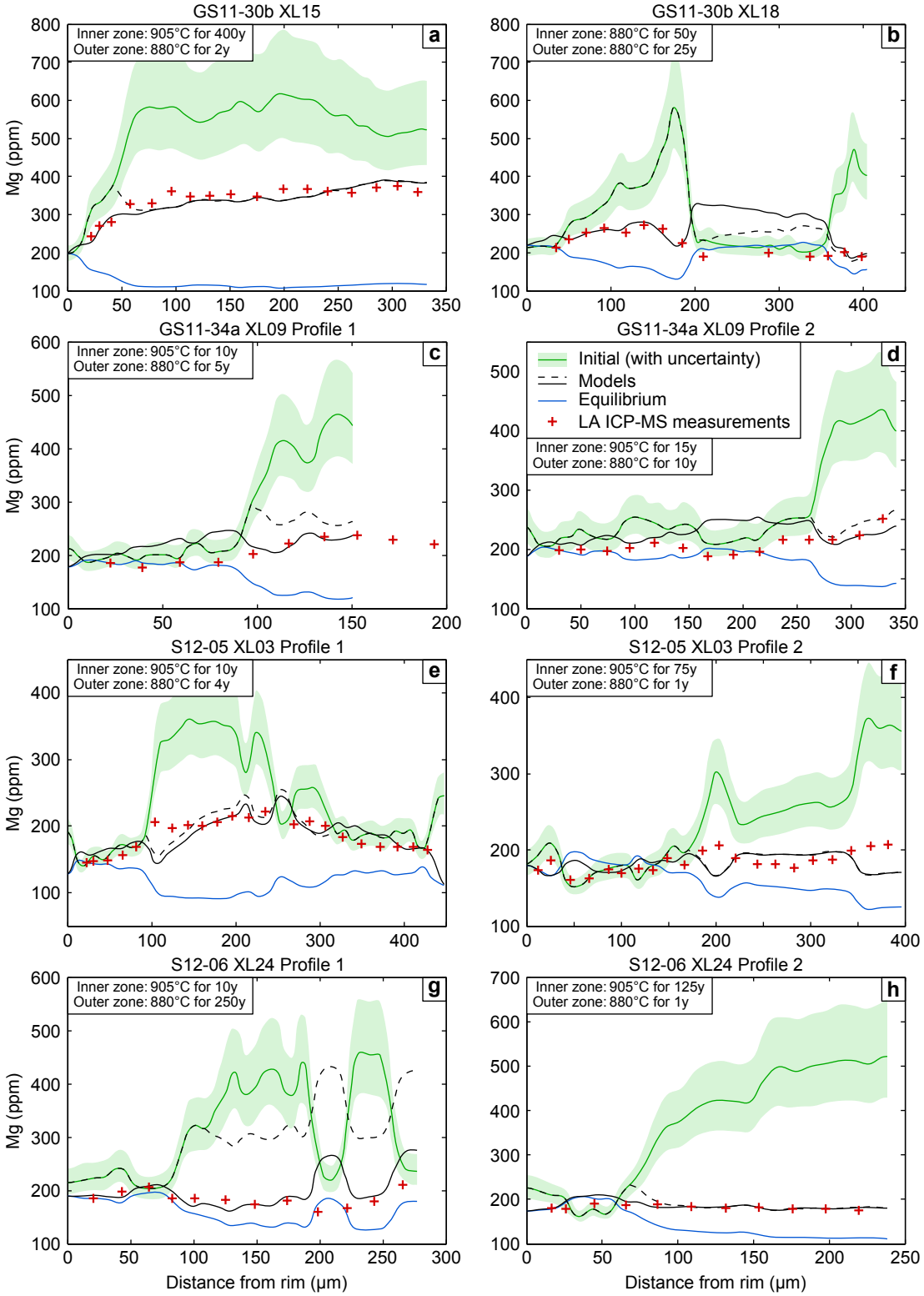

Figure 6.19: The results of two-stage diffusion models of plagioclase crystals from the Cape Riva dacite. Dashed black line is the modelled result after the first stage (inner zone only), solid black line is the result after both stages. The inner zone and outer zone times stated on the diagram are the times for each stage only; the total high-temperature residence times of the crystals is the inner zone residence time + outer zone residence time. The results are summarised in Table 6.3.

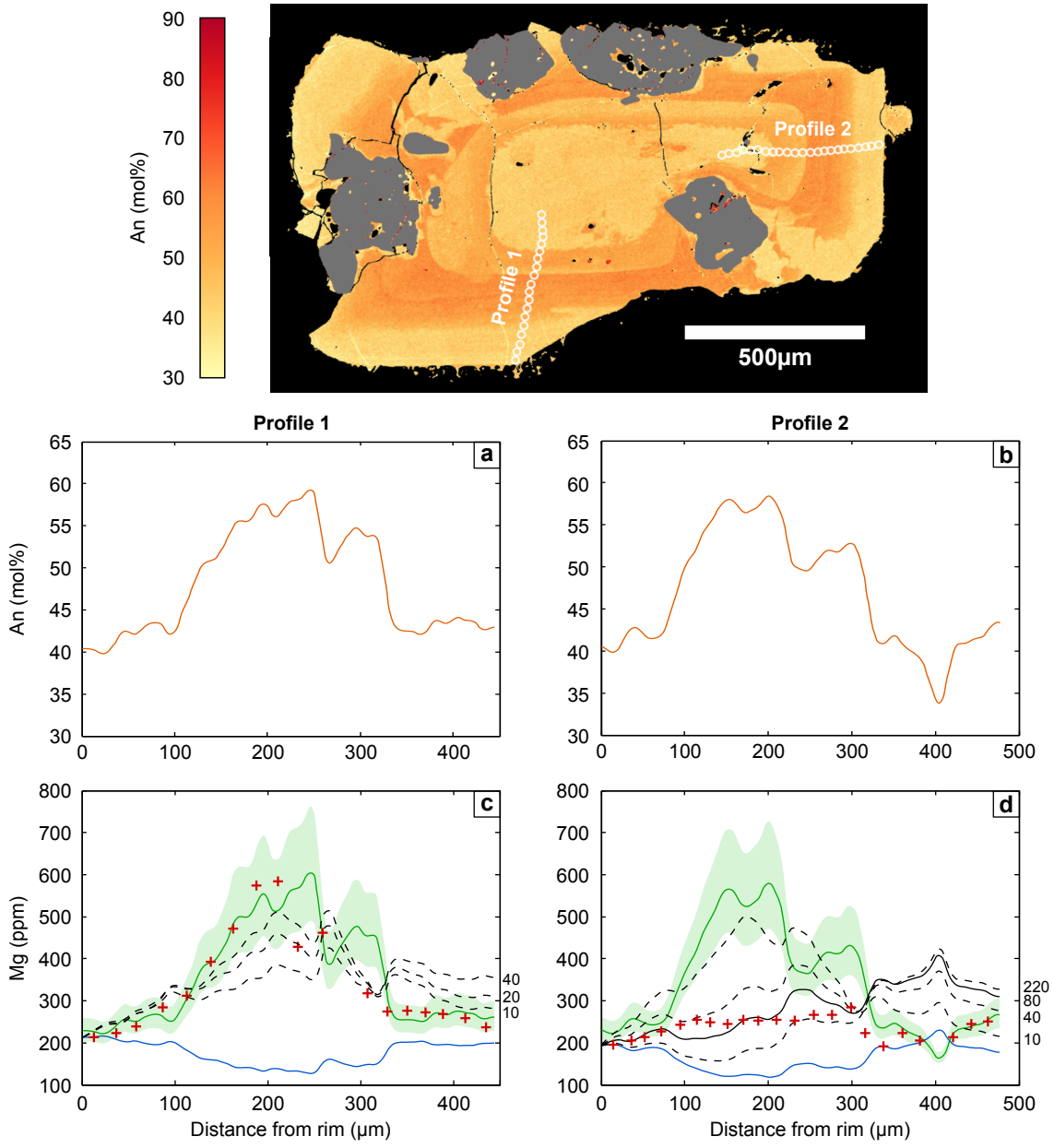

Figure 6.20: A plagioclase crystal from the Cape Riva dacite (GS11-34 XL14). (a,b) Anorthite contents along the two laser profiles, measured using the calibrated BSE image. (c,d) The results of one-stage diffusion models. Solid black lines are best fit models, while dashed lines show how the Mg profile evolves with time. No best-fit diffusion model shown for profile 1 (c), as the data are best fit by the initial profile. Labels on the right of each figure are the time in years for each of the models shown.

GS11-34a XL14 (Figure 6.20) also shows a common feature of the diffusion models: profile 2 appears to be more equilibrated than profile 1, and hence gives a longer high-temperature residence time. Where this is the case, the shorter time is taken as the better estimate of the crystal's high-temperature residence time. One-dimensional diffusion models, such as those presented here, may overestimate the time needed for diffusive re-equilibration (Costa et al., 2008). One-dimensional models assume that all the diffusion occurs parallel to the modelled profile. Where the geometry of the zoning pattern is complex, like it is around profile 2 of GS11-34a XL14, diffusion in other directions becomes more significant. Diffusion perpendicular to the modelled profile will allow the crystal to re-equilibrate faster than the models suggest.

There may be other fast paths for diffusion that are not obvious in the BSE images, such as cracks or grain boundaries. The zoning patterns of most of the plagioclase crystals from the Therasia and Cape Riva dacites have complex shapes, and even where the zoning patterns seem simple in the two dimensions visible in the BSE images, they may be complicated as you move out of the plane of the polished sections. Resorption also complicates the interpretation of the Mg profiles. Repeated cycles of growth, partial dissolution, re-equilibration and then renewed growth — as seen in GS11-34a XL14 (Figure 6.20), for example — will affect the shape of the Mg profile, and the one- and two-stage models presented here are clearly simplifications. It is for these reasons that the high-temperature residence times of the plagioclase crystals must be considered to be maximum residence times (except where the crystals appear to have fully equilibrated, as discussed below).

While some crystals were best fit by a one-stage model (GS11-34a XL14 and 23, discussed above; also GS10-16 XL148, Figure 6.16g and GS11-39b XL29, Figure 6.18i,j), most fits were improved by running a two-stage model. Figure 6.21 shows an example of one such crystal (GS11-30b XL15). In a one-stage model (Figure 6.21b), the calculated profile reaches the measured Mg concentrations in the edge of the crystal after less that 10 y. However, the Mg concentrations at the centre of the crystal are not

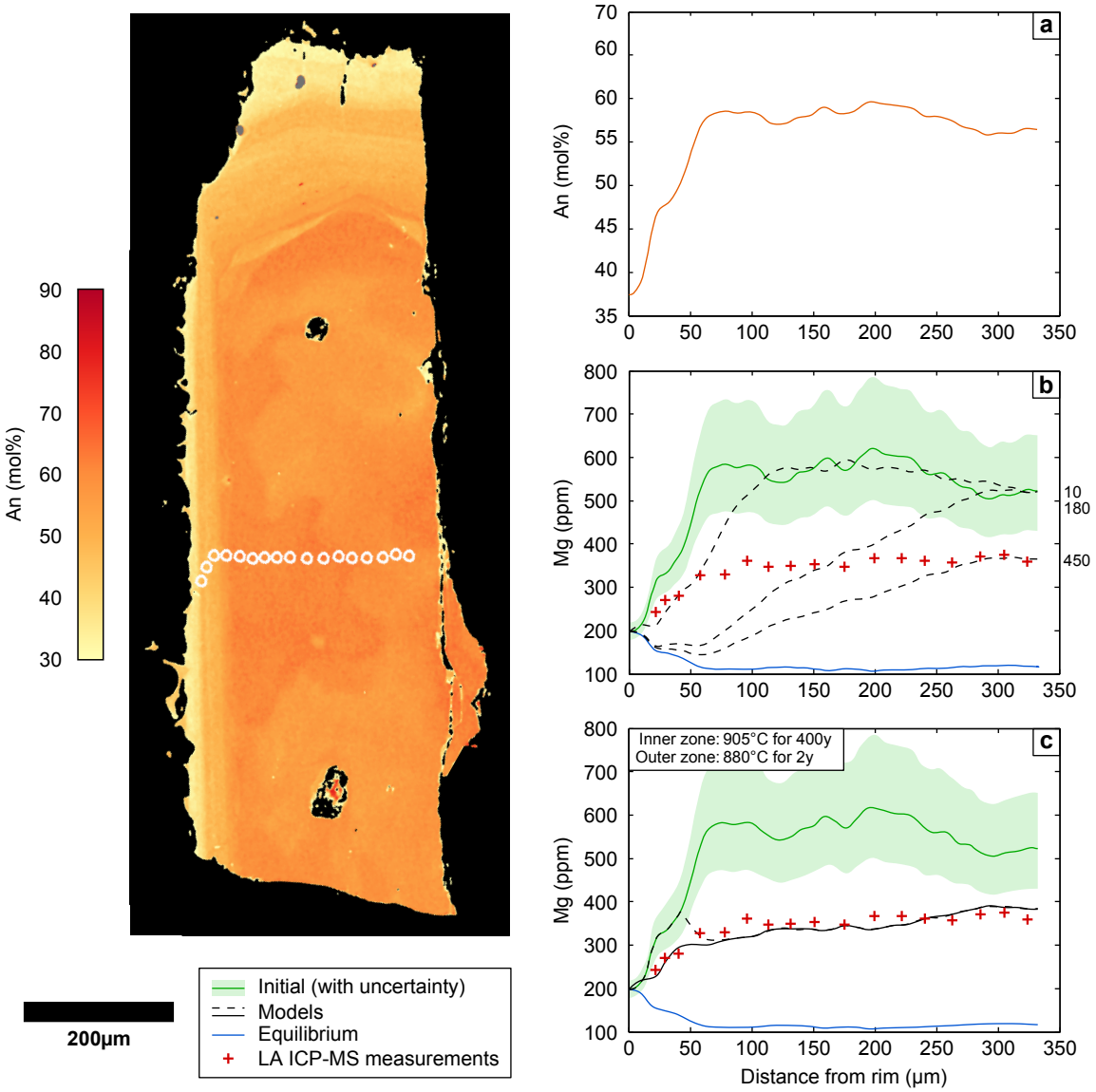

Figure 6.21: A plagioclase crystal from the Cape Riva dacite (GS11-30b XL15). (a) Anorthite contents along the laser profile, measured using the calibrated BSE image. (b) The results of one-stage diffusion models. Dashed lines show how the Mg profile evolves with time. Labels on the right are the time in years for each of the models shown. (c) The results of a two-stage diffusion model. Dashed black line is the modelled result after the first stage (inner zone only), solid black line is the result after both stages. The inner zone and outer zone times stated on the diagram are the times for each stage only; the total high-temperature residence times of the crystals is the inner zone residence time + outer zone residence time.

reached until about 450 y. In the two-stage model (Figure 6.21c), the inner zone is allowed to equilibrate for 400 y without the outer zone, and reaches the measured Mg concentrations. The outer zone then grows, and the crystal only remains in the melt for a short period (∼2 y) before being erupted.

A few crystals, however, are not well fit by either one-stage or two-stage diffusion models (e.g. GS10-14 XL32, Figure 6.22). The one-stage model for profile 1 (Figure 6.22c), for example, reaches the Mg concentration of the analyses between 170 and 250 µm from the outer zone after about 450 y. The Mg concentrations of the rest of the crystal are not reached until about 1,100 y. For the two-stage model, it is the analyses between 260 and 400 µm from the outer zone that cannot be fit at the same time as the rest of the crystal. A similar effect is seen in profile 2. One possible explanation is that not all the diffusion is occurring parallel to the measured profile. For GS10-14 XL32, it is possible that there is a join between two crystals at about 250 µm from the crystal outer zone along profile 1. This would provide a fast path for Mg to diffuse along. Another possibility is that the crystal grew in three stages rather than just two. Both explanations would require us to reduce the estimate of high-temperature crystal residence time, therefore even the poorly fit models can give us maximum high-temperature residence times.

The final feature of the diffusion models can also be seen in GS10-14 XL32 (Figure 6.22). The data can be fit by two-stage models where the inner zone first reaches equilibrium with its host melt, before the outer zone is grown. This is true of two other Therasia crystals (GS10-14 XL66, Figure 6.17c,d; GS10-17 XL60, Figure 6.17f). Once a crystal reaches equilibrium with its surroundings, it can remain at high temperature indefinitely without any changes to its composition. The timescales of these three inner zones, therefore, are minimum values. The fact that the inner zones are not in equilibrium with their outer zones, however, demonstrates that the outer zones must be younger than the inner zones, and allows us to estimate the time these crystals resided at high temperature after the growth of the outer zones.

6.6.6 Uncertainties

Uncertainty in the fit

The uncertainty in the high-temperature residence times due to the fit of the data was quantitatively assessed as follows. As the models were run, the time at which the calculated profile first reached the measured Mg concentrations was noted. The diffusion model was then allowed to continue until the calculated profile fell below most of the measured Mg concentrations. Although this approach is somewhat subjective, it was conservatively applied to produce the largest possible range of ages supported by the data.

Uncertainty in the initial conditions

Another major source of uncertainty in the diffusion models is the initial conditions. Three profiles were selected to investigate the effect of the initial Mg concentration on the residence times recovered from the diffusion models. The three profiles were run starting at the three different estimates of the initial concentration ('best', low, and high, as given by Equations 6.9, 6.10 and 6.11, respectively). The time each profile took to reach different levels of equilibration was then compared for the different starting conditions. The effect of using either the high or low initial Mg concentrations, rather than the 'best' initial concentrations, was to change the estimated high-temperature residence times by between 15 and 65 y (with an average difference of 40 y).

We can also asses the impact that the uncertainty in the initial conditions has on

Figure 6.22 ***(facing page)*:** A plagioclase crystal from the Therasia dacites (GS10-14 XL32). (a,b) Anorthite contents along the laser profiles, measured using the calibrated BSE image. (c,d) The results of one-stage diffusion models. Dashed lines show how the Mg profile evolves with time, and solid black lines are the best fit model. Labels on the right are the time in years for each of the models shown. (e,f) The results of a two-stage diffusion model. Dashed black line is the modelled result after the first stage (inner zone only), solid black line is the result after both stages. The inner zone and outer zone times stated on the diagram are the times for each stage only; the total high-temperature residence times of the crystals is the inner zone residence time + outer zone residence time.

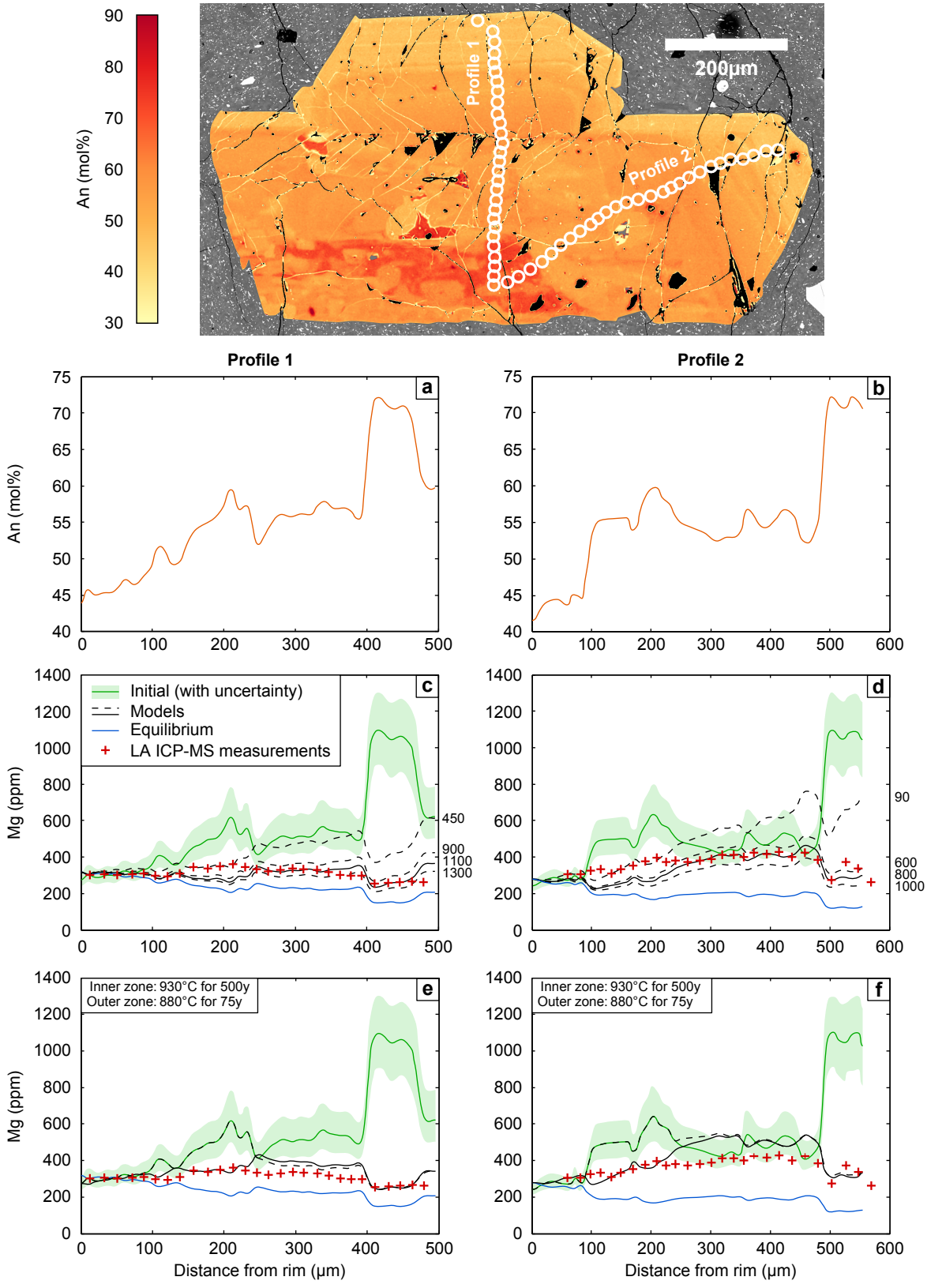
An (mol%)
90
80
70
60
50
40
30
Profile 1
Profile 2
200µm
Profile 1
Profile 2
a
b
c
d
e
f
An (mol%)
Mg (ppm)
Initial (with uncertainty)
Models
Equilibrium
LA ICP-MS measurements
450
900
1100
1300
90
600
800
1000
Inner zone: 930°C for 500y
Outer zone: 880°C for 75y
Distance from rim (µm)

the high-temperature residence times by looking at the time it takes for the calculated profile to drop from the 'best' initial profile to below the low bound of the initial concentration. In most cases this is less than 40 y. The exceptions are in the centres of long plateaus of the Mg concentration and regions affected by "uphill diffusion". For example, the very centre of Figure 6.21b stays at roughly the same Mg concentration for the first 180 y. This is due to the fact that the diffusion front has to migrate to the centre. In the case of "uphill diffusion" (e.g. Figure 6.22d), it is Mg diffusing out of regions with high initial Mg concentrations that stops the Mg profile from dropping (even driving the Mg concentrations "uphill", away from equilibrium). In both cases, changing the initial Mg concentration does not change this behaviour; instead it adds or subtracts ∼40 years on top of the time it takes for the Mg concentrations in the regions affected to start dropping. A value of ±40 y was taken as the uncertainty due to potential variations in the initial Mg concentration, and was added to the range of times estimated from the range of possible fits to the data (as described above). In crystals with high-temperature residence times shorter than 40 y, however, the time taken for the one-stage models to drop from the best estimate to below the lower bound of the estimates of the initial Mg concentrations was used instead.

Uncertainty in the diffusion coefficient

The final source of uncertainty in the models is the uncertainty in the diffusion coefficient. Because time is inversely proportional to the diffusion coefficient in Equation 6.4, we can assess this analytically. The biggest source of error in the diffusion coefficient is the temperature at which the diffusion is assumed to have taken place. The relationship between the diffusion coefficient and the temperature takes the form:

$$D = D_0 \exp\left(\frac{-Q}{RT}\right) \tag{6.18}$$

The ratio between the time diffusion takes at two different temperatures, T_1 and T_2, can therefore be written as:

$$\begin{aligned} \frac{t_1}{t_2} &= \frac{D_0 \exp\left(-Q/RT_2\right)}{D_0 \exp\left(-Q/RT_1\right)} \\ \ln\left(\frac{t_1}{t_2}\right) &= \frac{Q}{RT_1} - \frac{Q}{RT_2} \end{aligned} \tag{6.19}$$

Fe–Ti oxides from two of the three analysed pumice fall deposits from the Therasia dome complex, along with the Cape Riva eruption give temperatures of within about $\pm 25\,^{\circ}\mathrm{C}$ of $880\,^{\circ}\mathrm{C}$ (Chapter 5; Cadoux et al., 2014). This temperature range is therefore used to asses the uncertainty in the diffusion models. It is worth noting that the pumice fall deposit that falls outside this temperature range, pumice fall B, is significantly hotter. This would speed up Mg diffusion, again making the high-temperature residence times presented here overestimates.

Using the equation for the diffusion coefficient an An_{40} of Van Orman et al. (2014), diffusion at $855\,^{\circ}\mathrm{C}$ should take 1.94 times as long as at $880\,^{\circ}\mathrm{C}$, and diffusion at $905\,^{\circ}\mathrm{C}$ should take 0.53 times as long. This approach may not be strictly applicable, however, as the diffusion coefficient of Mg in plagioclase is not constant across the length of the crystal. This leads to a $\frac{\partial D_{\mathrm{Mg}}}{\partial x}$ term in the expansion of the diffusion equation (Equation 6.15). However, running models at 855 and $905\,^{\circ}\mathrm{C}$ confirms that a factor of two is a reasonable estimate of the uncertainty in the models due to variation in temperature. The lower and upper bounds on the range of high-temperature residence times estimated from the possible fits to the data and the uncertainties in the initial conditions were therefore multiplied or divided by a factor of two to take this into account.

6.7 Combining petrological and timescale information

The results of the diffusion models of the plagioclase crystals are presented in Table 6.3. Also shown are the range of possible high-temperature residence times, taking into account the uncertainties on the fit to the data, the initial conditions, and the temperature. The best estimate of the high-temperature residence time of each crystal, out of all the models presented, is shown in bold. The high-temperature crystal residence times are also plotted in Figure 6.23, along with timescale constraints from field data (Chapter 4). For the Therasia dacites, the average time between eruptions is calculated as the time between the youngest and oldest Therasia dacites, ∼15 ky, divided by the minimum number of pauses between the eruptions that took place during that time, 10 (≈ 1.5 ky per eruption). On the plot of Cape Riva high-temperature residence times (Figure 6.23b), the time between the youngest dated Therasia lava and the Cape Riva eruption is plotted, along with the uncertainty from the radiometric dating. Inner phenocryst zones are distinguished on the graph only where a separate high-temperature residence time could be determined using diffusion models. Outer zone residence times are either one stage models, or the second stage of two-stage models.

In order to properly interpret the crystal residence times recovered from diffusion modelling, they need to be seen in the context of the petrology and crystal textures. The three longest high-temperature residence times from the Therasia dacites come from calcic cores. As discussed in Section 6.5.1, these cores are probably xenocrystic. They could have either been introduced from a mafic recharge magma, or from an ancient plutonic mush. The high Sr content of some of the crystals suggested a plutonic origin, and the long timescales estimated here support this interpretation.

The high-temperature residence times of the outer crystal zones and one-stage models, which better represent the high-temperature residence times of phenocrysts in the Therasia magma reservoir, are all much shorter than the mean time between eruptions.

The phenocrysts from the Therasia dacites appear to have grown within a few decades, up to possibly a few centuries, prior to eruption. This tends to support the idea that there was no persistent magma reservoir during the construction of the Therasia dome complex. If there had been, we would expect to see phenocrysts recycled between eruptions.

The zoning patterns of the Cape Riva crystals record the repeated mixing of compositionally diverse magmas (silicic andesite to rhyodacite). The key result of the diffusion modelling of the Cape Riva plagioclase crystals is that all their high-temperature residence times are shorter than the $2,800 \pm 1,400$ y between the youngest dated Therasia lava and the Cape Riva eruption (Chapter 4). The depletion of incompatible elements in the Cape Riva whole rock relative to the Therasia magma suggests that much of the Cape Riva magma arrived during this time, and the short high-temperature residence times (mostly years to decades, up to a maximum of few centuries) support this interpretation.

6.8 Summary

In this chapter I have looked in detail at the plagioclase phenocrysts in the Therasia and Cape Riva dacites. I have characterised the anorthite zoning patterns of the phenocrysts, and compared these to zoning patterns of selected trace elements. I used the zoning patterns of slowly diffusing components (anorthite, Sr, Ti, La, Ce) to investigate the composition of the melts that the plagioclase phenocrysts came into contact with, and used the zoning patterns of Mg to estimate high-temperature residence times. The key findings of this chapter are:

- The plagioclase phenocrysts from the Therasia dacites have rims of An_{39} to An_{51}. Some of the crystals have sawtooth zoning, where anorthite contents cycle between An_{59-72} and the rim compositions. Other crystal have a calcic core, with compositions of An_{50} to An_{91}.

Table 6.3: High-temperature residence times, in years, calculated in diffusion models of Mg in plagioclase.

Therasia dacites

Crystal	Profile	1 Stage		2 Stage			
				Calcic core[a]		Outer zone[b]	
Flow 5 (GS10-17)							
XL60	—	2,200	(630–9,000)	**3,000**	**(1,000–)**	**15**	**(0–120)**
XL71	1	800	(100–3,400)		—		—
	2	330	(10–1,100)	**125**	**(30–480)**	**50**	**(0–330)**
Flow 8 (GS10-14)							
XL32	1	1,100	(200–3,700)	**500**	**(150–)**	**75**	**(5–330)**
	2	800	(25–2,100)	500	(7–)	75	(5–480)
XL66	1	9,000	(430–)	5,000	(1,200–)	400	(130–1,100)
	2	3,000	(25–)	**1,500**	**(400–)**	**15**	**(0–130)**
Flow 9 (GS10-16)							
XL148	—	**180**	**(10–1,700)**		—		—

Cape Riva dacite

Crystal	Profile	1 Stage		2 Stage			
				Inner sawtooth[a]		Outer sawtooth[b]	
Phase A (GS11-34a)							
XL09	1	20	(5–240)	**10**	**(2–120)**	**5**	**(0–100)**
	2	70	(10–440)	15	(5–120)	10	(0–110)
XL14	1	**0**	**(0–120)**		—		—
	2	80	(15–520)		—		—
XL23	1	**0**	**(0–260)**		—		—
	2	0	(0–400)		—		—
Phase B (S12-06)							
XL24	1	300	(45–1,500)	10	(5–)	250	(55–680)
	2	170	(20–480)	**125**	**(30–380)**	**1**	**(0–4)**
Phase C (GS11-30b)							
XL15	—	180	(5–980)	**400**	**(130–1,100)**	**2**	**(1–16)**
XL18	—	20	(5–280)	**50**	**(5–280)**	**25**	**(5–140)**
Phase C (S12-05)							
XL03	1	25	(2–180)	**10**	**(4–180)**	**4**	**(0–12)**
	2	220	(20–1,100)	75	(5–280)	1	(0–16)
Phase D (GS11-39b)							
XL29	1	60	(10–680)		—		—
	2	**4**	**(1–22)**		—		—

Figures in parentheses are the range of possible high-temperature residence times, taking into account the uncertainties in model fit, initial conditions, and temperature. Where an upper bound is not present, the Mg is at or close to equilibrium. Bold figures are the best estimate for each crystal. Outer zone and one-stage models run at 880 °C, inner zone models sometimes run at higher temperatures.

[a] Residence times of the inner zones up until the growth of the outer zone.

[b] Residence time of the outer zone, from its growth until eruption.

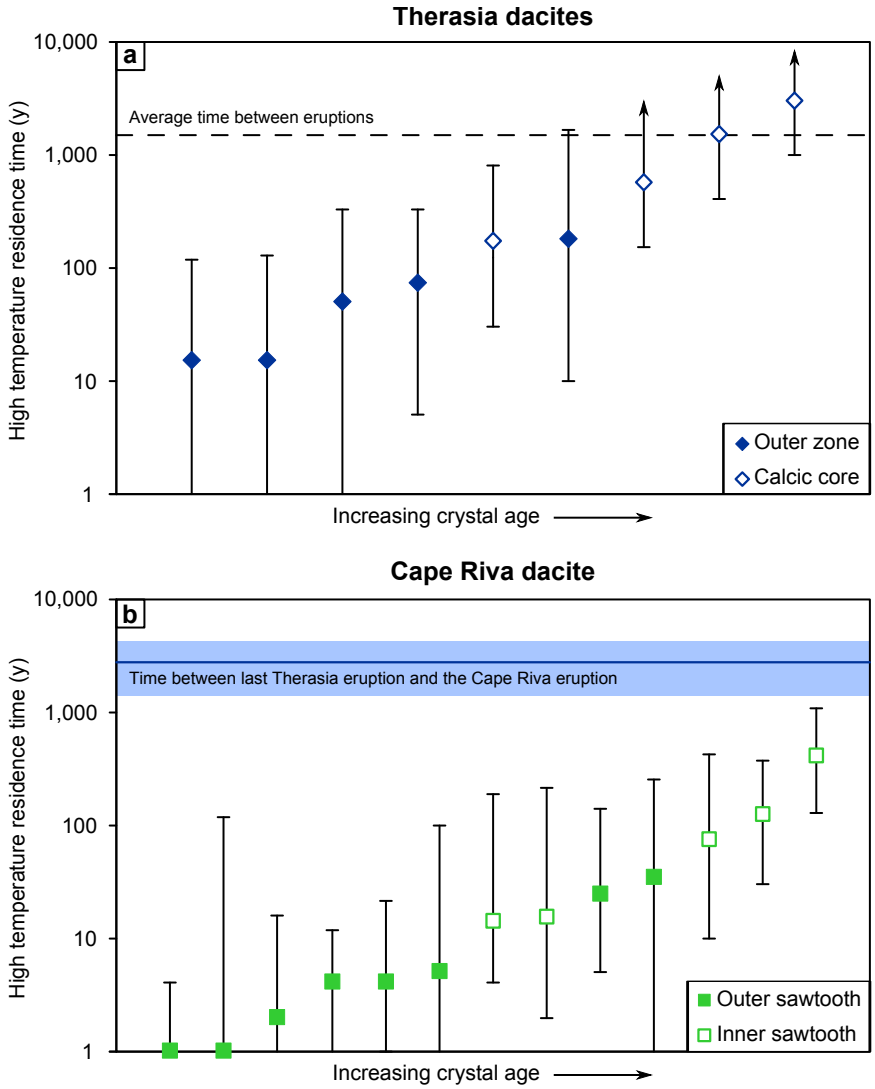

Figure 6.23: high-temperature Residence times of plagioclase crystals from (a) the Therasia and (b) the Cape Riva dacites. Outer zone residence times are either the duration of the second stage of the two stage models, or the residence times calculated from one-stage models where two-stage models were not run. Calcic core and inner sawtooth high-temperature residence times are the combined durations of the first and second stages of the two-stage models. Error bars represent the uncertainties in the estimates based on uncertainties in the model fit, the initial conditions and the temperature (as discussed in the text). Outer zone and one-stage models run at 880 °C, inner zone models sometimes run at higher temperatures (as discussed in the text). Average time between Therasia eruptions and the time between the last Therasia eruption and the Cape Riva eruption is calculated using the radiometric dates presented in Chapter 4.

- The compositions of the phenocryst rims vary between the different Therasia eruptions. There are also textural differences between the plagioclase found in each flow. Crystals with sawtooth zoning are present in some flows and absent in others. Some flows have crystals with large, brown, rounded glass inclusions, while these crystals are not found in others.

- The Cape Riva plagioclase phenocryst rims have compositions of An_{31-41}, with most clustering between An_{36} and An_{40}. Some Cape Riva plagioclase phenocrysts have sawtooth zones, cycling between An_{46-60} and rim compositions. No cores more calcic than the sawtooth zones were found. There are no obvious differences between crystals from the different phases of the eruption, suggesting that the Cape Riva magma reservoir was well mixed before eruption.

- The liquid equivalent Sr concentrations of the plagioclase phenocrysts in both the Therasia and Cape Riva eruptions are tightly correlated with anorthite content. This suggests that the changes in the anorthite content of the plagioclases correspond largely to changes in the melt composition. Using the Sr and Ti content of the plagioclase crystals, the composition of the melt that each zone grew from could be estimated.

- The Sr and Ti content of the Therasia plagioclase phenocrysts show that the rims grew in equilibrium with a dacitic melt. The calcic parts of the sawtooth zones demonstrate that the phenocrysts came into contact with a silicic andesitic melt during their growth. The Ti contents of these crystals suggest that most of the silicic andesite input into the Therasia plumbing system lay along fractional crystallisation trends. There is little evidence from the Ti content of the phenocrysts in the dacites for inputs of basaltic magma, apart from two crystals in the dacitic flow 9, close to the top of the sequence.

- The calcic cores found in some Therasia phenocrysts grew in a basaltic or andesitic melt, with a high Sr content characteristic of the much older (530-430 ka)

Peristeria magma. This suggests a xenocrystic origin, although it is possible that some of the calcic cores emanated from a mafic recharge magma.

- The Cape Riva plagioclase phenocrysts grew from dacitic to rhyodacitic melt compositions. The Ti content of the phenocrysts demonstrate that the incoming magma driving these composition cycles must be at least as evolved as a silicic andesite.

- The incompatible element concentrations (La, Ce, K) of the plagioclase crystals vary between the Therasia and Cape Riva magmas, in a similar fashion to the whole rock compositions (Chapter 5). While K diffuses quickly and may have re-equilibrated before eruption, La and Ce diffuse very slowly and the plagioclase crystals should preserve their original growth concentrations. Very few of the Cape Riva plagioclases have Therasia-like incompatible element concentrations, suggesting very little recycling of Therasia crystals into the Cape Riva magma. Only one crystal appears to have seen Therasia-like melt during its growth.

- Diffusion modelling of the Therasia plagioclase crystals shows that some of the calcic cores had extended histories of at least a few thousand years at high temperatures, while the bulk of the phenocrysts grew within a few decades (up to a maximum of a few centuries) before eruption.

- The Cape Riva plagioclases all have high-temperature residence times shorter than the $2{,}800 \pm 1{,}400$ years between the last Therasia eruption and the Cape Riva eruption deduced from the field data and radiometric dating (Chapter 4). This agrees with the suggestion, based on the whole rock chemistry (Chapter 5), that the Cape Riva magma only arrived in the shallow crust shortly before eruption. Most of the high-temperature residence times of the Cape Riva plagioclases are a few years to decades, up to perhaps a few hundred years.

Chapter 7

Orthopyroxene

7.1 Introduction

This chapter looks at the orthopyroxene crystals in the Therasia and Cape Riva dacites, in a similar way to how I investigated the plagioclase crystals in the previous chapter. The orthopyroxene crystals have been breifly described in Chapter 5 In this chapter, I look in more detail at the zoning patterns of both major and trace elements in orthopyroxene crystals. I consider only the phenocrysts, as these crystals provide a record of the events that took place within the magma reservoir, and I focus entirely on the dacites, as these make up the majority of the erupted material during both the Cape Riva eruption and the construction of the Therasia dome complex (Chapter 4).

Just as with the plagioclase phenocrysts, the zoning patterns of different elements with different diffusion coefficients were measured to provide complimentary information on the crystals' histories. Fe and Mg zoning patterns were measured quantitatively, using calibrated SEM images, while Al and Ca zoning patterns were imaged qualitatively using X-ray counts on the electron microprobe. The concentrations of fast-diffusing elements can be used to estimate timescales of magmatic processes through diffusion modelling. On the other hand, slowly-diffusing elements can be used to track growth conditions of crystals as they require long times to re-equilibrate with their

host magma. Their concentrations in crystals should therefore reflect the temperature, pressure and composition of the melt at the time of the crystals' growth, and they should be unaffected by any subsequent changes to its chemistry. Which elements can be considered "fast-" and which can be considered "slow-diffusing" depends on the temperature, the timescales and length-scales of interest. This is discussed later in the chapter, after the zoning patterns themselves are presented.

Of particular interest are the changes that occurred in the magma reservoir in the build-up to the Cape Riva eruption. In Chapter 5 we saw that a change in the concentration of incompatible elements between the Therasia and Cape Riva eruptions suggested that there was a large influx of new silicic magma shortly before the Cape Riva eruption. The field evidence constrains the timing of this influx to within $2{,}800 \pm 1{,}400$ y before the Cape Riva eruption (Chapter 4). The Cape Riva plagioclase crystals also appear to record the mixing of silicic magmas with slightly different compositions (Chapter 6). We can look for evidence of this in the zoning patterns of the orthopyroxene crystals.

Also of interest is the residence times of the phenocrysts in the Therasia and Cape Riva silicic magma reservoirs. Diffusion modelling of plagioclase crystals gave high-temperature residence times of years to centuries in both the Therasia and Cape Riva dacites (Chapter 6). This suggests that the shallow magma reservoirs that fed the Therasia and Cape Riva eruptions were short-lived.

7.2 Analytical techniques

Thin sections from three dacitic lavas from the Therasia dome complex were selected for study (flows 5, 8 and 9; samples GS10-17, GS10-14 and GS10-16, respectively), along with five pumices from the Cape Riva eruption, covering all four phases of the eruption (phase A: GS11-34a; phase B: S12-06; phase C: GS11-30b and S12-05; phase D: GS11-39b). These are the samples from which the plagioclases in Chapter 6 where taken.

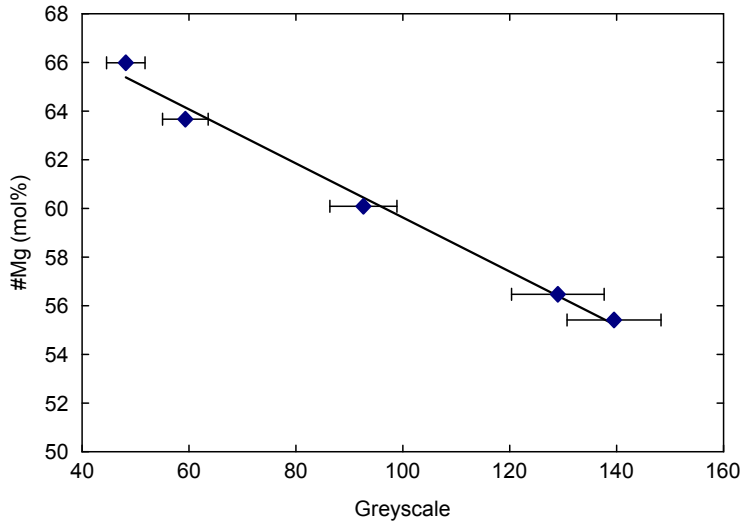

Figure 7.1: Typical calibration curve for #Mg (magnesium number; $100 \times$ molar Mg/[Mg + Fe]) for a BSE image of an orthopyroxene crystal (GS11-39b PYX29). Horizontal error bars are the standard deviation of the greyscale values within the circles measured in ImageJ, vertical error bars are calculated from the counting statistics of the electron microprobe but are smaller than the symbol.

The pumices were hand crushed, and orthopyroxene crystals were hand-picked, set in resin and polished. Crystals with adhering melt were preferred, as this demonstrates that those crystal face are original rather than fractures caused by crushing.

Mineral major element compositions were analysed using the Cameca SX 100 electron microprobe at the Laboratoire Magmas et Volcans, Université Blaise Pascal, Clermont-Ferrand, using a beam current of 15 nA. Orthopyroxene element maps were made of selected crystals with a beam current of 100 nA at 15 kV, and a dwell time of 100 ms per pixel. Pixel size varied between 1 and 3 µm, depending on the size of the crystal to be imaged.

Backscattered electron (BSE) images of selected orthopyroxene crystals were produced on the scanning electron microscope (SEM), and then calibrated for #Mg (magnesium number; $100 \times$ molar Mg/[Mg + Fe]) on the electron microprobe. Five points on each crystal were analysed using the electron microprobe for their #Mg. The average greyscale values in circles 2–5 µm in diameter around these same points was measured in the SEM images using the image analysis software package ImageJ (Rasband, 2012). The relationship between the greyscale value and composition was then calculated us-

ing a linear least-squares regression for each image (Figure 7.1). Correlation between greyscale values and anorthite content of the orthopyroxene was generally high, with correlation coefficients $r^2 > 0.95$ for most (and $r^2 > 0.80$ for all) of the images used. This corresponds to a standard error in #Mg of ±0.2–1 mol%, estimated from the regression parameters. With this relationship, the #Mg content of any spot on the image could be calculated. This allowed me to quickly plot profiles of #Mg against distance at much greater spatial resolution than would otherwise be practical (pixel size was 0.01–1 µm depending on the image).

7.3 Zoning patterns

7.3.1 Mg–Fe zoning

Most of the Therasia orthopyroxene phenocrysts are euhedral, weakly zoned and have a #Mg of 58–64 $Wo_{3-4}En_{53-60}Fs_{37-43}$, where Wo is molar Ca/(Ca + Mg + Fe), En is molar Mg/(Ca + Mg + Fe) and Fs is molar Fe/(Ca + Mg + Fe). A weakly zoned orthopyroxene is shown in Figure 7.2a. Some orthopyroxenes have a Mg-rich inner zone, with a #Mg of 65–71 ($Wo_{3-4}En_{62-68}Fs_{29-35}$). These inner zones have diffuse boundaries with the rims, and grade into similar compositions to the weakly zoned orthopyroxenes (Figure 7.2c). There are also rare crystals with three zones (Figure 7.2e). These crystals have inner and outer zones of a similar composition to the weakly zoned orthopyroxene (#Mg: 61–65), with an intermediate zone that has a similar composition to the Mg-rich cores (#Mg: 67–68).

The orthopyroxenes from the Cape Riva dacite are similar in appearance to those found in the Therasia dacites. The main differences are that more of the Cape Riva orthopyroxenes are zoned, and the Cape Riva orthopyroxenes are slightly more iron rich the Therasia orthopyroxenes. The weakly zoned Cape Riva orthopyroxenes have #Mg of 53–58 ($Wo_{3-4}En_{52-56}Fs_{41-44}$), and can be slightly normally or reversely zoned (Figure 7.2b). Many Cape Riva orthopyroxenes have Mg-rich inner zones with #Mg

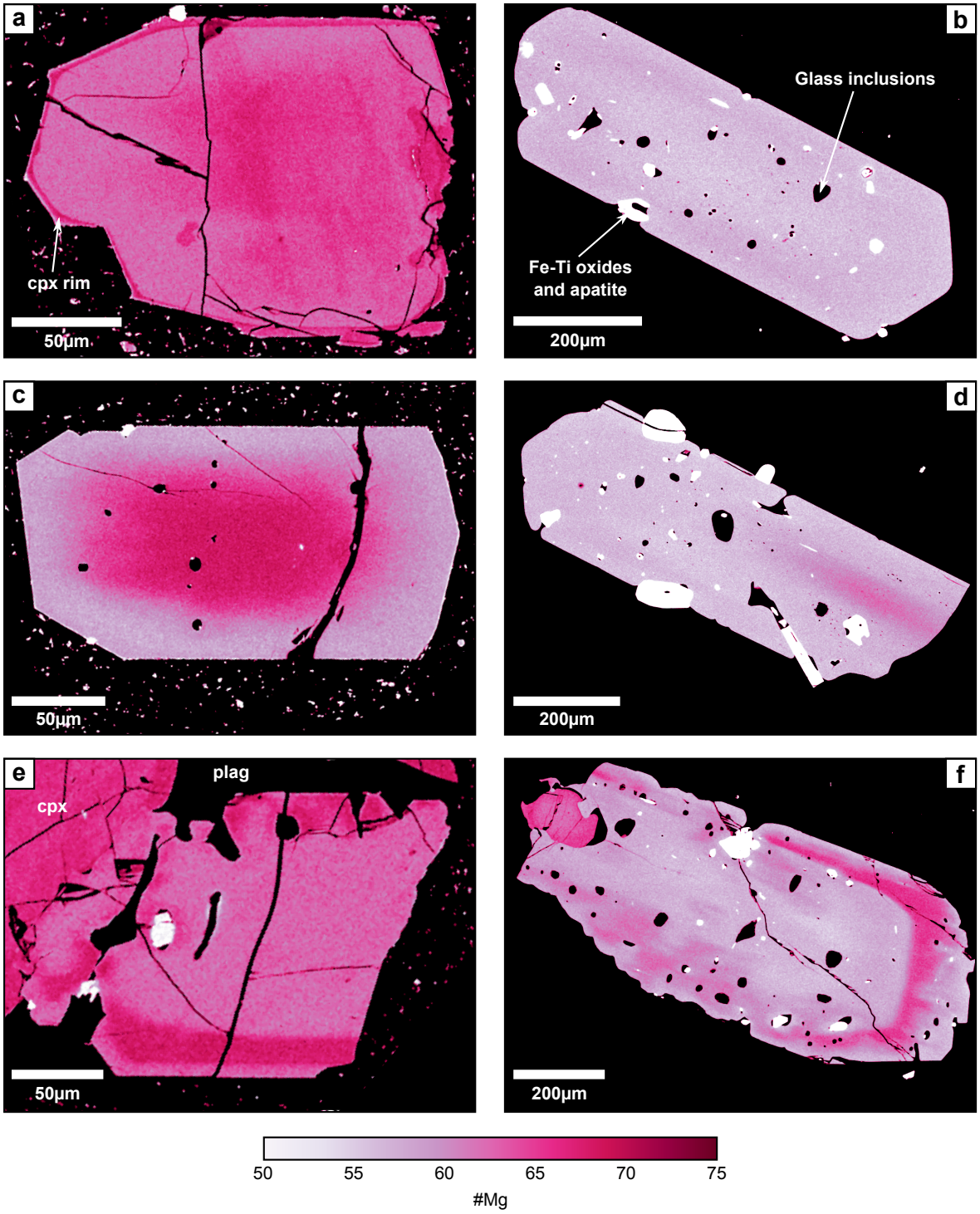

Figure 7.2: Calibrated BSE images of pyroxene crystals (a) a weakly zoned orthopyroxene from flow 8 of the Therasia dome complex (GS10-14 PYX01) (b) a weakly zoned orthopyroxene from the Cape Riva dacite (S12-05 PYX26) (c) an orthopyroxene with a Mg-rich rim from flow 5 of the Therasia dome complex (GS10-17 PYX30) (d) an orthopyroxene with a Mg-rich core from the Cape Riva dacite (S12-05 PYX12) (e) an orthopyroxene with a Mg-rich mantle from flow 8 of the Therasia dome complex (GS10-14 PYX26) (f) an orthopyroxene with a Mg-rich mantle from Cape Riva dacite (GS11-30b PYX08). cpx: clinopyroxene; plag: plagioclase.

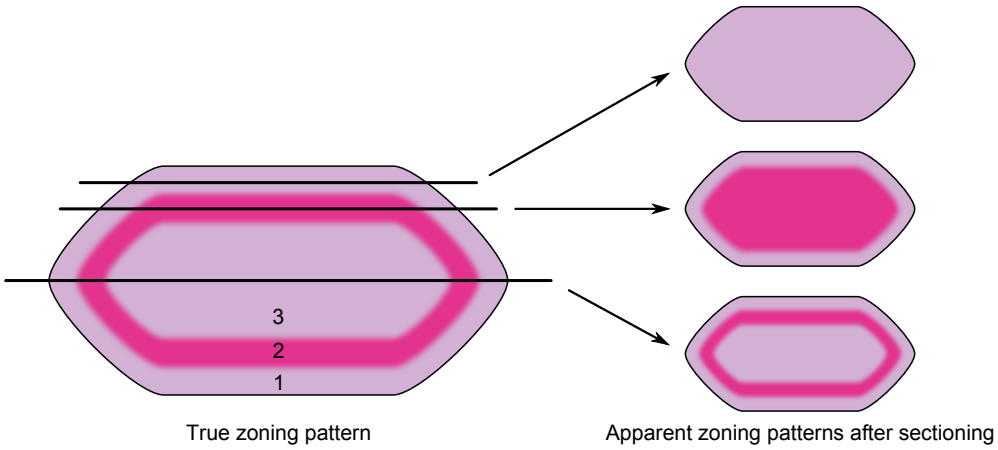

Figure 7.3: Sketch of the typical zoning pattern of Therasia and Cape Riva orthopyroxenes, showing how different cuts through one crystal can reveal three apparently different zoning patterns. The zones are numbered for reference.

of 60–68 ($Wo_{3-4}En_{57-65}Fs_{32-40}$). Like the Mg-rich inner zones in the Therasia dacites, these grade into rims of the same composition as the weakly zoned orthopyroxene crystals (Figure 7.2d). There are also orthopyroxenes with Mg-rich intermediate zones in the Cape Riva dacite (Figure 7.2f). Like in the Therasia dacites, the compositions of the intermediate zones match those of the Mg-rich cores, and the cores and rims match the weakly zoned crystals.

The different zoning patterns described above can all be related to a single, schematic zoning pattern, shown in Figure 7.3. The low-Mg zone 3 is overgrown by the high-Mg zone 2, which is in turn overgrown by the low-Mg zone 1. The BSE images are two-dimensional slices through three-dimensional crystals. The position of this slice relative to the zoning pattern of each crystal will be variable, and this could explain the variation in zoning patterns. A slice close to the centre of the crystal would reveal all three zones, and produce the orthopyroxenes with Mg-rich mantles. A cut closer to the edge of the crystal could go through zones 1 and 2, but miss zone 3. The BSE image would appear to show a crystal with a high-Mg core and a low-Mg rim. Cuts through just zone 1 would produce the weakly zoned crystals.

An alternative interpretation is that some of the weakly zoned crystals simply do not contain any zones 2 and 3, and the crystals with high-Mg cores do not contain any

zone 3. In either case, the high-Mg cores and high-Mg mantles can be considered to be equivalent to zone 2 of the general scheme (Figure 7.3). It is also possible that both explanations play a role in varying the zoning pattern between orthopyroxene, as the cut effect will be superimposed upon any real variation in zoning patterns.

The weakly zoned crystals have a similar composition to both zones 1 and 3. If we assume that all orthopyroxene crystals have all three zones, then the weakly zoned crystals cannot be zone 3. There is no single cut that would expose zone 3 without also exposing zone 2 (Figure 7.3). However, we cannot assume that all crystals have a zone 2. For weakly zoned orthopyroxenes without a zone 2 hidden from view outside of the plane of the section there are two possible scenarios: either they grew the same time as zone 1, but without a pre-existing orthopyroxene at their core, or they grew at the same time as zone 3 and were kept isolated from the strongly zoned orthopyroxenes during the growth of zone 2 (and possibly zone 1 as well).

7.3.2 Trace element zoning in the Cape Riva dacite

Figures 7.4–7.7 show element maps of Mg, Fe, Ca and Al of four typical orthopyroxene crystals from the Cape Riva, demonstrating the different types of apparent zoning pattern observed. Although these images are not calibrated, and therefore cannot give quantitative information on the composition, the raw X-ray counts for each element can be compared qualitatively. Fully calibrated electron microprobe spot analysis of the different zones are plotted in Figure 7.8, and these show the range of compositions found in the different zones. In all crystals examined Al zoning was sharper than Ca, which was in turn sharper than Mg and Fe. Sketches of the different features seen in the Al maps are shown in Figure 7.9.

Different types of inclusion can also be distinguished by comparing the different element maps (labelled in Figure 7.4). Glass inclusions (as well as adhering glass) have higher Al, similar Ca and lower Mg and Fe, than the orthopyroxene crystals themselves. Fe-Ti oxides have high Fe, moderately high Al, and low Mg and Ca. Apatite inclusions

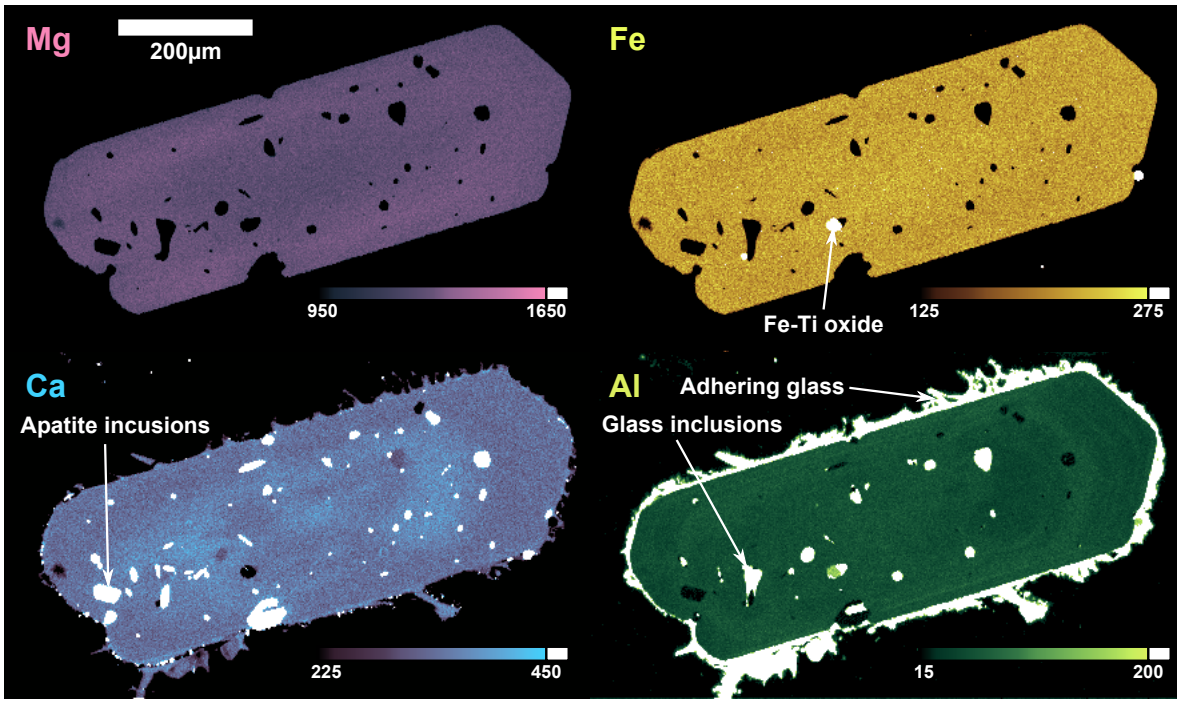

Figure 7.4: Element maps of a weakly zoned orthopyroxene from the Cape Riva eruption (S12-05 PYX26). Scale bars are the number of X-ray counts per 100 ms for each element measured on the electron microprobe.

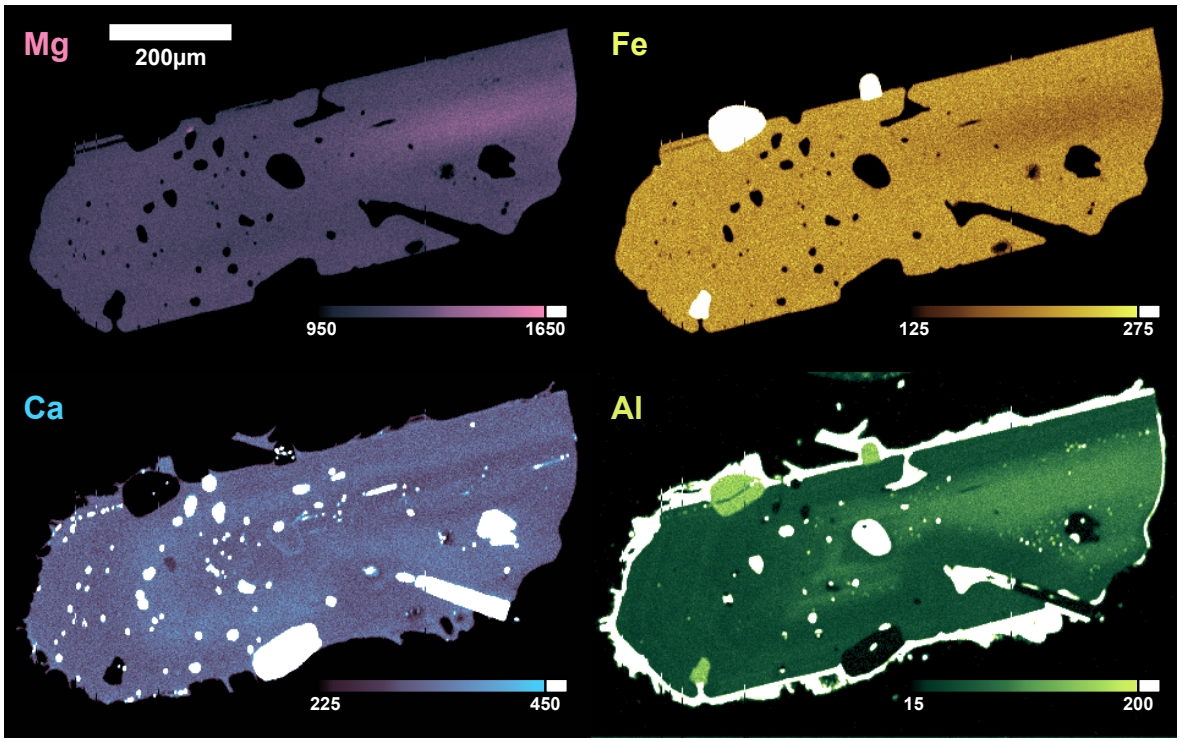

Figure 7.5: Element maps of an orthopyroxene with a Mg-rich inner zone (zone 2) from the Cape Riva eruption (S12-05 PYX12). Scale bars are the number of X-ray counts per 100 ms for each element measured on the electron microprobe.

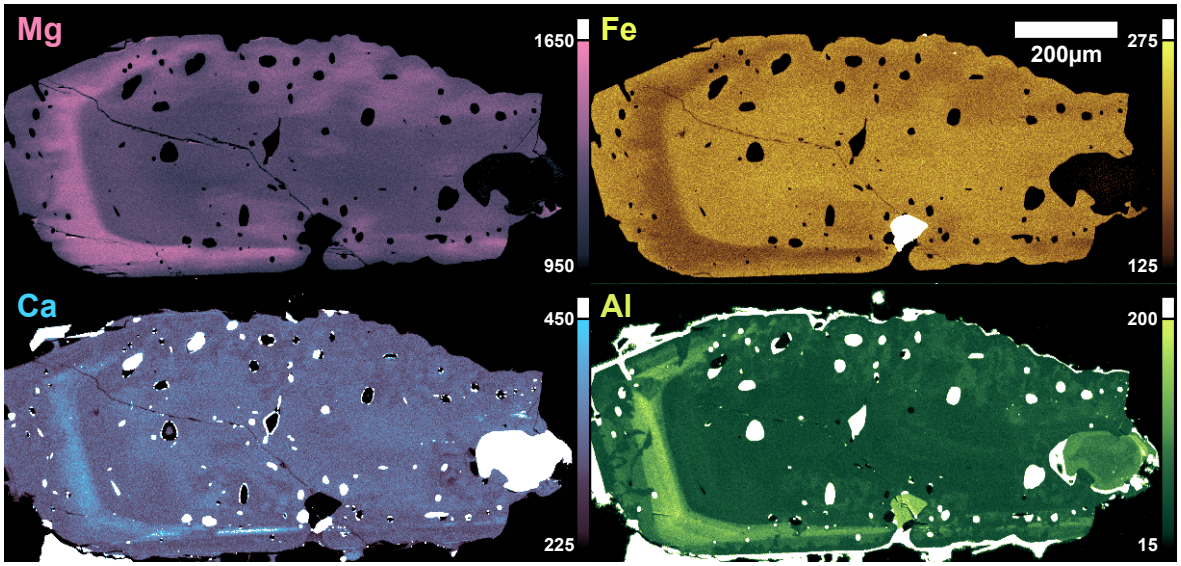

Figure 7.6: Element maps of an orthopyroxene with a Mg-rich intermediate zone (zone 2) from the Cape Riva eruption (GS11-30b PYX08). Scale bars are the number of X-ray counts per 100 ms for each element measured on the electron microprobe.

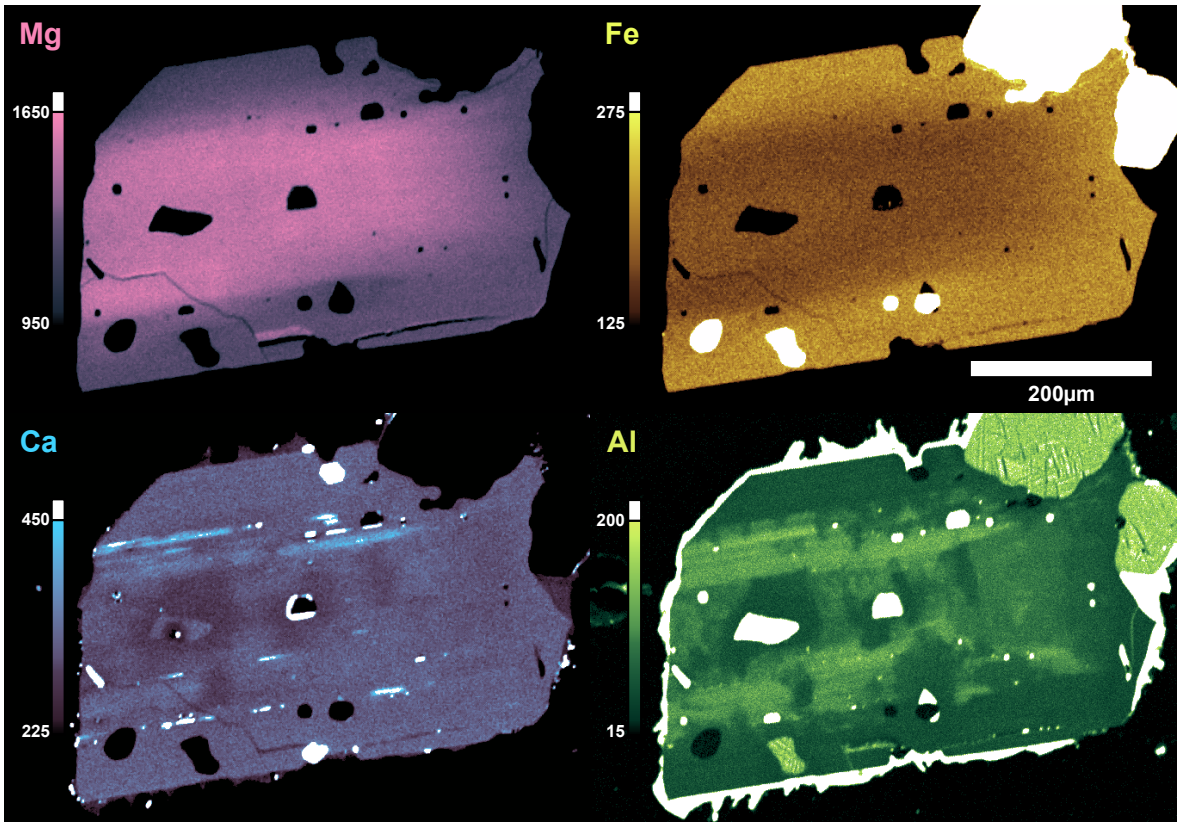

Figure 7.7: Element maps of an orthopyroxene with sector zoning or skeletal growth (S12-06 PYX17). Scale bars are the number of X-ray counts per 100 ms for each element measured on the electron microprobe.

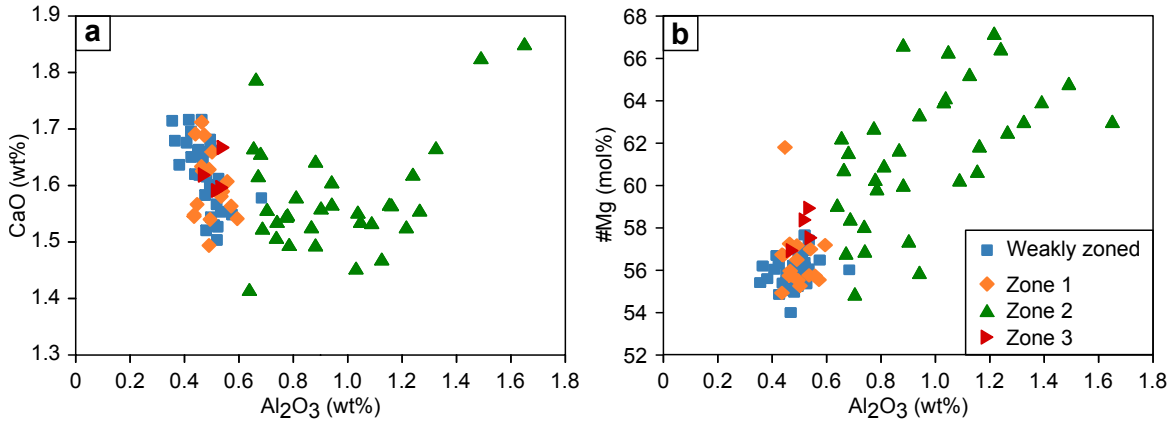

Figure 7.8: Compositions of the weakly zoned orthopyroxenes, and the different zones of the strongly zoned crystals, from electron microprobe spot analyses. The boundaries between the zones are defined using the Al maps.

have high Ca, and low Mg, Fe and Al.

The features of the different zones of the orthopyroxene crystals are as follows:

Weakly zoned crystals: In all of the six orthopyroxene crystals with weak Mg–Fe zonation that were imaged, there is only slight variations in Al and Ca. Al often show weak oscillatory growth zonation (Figures 7.4 and 7.9a). There are broad correlations between all four elements, with higher Al generally corresponding to higher Fe, and lower Mg and Ca (Figure 7.8). Electron microprobe point analyses on weakly zoned crystals show between 0.36 and 0.68 wt% Al_2O_3 and between 1.50 and 1.72 wt% CaO.

Figure 7.9 ***(facing page)*:** Sketches of the Al zoning patterns in typical Cape Riva orthopyroxenes, alongside EMP Al maps. (a) A weakly zoned crystal (S12-05 PYX26) (b) a crystal with a partially resorbed high-Al core (S12-05 PYX12) (c) a crystal with sector zoning or skeletal growth (S12-06 PYX17) (d) a crystal with a high-Al mantle (GS11-30b PYX07).

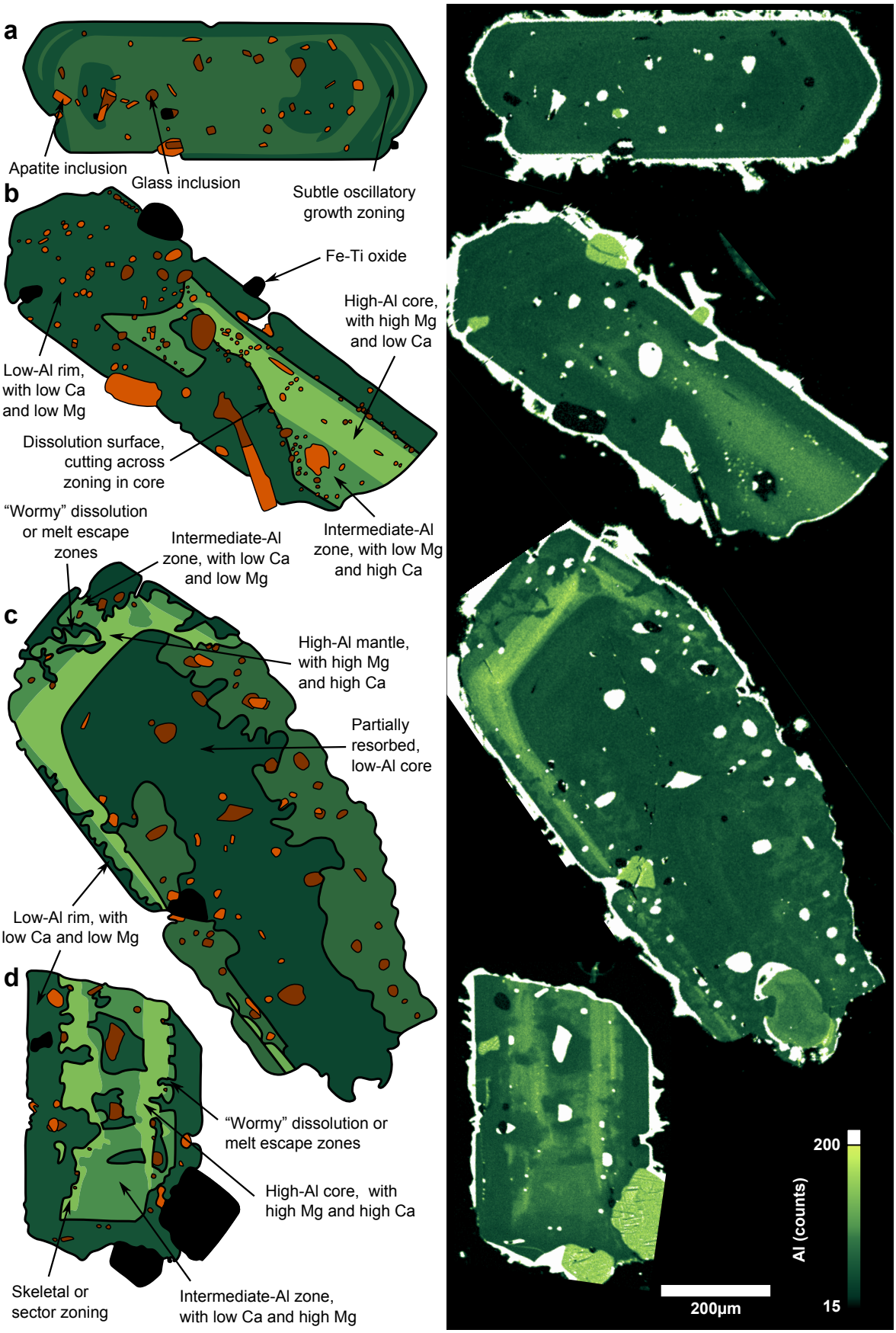
a
Apatite inclusion
Glass inclusion
Subtle oscillatory growth zoning
b
Fe-Ti oxide
High-Al core, with high Mg and low Ca
Low-Al rim, with low Ca and low Mg
Dissolution surface, cutting across zoning in core
"Wormy" dissolution or melt escape zones
Intermediate-Al zone, with low Ca and low Mg
Intermediate-Al zone, with low Mg and high Ca
c
High-Al mantle, with high Mg and high Ca
Partially resorbed, low-Al core
Low-Al rim, with low Ca and low Mg
d
"Wormy" dissolution or melt escape zones
High-Al core, with high Mg and high Ca
Skeletal or sector zoning
Intermediate-Al zone, with low Ca and high Mg
200
Al (counts)
15
200µm

Zone 1: Examples of strongly zoned orthopyroxenes are shown in Figures 7.5–7.7. Their outer, low-Mg zone (zone 1) also has low Al. Electron microprobe spot analyses record similar compositions to the weakly zoned crystals, with 0.44–0.69 wt% Al_2O_3 and 1.49–1.71 wt% CaO (Figure 7.8a).

Zone 2: The high-Mg inner and intermediate zones (zone 2) also have high Al (up to 1.26–1.65 wt% Al_2O_3, depending on the crystal). While there is sometimes correlation between the areas of high Al with areas of high Ca (e.g. Figure 7.5), in general Ca contents in zone 2 are decoupled from the concentrations of the other elements. Ca contents in zone 2 have a larger range than zone 1 (1.42–1.85 wt% CaO; Figure 7.8a). There is often more fine scale zoning visible in the Al maps, with zone 2 regularly split into an are of high Al and an area of intermediate Al (Figure 7.9b-d). A few crystals show repeated oscillation between intermediate and high Al contents within zone 2. The boundaries between zones 1 and 2 are sharp on Al maps, and often cut across the internal zoning in zone 2. There are often "wormy" structures, filled in with zone 1 orthopyroxene (Figure 7.9c,d). These are probably melt escape structures, as they often have glass inclusions trapped at their inner end. Alternatively, they may be due to partial dissolution of zone 2 before the growth of zone 1. One crystal (S12-06 PYX17; Figures 7.7 and 7.9d) shows evidence of skeletal growth or sector zoning during the growth of zone 2 preserved in the Al zoning patterns.

Zone 3: These zones have similar compositions to both zone 1 and the weakly zoned orthopyroxene crystals. It has between 0.47 and 0.54 wt% Al_2O_3 and between 1.59 and 1.67 wt% CaO (Figure 7.8a). The boundaries between zones 3 and 2 are sharp on maps of Al, and sometimes show signs of dissolution (Figure 7.9c).

7.4 Using fast and slow diffusing elements to elucidate magmatic processes

As previously discussed for plagioclase in Chapter 6, slow-diffusing elements can be used to reveal the crystals' histories, while fast-diffusing elements can be modelled to get timescales. The influence of diffusion on zoning patterns can be estimated using a back-of-the-envelope calculation for a characteristic length scale of diffusion, x:

$$x \approx \sqrt{Dt} \tag{7.1}$$

where D is the diffusion coefficient and t is the timescale that we are interested in. The variation of characteristic distance with time for the elements discussed here at 880 °C and at the FMQ buffer is shown in Figure 7.10, along with the timescales and distances of interest to this study.

The orthopyroxenes typically reach about 500 µm in length, so any element with a characteristic distance longer than this will have mostly re-equilibrated at the scale of whole crystals. These elements will not, therefore, record original growth compositions, and they will only provide information on minimum crystal residence times. On the other hand, elements with characteristic distances smaller than the size of the electron microprobe beam (1 µm) will remain close to their initial concentration. These slow-diffusing elements will be able to provide only maximum crystal high-temperature residence times. However, because their concentrations remain relatively unmodified even over extended periods, they can also be used to study the histories of the crystals. In between these two limits are the elements that will have partially re-equilibrated—these are the elements that can be modelled to estimate crystal high-temperature residence times.

For the Therasia–Cape Riva series, we are chiefly interested in processes that occur on timescales shorter than the ∼18 ky of dacitic eruption (the time between the

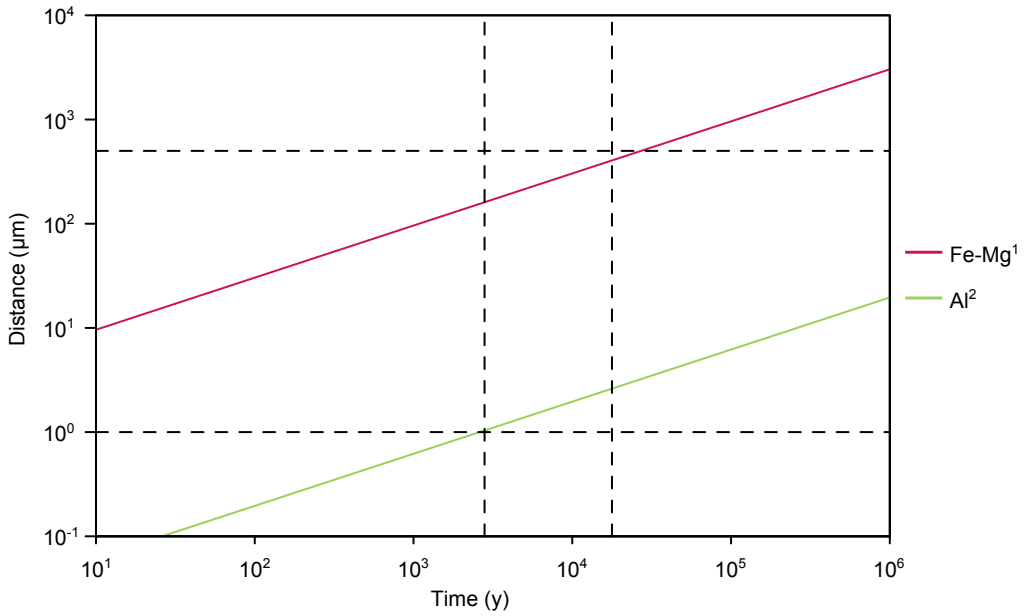

Figure 7.10: Characteristic diffusion distance against time, calculated using Equation 7.1 at 880 °C. The upper and lower horizontal dashed lines represent the typical orthopyroxene size (500 µm) and the size of the electron microprobe beam (1 µm), respectively. The left and right vertical dashed lines are the time between the youngest dated Therasia lava and the onset of the Cape Riva eruption (2,800 y), and the time between the first dacitic eruption of the Therasia dome complex and the onset of the Cape Riva eruption (18,000 y), respectively. References: 1: Nakagawa et al. (2005); 2: Ganguly and Tazzoli (1994), in orthopyroxene with a #Mg of 60 mol%, at the FMQ oxygen buffer.

oldest Therasia dacite and the Cape Riva eruption; Chapter 4). Elements that remain immobile over this length of time have been used in Section 7.5 to reconstruct crystal histories from orthopyroxene compositions. We are also particularly interested in the processes that occurred between the end of the construction of the Therasia dome complex and the onset of the Cape Riva eruption (2,800 ± 1,400 y; Chapter 4). The diffusion of elements that are expected to partially re-equilibrate over this period have been modelled in Section 7.6 in order to estimate crystal high-temperature residence times.

The diffusion coefficients of Al Fe–Mg have been discussed in detail in Chapter 3. Aluminium has a characteristic distance of ∼3 µm over 18 ky, and can be considered immobile here (Nakagawa et al., 2005; Smith and Barron, 1991). This is confirmed by the sharpness of the zoning patterns in the Al maps presented here (Figures 7.4–7.7).

Al contents should therefore be close to original, and the Al zoning can be used to reconstruct the crystals' growth histories (Section 7.5).

The Ca zoning patterns are not as sharp as the Al zoning patterns, but they are not as diffuse as the zoning patterns of Fe–Mg (Figure 7.2). It therefore appears the the diffusion coefficient of Ca is intermediate between that of Al and that of Fe–Mg, although there is no available experimental data to estimate the diffusion coefficient quantitatively. A diffusion coefficient between that of Al and that of Fe-Mg would agree with data for clinopyroxene (Cherniak and Dimanov, 2010).

Fe–Mg are the fastest diffusing elements considered in this chapter, and most orthopyroxene crystals will have completely re-equilibrated their Fe-Mg over 18 ky (Figure 7.10). The characteristic distance is ∼160 µm over the ∼2,800 y between the last Therasia eruption and the Cape Riva eruption, and this drops to 30 µm over 100 y. This means Fe–Mg diffusion should be useful to constrain the timescales of the magmatic processes that took place between the last Therasia eruption and the Cape Riva eruption, and it is modelled in Section 7.6.

7.5 Estimating melt compositions from orthopyroxene compositions

Despite the low diffusivity of Al and Ca in orthopyroxene, it is difficult to use their concentrations in the crystals to estimate melt compositions the same ways as Sr and Ti in plagioclase were used in Chapter 6. Whole-rock Al contents vary little at Santorini (Chapter 2), and the partitioning of Al between the melt and orthopyroxenes is complicated by the fact that Al can occupy either the tetrahedral or the metal ion sites (Bédard, 2007). Ca is not strictly a trace element, and experimental data for both Al and Ca shows that there is no simple relationship between their concentration in orthopyroxene and melt composition or other parameters (Bédard, 2007). This is true even when we look at the compositions of experimental orthopyroxenes from only

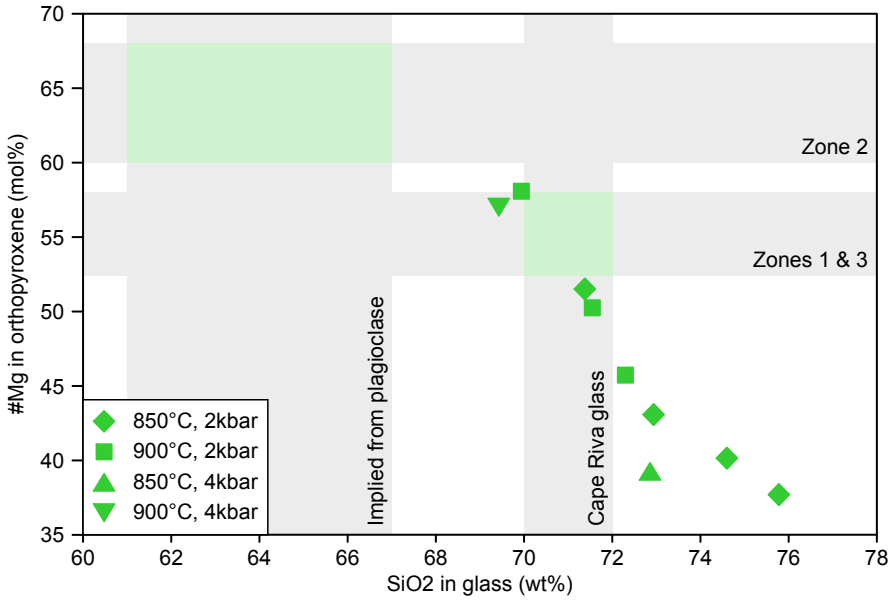

Figure 7.11: #Mg of orthopyroxenes plotted against the SiO_2 contents coexisting glasses produced in the experiments of Cadoux et al. (2014) using the Cape Riva dacite as a starting material. The horizontal grey bands represent the compositions of the natural orthopyroxenes from the Cape Riva (this chapter). The vertical grey bands are the compositions of the glass from the Cape Riva dacite (Chapter 5) and the melt compositions calculated from the trace element contents of the calcic parts of the sawtooth-zoned plagioclases (Chapter 6).

Cape Riva whole-rock compositions (Cadoux et al., 2014).

The low diffusivity of Al and Ca in orthopyroxene does mean that we can assume that the Al and Ca contents are primary, although they may have been affected by fast growth. The relationship between #Mg and Al content in the zoned crystals can therefore be used to interpret the lack of Fe-Mg zoning in the weakly zoned crystals. The high-Mg zone 2 also has high Al (Figure 7.8b), and if the weakly zoned crystals originally had a high-Mg zone 2 that was erased by diffusion, then we would expect them to still have a high-Al zone. Figures 7.4 and 7.8 show that this is not the case, the weakly zoned crystals have the same Al (and Ca) contents as the low-Mg zones 1 and 3 of the strongly zoned crystals. It seems unlikely, therefore, that the weakly zoned crystals were ever strongly zoned in Fe–Mg.

The #Mg of orthopyroxene is more useful than Al and Ca as an indicator of melt composition. Figure 7.11 shows how the #Mg of the orthopyroxenes produced in the phase-equilibrium experiments of Cadoux et al. (2014) varied with the SiO_2 content

of the coexisting glass during their runs using the Cape Riva dacite as the starting material. The orthopyroxenes range from a #Mg of 38 mol% at 76 wt% SiO_2 to 58 mol% at 69 wt% SiO_2. This is consistent with the weakly zoned crystals, zone 1 and zone 3 growing from the melt with the composition of the the Cape Riva glass (70–72 wt% SiO_2; Chapter 5), while zone 2 grew from a more mafic melt.

The growth histories of the orthopyroxene crystals can be compared to those of the plagioclase crystals, documented in Chapter 6. The trace element concentrations of the plagioclases implied that they had cycled between a melt similar in composition to the Cape Riva glass and another, more mafic melt, with between 61 and 67 wt% SiO_2. Although the data of Cadoux et al. do not extend back that far, the trend is consistent with the zone 2 orthopyroxene growing from the same 61–67 wt% SiO_2 melt.

7.6 Estimating timescales with diffusion chronometry

7.6.1 Method

As discussed in Chapter 3, Fe–Mg diffusion in orthopyroxene varies with orthopyroxene composition and oxygen fugacity as well as temperature (Ganguly and Tazzoli, 1994; Klügel, 2001). The equation for the diffusion coefficient, $D_{\text{Fe–Mg}}$, used for the models presented here is the same as that used by Allan et al. (2013):

$$D^{\text{opx}}_{\text{Fe–Mg}} = \exp\left(-6.77 - 5.99X_{\text{Mg}} - \frac{240,000}{RT}\right) \times \left(\frac{f\text{O}_2\,(\text{sample})}{f\text{O}_2\,(\text{IW buffer})}\right)^{\frac{1}{6}} \tag{7.2}$$

where X_{Mg} is the molar Mg fraction (Mg/[Mg + Fe]); R is the molar gas constant; and T is the temperature in Kelvin. Fe–Ti oxides from the Cape Riva dacite and two of the three Therasia pumice fall deposits analysed plot along the fayalite–magnetite–quartz (FMQ) oxygen buffer (Chapter 5), which is about four log units higher than the iron–würstite (IW) buffer used in the calibration of the equation above (Frost, 1991). The

diffusion coefficient is strongly dependent on the temperature, which for the Cape Riva dacite and two of the three analysed Therasia dacites is about $880 \pm 25\,^{\circ}\mathrm{C}$ (Figure 5.5). The models were therefore run at $880\,^{\circ}\mathrm{C}$, and at the FMQ oxygen buffer. The effect of using different temperatures and oxygen fugacities is discussed later, in Section 7.6.

The zone boundaries were assumed to initially be sharp, and modelled as a step function. The initial #Mg on either side of the boundary was estimated by taking the values of #Mg at a distance away from the boundary where they appeared to be unmodified by diffusion. The weakly zoned orthopyroxene crystals do not have obvious zone boundaries, however many of them do have small variations in the #Mg. These variations often have the curved profiles that are typical of diffusion. These profiles were modelled assuming they were initially a step function, to give the maximum times that the observed #Mg variations could survive at high temperature.

Because the variation in #Mg in each individual profile was always small ($<10\,\%$), the dependence of the Mg–Fe diffusion coefficient on #Mg within a single profile was ignored. This meant that the diffusion profiles could be fit by a simple analytical solution to the diffusion equation (Chapter 3):

$$X_{\mathrm{Mg}}(x,t) = X_{\mathrm{Mg}}^{\mathrm{left}} + \frac{X_{\mathrm{Mg}}^{\mathrm{left}} + X_{\mathrm{Mg}}^{\mathrm{right}}}{2}\left[1 + \mathrm{erf}\left(\frac{x}{\sqrt{tD}}\right)\right] \tag{7.3}$$

where $X_{\mathrm{Mg}}^{\mathrm{left}}$ and $X_{\mathrm{Mg}}^{\mathrm{right}}$ are the initial molar Mg fraction to the left and the right of the step function, respectively; x is the distance, centred on the initial step function; t is the time; and $\mathrm{erf}(u)$ is the error function, shown below:

$$\mathrm{erf}(u) = \frac{2}{\sqrt{\pi}}\int_0^u e^{-k^2}\mathrm{d}k \tag{7.4}$$

The diffusion coefficient was calculated using an X_{Mg} half way between $X_{\mathrm{Mg}}^{\mathrm{left}}$ and $X_{\mathrm{Mg}}^{\mathrm{right}}$.

Implicit in Equation 7.3 is the assumption that diffusion occurs in an infinitely long solid. This assumption is valid as long as the profiles are long compared to the length affected by diffusion (approximated by $\sqrt{tD}$ in Equation 7.3 above).

First, low resolution BSE images were taken with short acquisition times (∼60–90 s). Although these were noisy, they could be used to pick promising crystals for diffusion modelling. High-resolution images were then made across the zone boundaries, with acquisition times of ∼30 minutes. High-resolution images of selected weakly zoned crystals were also taken. Profiles perpendicular to zone boundaries were then plotted using the ImageJ software (Rasband, 2012). The profiles were made up of averages across a strip 20–50 pixels wide. The profiles were then fit by eye in a spreadsheet (LibreOffice Calc), allowing t, the diffusion time, to be extracted from Equation 7.3.

7.6.2 Results

The results of models of Mg–Fe diffusion in orthopyroxene crystals from the Therasia dacites are presented in Figures 7.12–7.14, and the results for crystals from the Cape Riva are shown in Figures 7.15–7.19. Low resolution BSE images with the location of the boundaries modelled are presented in Appendix F.

Most of the Mg–Fe profiles zone boundaries can be modelled as initial step functions that have broadened by diffusion. However, there is evidence that not all the gradients are entirely due to diffusion. There are sometimes large differences in the times calculated for different profiles in the same crystal. Profile 3 of S12-06 PYX17 (Figure 7.20c), for example, gives a high-temperature residence time of 450 y, while the other two profiles (Figure 7.20a,b) give diffusion times of only 11–33 y. The zoning pattern of this crystal suggests that it was originally elongated parallel to profile 3, which implies that growth was quickest along this direction. If crystal growth continued during a change in magma composition or another parameter that effects the orthopyroxene composition, then a compositional gradient reflecting this change will be preserved in the orthopyroxene. The faster growth is (relative to the change in magma composition), the shallower the gradient. The diffusion models presented here assume that the boundary was initially a step function, and any initial gradient due to growth will increase the apparent high-temperature residence times of the crystals. The

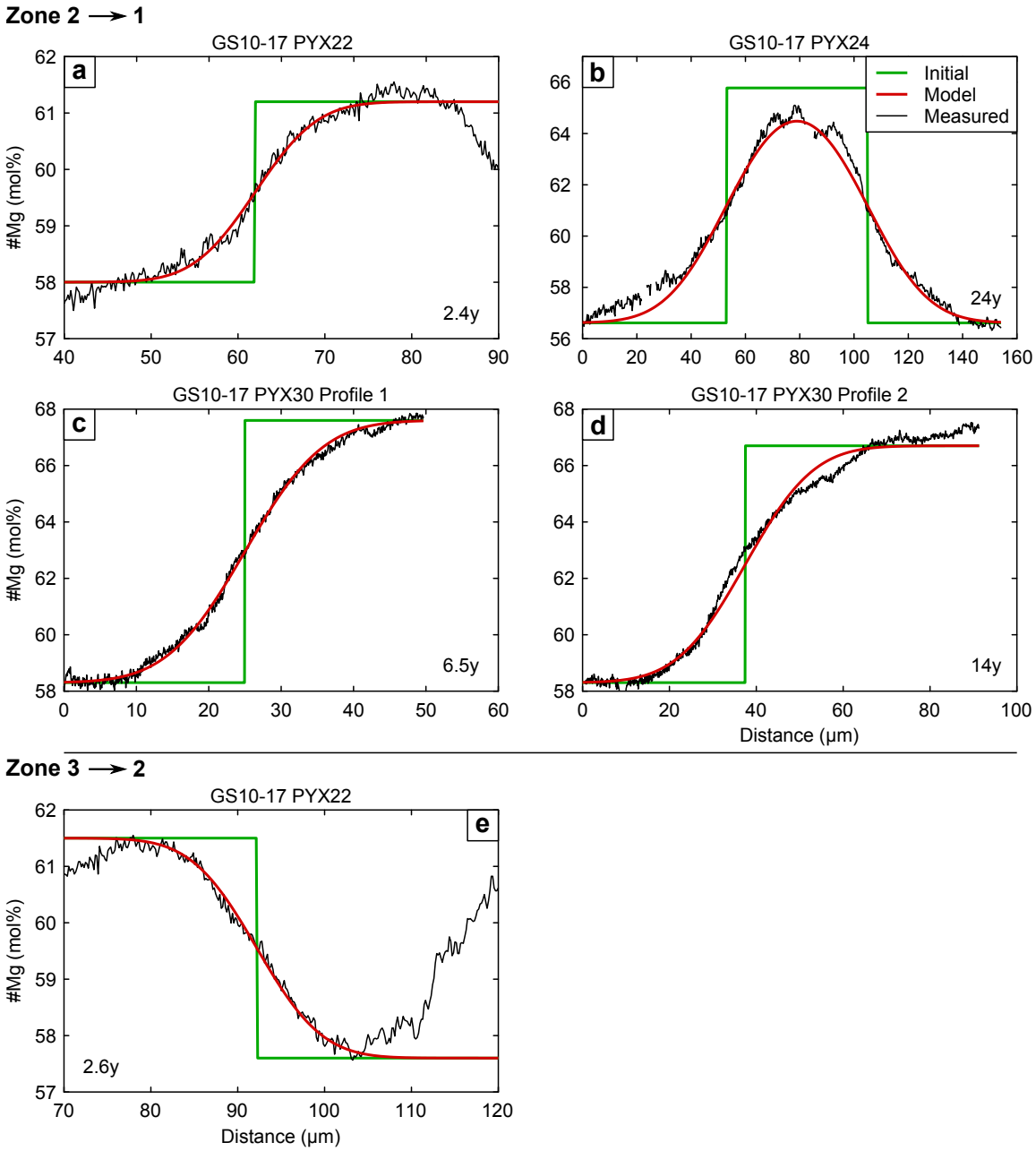

Figure 7.12: The results of models of Mg-Fe diffusion in orthopyroxenes from flow 5 of the Therasia dacites (GS10-17).

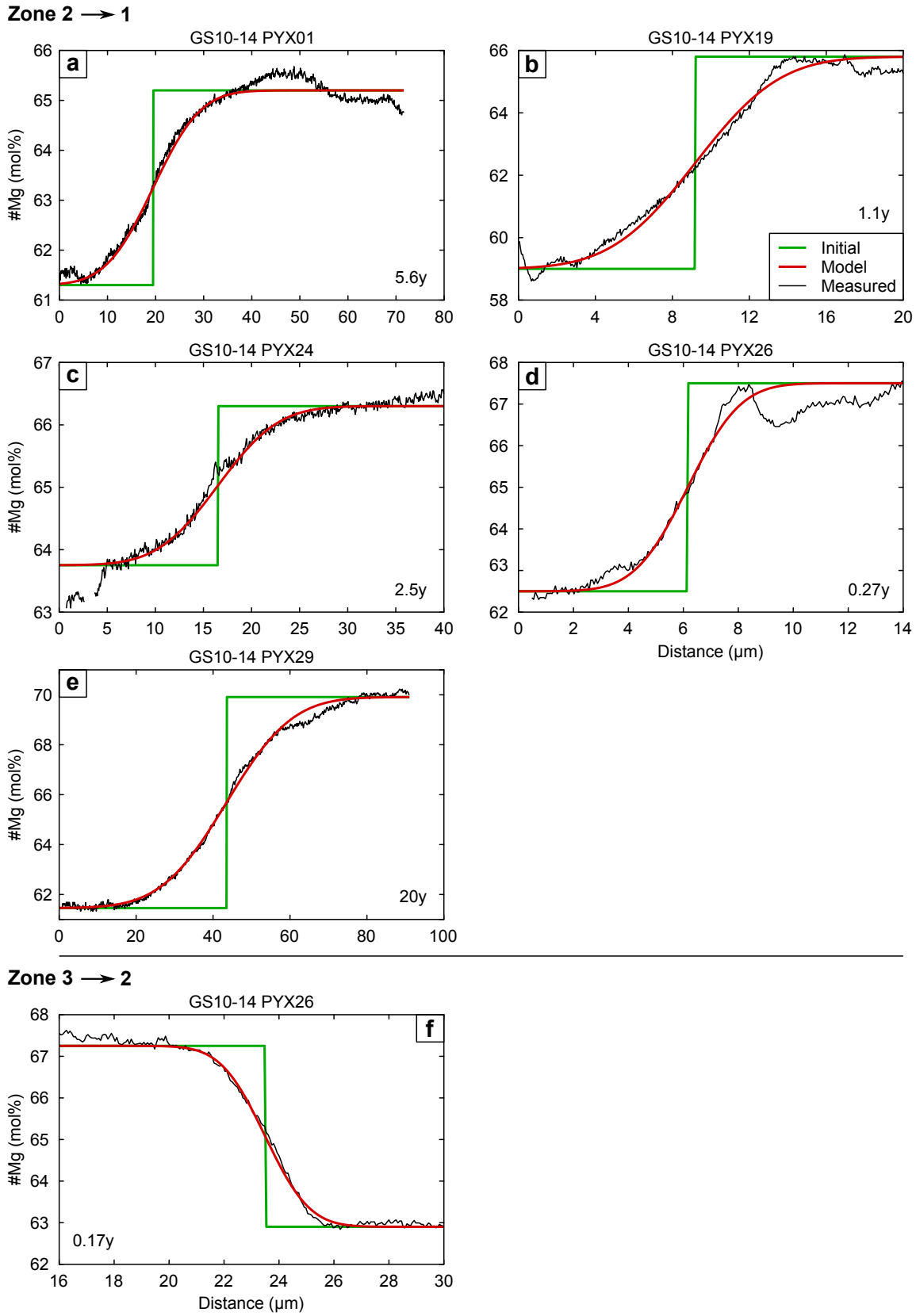

Figure 7.13: The results of models of Mg-Fe diffusion in orthopyroxenes from flow 8 of the Therasia dacites (GS10-14).

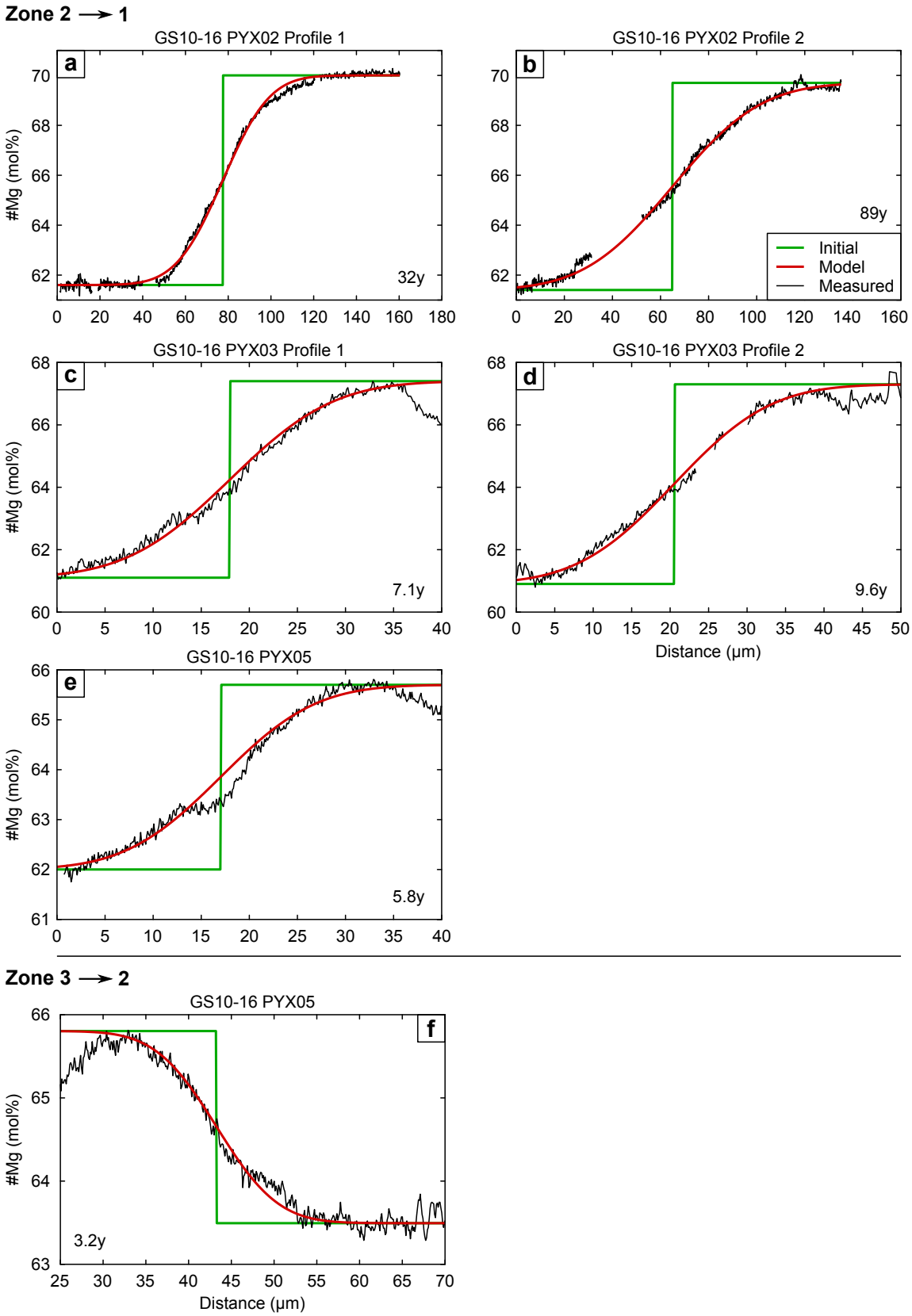

Figure 7.14: The results of models of Mg-Fe diffusion in orthopyroxenes from flow 9 of the Therasia dacites (GS10-16).

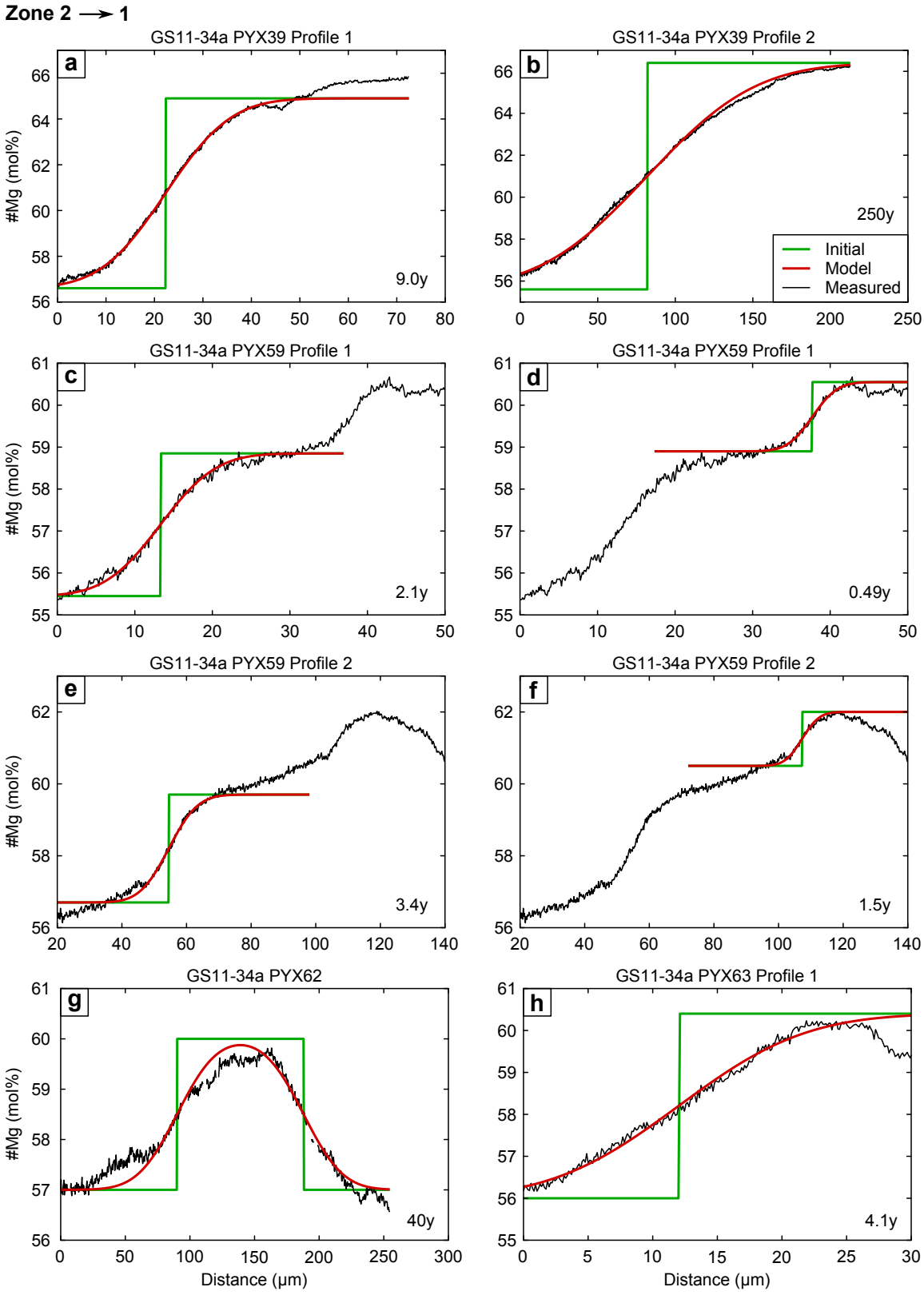

Figure 7.15: The results of models of Mg-Fe diffusion in orthopyroxenes from phase A of the Cape Riva eruption (GS11-34a).

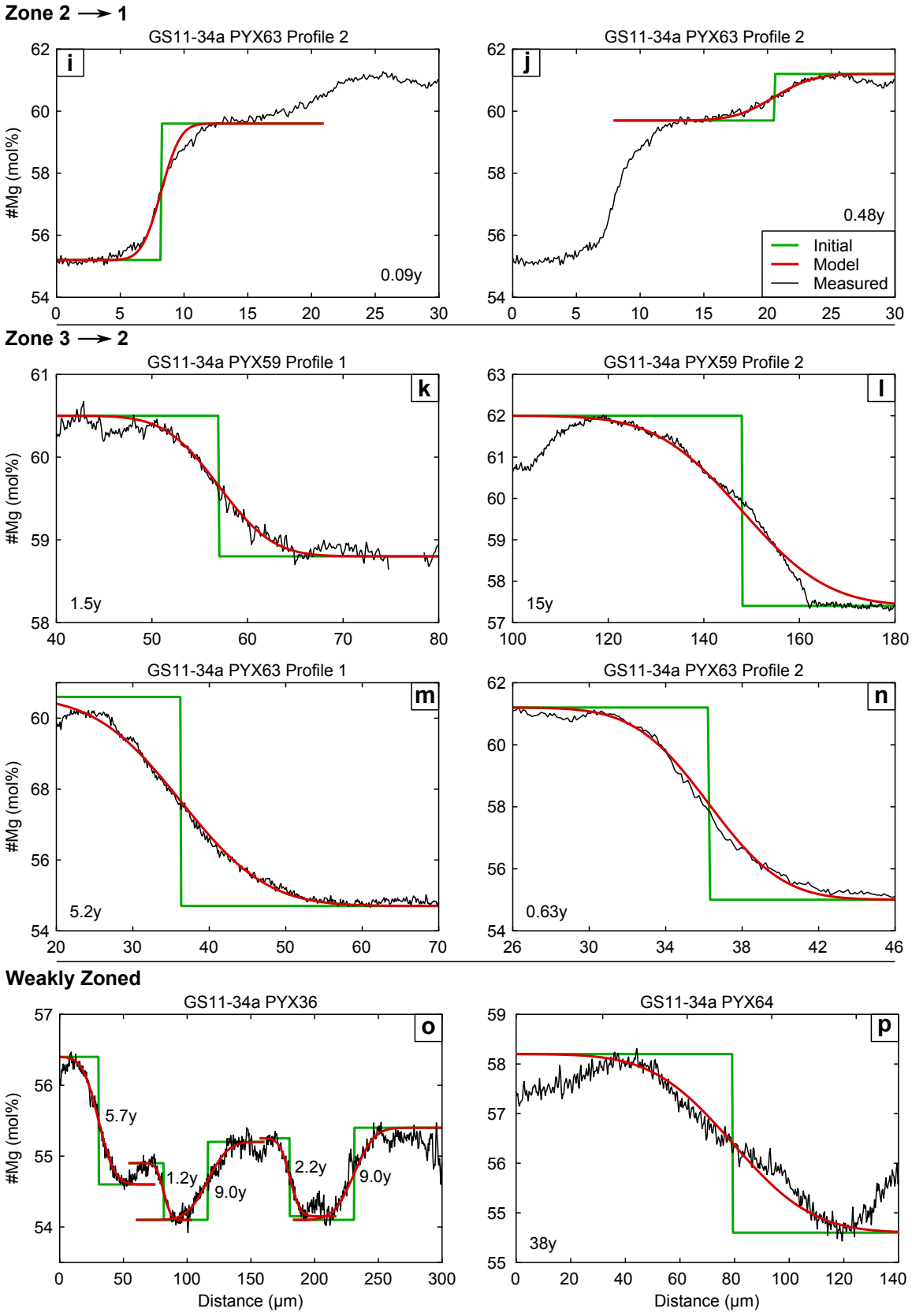

Figure 7.15 continued: The results of models of Mg-Fe diffusion in orthopyroxenes from phase A of the Cape Riva eruption (GS11-34a).

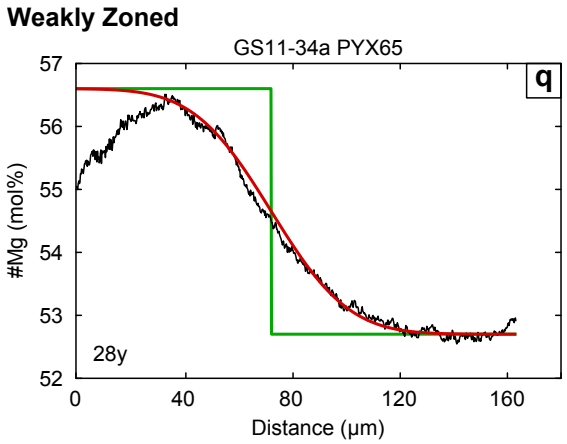

Figure 7.15 continued: The results of models of Mg-Fe diffusion in orthopyroxenes from phase A of the Cape Riva eruption (GS11-34a).

longer high-temperature residence time given by profile 3 can, therefore, be explained by faster growth in that direction.

While the diffusion coefficient for Fe–Mg diffusion in orthopyroxene is thought to be isotropic (Ganguly and Tazzoli, 1994), comparison of the Fe–Mg zoning patterns with those of Al suggest that growth is at least partially responsible for the longer apparent high-temperature residence time calculated for profile 3. The boundary between zones 2 and 1 in the Al map is sharp along profiles 1 and 2, but more diffuse along profile 3 (Figure 7.21). This is consistent with the results of Allan et al. (2013), who also found that gradients along the c axis, parallel to the direction of elongation of the orthopyroxene crystals, were best explained by a mix of growth and diffusion. Where only one profile in a crystal was modelled, it was chosen to be perpendicular to the long axis in order to minimise this effect. Where more than one profile was modelled, the shorter high-temperature residence time was used as the best estimate of the high-temperature residence time of the crystal. The sharpness of the zoning patterns in most of the Al maps of the strongly zoned crystals suggests that the effect of growth on the timescales calculated for the strongly zoned crystals is small (Section 7.3.2). This is less true for the weakly zoned crystals, as the Al and Ca often show gradual changes in their concentrations. However, correcting for the effect of growth will always reduce the high-temperature residence times. The high-temperature residence times

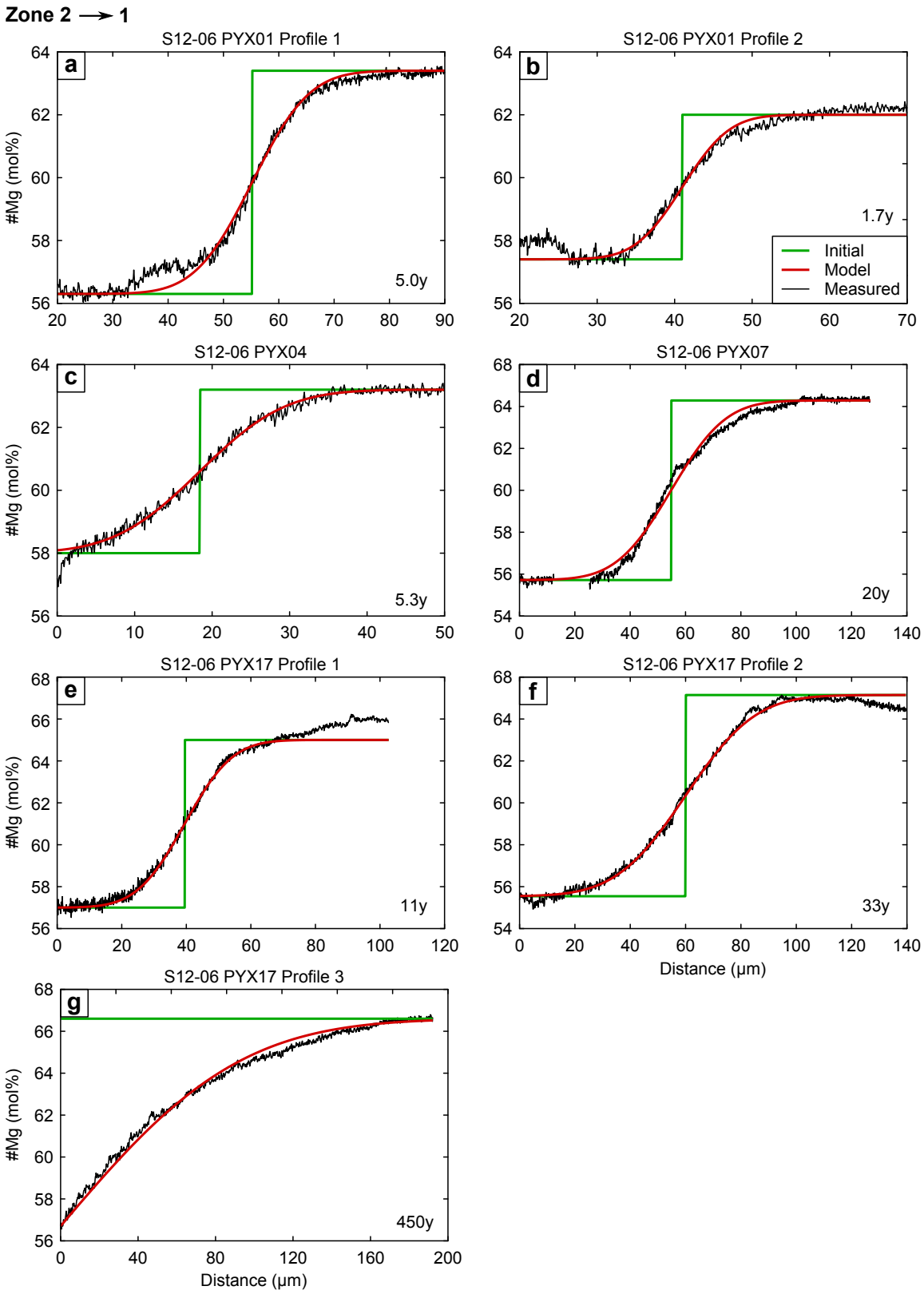

Figure 7.16: The results of models of Mg-Fe diffusion in orthopyroxenes from phase B of the Cape Riva eruption (S12-06).

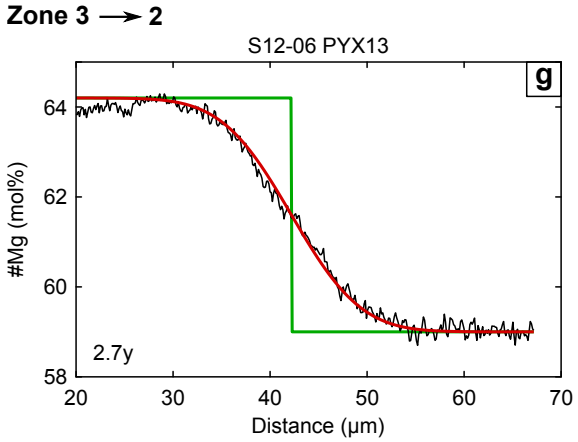

Figure 7.16 continued: The results of models of Mg-Fe diffusion in orthopyroxenes from phase B of the Cape Riva eruption (S12-06).

presented here are therefore maxima.

Another apparent contradiction in the data is that for many crystals the high-temperature residence times implied by the inner, zone 3/2 boundary is shorter than that implied by the outer, zone 2/1 boundary (e.g. GS11-30b PYX08; Figure 7.22). This cannot be explained by changes in the diffusion coefficient (through changes in the temperature or oxygen fugacity, for example) as any changes that affected the outer boundary would also affect the inner boundary. Instead, it is probable that the discrepancy can be explained by a mixture of growth and diffusion, in the same way as the different ages of the different profiles of the same boundary in S12-06 PYX17 are explained above. If orthopyroxene growth was more rapid — or the change in magma composition more gradual — during the transition from zone 2 to zone 1 than the transition from zone 3 to zone 2, then the outer boundary would initially be more diffuse than the inner boundary. This would increase the apparent high-temperature residence time of the outer boundary. Again, this shows that the high-temperature residence times presented here are maxima.

Most of the Fe–Mg zone boundaries can be fit by a single step function, however in a few crystals the boundary between zone 2 and zone 1 occurs in two steps (GS11-34a PYX59, Figure 7.15c–f; GS11-34a PYX63, Figure 7.15i,j; GS11-30b PYX08, Figure 7.17c,d; S12-05 PYX18 Figure 7.18e,f). Two steps are often seen in the Al zoning

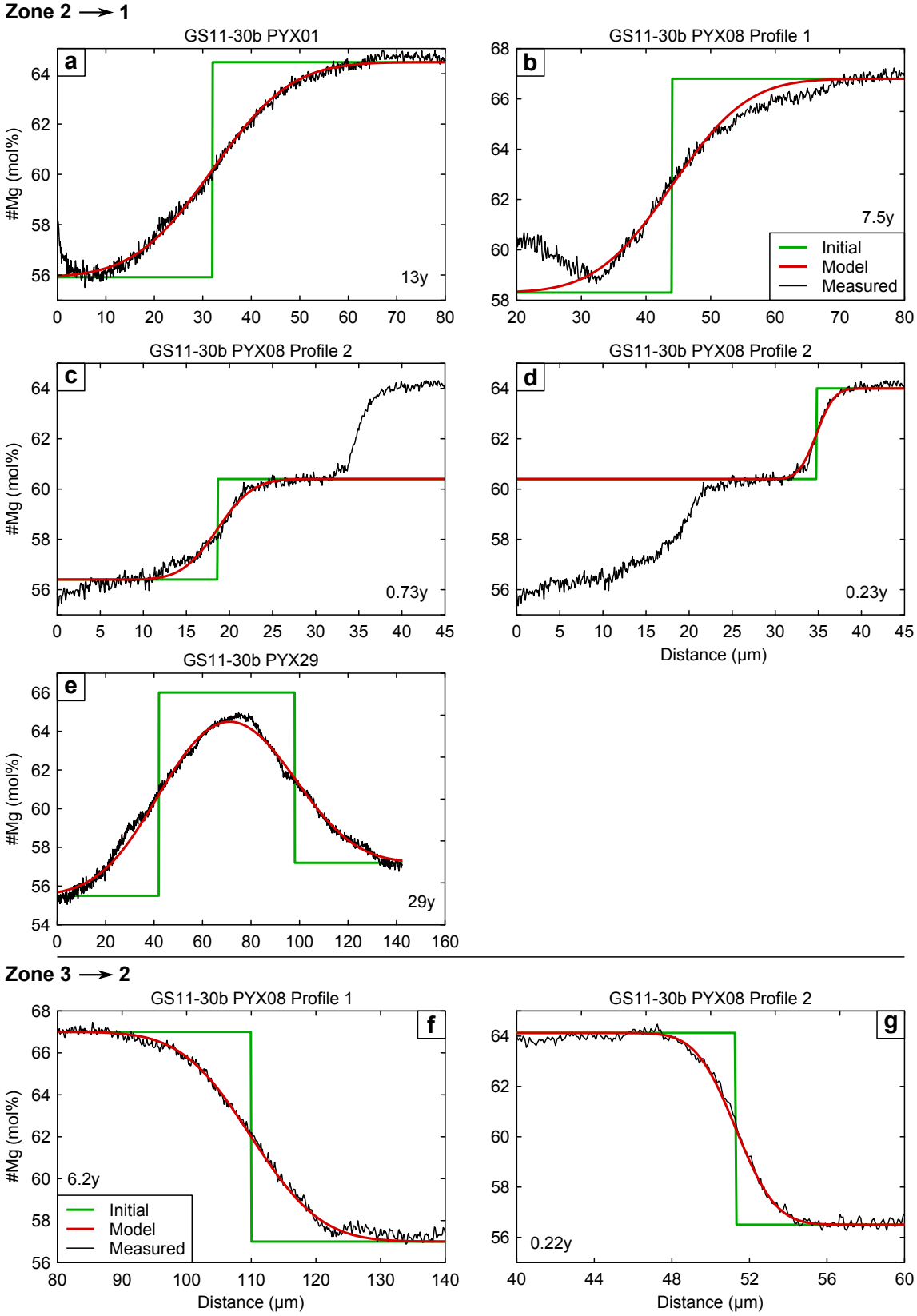

Figure 7.17: The results of models of Mg-Fe diffusion in orthopyroxenes from phase C of the Cape Riva eruption (GS11-30b).

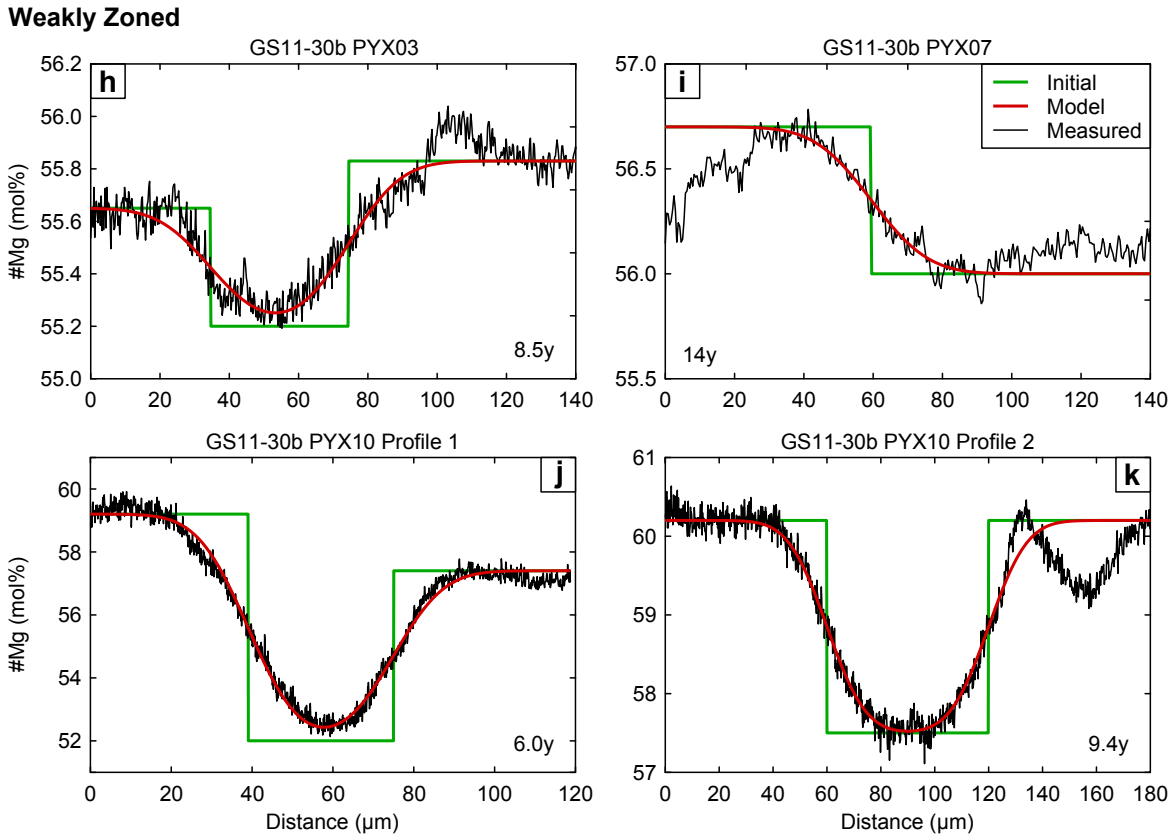

Figure 7.17 continued: The results of models of Mg-Fe diffusion in orthopyroxenes from phase C of the Cape Riva eruption (GS11-30b).

(e.g. Figure 7.9b,c), even in crystals where the zone 2 to zone 1 boundary occurs as a single step (e.g. Figure 7.5). This suggests that some of the one-step boundaries between zones 2 and 1 seen in Fe–Mg zoning initially had two steps. The two steps could have merged as they broadened by diffusion. Modelling these boundaries as a single step would give anomalously long high-temperature residence times.

7.6.3 Uncertainties

Temperature

The temperature will have an effect on all the residence times presented here. Because we are using an analytical solution to the diffusion equation (Equation 7.3), the

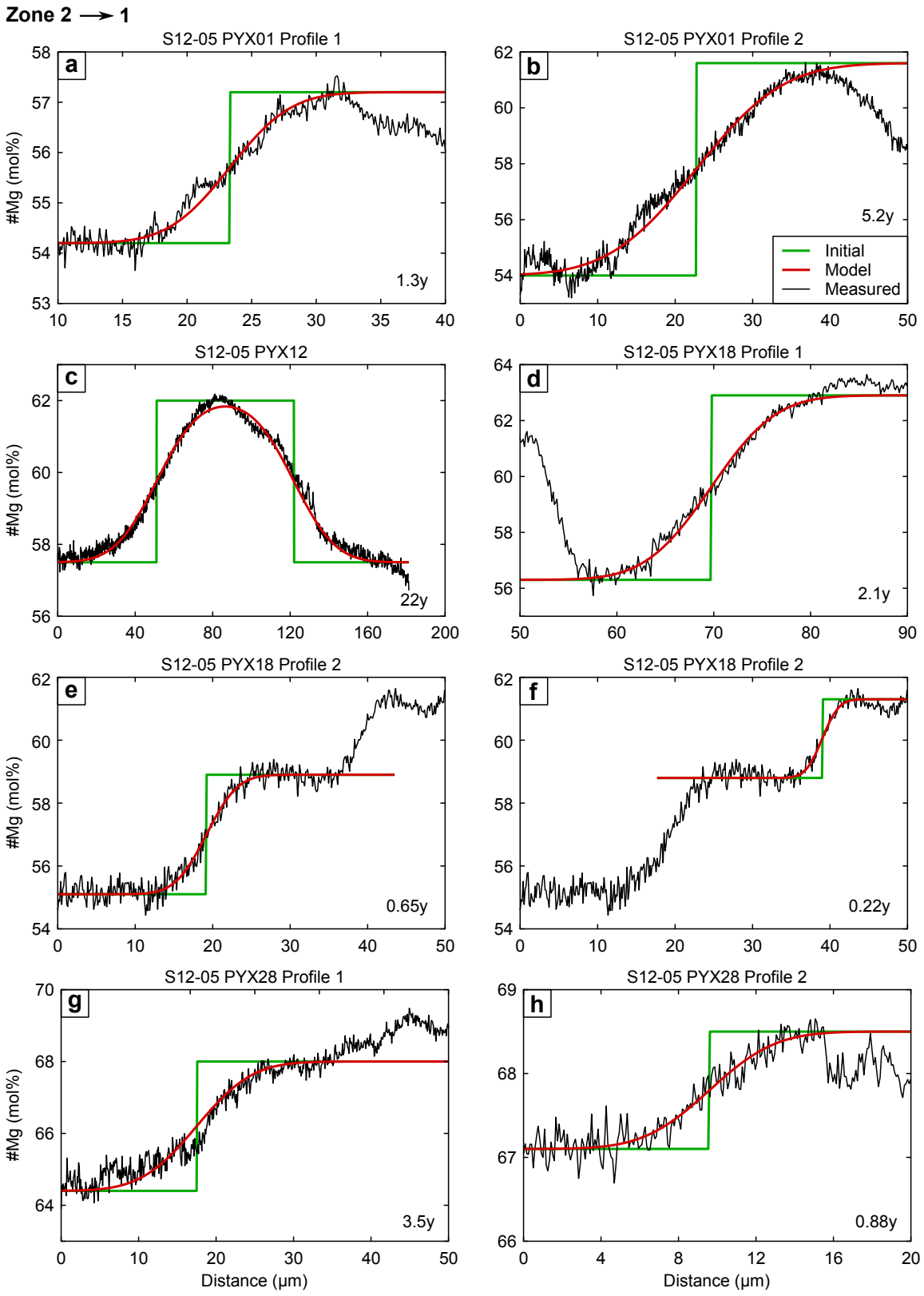

Figure 7.18: The results of models of Mg-Fe diffusion in orthopyroxenes from phase C of the Cape Riva eruption (S12-05).

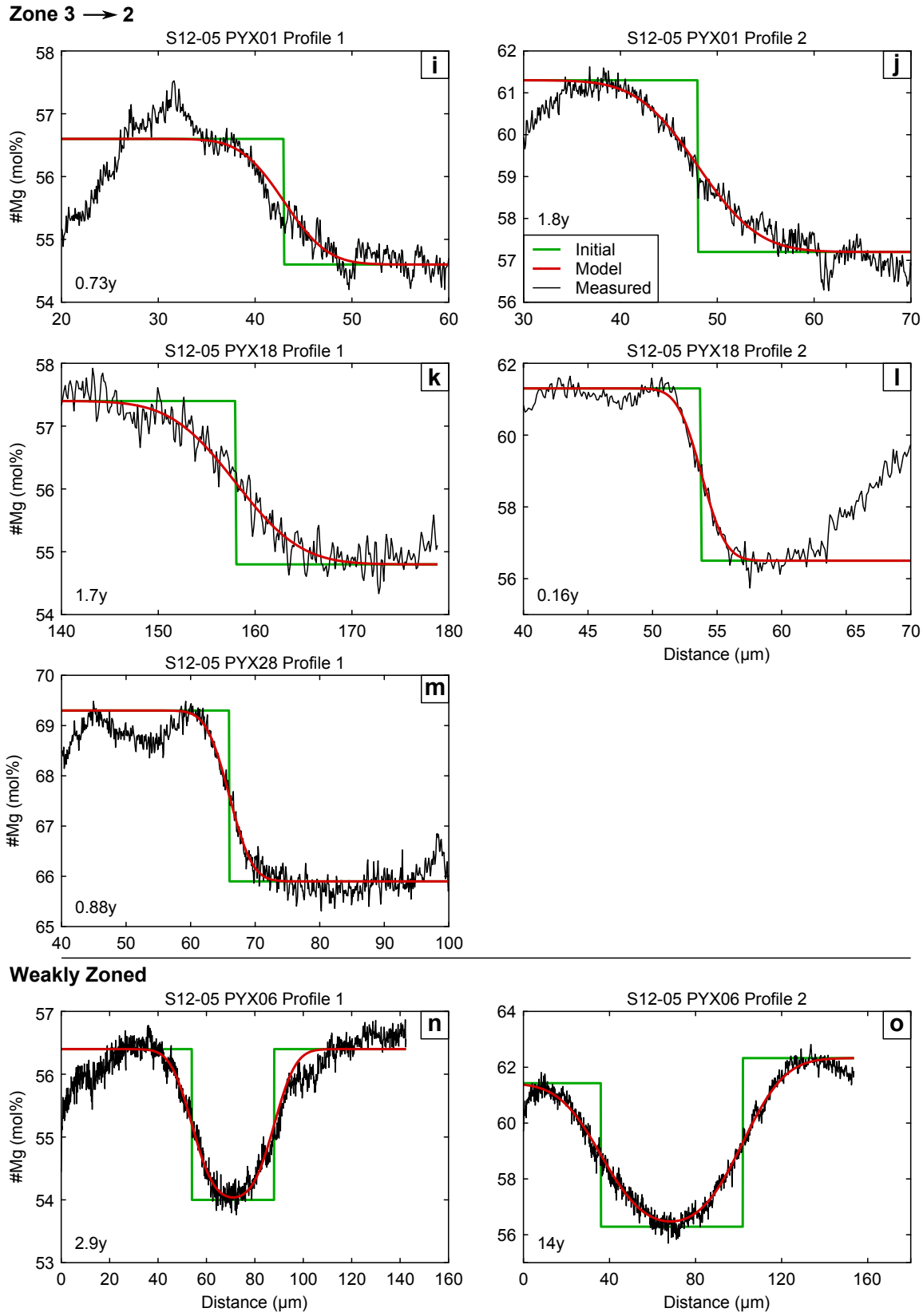

Figure 7.18 continued: The results of models of Mg-Fe diffusion in orthopyroxenes from phase C of the Cape Riva eruption (S12-05).

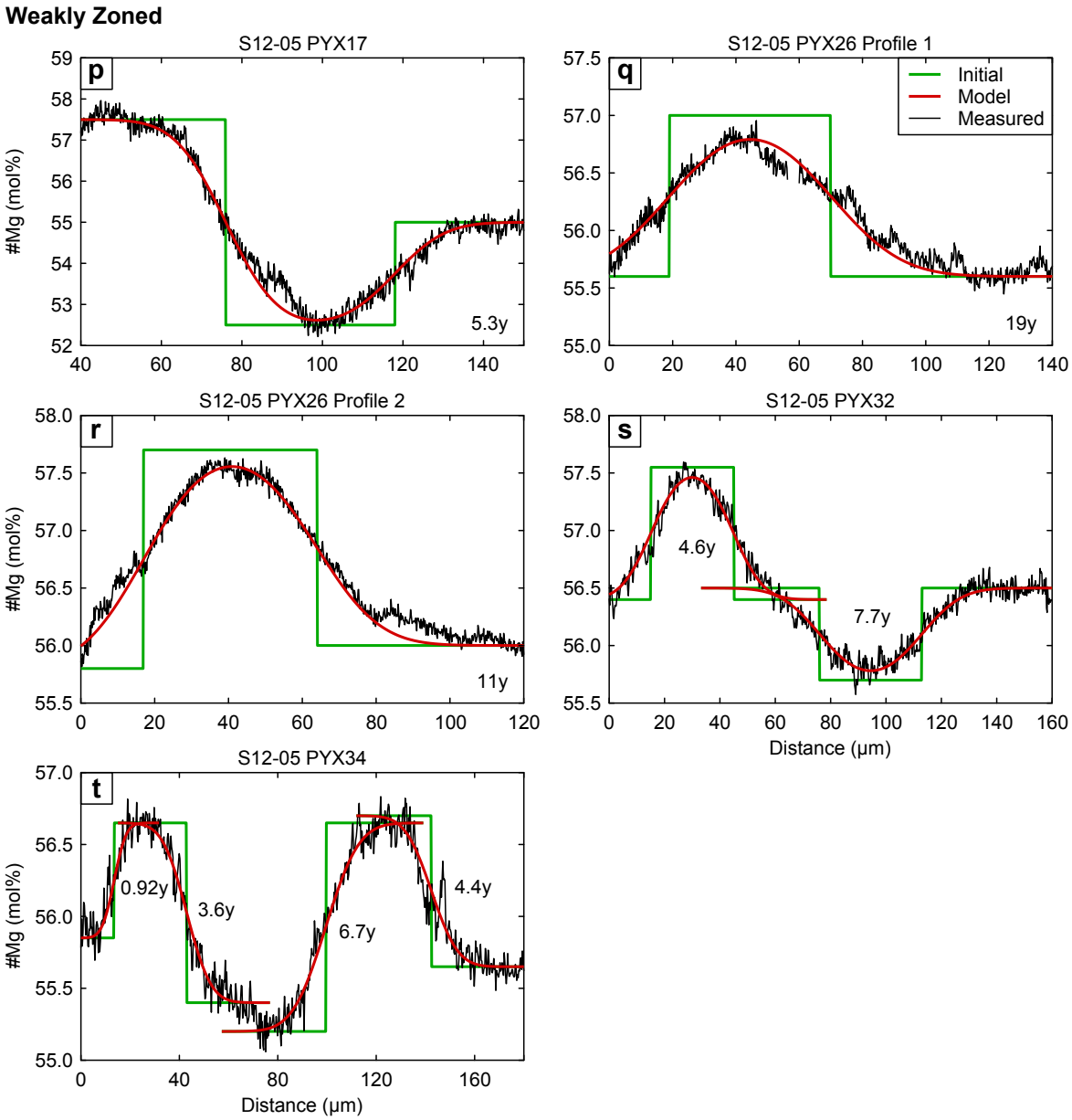

Figure 7.18 continued: The results of models of Mg-Fe diffusion in orthopyroxenes from phase C of the Cape Riva eruption (S12-05).

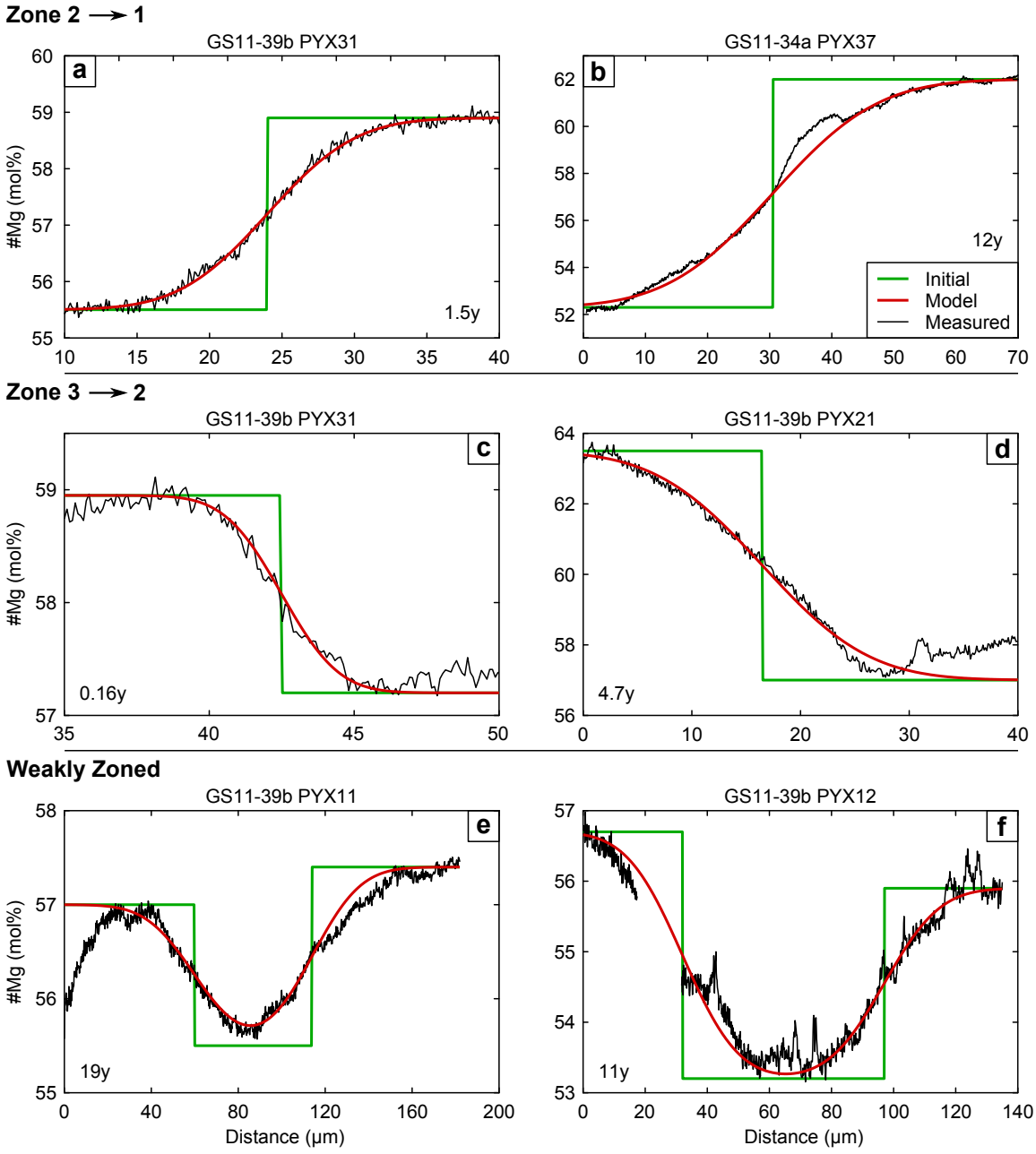

Figure 7.19: The results of models of Mg-Fe diffusion in orthopyroxenes from phase D of the Cape Riva eruption (GS11-39b).

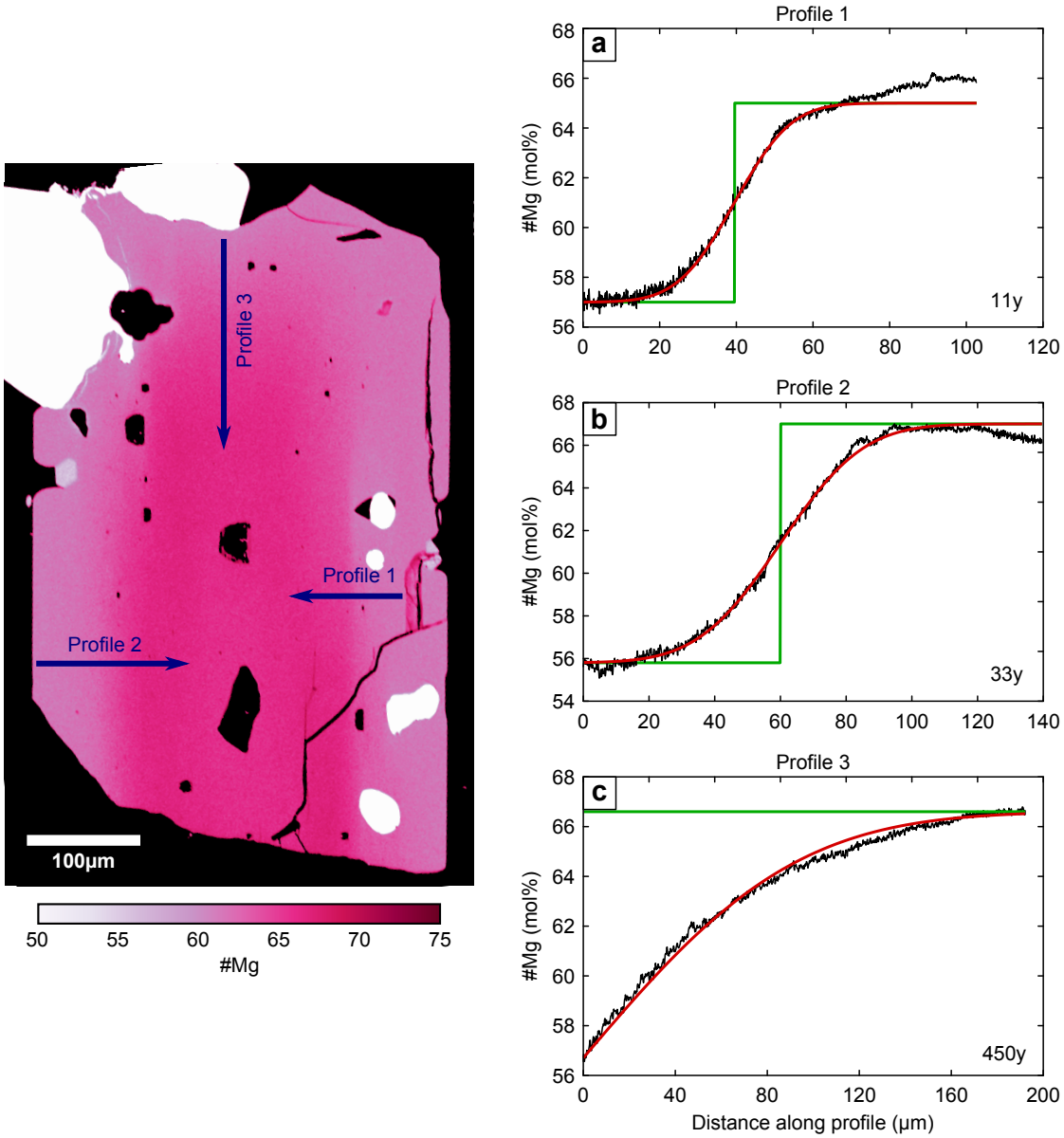

Figure 7.20: An orthopyroxene crystal from the Cape Riva dacite (S12-06 PYX17).

relationship between the residence time t and temperature T is given by:

$$t \propto \frac{1}{D} \propto \exp\left(\frac{240,000}{RT}\right) \tag{7.5}$$

where the diffusion coefficient D is given by Equation 7.2.

Pre-eruptive temperatures calculated from Fe–Ti oxides in the Cape Riva and two of the three analysed Therasia pumice fall deposits have a range of ±25 °C, centred around 880 °C (Chapter 5). The residence times quoted here are calculated at 880 °C;

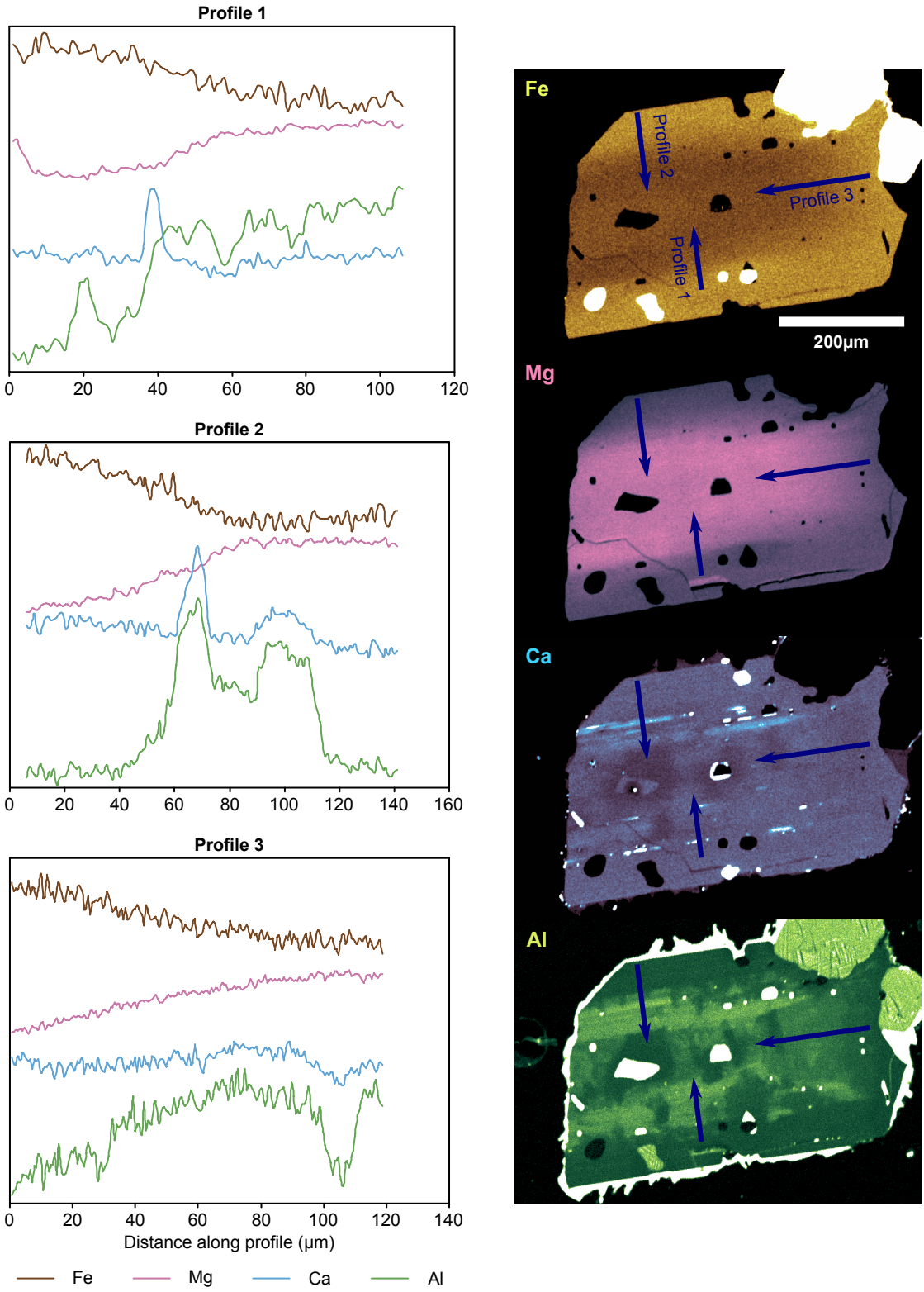

Figure 7.21: Profiles of Fe, Mg Ca and Al counts (arbitrary scale). Profiles are the same as those modelled using diffusion chronometry (Figure 7.20).

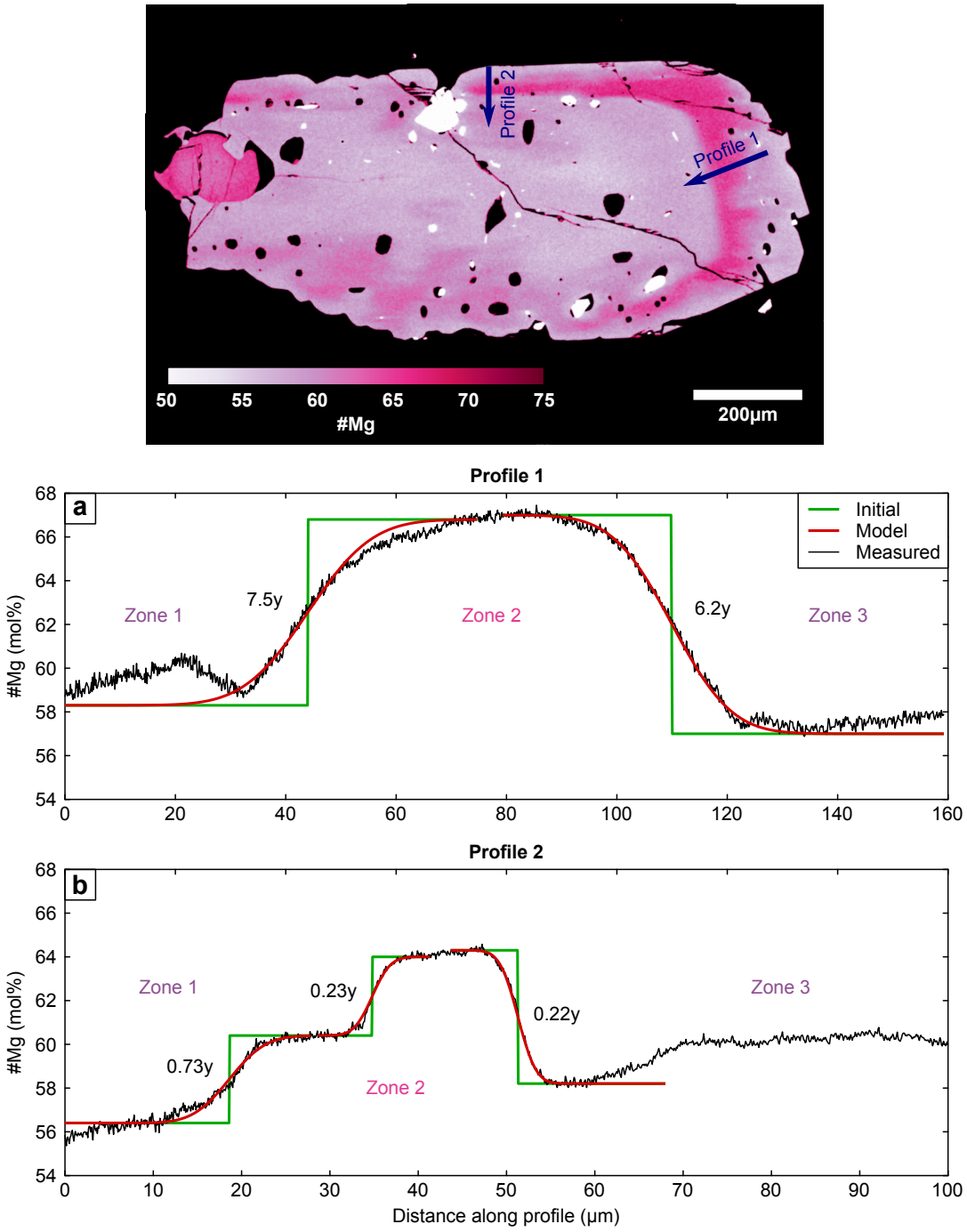

Figure 7.22: An orthopyroxene crystal from the Cape Riva dacite (GS11-03b PYX08).

using a temperature of 855 °instead changes the calculated residence times by a factor of 1.42, while calculations done at 905 °C change the residence times by a factor of 0.71.

Diffusion was modelled at constant temperature of 880 °C. However in Section 7.5 it was argued that zone 2 grew from a less evolved melt(61–66 wt% SiO_2), which would have been hotter. It is difficult to assess how much time the crystals resided in this hotter melt, but the fact that zone 1 appears to be in equilibrium with the Cape Riva glass suggests that the crystals were stored at 880 °C immediately prior to eruption. Because higher temperatures lead to faster diffusion, modelling the crystals at 880 °C for the duration of their pre-eruptive storage provides a maximum estimate of their high-temperature residence times.

Oxygen fugacity

The oxygen fugacity also has an effect on the diffusion coefficient. The relationship between the residence times and fO_2 is given by:

$$t \propto \frac{1}{D} \propto (fO_2)^{-\frac{1}{6}} \tag{7.6}$$

Pre-eruptive oxygen fugacities calculated from Fe–Ti oxides in the Cape Riva and two of the three analysed Therasia pumice fall deposits have a range of ±0.3 log units around the FMQ oxygen buffer. This translates to a difference in high-temperature residence times of ±12 % relative to the high-temperature residence times presented here, calculated at the FMQ buffer.

Pumice Fall B, however, was significantly hotter and more oxidised than both the Cape Riva dacite and the other two Therasia pumice fall deposits that were analysed (∼925 °C and FMQ + 0.7 log units). If Pumice Fall B better represents the pre-eruptive conditions, then high-temperature residence times would be reduced by a factor of 3.

7.7 Comparison of plagioclase and orthopyroxene timescales

The results of the diffusion models of orthopyroxene crystals from the Therasia dacites are presented in Table 7.1, and those from the Cape Riva in Table 7.2. The range of high-temperature residence times for each model is estimated by the range of times that still provide reasonable fits to most of the data, adjusted by $\pm 50\,\%$ to account for uncertainty in the diffusion coefficient due to uncertainty in the temperature and oxygen fugacity. The crystal high-temperature residence times are also plotted in Figure 7.23, along with timescale constraints from field data (Chapter 4). For the Therasia dacites, the average time between eruptions is calculated as the time between the youngest and oldest Therasia dacites, $\sim$15 ky, divided by the minimum number of pauses between the eruptions that took place during that time, 10 (≈ 1.5 ky per eruption). On the plot of Cape Riva high-temperature residence times, the time between the youngest dated Therasia lava and the Cape Riva eruption is plotted, along with the uncertainty from the radiometric dating.

All the modelled Therasia orthopyroxenes have high-temperature residence times significantly shorter than the average time between eruptions, with estimated high-temperature residence times varying from a few months up to a few decades. These times are similar, but slightly shorter than those estimated for the plagioclase phenocrysts (decades to a few centuries). This difference may be real, and the plagioclase crystals may have grown before the orthopyroxene crystals, however it is more likely to be an artefact. Both the orthopyroxene and plagioclases residence times are maximum high-temperature residence times. The tabular shapes and complex resorption surfaces found in the plagioclase crystals means that diffusion in two and three dimensions will be significant. In contrast, the orthopyroxene crystals have prismatic shapes and planar zone boundaries. This make the assumption of diffusion in 1D more realistic for the orthopyroxenes. It is likely that the plagioclase models overestimate the true

Table 7.1: Residence times, in years, calculated in diffusion models of Fe–Mg in orthopyroxene from the Therasia dacites.

Crystal	Profile	Zone 3 → Zone 2		Zone 2 → Zone 1	
Flow 5 (GS10-17)					
PYX22	—	**2.6**	**(0.90–6.8)**	**2.4**	**(0.46–6.8)**
PYX24	—		—	**24**	**(3.8–60)**
PYX30	1		—	**6.5**	**(1.8–15)**
	2		—	14	(5.0–45)
Flow 8 (GS10-14)					
PYX01	—		—	**5.6**	**(1.2–14)**
PYX19	—		—	**1.1**	**(0.34–2.8)**
PYX24	—		—	**2.5**	**(0.60–7.8)**
PYX26	—	**0.17**	**(0.08–0.38)**	**0.27**	**(0.06–0.94)**
PYX29	—		—	**20**	**(8.0–60)**
Flow 9 (GS10-16)					
PYX02	1		—	**32**	**(11–88)**
	2		—	89	(34–190)
PYX03	1		—	**7.1**	**(2.2–20)**
	2		—	9.6	(3.2–27)
PYX05	—	**3.2**	**(0.90–11)**	**5.8**	**(1.8-16)**

Figures in parentheses are the range of possible residence times, taking into account the uncertainties discussed in the text. Bold figures are the best estimate for each crystal.

high-temperature residence times by a greater amount than the orthopyroxene models do.

The orthopyroxenes from the Cape Riva dacite have also have short high-temperature residence times, of months to decades. There is no significant difference between the timescales estimated for crystals in each of the four eruptive phases. This is also true for diffusion models of both the zone 3 to zone 2 and the zone 2 to zone 1 boundary, as well as chemical gradients in the weakly zoned orthopyroxene crystals. This suggests that the majority of the orthopyroxene crystals in the Cape Riva are young. Although some of these gradients may be due to growth rather than

Table 7.2: Residence times, in years, calculated in diffusion models of Fe–Mg in orthopyroxene from the Cape Riva dacite.

Crystal Profile		Zone 3 → Zone 2		Zone 2 → Zone 1		Weakly Zoned	
Phase A (GS11-34a)							
PYX36	—		—		—	**1.2**	**(0.28–3.3)**
PYX39	1		—	**9.0**	**(3.6–21)**		—
	2		—	250	(95-520)		—
PYX59	1	**1.5**	**(0.38–3.6)**	**0.49**	**(0.12–1.5)**		—
	2	15	(2.7–30)	1.5	(0.33–7.5)		—
PYX62	—		—	**40**	**(9.0–220)**		—
PYX63	1	5.2	(1.5–11)	4.1	(1.2–10)		—
	2	**0.63**	**(0.21–1.5)**	**0.09**	**(0.03–0.50)**		—
PYX64	—		—		—	**38**	**(13–120)**
PYX65	—		—		—	**28**	**(10–70)**
Phase B (S12-06)							
PYX01	1		—	5.0	(1.2–11)		—
	2		—	**1.7**	**(0.60–5.6)**		—
PYX04	—		—	**5.3**	**(1.2–10)**		—
PYX07	—		—	**20**	**(6.0–54)**		—
PYX13	—	**2.7**	**(1.0–6.6)**		—		—
PYX17	1		—	**11**	**(3.9–24)**		—
	2		—	33	(10–63)		—
	3		—	450	(160–940)		—
Phase C (GS11-30b)							
PYX01	—		—	**13**	**(4.4–28)**		—
PYX03	—		—		—	**8.5**	**(1.4–32)**
PYX07	—		—		—	**14**	**(2.8–36)**
PYX08	1	6.2	(2.4–14)	7.5	(2.0–33)		—
	2	**0.22**	**(0.08–0.48)**	**0.23**	**(0.04–0.58)**		—
PYX10	1		—		—	**6.0**	**(1.2–16)**
	2		—		—	9.4	(2.6–22)
PYX29	—		—	**29**	**(10–64)**		—

Figures in parentheses are the range of possible residence times, taking into account the uncertainties discussed in the text. Bold figures are the best estimate for each crystal.

Table 7.2 continued: Residence times, in years, calculated in diffusion models of Fe–Mg in orthopyroxene from the Cape Riva dacite.

Crystal Profile		Zone 3 → Zone 2		Zone 2 → Zone 1		Weakly Zoned	
Phase C (S12-05)							
PYX01	1	**0.73**	**(0.20–1.8)**	**1.3**	**(0.22–3.2)**		—
	2	1.8	(0.60–3.4)	5.2	(1.8–16)		—
PYX06	1		—		—	**2.9**	**(0.80–7.2)**
	2		—		—	14	(4.3–30)
PYX12	—		—	**22**	**(4.8–51)**		—
PYX17	—		—		—	**5.3**	**(1.6–15)**
PYX18	1	1.7	(0.22–3.3)	2.1	(0.75–6.0)		—
	2	**0.16**	**(0.05–0.33)**	**0.22**	**(0.05–0.70)**		—
PYX26	1		—		—	19	(5.5–56)
	2		—		—	**11**	**(3.6–39)**
PYX28	1	**0.88**	**(0.22–2.1)**	3.5	(0.95–13)		—
	2		—	**0.88**	**(0.16–3.3)**		—
PYX34	—		—		—	**3.6**	**(0.55–10)**
Phase D (GS11-39b)							
PYX11	—		—		—	**19**	**(5.5–39)**
PYX12	—		—		—	**11**	**(2.8–30)**
PYX21	—	**4.7**	**(1.2–11)**		—		—
PYX31	—	**0.16**	**(0.06–0.46)**	**1.5**	**(0.46–2.8)**		—
PYX37	—		—	**12**	**(4.9–24)**		—

Figures in parentheses are the range of possible residence times, taking into account the uncertainties discussed in the text. Bold figures are the best estimate for each crystal.

diffusion, the diffusion models still place constraints on the maximum time that the orthopyroxenes resided at high temperature before eruption. Significantly, the models show that this is much shorter than the $2{,}800 \pm 1{,}400$ y between the youngest dated Therasia eruption and the Cape Riva eruption (Chapter 4). This supports the short high-temperature residence times calculated for the Cape Riva plagioclase phenocrysts (Chapter 6). Like in the Therasia dacites, the Cape Riva orthopyroxenes appear to have shorter high-temperature residence times than the plagioclases. As described for the Therasia dacites above, this is probably an artefact of the different modelling pro-

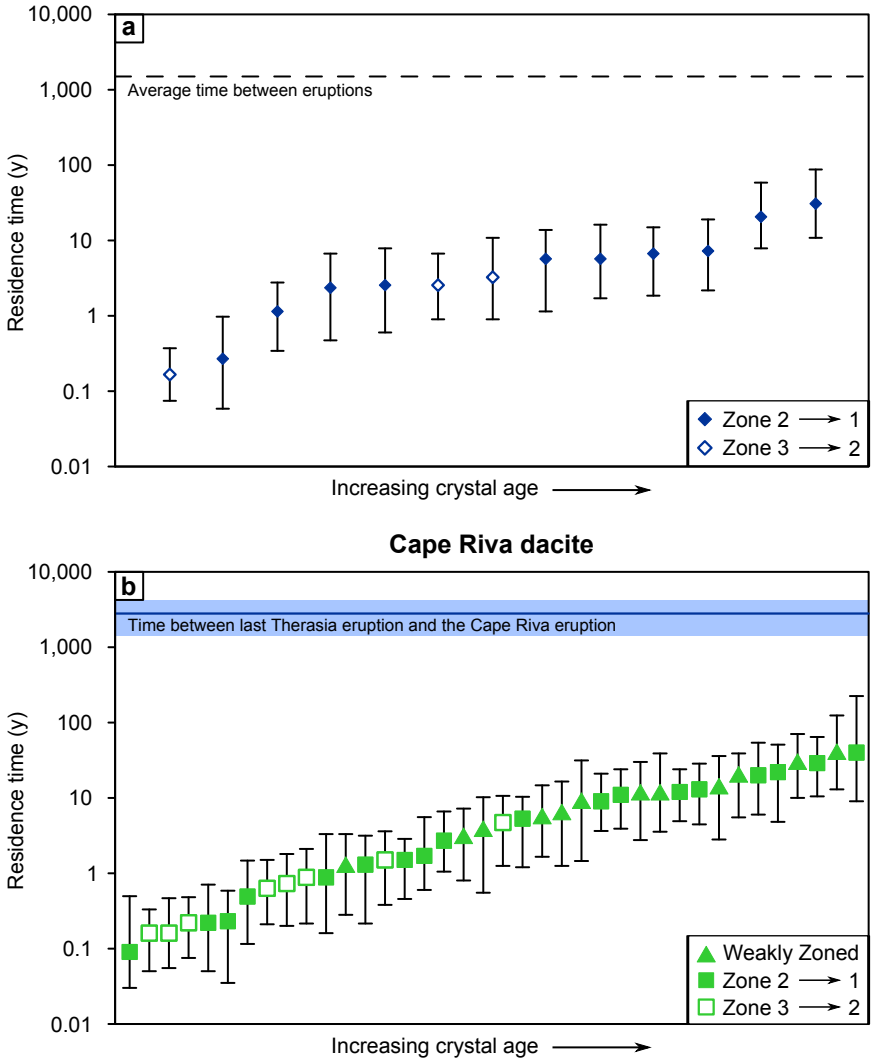

Figure 7.23: High-temperature residence times of plagioclase crystals from (a) the Therasia and (b) the Cape Riva dacites.

cedures rather than indicating that the orthopyroxene crystals are in fact younger than the plagioclase crystals.

There is still ambiguity over whether the weakly zoned crystals are the equivalent of zones 1 or 3 of the strongly zoned crystals. Their relatively long high-temperature residence times — at the upper end of the range shown by the strongly zoned crystals — would seem to suggest that they are too old to be equivalent to zone 1. However, the gradients in the weakly zoned crystals are probably at least partly due to growth, and that the calculated high-temperature residence times for the weakly zoned crystals are overestimates. Even if the calculated high-temperature residence times are overestim-

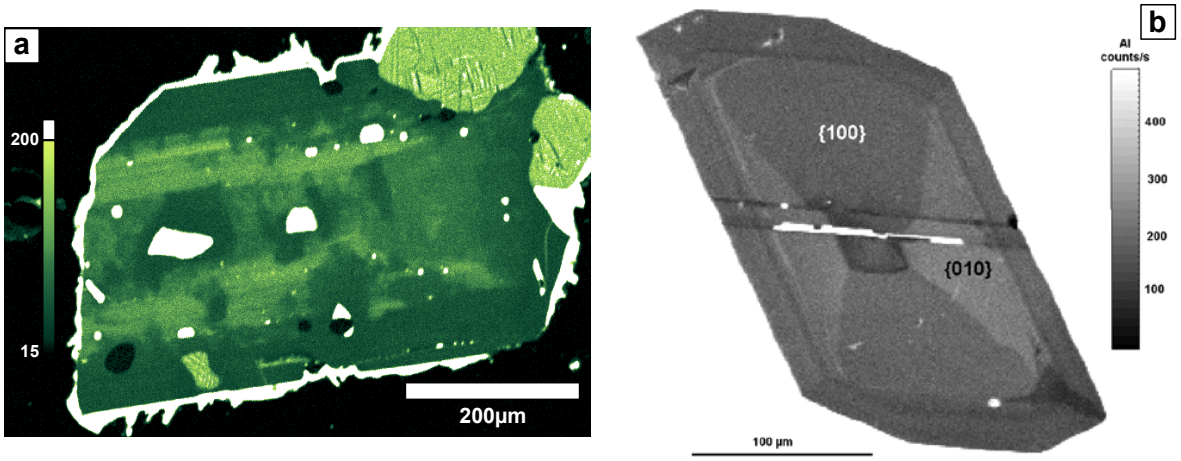

Figure 7.24: (a) An orthopyroxene crystal from the Cape Riva dacite (S12-06 PYX17) and (b) an orthopyroxene from the experiments of Schwandt and McKay (2006), showing possible sector zoning

ates, they are still short (up to a few decades). This, along with the lack of strong Al zonation, makes it unlikely that the weakly zoned crystals were once strongly zoned before they re-equilibrated with their host melt.

There is evidence for rapid growth of zone 2, which is consistent with the short high-temperature residence times. Many of the crystals' zone 2 has melt escape features typical of rapid growth visible in the Al zoning (Figure 7.9). Another orthopyroxene crystal (S12-06 PYX17) appears to have sector zoning (Figure 7.24). Schwandt and McKay (2006) found Al sector zoning in some of the orthopyroxene crystal that were produced in their experiments, but only when crystal growth was sufficiently fast.

7.8 Summary

- Many of the orthopyroxene phenocrysts found in the Therasia are weakly zoned $Wo_{3-4}En_{53-60}Fs_{37-43}$ (#Mg: 58–64). Those that have strong Fe-Mg zoning can be described schematically as different cuts through a crystal with three zones: a core (zone 3) and rim (zone 1) with similar compositions to the weakly zoned orthopyroxene crystals, and in between these a high-Mg mantle (zone 2) of $Wo_{3-4}En_{62-68}Fs_{29-35}$ (#Mg: 65–71). The boundaries between the different

zones are diffuse, and can be used to estimate high-temperature residence times for the different zones.

- The orthopyroxene phenocrysts found in the Cape Riva dacite have similar zoning patterns to those found in the Therasia dacites. Weakly zoned crystals have compositions of $Wo_{3-4}En_{52-56}Fs_{41-44}$ (#Mg: 53–58). Strongly zoned crystals are more common than in the Therasia dacites, but have a similar, diffuse Fe–Mg zoning patterns. The cores (zone 3) and rims (zone 1) of strongly zoned Cape Riva phenocrysts have similar compositions to the weakly zoned crystals found in the Cape Riva dacite. Zone 2, the mantles, have compositions of $Wo_{3-4}En_{57-65}Fs_{32-40}$ (#Mg: 60–68).

- Electron microprobe X-ray count maps show that the high-Mg zone 2 also has high Al. Because Al diffuses very slowly in orthopyroxene (Nakagawa et al., 2005; Smith and Barron, 1991), the Al concentrations seen in the element maps are close to original. The sharp boundaries between different zones in most of the Al maps suggest that the Fe–Mg zoning was also originally sharp, and this is assumed in the timescale modelling. The present gradients seen in Fe–Mg are therefore mostly due to diffusion. The lack of significant Al zoning in the crystals with weak Fe–Mg zoning suggests that they were never strongly zoned.

- The experiments of Cadoux et al. (2014) show that the composition of zones 1, 3 and the weakly zoned orthopyroxene crystals is consistent with them growing from a melt with the composition of the Cape Riva, between 70–72 wt% SiO_2. The high-Mg zone 2 could have grown from a melt with between 61 and 67 wt% SiO_2, as proposed for the Ca-rich parts of the sawtooth zoned plagioclase crystals (Chapter 6).

- Modelling the diffusion of Fe–Mg across the zone boundaries in the Therasia orthopyroxenes give high-temperature residence times of months to decades. This is consistent with high-temperature residence times of years to centuries calculated

by modelling Mg diffusion in plagioclase (Chapter 6). The plagioclase diffusion models probably overestimate the true high-temperature residence times of the plagioclase crystals, due to diffusion in 2/3D. These ages are significantly shorter than the average time between eruptions during the construction of the Therasia dome complex.

- Modelling the diffusion of Fe–Mg across the zone boundaries of the strongly zoned orthopyroxene crystals found in the Cape Riva dacite, as well as the more gentle gradients in the weakly zoned crystals, also gives high-temperature residence times of months to decades. The timescale for all four eruptive phases is the same.

Chapter 8

Conclusions

8.1 Introduction

There is currently much discussion over the processes that allow the accumulation of large bodies of eruptible silicic magma in the shallow crust, and particularly over the timescales over which these processes operate (Chapter 1). For example, radiometric ages of accessory minerals such as zircon are often found to be 10^5–10^6 y older than eruption ages, which suggests long-term storage for these magmas (e.g. Brown and Fletcher, 1999; Chamberlain et al., 2014). However, diffusion chronometry often suggests much shorter times for the assembly of these magma bodies, of 10^1–10^3 y (e.g. Allan et al., 2013; Druitt et al., 2012). This apparent dichotomy between short and long timescales is usually explained by long-term storage in a rigid crystal mush, followed by rapid remobilisation or segregation shortly before eruption (e.g. Bachmann and Bergantz, 2004; Bachmann et al., 2007a; Burgisser and Bergantz, 2011).

With this in mind, I studied the >10 km^3, dacitic Cape Riva eruption of Santorini, Greece (Chapter 2). Over a period of about 18 ky prior to the Cape Riva eruption, the volcano extruded a series of dacitic domes and coulées: the Therasia dome complex. This allowed me to investigate the evolution of the plumbing system of Santorini during the build-up to a caldera-forming eruption. I focused in particular on answering the

following three questions:

1. How are large, shallow crustal bodies of volatile-rich, crystal-poor magma assembled?

2. How and where do the crystals in these eruptions form, and what do the zoning patterns of the crystals record?

3. What are the associated timescales of these processes?

I attempted to answer these questions by combining information acquired using multiple approaches. The first technique I used was field mapping (Chapter 4). The stratigraphic relationships between the different units provided the context into which I could place the subsequent results. These relative dates were augmented with $^{40}Ar/^{39}Ar$ absolute dates of four key lava flows provided by Dr S. Scaillet (Fabbro et al., 2013). The Y-4 ash layer in the Aegean was found to correlate with the one of the pumice fall deposits intercalated between the Therasia lavas (the Cape Tripiti Pumice), and this provided further constraints on the absolute ages of the Therasia dacites. A key finding was that the last Therasia eruption occurred no more the $2{,}800 \pm 1{,}400$ y before the Cape Riva eruption.

Following the field mapping, I analysed the chemistry and petrology of the Therasia dome complex and the Cape Riva eruption (Chapter 5). Using the stratigraphic relationships identified in the field, I could show that there were no systematic trends in the composition of the magma emitted in the build-up to the Cape Riva eruption. The chemistry and petrology allowed me to distinguish hybrid andesites from fractionated andesites, which allowed me to place constraints on mafic recharge. Comparing the chemistry of the Therasia dacites with that of the Cape Riva dacite allowed me to rule out the possibility that the Therasia dacites were precursory leaks from the growing Cape Riva magma reservoir, contrary to previous interpretations (Bacon, 1985; Druitt, 1985).

I then looked in more detail at the zoning patterns of plagioclase and orthopyroxene crystals in both the Therasia and Cape Riva dacites (Chapters 6 and 7). I examined the zoning patterns of multiple elements with different diffusion coefficients in each mineral, as these provided complimentary information. The distribution of slowly diffusing elements, such as NaSi–CaAl and Ti in plagioclase and Al in orthopyroxene, would not be modified by diffusion during the crystals' storage in the magma reservoir. This meant they could be used to recreate the melt compositions those crystals came into contact with, and study the magmatic processes that the crystals witnessed. After interpreting the histories recorded by the crystals' zoning patterns, the timescales associated with the identified processes could be estimated by modelling the diffusion of fast-diffusing elements (Mg in plagioclase and Fe–Mg in orthopyroxene). Using diffusion models of two different minerals in the same samples provides more robust constraints on the timescales.

Below, I first summarise the key findings of this thesis. I then discuss how these findings can be used to place constraints on the ascent and storage of the Therasia and Cape Riva magmas, on the growth of the phenocrysts, and on the timescales calculated in the diffusion models. Finally, I bring together all the different pieces of evidence in order to present a coherent model for the evolution of the plumbing system of Santorini in the build-up to the Cape Riva eruption.

8.2 Summary of the Therasia–Cape Riva sequence

8.2.1 The Therasia dome complex

- The Therasia dacites were preceded by the construction of the $\sim$10 km^3 Skaros shield from 67 ± 9 ka, which culminated in the 54 ± 3 ka large, explosive, andesitic Upper Scoria 2 eruption (Chapter 2).

- Between the Upper Scoria 2 eruption and the first Therasia dacite there was a

period of 15 ± 4 ky of near repose, with a low eruptive rate ($<0.1\,km^3\,ky^{-1}$). Lavas emitted during this period were andesitic (Chapter 4).

- Starting at 39.4 ± 2.2 ka, dacite began to be erupted from diffuse vents across the Skaros edifice. Two feeder dykes from these lavas are visible on the south-east corner of Therasia (Chapter 4).

- Dacite eruption continued for a period of 14.8 ± 2.6 ky, during which time $\sim 2\,km^3$ was emitted over at least 11 extrusive eruptions and 5 explosive eruptions. This give a maximum mean repose time between eruptions of ~1,000 y (Chapter 4).

- Pumice fall deposits intercalated between the lavas are concentrated towards the top of the sequence, suggesting increased explosivity with time (Chapter 4).

- There are only minor, non-systematic variations with stratigraphic height in both whole-rock and groundmass (i.e. melt) compositions of the Therasia dacites (Chapter 5).

- The compositions of both the plagioclase and orthopyroxene phenocryst rims vary between lava flows. There are also textural differences in plagioclases in different flows (Chapter 6).

- There are also variations in the pre-eruptive temperatures and oxygen fugacities of different pumice fall deposits. Fe–Ti oxides in the Cape Tripiti pumice fall and Pumice Fall C record temperatures of ~880 °C and oxygen fugacities close to the FMQ buffer. Fe–Ti oxides from Pumice Fall B, however, record temperatures ~50 °C hotter and oxygen fugacities close to the NNO buffer (Chapter 5).

- The Therasia dacites contain glass-bearing clusters of plagioclase and orthopyroxene. The crystals in these clusters have similar compositions and textures to the phenocrysts. These clusters are interpreted as having grown on the margins of the magma reservoir at the same time as the phenocrysts (Chapter 5).

- The lavas also contain holocrystalline gabbroic nodules, composed of plagioclase, two pyroxenes and olivine. These nodules are interpreted as remobilised plutonic material intruded during previous episodes of volcanism at Santorini. The textures of these nodules, as well as the compositions of the minerals of which they consist, vary from lava flow to lava flow (Chapter 5).

- Some plagioclase phenocrysts have calcic cores, with compositions of An_{62-91}. These are often resorbed, in equilibrium with a high Sr melt, and have high-temperature residence times of at least a few thousand years. They are probably derived from plutons related to previous volcanic activity on Santorini, although some may have been introduced by basaltic or andesitic recharge magmas. These calcic cores are overgrown by rims with the same composition as the phenocrysts (Chapter 6).

- Some plagioclase phenocrysts have sawtooth zoning, cycling between An_{59-72} and An_{41-51}, the latter being similar to rim compositions. The tight correlation of Sr with anorthite content suggests that the sawtooth zones grew from melts ranging in composition from andesite to dacite. The Ti contents of these crystals suggest that most of the melts injected into the Therasia reservoir were the products of fractional crystallisation; these plagioclase crystals do not record evidence of basaltic recharge (Chapter 6).

- The compositions of the orthopyroxene crystals are also consistent with growth from andesitic to dacitic melts (Chapter 7).

- Plagioclase phenocrysts in the Therasia dacites have maximum high-temperature residence times of a few decades to a few centuries at 880 °C, as estimated by diffusion chronometry (Chapter 6). Orthopyroxene yield shorter maximum high-temperature residence times, of a few months to a few decades (Chapter 7). These timescales are shorter that the estimated repose times between eruptions (∼1,000 y).

- After the eruption of the first Therasia dacite at ∼39 ka, up until the final lava flow discharged before the Cape Riva eruption, mafic magma only reaches the surface as minor (≪1 %) chilled basaltic enclaves (Chapter 5).
- The final eruption of the Therasia period, the upper Therasia andesite, is a hybrid andesite that formed through a ∼60:40 mix of dacite and basalt (Chapter 5).
- The youngest dated Therasia lava was erupted at 24.6 ± 1.3 ka (Chapter 4).

8.2.2 The Cape Riva eruption

- The Cape Riva eruption occurred at 21.8±0.4 ka, 2,800 ± 1,400 y after the youngest dated Therasia eruption (Chapter 4).
- >10 km^3 of mainly dacitic magma was erupted, with a minor (>1 %) hybrid andesite component formed by mixing olivine basalt and dacite in the ratio 60:40 (Chapter 4).
- The Skaros–Therasia edifice collapsed during the eruption, creating a caldera 5–6 km in diameter in the north of the volcanic field (Chapter 2).
- The dacite discharged during all four phases of the eruption has the same composition and pre-eruptive temperatures and oxygen fugacities (Chapter 5).
- The rim compositions of the plagioclases and orthopyroxene crystals erupted during all four phases is the same (Chapter 5).
- Many plagioclase phenocrysts have sawtooth zoning, cycling between An_{46-60} and An_{36-41} rim compositions. The tight correlation of Sr with anorthite content suggests that these plagioclase compositions grew from melts that range from dacitic to rhyodacitic compositions. The Ti content of the sawtooth zones of the plagioclase crystals rule out the injection and mixing into the Cape Riva magma reservoir of melts less evolved than a silicic andesite as the cause of the changes in melt composition (Chapter 6).

- The orthopyroxene phenocrysts have compositions that are consistent with growth from melts with compositions ranging between that of the Cape Riva glass and a dacitic melt (Chapter 7).

- Major element contents of the Cape Riva dacite are similar to those found in the Therasia dacites. In addition, the major element contents of the Cape Riva hybrid andesite are similar to the upper Therasia hybrid andesite. However, the Cape Riva dacite is depleted in incompatible elements compared to the Therasia dacites (K, Rb, Zr, LREE, HREE). A similar depletion is implied for both the mafic and silicic endmembers that mixed to form the Cape Riva hybrid andesite (Chapter 5).

- Plagioclase phenocrysts in the Cape Riva dacite are also depleted in La and Ce compared to plagioclase phenocrysts in the Therasia dacite (Chapter 6).

- Maximum high-temperature residence times of the plagioclase phenocrysts in the Cape Riva are a few years up to a few centuries at 880 °C, as measured by diffusion chronometry (Chapter 6). Maximum high-temperature residence times of the orthopyroxene phenocrysts at the same temperature are months to decades (Chapter 7). This is short compared to the 2,800 ± 1,400 y maximum repose time after the last Therasia dacite eruption.

8.3 Constraints on the volcanic plumbing system

8.3.1 Magma reservoir depths

Figure 8.1 shows the estimated storage depths of Santorini magmas. Andújar et al. (2010) examined a basalt from a cinder cone erupted during the Peristeria period along with the andesitic Upper Scoria 1 (Chapter 2). Their phase equilibria experiments suggest that the basalt was stored at around 4 kbar (∼15 km) prior to eruption. They also suggest that the Upper Scoria 1 differentiated from basalt to andesite at about

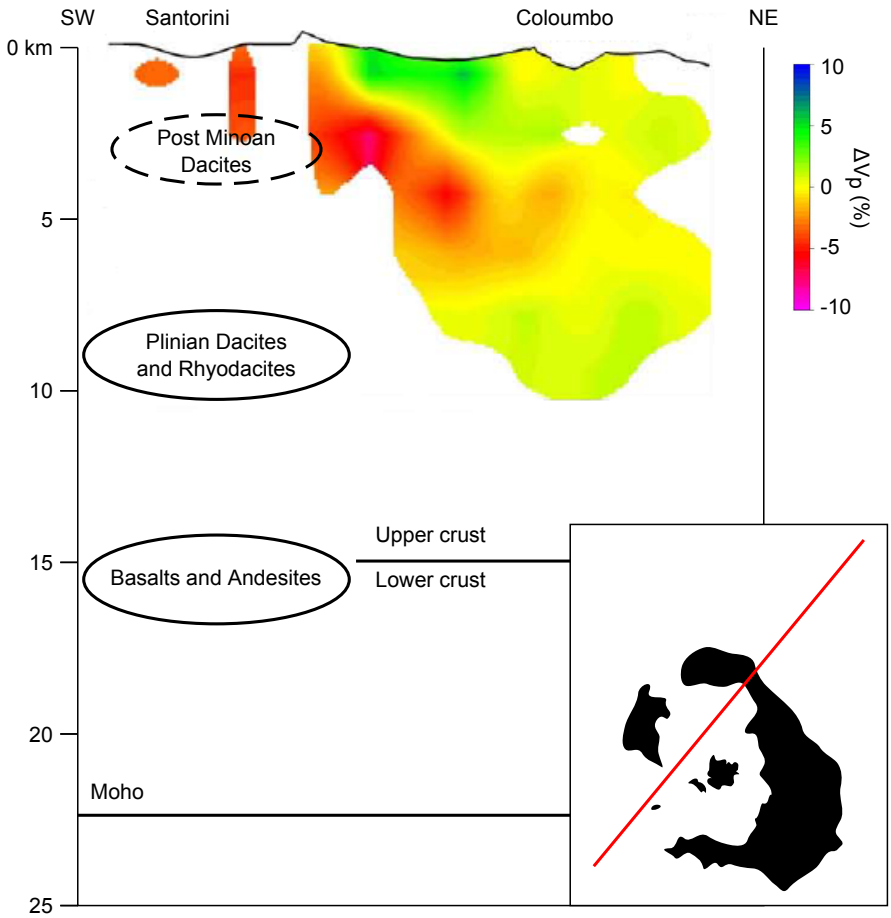

Figure 8.1: Schematic interpretative illustration of the Santorini-Coloumbo magma plumbing system along a SW–NE cross-section from the Santorini caldera towards the Coloumbo seamount, after Cadoux et al. (2014). P-waves velocity variations beneath Coloumbo from Dimitriadis et al. (2010) are shown. Moho and upper/lower crust boundary depths from Endrun et al. (2008); Karagianni and Papazachos (2007); Konstantinou (2010); Sachpazi et al. (1997). Basaltic and andesitic reservoir from Andújar et al. (2010), Plinian dacite and rhyodacite reservoir from Cadoux et al. (2013, 2014). Post-Minoan dacite reservoir from Foumelis et al. (2013); Newman et al. (2012); Papoutsis et al. (2013); Parks et al. (2012)

4 kbar. This is close to the boundary between the upper and lower crust (Endrun et al., 2008; Karagianni et al., 2005; Konstantinou, 2010).

Cadoux et al. (2013, 2014) carried out phase equilibria experiments using the Cape Riva dacite as their starting material, and the phase relationships they calculated are shown in Figure 8.2. They estimated the depth of storage of the Cape Riva magma was 2 ± 0.5 kbar (8 ± 2 km). The similar chemistry and petrology of the Cape Riva and Therasia dacites suggests that they were stored at comparable depths. In the following

discussion, I shall refer to this reservoir at ∼2 kbar as the "shallow" reservoir.

The storage depths of other silicic magmas from Santorini have also been estimated. Cadoux et al. (2013, 2014) also carried out experiments on the deposits of three other Plinian eruptions of Santorini, the Minoan, Lower Pumice 1 and Lower Pumice 2. Their results indicate that all four magmas were stored at about 2 kbar. Cottrell et al. (1999) also studied the products of the Minoan eruption. They suggested that the Minoan magma underwent two stages of evolution, the first at >2 kbar, and the second at ∼0.5 kbar. However, Cottrell et al. (1999) carried out their experiments at water-saturated conditions. Cadoux et al. (2013, 2014) demonstrate that the Minoan eruption was not water saturated, and that the phase relationships observed in the Minoan products can be explained by a single stage of evolution at 2 kbar. Gertisser et al. (2009) used the aluminium content of rare amphibole crystals to estimate a storage depth of about 4 kbar for the Lower Pumice 2 magma. A shallower magma reservoir, at about 2–4 km depth, has been suggested for the youngest dacites, based on modelling recent deformation at Santorini (Foumelis et al., 2013; Newman et al., 2012; Papoutsis et al., 2013; Parks et al., 2012).

8.3.2 Magma ascent and storage during the Therasia period

The vents of the Therasia dacites were located across the flanks and summit area of the Skaros shield. This suggests that they were fed from one or more reservoirs situated beneath the Skaros shield. The depth at which these dacites were stored is not well constrained. However, the mineralogy and major element composition of the Therasia dacites is similar to that of the Cape Riva dacite, suggesting they were stored at similar depths (about 8 km).

The Therasia dacites have been previously interpreted as "precursory leaks" from the growing Cape Riva magma body (Druitt, 1985). Precursory leaks of silicic magma from diffuse vents prior to caldera-forming eruptions are believed to record the prolonged, incremental growth of large crustal magma reservoirs (Bacon, 1985). For ex-

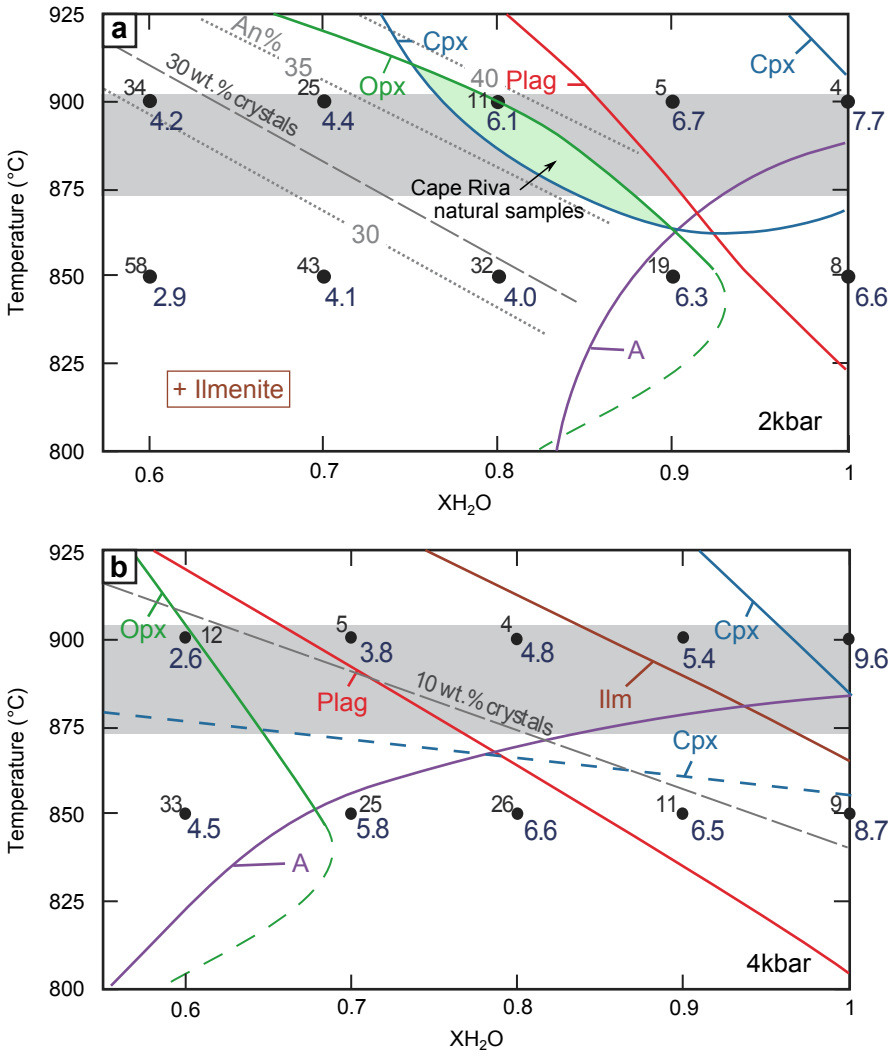

Figure 8.2: Isobaric phase relationships of the Cape Riva dacite at (a) 2 and (b) 4 kbar, at the FMQ oxygen buffer and as a function of the molar water fraction (X_{H_2O}) of the coexisting fluid phase and of temperature (°C). Taken from Cadoux et al. (2014). Curves are labelled with mineral names lying inside their stability fields. Plg: plagioclase, Opx: orthopyroxene, Cpx: clinopyroxene, A: amphibole, Ilm: ilmenite. Each black circle represents an experimental charge. Dark blue numbers: by-difference H_2O melt values in wt%. Smaller italic black numbers are charge crystallinity in wt%. Light grey dashed-lines indicate the anorthite content (mol%) of the experimental plagioclases. Grey band: pre-eruptive temperature range inferred from natural Fe-Ti oxides (Chapter 5).

ample, leaks of rhyodacite at Mount Mazama (Crater Lake, Oregon) bear witness to the progressive growth, over about 20,000 y, of the magma body that was discharged 6,850 years ago (Bacon, 1985; Bacon and Lanphere, 2006). The Glass Mountain rhyolites at Long Valley, California, have also been described as precursory leaks recording the growing Bishop Tuff magma chamber over about 300 ky (Chapter 1; Halliday et al., 1989; Hildreth and Wilson, 2007), although this interpretation is somewhat controversial (Chamberlain et al., 2014; Reid and Coath, 2000; Simon and Reid, 2005).

However, there are several lines of evidence that suggest that the Therasia dacites were fed by multiple small magma reservoirs, rather than one single, long-lived reservoir. Whole rock and melt compositions vary slightly throughout the sequence, along with temperature and oxygen fugacity, but not in any systematic way (Figure 4.7). The crystals found in one flow do not appear to be the same as the crystals found in another. The composition of the rims of the plagioclase and orthopyroxene phenocrysts vary from flow to flow, and the plagioclase crystals have a range of textures in different units. In some lavas some of the plagioclase crystals have large, brown glass inclusions, while these crystals are absent in others. Similarly, plagioclase crystals with sawtooth zoning are only present in some lava flows. Although plagioclase crystals with calcic cores are present in most lava flows, the composition of these cores varies from flow to flow. The composition and zoning patterns of the plagioclases found in the gabbroic also differs between flows. Finally, the high-temperature residence times of both the plagioclase and orthopyroxene phenocrysts are short compared to the repose time between eruptions. This implies that there is little recycling of crystals between eruptions, contrary to what would be expected if the Therasia lavas were fed from a single, long-lived reservoir.

There are three potential ways of producing multiple, small batches of silicic magma in the shallow crust: (1) fractional crystallisation from basalt to dacite, followed by the upward transfer to the shallow reservoir in small batches; (2) the defrosting and bulk remobilisation of a crystal mush stored in the shallow crust; (3) mush defrosting,

followed by melt segregation.

Fractional crystallisation and upward transfer

The Therasia dacites could be produced by fractional crystallisation from basalt at depth. Small parcels of dacite could be transferred to a shallow holding reservoir at about 2 kbar, where the phenocrysts would would grow. Each individual parcel would then either promptly be erupted, or would rapidly freeze. There is little constraint on the depth at which this fractionation would happen, but one possibility is that it occurred in the 4 kbar reservoir identified by Andújar et al. (2010) as the location where basalt fractionates to andesite (Figure 8.1).

Defrosting and bulk remobilisation of a crystal mush

In situ melting and remobilising of a shallow crystal mush could have been caused by the injection of basalt into the shallow plumbing system. The injection of basalt is recorded by the presence of mafic enclaves in many of the Therasia dacites; the injected mafic magma could have melted some of the overlying crystal mush by conduction or gas sparging, without large-scale mixing and hybridisation (Bachmann and Bergantz, 2006). The gabbroic nodules attest to at least some assimilation of plutonic material. The glass-bearing clusters appear to once have been part of a network of touching crystals, which is consistent with them having grown in a mush zone.

However, there is little textural evidence that the crystals in the Therasia dacites are derived from a partially remelted crystal mush. The plutonic nodules are holocrystalline, and appear to have been incorporated by mechanical disaggregation rather than melting and resorption. The phenocrysts are euhedral, and they often are normally zoned towards their rims. This is true of phenocrysts found as individual crystals as well as those found in the glass-bearing clusters. The last thing the phenocrysts appear to record is a period of growth, not a period of dissolution.

Mush defrosting followed by melt segregation

If the Therasia dacites were produced by the defrosting of a crystal mush, then the melt must have been segregated and transferred into a shallow holding reservoir before eruption. It is not possible to place constraints on the depth of the source mush. One possibility is that the source mush may have been located at about 4 kbar (Figure 8.1. Another possibility is that the source mush was already in the shallow crust, and segregation only occurred locally. In either case, most of the phenocrysts would have grown in the shallow holding reservoir after segregation.

Conclusion

The Therasia dacites formed either by remelting and remobilising a rigid crystal mush or by fractional crystallisation; however in both cases the melts that were produced must have segregated and been stored for a period in small, short-lived holding reservoirs before eruption. Most of the phenocrysts would have grown in these holding reservoirs.

8.3.3 The ascent and storage of the Cape Riva magma

The Cape Riva dacite was probably stored in a single, well-mixed reservoir immediately prior to eruption. The evidence for this is that all four phases of the Cape Riva eruption have the same whole rock and melt compositions (Druitt, 1983; Druitt et al., 1999); the phenocrysts found in all four phase have the same rim compositions and the same textures; and the temperature and oxygen fugacity does not vary between different phases (Cadoux et al., 2013, 2014).

Despite the similar major-element chemistry and petrology of the Cape Riva and Therasia dacites, the Cape Riva dacite is depleted in incompatible elements compared to the Therasia dacites (Figure 5.4). This depletion cannot be produced by fractional crystallisation of the Therasia dacite, or by back-mixing of the Therasia dacite with an incompatible-depleted basalt. The similar $^{87}Sr/^{86}Sr$ of the Cape Riva and Therasia

dacites rules out significant crustal assimilation (Briqueu et al., 1986; Druitt et al., 1999; Zellmer et al., 2000). This depletion is part of a longer term trend, and is probably related to processes occurring in the source region of the magmas (Bailey et al., 2009; Clift and Blusztajn, 1999; Francalanci et al., 2005; Huijsmans et al., 1988; Zellmer et al., 2000). This suggests that the Therasia and Cape Riva magmas are separate batches that evolved independently.

One possible model for the storage of these two dacite types is that they were emplaced in separate, long-lived reservoirs that coexisted in the upper crust, perhaps for much of the 30 ky since the Upper Scoria 2 eruption. The Therasia eruptions would have been fed from one or more small reservoirs, and the Cape Riva eruption from another, larger reservoir. The Cape Tripiti pumice, with its intermediate chemical character, might have resulted from a temporary connection between the two reservoirs.

However, field and phase equilibria data provide quite stringent constraints on the possible locations of the two reservoirs in such a model. First, the vents that fed the Therasia lavas lay within the area that subsequently collapsed to form the Cape Riva caldera (Druitt, 1985, 2014; Druitt and Francaviglia, 1992), showing that the reservoirs were geographically coincident. Second, the similarities in whole rock major element composition, phenocryst assemblage, phenocryst rim compositions and Fe–Ti oxide temperatures, show that the Therasia dacites must have been stored immediately prior to eruption at a pressure (2 ± 0.5 kbar, equivalent to 8 ± 2 km) similar to that determined experimentally for the Cape Riva dacite by Cadoux et al. (2013, 2014). The two reservoirs must therefore have been situated within the $\sim$4 km vertical distance represented by the $\pm$0.5 kbar uncertainty on the pressure. Moreover, this uncertainty is on the absolute pressure, not on the relative pressure difference between the two dacite types. It is difficult to see how two magma reservoirs within this confined space could remain largely isolated over many thousands of years. This model cannot be ruled out, but it raises problems that are hard to surmount.

My preferred interpretation is that the Therasia and Cape Riva magma batches

were emplaced sequentially into the upper crust beneath the summit of the volcano, the first then being partially, or wholly, flushed out by the arrival of the second. The new input magma mixed with any remaining Therasia magma to generate the dacite that subsequently discharged during the Cape Riva eruption. This may have had the composition of pure Cape Riva dacite, or may have been a dacite even poorer in incompatibles (e.g. Kameni-like dacite). However, the lower La and Ce contents of the Cape Riva plagioclase phenocrysts relative to the Therasia phenocrysts suggest that few of the crystals in the Cape Riva dacite were derived from remnant Therasia magma. Either there was little Therasia magma remaining in the shallow plumbing system when the Cape Riva magma arrived, or the remnant Therasia magma was mostly aphyric.

8.4 Constraints on the growth of the phenocrysts

8.4.1 Cause of the zoning in the phenocrysts

Understanding the cause of the zoning patterns of the crystals is key to interpreting the high-temperature residence times estimated from the diffusion modelling. The orthopyroxene and plagioclase phenocrysts appear to be recording the same events, with a similar story in both the Therasia and Cape Riva dacites. The Therasia phenocrysts mostly grew in a dacitic melt, however the calcic peaks of the sawtooth zones of some plagioclases and the Mg-rich zones of some orthopyroxenes show that they occasionally came into contact with an andesitic melt. Zoning in the Cape Riva dacite shows cycling between slightly more evolved melts (dacites and rhyodacites).

The high Ti contents of most of the Therasia and all of the Cape Riva plagioclase phenocrysts that were analysed, along with the tight correlation of Sr with anorthite content, implies that the majority of the melts that the phenocrysts came into contact with lay along fractionation trends for Santorini magmas (Figure 6.11). The reversely zoned sections of the phenocrysts must record a period when the melt was driven back

down the fractional crystallisation trends, towards more primitive compositions. This suggests that magma mixing occurred during the growth of the phenocrysts. The mafic endmember would have to be at least as evolved as a silicic andesite to explain the high Ti contents of the plagioclase phenocrysts.

The mixing would not necessarily have had to involve the entire reservoir simultaneously. This is particularly evident in the Cape Riva phenocrysts, where the range of residence times recovered suggests that mixing was a continuous process, affecting different crystals at different times. The zoning patterns could record mingling and mixing between small batches of differing compositions, or the injection of small batches into a growing Cape Riva magma reservoir. Either way, these different batches must have amalgamated into a single reservoir and been homogenised prior to eruption.

8.4.2 Triggering crystal growth

Although the zoning patterns of the phenocrysts suggest that their growth coincided with a period of magma mixing, it does not tell us what is causing the crystals to grow in the first place.

The experiments of Cadoux et al. (2013, 2014) show that both plagioclase and orthopyroxene growth in the Cape Riva dacite can be caused either by a reduction in the temperature, or by a reduction in the pressure of the magma (Figure 8.2). For example, a melt with $X_{H_2O} = 0.8$ at 2 kbar cooling from 925 to 880 °C will first start to crystallise plagioclase, then orthopyroxene. Similarly, a melt with $X_{H_2O} = 0.8$ and a temperature of 880 °C decompressing from 4 to 2 kbar will also grow first plagioclase then orthopyroxene.

There are several potential magmatic processes that could trigger crystal growth on a timescale of decades to centuries:

1. Decompression of the dacitic melt through upward transfer through the crust.

2. Cooling of the dacitic melt due to mixing with cooler resident magma at shallow

levels.

3. Transfer of dacitic melt upwards through the crust to a cooler environment.

4. Depressurisation of the shallow magma reservoir through precursory eruptions or degassing.

These processes are not mutually exclusive, and the data presented here is not sufficient to definitively rule out any of them.

The phase relationships shown in Figure 8.2 suggest that the magma reservoir would have to cool by about 25 °C in order to grow the observed plagioclase and orthopyroxene phenocrysts. The high-temperature residence times of the phenocrysts requires that this cooling occurred within decades to a few centuries of eruption; it is difficult to reconcile such a sudden drop in temperature with a model of a long-lived, stable magma reservoir. If cooling of the reservoir did cause crystal growth, then some other process — such as the transfer of the magma to a cooler part of the crust — must have triggered the cooling.

Precursory eruptions prior to the Cape Riva are unlikely to have caused the growth of the Cape Riva crystals No products of precursory volcanic activity are preserved on Santorini after the last Therasia dacite at 39.4 ± 2.2 ka. Precursory degassing would not leave much evidence in the geological record, however precursory degassing raises much the same questions as cooling. If the reservoir is present in the shallow crust for long periods of time, what would cause it to start degassing only shortly before eruption?

The zoning patterns of the phenocrysts show that crystal growth was coincident with the amalgamation of compositionally diverse melts (silicic andesite to rhyodacite), and a major reorganisation of the plumbing system must have occurred a few decades before the Cape Riva eruption. If a hotter dacitic melts were mixed into cooler rhyodacitic melts, then the dacites would cool and start to crystallise.

The final process capable of triggering the growth of the phenocrysts is through the upward movement and decompression of the magma. The the Cape Riva dacite was probably stored at about 2 kbar had about 6 wt% water in the melt (Cadoux et al., 2013, 2014). The same magma at 4 kbar would be close to its liquidus, and would not contain any plagioclase or orthopyroxene crystals. Transferring the magma upwards from about 4 kbar to about 2 kbar would trigger the growth of ∼10 % phenocrysts. This interpretation is consistent with magma storage depths estimated from experimental petrology (Figure 8.1). It is possible that the mafic parental magma for the Cape Riva was stored in the lower reservoir, where it partially crystallised. The melt from this stage, which had the same composition as the bulk Cape Riva, then separated from its crystals and ascended in to the upper reservoir.

In summary: the growth of the phenocrysts in the both the Cape Riva and Therasia dacites was probably caused by a mixture of cooling and decompression triggered by the amalgamation and emplacement of multiple batches of compositionally diverse melts (silicic andesite to rhyodacite) in the shallow crust.

8.5 The evolution of the volcanic plumbing system prior to the Cape Riva eruption

I now bring together all of the evidence presented in this thesis in order to put forward an integrated model of the evolution of the plumbing system of Santorini in the build-up to the Cape Riva eruption.

8.5.1 Skaros–Upper Scoria 2 (67–54 ka)

The Skaros shield was studied in detail by Huijsmans (1985) and Huijsmans and Barton (1989), and their conclusions are presented here for completeness. The oldest Skaros lava has been dated at 67 ± 9 ka (Druitt et al., 1999). During the Skaros period the volcano is interpreted as having behaved as an open conduit. The eruptive rate was

high, and close to the long-term average for Santorini ($\sim$1 km^3). The volcanic activity mostly involved the extrusion of andesites and relatively primitive basalts.

A few times during this period, the system began to stagnate and the composition of the erupted magma became steadily more evolved. Each of these cycles ended with a minor explosive eruption, leaving pumice fall and phreatomagmatic deposits. The last of these failed stagnations ended with the Upper Scoria 2 eruption, at 54 ± 3 ka (Druitt et al., 1999). The Upper Scoria 2 eruption began with a small dacitic pumice and ash fall, before discharging several km^3 of andesitic scoria as pyroclastic flows (Mellors and Sparks, 1991). This was the first time dacite had been erupted at Santorini since the beginning of the Skaros period.

8.5.2 Early Therasia period (54–39 ka)

After the Upper Scoria 2 eruption, the volcano entered a period of near-repose where the eruption rate dropped to <0.1 km^3 ky^{-1}. The activity consisted of only a few andesitic lavas, such as the Lower Therasia andesite (48.2 ± 24 ka). The Andesite of Oia was probably also erupted during this period; its composition is very similar to that of the Upper Scoria 2 andesite, and it is probably remnant magma from that eruption. It is possible that the weight of the Skaros edifice during this period prevented the ascent of magma to the surface, trapping the incoming mafic magma at depth (Pinel and Jaupart, 2000, 2004).

8.5.3 The Therasia dacites (39–25 ka)

The first erupted dacite after the Upper Scoria 2 eruption was erupted at 39.4 ± 2.2 ka. From this point on, mafic magma was only erupted as minor ($\ll 0.1$ %) basaltic enclaves. Incoming mafic magma was probably still being trapped at depth. Accumulation of heat from prolonged, deep intrusion probably generated silicic melt by a combination of fractional crystallisation, partial melting of crustal rocks and defrosting of extant

mushy intrusions (Barton et al., 1983; Druitt et al., 1999; Huijsmans, 1985; Huijsmans and Barton, 1989; Mann, 1983).

While the Therasia dacites have been interpreted as leaks from the growing Cape Riva magma reservoir (Druitt, 1985), the differences in incompatible element concentrations in the Therasia and Cape Riva dacites suggest this is not the case. While I cannot rule out the possibility that the Therasia dacites were fed from a single, long-lived reservoir, it is more likely that they were fed from a series of small, ephemeral reservoirs. Small batches of dacitic melt would have been sequentially emplaced in the shallow crust, at a depth corresponding to a presure of about 2 kbar (∼8 km; Figure 8.1). This emplacement would have driven crystal growth through a mixture of cooling and decompression. Occasional inputs of less evolved magma would have caused the sawtooth zoning in the plagioclases and the high-Mg zones in the orthopyroxenes. Gabbroic nodules were incorporated into the magma from plutonic material intruded during previous volcanic activity at Santorini, and some plagioclase crystals from this plutonic material became the cores of new plagioclase phenocrysts. Eruption occurred within a few decades to centuries of the onset of crystallisation.

The Therasia period ended with the eruption of the upper Therasia andesite, a hybrid andesite formed by mixing ∼60 wt% Therasia dacite with ∼40 wt% basalt. This hybrid andesite represents the first time that basaltic magma had ascended into the shallow crust since the eruption of the first Therasia dacite, and may have signalled an increase in the rate magma supply from depth. Increasing explosivity towards the top of the Therasia sequence was also potentially a result of this increase in magma flux.

The youngest dated Therasia lava was erupted at 24.6 ± 1.3 ka, $2{,}800 \pm 1{,}400$ y before the Cape Riva eruption.

8.5.4 The build-up to the Cape Riva eruption (25–22 ka)

As argued above, most of the Cape Riva magma probably arrived in the shallow crust after the extrusion of the last Therasia dacite. At 26 ka the system may have been

replenished by incompatible-depleted silicic melt, which mixed with Therasia dacite and was discharged as the Cape Tripiti Pumice. The subsequent return to eruption of "pure" Therasia dacite suggests that if a discrete Cape Riva reservoir already existed below the summit at this time, it had probably not yet reached its full size. Following extrusion of the last Therasia lava flow, the input of incompatible-depleted silicic melt continued, and perhaps accelerated, during the $< 2\,800 \pm 1\,400$ y preceding the Cape Riva eruption.

The Cape Riva magma reservoir formed through the amalgamation of multiple compositionally diverse melts (silicic andesite to rhyodacite). Crystallisation of plagioclase and orthopyroxene was triggered by a mixture of decompression and cooling. Sawtooth zoning in the plagioclases was generated as the crystals cycled between hotter and cooler melts. Crystals transferred from a cooler rhyodacite to a hotter, less evolved melt were first partially resorbed, then overgrown with more calcic plagioclase. A similar story is recorded in the orthopyroxene crystals. Crystal high-temperature residence times indicate that this occurred within a few decades to centuries before eruption. The entire reservoir was then homogenised prior to eruption.

If the Cape Riva magma reservoir did not exist in the shallow crust during the Therasia period, then a robust minimum magma supply rate can be calculated assuming that most of the $>10\,km^3$ of Cape Riva magma was injected into the shallow crust in the $<2{,}800 \pm 1{,}400$ y between the last Therasia eruption and the onset of the Cape Riva eruption. This yields a time-averaged supply rate of $>0.004 \pm 0.002\,km^3\,y^{-1}$. The high-temperature residence times of the phenocrysts are much shorter than the break between the end of the Therasia period and the Cape Riva eruption. This suggests that supply rates could be much greater, although the phenocrysts may only record the last few pulses of reservoir assembly rather than the accumulation of the entire Cape Riva magma body. Using the longest high-temperature residence time found in the plagioclase phenocrysts (400 y), the magma supply rate rises to $>0.025\,km^3\,y^{-1}$, and using the longest high-temperature residence time found for the orthopyroxene crystals

(40 y) gives a supply rate of $>0.25\,km^3\,y^{-1}$.

For comparison, the mean accumulation rate estimated over the 1600 y to prior the Oruanui eruption has been estimated as $>0.33\,km^3\,y^{-1}$, culminating in values of $\sim 1\,km^3\,y^{-1}$ (Allan et al., 2013; Wilson and Charlier, 2009). A late-stage growth spurt of the Minoan magma reservoir has been estimated as $>0.05\,km^3\,y^{-1}$ (Druitt et al., 2012). Intrusion rates comparable to, or higher than, that estimated for the Cape Riva are implied by measured deformation rates at silicic volcanoes such as Uturuncu ($\sim 0.01\,km^3\,y^{-1}$; Pritchard and Simons, 2004; Sparks et al., 2008), Kameni ($\sim 0.01\,km^3\,y^{-1}$; Parks et al., 2012), Yellowstone ($\sim 0.1\,km^3\,y^{-1}$; Chang et al., 2010), and Lazufre ($\sim 0.01\,km^3\,y^{-1}$; Froger et al., 2007; Ruch et al., 2009).

Rapid intrusion of the Cape Riva dacite into the upper crust would have favoured runaway growth of a melt-dominated magma reservoir (Annen, 2009; Gelman et al., 2013; Schöpa and Annen, 2013). Driving mechanisms for magma ascent may have included increased basaltic flux from the mantle, tectonic forces, or gravitational instability of crustal magma storage regions. Possible evidence of increased basaltic flux is provided by the production of hybrid andesites (formed by mixing of basalt and dacite in approximately equal proportions) in the few thousand years prior to the Cape Riva eruption, as well as in the Cape Riva reservoir itself. Pressurization of the upper crustal plumbing system by sustained, high-flux injection of dacite and basalt may have triggered the transition from prolonged, largely effusive activity to catastrophic explosive eruption and caldera collapse.

References

Ague, J. J. and Baxter, E. F. (2007). Brief thermal pulses during mountain building recorded by Sr diffusion in apatite and multicomponent diffusion in garnet. *Earth and Planetary Science Letters*, 261(3-4):500–516. doi:10.1016/j.epsl.2007.07.017.

Allan, A. S. R., Morgan, D. J., Wilson, C. J. N., and Millet, M.-A. (2013). From mush to eruption in centuries: assembly of the super-sized Oruanui magma body. *Contributions to Mineralogy and Petrology*, 166(1):143–164. doi:10.1007/s00410-013-0869-2.

Allan, A. S. R., Wilson, C. J. N., Millet, M.-A., and Wysoczanski, R. J. (2012). The invisible hand: Tectonic triggering and modulation of a rhyolitic supereruption. *Geology*, 40(6):563–566. doi:10.1130/G32969.1.

Allen, S. R. and Cas, R. A. F. (1998). Rhyolitic fallout and pyroclastic density current deposits from a phreatoplinian eruption in the eastern Aegean Sea, Greece. *Journal of Volcanology and Geothermal Research*, 86(1-4):219–251. doi:10.1016/S0377-0273(98)00080-8.

Allen, S. R., Stadlbauer, E., and Keller, J. (1999). Stratigraphy of the Kos Plateau Tuff: product of a major Quaternary explosive rhyolitic eruption in the eastern Aegean, Greece. *International Journal of Earth Sciences*, 88:132–156. doi:10.1007/s005310050251.

Andersen, D. J. and Lindsley, D. H. (1985). New (and final!) models for the Ti-magnetite/ilmenite geothermometer and oxygen barometer. *Eos, Transactions of the American Geophysical Union*, 66(18):416.

Anderson, A. T., Davis, A. M., and Lu, F. (2000). Evolution of Bishop Tuff rhyolitic magma based on melt and magnetite inclusions and zoned phenocrysts. *Journal of Petrology*, 41(3):449–473.

Andrews, B. J., Gardner, J. E., and Housh, T. B. (2008). Repeated recharge, assimilation, and hybridization in magmas erupted from El Chichón as recorded by plagioclase and amphibole phenocrysts. *Journal of Volcanology and Geothermal Research*, 175(4):415–426. doi:10.1016/j.jvolgeores.2008.02.017.

Andújar, J., Scaillet, B., Pichavant, M., and Druitt, T. H. (2010). Differentiation conditions of a basaltic magma from Santorini and its bearing on andesitic/dacitic magma production. Abstract V43A-2354 presented at AGU Fall Meeting, San Francisco, California, 13-17 December.

Annen, C. (2009). From plutons to magma chambers: Thermal constraints on the accumulation of eruptible silicic magma in the upper crust. *Earth and Planetary Science Letters*, 284(3-4):409–416. doi:10.1016/j.epsl.2009.05.006.

Annen, C., Blundy, J. D., and Sparks, R. S. J. (2006). The genesis of intermediate and silicic magmas in deep crustal hot zones. *Journal of Petrology*, 47(3):505–539. doi:10.1093/petrology/egi084.

Annen, C., Paulatto, M., Sparks, R. S. J., Minshull, T. A., and Kiddle, E. J. (2014). Quantification of the intrusive magma fluxes during magma chamber growth at Soufrière Hills Volcano (Montserrat, Lesser Antilles). *Journal of Petrology*, 55(3):529–548. doi:10.1093/petrology/egt075.

Arce, J. L., Gardner, J. E., and Macías, J. L. (2012). Pre-eruptive conditions of dacitic magma erupted during the 21.7 ka Plinian event at Nevado de Toluca volcano, Central Mexico. *Journal of Volcanology and Geothermal Research*. doi:10.1016/j.jvolgeores.2012.09.012.

Asku, A. E., Jenner, G., Hiscott, R. N., and İşler, E. B. (2008). Occurrence, stratigraphy and geochemistry of Late Quaternary tephra layers in the Aegean Sea and the Marmara Sea. *Marine Geology*, 252(3-4):174–192. doi:10.1016/j.margeo.2008.04.004.

Avigad, D. and Garfunkel, Z. (1991). Uplift and exhumation of high-pressure metamorphic terrains: the example of the Cycladic blueschist belt (Aegean Sea). *Tectonophysics*, 188(3-4):357–372. doi:10.1016/0040-1951(91)90464-4.

Bachmann, O. and Bergantz, G. W. (2004). On the origin of crystal-poor rhyolites: Extracted from batholithic crystal mushes. *Journal of Petrology*, 45(8):1565 –1582. doi:10.1093/petrology/egh019.

Bachmann, O. and Bergantz, G. W. (2006). Gas percolation in upper-crustal silicic crystal mushes as a mechanism for upward heat advection and rejuvenation of near-solidus magma bodies. *Journal of Volcanology and Geothermal Research*, 149(1–2):85–102. doi:10.1016/j.jvolgeores.2005.06.002.

Bachmann, O. and Bergantz, G. W. (2008a). The magma reservoirs that feed supereruptions. *Elements*, 4(1):17–21. doi:10.2113/GSELEMENTS.4.1.17.

Bachmann, O. and Bergantz, G. W. (2008b). Rhyolites and their source mushes across tectonic settings. *Journal of Petrology*, 49(12):2277 –2285. doi:10.1093/petrology/egn068.

Bachmann, O., Charlier, B. L. A., and Lowenstern, J. B. (2007a). Zircon crystallization and recycling in the magma chamber of the rhyolitic Kos Plateau Tuff (Aegean Arc). *Geology*, 35(1):73–76. doi:10.1130/G23151A.1.

Bachmann, O., Dungan, M., and Lipman, P. W. (2002). The Fish Canyon magma body, San Juan Volcanic Field, Colorado: Rejuvenation and eruption of an upper-crustal batholith. *Journal of Petrology*, 43(8):1469–1503. doi:10.1093/petrology/43.8.1469.

Bachmann, O., Oberli, F., Dungan, M. A., Meier, M., Mundil, R., and Fischer, H. (2007b). $^{40}Ar/^{39}Ar$ and U–Pb dating of the Fish Canyon magmatic system, San Juan Volcanic Field, Colorado: Evidence for an extended crystallization history. *Chemical Geology*, 236(1–2):134–166. doi:10.1016/j.chemgeo.2006.09.005.

Bacon, C. R. (1985). Implications of silicic vent patterns for the presence of large crustal magma chambers. *Journal of Geophysical Research*, 90(B13):11,243–11,252. doi:10.1029/JB090iB13p11243.

Bacon, C. R., Adami, L. H., and Lanphere, M. A. (1989). Direct evidence for the origin of low-^{18}O silicic magmas: quenched samples of a magma chamber's partially-fused granitoid walls, Crater Lake, Oregon. *Earth and Planetary Science Letters*, 96(1–2):199–208. doi:10.1016/0012-821X(89)90132-5.

Bacon, C. R. and Druitt, T. H. (1988). Compositional evolution of the zoned calcalkaline magma chamber of Mount Mazama, Crater Lake, Oregon. *Contributions to Mineralogy and Petrology*, 98(2):224–256. doi:10.1007/BF00402114.

Bacon, C. R. and Lanphere, M. A. (2006). Eruptive history and geochronology of Mount Mazama and the Crater Lake region, Oregon. *Geological Society of America Bulletin*, 118(11-12):1331–1359. doi:10.1130/B25906.1.

Bacon, C. R. and Lowenstern, J. B. (2005). Late Pleistocene granodiorite source for recycled zircon and phenocrysts in rhyodacite lava at Crater Lake, Oregon. *Earth and Planetary Science Letters*, 233(3-4):277–293. doi:10.1016/j.epsl.2005.02.012.

Bacon, C. R., Persing, H. M., Wooden, J. L., and Ireland, T. R. (2000). Late Pleistocene granodiorite beneath Crater Lake caldera, Oregon, dated by ion microprobe. *Geology*, 28(5):467–470. doi:10.1130/0091-7613(2000)28<467:LPGBCL>2.0.CO;2.

Bailey, J., Jensen, E., Hansen, A., Kann, A., and Kann, K. (2009). Formation of heterogeneous magmatic series beneath north Santorini, south Aegean island arc. *Lithos*, 110(1-4):20–36. doi:10.1016/j.lithos.2008.12.002.

Barth, A. P., Feilen, A. D. G., Yager, S. L., Douglas, S. R., Wooden, J. L., Riggs, N. R., and Walker, J. D. (2012). Petrogenetic connections between ash-flow tuffs and a granodioritic to granitic intrusive suite in the Sierra Nevada arc, California. *Geosphere*. doi:10.1130/GES00737.1.

Barton, M. and Huijsmans, J. P. P. (1986). Post-caldera dacites from the Santorini volcanic complex, Aegean Sea, Greece: an example of the eruption of lavas of near-constant composition over a 2,200 year period. *Contributions to Mineralogy and Petrology*, 94(4):472–495. doi:10.1007/BF00376340.

Barton, M., Salters, V. J. M., and Huijsmans, J. P. P. (1983). Sr isotope and trace element evidence for the role of continental crust in calc-alkaline volcanism on Santorini and Milos, Aegean Sea, Greece. *Earth and Planetary Science Letters*, 63(2):273–291. doi:10.1016/0012-821X(83)90042-0.

Baschek, G. and Johannes, W. (1995). The estimation of NaSi–CaAl interdiffusion rates in peristerite by homogenization experiments. *European Journal of Mineralogy*, 7(2):295–307.

Bédard, J. H. (2006). Trace element partitioning in plagioclase feldspar. *Geochimica et Cosmochimica Acta*, 70(14):3717–3742. doi:10.1016/j.gca.2006.05.003.

Bédard, J. H. (2007). Trace element partitioning coefficients between silicate melts and orthopyroxene: Parameterizations of D variations. *Chemical Geology*, 244(1–2):263–303. doi:10.1016/j.chemgeo.2007.06.019.

Behrens, H., Johannes, W., and Schmalzried, H. (1990). On the mechanisms of cation diffusion processes in ternary feldspars. *Physics and Chemistry of Minerals*, 17(1):62–78. doi:10.1007/BF00209227.

Béjina, F., Jaoul, O., and Liebermann, R. C. (2003). Diffusion in minerals at high pressure: a review. *Physics of The Earth and Planetary Interiors*, 139(1-2):3–20. doi:10.1016/S0031-9201(03)00140-7.

Béjina, F., Sautter, V., and Jaoul, O. (2009). Cooling rate of chondrules in ordinary chondrites revisited by a new geospeedometer based on the compensation rule. *Physics of the Earth and Planetary Interiors*, 172(1-2):5–12. doi:10.1016/j.pepi.2008.08.014.

Benetatos, C., Kiratzi, A., Papazachos, C., and Karakaisis, G. (2004). Focal mechanisms of shallow and intermediate depth earthquakes along the Hellenic arc. *Journal of Geodynamics*, 37(2):253–296. doi:10.1016/j.jog.2004.02.002.

Bindeman, I. N., Davis, A. M., and Drake, M. J. (1998). Ion microprobe study of plagioclase-basalt partition experiments at natural concentration levels of trace elements. *Geochimica et Cosmochimica Acta*, 62(7):1175–1193. doi:10.1016/S0016-7037(98)00047-7.

Bindeman, I. N., Sigmarsson, O., and Eiler, J. (2006). Time constraints on the origin of large volume basalts derived from O-isotope and trace element mineral zoning and U-series disequilibria in the Laki and Grímsvötn volcanic system. *Earth and Planetary Science Letters*, 245(1-2):245–259. doi:10.1016/j.epsl.2006.02.029.

Bindeman, I. N. and Valley, J. W. (2001). Low-δ^{18}O rhyolites from Yellowstone: Magmatic evolution based on analyses of zircons and individual phenocrysts. *Journal of Petrology*, 42(8):1491 –1517. doi:10.1093/petrology/42.8.1491.

Bindeman, I. N. and Valley, J. W. (2002). Oxygen isotope study of the Long Valley magma system, California: isotope thermometry and convection in large silicic magma bodies. *Contributions to Mineralogy and Petrology*, 144(2):185–205. doi:10.1007/s00410-002-0371-8.

Bindeman, I. N. and Valley, J. W. (2003). Rapid generation of both high- and low-δ^{18}O, large-volume silicic magmas at the Timber Mountain/Oasis Valley caldera complex, Nevada. *Geological Society of America Bulletin*, 115(5):581–595. doi:10.1130/0016-7606(2003)115<0581:RGOBHA>2.0.CO;2.

Blundy, J. and Cashman, K. (2008). Petrologic reconstruction of magmatic system variables and processes. *Reviews in Mineralogy and Geochemistry*, 69(1):179–239. doi:10.2138/rmg.2008.69.6.

Blundy, J. and Wood, B. (2003). Partitioning of trace elements between crystals and melts. *Earth and Planetary Science Letters*, 210(3-4):383–397. doi:10.1016/S0012-821X(03)00129-8.

Blundy, J. D. and Wood, B. J. (1991). Crystal-chemical controls on the partitioning of Sr and Ba between plagioclase feldspar, silicate melts, and hydrothermal solutions. *Geochimica et Cosmochimica Acta*, 55(1):193–209. doi:10.1016/0016-7037(91)90411-W.

Bohnhoff, M., Rische, M., Meier, T., Becker, D., Stavrakakis, G., and Harjes, H. (2006). Microseismic activity in the Hellenic Volcanic Arc, Greece, with emphasis on the seismotectonic setting of the Santorini-Amorgos zone. *Tectonophysics*, 423(1-4):17–33. doi:10.1016/j.tecto.2006.03.024.

Bolhar, R., Ring, U., and Allen, C. (2010). An integrated zircon geochronological and geochemical investigation into the miocene plutonic evolution of the Cyclades, Aegean Sea, Greece: Part 1: Geochronology. *Contributions to Mineralogy and Petrology*, 160(5):719–742. doi:10.1007/s00410-010-0504-4.

Bowen, N. L. (1915). Supplement: The later stages of the evolution of the igneous rocks. *The Journal of Geology*, 23(8):1–91.

Boyce, J. W. and Hervig, R. L. (2008). Magmatic degassing histories from apatite volatile stratigraphy. *Geology*, 36(1):63–66. doi: 10.1130/G24184A.1 .

Brady, J. B. (1995). Diffusion data for silicate minerals, glasses and liquids. In Ahrens, T. J., editor, *Mineral physics & crystallography: A handbook of physical constants*, number 2 in AGU Reference Shelf, pages 269–290. American Geophysical Union, Washington, D.C.

Briqueu, L., Javoy, M., Lancelot, J. R., and Tatsumoto, M. (1986). Isotope geochemistry of recent magmatism in the Aegean arc: Sr, Nd, Hf, and O isotopic ratios in the lavas of Milos and Santorini—geodynamic implications. *Earth and Planetary Science Letters*, 80(1-2):41–54. doi:10.1016/0012-821X(86)90018-X.

Brombach, T., Caliro, S., Chiodini, G., Fiebig, J., Hunziker, J. C., and Raco, B. (2003). Geochemical evidence for mixing of magmatic fluids with seawater, Nisyros hydrothermal system, Greece. *Bulletin of Volcanology*, 65:505–516. doi:10.1007/s00445-003-0278-x.

Brown, E. H., Talbot, J. L., McClelland, W. C., Feltman, J. A., Lapen, T. J., Bennett, J. D., Hettinga, M. A., Troost, M. L., Alvarez, K. M., and Calvert, A. T. (2000). Interplay of plutonism and regional deformation in an obliquely convergent arc, southern Coast Belt, British Columbia. *Tectonics*, 19(3):493–511. doi:10.1029/1999TC001168.

Brown, M. and Solar, G. S. (1998). Shear-zone systems and melts: feedback relations and self-organization in orogenic belts. *Journal of Structural Geology*, 20(2–3):211–227. doi:10.1016/S0191-8141(97)00068-0.

Brown, S. J. A. and Fletcher, I. R. (1999). SHRIMP U–Pb dating of the preeruption growth history of zircons from the 340 ka Whakamaru Ignimbrite, New Zealand: Evidence for >250 k.y. magma residence times. *Geology*, 27(11):1035–1038. doi:10.1130/0091-7613(1999)027<1035:SUPDOT>2.3.CO;2.

Bruins, H. J., MacGillivray, J. A., Synolakis, C. E., Benjamini, C., Keller, J., Kisch, H. J., Klügel, A., and van der Plicht, J. (2008). Geoarchaeological tsunami deposits at Palaikastro (Crete) and the Late Minoan IA eruption of Santorini. *Journal of Archaeological Science*, 35(1):191–212. doi:16/j.jas.2007.08.017.

Buening, D. K. and Buseck, P. R. (1973). Fe–Mg lattice diffusion in olivine. *Journal of Geophysical Research*, 78(29):6852–6862. doi:10.1029/JB078i029p06852.

Buettner, A., Kleinhanns, I. C., Rufer, D., Hunziker, J. C., and Villa, I. M. (2005). Magma generation at the easternmost section of the hellenic arc: Hf, Nd, Pb and Sr isotope geochemistry of Nisyros and Yali volcanoes (Greece). *Lithos*, 83(1-2):29–46. doi:10.1016/j.lithos.2005.01.001.

Burgisser, A. and Bergantz, G. W. (2011). A rapid mechanism to remobilize and homogenize highly crystalline magma bodies. *Nature*, 471(7337):212–215. doi:10.1038/nature09799.

Cadoux, A., Andújar, J., Scaillet, B., Druitt, T. H., and Deloule, E. (2013). Santorini volcano magma plumbing system: constraints from a combined experimental and natural products study. Abstract 4W_1B-P9, IAVCEI Scientific Assembly, 20–24 July 2013, Kagoshima, Japan.

Cadoux, A., Scaillet, B., Druitt, T. H., and Deloule, E. (2014). Magma storage conditions of large Plinian eruptions of Santorini Volcano. *Submitted to Journal of Petrology*.

Caliro, S., Chiodini, G., Galluzzo, D., Granieri, D., La Rocca, M., Saccorotti, G., and Ventura, G. (2004). Recent activity of Nisyros volcano (Greece) inferred from structural, geochemical and seismological data. *Bulletin of Volcanology*, 67:358–369. doi:10.1007/s00445-004-0381-7.

Cantner, K., Carey, S., and Nomikou, P. (2014). Integrated volcanologic and petrologic analysis of the 1650 AD eruption of Kolumbo submarine volcano, Greece. *Journal of Volcanology and Geothermal Research*, 269:28–43. doi:10.1016/j.jvolgeores.2013.10.004.

Carey, S., Nomikou, P., Croff Bell, K. L., Lilley, M., Lupton, J., Roman, C., Stathopoulou, E., Bejelou, K., and Ballard, R. (2013). CO_2 degassing from hydrothermal vents at Kolumbo submarine volcano, Greece, and the accumulation of acidic crater water. *Geology*, 41(9):1035–1038. doi:10.1130/G34286.1.

Caricchi, L., Annen, C., Blundy, J., Simpson, G., and Pinel, V. (2014). Frequency and magnitude of volcanic eruptions controlled by magma injection and buoyancy. *Nature Geoscience*, 7(2):126–130. doi:10.1038/ngeo2041.

Chakraborty, S. (2008). Diffusion in solid silicates: A tool to track timescales of processes comes of age. *Annual Review of Earth and Planetary Sciences*, 36(1):153–190. doi:10.1146/annurev.earth.36.031207.124125.

Chamberlain, K. J., Wilson, C. J. N., Wooden, J. L., Charlier, B. L. A., and Ireland, T. R. (2014). New perspectives on the Bishop Tuff from zircon textures, ages and trace elements. *Journal of Petrology*, 55(2):395–426. doi:10.1093/petrology/egt072.

Chang, W.-L., Smith, R. B., Farrell, J., and Puskas, C. M. (2010). An extraordinary episode of Yellowstone caldera uplift, 2004-–2010, from GPS and InSAR observations. *Geophysical Research Letters*, 37:L23302. doi:201010.1029/2010GL045451.

Charlier, B. L. A., Morgan, D. J., Wilson, C. J. N., Wooden, J. L., Allan, A. S. R., and Baker, J. A. (2012). Lithium concentration gradients in feldspar and quartz record the final minutes of magma ascent in an explosive supereruption. *Earth and Planetary Science Letters*, 319-320:218–227. doi:10.1016/j.epsl.2011.12.016.

Charlier, B. L. A., Wilson, C. J. N., Lowenstern, J. B., Blake, S., van Calsteren, P. W., and Davidson, J. P. (2005). Magma generation at a large, hyperactive silicic volcano (Taupo, New Zealand) revealed by U–Th and U–Pb systematics in zircons. *Journal of Petrology*, 46(1):3 –32. doi:10.1093/petrology/egh060.

Cherniak, D. J. (1995). Diffusion of lead in plagioclase and K-feldspar: an investigation using Rutherford backscattering and resonant nuclear reaction analysis. *Contributions to Mineralogy and Petrology*, 120(3-4):358–371. doi:10.1007/BF00306513.

Cherniak, D. J. (2002a). Ba diffusion in feldspar. *Geochimica et Cosmochimica Acta*, 66(9):1641–1650. doi:10.1016/S0016-7037(01)00866-3.

Cherniak, D. J. (2002b). REE diffusion in feldspar. *Chemical Geology*, 193(1-2):25–41. doi:10.1016/S0009-2541(02)00246-2.

Cherniak, D. J. (2003). Silicon self-diffusion in single-crystal natural quartz and feldspar. *Earth and Planetary Science Letters*, 214(3-4):655–668. doi:10.1016/S0012-821X(03)00394-7.

Cherniak, D. J. (2010). Cation diffusion in feldspars. *Reviews in Mineralogy and Geochemistry*, 72(1):691–733. doi:10.2138/rmg.2010.72.15.

Cherniak, D. J. and Dimanov, A. (2010). Diffusion in pyroxene, mica and amphibole. *Reviews in Mineralogy and Geochemistry*, 72(1):641–690. doi:10.2138/rmg.2010.72.14.

Cherniak, D. J., Hervig, R., Koepke, J., Zhang, Y., and Zhao, D. (2010). Analytical methods in diffusion studies. *Reviews in Mineralogy and Geochemistry*, 72(1):107–170. doi:10.2138/rmg.2010.72.4.

Cherniak, D. J. and Watson, E. B. (1992). A study of strontium diffusion in K-feldspar, Na-K feldspar and anorthite using Rutherford backscattering spectroscopy. *Earth and Planetary Science Letters*, 113(3):411–425. doi:10.1016/0012-821X(92)90142-I.

Cherniak, D. J. and Watson, E. B. (1994). A study of strontium diffusion in plagiclase using Rutherford backscattering spectroscopy. *Geochimica et Cosmochimica Acta*, 58(23):5179–5190. doi:10.1016/0016-7037(94)90303-4.

Cherniak, D. J. and Watson, E. B. (2001). Pb diffusion in zircon. *Chemical Geology*, 172(1–2):5–24. doi:10.1016/S0009-2541(00)00233-3.

Cherniak, D. J. and Watson, E. B. (2012). Diffusion of helium in olivine at 1 atmosphere and 2.7 GPa. *Geochimica et Cosmochimica Acta*, 84:269–279. doi:10.1016/j.gca.2012.01.042.

Christensen, J. N. and DePaolo, D. J. (1993). Time scales of large volume silicic magma systems: Sr isotopic systematics of phenocrysts and glass from the Bishop Tuff, Long Valley, California. *Contributions to Mineralogy and Petrology*, 113(1):100–114. doi:10.1007/BF00320834.

Cioni, R., Gurioli, L., Sbrana, A., and Vougioukalakis, G. (2000). Precursors to the Plinian eruptions of Thera (Late Bronze Age) and Vesuvius (AD 79): Data from archaeological areas. *Physics and Chemistry of the Earth, Part A: Solid Earth and Geodesy*, 25(9-11):719–724. doi:10.1016/S1464-1895(00)00111-3.

Claiborne, L. L., Miller, C. F., Flanagan, D. M., Clynne, M. A., and Wooden, J. L. (2010). Zircon reveals protracted magma storage and recycling beneath Mount St. Helens. *Geology*, 38(11):1011–1014. doi:10.1130/G31285.1.

Clift, P. and Blusztajn, J. (1999). The trace-element characteristics of Aegean and Aeolian volcanic arc marine tephra. *Journal of Volcanology and Geothermal Research*, 92(3-4):321–347. doi:10.1016/S0377-0273(99)00059-1.

Coleman, D. S., Gray, W., and Glazner, A. F. (2004). Rethinking the emplacement and evolution of zoned plutons: Geochronologic evidence for incremental assembly of the Tuolumne Intrusive Suite, California. *Geology*, 32(5):433–436. doi:10.1130/G20220.1.

Coogan, L. A., Kasemann, S. A., and Chakraborty, S. (2005). Rates of hydrothermal cooling of new oceanic upper crust derived from lithium-geospeedometry. *Earth and Planetary Science Letters*, 240(2):415–424. doi:10.1016/j.epsl.2005.09.020.

Coombs, M. L., Eichelberger, J. C., and Rutherford, M. J. (2000). Magma storage and mixing conditions for the 1953–1974 eruptions of Southwest Trident volcano, Katmai National Park, Alaska. *Contributions to Mineralogy and Petrology*, 140(1):99–118. doi:10.1007/s004100000166.

Cooper, K. M. and Kent, A. J. R. (2014). Rapid remobilization of magmatic crystals kept in cold storage. *Nature*, 506:480–483. doi:10.1038/nature12991.

Costa, F. (2008). Residence times of silicic magmas associated with calderas. In Gottsmann, J. and Martí, J., editors, *Caldera volcanism: analysis, modelling and response*, volume 10 of *Developments in Volcanology*, pages 1–55. Elsevier.

Costa, F. and Chakraborty, S. (2004). Decadal time gaps between mafic intrusion and silicic eruption obtained from chemical zoning patterns in olivine. *Earth and Planetary Science Letters*, 227(3-4):517–530. doi:10.1016/j.epsl.2004.08.011.

Costa, F. and Chakraborty, S. (2008). The effect of water on Si and O diffusion rates in olivine and implications for transport properties and processes in the upper mantle. *Physics of the Earth and Planetary Interiors*, 166(1-2):11–29. doi:10.1016/j.pepi.2007.10.006.

Costa, F., Chakraborty, S., and Dohmen, R. (2003). Diffusion coupling between trace and major elements and a model for calculation of magma residence times using plagioclase. *Geochimica et Cosmochimica Acta*, 67(12):2189–2200. doi:10.1016/S0016-7037(02)01345-5.

Costa, F., Coogan, L. A., and Chakraborty, S. (2009). The time scales of magma mixing and mingling involving primitive melts and melt–mush interaction at mid-ocean ridges. *Contributions to Mineralogy and Petrology*, 159(3):371–387. doi:10.1007/s00410-009-0432-3.

Costa, F., Dohmen, R., and Chakraborty, S. (2008). Time scales of magmatic processes from modelling the zoning patterns of crystals. *Reviews in Mineralogy and Geochemistry*, 69(1):545–594. doi:10.2138/rmg.2008.69.14.

Cottrell, E., Gardner, J. E., and Rutherford, M. J. (1999). Petrologic and experimental evidence for the movement and heating of the pre-eruptive Minoan rhyodacite (Santorini, Greece). *Contributions to Mineralogy and Petrology*, 135(4):315–331. doi:10.1007/s004100050514.

D'Alessandro, W., Brusca, L., Kyriakopoulos, K., Michas, G., and Papadakis, G. (2008). Methana, the westernmost active volcanic system of the south Aegean arc (Greece): insight from fluids geochemistry. *Journal of Volcanology and Geothermal Research*, 178(4):818–828. doi:10.1016/j.jvolgeores.2008.09.014.

D'Alessandro, W., Brusca, L., Kyriakopoulos, K., Rotolo, S., Michas, G., Minio, M., and Papadakis, G. (2006). Diffuse and focused carbon dioxide and methane emissions from the Sousaki geothermal system, Greece. *Geophysical Research Letters*, 33:L05307. doi:200610.1029/2006GL025777.

Daly, R. A. (1914). *Igneous rocks and their origin*. McGraw-Hill Book Company, New York.

Davidson, J., Tepley III, F., Palacz, Z., and Meffan-Main, S. (2001). Magma recharge, contamination and residence times revealed by in situ laser ablation isotopic analysis of feldspar in volcanic rocks. *Earth and Planetary Science Letters*, 184(2):427–442. doi:10.1016/S0012-821X(00)00333-2.

Davies, G. R. and Halliday, A. N. (1998). Development of the Long Valley rhyolitic magma system: strontium and neodymium isotope evidence from glasses and individual phenocrysts. *Geochimica et Cosmochimica Acta*, 62(21-22):3561–3574. doi:10.1016/S0016-7037(98)00247-6.

Davies, G. R., Halliday, A. N., Mahood, G. A., and Hall, C. M. (1994). Isotopic constraints on the production rates, crystallisation histories and residence times of pre-caldera silicic magmas, Long Valley, California. *Earth and Planetary Science Letters*, 125(1-4):17–37. doi:10.1016/0012-821X(94)90204-6.

Davis, J. W., Coleman, D. S., Gracely, J. T., Gaschnig, R., and Stearns, M. (2011). Magma accumulation rates and thermal histories of plutons of the Sierra Nevada batholith, CA. *Contributions to Mineralogy and Petrology*. doi:10.1007/s00410-011-0683-7.

Deering, C. D., Bachmann, O., and Vogel, T. A. (2011). The Ammonia Tanks Tuff: Erupting a melt-rich rhyolite cap and its remobilized crystal cumulate. *Earth and Planetary Science Letters*, 310(3-4):518–525. doi:10.1016/j.epsl.2011.08.032.

Demouchy, S., Jacobsen, S. D., Gaillard, F., and Stern, C. R. (2006). Rapid magma ascent recorded by water diffusion profiles in mantle olivine. *Geology*, 34(6):429–432. doi:10.1130/G22386.1.

Di Paola, G. M. (1974). Volcanology and petrology of Nisyros island (Dodecanese, Greece). *Bulletin Volcanologique*, 38:944–987. doi:10.1007/BF02597100.

Dimanov, A. and Sautter, V. (2000). "Average" interdiffusion of (Fe,Mn)–Mg in natural diopside. *European Journal of Mineralogy*, 12(4):749–760. doi:10.1127/0935-1221/2000/0012-0749.

Dimanov, A. and Wiedenbeck, M. (2006). (Fe,Mn)–Mg interdiffusion in natural diopside: effect of pO_2. *European Journal of Mineralogy*, 18(6):705–718. doi:10.1127/0935-1221/2006/0018-0705.

Dimitriadis, I., Karagianni, E., Panagiotopoulos, D., Papazachos, C., Hatzidimitriou, P., Bohnhoff, M., Rische, M., and Meier, T. (2009). Seismicity and active tectonics at Coloumbo reef (Aegean Sea, Greece): Monitoring an active volcano at Santorini volcanic center using a temporary seismic network. *Tectonophysics*, 465(1-4):136–149. doi:10.1016/j.tecto.2008.11.005.

Dimitriadis, I., Papazachos, C., Panagiotopoulos, D., Hatzidimitriou, P., Bohnhoff, M., Rische, M., and Meier, T. (2010). P and S velocity structures of the Santorini–Coloumbo volcanic system (Aegean Sea, Greece) obtained by non-linear inversion of travel times and its tectonic implications. *Journal of Volcanology and Geothermal Research*, 195(1):13–30. doi:10.1016/j.jvolgeores.2010.05.013.

Dodson, M. H. (1973). Closure temperature in cooling geochronological and petrological systems. *Contributions to Mineralogy and Petrology*, 40(3):259–274. doi:10.1007/BF00373790.

Dohmen, R., Becker, H., and Chakraborty, S. (2007). Fe–Mg diffusion in olivine I: experimental determination between 700 and 1,200°C as a function of composition, crystal orientation and oxygen fugacity. *Physics and Chemistry of Minerals*, 34(6):389–407. doi:10.1007/s00269-007-0157-7.

Dohmen, R. and Chakraborty, S. (2007). Fe–Mg diffusion in olivine II: point defect chemistry, change of diffusion mechanisms and a model for calculation of diffusion coefficients in natural olivine. *Physics and Chemistry of Minerals*, 34(6):409–430. doi:10.1007/s00269-007-0158-6.

Dominey-Howes, D. T. M., Papadopoulos, G. A., and Dawson, A. G. (2000). Geological and historical investigation of the 1650 Mt. Columbo (Thera island) eruption and tsunami, Aegean Sea, Greece. *Natural Hazards*, 21(1):83–96. doi:10.1023/A:1008178100633.

Dotsika, E., Poutoukis, D., and Raco, B. (2010). Fluid geochemistry of the Methana peninsula and Loutraki geothermal area, Greece. *Journal of Geochemical Exploration*, 104(3):97–104. doi:10.1016/j.gexplo.2010.01.001.

Druitt, T. H. (1983). *Explosive volcanism on Santorini, Greece*. Ph.D., University of Cambridge, Cambridge.

Druitt, T. H. (1985). Vent evolution and lag breccia formation during the Cape Riva eruption of Santorini, Greece. *The Journal of Geology*, 93(4):439–454. doi:10.1086/628965.

Druitt, T. H. (2014). New insights into the initiation and venting of the Bronze-Age eruption of Santorini (Greece), from component analysis. *Bulletin of Volcanology*, 76(2):1–21. doi:10.1007/s00445-014-0794-x.

Druitt, T. H. and Bacon, C. R. (1989). Petrology of the zoned calcalkaline magma chamber of Mount Mazama, Crater Lake, Oregon. *Contributions to Mineralogy and Petrology*, 101(2):245–259. doi:10.1007/BF00375310.

Druitt, T. H., Costa, F., Deloule, E., Dungan, M., and Scaillet, B. (2012). Decadal to monthly timescales of magma transfer and reservoir growth at a caldera volcano. *Nature*, 482(7383):77–80. doi:10.1038/nature10706.

Druitt, T. H., Edwards, L., Mellors, R. M., Pyle, D. M., Sparks, R. S. J., Lanphere, M., Davies, M., and Barriero, B. (1999). *Santorini Volcano*, volume 19 of *Geological Society Memoirs*. Geological Society, London.

Druitt, T. H. and Francaviglia, V. (1992). Caldera formation on Santorini and the physiography of the islands in the late Bronze Age. *Bulletin of Volcanology*, 54(6):484–493. doi:10.1007/BF00301394.

Druitt, T. H. and Sparks, R. S. J. (1982). A proximal ignimbrite breccia facies on Santorini, Greece. *Journal of Volcanology and Geothermal Research*, 13(1-2):147–171. doi:10.1016/0377-0273(82)90025-7.

Eichelberger, J. C. and Izbekov, P. E. (2000). Eruption of andesite triggered by dyke injection: contrasting cases at Karymsky Volcano, Kamchatka and Mt Katmai, Alaska. *Philosophical Transactions of the Royal Society of London. Series A: Mathematical, Physical and Engineering Sciences*, 358(1770):1465–1485. doi:10.1098/rsta.2000.0599.

Endrun, B., Meier, T., Lebedev, S., Bohnhoff, M., Stavrakakis, G., and Harjes, H.-P. (2008). S velocity structure and radial anisotropy in the Aegean region from surface wave dispersion. *Geophysical Journal International*, 174(2):593–616. doi:10.1111/j.1365-246X.2008.03802.x.

Eppich, G. R., Cooper, K. M., Kent, A. J. R., and Koleszar, A. (2012). Constraints on crystal storage timescales in mixed magmas: Uranium-series disequilibria in plagioclase from Holocene magmas at Mount Hood, Oregon. *Earth and Planetary Science Letters*, 317-318:319–330. doi:10.1016/j.epsl.2011.11.019.

Eriksen, U., Friedrich, W. L., Buchardt, B., Tauber, H., and Thomsen, M. S. (1990). The Stronghyle caldera: geological, palaeontological and stable isotope evidence from radiocarbon dated stromatolites from Santorini. In Hardy, D. A., Keller, J., Galanopoulos, V. P., Flemming, N. C., and Druitt, T. H., editors, *Thera and the Aegean world III*, volume 2, pages 139–150. The Thera Foundation, London.

Faak, K., Chakraborty, S., and Coogan, L. A. (2013). Mg in plagioclase: Experimental calibration of a new geothermometer and diffusion coefficients. *Geochimica et Cosmochimica Acta*, 123:195–217. doi:10.1016/j.gca.2013.05.009.

Fabbro, G. N., Druitt, T. H., and Scaillet, S. (2013). Evolution of the crustal magma plumbing system during the build-up to the 22-ka caldera-forming eruption of Santorini (Greece). *Bulletin of Volcanology*, 75(12):1–22. doi:10.1007/s00445-013-0767-5.

Fairbanks, R. G., Mortlock, R. A., Chiu, T.-C., Cao, L., Kaplan, A., Guilderson, T. P., Fairbanks, T. W., Bloom, A. L., Grootes, P. M., and Nadeau, M.-J. (2005). Radiocarbon calibration curve spanning 0 to 50,000 years BP based on paired $^{230}Th/^{234}U/^{238}U$ and ^{14}C dates on pristine corals. *Quaternary Science Reviews*, 24(16–17):1781–1796. doi:10.1016/j.quascirev.2005.04.007.

Farver, J. R. and Yund, R. A. (1990). The effect of hydrogen, oxygen, and water fugacity on oxygen diffusion in alkali feldspar. *Geochimica et Cosmochimica Acta*, 54(11):2953–2964. doi:10.1016/0016-7037(90)90113-Y.

Faryad, S. W. and Chakraborty, S. (2005). Duration of Eo-Alpine metamorphic events obtained from multicomponent diffusion modeling of garnet: a case study from the eastern Alps. *Contributions to Mineralogy and Petrology*, 150(3):306–318. doi:10.1007/s00410-005-0020-0.

Federman, A. N. and Carey, S. N. (1980). Electron microprobe correlation of tephra layers from Eastern Mediterranean abyssal sediments and the Island of Santorini. *Quaternary Research*, 13(2):160–171. doi:10.1016/0033-5894(80)90026-5.

Feuillet, N. (2013). The 2011–2012 unrest at Santorini rift: Stress interaction between active faulting and volcanism. *Geophysical Research Letters*, 40(14):3532–3537. doi:10.1002/grl.50516.

Fick, A. (1855). Ueber diffusion. *Annalen der Physik*, 170(1):59–86. doi:10.1002/andp.18551700105.

Finney, B., Turner, S., Hawkesworth, C., Larsen, J., Nye, C., George, R., Bindeman, I., and Eichelberger, J. (2008). Magmatic differentiation at an island-arc caldera: Okmok Volcano, Aleutian Islands, Alaska. *Journal of Petrology*, 49(5):857 –884. doi:10.1093/petrology/egn008.

Floyd, M. A., Billiris, H., Paradissis, D., Veis, G., Avallone, A., Briole, P., McClusky, S., Nocquet, J., Palamartchouk, K., Parsons, B., and England, P. C. (2010). A new velocity field for Greece: Implications for the kinematics and dynamics of the Aegean. *Journal of Geophysical Research*, 115(B10):B10403. doi:10.1029/2009JB007040.

Foland, K. A. (1994). Argon diffusion in feldspars. In Parsons, I., editor, *Feldspars and their Reactions*, number 421 in NATO ASI Series, pages 415–447. Springer Netherlands.

Folkes, C. B., de Silva, S. L., Schmitt, A. K., and Cas, R. A. (2011). A reconnaissance of U–Pb zircon ages in the Cerro Galán system, NW Argentina: Prolonged magma residence, crystal recycling, and crustal assimilation. *Journal of Volcanology and Geothermal Research*, 206(3–4):136–147. doi:10.1016/j.jvolgeores.2011.06.001.

Foumelis, M., Trasatti, E., Papageorgiou, E., Stramondo, S., and Parcharidis, I. (2013). Monitoring Santorini volcano (Greece) breathing from space. *Geophysical Journal International*, 193(1):161–170. doi:10.1093/gji/ggs135.

Fouqué, F. A. (1879). *Santorin et ses éruptions*. G. Masson., Paris.

Francalanci, L., Varekamp, J. C., Vougioukalakis, G., Delant, M. J., Innocenti, F., and Manetti, P. (1995). Crystal retention, fractionation and crustal assimilation in a convecting magma chamber, Nisyros volcano, Greece. *Bulletin of Volcanology*, 56(8):601–620. doi:10.1007/BF00301465.

Francalanci, L., Vougioukalakis, G., Perini, G., and Manetti, P. (2005). A west–east traverse along the magmatism of the south Aegean volcanic arc in the light of volcanological, chemical and isotope data. In Fytikas, M. and Vougioukalakis, G. E., editors, *The South Aegean active volcanic arc: present knowledge and future perspectives*, volume 7 of *Developments in Volcanology*, pages 65–111. Elsevier.

Friedrich, W. L., Eriksen, U., Tauber, H., Heinemeier, J., Rud, N., Thomsen, M. S., and Buchardt, B. (1988). Existence of a water-filled caldera prior to the Minoan eruption of Santorini, Greece. *Naturwissenschaften*, 75(11):567–569. doi:10.1007/BF00377720.

Friedrich, W. L., Kromer, B., Friedrich, M., Heinemeier, J., Pfeiffer, T., and Talamo, S. (2006). Santorini eruption radiocarbon dated to 1627–1600 B.C. *Science*, 312(5773):548–548. doi:10.1126/science.1125087.

Froger, J.-L., Remy, D., Bonvalot, S., and Legrand, D. (2007). Two scales of inflation at Lastarria-Cordon del Azufre volcanic complex, central Andes, revealed from ASAR-ENVISAT interferometric data. *Earth and Planetary Science Letters*, 255(1–2):148–163. doi:10.1016/j.epsl.2006.12.012.

Frost, B. R. (1991). Introduction to oxygen fugacity and its petrologic importance. *Reviews in Mineralogy and Geochemistry*, 25(1):1–9.

Fytikas, M., Innocenti, F., Kolios, N., Manetti, P., Mazzuoli, R., Poli, G., Rita, F., and Villari, L. (1986). Volcanology and petrology of volcanic products from the island of Milos and neighbouring islets. *Journal of Volcanology and Geothermal Research*, 28(3-4):297–317. doi:10.1016/0377-0273(86)90028-4.

Fytikas, M., Innocenti, F., Manetti, P., Mazzuoli, R., Peccerillo, A., and Villari, L. (1984). Tertiary to Quaternary evolution of volcanism in the Aegean region. In Dixon, J. E. and Robertson, A. H. F., editors, *The geological evolution of the eastern Mediterranean*, volume 17 of *Geological Society Special Publications*, pages 687–699. Geological Society, London.

Ganguly, J. and Tazzoli, V. (1994). Fe^{2+}–Mg interdiffusion in orthopyroxene; retrieval from the data on intracrystalline exchange reaction. *American Mineralogist*, 79(9-10):930–937.

Gansecki, C. A., Mahood, G. A., and McWilliams, M. O. (1996). $^{40}Ar/^{39}Ar$ geochronology of rhyolites erupted following collapse of the Yellowstone caldera, Yellowstone Plateau volcanic field: implications for crustal contamination. *Earth and Planetary Science Letters*, 142(1–2):91–107. doi:10.1016/0012-821X(96)00088-X.

Gelman, S. E., Gutiérrez, F. J., and Bachmann, O. (2013). On the longevity of large upper crustal silicic magma reservoirs. *Geology*, 41(7):759–762. doi:10.1130/G34241.1.

Gertisser, R., Preece, K., and Keller, J. (2009). The Plinian Lower Pumice 2 eruption, Santorini, Greece: Magma evolution and volatile behaviour. *Journal of Volcanology and Geothermal Research*, 186(3–4):387–406. doi:10.1016/j.jvolgeores.2009.07.015.

Gertisser, R., Self, S., Thomas, L. E., Handley, H. K., Van Calsteren, P., and Wolff, J. A. (2012). Processes and timescales of magma genesis and differentiation leading to the great Tambora eruption in 1815. *Journal of Petrology*, 53(2):271–297. doi:10.1093/petrology/egr062.

Ghiorso, M. S. and Evans, B. W. (2008). Thermodynamics of rhombohedral oxide solid solutions and a revision of the Fe-Ti two-oxide geothermometer and oxygen-barometer. *American Journal of Science*, 308(9):957–1039. doi:10.2475/09.2008.01.

Giletti, B. J. (1991). Rb and Sr diffusion in alkali feldspars, with implications for cooling histories of rocks. *Geochimica et Cosmochimica Acta*, 55(5):1331–1343. doi:10.1016/0016-7037(91)90311-R.

Giletti, B. J. and Casserly, J. E. D. (1994). Strontium diffusion kinetics in plagioclase feldspars. *Geochimica et Cosmochimica Acta*, 58(18):3785–3793. doi:10.1016/0016-7037(94)90363-8.

Giletti, B. J. and Shanahan, T. M. (1997). Alkali diffusion in plagioclase feldspar. *Chemical Geology*, 139(1-4):3–20. doi:10.1016/S0009-2541(97)00026-0.

Gioncada, A., Mazzuoli, R., and Milton, A. J. (2005). Magma mixing at Lipari (Aeolian Islands, Italy): Insights from textural and compositional features of phenocrysts. *Journal of Volcanology and Geothermal Research*, 145(1-2):97–118. doi:10.1016/j.jvolgeores.2005.01.002.

Girard, G. and Stix, J. (2010). Rapid extraction of discrete magma batches from a large differentiating magma chamber: the Central Plateau Member rhyolites, Yellowstone Caldera, Wyoming. *Contributions to Mineralogy and Petrology*, 160(3):441–465. doi:10.1007/s00410-009-0487-1.

Glazner, A. F., Bartley, J. M., Coleman, D. S., Gray, W., and Taylor, R. Z. (2004). Are plutons assembled over millions of years by amalgamation from small magma chambers? *GSA Today*, 14(4):4. doi:10.1130/1052-5173(2004)014<0004:APAOMO>2.0.CO;2.

Graham, C. M. and Elphick, S. C. (1990). A re-examination of the role of hydrogen in Al–Si interdiffusion in feldspars. *Contributions to Mineralogy and Petrology*, 104(4):481–491. doi:10.1007/BF01575625.

Gregg, P. M., de Silva, S. L., and Grosfils, E. B. (2013). Thermomechanics of shallow magma chamber pressurization: Implications for the assessment of ground deformation data at active volcanoes. *Earth and Planetary Science Letters*, 384:100–108. doi:10.1016/j.epsl.2013.09.040.

Grove, M. and Harrison, T. M. (1996). ^{40}Ar* diffusion in Fe-rich biotite. *American Mineralogist*, 81(7-8):940–951.

Grove, T. L., Baker, M. B., and Kinzler, R. J. (1984). Coupled CaAl–NaSi diffusion in plagioclase feldspar: Experiments and applications to cooling rate speedometry. *Geochimica et Cosmochimica Acta*, 48(10):2113–2121. doi:10.1016/0016-7037(84)90391-0.

Gualda, G. A. R., Ghiorso, M. S., Lemons, R. V., and Carley, T. L. (2012a). Rhyolite-MELTS: a modified calibration of MELTS optimized for silica-rich, fluid-bearing magmatic systems. *Journal of Petrology*. doi:10.1093/petrology/egr080.

Gualda, G. A. R., Pamukcu, A. S., Ghiorso, M. S., Anderson, A. T., Sutton, S. R., and Rivers, M. L. (2012b). Timescales of quartz crystallization and the longevity of the Bishop giant magma body. *PLoS ONE*, 7(5):e37492. doi:10.1371/journal.pone.0037492.

Halliday, A., Mahood, G., Holden, P., Metz, J., Dempster, T., and Davidson, J. (1989). Evidence for long residence times of rhyolitic magma in the Long Valley magmatic system: the isotopic record in precaldera lavas of Glass Mountain. *Earth and Planetary Science Letters*, 94(3-4):274–290. doi:10.1016/0012-821X(89)90146-5.

Harris, N., Hunt, A., Parkinson, I., Tindle, A., Yondon, M., and Hammond, S. (2009). Tectonic implications of garnet-bearing mantle xenoliths exhumed by Quaternary magmatism in the Hangay dome, central Mongolia. *Contributions to Mineralogy and Petrology*, 160(1):67–81. doi:10.1007/s00410-009-0466-6.

Heiken, G. and McCoy, F. (1984). Caldera development during the Minoan eruption, Thira, Cyclades, Greece. *Journal of Geophysical Research*, 89(B10):8441–8462. doi:10.1029/JB089iB10p08441.

Hermeling, J. and Schmalzried, H. (1984). Tracerdiffusion of the Fe-cations in olivine $(Fe_xMg_{1-x})_2SiO_4$ (III). *Physics and Chemistry of Minerals*, 11(4):161–166. doi:10.1007/BF00387846.

Hervig, R. L. and Dunbar, N. W. (1992). Cause of chemical zoning in the Bishop (California) and Bandelier (New Mexico) magma chambers. *Earth and Planetary Science Letters*, 111(1):97–108. doi:10.1016/0012-821X(92)90172-R.

Hier-Majumder, S., Anderson, I. M., and Kohlstedt, D. L. (2005). Influence of protons on Fe–Mg interdiffusion in olivine. *Journal of Geophysical Research*, 110(2):B02202. doi:200510.1029/2004JB003292.

Hildreth, W. (1979). The Bishop Tuff: Evidence for the origin of compositional zonation in silicic magma chambers. *Geological Society of America Special Papers*, 180:43–76. doi:10.1130/SPE180-p43.

Hildreth, W. (1981). Gradients in silicic magma chambers: Implications for lithospheric magmatism. *Journal of Geophysical Research: Solid Earth*, 86(B11):10153–10192. doi:10.1029/JB086iB11p10153.

Hildreth, W. (2004). Volcanological perspectives on Long Valley, Mammoth Mountain, and Mono Craters: several contiguous but discrete systems. *Journal of Volcanology and Geothermal Research*, 136(3–4):169–198. doi:10.1016/j.jvolgeores.2004.05.019.

Hildreth, W. and Moorbath, S. (1988). Crustal contributions to arc magmatism in the Andes of Central Chile. *Contributions to Mineralogy and Petrology*, 98(4):455–489. doi:10.1007/BF00372365.

Hildreth, W. and Wilson, C. J. N. (2007). Compositional zoning of the Bishop Tuff. *Journal of Petrology*, 48(5):951–999. doi:10.1093/petrology/egm007.

Holness, M. B., Martin, V. M., and Pyle, D. (2005). Information about open-system magma chambers derived from textures in magmatic enclaves: the Kameni Islands, Santorini, Greece. *Geological Magazine*, 142(6):637–649. doi:10.1017/S0016756805001172.

Huber, C., Bachmann, O., and Dufek, J. (2011). Thermo-mechanical reactivation of locked crystal mushes: Melting-induced internal fracturing and assimilation processes in magmas. *Earth and Planetary Science Letters*, 304(3-4):443–454. doi:10.1016/j.epsl.2011.02.022.

Huber, C., Bachmann, O., and Dufek, J. (2012). Crystal-poor versus crystal-rich ignimbrites: A competition between stirring and reactivation. *Geology*, 40(2):115 –118. doi:10.1130/G32425.1.

Huber, C., Bachmann, O., and Manga, M. (2009). Homogenization processes in silicic magma chambers by stirring and mushification (latent heat buffering). *Earth and Planetary Science Letters*, 283(1-4):38–47. doi:10.1016/j.epsl.2009.03.029.

Huebner, J. S. and Sato, M. (1970). The oxygen fugacity-temperature relationships of manganese oxide and nickel oxide buffers. *The American Mineralogist*, 55:934–952.

Huijsmans, J. P. P. (1985). *Calc-alkaline lavas from the volcanic complex of Santorini, Aegean Sea, Greece. A petrological and stratigraphical study.* Ph.D., Rijksuniversiteit te Utrecht, Utrecht.

Huijsmans, J. P. P. and Barton, M. (1989). Polybaric geochemical evolution of two shield volcanoes from Santorini, Aegean Sea, Greece: Evidence for zoned magma chambers from cyclic compositional variations. *Journal of Petrology*, 30(3):583–625. doi:10.1093/petrology/30.3.583.

Huijsmans, J. P. P., Barton, M., and Salters, V. J. M. (1988). Geochemistry and evolution of the calc-alkaline volcanic complex of Santorini, Aegean Sea, Greece. *Journal of Volcanology and Geothermal Research*, 34(3-4):283–306. doi:10.1016/0377-0273(88)90039-X.

Innocenti, F., Manetti, P., Peccerillo, A., and Poli, G. (1981). South Aegean volcanic arc: Geochemical variations and geotectonic implications. *Bulletin Volcanologique*, 44:377–391. doi:10.1007/BF02600571.

Jackson, J. (1994). Active tectonics of the Aegean region. *Annual Review of Earth and Planetary Sciences*, 22(1):239–271. doi:10.1146/annurev.ea.22.050194.001323.

Jaoul, O. and Raterron, P. (1994). High-temperature deformation of diopside crystal: 3. Influences of pO_2 and SiO_2 precipitation. *Journal of Geophysical Research: Solid Earth*, 99(B5):9423–9439. doi:10.1029/93JB03363.

Jellinek, A. M. and DePaolo, D. J. (2003). A model for the origin of large silicic magma chambers: precursors of caldera-forming eruptions. *Bulletin of Volcanology*, 65(5):363–381. doi:10.1007/s00445-003-0277-y.

Jolivet, L. and Brun, J.-P. (2010). Cenozoic geodynamic evolution of the Aegean. *International Journal of Earth Sciences*, 99(1):109–138. doi:10.1007/s00531-008-0366-4.

Jolivet, L. and Faccenna, C. (2000). Mediterranean extension and the Africa-Eurasia collision. *Tectonics*, 19(6):1095–1106. doi:10.1029/2000TC900018.

Jolivet, L., Faccenna, C., Huet, B., Labrousse, L., Le Pourhiet, L., Lacombe, O., Lecomte, E., Burov, E., Denèle, Y., Brun, J.-P., Philippon, M., Paul, A., Salaün, G., Karabulut, H., Piromallo, C., Monié, P., Gueydan, F., Okay, A. I., Oberhänsli, R., Pourteau, A., Augier, R., Gadenne, L., and Driussi, O. (2013). Aegean tectonics: Strain localisation, slab tearing and trench retreat. *Tectonophysics*, 597–598:1–33. doi:10.1016/j.tecto.2012.06.011.

Kahl, M., Chakraborty, S., Costa, F., and Pompilio, M. (2011). Dynamic plumbing system beneath volcanoes revealed by kinetic modelling, and the connection to monitoring data: An example from Mt. Etna. *Earth and Planetary Science Letters*, In Press, Corrected Proof. doi:16/j.epsl.2011.05.008.

Karagianni, E. E. and Papazachos, C. B. (2007). Shear velocity structure in the Aegean region obtained by joint inversion of Rayleigh and Love waves. *Geological Society, London, Special Publications*, 291(1):159–181. doi:10.1144/SP291.8.

Karagianni, E. E., Papazachos, C. B., Panagiotopoulos, D. G., Suhadolc, P., Vuan, A., and Panza, G. F. (2005). Shear velocity structure in the Aegean area obtained by inversion of Rayleigh waves. *Geophysical Journal International*, 160(1):127–143. doi:10.1111/j.1365-246X.2005.02354.x.

Karlstrom, L., Dufek, J., and Manga, M. (2010). Magma chamber stability in arc and continental crust. *Journal of Volcanology and Geothermal Research*, 190(3-4):249–270. doi:10.1016/j.jvolgeores.2009.10.003.

Kasper, R. B. (1975). *Cation and oxygen diffusion in albite*. Ph.D., Brown University, Providence, Rhode Island.

Keller, J. (1969). Origin of rhyolites by anatectic melting of granitic crustal rocks. *Bulletin Volcanologique*, 33(3):942–959. doi:10.1007/BF02596758.

Keller, J., Dietrich, V., Reusser, E., and Gertisser, R. (2012). The Christiani Ignimbrite: Recognition of a major ignimbrite in the early evolution of the Santorini Group. Presented at VOLSAM: Volcanism of the Southern Aegean in the frame of the broader Mediterranean area, Fira, Santorini, Greece, 10-12 October.

Keller, J., Kraml, M., and Schwarz, M. (2000). Dating major volcanic paroxysms within the deep-sea record: the example of the Thera Formation, Santorini, Greece. Presented at IAVCEI General Assembly, Bali, Indonesia, July 2000.

Keller, J., Ryan, W. B. F., Ninkovich, D., and Altherr, R. (1978). Explosive volcanic activity in the Mediterranean over the past 200,000 yr as recorded in deep-sea sediments. *Geological Society of America Bulletin*, 89(4):591–604. doi:10.1130/0016-7606(1978)89<591:EVAITM>2.0.CO;2.

Kelley, S. P. and Wartho, J.-A. (2000). Rapid kimberlite ascent and the significance of Ar–Ar ages in xenolith phlogopites. *Science*, 289(5479):609–611. doi:10.1126/science.289.5479.609. PMID: 10915621.

Kent, A. J. R., Blundy, J., Cashman, K. V., Cooper, K. M., Donnelly, C., Pallister, J. S., Reagan, M., Rowe, M. C., and Thornber, C. R. (2007). Vapor transfer prior to the October 2004 eruption of Mount St. Helens, Washington. *Geology*, 35(3):231–234. doi:10.1130/G22809A.1.

Kilias, S. P., Nomikou, P., Papanikolaou, D., Polymenakou, P. N., Godelitsas, A., Argyraki, A., Carey, S., Gamaletsos, P., Mertzimekis, T. J., Stathopoulou, E., Goettlicher, J., Steininger, R., Betzelou, K., Livanos, I., Christakis, C., Croff Bell, K. L., and Scoullos, M. (2013). New insights into hydrothermal vent processes in the unique shallow-submarine arc-volcano, Kolumbo (Santorini), Greece. *Scientific Reports*, 3:2421. doi:10.1038/srep02421.

Klemetti, E. W., Deering, C. D., Cooper, K. M., and Roeske, S. M. (2011). Magmatic perturbations in the Okataina Volcanic Complex, New Zealand at thousand-year timescales recorded in single zircon crystals. *Earth and Planetary Science Letters*, 305(1–2):185–194. doi:10.1016/j.epsl.2011.02.054.

Klügel, A. (1998). Reactions between mantle xenoliths and host magma beneath La Palma (Canary Islands): constraints on magma ascent rates and crustal reservoirs. *Contributions to Mineralogy and Petrology*, 131(2-3):237–257. doi:10.1007/s004100050391.

Klügel, A. (2001). Prolonged reactions between harzburgite xenoliths and silica-undersaturated melt: implications for dissolution and Fe–Mg interdiffusion rates of orthopyroxene. *Contributions to Mineralogy and Petrology*, 141(1):1–14. doi:10.1007/s004100000222.

Kokkalas, S. and Aydin, A. (2013). Is there a link between faulting and magmatism in the south-central Aegean Sea? *Geological Magazine*, 150(2):193–224. doi:10.1017/S0016756812000453.

Konstantinou, K. I. (2010). Crustal rheology of the Santorini–Amorgos zone: Implications for the nucleation depth and rupture extent of the 9 July 1956 Amorgos earthquake, southern Aegean. *Journal of Geodynamics*, 50(5):400–409. doi:10.1016/j.jog.2010.05.002.

Koyaguchi, T. and Kaneko, K. (1999). A two-stage thermal evolution model of magmas in continental crust. *Journal of Petrology*, 40(2):241–254. doi:10.1093/petroj/40.2.241.

Koyaguchi, T. and Kaneko, K. (2000). Thermal evolution of silicic magma chambers after basalt replenishments. *Transactions of the Royal Society of Edinburgh: Earth Sciences*, 91(1-2):47–60. doi:10.1017/S0263593300007288.

Lagios, E., Sakkas, V., Parcharidis, I., and Dietrich, V. (2005). Ground deformation of Nisyros Volcano (Greece) for the period 1995–2002: Results from DInSAR and DGPS observations. *Bulletin of Volcanology*, 68:201–214. doi:10.1007/s00445-005-0004-y.

Lasaga, A. C. (1998). *Kinetic theory in the earth sciences*. Princetown series in geochemistry. Princeton University Press, Princeton, N.J.

LaTourrette, T. and Wasserburg, G. J. (1998). Mg diffusion in anorthite: implications for the formation of early solar system planetesimals. *Earth and Planetary Science Letters*, 158(3-4):91–108. doi:10.1016/S0012-821X(98)00048-X.

Le Pichon, X. and Angelier, J. (1979). The Hellenic arc and trench system: A key to the neotectonic evolution of the eastern Mediterranean area. *Tectonophysics*, 60(1-2):1–42. doi:10.1016/0040-1951(79)90131-8.

Lejeune, A.-M. and Richet, P. (1995). Rheology of crystal-bearing silicate melts: An experimental study at high viscosities. *Journal of Geophysical Research: Solid Earth*, 100(B3):4215–4229. doi:10.1029/94JB02985.

Lepage, L. D. (2003). ILMAT: an Excel worksheet for ilmenite–magnetite geothermometry and geobarometry. *Computers & Geosciences*, 29(5):673–678. doi:10.1016/S0098-3004(03)00042-6.

Limburg, E. M. and Varekamp, J. C. (1991). Young pumice deposits on Nisyros, Greece. *Bulletin of Volcanology*, 54(1):68–77. doi:10.1007/BF00278207.

Lindsay, J. M., Schmitt, A. K., Trumbull, R. B., de Silva, S. L., Siebel, W., and Emmermann, R. (2001). Magmatic evolution of the La Pacana caldera system, central Andes, Chile: compositional variation of two cogenetic, large-volume felsic ignimbrites. *Journal of Petrology*, 42(3):459–486. doi:10.1093/petrology/42.3.459.

Lipman, P. W. (2007). Incremental assembly and prolonged consolidation of Cordilleran magma chambers: Evidence from the Southern Rocky Mountain volcanic field. *Geosphere*, 3(1):42–70. doi:10.1130/GES00061.1.

Lister, G. S., Banga, G., and Feenstra, A. (1984). Metamorphic core complexes of Cordilleran type in the Cyclades, Aegean Sea, Greece. *Geology*, 12(4):221–225. doi:10.1130/0091-7613(1984)12<221:MCCOCT>2.0.CO;2.

Liu, M. and Yund, R. A. (1992). NaSi–CaAl interdiffusion in plagioclase. *American Mineralogist*, 77(3-4):275–283.

Liu, Y., Anderson, A. T., Wilson, C. J. N., Davis, A. M., and Steele, I. M. (2005). Mixing and differentiation in the Oruanui rhyolitic magma, Taupo, New Zealand: evidence from volatiles and trace elements in melt inclusions. *Contributions to Mineralogy and Petrology*, 151(1):71–87. doi:10.1007/s00410-005-0046-3.

Lowe, D. J., Shane, P. A. R., Alloway, B. V., and Newnham, R. M. (2008). Fingerprints and age models for widespread New Zealand tephra marker beds erupted since 30,000 years ago: a framework for NZ-INTIMATE. *Quaternary Science Reviews*, 27(1–2):95–126. doi:10.1016/j.quascirev.2007.01.013.

Mackwell, S. J. and Kohlstedt, D. L. (1990). Diffusion of hydrogen in olivine: Implications for water in the mantle. *Journal of Geophysical Research*, 95(B4):5079–5088. doi:10.1029/JB095iB04p05079.

Mahood, G. (1990). Second reply to comment of R.S.J. Sparks, H.E. Huppert and C.J.N. Wilson on "Evidence for long residence times of rhyolitic magma in the Long Valley magmatic system: the isotopic record in the precaldera lavas of Glass Mountain". *Earth and Planetary Science Letters*, 99(4):395–399. doi:10.1016/0012-821X(90)90145-N.

Mann, A. C. (1983). Trace element geochemistry of high alumina basalt-andesite-dacite-rhyodacite lavas of the Main Volcanic Series of Santorini Volcano, Greece. *Contributions to Mineralogy and Petrology*, 84(1):43–57. doi:10.1007/BF01132329.

Manning, S. W., Ramsey, C. B., Kutschera, W., Higham, T., Kromer, B., Steier, P., and Wild, E. M. (2006). Chronology for the Aegean Late Bronze Age 1700–1400 B.C. *Science*, 312(5773):565 –569. doi:10.1126/science.1125682.

Margari, V., Pyle, D. M., Bryant, C., and Gibbard, P. L. (2007). Mediterranean tephra stratigraphy revisited: Results from a long terrestrial sequence on Lesvos Island, Greece. *Journal of Volcanology and Geothermal Research*, 163(1-4):34–54. doi:10.1016/j.jvolgeores.2007.02.002.

Martí, J., Castro, A., Rodríguez, C., Costa, F., Carrasquilla, S., Pedreira, R., and Bolos, X. (2013). Correlation of magma evolution and geophysical monitoring during the 2011–2012 El Hierro (Canary Islands) submarine eruption. *Journal of Petrology*. doi:10.1093/petrology/egt014.

Martin, V. M. (2005). *Geochemical and Textural Analysis of Mafic Enclaves from Nea Kameni, Santorini, Greece*. Ph.D., University of Cambridge, Cambridge.

Martin, V. M., Davidson, J., Morgan, D., and Jerram, D. A. (2010). Using the Sr isotope compositions of feldspars and glass to distinguish magma system components and dynamics. *Geology*, 38(6):539–542. doi:10.1130/G30758.1.

Martin, V. M., Holness, M. B., and Pyle, D. M. (2006). Textural analysis of magmatic enclaves from the Kameni Islands, Santorini, Greece. *Journal of Volcanology and Geothermal Research*, 154(1-2):89–102. doi:10.1016/j.jvolgeores.2005.09.021.

Martin, V. M., Morgan, D. J., Jerram, D. A., Caddick, M. J., Prior, D. J., and Davidson, J. P. (2008). Bang! Month-scale eruption triggering at Santorini volcano. *Science*, 321(5893):1178. doi:10.1126/science.1159584.

Mason, B. G., Pyle, D. M., and Oppenheimer, C. (2004). The size and frequency of the largest explosive eruptions on earth. *Bulletin of Volcanology*, 66(8):735–748. doi:10.1007/s00445-004-0355-9.

Matthews, N. E., Huber, C., Pyle, D. M., and Smith, V. C. (2012a). Timescales of magma recharge and reactivation of large silicic systems from Ti diffusion in quartz. *Journal of Petrology*. doi:10.1093/petrology/egs020.

Matthews, N. E., Pyle, D. M., Smith, V. C., Wilson, C. J. N., Huber, C., and Hinsberg, V. (2012b). Quartz zoning and the pre-eruptive evolution of the ∼340-ka Whakamaru magma systems, New Zealand. *Contributions to Mineralogy and Petrology*, 163(1):87–107. doi:10.1007/s00410-011-0660-1.

McKenzie, D. (1985). The extraction of magma from the crust and mantle. *Earth and Planetary Science Letters*, 74(1):81–91. doi:10.1016/0012-821X(85)90168-2.

McKenzie, D. P. (1970). Plate tectonics of the Mediterranean region. *Nature*, 226(5242):239–243. doi:10.1038/226239a0.

McKenzie, D. P. (1972). Active tectonics of the Mediterranean region. *Geophysical Journal of the Royal Astronomical Society*, 30(2):109–185. doi:10.1111/j.1365-246X.1972.tb02351.x.

Mellors, R. A. and Sparks, R. S. J. (1991). Spatter-rich pyroclastic flow deposits on Santorini, Greece. *Bulletin of Volcanology*, 53(5):327–342. doi:10.1007/BF00280225.

Menand, T. (2008). The mechanics and dynamics of sills in layered elastic rocks and their implications for the growth of laccoliths and other igneous complexes. *Earth and Planetary Science Letters*, 267(1–2):93–99. doi:10.1016/j.epsl.2007.11.043.

Mercier, M., Druitt, T. H., Deloule, E., and Nicolas, C. (2013). Santorini Volcano plumbing system: constraints from melt inclusion volatile contents. Abstract 4W_1B–P23, IAVCEI Scientific Assembly, 20–24 July, Kagoshima, Japan.

Metz, J. M. and Mahood, G. A. (1985). Precursors to the Bishop Tuff eruption: Glass Mountain, Long Valley, California. *Journal of Geophysical Research*, 90(B13):11,121–11,126. doi:10.1029/JB090iB13p11121.

Metz, J. M. and Mahood, G. A. (1991). Development of the Long Valley, California, magma chamber recorded in precaldera rhyolite lavas of Glass Mountain. *Contributions to Mineralogy and Petrology*, 106(3):379–397. doi:10.1007/BF00324565.

Michaud, V., Clocchiatti, R., and Sbrana, S. (2000). The Minoan and post-Minoan eruptions, Santorini (Greece), in the light of melt inclusions: chlorine and sulphur behaviour. *Journal of Volcanology and Geothermal Research*, 99(1-4):195–214. doi:10.1016/S0377-0273(00)00173-6.

Miller, C. F. and Wark, D. A. (2008). Supervolcanoes and their explosive supereruptions. *Elements*, 4(1):11–15. doi:10.2113/GSELEMENTS.4.1.11.

Miller, J. S., Matzel, J. E., Miller, C. F., Burgess, S. D., and Miller, R. B. (2007). Zircon growth and recycling during the assembly of large, composite arc plutons. *Journal of Volcanology and Geothermal Research*, 167(1-4):282–299. doi:10.1016/j.jvolgeores.2007.04.019.

Miller, J. S. and Wooden, J. L. (2004). Residence, resorption and recycling of zircons in Devils Kitchen Rhyolite, Coso Volcanic Field, California. *Journal of Petrology*, 45(11):2155–2170. doi:10.1093/petrology/egh051.

Morgan, D. J. and Blake, S. (2005). Magmatic residence times of zoned phenocrysts: introduction and application of the binary element diffusion modelling (BEDM) technique. *Contributions to Mineralogy and Petrology*, 151(1):58–70. doi:10.1007/s00410-005-0045-4.

Morgan, D. J., Blake, S., Rogers, N. W., DeVivo, B., Rolandi, G., and Davidson, J. P. (2006). Magma chamber recharge at Vesuvius in the century prior to the eruption of A.D. 79. *Geology*, 34(10):845–848. doi:10.1130/G22604.1.

Morgan, D. J., Blake, S., Rogers, N. W., DeVivo, B., Rolandi, G., Macdonald, R., and Hawkesworth, C. J. (2004). Time scales of crystal residence and magma chamber volume from modelling of diffusion profiles in phenocrysts: Vesuvius 1944. *Earth and Planetary Science Letters*, 222(3-4):933–946. doi:10.1016/j.epsl.2004.03.030.

Müller, T., Dohmen, R., Becker, H. W., ter Heege, J. H., and Chakraborty, S. (2013). Fe–Mg interdiffusion rates in clinopyroxene: experimental data and implications for Fe–Mg exchange geothermometers. *Contributions to Mineralogy and Petrology*, 166(6):1563–1576. doi:10.1007/s00410-013-0941-y.

Nakagawa, K., Nagahara, H., Ozawa, K., Tachibana, S., and Yasuda, A. (2005). Experimental determination of AlAl–SiMg interdiffusion coefficient in orthopyroxene. Abstract K038–013 presented at the Japan Earth and Planetary Science Joint Meeting, http://www2.jpgu.org/meeting/2005/pdf/k038/k038-013_e.pdf.

Nakamura, M. (1995). Continuous mixing of crystal mush and replenished magma in the ongoing Unzen eruption. *Geology*, 23(9):807–810. doi:10.1130/0091-7613(1995)023<0807:CMOCMA>2.3.CO;2.

Narcisi, B. and Vezzoli, L. (1999). Quaternary stratigraphy of distal tephra layers in the Mediterranean—an overview. *Global and Planetary Change*, 21(1-3):31–50. doi:10.1016/S0921-8181(99)00006-5.

Newman, A. V., Stiros, S., Feng, L., Psimoulis, P., Moschas, F., Saltogianni, V., Jiang, Y., Papazachos, C., Panagiotopoulos, D. G., Karagianni, E., and Vamvakaris, D. (2012). Recent geodetic unrest at Santorini caldera, Greece. *Geophysical Research Letters*, 39(6):L06309. doi:10.1029/2012GL051286.

Nicholls, I. A. (1971). Petrology of Santorini Volcano, Cyclades, Greece. *Journal of Petrology*, 12(1):67–119. doi:10.1093/petrology/12.1.67.

Nocquet, J.-M. (2012). Present-day kinematics of the Mediterranean: A comprehensive overview of GPS results. *Tectonophysics*, 579:220–242. doi:10.1016/j.tecto.2012.03.037.

Nomikou, P., Carey, S., Croff Bell, K. L., Papanikolaou, D., Bejelou, K., Alexandri, M., Cantner, K., and Martin, J. F. (2013a). Morphological analysis and related volcanic features of the Kolumbo submarine volcanic chain (NE of Santorini Island, Aegean Volcanic Arc). *Zeitschrift für Geomorphologie, Supplementary Issues*, 57(3):29–47. doi:10.1127/0372-8854/2013/S-00142.

Nomikou, P., Carey, S., Croff Bell, K. L., Papanikolaou, D., Bejelou, K., Cantner, K., Sakellariou, D., and Perros, I. (2012a). Tsunami hazard risk of a future volcanic eruption of Kolumbo submarine volcano, NE of Santorini Caldera, Greece. *Natural Hazards*. doi:10.1007/s11069-012-0405-0.

Nomikou, P., Carey, S., Papanikolaou, D., Croff Bell, K. L., Sakellariou, D., Alexandri, M., and Bejelou, K. (2012b). Submarine volcanoes of the Kolumbo volcanic zone NE of Santorini Caldera, Greece. *Global and Planetary Change*, 90–91:135–151. doi:10.1016/j.gloplacha.2012.01.001.

Nomikou, P., Papanikolaou, D., Alexandri, M., Sakellariou, D., and Rousakis, G. (2013b). Submarine volcanoes along the Aegean volcanic arc. *Tectonophysics*, 597-598:123–146. doi:10.1016/j.tecto.2012.10.001.

Nomikou, P., Parks, M. M., Papanikolaou, D., Pyle, D. M., Mather, T. A., Carey, S., Watts, A. B., Paulatto, M., Kalnins, M. L., Livanos, I., Bejelou, K., Simou, E., and Perros, I. (2014). The emergence and growth of a submarine volcano: The Kameni islands, Santorini (Greece). *GeoResJ*, 1–2:8–18. doi:10.1016/j.grj.2014.02.002.

Nyst, M. and Thatcher, W. (2004). New constraints on the active tectonic deformation of the Aegean. *Journal of Geophysical Research*, 109:B11406. doi:200410.1029/2003JB002830.

Okal, E. A., Synolakis, C. E., Uslu, B., Kalligeris, N., and Voukouvalas, E. (2009). The 1956 earthquake and tsunami in Amorgos, Greece. *Geophysical Journal International*, 178(3):1533–1554. doi:10.1111/j.1365-246X.2009.04237.x.

Pallister, J. S., Hoblitt, R. P., and Reyes, A. G. (1992). A basalt trigger for the 1991 eruptions of Pinatubo volcano? *Nature*, 356(6368):426–428. doi:10.1038/356426a0.

Pan, Y. and Batiza, R. (2002). Mid-ocean ridge magma chamber processes: Constraints from olivine zonation in lavas from the East Pacific Rise at 9°30′N and 10°30′N. *Journal of Geophysical Research*, 107(B1):2022. doi:200210.1029/2001JB000435.

Papadopoulos, G. A. and Pavlides, S. B. (1992). The large 1956 earthquake in the south Aegean: Macroseismic field configuration, faulting, and neotectonics of Amorgos island. *Earth and Planetary Science Letters*, 113(3):383–396. doi:16/0012-821X(92)90140-Q.

Papazachos, B. C., Karakostas, V. G., Papazachos, C. B., and Scordilis, E. M. (2000). The geometry of the Wadati-Benioff zone and lithospheric kinematics in the Hellenic arc. *Tectonophysics*, 319(4):275–300. doi:10.1016/S0040-1951(99)00299-1.

Papazachos, B. C. and Panagiotopoulos, D. G. (1993). Normal faults associated with volcanic activity and deep rupture zones in the southern Aegean volcanic arc. *Tectonophysics*, 220(1-4):301–308. doi:16/0040-1951(93)90237-E.

Papazachos, C. and Nolet, G. (1997). P and S deep velocity structure of the Hellenic area obtained by robust nonlinear inversion of travel times. *Journal of Geophysical Research*, 102(B4):8349–8367. doi:199710.1029/96JB03730.

Papoutsis, I., Papanikolaou, X., Floyd, M., Ji, K. H., Kontoes, C., Paradissis, D., and Zacharis, V. (2013). Mapping inflation at Santorini volcano, Greece, using GPS and InSAR. *Geophysical Research Letters*, 40(2):267–272. doi:10.1029/2012GL054137.

Parkinson, I. J., Hammond, S. J., James, R. H., and Rogers, N. W. (2007). High-temperature lithium isotope fractionation: Insights from lithium isotope diffusion in magmatic systems. *Earth and Planetary Science Letters*, 257(3-4):609–621. doi:10.1016/j.epsl.2007.03.023.

Parks, M. M., Biggs, J., England, P., Mather, T. A., Nomikou, P., Palamartchouk, K., Papanikolaou, X., Paradissis, D., Parsons, B., Pyle, D. M., Raptakis, C., and Zacharis, V. (2012). Evolution of Santorini Volcano dominated by episodic and rapid fluxes of melt from depth. *Nature Geoscience*, 5(10):749–754. doi:10.1038/ngeo1562.

Paulatto, M., Annen, C., Henstock, T. J., Kiddle, E., Minshull, T. A., Sparks, R. S. J., and Voight, B. (2012). Magma chamber properties from integrated seismic tomography and thermal modelling at Montserrat. *Geochemistry Geophysics Geosystems*, 13:Q01014. doi:201210.1029/2011GC003892.

Pe, G. G. (1973). Petrology and geochemistry of volcanic rocks of Aegina, Greece. *Bulletin Volcanologique*, 37:491–514. doi:10.1007/BF02596888.

Pe-Piper, G. and Hatzipanagiotou, K. (1997). The Pliocene volcanic rocks of Crommyonia, western Greece and their implications for the early evolution of the South Aegean Arc. *Geological Magazine*, 134(1):55–66.

Pe-Piper, G. and Moulton, B. (2008). Magma evolution in the Pliocene–Pleistocene succession of Kos, South Aegean arc (Greece). *Lithos*, 106(1-2):110–124. doi:10.1016/j.lithos.2008.07.002.

Pe-Piper, G., Piper, D. J. W., and Reynolds, P. H. (1983). Paleomagnetic stratigraphy and radiometric dating of the Pliocene volcanic rocks of Aegina, Greece. *Bulletin Volcanologique*, 46(1):1–7. doi:10.1007/BF02598241.

Pearce, F. D., Rondenay, S., Sachpazi, M., Charalampakis, M., and Royden, L. H. (2012). Seismic investigation of the transition from continental to oceanic subduction along the western Hellenic Subduction Zone. *Journal of Geophysical Research*, 117(B7):B07306. doi:10.1029/2011JB009023.

Petrelli, M., Poli, G., Perugini, D., and Peccerillo, A. (2005). PetroGraph: a new software to visualize, model, and present geochemical data in igneous petrology. *Geochemistry Geophysics Geosystems*, 6:Q07011. doi:10.1029/2005GC000932.

Pichler, H. and Friedrich, W. (1976). Radiocarbon dates of Santorini volcanics. *Nature*, 262(5567):373–374. doi:10.1038/262373a0.

Pinel, V. and Jaupart, C. (2000). The effect of edifice load on magma ascent beneath a volcano. *Philosophical Transactions of the Royal Society of London. Series A: Mathematical, Physical and Engineering Sciences*, 358(1770):1515–1532. doi:10.1098/rsta.2000.0601.

Pinel, V. and Jaupart, C. (2004). Magma storage and horizontal dyke injection beneath a volcanic edifice. *Earth and Planetary Science Letters*, 221(1–4):245–262. doi:10.1016/S0012-821X(04)00076-7.

Piromallo, C. and Morelli, A. (2003). P wave tomography of the mantle under the Alpine–Mediterranean area. *Journal of Geophysical Research: Solid Earth*, 108(B2):2065. doi:10.1029/2002JB001757.

Pistone, M., Caricchi, L., Ulmer, P., Reusser, E., and Ardia, P. (2013). Rheology of volatile-bearing crystal mushes: Mobilization vs. viscous death. *Chemical Geology*, 345:16–39. doi:10.1016/j.chemgeo.2013.02.007.

Pritchard, M. E. and Simons, M. (2004). An InSAR-based survey of volcanic deformation in the central Andes. *Geochemistry, Geophysics, Geosystems*, 5(2):Q02002. doi:10.1029/2003GC000610.

Putirka, K. D. (2008). Thermometers and barometers for volcanic systems. *Reviews in Mineralogy and Geochemistry*, 69(1):61–120. doi:10.2138/rmg.2008.69.3.

Pyle, D. M. (1990). New estimates for the volume of the Minoan eruption. In Hardy, D. A., Keller, J., Galanopoulos, V. P., Flemming, N. C., and Druitt, T. H., editors, *Thera and the Aegean world III*, volume 2, pages 113–121. The Thera Foundation, London.

Pyle, D. M. and Elliott, J. R. (2006). Quantitative morphology, recent evolution, and future activity of the Kameni Islands volcano, Santorini, Greece. *Geosphere*, 2(5):253–268. doi:10.1130/GES00028.1.

Qian, Q., O'Neill, H. St. C., and Hermann, J. (2010). Comparative diffusion coefficients of major and trace elements in olivine at ∼950 °C from a xenocryst included in dioritic magma. *Geology*, 38(4):331–334. doi:10.1130/G30788.1.

Ramos, F. C., Wolff, J. A., and Tollstrup, D. L. (2005). Sr isotope disequilibrium in Columbia River flood basalts: Evidence for rapid shallow-level open-system processes. *Geology*, 33(6):457–460. doi:10.1130/G21512.1.

Rasband, W. S. (1997–2012). ImageJ, U.S. National Institutes of Health, Bethesda, Maryland, USA. http://rsb.info.nih.gov/ij/.

Reid, M. R. (2008). How long does it take to supersize an eruption? *Elements*, 4(1):23–28. doi:10.2113/GSELEMENTS.4.1.23.

Reid, M. R. and Coath, C. D. (2000). In situ U-Pb ages of zircons from the Bishop Tuff: No evidence for long crystal residence times. *Geology*, 28(5):443–446. doi:10.1130/0091-7613(2000)28<443:ISUAOZ>2.0.CO;2.

Reilinger, R., McClusky, S., Paradissis, D., Ergintav, S., and Vernant, P. (2010). Geodetic constraints on the tectonic evolution of the Aegean region and strain accumulation along the Hellenic subduction zone. *Tectonophysics*, 488(1-4):22–30. doi:10.1016/j.tecto.2009.05.027.

Reilinger, R., McClusky, S., Vernant, P., Lawrence, S., Ergintav, S., Cakmak, R., Ozener, H., Kadirov, F., Guliev, I., Stepanyan, R., Nadariya, M., Hahubia, G., Mahmoud, S., Sakr, K., ArRajehi, A., Paradissis, D., Al-Aydrus, A., Prilepin, M., Guseva, T., Evren, E., Dmitrotsa, A., Filikov, S. V., Gomez, F., Al-Ghazzi, R., and Karam, G. (2006). GPS constraints on continental deformation in the Africa-Arabia-Eurasia continental collision zone and implications for the dynamics of plate interactions. *Journal of Geophysical Research*, 111:26 PP. doi:200610.1029/2005JB004051.

Renne, P. R., Balco, G., Ludwig, K. R., Mundil, R., and Min, K. (2011). Response to the comment by W. H. Schwarz et al. on "Joint determination of ^{40}K decay constants and ^{40}Ar*/^{40}K for the Fish Canyon sanidine standard, and improved accuracy for ^{40}Ar/^{39}Ar geochronology" by P. R. Renne et al. (2010). *Geochimica et Cosmochimica Acta*, 75(17):5097–5100. doi:10.1016/j.gca.2011.06.021.

Renne, P. R., Mundil, R., Balco, G., Min, K., and Ludwig, K. R. (2010). Joint determination of ^{40}K decay constants and ^{40}Ar*/^{40}K for the Fish Canyon sanidine standard, and improved accuracy for ^{40}Ar/^{39}Ar geochronology. *Geochimica et Cosmochimica Acta*, 74(18):5349–5367. doi:10.1016/j.gca.2010.06.017.

Rivera, T. A., Storey, M., Zeeden, C., Hilgen, F. J., and Kuiper, K. (2011). A refined astronomically calibrated ^{40}Ar/^{39}Ar age for Fish Canyon sanidine. *Earth and Planetary Science Letters*, 311(3–4):420–426. doi:10.1016/j.epsl.2011.09.017.

Roberge, J., Wallace, P., and Kent, A. (2013). Magmatic processes in the Bishop Tuff rhyolitic magma based on trace elements in melt inclusions and pumice matrix glass. *Contributions to Mineralogy and Petrology*, 165(2):237–257. doi:10.1007/s00410-012-0807-8.

Roeder, P. L. and Emslie, R. F. (1970). Olivine–liquid equilibrium. *Contributions to Mineralogy and Petrology*, 29(4):275–289. doi:10.1007/BF00371276.

Rowland, J. V., Wilson, C. J. N., and Gravley, D. M. (2010). Spatial and temporal variations in magma-assisted rifting, Taupo Volcanic Zone, New Zealand. *Journal of Volcanology and Geothermal Research*, 190(1-2):89–108. doi:10.1016/j.jvolgeores.2009.05.004.

Rubin, A. M. (1995). Propagation of magma-filled cracks. *Annual Review of Earth and Planetary Sciences*, 23(1):287–336. doi:10.1146/annurev.ea.23.050195.001443.

Ruch, J., Manconi, A., Zeni, G., Solaro, G., Pepe, A., Shirzaei, M., Walter, T. R., and Lanari, R. (2009). Stress transfer in the Lazufre volcanic area, central Andes. *Geophysical Research Letters*, 36(22):L22303. doi:10.1029/2009GL041276.

Ruprecht, P. and Cooper, K. M. (2012). Integrating the uranium-series and elemental diffusion geochronometers in mixed magmas from Volcán Quizapu, central Chile. *Journal of Petrology*. doi:10.1093/petrology/egs001.

Ruprecht, P. and Plank, T. (2013). Feeding andesitic eruptions with a high-speed connection from the mantle. *Nature*, 500(7460):68–72. doi:10.1038/nature12342.

Sachpazi, M., Hirn, A., Nercessian, A., Avedik, F., Mc Bride, J., Loucoyannakis, M., Nicolich, R., and the STREAMERS-PROFILES group (1997). A first coincident normal-incidence and wide-angle approach to studying the extending Aegean crust. *Tectonophysics*, 270(3–4):301–312. doi:10.1016/S0040-1951(96)00160-6.

Sachpazi, M., Kontoes, C., Voulgaris, N., Laigle, M., Vougioukalakis, G., Sikioti, O., Stavrakakis, G., Baskoutas, J., Kalogeras, J., and Lepine, J. (2002). Seismological and SAR signature of unrest at Nisyros caldera, Greece. *Journal of Volcanology and Geothermal Research*, 116(1-2):19–33. doi:10.1016/S0377-0273(01)00334-1.

Saito, G., Morishita, Y., and Shinohara, H. (2010). Magma plumbing system of the 2000 eruption of Miyakejima volcano, Japan, deduced from volatile and major component contents of olivine-hosted melt inclusions. *Journal of Geophysical Research*, 115:B11202. doi:10.1029/2010JB007433.

Sakellariou, D., Sigurdsson, H., Alexandri, M., Carey, S., Rousakis, G., Nomikou, P., Georgiou, P., and Ballas, D. (2010). Active tectonics in the Hellenic Volcanic Arc: the Kolumbo submarine volcanic zone. *Bulletin of the Geological Society of Greece*, 43(2):1056–1063.

Saunders, K. E., Morgan, D. J., Baker, J. A., and Wysoczanski, R. J. (2010). The magmatic evolution of the Whakamaru supereruption, New Zealand, constrained by a microanalytical study of plagioclase and quartz. *Journal of Petrology*, 51(12):2465 –2488. doi:10.1093/petrology/egq064.

Scaillet, B. and Evans, B. W. (1999). The 15 June 1991 eruption of Mount Pinatubo. I. Phase equilibria and pre-eruption P–T–fO_2–fH_2O conditions of the dacite magma. *Journal of Petrology*, 40(3):381–411. doi:10.1093/petroj/40.3.381.

Scaillet, S., Rotolo, S. G., La Felice, S., and Vita-Scaillet, G. (2011). High-resolution $^{40}Ar/^{39}Ar$ chronostratigraphy of the post-caldera (<20 ka) volcanic activity at Pantelleria, Sicily Strait. *Earth and Planetary Science Letters*, 309(3–4):280–290. doi:10.1016/j.epsl.2011.07.009.

Scaillet, S., Vita-Scaillet, G., and Guillou, H. (2008). Oldest human footprints dated by Ar/Ar. *Earth and Planetary Science Letters*, 275(3–4):320–325. doi:10.1016/j.epsl.2008.08.026.

Schöpa, A. and Annen, C. (2013). The effects of magma flux variations on the formation and lifetime of large silicic magma chambers. *Journal of Geophysical Research: Solid Earth*, 118(3):926–942. doi:10.1002/jgrb.50127.

Schwandt, C. S. and McKay, G. A. (2006). Minor- and trace-element sector zoning in synthetic enstatite. *American Mineralogist*, 91(10):1607–1615. doi:10.2138/am.2006.2093.

Schwarz, M. (2000). *Tephrakorrelation im östlichen Mittelmeer (Meteor M40/4 Kerne)*. MSc, Albert-Ludwigs-Universität Freiburg i. Br., Freiburg.

Shaw, B. and Jackson, J. (2010). Earthquake mechanisms and active tectonics of the Hellenic subduction zone. *Geophysical Journal International*, 181(2):966–984. doi:10.1111/j.1365-246X.2010.04551.x.

Sigmarsson, O., Vlastelic, I., Andreasen, R., Bindeman, I., Devidal, J.-L., Moune, S., Keiding, J. K., Larsen, G., Höskuldsson, A., and Thordarson, Th. (2011). Remobilization of silicic intrusion by mafic magmas during the 2010 Eyjafjallajökull eruption. *Solid Earth*, 2(2):271–281. doi:10.5194/se-2-271-2011.

Sigmundsson, F., Hreinsdóttir, S., Hooper, A., Árnadóttir, T., Pedersen, R., Roberts, M. J., Óskarsson, N., Auriac, A., Decriem, J., Einarsson, P., Geirsson, H., Hensch, M., Ófeigsson, B. G., Sturkell, E., Sveinbjörnsson, H., and Feigl, K. L. (2010). Intrusion triggering of the 2010 Eyjafjallajökull explosive eruption. *Nature*, 468(7322):426–430. doi:10.1038/nature09558.

Sigurdsson, H., Carey, S., Alexandri, M., Vougioukalakis, G., Croff, K., Roman, C., Sakellariou, D., Anagnostou, C., Rousakis, G., Ioakim, C., Gogou, A., Ballas, D., Misaridis, T., and Nomikou, P. (2006). Marine investigations of Greece's Santorini volcanic field. *Eos*, 87(34):337–348. doi:200610.1029/2006EO340001.

Simkin, T. and Baker, L. (2014). Smithsonian Institution — Global Volcanism Program: Worldwide Holocene volcano and eruption information. http://www.volcano.si.edu.

Simon, J. I. and Reid, M. R. (2005). The pace of rhyolite differentiation and storage in an 'archetypical' silicic magma system, Long Valley, California. *Earth and Planetary Science Letters*, 235(1-2):123–140. doi:10.1016/j.epsl.2005.03.013.

Sio, C. K. I., Dauphas, N., Teng, F.-Z., Chaussidon, M., Helz, R. T., and Roskosz, M. (2013). Discerning crystal growth from diffusion profiles in zoned olivine by in situ Mg–Fe isotopic analyses. *Geochimica et Cosmochimica Acta*, 123:302–321. doi:10.1016/j.gca.2013.06.008.

Sisson, T. W. and Bacon, C. R. (1999). Gas-driven filter pressing in magmas. *Geology*, 27(7):613–616. doi:10.1130/0091-7613(1999)027<0613:GDFPIM>2.3.CO;2.

Smith, D. and Barron, B. R. (1991). Pyroxene–garnet equilibration during cooling in the mantle. *American Mineralogist*, 76(11-12):1950–1963.

Smith, R. L. (1979). Ash-flow magmatism. *Geological Society of America Special Papers*, 180:5–28. doi:10.1130/SPE180-p5.

Smith, V. C., Shane, P., and Nairn, I. A. (2004). Reactivation of a rhyolitic magma body by new rhyolitic intrusion before the 15.8 ka Rotorua eruptive episode: implications for magma storage in the Okataina Volcanic Centre, New Zealand. *Journal of the Geological Society*, 161(5):757–772. doi:10.1144/0016-764903-092.

Smith, V. C., Shane, P., and Nairn, I. A. (2010). Insights into silicic melt generation using plagioclase, quartz and melt inclusions from the caldera-forming Rotoiti eruption, Taupo volcanic zone, New Zealand. *Contributions to Mineralogy and Petrology*, 160(6):951–971. doi:10.1007/s00410-010-0516-0.

Solano, J. M. S., Jackson, M. D., Sparks, R. S. J., Blundy, J. D., and Annen, C. (2012). Melt segregation in deep crustal hot zones: a mechanism for chemical differentiation, crustal assimilation and the formation of evolved magmas. *Journal of Petrology*, 53(10):1999–2026. doi:10.1093/petrology/egs041.

Sparks, R. J., Huppert, H. E., and Wilson, C. J. (1990). Comment on "Evidence for long residence times of rhyolitic magma in the Long Valley magmatic system: the isotopic record in precaldera lavas of Glass Mountain" by A.N. Halliday, G.A. Mahood, P. Holden, J.M. Metz, T.J. Dempster and J.P. Davidson. *Earth and Planetary Science Letters*, 99(4):387–389. doi:10.1016/0012-821X(90)90143-L.

Sparks, R. S. J., Folkes, C. B., Humphreys, M. C., Barfod, D. N., Clavero, J., Sunagua, M. C., McNutt, S. R., and Pritchard, M. E. (2008). Uturuncu volcano, Bolivia: Volcanic unrest due to mid-crustal magma intrusion. *American Journal of Science*, 308(6):727–769. doi:10.2475/06.2008.01.

St Seymour, K., Christanis, K., Bouzinos, A., Papazisimou, S., Papatheodorou, G., Moran, E., and Denes, G. (2004). Tephrostratigraphy and tephrochronology in the Philippi peat basin, Macedonia, Northern Hellas (Greece). *Quaternary International*, 121(1):53–65. doi:10.1016/j.quaint.2004.01.023.

Stevenson, D. J. (1989). Spontaneous small-scale melt segregation in partial melts undergoing deformation. *Geophysical Research Letters*, 16(9):1067–1070. doi:10.1029/GL016i009p01067.

Stewart, A. L. and McPhie, J. (2006). Facies architecture and Late Pliocene – Pleistocene evolution of a felsic volcanic island, Milos, Greece. *Bulletin of Volcanology*, 68:703–726. doi:10.1007/s00445-005-0045-2.

Stimpfl, M., Ganguly, J., and Molin, G. (2005). Kinetics of Fe^{2+}–Mg order–disorder in orthopyroxene: experimental studies and applications to cooling rates of rocks. *Contributions to Mineralogy and Petrology*, 150(3):319–334. doi:10.1007/s00410-005-0016-9.

Storm, S., Shane, P., Schmitt, A. K., and Lindsay, J. M. (2011). Decoupled crystallization and eruption histories of the rhyolite magmatic system at Tarawera volcano revealed by zircon ages and growth rates. *Contributions to Mineralogy and Petrology*. doi:10.1007/s00410-011-0682-8.

Stormer, J. C. (1983). The effects of recalculation on estimates of temperature and oxygen fugacity from analyses of multicomponent iron-titanium oxides. *American Mineralogist*, 68(5-6):586–594.

Sutton, A. N., Blake, S., and Wilson, C. J. (1995). An outline geochemistry of rhyolite eruptives from Taupo volcanic centre, New Zealand. *Journal of Volcanology and Geothermal Research*, 68(1–3):153–175. doi:10.1016/0377-0273(95)00011-I.

Sutton, A. N., Blake, S., Wilson, C. J. N., and Charlier, B. L. A. (2000). Late Quaternary evolution of a hyperactive rhyolite magmatic system: Taupo volcanic centre, New Zealand. *Journal of the Geological Society*, 157(3):537–552. doi:10.1144/jgs.157.3.537.

Suzuki, Y., Yasuda, A., Hokanishi, N., Kaneko, T., Nakada, S., and Fujii, T. (2013). Syneruptive deep magma transfer and shallow magma remobilization during the 2011 eruption of Shinmoe-dake, Japan—constraints from melt inclusions and phase equilibria experiments. *Journal of Volcanology and Geothermal Research*. doi:10.1016/j.jvolgeores.2013.03.017.

ter Heege, J. H., Dohmen, R., Becker, H., and Chakraborty, S. (2006). Experimental determination of Fe–Mg interdiffusion coefficients in orthopyroxene using pulsed laser ablation and nanoscale thin films. Abstract MR21A-0004 presented at AGU Fall Meeting, San Francisco, California, 11-15 December.

Thunell, R., Federman, A., Sparks, S., and Williams, D. (1979). The age, origin, and volcanological significance of the Y-5 ash layer in the Mediterranean. *Quaternary Research*, 12(2):241–253. doi:10.1016/0033-5894(79)90060-7.

Tirel, C., Gueydan, F., Tiberi, C., and Brun, J.-P. (2004). Aegean crustal thickness inferred from gravity inversion. Geodynamical implications. *Earth and Planetary Science Letters*, 228(3-4):267–280. doi:10.1016/j.epsl.2004.10.023.

Tomiya, A. and Takahashi, E. (2005). Evolution of the magma chamber beneath Usu volcano since 1663: a natural laboratory for observing changing phenocryst compositions and textures. *Journal of Petrology*, 46(12):2395 –2426. doi:10.1093/petrology/egi057.

Traineau, H. and Dalabakis, P. (1989). Mise en evidence d'une éruption phreatique historique sur l'ile de Milos (Grece). *Comptes rendus de l'Académie des sciences, Paris*, 308(2):247–252.

Trotet, F., Jolivet, L., and Vidal, O. (2001). Tectono-metamorphic evolution of Syros and Sifnos islands (Cyclades, Greece). *Tectonophysics*, 338(2):179–206. doi:10.1016/S0040-1951(01)00138-X.

Ulvrová, M., Paris, R., Kelfoun, K., and Nomikou, P. (2013). Numerical simulations of tsunami generated by underwater volcanic explosions at Karymskoye lake (Kamchatka, Russia) and Kolumbo volcano (Aegean Sea, Greece). *Natural Hazards and Earth System Sciences Discussions*, 1(6):6399–6432. doi:10.5194/nhessd-1-6399-2013.

Vaggelli, G., Pellegrini, M., Vougioukalakis, G., Innocenti, S., and Francalanci, L. (2009). Highly Sr radiogenic tholeiitic magmas in the latest inter-Plinian activity of Santorini volcano, Greece. *Journal of Geophysical Research*, 114:B06201. doi:10.1029/2008JB005936.

Valsami-Jones, E., Baltatzis, E., Bailey, E., Boyce, A. J., Alexander, J. L., Magganas, A., Anderson, L., Waldron, S., and Ragnarsdottir, K. V. (2005). The geochemistry of fluids from an active shallow submarine hydrothermal system: Milos island, Hellenic Volcanic Arc. *Journal of Volcanology and Geothermal Research*, 148(1-2):130–151. doi:10.1016/j.jvolgeores.2005.03.018.

van den Bogaard, P. and Schirnick, C. (1995). $^{40}Ar/^{39}Ar$ laser probe ages of Bishop Tuff quartz phenocrysts substantiate long-lived silicic magma chamber at Long Valley, United States. *Geology*, 23(8):759–762. doi:10.1130/0091-7613(1995)023<0759:AALPAO>2.3.CO;2.

van Hinsbergen, D. J. J., Snel, E., Garstman, S. A., Mărunţeanu, M., Langereis, C. G., Wortel, M. J. R., and Meulenkamp, J. E. (2004). Vertical motions in the Aegean volcanic arc: evidence for rapid subsidence preceding volcanic activity on Milos and Aegina. *Marine Geology*, 209(1-4):329–345. doi:10.1016/j.margeo.2004.06.006.

Van Orman, J. A., Cherniak, D. J., and Kita, N. T. (2014). Magnesium diffusion in plagioclase: Dependence on composition, and implications for thermal resetting of the ^{26}Al–^{26}Mg early solar system chronometer. *Earth and Planetary Science Letters*, 385:79–88. doi:10.1016/j.epsl.2013.10.026.

Vazquez, J. A. and Reid, M. R. (2004). Probing the accumulation history of the voluminous Toba magma. *Science*, 305(5686):991–994. doi:10.1126/science.1096994.

Vespa, M., Keller, J., and Gertisser, R. (2006). Interplinian explosive activity of Santorini volcano (Greece) during the past 150,000 years. *Journal of Volcanology and Geothermal Research*, 153(3-4):262–286. doi:10.1016/j.jvolgeores.2005.12.009.

Vinci, A. (1985). Distribution and chemical composition of tephra layers from Eastern Mediterranean abyssal sediments. *Marine Geology*, 64(1-2):143–155. doi:10.1016/0025-3227(85)90165-3.

Walcott, C. R. and White, S. H. (1998). Constraints on the kinematics of post-orogenic extension imposed by stretching lineations in the Aegean region. *Tectonophysics*, 298(1-3):155–175. doi:10.1016/S0040-1951(98)00182-6.

Wang, Z., Hiraga, T., and Kohlstedt, D. L. (2004). Effect of H^+ on Fe–Mg interdiffusion in olivine, $(Fe,Mg)_2SiO_4$. *Applied Physics Letters*, 85(2):209. doi:10.1063/1.1769593.

Wark, D. A., Hildreth, W., Spear, F. S., Cherniak, D. J., and Watson, E. B. (2007). Pre-eruption recharge of the Bishop magma system. *Geology*, 35(3):235–238. doi:10.1130/G23316A.1.

Wiebe, R. A. (1993). The Pleasant Bay layered gabbro–diorite, coastal Maine: Ponding and crystallization of basaltic injections into a silicic magma chamber. *Journal of Petrology*, 34(3):461–489. doi:10.1093/petrology/34.3.461.

Wiebe, R. A. and Collins, W. J. (1998). Depositional features and stratigraphic sections in granitic plutons: implications for the emplacement and crystallization of granitic magma. *Journal of Structural Geology*, 20(9–10):1273–1289. doi:10.1016/S0191-8141(98)00059-5.

Wilcock, J., Goff, F., Minarik, W. G., and Stix, J. (2012). Magmatic recharge during the formation and resurgence of the Valles Caldera, New Mexico, USA: Evidence from quartz compositional zoning and geothermometry. *Journal of Petrology*. doi:10.1093/petrology/egs078.

Wilson, C. J. N. (2001). The 26.5 ka Oruanui eruption, New Zealand: an introduction and overview. *Journal of Volcanology and Geothermal Research*, 112(1–4):133–174. doi:10.1016/S0377-0273(01)00239-6.

Wilson, C. J. N. and Charlier, B. L. A. (2009). Rapid rates of magma generation at contemporaneous magma systems, Taupo Volcano, New Zealand: Insights from U–Th model-age spectra in zircons. *Journal of Petrology*, 50(5):875–907. doi:10.1093/petrology/egp023.

Winick, J. A., McIntosh, W. C., and Dunbar, N. W. (2001). Melt-inclusion-hosted excess ^{40}Ar in quartz crystals of the Bishop and Bandelier magma systems. *Geology*, 29(3):275–278. doi:10.1130/0091-7613(2001)029<0275:MIHEAI>2.0.CO;2.

Wolff, J. A., Balsley, S. D., and Gregory, R. T. (2002). Oxygen isotope disequilibrium between quartz and sanidine from the Bandelier Tuff, New Mexico, consistent with a short residence time of phenocrysts in rhyolitic magma. *Journal of Volcanology and Geothermal Research*, 116(1–2):119–135. doi:10.1016/S0377-0273(02)00214-7.

Wolff, J. A. and Ramos, F. C. (2003). Pb isotope variations among Bandelier Tuff feldspars: No evidence for a long-lived silicic magma chamber. *Geology*, 31(6):533–536. doi:10.1130/0091-7613(2003)031<0533:PIVABT>2.0.CO;2.

Wotzlaw, J.-F., Schaltegger, U., Frick, D. A., Dungan, M. A., Gerdes, A., and Günther, D. (2013). Tracking the evolution of large-volume silicic magma reservoirs from assembly to supereruption. *Geology*, 41(8):867–870. doi:10.1130/G34366.1.

Wulf, S., Kraml, M., Kuhn, T., Schwarz, M., Inthorn, M., Keller, J., Kuscu, I., and Halbach, P. (2002). Marine tephra from the Cape Riva eruption (22 ka) of Santorini in the Sea of Marmara. *Marine Geology*, 183(1-4):131–141. doi:10.1016/S0025-3227(01)00302-4.

Yund, R. A. (1986). Interdiffusion of NaSi–CaAl in peristerite. *Physics and Chemistry of Minerals*, 13(1):11–16. doi:10.1007/BF00307308.

Yund, R. A. and Snow, E. (1989). Effects of hydrogen fugacity and confining pressure on the interdiffusion rate of NaSi–CaAl in plagiolcalse. *Journal of Geophysical Research B: Solid Earth*, 94(B8):10662–10668. doi:10.1029/JB094iB08p10662.

Zellmer, G., Turner, S., and Hawkesworth, C. (2000). Timescales of destructive plate margin magmatism: new insights from Santorini, Aegean volcanic arc. *Earth and Planetary Science Letters*, 174(3-4):265–281. doi:10.1016/S0012-821X(99)00266-6.

Zellmer, G. F., Blake, S., Vance, D., Hawkesworth, C., and Turner, S. (1999). Plagioclase residence times at two island arc volcanoes (Kameni Islands, Santorini, and Soufriere, St. Vincent) determined by Sr diffusion systematics. *Contributions to Mineralogy and Petrology*, 136(4):345–357. doi:10.1007/s004100050543.

Zellmer, G. F., Dulski, P., Iizuka, Y., and Perfit, M. R. (2012). Rates and processes of crystallization in on-axis and off-axis MOR basaltic melts. *Lithos*, 154:1–15. doi:10.1016/j.lithos.2012.07.019.

Zellmer, G. F., Rubin, K. H., Dulski, P., Iizuka, Y., Goldstein, S. L., and Perfit, M. R. (2011). Crystal growth during dike injection of MOR basaltic melts: evidence from preservation of local Sr disequilibria in plagioclase. *Contributions to Mineralogy and Petrology*, 161(1):153–173. doi:10.1007/s00410-010-0518-y.

Zellmer, G. F., Sparks, R. S. J., Hawkesworth, C. J., and Wiedenbeck, M. (2003). Magma emplacement and remobilization timescales beneath Montserrat: Insights from Sr and Ba zonation in plagioclase phenocrysts. *Journal of Petrology*, 44(8):1413 –1431. doi:10.1093/petrology/44.8.1413.

Zhang, Y., Ni, H., and Chen, Y. (2010). Diffusion data in silicate melts. *Reviews in Mineralogy and Geochemistry*, 72(1):311–408. doi:10.2138/rmg.2010.72.8.

Zimmerer, M. J. and McIntosh, W. C. (2012). The geochronology of volcanic and plutonic rocks at the Questa caldera: Constraints on the origin of caldera-related silicic magmas. *Geological Society of America Bulletin*, 124(7-8):1394–1408. doi:10.1130/B30544.1.

Zimmerer, M. J. and McIntosh, W. C. (2013). Geochronologic evidence of upper-crustal in situ differentiation: Silicic magmatism at the Organ caldera complex, New Mexico. *Geosphere*, 9(1):155–169. doi:10.1130/GES00841.1.

Appendix A

Sample locations

Sample	Locality	Unit	Description	Latitude	Longitude
GS10-03	Manolas	Therasia 19	lava	36.4417	25.3527
GS10-06	Manolas	Therasia 27	lava	36.4406	25.3565
GS10-14	South Therasia	Therasia 8	lava	36.4122	25.3507
GS10-16	South Therasia	Therasia 9	lava	36.4122	25.3507
GS10-17	South Therasia	Therasia 5	lava	36.4122	25.3507
GS10-18	South Therasia	Therasia 14	lava	36.4184	25.3483
GS10-20	Mt. Vigalos	Therasia 22	lava	36.4265	25.3468
GS10-22	Mt. Vigalos	Therasia 22	lava	36.4265	25.3468
GS10-27a	South Therasia	Therasia 3	lava	36.4139	25.3440
GS10-27b	South Therasia	Therasia 3	lava	36.4139	25.3440
GS10-27c	South Therasia	Therasia 3	enclave	36.4139	25.3440
GS10-27d	South Therasia	Therasia A	single pumice clast	36.4139	25.3440
GS10-27e	South Therasia	Therasia A	single pumice clast	36.4139	25.3440
GS10-27f	South Therasia	Therasia A	pumice	36.4139	25.3440
GS10-27g	South Therasia	Therasia B	pumice and obsidian	36.4139	25.3440
GS10-27h	South Therasia	Therasia C	pumice	36.4139	25.3440
GS10-28a	South Therasia	Therasia D	banded pumice	36.4144	25.3508
GS10-28b	South Therasia	Therasia D	single scoria clast	36.4144	25.3508
GS10-28c	South Therasia	Therasia D	single scoria clast	36.4144	25.3508
GS10-28d	South Therasia	Therasia D	single pumice clast	36.4144	25.3508
GS10-28e	South Therasia	Therasia D	single pumice clast	36.4144	25.3508
GS10-28f	South Therasia	Therasia D	pumice	36.4144	25.3508
GS10-30a	Mt. Vigalos	Therasia 19	lava	36.4211	25.3477
GS10-30b	Mt. Vigalos	Therasia 15	lava	36.4211	25.3477
GS10-31a	Mt. Vigalos	Therasia D	single scoria clast	36.4267	25.3468
GS10-31b	Mt. Vigalos	Therasia D	single pumice clast	36.4267	25.3468
GS10-31c	Mt. Vigalos	Therasia D	single pumice clast	36.4267	25.3468
GS10-31d	Mt. Vigalos	Therasia D	single pumice clast	36.4267	25.3468
GS10-31e	Mt. Vigalos	Therasia D	pumice	36.4267	25.3468
GS10-32	Manolas	Therasia E	pumice	36.4373	25.3475
GS10-33	Manolas	Therasia 27	lava	36.4374	25.3478
GS10-36	Oia	Therasia 26	lava	36.4628	25.3699
GS10-37b	Oia	Therasia 26	enclave	36.4659	25.3681
GS10-38a	Oia	Oia A	pumice	36.4659	25.3682

Sample	Locality	Unit	Description	Latitude	Longitude
GS10-38b	Oia	Oia B	pumice	36.4659	25.3682
GS10-38c	Oia	Oia C	pumice	36.4659	25.3682
GS10-38d	Oia	Oia D	pumice	36.4659	25.3682
GS10-39a	Oia	Cape Riva A	scoria	36.4663	25.3684
GS10-39b	Oia	Cape Riva A	banded pumice	36.4663	25.3684
GS10-39c	Oia	Cape Riva A	pumice	36.4663	25.3684
GS10-40	Phira	Therasia 25	lava	36.4198	25.4297
GS10-41	Cape Skaros	Skaros	lava	36.4324	25.4196
GS10-43	South Therasia	Therasia 11	enclave	36.4168	25.3377
GS10-44b	South Therasia	Therasia 1	lava	36.4181	25.3363
GS10-46	South Therasia	Therasia 11	lava	36.4168	25.3377
GS10-48	Mt. Vigalos	Therasia 21	lava	36.4311	25.3445
GS10-49	Balos	Upper Scoria 2	scoria	36.3617	25.3934
GS10-50	Ammoudi	Andesite of Oia	lava	36.4659	25.3680
GS11-07a	Balos	Cape Riva B	single pumice clast	36.3603	25.4044
GS11-07b	Balos	Cape Riva B	single pumice clast	36.3603	25.4044
GS11-07c	Balos	Cape Riva B	single pumice clast	36.3603	25.4044
GS11-12a	Akrotiri Quary	Therasia	pumice	36.3628	25.4178
GS11-12b	Akrotiri Quary	Therasia	pumice	36.3628	25.4178
GS11-30a	Cape Riva	Cape Riva C	single pumice clast	36.4505	25.3466
GS11-30b	Cape Riva	Cape Riva C	single pumice clast	36.4505	25.3466
GS11-30c	Cape Riva	Cape Riva C	single pumice clast	36.4505	25.3466
GS11-32a	Red Beach	Cape Riva B	single pumice clast	36.3481	25.4151
GS11-32b	Red Beach	Cape Riva B	single pumice clast	36.3481	25.4151
GS11-32c	Red Beach	Cape Riva B	single pumice clast	36.3481	25.4151
GS11-34a	Katheros	Cape Riva A	single dacite pumice	36.4661	25.3682
GS11-34b	Katheros	Cape Riva A	dacite pumice	36.4661	25.3682
GS11-34c	Katheros	Cape Riva A	single dacite pumice	36.4661	25.3682
GS11-34d	Katheros	Cape Riva A	single dacite pumice	36.4661	25.3682
GS11-34e	Katheros	Cape Riva A	single dacite pumice	36.4661	25.3682
GS11-34f	Katheros	Cape Riva A	single dacite pumice	36.4661	25.3682
GS11-34g	Katheros	Cape Riva A	single dacite pumice	36.4661	25.3682
GS11-34h	Katheros	Cape Riva A	andesite scoria	36.4661	25.3682
GS11-34i	Katheros	Cape Riva A	single andesite scoria	36.4661	25.3682
GS11-39a	Ammoudi	Cape Riva D	single pumice clast	36.4629	25.3708
GS11-39b	Ammoudi	Cape Riva D	single pumice clast	36.4629	25.3708
GS11-39c	Ammoudi	Cape Riva D	single pumice clast	36.4629	25.3708

Appendix B

Whole rock and groundmass chemical analyses

	Andesite of Oia	Lower Therasia Andesite		Therasia Dacites			
Sample	GS10-50	GS10-44b	GS10-33	GS10-27a	GS10-17	GS10-14	GS10-16
Unit	Flow 26	Flow 1	Flow 24	Flow 3	Flow 5	Flow 8	Flow 9
Type	Lava	Lava	Lava	Lava	Lava	Lava	Lava
Major elements (wt% dry)							
SiO_2	57.26	56.26	56.19	65.83	66.00	65.36	65.80
Al_2O_3	15.74	17.73	17.45	15.73	15.38	15.86	15.65
TiO_2	1.28	1.04	1.01	0.81	0.75	0.80	0.80
FeO_T	9.15	8.05	7.78	5.23	4.66	4.71	4.64
MgO	3.54	4.16	4.07	1.25	1.08	1.31	1.21
CaO	7.28	8.26	8.05	3.69	3.15	3.83	3.53
Na_2O	3.96	2.87	3.74	4.33	5.48	5.04	5.21
K_2O	1.40	1.32	1.39	2.77	3.19	2.75	2.78
MnO	0.18	0.16	0.16	0.14	0.13	0.13	0.13
P_2O_5	0.21	0.16	0.16	0.22	0.18	0.20	0.24
Trace elements (ppm)							
Li	11.4	10.3	9.6	24.3	25.5	23.7	24.2
Sc	30.1	26.3	25.7	13.1	13.9	13.7	13.3
V	275	215	206	40	30	50	41
Cr	5.23	13.30	17.50	2.76	1.17	2.27	1.17
Co	23.00	22.30	22.00	7.08	5.77	6.92	6.17
Ni	7.84	11.10	11.90	1.69	0.86	1.13	0.79
Cu	48.4	37.0	44.4	20.4	17.5	14.5	12.7
Zn	92.0	79.1	73.8	77.2	76.4	71.6	71.2
As	1.98	0.91	1.02	1.99	2.18	1.90	2.00
Rb	52.7	42.8	45.1	95.0	104.0	91.6	92.6
Sr	183	247	247	166	133	180	177
Y	38.9	31.2	31.1	41.4	50.8	46.0	46.8
Zr	175	140	146	243	321	272	281
Nb	6.44	5.99	6.03	11.70	12.90	12.50	12.60
Cd	0.070	<DL	0.081	0.078	0.129	0.108	0.117
Cs	1.77	0.65	0.70	2.90	3.21	2.74	2.80
Ba	236	253	256	450	513	482	489
La	16.4	16.5	16.8	28.6	32.2	30.3	30.6
Ce	36.1	35.2	35.3	57.9	66.5	63.1	63.8
Pr	4.62	4.36	4.32	6.60	7.70	7.33	7.49
Nd	19.3	18.3	18.0	25.6	30.1	29.1	29.4
Sm	5.08	4.41	4.35	5.83	6.91	6.51	6.54
Eu	1.33	1.18	1.17	1.28	1.43	1.42	1.39
Gd	5.74	4.79	4.63	5.92	7.14	6.62	6.73
Tb	0.99	0.80	0.79	1.00	1.20	1.12	1.11
Dy	6.27	5.17	5.17	6.45	7.94	7.09	7.12
Ho	1.36	1.08	1.08	1.40	1.68	1.54	1.58
Er	4.10	3.30	3.26	4.26	5.20	4.76	4.75
Yb	4.13	3.33	3.20	4.36	5.30	4.71	4.79
Lu	0.598	0.501	0.483	0.665	0.810	0.725	0.722
Hf	4.82	3.80	3.85	6.06	7.51	6.55	6.76
Ta	0.488	0.423	0.436	0.886	0.920	0.869	0.868
Tl	0.111	0.170	0.161	0.455	0.491	0.418	0.441
Pb	8.1	6.6	6.5	15.2	16.9	14.7	14.9
Th	9.8	8.2	8.4	15.7	17.9	15.1	15.4
U	2.91	2.34	2.41	4.40	5.15	4.14	4.23

	Therasia Dacites				Upper Therasia Andesite	
Sample	GS10-30a	GS10-20	GS10-48	GS10-40	GS10-46	GS10-22
Unit	Flow 19	Flow 20	Flow 21	Flow 25	Flow 11	Flow 22
Type	Lava	Lava	Lava	Lava	Lava	Lava
Major elements (wt% dry)						
SiO_2	67.46	65.08	67.87	68.67	60.79	60.26
Al_2O_3	15.26	15.65	15.17	15.25	17.04	17.16
TiO_2	0.72	0.82	0.67	0.61	0.85	0.86
FeO_T	4.42	5.18	4.25	4.09	6.01	6.05
MgO	0.87	1.43	0.67	0.65	2.58	2.66
CaO	2.68	3.79	2.39	2.37	5.85	5.98
Na_2O	5.23	4.97	5.50	5.60	4.43	4.52
K_2O	3.07	2.75	3.21	2.50	2.09	2.18
MnO	0.12	0.14	0.12	0.12	0.14	0.14
P_2O_5	0.17	0.21	0.16	0.14	0.20	0.19
Trace elements (ppm)						
Li	25.2	24.3	26.4	28.2	16.7	18.1
Sc	13.2	15.3	12.8	14.9	17.5	17.4
V	22	51	8	8	106	109
Cr	0.42	2.88	0.64	0.98	8.44	9.52
Co	4.88	7.91	3.35	3.38	13.10	13.80
Ni	0.75	2.01	0.23	<DL	4.85	5.65
Cu	14.9	20.4	10.6	16.3	21.7	16.5
Zn	76.4	77.8	79.6	75.4	68.7	71.9
As	2.26	2.03	2.36	2.70	1.39	1.54
Rb	107.0	95.6	109.0	106.0	69.0	68.1
Sr	123	146	117	108	232	231
Y	51.1	48.5	53.7	55.4	38.0	37.9
Zr	333	296	354	352	201	200
Nb	13.30	11.80	13.40	14.70	9.58	9.47
Cd	0.119	0.116	0.112	0.150	0.069	0.077
Cs	3.29	2.97	3.40	3.34	1.40	2.09
Ba	528	480	542	533	400	391
La	33.1	30.4	33.4	32.7	24.0	23.5
Ce	68.7	62.9	69.0	66.5	50.5	49.5
Pr	7.96	7.41	8.11	8.11	6.01	5.93
Nd	30.8	28.9	31.5	32.0	23.9	23.4
Sm	7.04	6.69	7.18	7.30	5.60	5.40
Eu	1.37	1.39	1.46	1.40	1.30	1.29
Gd	7.21	6.82	7.44	7.67	5.66	5.57
Tb	1.22	1.13	1.25	1.27	0.94	0.92
Dy	8.04	7.56	8.29	8.76	6.03	5.96
Ho	1.73	1.65	1.82	1.88	1.30	1.27
Er	5.20	4.98	5.49	5.73	3.96	3.89
Yb	5.35	5.06	5.68	5.88	3.99	3.94
Lu	0.821	0.767	0.854	0.883	0.597	0.589
Hf	7.80	7.05	8.32	8.62	5.25	5.27
Ta	0.933	0.833	0.928	1.050	0.643	0.634
Tl	0.484	0.436	0.348	0.454	0.279	0.287
Pb	17.1	15.8	16.9	18.3	10.8	11.6
Th	18.8	16.5	18.7	17.7	11.3	11.3
U	5.25	4.71	5.34	5.06	3.20	3.15

	Therasia Pumices					
Sample	GS10-27d	GS10-27g(o)	GS10-27g(p)	GS10-27h	GS10-28c	GS10-28d
Unit	CTP	PF B	PF B	PF C	PF D	PF D
Type	Pumice	Obsidian	Pumice	Pumice	Pumice	Pumice
Major elements (wt% dry)						
SiO_2	67.50	64.60	64.82	68.14	65.16	66.24
Al_2O_3	15.10	15.61	15.62	15.15	15.31	15.41
TiO_2	0.72	0.97	0.98	0.60	0.86	0.87
FeO_T	4.35	5.39	5.54	4.14	4.79	4.83
MgO	0.88	1.42	1.46	0.78	1.07	1.07
CaO	2.68	3.70	3.80	2.29	3.10	3.16
Na_2O	5.54	5.38	5.05	5.36	6.52	5.34
K_2O	2.92	2.48	2.28	3.27	2.81	2.68
MnO	0.13	0.15	0.15	0.12	0.14	0.14
P_2O_5	0.17	0.30	0.31	0.15	0.25	0.26
Trace elements (ppm)						
Li	20.2	23.5	23.1	22.4	25.3	24.7
Sc	13.6	16.3	16.8	12.0	15.2	14.8
V	9	44	48	11	21	20
Cr	<DL	4.77	1.02	0.93	0.81	0.43
Co	5.66	6.69	7.26	3.50	4.73	4.64
Ni	1.09	2.61	0.90	0.65	0.78	1.66
Cu	6.5	8.9	10.5	13.6	5.8	8.7
Zn	71.4	85.9	86.1	71.1	83.0	82.2
As	2.12	1.96	2.06	2.94	2.08	2.09
Rb	86.6	80.2	79.8	104.0	91.4	90.7
Sr	112	164	168	108	145	143
Y	46.6	52.1	51.7	55.2	51.9	52.3
Zr	279	280	287	362	296	308
Nb	11.90	11.20	11.10	13.30	12.00	11.90
Cd	0.136	0.115	0.128	0.140	0.127	0.108
Cs	2.71	2.54	2.54	3.33	2.90	2.87
Ba	454	450	442	508	486	480
La	28.3	29.5	29.4	32.2	31.2	31.1
Ce	56.7	62.8	62.4	67.6	65.1	64.5
Pr	6.88	7.61	7.57	7.99	7.78	7.54
Nd	27.7	30.8	30.6	31.6	30.7	30.5
Sm	6.27	7.29	7.05	7.23	7.20	7.23
Eu	1.24	1.64	1.58	1.35	1.54	1.54
Gd	6.50	7.73	7.47	7.45	7.51	7.31
Tb	1.09	1.26	1.25	1.30	1.23	1.24
Dy	7.20	8.23	8.03	8.52	8.13	8.06
Ho	1.55	1.76	1.77	1.85	1.76	1.75
Er	4.78	5.48	5.27	5.64	5.33	5.33
Yb	4.91	5.41	5.34	5.83	5.43	5.38
Lu	0.743	0.837	0.822	0.888	0.831	0.832
Hf	6.85	6.96	6.88	8.55	7.39	7.30
Ta	0.852	0.758	0.755	0.905	0.820	0.833
Tl	0.481	0.384	0.408	0.512	0.452	0.417
Pb	15.3	14.1	14.4	17.6	15.9	15.5
Th	15.2	14.2	13.7	17.5	15.7	15.7
U	4.33	4.11	3.92	4.94	4.49	4.52

	Therasia Pumices			Therasia Mafic Enclaves		Andesite of Oia	L. Therasia Andesite
Sample	GS10-28f	GS10-32	GS10-38d	GS10-27c	GS10-43	GS10-50	GS10-44b
Unit	PF D	PF E	Oia PF D	Flow 3	Flow 11	Flow 26	Flow 1
Type	Pumice	Pumice	Pumice	Enclave	Enclave	Gdms	Gdms
Major elements (wt% dry)							
SiO_2	65.49	65.32	66.34	49.62	51.87	58.44	57.39
Al_2O_3	14.94	15.37	15.55	17.41	19.07	15.71	17.35
TiO_2	0.72	0.78	0.83	0.51	0.89	1.31	1.08
FeO_T	4.36	5.06	4.71	7.39	8.08	9.41	8.19
MgO	0.91	1.29	1.04	8.58	5.44	3.50	3.79
CaO	2.65	3.46	3.00	14.53	10.16	7.35	7.39
Na_2O	7.75	5.65	5.29	1.39	3.30	3.77	3.94
K_2O	2.87	2.70	2.87	0.36	0.90	1.42	1.59
MnO	0.13	0.14	0.14	0.16	0.16	0.18	0.16
P_2O_5	0.17	0.21	0.22	0.05	0.14	0.21	0.19
Trace elements (ppm)							
Li	23.6	29.4	22.7	9.5	16.2	11.4	9.6
Sc	13.3	14.0	13.8	46.2	25.9	30.5	28.9
V	13	29	24	201	193	285	192
Cr	0.92	1.83	2.17	44.20	31.30	5.40	8.92
Co	4.40	5.99	4.75	37.50	27.40	23.90	21.30
Ni	1.70	0.92	1.46	32.80	15.80	8.93	10.40
Cu	8.9	33.1	6.4	17.6	54.4	48.3	40.8
Zn	78.9	82.1	77.4	50.3	72.6	98.8	85.7
As	2.31	2.39	2.61	0.27	0.77	1.91	1.12
Rb	97.5	91.8	89.7	10.1	25.8	55.7	52.8
Sr	124	155	153	215	323	183	261
Y	51.7	47.7	52.6	14.2	23.8	39.6	37.9
Zr	323	265	318	40	108	191	186
Nb	12.20	11.20	13.10	1.24	4.71	6.23	7.24
Cd	0.148	0.130	0.145	0.047	0.072	0.075	0.083
Cs	3.02	5.30	3.02	0.29	0.52	1.86	0.77
Ba	496	451	476	65.2	251	235	295
La	31.3	29.4	31.7	3.8	11.9	16.2	19.2
Ce	64.7	60.7	69.3	9.0	26.9	38.1	41.4
Pr	7.60	7.14	7.88	1.19	3.37	4.59	5.20
Nd	29.9	28.0	31.5	5.4	14.2	19.5	20.9
Sm	6.89	6.27	7.18	1.68	3.43	4.96	5.04
Eu	1.43	1.37	1.46	0.56	0.97	1.26	1.30
Gd	7.05	6.66	7.58	1.98	3.67	5.53	5.27
Tb	1.21	1.10	1.25	0.35	0.62	0.96	0.88
Dy	7.88	7.35	8.25	2.40	3.92	6.32	5.82
Ho	1.72	1.59	1.77	0.50	0.84	1.37	1.25
Er	5.23	4.74	5.36	1.56	2.53	4.08	3.82
Yb	5.40	4.81	5.57	1.43	2.42	4.15	3.76
Lu	0.814	0.757	0.830	0.226	0.369	0.622	0.573
Hf	7.58	6.61	7.87	1.18	2.78	4.89	4.63
Ta	0.843	0.789	0.872	0.090	0.285	0.477	0.524
Tl	0.464	0.609	0.503	0.083	0.110	0.126	0.199
Pb	17.5	17.5	16.5	2.9	15.9	8.2	7.9
Th	16.6	15.4	16.4	1.3	3.5	9.8	11.0
U	4.74	4.67	4.37	0.45	1.02	2.97	2.94

	Therasia Dacites						
Sample	GS10-27a	GS10-17	GS10-14	GS10-16	GS10-30a	GS10-20	GS10-48
Unit	Flow 3	Flow 5	Flow 8	Flow 9	Flow 19	Flow 20	Flow 21
Type	Gdms	Gdms	Gdms	Gdms	Gdms	Gdms	Gdms
Major elements (wt% dry)							
SiO_2	66.06	67.99	67.35	67.44	68.99	67.07	68.93
Al_2O_3	15.36	14.70	15.35	15.13	14.93	15.22	15.23
TiO_2	0.73	0.63	0.68	0.73	0.60	0.66	0.60
FeO_T	4.91	4.03	4.00	4.28	3.88	4.36	3.97
MgO	1.14	0.85	1.05	1.08	0.76	1.17	0.64
CaO	3.35	2.34	3.13	2.80	2.23	3.07	2.31
Na_2O	5.25	5.91	5.19	5.10	5.45	5.09	5.48
K_2O	2.86	3.25	2.94	3.06	3.49	3.04	3.16
MnO	0.14	0.12	0.12	0.13	0.12	0.12	0.12
P_2O_5	0.19	0.19	0.20	0.24	0.15	0.20	0.15
Trace elements (ppm)							
Li	23.6	26.9	24.5	24.8	24.1	25.1	25.4
Sc	15.5	14.2	13.1	13.4	12.9	15.5	14.1
V	27	15	24	25	9	29	5
Cr	2.54	0.76	1.09	1.05	<DL	2.28	0.85
Co	6.96	4.48	5.25	5.33	3.93	6.28	3.08
Ni	1.95	0.75	1.02	1.19	0.80	4.39	0.75
Cu	24.6	22.9	16.5	15.6	18.0	25.3	13.0
Zn	82.5	75.9	68.5	73.1	71.5	77.2	78.3
As	1.88	3.06	1.97	2.60	3.04	2.85	2.03
Rb	106.0	105.0	100.0	102.0	106.0	105.0	110.0
Sr	172	108	160	146	99	125	125
Y	46.5	53.6	48.4	50.5	52.7	50.9	50.8
Zr	267	334	287	302	341	312	365
Nb	12.30	13.30	12.90	13.20	13.50	12.40	13.60
Cd	0.101	0.117	0.107	0.113	0.128	0.116	0.110
Cs	2.92	3.55	3.00	3.05	3.57	3.26	3.28
Ba	463	542	514	520	510	511	548
La	29.3	33.9	32.2	32.3	33.6	31.9	29.1
Ce	59.5	70.2	66.4	67.9	69.8	66.6	63.4
Pr	6.90	8.22	7.77	8.05	8.22	7.80	7.40
Nd	26.6	31.9	30.5	31.4	31.5	30.4	29.5
Sm	5.96	7.16	6.72	7.04	7.17	7.04	6.63
Eu	1.26	1.33	1.35	1.39	1.32	1.33	1.35
Gd	6.08	7.35	6.89	7.07	7.27	7.13	6.88
Tb	1.01	1.27	1.13	1.19	1.24	1.22	1.19
Dy	6.71	8.43	7.42	7.74	8.20	8.00	8.04
Ho	1.44	1.80	1.61	1.67	1.76	1.71	1.70
Er	4.43	5.53	4.92	5.18	5.39	5.27	5.27
Yb	4.48	5.74	5.03	5.25	5.58	5.40	5.56
Lu	0.699	0.871	0.777	0.806	0.851	0.833	0.855
Hf	6.42	8.38	7.18	7.52	8.43	7.82	8.62
Ta	0.896	0.982	0.929	0.969	0.992	0.917	0.942
Tl	0.461	0.546	0.466	0.477	0.531	0.484	0.355
Pb	16.3	18.8	16.3	16.4	18.5	17.3	17.7
Th	18.3	20.5	16.6	17.2	20.5	18.8	17.3
U	4.64	5.84	4.64	4.77	5.78	5.35	5.56

	Therasia Dacites	U. Therasia Andesite	Therasia Pumices				
Sample	GS10-40	GS10-22	GS10-27d	GS10-27h	GS10-28c	GS10-28d	GS10-28f
Unit	Flow 25	Flow 22	CTP	PF C	PF D	PF D	PF D
Type	Gdms	Gdms	Glass	Glass	Glass	Glass	Glass
Major elements (wt% dry)							
SiO_2	68.97	63.67	67.87	69.13	65.82	66.69	68.38
Al_2O_3	15.23	15.44	15.28	14.89	15.11	15.16	15.44
TiO_2	0.56	0.79	0.64	0.49	0.93	0.81	0.66
FeO_T	3.90	5.60	4.05	3.74	4.93	4.60	4.05
MgO	0.60	2.39	0.74	0.57	1.33	1.05	0.79
CaO	2.20	4.62	2.63	1.99	3.02	2.87	2.63
Na_2O	5.58	4.55	5.51	5.47	5.72	5.64	5.41
K_2O	3.27	2.60	2.97	3.47	2.70	2.79	3.02
MnO	0.12	0.14	0.13	0.11	0.15	0.14	0.13
P_2O_5	0.13	0.20	0.19	0.13	0.28	0.25	0.16
Trace elements (ppm)							
Li	29.7	20.3	24.1	24.1	24.6	25.1	24.8
Sc	13.5	18.5	15.4	14.4	16.7	14.8	15.7
V	6	81	7	5	16	13	9
Cr	0.82	8.41	2.20	0.63	<DL	<DL	1.09
Co	3.17	12.00	5.10	2.83	5.30	4.24	3.30
Ni	0.57	4.62	1.12	0.66	1.12	0.72	1.01
Cu	17.8	21.8	12.7	13.0	19.6	14.0	11.5
Zn	77.7	71.9	88.6	86.4	93.1	85.5	85.0
As	3.29	2.31	2.10	2.52	1.94	2.07	1.99
Rb	105.0	88.5	106.0	118.0	91.0	83.2	105.0
Sr	107	176	143	111	144	134	136
Y	57.9	44.9	56.7	60.6	52.2	50.9	55.3
Zr	369	271	336	380	298	309	327
Nb	13.70	11.40	12.70	13.60	12.00	11.90	12.00
Cd	0.136	0.097	0.123	0.143	0.111	0.104	0.120
Cs	3.54	2.72	3.06	3.45	2.83	2.89	2.98
Ba	554	455	511	537	478	486	502
La	33.8	27.9	31.5	32.8	30.7	28.9	31.5
Ce	71.1	63.2	65.7	68.8	65.3	62.0	65.1
Pr	8.45	7.07	7.77	8.32	7.73	7.33	7.78
Nd	33.2	27.9	30.1	32.7	30.8	29.5	30.2
Sm	7.53	6.31	7.02	7.40	7.15	6.73	7.02
Eu	1.40	1.20	1.41	1.29	1.52	1.42	1.39
Gd	7.76	6.40	7.10	7.62	7.25	7.09	7.03
Tb	1.32	1.09	1.23	1.29	1.23	1.20	1.19
Dy	8.91	7.12	8.30	8.61	8.09	8.05	8.13
Ho	1.90	1.51	1.75	1.88	1.75	1.74	1.72
Er	5.96	4.64	5.41	5.85	5.35	5.33	5.35
Yb	6.12	4.69	5.55	5.90	5.46	5.44	5.52
Lu	0.942	0.718	0.861	0.923	0.829	0.835	0.844
Hf	9.16	6.73	7.91	8.96	7.35	7.54	7.79
Ta	0.963	0.813	0.878	0.934	0.855	0.856	0.844
Tl	0.488	0.387	0.527	0.552	0.430	0.440	0.506
Pb	18.7	14.4	17.3	19.0	16.5	16.7	17.2
Th	19.0	14.6	18.6	20.1	15.7	14.8	18.7
U	5.47	4.07	4.97	5.30	4.59	4.70	4.88

	Cape Riva Andesite			Cape Riva Dacite			
Sample	S09-41	S80-145	S09-64	S09-40	S09-38	S82-52	S09-62
Unit	A	A	A	A	A	A	A
Type	Scoria	Scoria	Scoria	Pumice	Pumice	Pumice	Pumice
Major elements (wt% dry)							
SiO_2	60.19	60.41	60.46	65.84	66.38	66.68	67.11
Al_2O_3	16.43	16.61	16.77	15.40	15.41	15.58	15.17
TiO_2	0.88	0.83	0.84	0.76	0.78	0.73	0.71
FeO_T	6.58	6.33	6.44	4.88	4.78	4.57	4.61
MgO	3.17	3.03	3.08	1.16	1.19	1.05	1.02
CaO	6.20	6.22	6.29	3.28	3.28	3.12	2.88
Na_2O	4.63	4.65	4.30	5.84	5.85	5.49	5.55
K_2O	1.56	1.60	1.49	2.45	1.98	2.44	2.60
MnO	0.16	0.16	0.16	0.16	0.16	0.15	0.15
P_2O_5	0.19	0.16	0.17	0.22	0.20	0.19	0.19
Trace elements (ppm)							
Li	16.4	16.9	16.8	17.4	17.9	19.2	20.2
Sc	23.4	22.7	22.7	13.8	13.9	14.8	14.0
V	139	127	131	30	26	30	25
Cr	27.10	29.20	25.80	0.60	0.23	0.71	0.55
Co	15.50	14.70	15.00	6.39	4.79	4.39	4.65
Ni	14.20	12.00	11.10	2.57	3.51	2.38	1.11
Cu	37.0	35.8	33.3	7.4	10.2	7.8	7.8
Zn	82.1	82.6	78.6	75.5	71.6	80.8	76.0
As	1.47	1.42	1.34	1.82	1.89	1.98	2.27
Rb	50.0	50.2	50.4	71.7	72.2	78.7	84.9
Sr	185	188	186	127	132	139	120
Y	38.5	38.3	38.5	45.9	48.4	50.2	53.0
Zr	175	184	178	250	246	279	306
Nb	7.12	7.27	7.30	9.44	9.28	10.20	10.80
Cd	0.080	0.098	0.082	0.097	0.109	0.122	0.138
Cs	1.56	1.57	1.60	2.22	2.24	2.46	2.73
Ba	297	298	299	375	388	409	430
La	19.0	18.9	18.9	23.7	24.4	25.6	27.0
Ce	40.7	40.3	40.9	50.5	51.4	54.3	57.3
Pr	4.98	4.96	4.95	6.09	6.34	6.59	6.95
Nd	20.4	20.3	20.5	24.6	25.1	26.8	27.8
Sm	5.14	4.99	4.90	5.77	6.32	6.31	6.80
Eu	1.29	1.28	1.30	1.34	1.37	1.47	1.36
Gd	5.56	5.42	5.54	6.44	6.50	6.94	7.14
Tb	0.95	0.92	0.93	1.07	1.13	1.17	1.21
Dy	6.16	6.05	6.06	7.06	7.38	7.84	8.15
Ho	1.33	1.35	1.33	1.54	1.63	1.71	1.78
Er	4.11	4.02	4.13	4.77	4.89	5.12	5.38
Yb	4.08	4.00	4.12	4.92	5.02	5.22	5.60
Lu	0.624	0.609	0.622	0.747	0.766	0.799	0.829
Hf	4.69	4.61	4.74	6.22	6.03	6.66	7.24
Ta	0.498	0.498	0.498	0.640	0.648	0.697	0.745
Tl	0.217	0.193	0.225	0.353	0.324	0.374	0.398
Pb	9.5	13.0	9.5	12.5	11.8	14.6	14.3
Th	8.5	8.7	8.9	11.9	12.2	13.0	14.1
U	2.44	2.47	2.54	3.48	3.42	3.74	4.06

	Cape Riva Andesite		Cape Riva Dacite	Upper Scoria 2		Skaros
Sample	S09-41	S09-64	S09-40	GS10-49	GS10-49	GS10-41
Unit	A	A	A			Top flow
Type	Glass	Glass	Glass	Scoria	Gdms	Lava
Major elements (wt% dry)						
SiO_2	61.53	62.83	69.88	58.70	59.19	57.65
Al_2O_3	16.98	16.59	15.05	16.38	16.47	15.88
TiO_2	0.74	0.71	0.48	1.34	1.32	1.26
FeO_T	5.96	5.57	3.31	8.60	8.56	8.42
MgO	2.62	2.53	0.53	2.95	2.93	3.64
CaO	5.86	5.67	2.14	6.58	6.63	7.15
Na_2O	4.92	4.68	5.86	3.44	4.35	3.94
K_2O	1.82	1.81	2.95	1.59	1.54	1.63
MnO	0.15	0.14	0.12	0.18	0.18	0.17
P_2O_5	0.17	0.18	0.16	0.23	0.13	0.25
Trace elements (ppm)						
Li	17.7	17.2	20.4	15.5	15.1	13.3
Sc	24.6	19.6	14.8	25.5	28.6	28.9
V	126	111	8	200	198	194
Cr	21.20	20.80	4.33	1.17	1.93	54.70
Co	14.20	14.60	5.62	17.50	17.60	20.70
Ni	14.60	11.60	5.48	2.78	1.69	19.60
Cu	39.2	34.8	10.3	13.2	15.9	83.5
Zn	132.0	387.0	92.3	96.2	98.5	90.8
As	1.60	1.76	2.10	2.21	1.85	1.82
Rb	60.2	53.7	101.0	59.3	61.6	59.6
Sr	197	171	105	190	209	181
Y	44.2	39.5	61.1	40.4	42.9	43.4
Zr	214	212	341	177	194	198
Nb	7.58	7.40	11.60	7.09	7.09	7.41
Cd	0.087	0.089	0.124	0.079	0.086	0.084
Cs	1.70	1.83	2.82	2.10	2.06	1.47
Ba	323	331	460	224	225	244
La	20.5	19.3	28.9	17.5	17.4	18.6
Ce	43.6	44.9	61.6	38.6	38.1	41.6
Pr	5.41	5.17	7.40	4.9	4.89	5.3
Nd	21.6	21.2	29.5	20.7	20.6	22.0
Sm	5.28	5.16	7.09	5.37	5.20	5.59
Eu	1.27	1.24	1.28	1.38	1.43	1.42
Gd	5.68	5.45	7.50	5.97	5.84	6.43
Tb	0.97	0.94	1.29	0.99	0.99	1.09
Dy	6.58	6.34	8.58	6.56	6.60	7.06
Ho	1.41	1.37	1.87	1.41	1.42	1.50
Er	4.32	4.17	5.81	4.20	4.37	4.55
Yb	4.37	4.27	6.09	4.26	4.29	4.49
Lu	0.663	0.655	0.938	0.641	0.655	0.680
Hf	5.14	5.21	8.07	4.91	4.89	5.36
Ta	0.520	0.529	0.819	0.531	0.538	0.535
Tl	0.242	0.319	0.427	0.189	0.182	0.154
Pb	11.1	11.8	16.0	9.6	9.7	10.3
Th	10.9	9.2	17.3	10.3	11.3	10.4
U	2.86	2.90	4.56	3.12	3.18	3.05

Appendix C

LA ICP-MS data

Table C.1: GS10-14 XL32 Profile 1

Distance from rim (µm)	An (mol%)	Li (ppm)	Mg (ppm)	K (ppm)	Ca (ppm)	Ti (ppm)	Fe (ppm)	Sr (ppm)	Ba (ppm)	La (ppm)	Ce (ppm)	Nd (ppm)	Pb (ppm)
13	45.6	16.7	302	2996	67110	—	2968	565	208	5.84	8.44	2.07	4.25
33	44.9	17.7	304	3107	66184	—	2926	585	225	6.05	8.46	2.86	3.42
51	46.9	17.9	302	3331	69064	—	3144	606	231	6.22	9.17	2.61	3.32
71	46.4	17.7	306	3050	68418	—	3011	603	218	6.10	8.75	2.67	3.33
89	47.4	18.4	308	2814	69831	—	3037	588	186	5.53	7.56	2.64	3.49
104	51.2	17.0	298	2315	75361	—	2842	578	154	4.68	7.16	2.34	3.23
121	51.7	17.4	294	2483	76101	—	2918	579	146	4.86	6.92	2.41	2.89
138	50.8	18.7	308	2255	74810	—	2829	530	139	4.42	6.59	2.24	3.13
157	53.7	20.2	346	2234	79063	—	3339	551	143	3.94	6.39	1.90	3.49
178	55.8	18.8	336	2014	82146	—	3194	540	128	3.50	5.61	1.89	3.45
194	57.1	19.5	350	2051	84050	—	3426	542	127	3.33	5.54	2.34	3.53
213	56.4	19.5	359	2083	83072	—	3363	557	133	3.30	5.81	1.96	4.72
230	55.9	18.9	345	2117	82370	—	3319	555	140	3.69	5.74	1.91	4.37
246	55.3	18.5	334	1977	81446	—	3163	534	141	4.34	7.26	2.08	4.93
262	54.1	17.3	323	2024	79754	—	3125	516	115	3.42	5.35	1.83	3.15
279	55.4	17.7	329	2067	81649	—	3243	515	123	3.36	5.10	1.66	2.92
296	55.2	17.8	336	2101	81334	—	3189	522	121	3.32	5.27	1.63	3.66
311	56.0	18.0	331	1941	82482	—	3220	521	121	3.21	5.12	1.57	2.71
330	57.5	17.1	330	1884	84694	—	3299	544	121	3.20	4.93	1.70	2.51
347	57.5	16.9	319	1863	84679	—	3185	545	122	3.54	5.03	1.69	2.18
362	57.1	15.6	302	1696	84098	—	3091	540	123	3.19	4.93	2.03	2.69
377	55.0	14.8	300	1783	81084	—	3082	532	117	2.92	4.78	1.96	3.63
393	55.5	15.2	300	1890	81803	—	3029	544	128	3.50	5.25	1.69	2.44
411	70.9	9.1	254	705	104470	—	3314	490	76	3.97	6.14	2.58	1.84
430	70.5	9.4	258	747	103803	—	3292	486	76	3.64	5.77	2.00	2.74
446	71.5	10.2	261	830	105265	—	3419	492	78	3.64	5.97	2.57	2.47
463	68.7	11.7	266	999	101154	—	3402	485	83	3.28	5.50	2.45	2.20
479	61.9	11.9	262	1044	91253	—	3251	447	80	2.69	4.66	2.20	1.57

Table C.2: GS10-14 XL32 Profile 2

Distance from rim (µm)	An (mol%)	Li (ppm)	Mg (ppm)	K (ppm)	Ca (ppm)	Ti (ppm)	Fe (ppm)	Sr (ppm)	Ba (ppm)	La (ppm)	Ce (ppm)	Nd (ppm)	Pb (ppm)
60	44.9	17.0	304	3087	66192	—	2988	579	214	6.04	8.66	2.95	3.69
81	45.9	17.8	306	2969	67597	—	2969	560	198	5.42	8.11	2.47	3.54
99	51.3	18.5	325	2722	75615	—	3239	603	187	6.20	8.88	2.33	3.90
115	51.5	17.0	334	2565	75925	—	3191	570	159	4.76	7.16	2.59	5.80
133	50.5	16.2	311	2374	74342	—	2983	543	142	4.98	7.37	2.42	3.86
149	52.4	17.3	332	2246	77252	—	3422	556	134	4.42	6.93	2.51	3.22
170	55.3	17.2	353	2144	81436	—	3570	538	131	4.01	6.04	2.13	2.85
190	59.0	16.6	377	2007	86887	—	3798	552	120	3.74	5.61	2.18	3.12
209	58.9	17.6	395	2072	86759	—	3808	548	120	3.42	5.56	2.27	4.95
225	57.7	16.3	372	1874	84988	—	3573	524	119	3.37	5.20	2.40	2.67
240	56.0	18.3	381	2207	82534	—	3668	541	124	3.28	5.01	1.70	2.47
262	57.2	17.8	372	2174	84334	—	3671	529	123	3.45	5.32	1.79	2.62
282	57.2	18.7	380	2222	84206	—	3675	536	123	3.20	5.36	1.46	2.54
301	56.4	15.8	389	2236	83108	—	3720	537	129	3.39	5.35	1.94	2.50
319	54.2	10.9	414	2467	79803	—	3763	534	144	3.54	5.73	2.10	2.89
339	55.9	10.8	413	2390	82353	—	3577	540	131	3.77	5.86	2.21	4.03
356	57.2	9.9	401	2185	84195	—	3642	519	129	3.53	5.61	1.63	3.09
372	56.7	16.6	423	2246	83551	—	3894	533	132	3.64	5.73	2.34	3.09
394	53.0	20.2	414	2330	78046	—	3735	522	137	3.50	5.90	1.87	2.76
415	53.7	22.2	430	2496	79046	—	3700	534	143	3.60	5.54	1.73	2.82
436	55.1	22.5	402	2471	81185	—	3669	555	150	3.86	6.10	2.14	2.62
458	52.0	22.9	423	2591	76666	—	3732	531	145	3.29	5.30	1.63	2.61
479	54.6	20.2	386	2100	80402	—	3507	537	135	3.42	5.50	2.07	2.11
503	71.1	13.4	276	1382	104719	—	3837	461	80	3.12	4.96	3.18	2.07
528	70.1	17.7	374	1204	103201	—	3798	584	127	3.60	6.38	<1.41	2.17
548	69.6	15.4	337	1359	102596	—	4287	511	97	2.98	5.73	2.45	3.77
569	61.9	11.9	262	1044	91253	—	3251	447	80	2.69	4.66	2.20	1.57

Table C.3: GS10-14 XL66 Profile 1

Distance from rim (µm)	An (mol%)	Li (ppm)	Mg (ppm)	K (ppm)	Ca (ppm)	Ti (ppm)	Fe (ppm)	Sr (ppm)	Ba (ppm)	La (ppm)	Ce (ppm)	Nd (ppm)	Pb (ppm)
12	47.0	20.5	340	3390	69215	—	3455	598	228	6.22	9.03	2.34	6.64
20	48.4	21.8	350	3682	71352	—	3538	637	255	6.61	9.59	2.48	4.42
42	45.6	19.8	323	3424	67167	—	3253	601	246	6.54	9.36	1.94	4.52
62	45.2	19.4	315	3665	66532	—	3289	612	256	6.61	9.64	3.13	4.52
82	46.7	18.2	309	3464	68820	—	3411	632	258	6.85	9.97	3.25	4.72
103	45.6	19.1	312	3408	67219	—	3351	601	241	6.27	9.51	2.86	4.10
122	46.4	19.7	309	3296	68409	—	3373	616	243	6.62	9.26	2.99	4.06
139	46.9	18.8	306	3282	69091	—	3216	626	242	6.78	9.51	2.75	3.66
155	47.2	18.2	305	3200	69462	—	3318	607	226	6.52	9.84	2.24	3.73
170	45.7	18.4	307	3397	67349	—	3340	610	225	5.88	8.34	1.97	3.83
188	52.6	17.0	306	2662	77424	—	3445	640	178	4.86	7.54	2.24	3.87
206	59.2	15.4	305	1903	87163	—	3538	660	147	4.68	6.93	2.25	4.37
223	64.1	15.2	301	1580	94414	—	3895	637	109	3.26	5.19	1.72	3.71
241	72.8	13.0	292	1113	107282	—	4178	622	73	2.38	3.81	1.84	3.40
255	71.0	15.1	299	1219	104617	—	4179	601	65	1.50	2.57	<0.55	2.98
275	81.0	10.5	265	826	119388	—	4487	578	41	0.94	1.81	1.40	2.51
299	87.3	4.9	214	374	128655	—	4501	574	26	0.69	1.03	<0.72	1.76
324	87.3	5.2	183	314	128669	—	4341	587	24	0.57	1.03	<0.66	1.26
342	88.4	5.2	180	267	130214	—	4278	576	21	0.59	0.95	1.16	<0.39
360	88.3	3.4	146	167	130118	—	3695	549	20	0.32	1.02	<0.71	0.65
376	89.0	4.6	177	301	131115	—	4142	577	24	0.71	0.97	<0.68	<0.42
394	87.4	4.4	176	294	128748	—	4202	567	22	0.53	1.02	<0.71	<0.44
413	85.8	6.2	180	314	126463	—	3989	563	24	0.41	0.92	<0.66	<0.41
431	85.7	5.9	190	298	126309	—	4231	568	24	0.66	0.99	<0.78	<0.46
452	86.0	6.2	200	398	126663	—	4258	574	24	0.63	1.08	<0.73	<0.43

Table C.4: GS10-14 XL66 Profile 2

Distance from rim (µm)	An (mol%)	Li (ppm)	Mg (ppm)	K (ppm)	Ca (ppm)	Ti (ppm)	Fe (ppm)	Sr (ppm)	Ba (ppm)	La (ppm)	Ce (ppm)	Nd (ppm)	Pb (ppm)
50	46.8	15.9	304	3020	68968	—	3343	599	224	6.11	8.56	1.84	2.96
65	46.7	17.5	299	3056	68815	—	3343	605	226	6.03	8.34	2.71	3.13
88	45.9	16.7	287	3006	67594	—	3310	592	225	6.22	8.42	2.24	3.16
106	54.4	17.3	327	3044	80182	—	3779	688	217	5.83	7.81	1.96	3.09
122	66.7	15.2	310	1707	98201	—	3884	668	114	3.54	5.54	1.21	2.94
143	82.9	8.1	249	643	122150	—	4105	610	50	1.29	2.27	1.23	2.55
160	86.9	6.9	203	483	128019	—	4089	572	35	0.76	1.58	0.81	1.63
181	87.3	6.3	197	388	128655	—	4303	564	31	0.61	1.31	<0.55	1.15
204	87.3	6.8	207	398	128669	—	4370	565	34	0.65	1.53	<0.52	1.12
229	87.6	6.1	217	508	129035	—	4553	598	45	0.61	1.78	<0.54	1.25
251	87.3	7.8	460	1233	128655	—	4552	590	52	1.09	2.81	1.06	4.27
280	87.3	5.2	183	314	128669	—	4341	587	24	0.57	1.03	<0.66	1.26

Table C.5: GS10-16 XL148 Profile 1

Distance from rim (µm)	An (mol%)	Li (ppm)	Mg (ppm)	K (ppm)	Ca (ppm)	Ti (ppm)	Fe (ppm)	Sr (ppm)	Ba (ppm)	La (ppm)	Ce (ppm)	Nd (ppm)	Pb (ppm)
66	47.6	19.1	318	3068	70135	274	3356	607	228	5.53	7.30	1.14	2.80
79	50.1	19.2	318	2726	73860	254	3414	620	187	4.62	6.47	2.53	2.48
97	53.3	19.8	315	2435	78555	238	3366	600	143	3.97	6.00	1.58	2.29
117	54.0	19.4	321	2357	79579	249	3540	591	129	3.59	5.08	1.22	2.45
140	62.5	18.1	325	1707	92002	240	3838	578	100	3.00	4.84	1.79	2.67
164	68.7	19.0	347	1576	101262	231	4175	582	96	2.69	4.64	1.28	2.07
194	68.3	27.3	467	3486	100600	310	5112	737	196	5.37	8.07	2.57	4.20
240	71.2	17.6	443	1794	104898	382	5324	535	92	3.93	6.76	2.39	3.44
263	70.0	19.2	350	1540	103082	269	4317	555	90	3.26	5.46	2.33	2.79
286	67.3	17.0	307	1316	99212	206	3665	552	82	2.90	4.78	2.14	2.36
311	70.7	15.2	292	1160	104155	198	3722	545	75	3.10	5.12	1.52	2.49

Table C.6: GS10-16 XL148 Profile 2

Distance from rim (µm)	An (mol%)	Li (ppm)	Mg (ppm)	K (ppm)	Ca (ppm)	Ti (ppm)	Fe (ppm)	Sr (ppm)	Ba (ppm)	La (ppm)	Ce (ppm)	Nd (ppm)	Pb (ppm)
16	45.5	17.7	314	3341	67070	231	3341	601	239	6.30	8.61	3.11	3.54
31	46.2	18.4	301	2988	68024	242	3162	573	211	4.76	7.02	1.97	2.64
51	53.7	18.7	318	2467	79068	262	3585	588	141	3.60	5.19	1.79	2.62
77	62.8	17.6	332	1917	92468	248	4119	577	102	3.08	5.01	1.25	2.07
102	57.6	18.0	306	1936	84832	260	3716	515	112	3.29	5.10	1.59	1.87
125	60.3	18.8	317	2033	88894	275	3766	540	117	3.43	5.49	2.28	2.20
147	60.3	17.9	316	2243	88847	290	3642	573	128	3.49	5.80	1.91	2.52
174	51.3	17.9	320	3002	75530	236	3496	587	196	5.63	8.17	1.35	2.76
199	48.6	12.8	277	2441	71534	208	3012	542	169	5.12	7.50	2.64	3.01
228	48.7	13.4	330	3732	71803	256	3659	613	225	7.08	9.98	3.11	3.84
254	48.1	13.8	318	3327	70904	221	3409	608	222	6.58	9.33	2.98	3.52
279	48.1	9.4	432	4852	70889	372	4267	592	242	8.37	12.28	4.24	4.20
301	55.9	15.8	330	2582	82309	313	3669	580	125	3.14	4.82	1.26	3.16
325	60.7	17.8	320	2168	89359	283	3748	556	118	3.70	5.23	1.72	2.42
350	60.2	18.7	311	2049	88674	268	3586	541	109	3.35	5.35	1.87	2.03
372	58.9	18.2	316	1939	86773	267	3665	531	108	3.33	4.65	1.84	2.04
393	61.3	19.8	330	2046	90298	262	3932	566	102	3.19	4.64	1.73	2.01
413	60.2	18.6	334	2312	88697	263	3900	618	125	3.42	4.65	1.70	2.51
435	51.8	18.8	326	2946	76272	252	3584	628	193	4.79	6.65	2.35	3.08

Table C.7: GS10-17 XL60 Profile 1

Distance from rim (µm)	An (mol%)	Li (ppm)	Mg (ppm)	K (ppm)	Ca (ppm)	Ti (ppm)	Fe (ppm)	Sr (ppm)	Ba (ppm)	La (ppm)	Ce (ppm)	Nd (ppm)	Pb (ppm)
20	45.7	21.0	313	4437	67320	227	3584	543	320	7.02	9.87	2.58	6.14
37	47.3	18.4	286	3549	69705	220	3456	533	253	6.05	8.44	2.01	3.86
50	51.6	19.9	299	3447	75948	228	3755	569	244	6.07	8.90	2.69	4.65
66	47.1	20.9	268	4133	69409	212	3488	555	309	6.71	9.90	2.27	3.90
86	45.7	22.3	289	4988	67320	210	3544	573	374	7.54	10.44	3.03	5.43
106	43.5	21.0	267	4395	64019	216	3339	551	342	6.96	9.59	2.47	3.86
126	51.8	19.9	288	3145	76252	214	3501	578	221	5.87	8.78	1.90	4.08
143	54.1	21.4	300	3166	79716	225	3789	609	226	5.97	8.99	2.01	3.84
158	48.5	22.1	298	3897	71469	228	3932	600	284	6.45	8.86	2.13	3.90
176	53.6	22.2	312	3297	79018	229	3869	586	219	5.79	8.42	2.85	3.94
195	61.0	19.0	294	2438	89869	206	4067	556	146	4.62	7.13	2.03	3.33
216	75.0	14.4	264	1398	110561	246	4351	513	103	3.11	6.03	2.37	3.37
233	61.0	20.8	295	2490	89918	241	3950	505	167	5.23	8.35	2.34	4.59
252	48.3	17.8	275	2860	71116	197	3823	441	213	7.10	9.90	2.62	3.22
272	54.4	23.4	298	3178	80090	298	3730	483	199	4.96	8.76	2.07	5.06
293	65.1	19.2	265	1855	95872	244	3828	474	142	4.58	8.31	3.02	4.54
315	79.2	22.2	311	2114	116636	315	4768	570	167	6.54	12.08	4.68	5.56
337	64.7	21.3	280	1963	95308	263	3763	485	141	4.03	6.64	1.97	4.96
364	76.2	16.1	248	1314	112276	263	3756	459	137	5.56	9.94	3.50	3.63
385	66.1	18.9	268	2027	97312	284	3861	491	153	5.16	9.19	3.80	5.01
407	70.5	17.0	256	1768	103880	255	3740	492	152	5.83	10.49	4.20	4.76
426	57.7	16.6	243	2090	84972	216	3358	439	162	6.79	11.66	3.52	4.28
447	70.9	20.5	303	2590	104459	301	4259	557	203	7.88	13.67	4.91	5.42
466	75.4	16.3	303	1772	111027	234	4860	526	118	4.66	8.20	3.57	34.88
487	63.9	14.2	232	1550	94193	205	3265	472	110	3.57	6.45	1.26	3.76
505	57.0	14.8	232	1774	83900	203	3263	445	133	4.48	7.39	2.51	3.64

Table C.8: GS10-17 XL71 Profile 1

Distance from rim (µm)	An (mol%)	Li (ppm)	Mg (ppm)	K (ppm)	Ca (ppm)	Ti (ppm)	Fe (ppm)	Sr (ppm)	Ba (ppm)	La (ppm)	Ce (ppm)	Nd (ppm)	Pb (ppm)
43	40.1	14.5	856	3513	59132	188	4272	398	228	5.46	7.91	2.88	8.61
68	39.3	14.3	740	3149	57849	193	3332	436	228	5.56	7.91	2.79	6.11
119	82.4	14.9	283	1065	121410	187	4460	580	78	1.93	3.15	1.33	4.21
140	80.6	11.2	255	753	118766	142	4719	507	49	1.37	2.37	0.86	4.49
166	78.4	12.7	509	942	115428	190	6837	498	49	1.59	3.05	1.96	38.37
191	78.4	13.5	476	1208	115428	200	6813	498	60	1.64	3.06	1.59	55.30
223	77.8	13.9	284	884	114606	158	4682	501	56	1.12	2.05	<0.53	1.16

Table C.9: GS10-17 XL71 Profile 2

Distance from rim (µm)	An (mol%)	Li (ppm)	Mg (ppm)	K (ppm)	Ca (ppm)	Ti (ppm)	Fe (ppm)	Sr (ppm)	Ba (ppm)	La (ppm)	Ce (ppm)	Nd (ppm)	Pb (ppm)
30	38.9	15.3	221	3352	57293	180	2540	455	250	5.84	7.80	1.87	3.66
48	39.9	16.4	240	3412	58839	179	2853	465	244	5.74	8.25	2.71	3.81
70	41.9	16.7	247	3440	61685	175	2964	479	227	5.96	7.91	2.55	3.84
94	67.1	14.2	297	1511	98784	211	3721	533	122	2.31	3.67	1.42	4.15
120	74.3	13.6	288	1132	109499	177	3996	512	61	1.57	2.58	<0.60	3.46
143	84.2	9.6	236	575	124095	118	4399	500	51	1.43	2.24	1.01	1.62
165	81.0	12.8	539	939	119267	179	5672	493	54	1.39	2.71	<0.58	2.57

Table C.10: GS11-30b XL15 Profile 1

Distance from rim (µm)	An (mol%)	Li (ppm)	Mg (ppm)	K (ppm)	Ca (ppm)	Ti (ppm)	Fe (ppm)	Sr (ppm)	Ba (ppm)	La (ppm)	Ce (ppm)	Nd (ppm)	Pb (ppm)
22	46.1	3.7	242	2756	67923	209	3355	508	154	4.03	5.41	1.94	3.16
29	47.9	5.8	270	2595	70558	209	3519	513	131	3.56	5.62	0.00	3.30
40	49.5	5.9	279	2269	72889	196	3388	497	130	4.41	6.17	2.02	2.45
58	56.6	10.8	327	1809	83369	192	3860	511	127	4.89	7.08	2.61	2.74
78	58.6	16.2	330	1662	86278	222	3888	484	130	4.26	6.87	2.04	2.78
96	58.5	27.7	361	1933	86185	223	3887	484	125	3.82	5.86	1.72	3.11
114	57.4	36.5	347	1986	84613	212	3754	476	119	3.84	5.45	1.36	2.94
132	57.2	44.9	350	2243	84258	229	3773	468	116	3.81	5.55	1.83	2.81
151	58.1	53.2	353	2258	85626	226	3963	472	120	3.62	5.48	1.95	3.03
176	58.1	54.0	347	2195	85646	227	3821	460	113	3.43	5.39	2.15	2.97
200	59.6	56.4	367	2234	87840	225	3960	481	107	3.76	5.68	2.45	3.01
222	59.1	54.1	367	2302	87018	216	4028	474	110	3.69	5.93	2.19	3.34
241	58.3	55.7	361	2404	85864	229	4080	471	109	3.70	5.66	2.47	3.12
263	57.4	50.8	357	2417	84556	234	3887	471	111	3.69	5.50	2.41	3.45
286	56.3	43.2	370	2559	82914	225	3959	471	112	3.58	5.43	2.09	3.03
305	56.3	26.9	374	2787	82907	218	4030	474	117	3.34	5.51	1.48	3.72
324	56.6	13.7	360	2522	83405	226	3882	465	109	3.54	5.52	2.23	3.27

Table C.11: GS11-30b XL18 Profile 1

Distance from rim (µm)	An (mol%)	Li (ppm)	Mg (ppm)	K (ppm)	Ca (ppm)	Ti (ppm)	Fe (ppm)	Sr (ppm)	Ba (ppm)	La (ppm)	Ce (ppm)	Nd (ppm)	Pb (ppm)
35	38.7	5.7	214	3509	56972	210	3028	502	243	5.01	6.65	1.65	2.80
51	42.3	6.4	235	3116	62328	202	3128	539	206	4.16	5.91	1.77	2.57
71	45.4	8.5	254	2675	66874	202	3257	535	163	4.00	5.60	2.11	2.26
93	46.9	11.8	265	2467	69030	226	3245	539	139	4.10	6.47	2.28	2.29
118	50.0	11.0	252	1984	73612	218	3096	551	116	2.98	4.86	1.07	2.16
139	49.9	12.0	273	2122	73537	232	3457	543	113	3.06	4.49	1.88	1.94
162	54.0	9.0	262	1890	79500	231	3555	542	93	2.96	4.44	1.41	1.80
186	55.3	3.3	225	1569	81489	209	3292	480	77	2.33	3.69	1.30	2.28
211	44.0	3.3	190	2302	64787	175	2675	439	151	4.29	5.96	1.89	2.98
288	39.8	1.8	199	2765	58649	160	2555	456	201	4.88	7.22	2.58	2.89
337	37.8	2.4	189	3192	55692	157	2722	465	223	5.23	7.46	2.42	3.72
358	41.1	1.9	192	3110	60547	172	2808	493	219	5.40	7.42	2.16	3.57
378	49.2	2.1	201	2167	72449	190	2957	507	134	3.69	5.58	2.39	3.50
398	52.3	1.1	189	1879	77115	207	2729	563	206	6.53	9.03	2.31	4.01

Table C.12: GS11-34a XL09 Profile 1

Distance from rim (µm)	An (mol%)	Li (ppm)	Mg (ppm)	K (ppm)	Ca (ppm)	Ti (ppm)	Fe (ppm)	Sr (ppm)	Ba (ppm)	La (ppm)	Ce (ppm)	Nd (ppm)	Pb (ppm)
22	37.1	16.6	185	3029	54721	—	2562	447	214	4.92	7.20	1.94	3.26
39	36.8	18.3	177	3235	54316	—	2377	462	220	5.36	7.17	2.34	3.19
59	38.1	14.2	186	3146	56140	—	2502	481	211	5.37	7.46	2.16	3.09
80	39.0	9.8	187	2917	57458	—	2524	480	195	5.27	7.43	2.71	2.82
98	46.3	7.9	202	2150	68098	—	2656	495	158	4.07	5.97	1.83	2.69
117	51.3	6.6	221	1573	75597	—	2988	496	115	2.95	3.97	1.67	2.45
136	52.3	4.9	235	1500	77117	—	3133	510	96	2.66	3.96	1.57	2.17
153	52.5	6.5	238	1674	77319	—	3155	542	103	2.97	4.27	1.21	2.48
172	51.8	6.5	229	1653	76306	—	3092	542	95	2.59	3.98	1.45	1.87
194	52.6	5.9	220	1576	77522	—	2912	547	92	2.73	3.57	0.99	1.69

Table C.13: GS11-34a XL09 Profile 2

Distance from rim (µm)	An (mol%)	Li (ppm)	Mg (ppm)	K (ppm)	Ca (ppm)	Ti (ppm)	Fe (ppm)	Sr (ppm)	Ba (ppm)	La (ppm)	Ce (ppm)	Nd (ppm)	Pb (ppm)
30	38.8	20.5	198	3443	57154	—	2814	481	246	5.59	8.15	2.28	3.84
50	40.6	16.1	200	3541	59788	—	2831	488	234	5.56	7.59	1.90	3.60
75	39.7	10.5	197	3476	58572	—	2771	493	239	5.76	8.22	2.40	3.57
96	41.8	9.3	202	3297	61612	—	2827	493	225	5.30	7.93	2.69	3.63
118	42.0	7.8	211	3335	61916	—	2930	514	227	5.46	7.88	2.34	3.71
145	41.4	8.0	202	3218	61004	—	2754	490	221	5.66	7.71	2.79	3.50
167	39.2	8.1	188	3332	57762	—	2579	471	227	5.23	7.36	2.75	3.28
191	39.3	7.9	191	3425	57964	—	2591	488	227	5.70	7.60	2.50	3.36
216	40.4	7.7	196	3068	59484	—	2633	476	207	5.39	7.40	2.10	3.26
237	41.8	8.4	216	2944	61511	—	2823	488	200	5.09	7.29	2.65	3.54
261	42.6	7.9	216	2929	62727	—	2888	482	180	4.64	7.16	2.00	3.30
283	50.2	7.3	216	2023	73975	—	2960	499	133	3.33	5.39	1.67	2.91
308	52.0	6.5	223	1726	76610	—	3080	511	91	2.55	4.28	1.09	2.98
329	52.9	9.2	251	1975	77927	—	3370	533	99	2.73	4.85	1.43	2.85

Table C.14: GS11-34a XL14 Profile 1

Distance from rim (µm)	An (mol%)	Li (ppm)	Mg (ppm)	K (ppm)	Ca (ppm)	Ti (ppm)	Fe (ppm)	Sr (ppm)	Ba (ppm)	La (ppm)	Ce (ppm)	Nd (ppm)	Pb (ppm)
13	39.7	15.2	214	3143	58471	—	2901	478	239	5.39	7.29	2.08	3.59
37	41.3	17.8	224	2771	60903	—	2817	474	194	4.84	7.23	2.47	3.01
58	42.1	13.3	239	2981	62018	—	2961	489	200	5.39	7.40	2.40	3.12
87	43.0	10.7	284	3242	63335	—	3369	525	219	4.88	6.83	2.03	3.09
113	44.7	8.3	312	2327	65868	—	3512	494	135	3.45	5.26	1.63	2.35
139	50.3	7.8	393	2009	74077	—	4404	519	108	3.16	4.88	1.59	2.17
163	54.0	7.7	471	1827	79549	—	4729	519	83	2.53	4.49	1.64	1.63
188	56.0	7.4	575	1790	82488	—	5083	525	79	2.41	4.45	1.26	1.79
211	55.9	8.4	585	1763	82386	—	5057	505	82	2.09	4.25	1.60	1.99
233	58.1	7.9	428	1282	85629	—	3689	499	68	2.04	3.70	0.82	1.33
259	55.9	8.9	461	2505	82386	—	4314	572	136	3.28	5.19	2.11	2.13
308	55.2	7.1	318	1796	81271	—	3367	541	105	3.07	4.84	1.38	2.01
329	51.0	7.0	275	1765	75090	—	2953	519	119	3.66	5.18	1.49	1.97
350	42.5	6.8	276	2723	62524	—	2843	519	150	4.57	5.49	1.62	2.41
370	42.7	8.0	272	2957	62828	—	2896	523	163	4.98	6.51	1.81	2.28
389	43.3	7.7	269	3062	63842	—	2882	535	173	5.08	7.03	2.50	2.51
413	43.4	8.5	258	2999	63943	—	2737	534	172	5.25	7.02	2.03	2.72
436	42.7	7.8	238	2941	62930	—	2571	525	169	5.05	6.62	1.91	2.69

Table C.15: GS11-34a XL14 Profile 2

Distance from rim (µm)	An (mol%)	Li (ppm)	Mg (ppm)	K (ppm)	Ca (ppm)	Ti (ppm)	Fe (ppm)	Sr (ppm)	Ba (ppm)	La (ppm)	Ce (ppm)	Nd (ppm)	Pb (ppm)
15	40.3	15.9	196	3166	59384	—	2618	483	227	5.52	7.86	2.44	3.84
36	42.2	19.1	205	3028	62221	—	2699	489	206	5.42	7.71	2.61	3.36
52	42.2	12.0	214	2963	62221	—	2815	497	189	5.69	7.53	2.88	3.35
72	42.7	9.6	227	2983	62829	—	2873	501	176	4.76	6.74	2.50	3.22
95	48.9	7.6	242	2390	72051	—	3102	518	138	3.49	5.52	1.80	2.88
114	52.3	7.0	255	1982	77016	—	3325	531	106	2.96	4.58	1.53	2.65
130	55.3	6.9	250	1618	81475	—	3281	517	81	2.48	3.97	1.38	2.04
152	57.4	6.5	244	1446	84617	—	3310	507	67	2.15	3.60	1.28	2.14
170	55.9	6.3	255	1579	82387	—	3362	520	67	2.23	3.42	1.36	1.79
188	57.2	6.4	254	1477	84211	—	3399	514	68	1.93	2.99	1.13	1.83
210	57.9	6.8	255	1545	85225	—	3437	525	76	2.01	3.13	1.33	1.99
232	48.4	7.7	254	2185	71240	—	3141	517	99	3.00	4.10	1.45	1.69
254	50.6	7.9	267	2328	74483	—	3371	555	120	3.54	5.56	2.28	1.89
276	52.1	7.6	267	2185	76814	—	3264	554	116	3.60	5.27	2.08	1.87
299	52.9	8.5	284	2189	78030	—	3420	552	117	3.39	4.96	1.89	2.08
316	46.9	6.7	223	1678	69112	—	2823	468	100	2.89	4.58	1.89	1.94
338	41.8	5.6	191	1481	61512	—	2399	417	91	2.69	3.94	1.64	1.90
360	40.7	7.0	223	2760	59992	—	2684	512	156	4.44	5.35	2.10	2.00
382	39.0	6.6	206	2636	57357	—	2524	485	150	4.54	5.50	1.02	2.24
421	38.1	7.2	213	2711	56141	—	2573	477	145	4.68	5.88	2.01	2.21
443	41.6	7.7	244	3134	61309	—	2938	520	159	4.93	6.51	2.04	2.51
463	42.7	7.7	251	3151	62931	—	3074	541	164	4.76	6.21	2.24	3.03

Table C.16: GS11-34a XL23 Profile 1

Distance from rim (µm)	An (mol%)	Li (ppm)	Mg (ppm)	K (ppm)	Ca (ppm)	Ti (ppm)	Fe (ppm)	Sr (ppm)	Ba (ppm)	La (ppm)	Ce (ppm)	Nd (ppm)	Pb (ppm)
15	38.4	12.2	205	2960	56546	—	2607	453	213	5.22	7.60	2.47	3.76
28	40.1	21.4	206	3307	59080	—	2642	494	207	5.23	7.19	2.34	3.18
45	47.2	17.2	241	2627	69517	—	3096	532	156	4.48	6.39	1.93	2.98
63	49.9	11.0	258	2097	73470	—	3137	538	119	4.04	5.91	2.38	2.74
80	50.5	9.0	289	2239	74280	—	3265	552	112	3.71	5.63	1.80	2.31
98	51.9	7.9	313	1935	76510	—	3422	549	99	3.43	5.09	1.38	2.25
117	52.6	8.3	325	1935	77422	—	3571	557	99	3.11	4.64	1.22	1.87
137	53.5	8.0	339	1965	78841	—	3513	592	94	3.17	4.52	0.95	1.84
156	53.3	8.3	333	1826	78435	—	3488	573	86	2.78	4.07	1.43	1.72
172	51.1	8.0	344	2059	75395	—	3416	567	103	3.16	4.78	1.33	2.06
195	52.9	8.9	350	2276	77928	—	3525	582	120	3.71	5.69	1.83	2.23
213	52.2	8.8	377	2397	77016	—	3855	564	113	3.54	5.40	2.01	2.31
234	54.3	7.8	367	1927	80057	—	3615	559	98	3.23	4.88	1.16	2.00
250	57.4	8.2	404	2043	84617	—	4128	587	102	3.24	4.75	1.91	1.89
270	60.5	8.0	433	1825	89076	—	4628	590	86	2.58	3.97	1.56	1.99
284	61.1	7.9	435	1776	90089	—	4644	571	74	1.92	3.15	1.12	1.96
302	56.4	6.3	326	1513	83097	—	3605	517	77	1.80	3.32	1.13	1.72
321	49.1	8.1	321	2090	72355	—	3445	526	104	2.91	4.34	1.62	1.69
339	48.1	7.6	312	2348	70936	—	3175	536	127	3.83	5.40	1.97	2.20
364	47.1	8.5	299	2434	69416	—	3181	533	138	3.81	5.80	1.84	2.48
383	46.9	8.2	300	2633	69011	—	3177	544	151	4.30	6.32	2.00	2.57
405	48.4	8.0	303	2697	71342	—	3195	564	161	4.64	6.71	2.14	2.52
424	47.6	8.3	284	2493	70126	—	3050	539	152	4.41	6.68	2.21	2.52
446	44.4	8.0	258	2385	65464	—	2842	511	145	4.13	5.90	2.00	2.55
466	45.5	8.4	254	2452	66984	—	2886	517	152	4.24	6.24	1.96	2.67
487	46.1	9.1	250	2385	67795	—	2908	520	158	4.07	6.10	1.97	2.76
504	43.2	7.7	228	2163	63640	—	2620	476	152	4.00	5.81	1.94	2.51
520	42.8	10.9	226	2611	63032	—	2720	511	207	5.88	7.57	1.90	2.71
539	42.0	9.2	213	2531	61816	—	2603	509	197	6.21	7.86	3.47	2.71

Table C.17: GS11-34a XL23 Profile 2

Distance from rim (µm)	An (mol%)	Li (ppm)	Mg (ppm)	K (ppm)	Ca (ppm)	Ti (ppm)	Fe (ppm)	Sr (ppm)	Ba (ppm)	La (ppm)	Ce (ppm)	Nd (ppm)	Pb (ppm)
19	38.7	16.3	207	2827	56952	—	2647	455	194	4.69	6.10	2.24	3.62
38	41.5	13.4	215	2492	61106	—	2625	474	149	4.28	5.81	1.94	3.64
56	46.7	12.5	273	2484	68808	—	3204	523	128	3.54	5.66	1.74	3.18
75	47.6	9.4	277	2179	70125	—	3195	497	111	3.45	5.02	1.33	2.75
96	51.2	9.8	331	2342	75496	—	3682	534	115	3.37	5.22	2.08	2.82
115	51.7	8.3	346	2206	76104	—	3684	533	110	3.45	4.89	1.94	2.23
135	52.7	8.0	336	2198	77523	—	3429	566	106	3.30	4.71	1.42	1.96
155	51.8	8.6	331	2057	76307	—	3255	573	98	2.94	4.47	1.49	2.16
174	52.8	9.2	366	2014	77726	—	3478	559	87	2.51	4.42	1.81	2.21
194	53.4	8.7	379	2002	78739	—	3744	575	100	2.77	4.24	1.30	2.13
213	54.4	9.0	387	2233	80056	—	3842	591	111	3.63	5.53	1.74	1.99
232	53.4	8.5	359	2028	78638	—	3521	553	112	3.14	5.40	1.80	2.11
252	53.1	7.9	368	1997	78131	—	3613	547	106	3.34	4.89	1.60	2.11
276	54.8	8.7	373	2001	80766	—	3779	559	102	3.08	4.88	1.36	2.08
297	56.3	7.9	394	1911	82894	—	3893	556	101	2.96	4.79	1.46	2.11
319	57.3	8.2	421	1879	84414	—	3996	558	94	3.01	4.69	1.94	2.14
339	57.8	9.3	514	2132	85123	—	4826	543	90	2.71	4.40	1.46	2.23
366	60.2	9.9	463	1863	88670	—	4391	560	94	2.61	4.23	1.81	2.06
385	61.1	7.0	406	1392	90089	—	4275	584	97	2.14	4.06	1.52	1.66
404	54.6	7.1	371	1517	80360	—	3741	505	81	1.98	3.06	1.19	1.84
432	49.2	8.1	337	2249	72558	—	3224	538	120	3.71	5.47	1.70	2.21
456	48.5	8.8	321	2245	71443	—	3118	540	136	4.17	5.91	1.74	2.54
478	47.7	8.4	320	2378	70328	—	3008	533	140	3.94	5.94	2.30	2.50
495	47.5	8.3	310	2468	69923	—	2958	539	149	4.30	6.20	2.04	2.57
515	47.8	8.9	306	2513	70429	—	3051	556	159	4.45	6.64	2.24	2.44
536	48.6	8.8	309	2572	71645	—	3035	560	162	4.62	6.66	2.48	2.82
567	47.1	7.5	309	2566	69315	—	3105	532	156	4.45	6.52	2.45	2.50
597	46.7	8.5	286	2396	68808	—	2907	529	159	4.11	6.17	1.57	2.89
626	46.3	7.9	285	2442	68099	—	3031	522	166	4.17	6.28	1.67	2.89
650	49.1	8.2	408	3523	72254	—	4171	555	186	5.12	7.98	2.61	3.96
676	46.6	8.3	266	2662	68605	—	3091	518	189	4.75	7.03	1.84	3.01
699	44.4	8.9	248	2628	65363	—	2962	501	181	4.59	6.91	2.67	3.18
719	44.7	10.1	265	2870	65869	—	3050	525	173	4.85	7.37	1.60	3.19

Table C.18: GS11-34c XL06 Profile 1

Distance from rim (µm)	An (mol%)	Li (ppm)	Mg (ppm)	K (ppm)	Ca (ppm)	Ti (ppm)	Fe (ppm)	Sr (ppm)	Ba (ppm)	La (ppm)	Ce (ppm)	Nd (ppm)	Pb (ppm)
27	41.3	9.2	157	1948	60904	—	2239	426	148	3.69	5.33	1.46	3.06
49	53.7	8.8	197	1827	79043	—	2762	520	126	2.71	4.17	1.29	3.71
70	53.4	5.3	202	1912	78638	—	2759	515	109	3.17	4.72	1.55	3.29
92	49.9	7.6	187	1837	73470	—	2673	492	112	3.32	4.96	1.69	3.03
117	51.2	7.8	189	1865	75496	—	2569	506	135	3.77	5.93	2.44	2.94
138	43.5	7.6	188	2610	64045	—	2627	489	170	4.92	6.85	2.50	3.25
159	41.8	7.6	202	2956	61512	—	2812	486	192	5.26	7.74	2.38	3.49
180	42.1	9.1	237	3539	62120	—	3119	477	207	5.71	8.68	2.50	4.14

Table C.19: GS11-39b XL29 Profile 1

Distance from rim (µm)	An (mol%)	Li (ppm)	Mg (ppm)	K (ppm)	Ca (ppm)	Ti (ppm)	Fe (ppm)	Sr (ppm)	Ba (ppm)	La (ppm)	Ce (ppm)	Nd (ppm)	Pb (ppm)
29	34.1	4.3	168	3297	50185	153	2378	444	234	4.92	6.72	1.43	3.22
38	36.0	4.3	170	2862	53040	148	2342	440	215	4.85	6.65	1.28	2.84
55	37.0	5.3	173	2793	54521	144	2372	451	205	5.13	6.61	1.82	3.10
75	34.8	4.5	166	2947	51249	148	2287	442	207	5.16	6.63	2.58	3.18
98	40.8	5.9	184	2663	60095	159	2531	482	199	4.99	6.91	2.41	3.23
122	43.2	6.6	190	2460	63610	228	2599	477	175	4.57	6.50	1.80	3.10
146	48.9	5.4	191	2081	72070	220	2510	509	142	3.72	5.36	2.37	2.93
169	47.9	6.2	195	2185	70576	219	2537	511	149	4.16	5.66	1.57	2.62
193	51.0	5.5	178	1720	75112	214	2409	500	129	4.19	5.89	1.93	2.62
214	50.0	4.9	182	1876	73638	237	2434	486	133	4.19	5.96	2.02	3.39
234	40.8	4.8	187	2755	60149	176	2431	465	204	5.34	7.04	3.72	2.77

Table C.20: GS11-39b XL29 Profile 2

Distance from rim (µm)	An (mol%)	Li (ppm)	Mg (ppm)	K (ppm)	Ca (ppm)	Ti (ppm)	Fe (ppm)	Sr (ppm)	Ba (ppm)	La (ppm)	Ce (ppm)	Nd (ppm)	Pb (ppm)
30	36.8	4.1	169	2652	54284	147	2364	442	200	5.32	7.00	2.40	2.63
51	36.9	4.6	171	2646	54373	147	2385	443	196	5.01	6.90	2.41	2.82
75	39.7	5.3	185	2615	58555	155	2569	463	200	4.99	7.16	1.95	3.28
100	36.7	5.4	186	3327	54009	161	2616	459	232	5.33	7.26	2.10	2.93
123	38.4	5.1	191	3243	56508	170	2631	473	233	5.27	6.91	2.23	2.99
146	49.4	4.7	185	1877	72706	216	2500	490	161	4.40	6.11	1.61	3.19
171	50.9	5.0	192	2039	75012	254	2588	513	149	3.89	5.66	2.19	3.40
193	37.5	4.1	183	3311	55224	167	2571	474	202	4.66	6.26	1.59	2.79
215	34.3	3.6	177	3265	50554	150	2431	439	212	4.80	6.22	2.24	2.97
238	37.8	2.3	197	3542	55633	153	2777	480	223	6.21	8.72	3.54	3.86

Table C.21: S12-05 XL03 Profile 1

Distance from rim (µm)	An (mol%)	Li (ppm)	Mg (ppm)	K (ppm)	Ca (ppm)	Ti (ppm)	Fe (ppm)	Sr (ppm)	Ba (ppm)	La (ppm)	Ce (ppm)	Nd (ppm)	Pb (ppm)
23	31.9	12.9	146	3675	46954	133	2209	423	229	5.37	6.82	1.99	2.95
31	32.8	11.9	148	3480	48301	130	2206	413	224	5.18	6.78	1.91	3.23
48	32.4	9.4	148	3440	47743	135	2152	408	216	5.24	7.00	2.44	3.45
66	34.6	7.1	156	3432	50951	142	2292	419	224	4.85	6.70	2.25	3.33
82	34.2	7.5	169	3556	50406	171	2400	434	220	5.06	6.81	1.99	3.10
104	44.2	8.4	207	3619	65096	177	3020	514	235	6.45	8.47	3.00	4.24
124	47.6	7.4	197	2710	70113	117	2895	500	204	7.66	10.79	2.73	4.44
144	48.9	7.7	201	2481	72048	133	2824	494	196	7.49	11.00	2.00	4.51
160	48.8	7.7	200	2589	71963	132	2841	506	201	7.91	10.92	2.26	4.33
178	48.8	7.9	206	2738	71924	137	2939	511	211	7.59	10.81	2.91	4.66
196	48.6	8.2	215	2956	71543	151	3107	525	226	7.44	10.24	2.75	4.59
215	45.0	8.6	212	3355	66273	172	2990	512	243	5.65	8.52	2.25	4.27
235	46.4	8.1	222	3787	68314	197	3294	551	274	5.78	8.26	3.74	4.57
269	40.9	7.8	203	3397	60194	176	3005	506	272	5.51	7.09	2.36	3.62
288	42.7	8.4	208	3864	62886	185	3064	527	327	6.01	7.85	2.25	4.28
307	40.5	8.1	200	3909	59725	185	2949	517	337	6.17	7.99	2.34	3.59
327	36.9	8.3	183	3673	54355	166	2708	470	322	5.78	7.56	3.02	3.26
350	35.9	8.1	174	3574	52863	151	2529	458	313	5.68	7.45	2.10	3.00
372	36.0	8.8	169	3425	53031	146	2482	455	293	5.52	7.40	2.23	3.38
393	36.8	11.0	169	3299	54197	149	2546	460	273	5.54	7.39	2.29	3.28
411	36.5	13.9	169	3098	53710	149	2518	448	240	5.52	6.80	2.73	3.19
428	35.3	16.8	164	2807	51937	144	2386	431	208	5.10	6.42	2.28	3.47

Table C.22: S12-05 XL03 Profile 2

Distance from rim (µm)	An (mol%)	Li (ppm)	Mg (ppm)	K (ppm)	Ca (ppm)	Ti (ppm)	Fe (ppm)	Sr (ppm)	Ba (ppm)	La (ppm)	Ce (ppm)	Nd (ppm)	Pb (ppm)
12	37.0	15.0	173	3609	54563	162	2625	455	221	5.15	7.03	2.14	3.66
26	38.5	12.4	186	3524	56735	163	2642	463	220	5.35	7.02	2.49	3.54
46	32.6	8.0	160	4185	48014	146	2382	423	241	5.31	6.82	1.85	3.37
67	33.7	7.4	163	4098	49606	154	2431	439	243	5.18	7.24	1.64	3.21
87	35.1	8.3	174	3918	51762	132	2494	446	250	5.21	7.28	2.79	3.47
100	35.5	8.4	170	4003	52340	150	2359	443	239	5.42	7.61	1.70	3.38
119	34.5	8.2	175	3715	50805	170	2471	441	231	5.14	6.81	2.54	3.25
134	35.6	7.7	173	3869	52389	164	2473	447	227	5.06	6.80	1.99	3.32
149	37.2	7.9	189	3812	54829	174	2741	463	225	5.06	6.71	1.55	3.32
167	37.3	7.5	180	3555	54989	163	2603	461	220	5.03	6.89	2.29	3.51
186	40.8	7.8	199	3680	60143	190	2894	494	228	5.84	7.63	2.23	3.64
204	45.9	7.1	206	3202	67633	126	2912	514	218	6.80	9.60	3.22	3.81
221	41.7	7.7	189	3103	61430	110	2696	476	212	6.13	8.94	2.05	3.70
244	41.7	8.0	181	2708	61411	92	2589	447	188	6.73	9.34	2.55	3.84
263	41.8	7.2	182	2603	61616	94	2556	434	181	6.93	9.85	2.10	3.81
283	42.6	7.7	176	2597	62733	101	2520	444	189	6.71	9.61	2.75	3.88
303	43.0	7.9	186	2935	63348	90	2640	454	201	6.70	10.04	3.42	3.94
323	42.8	7.6	188	2798	62982	94	2646	457	192	7.22	10.00	2.67	4.17
343	44.2	8.4	199	2793	65130	108	2837	474	207	7.34	10.48	3.70	4.67
364	49.9	8.4	205	2778	73557	122	3066	513	206	7.95	11.68	3.64	4.96
382	49.3	8.5	207	2757	72676	139	2914	506	203	7.96	10.75	3.07	4.37

Table C.23: S12-06 XL24 Profile 1

Distance from rim (µm)	An (mol%)	Li (ppm)	Mg (ppm)	K (ppm)	Ca (ppm)	Ti (ppm)	Fe (ppm)	Sr (ppm)	Ba (ppm)	La (ppm)	Ce (ppm)	Nd (ppm)	Pb (ppm)
21	40.1	3.1	185	2770	59036	163	2681	472	213	5.13	7.01	2.27	3.27
43	38.8	4.3	197	3189	57221	224	2871	477	243	4.36	5.91	1.71	3.20
64	41.5	4.5	206	3021	61143	232	2937	494	229	4.29	5.44	0.00	3.53
83	40.4	3.4	186	2489	59588	196	2549	456	176	3.49	5.37	1.43	3.17
101	46.8	3.2	186	2147	68936	216	2575	492	159	3.34	5.04	1.88	3.19
125	50.8	3.7	182	1884	74864	238	2569	499	144	3.10	4.31	1.25	3.32
148	51.4	3.8	173	1583	75680	244	2433	491	140	2.80	4.52	1.99	2.94
174	51.8	3.1	181	1735	76275	264	2597	511	133	3.63	5.90	2.15	3.36
199	43.3	3.1	159	1722	63791	255	2258	450	114	3.95	5.94	1.79	2.53
221	47.6	2.6	166	1669	70063	231	2305	481	99	2.91	4.39	0.00	2.83
243	53.7	2.3	179	1711	79044	242	2545	515	105	2.49	3.75	1.44	3.49
266	42.3	2.6	211	3052	62319	160	3019	490	206	5.62	7.46	1.77	3.51

Table C.24: S12-06 XL24 Profile 2

Distance from rim (µm)	An (mol%)	Li (ppm)	Mg (ppm)	K (ppm)	Ca (ppm)	Ti (ppm)	Fe (ppm)	Sr (ppm)	Ba (ppm)	La (ppm)	Ce (ppm)	Nd (ppm)	Pb (ppm)
17	38.6	3.0	181	3033	56913	163	2680	465	216	5.12	7.58	2.64	3.36
26	36.8	3.0	179	3129	54212	154	2654	447	216	5.04	7.02	1.77	2.97
45	34.6	4.5	191	3869	50962	205	2762	455	268	5.14	6.47	2.52	3.44
66	40.1	4.9	187	3030	59090	213	2724	472	231	4.73	5.88	1.97	2.84
87	48.2	6.7	188	2240	70932	208	2643	503	148	3.43	5.03	1.62	3.48
109	51.1	9.6	184	2012	75336	250	2627	521	110	2.56	3.81	1.38	2.59
132	52.3	12.9	180	1751	77054	231	2559	526	91	2.31	3.45	1.05	2.91
154	53.9	14.3	181	1704	79405	243	2616	535	82	2.07	3.04	0.99	2.38
176	55.4	11.0	178	1567	81601	236	2614	531	68	2.06	2.85	1.03	2.19
198	55.8	7.2	179	1553	82227	244	2694	519	66	1.88	2.65	1.13	2.63
220	55.7	4.7	176	1547	81986	245	2626	515	68	1.74	3.01	0.00	2.65

Appendix D

Plagioclase diffusion model code

D.1 1 Stage model

```
An      = % Anorthite profile
x_An    = % Positions of the anorthite profile points
C_mes   = % Measured Mg
x_C     = % Location of measured Mg points
T       = % Temperature in Kelvin
delta_t = % Time step in seconds
j_max   = % Number of time steps to run diffusion model
a       = % Parameter from partition coefficient equation
b       = % Parameter from partition coefficient equation
Title   = % Title for graphs

i_max   = length(x_An);
C_eq    = zeros(i_max,1);
C_init  = zeros(i_max,1);
C_High  = zeros(i_max,1);
C_Low   = zeros(i_max,1);

% Calculate initial Mg profile from An [via Ti]
for i = 1:i_max
    if An(i) < 0.69
        C_init(i) = 3 * 310 * exp((6.13 - ...
            (26100 / (7670 + 4160 * An(i)))) * An(i) ...
            - (25700 / (7670 + 4160 * An(i))));
    else
        C_init(i) = 3 * 2130 * exp((3.33 - ...
            (26100 / (7670 + 4160 * An(i)))) * An(i) ...
            - (25700 / (7670 + 4160 * An(i))));
    end
end
```

```
% Upper bound on the initial Mg
for i = 1:i_max
    if An(i) < 0.66
        C_High(i) = 3 * 276 * exp((6.72 - ...
            (26100 / (7670 + 4160 * An(i)))) * An(i) ...
            - (25700 / (7670 + 4160 * An(i))));
    else
        C_High(i) = 3 * 3150 * exp((3.03 - ...
            (26100 / (7670 + 4160 * An(i)))) * An(i) ...
            - (25700 / (7670 + 4160 * An(i))));
    end
end

% Lower bound on the initial Mg
for i = 1:i_max
    if An(i) < 0.72
        C_Low(i) = 3 * 340 * exp((5.62 - ...
            (26100 / (7670 + 4160 * An(i)))) * An(i) ...
            - (25700 / (7670 + 4160 * An(i))));
    else
        C_Low(i) = 3 * 1320 * exp((3.73 - ...
            (26100 / (7670 + 4160 * An(i)))) * An(i) ...
            - (25700 / (7670 + 4160 * An(i))));
    end
end

% Find location of the first measurement
first_C = find(abs(x_An - min(x_C)) ...
   ==min(abs(x_An - min(x_C))));

C_eq(first_C) = C_mes(length(C_mes));


for i = first_C+1:1:i_max
    C_eq(i) = C_eq(i-1) * exp(a * (An(i)-An(i-1)) ...
                        / (8.3144621*T));
end

for i = first_C-1:-1:1
    C_eq(i) = C_eq(i+1) * exp(a * (An(i)-An(i+1)) ...
                        / (8.3144621*T));
end

% Plot initial and equilibrium profiles
```

```
figure

plot(x_An,C_init,'LineStyle','-','Color',[0 170/255 0],...
    'DisplayName','Initial')

plot(x_An,C_High,'LineStyle','-','Color',[85/255 1 85/255],...
    'DisplayName','Uncertainty')

plot(x_An,C_Low,'LineStyle','-','Color',[85/255 1 85/255],...
    'DisplayName','Uncertainty')

plot(x_An,C_eq,'LineStyle','-','Color',[0 85/255 212/255],...
    'DisplayName','Equilibrium')

plot(x_C,C_mes,'LineStyle','none','Color',[212/255 0 0],...
    'DisplayName','Measured', ...
        'Marker','+')

title(Title)

legend('show', 'Location', 'NorthWest')

% Calculate initial parameters

% Calculate the distance between points
delta_x       = (x_An(2) - x_An(1));

% Calculate total time for model
t_max         = j_max * delta_t;

% Add an extra row rather than overwrite An data in making
% crystal "symmetrical"
i_max         = length(x_An)+1;
x2            = x_An;
x2(i_max)     = x_An(i_max-1) + delta_x;

% Variables for before and after each diffusion step
C_old         = C_init;
C_new         = C_init;

% External boundary condition
Out_BC        = C_eq(1);

% make crystal "symmetrical"
An(i_max)     = An(i_max-1);
```

```
C_init(i_max) = C_init(i_max-1);

% Diffusion coefficient equation
% D = 10^(m_An * An + c_An) * exp(-act_en/RT)
m_An        = -3.46;
c_An        = -2.63;
act_en      = 287000;

% Check for stability
D_max = 10^(m_An*min(An)+c_An) * exp(-act_en/(8.3144621*T)) ...
        * 10^12;
r     = D_max * delta_t / delta_x^2 %#ok<NOPRT>

if r >= 0.5;
    t_max = 0;
    error('plag_diff:Courant', strcat( ...
        'Courant condition unfulfilled: r = ', ...
        num2str(r,3), ' >= 0.5'))
end

% Diffusion model

% Calculate constants invariant with time, so they are only
% calculated once
rr                = delta_t / delta_x^2;
ART               = a / (8.3144621*T);
D                 = 10.^(m_An * An + c_An) * exp( -act_en ...
                    / (8.3144621 * T)) * 10^12;
delta_D           = zeros(i_max,1);
delta_An          = zeros(i_max,1);
delta_An2         = zeros(i_max,1);
for i = 2:1:i_max-1
    delta_D(i)    = (D(i+1) - D(i));
    delta_An(i)   = (An(i+1) - An(i));
    delta_An2(i) = An(i+1) - 2*An(i) + An(i-1);
end
D_delta_An        = D .* delta_An;
D_delta_An2       = D .* delta_An2;
delta_D_delta_An = delta_D .* delta_An;

% Diffuse
for j = 1:j_max
     C_new(1)= Out_BC;
    for i = 2:1:i_max-1
        C_new(i) = C_old(i) + rr * (...
```

```
            D(i) * (C_old(i+1) - 2*C_old(i) + C_old(i-1)) ...
            + delta_D(i) * (C_old(i+1) - C_old(i)) ...
            - ART * (D_delta_An(i) * (C_old(i+1) - C_old(i))...
            + C_old(i) * delta_D_delta_An(i) ...
            + C_old(i) * D_delta_An2(i)));
    end

  % Symmetrical crystal (internal boundary condition)
  C_new(i_max) = C_new(i_max-1);

  C_old = C_new;
end

% remove the extra datapoint added to make the crystal
% symmetrical
C_new(i_max)=[];

%Plot the results

% Calculate the length of time diffusion has taken place over
% in a sensible unit, and append it to graph label
time_in = 'years';

if strcmp(time_in,'days')
    t_max = t_max/(60*60*24) %#ok<NOPTS>
elseif strcmp(time_in,'years')
    t_max = t_max/(60*60*24*365.25) %#ok<NOPTS>
else
    time_in = 'seconds';
end

% Plot results
figure('Name', [Title, ' for ', num2str(t_max,3), ' ', ...
        time_in])

plot(x_An,C_init,'LineStyle','-','Color',[0 170/255 0],...
    'DisplayName','Initial')

hold on

plot(x_An,C_new,'LineStyle','-','Color','k','DisplayName', ...
    [num2str(t_max,3), ' ', time_in, ' @ ', num2str(T), 'K'])

plot(x_An,C_eq,'LineStyle','-','Color',[0 85/255 212/255],...
    'DisplayName','Equilibrium')
```

```
plot(x_C,C_mes,'LineStyle','none','Color',[212/255 0 0],...
    'DisplayName','Measured', 'Marker','+')

plot(x_An,C_High,'LineStyle','-','Color',[85/255 1 85/255],...
    'DisplayName','Uncertainty')

plot(x_An,C_Low,'LineStyle','-','Color',[85/255 1 85/255],...
    'DisplayName','Uncertainty')

% Plot labels
ylabel('Mg (ppm)')
xlabel('Distance from rim (microns)')
title(Title)
legend('show', 'Location', 'NorthWest')
```

D.2 2 stage model

```
An      = % Anorthite profile
x_An    = % Positions of the anorthite profile points
C_mes   = % Measured Mg
x_C     = % Location of measured Mg points
T_core  = % Temperature for the first (core) stage
T_rim   = % Temperature for the second (whole crystal) stage
i_min   = % Location of the core/rim boundary (in steps)
delta_t = % Time step in seconds
j_max   = % Number of time steps to run diffusion model
a       = % Parameter from partition coefficient equation
b       = % Parameter from partition coefficient equation
Title   = % Title for graphs
Core_Yr = % Time(s) in years to run the first stage
Rim_Yr  = % Time(s) in years to run the second stage

i_max   = length(x_An);
C_eq    = zeros(i_max,1);
C_init  = zeros(i_max,1);
C_High  = zeros(i_max,1);
C_Low   = zeros(i_max,1);

% Calculate initial Mg profile from An [via Ti]
for i = 1:i_max
    if An(i) < 0.69
        C_init(i) = 3 * 310 * exp((6.13 - ...
            (26100 / (7670 + 4160 * An(i)))) * An(i) ...
            - (25700 / (7670 + 4160 * An(i))));
    else
        C_init(i) = 3 * 2130 * exp((3.33 - ...
            (26100 / (7670 + 4160 * An(i)))) * An(i) ...
            - (25700 / (7670 + 4160 * An(i))));
    end
end

% Upper bound on the initial Mg
for i = 1:i_max
    if An(i) < 0.66
        C_High(i) = 3 * 276 * exp((6.72 - ...
            (26100 / (7670 + 4160 * An(i)))) * An(i) ...
            - (25700 / (7670 + 4160 * An(i))));
    else
        C_High(i) = 3 * 3150 * exp((3.03 - ...
            (26100 / (7670 + 4160 * An(i)))) * An(i) ...
```

```
            - (25700 / (7670 + 4160 * An(i))));
    end
end

% Lower bound on the initial Mg
for i = 1:i_max
    if An(i) < 0.72
        C_Low(i) = 3 * 340 * exp((5.62 - ...
            (26100 / (7670 + 4160 * An(i)))) * An(i) ...
            - (25700 / (7670 + 4160 * An(i))));
    else
        C_Low(i) = 3 * 1320 * exp((3.73 - ...
            (26100 / (7670 + 4160 * An(i)))) * An(i) ...
            - (25700 / (7670 + 4160 * An(i))));
    end
end

% Find location of the first measurement
first_C = find(abs(x_An - min(x_C)) ...
   ==min(abs(x_An - min(x_C))));

C_eq(first_C) = C_mes(length(C_mes));


for i = first_C+1:1:i_max
    C_eq(i) = C_eq(i-1) * exp(a * (An(i)-An(i-1)) ...
                          / (8.3144621*T));
end

for i = first_C-1:-1:1
    C_eq(i) = C_eq(i+1) * exp(a * (An(i)-An(i+1)) ...
                          / (8.3144621*T));
end

% Plot initial and equilibrium profiles
figure

plot(x_An,C_init,'LineStyle','-','Color',[0 170/255 0],...
    'DisplayName','Initial')

plot(x_An,C_High,'LineStyle','-','Color',[85/255 1 85/255],...
    'DisplayName','Uncertainty')

plot(x_An,C_Low,'LineStyle','-','Color',[85/255 1 85/255],...
    'DisplayName','Uncertainty')
```

```
plot(x_An,C_eq,'LineStyle','-','Color',[0 85/255 212/255],...
    'DisplayName','Equilibrium')

plot(x_C,C_mes,'LineStyle','none','Color',[212/255 0 0],...
    'DisplayName','Measured', ...
        'Marker','+')

title(Title)

legend('show', 'Location', 'NorthWest')

% Contestants for calculating the diffusion coefficient using
% D = 10^(m_An * An + c_An) * \exp(act_en / RT
m_An        = -3.46;
c_An        = -2.63;
act_en      = 287000;

% Combine upper and lower bounds of the initial profile
C_un = [C_High; NaN; C_Low];

% Calculate delta_t to give a maximum r of 0.48 (fulfilling the
% Courant condition) for both the rim and core separately
delta_x = x_An(2) - x_An(1);

D_max = 10 ^ (m_An * min(An) + c_An) * exp(-act_en / ...
    (8.3144621 * T_core)) * 10^12;
delta_t_core = 0.48 * delta_x^2 / D_max;

D_max = 10 ^ (m_An * min(An) + c_An) * exp(-act_en / ...
    (8.3144621 * T_rim )) * 10^12;
delta_t_rim = 0.48 * delta_x^2 / D_max;

% Turn times from years into multiples of delta_t (in s)
Core = fix(Core_Yr * 31557600 / delta_t_core);
Rim  = fix(Rim_Yr * 31557600 / delta_t_rim);


% Call the diffusion functions
for n1 = 1:1:length(Core)

    if n1 == 1
        [C_new_core, t_max] = DiffCore (delta_t_core, ...
            Core(n1), T_core, An, x_An, C_init, i_min, ...
            element, m_An, c_An, act_en);
```

```
    else
        [C_new_core, t_maxb] = DiffCore (delta_t_core, ...
            Core(n1) - Core(n1-1), T_core, An, x_An, ...
            C_new_core, i_min, element, m_An, c_An, act_en);
        t_max = t_max + t_maxb;
    end

    for n2 = 1:1:length(Rim)
        if n2 == 1
            [C_new_rim, t_max2] = DiffRim(delta_t_rim, ...
                Rim(n2), T_rim, An, x_An, C_new_core, C_eq, ...
                element, m_An, c_An, act_en);
        else
            [C_new_rim, t_max2b] = DiffRim(delta_t_rim, ...
                Rim(n2) - Rim(n2-1), T_rim, An, x_An, ...
                C_new_rim, C_eq, element, m_An, c_An, act_en);
            t_max2 = t_max2 + t_max2b;
        end

        PlotDiff(Title, t_max, t_max2, x_An, C_init, C_un, ...
            C_eq, x_C, C_mes, C_new_core, T_core, ...
            C_new_rim, T_rim, element);

    end

end

function [C_new, t_max] = DiffCore (delta_t, j_max, ...
    T_core, An, x_An, C_init, i_min, element, m_An, ...
    c_An, act_en)

% Calculate the first stage in a 2 stage diffusion model
%
% Output:
% C_new   = final profile
% C_old   = profile after diffusion in just the core
%
% Inputs:
% delta_t = seconds per time step
% j_max   = number of time steps for the core
% j_max2  = number of time steps for the core + rim
% T_core  = temperature for core diffusion (in K)
% T_rim   = temperature for rim diffusion (in K)
% An      = anorthite profile
% x_An    = location of the anorthite measurements (in microns)
```

```
% C_eq    = equilibrium profile
% C_init  = initial profile
% C_un    = uncertainty in the initial profile
% i_min   = location of the core/rim boundary (in pixels)
% element = element diffusing
% m_An    = Diffusion coefficient parameter
% c_An    = Diffusion coefficient parameter
% act_en  = Diffusion coefficient parameter
% Title   = title for the graph
%
% Diffusion coefficient is in the form:
% D = 10^(m_An * An + c_An) * \exp(act_en / RT

% adding an extra row rather than overwriting An data
% in making crystal "symetrical"
i_max          = length(x_An)+1;
x_An(i_max)    = x_An(i_max-1);
An(i_max)      = An(i_max-1);

% Calculate the time core diffuses in years
t_max          = delta_t * j_max / 31557600;

C_old          = C_init;
C_old(i_max)   = C_init(i_max-1);
C_new          = C_old;

A              = -21600;

% Calculate constants invariant with time, so they are only
% calculated once
delta_x           = x_An(2) - x_An(1);
rr                = delta_t / delta_x^2;
delta_An          = zeros(i_max,1);
delta_An2         = zeros(i_max,1);
for i = 2:1:i_max-1
    delta_An(i)  = (An(i+1) - An(i));
    delta_An2(i) = An(i+1) - 2*An(i) + An(i-1);
end

% Core

% Calculate constants invariant with time at core temperatures
ART               = A / (8.3144621*T_core);
D                 = 10 .^ (m_An * An + c_An) * ...
                        exp(-act_en / (8.3144621 * T_core)) ...
```

```
                        * 10^12;
delta_D           = zeros(i_max,1);
for i = 2:1:i_max-1
    delta_D(i)    = (D(i+1) - D(i));
end
D_delta_An        = D .* delta_An;
D_delta_An2       = D .* delta_An2;
delta_D_delta_An = delta_D .* delta_An;

% Diffuse
for j = 1:j_max
    for i = i_min:1:i_max-1
        C_new(i) = C_old(i) + rr * (...
            D(i) * (C_old(i+1) - 2*C_old(i) + C_old(i-1)) ...
            + delta_D(i) * (C_old(i+1) - C_old(i)) ...
            - ART * (D_delta_An(i) * (C_old(i+1) - C_old(i))...
            + C_old(i) * delta_D_delta_An(i) ...
            + C_old(i) * D_delta_An2(i)));
    end

    % symmetrical crystal (internal boundary condition)
    C_new(i_max) = C_new(i_max-1);

    C_old = C_new;
end

% remove the extra datapoint added to make the crystal
% symmetrical
C_new(i_max)=[];

end

function [C_new, t_max2] = DiffRim (delta_t, j_max2, T_rim, ...
    An, x_An, C_init, C_eq, element, m_An, c_An, act_en)

% Calculate the second stage in a 2 stage diffusion model
%
% Output:
% C_new   = final profile
% C_old   = profile after diffusion in just the core
%
% Inputs:
% delta_t = seconds per time step
% j_max   = number of time steps for the core
% j_max2  = number of time steps for the core + rim
```

```
% T_core  = temperature for core diffusion (in K)
% T_rim   = temperature for rim diffusion (in K)
% An      = anorthite profile
% x_An    = location of the anorthite measurements (in microns)
% C_eq    = equilibrium profile
% C_init  = initial profile
% C_un    = uncertainty in the initial profile
% i_min   = location of the core/rim boundary (in pixels)
% element = element diffusing
% m_An    = Diffusion coefficient parameter
% c_An    = Diffusion coefficient parameter
% act_en  = Diffusion coefficient parameter
% Title   = title for the graph
%
% Diffusion coefficient is in the form:
% D = 10^(m_An * An + c_An) * \exp(act_en / RT

% adding an extra row rather than overwriting An data
% in making crystal "symmetrical"
i_max          = length(x_An)+1;
x_An(i_max)    = x_An(i_max-1);
An(i_max)      = An(i_max-1);

% Time whole crystal diffuses
t_max2         = delta_t * j_max2 / 31557600;

C_old          = C_init;
C_old(i_max)   = C_init(i_max-1);
C_old(1)       = C_eq(1);
C_new          = C_old;

A              = -21600;

% Calculate constants invariant with time, so they are only
% calculated once
delta_x           = x_An(2) - x_An(1);
rr                = delta_t / delta_x^2;
delta_An          = zeros(i_max,1);
delta_An2         = zeros(i_max,1);
for i = 2:1:i_max-1
    delta_An(i)  = (An(i+1) - An(i));
    delta_An2(i) = An(i+1) - 2*An(i) + An(i-1);
end

% Core
```

```
% Calculate constants invariant with time at rim temperatures
ART               = A / (8.3144621*T_rim);
D                 = 10 .^ (m_An * An + c_An) * ...
                        exp(-act_en / (8.3144621 * T_rim)) ...
                        * 10^12;
delta_D           = zeros(i_max,1);
for i = 2:1:i_max-1
    delta_D(i)    = (D(i+1) - D(i));
end
D_delta_An        = D .* delta_An;
D_delta_An2       = D .* delta_An2;
delta_D_delta_An = delta_D .* delta_An;

for j = 1:j_max2
    for i = 2:1:i_max-1
        C_new(i) = C_old(i) + rr * (...
            D(i) * (C_old(i+1) - 2*C_old(i) + C_old(i-1)) ...
            + delta_D(i) * (C_old(i+1) - C_old(i)) ...
            - ART * (D_delta_An(i) * (C_old(i+1) - C_old(i))...
            + C_old(i) * delta_D_delta_An(i) ...
            + C_old(i) * D_delta_An2(i)));
    end

    % symmetrical crystal (internal boundary condition)
    C_new(i_max) = C_new(i_max-1);
    C_old = C_new;
end

% remove the extra datapoint added to make the crystal
% symmetrical
C_new(i_max)=[];

end
```

Appendix E

Plagioclase diffusion model results

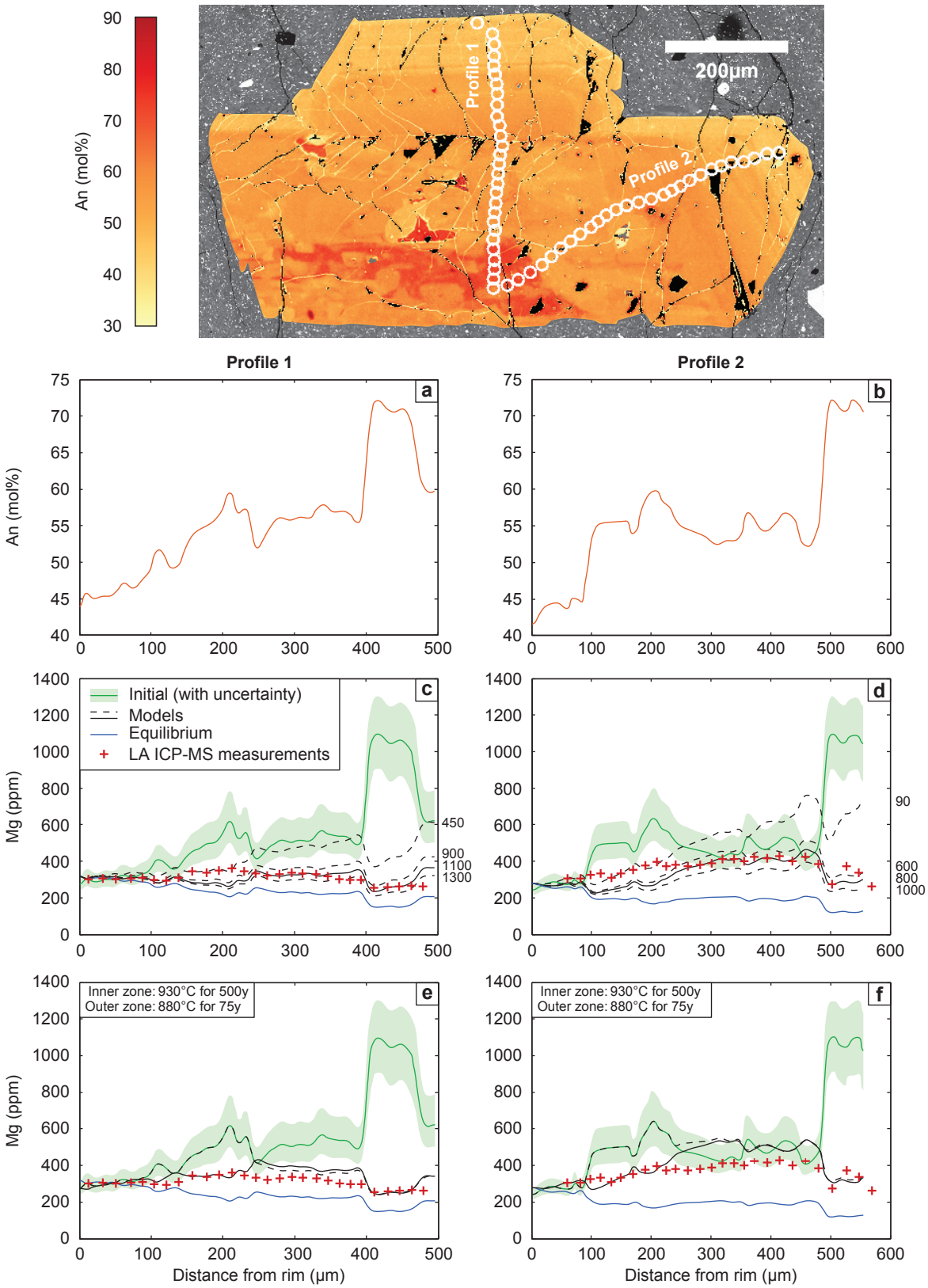

Figure E.1: GS10-14 XL32

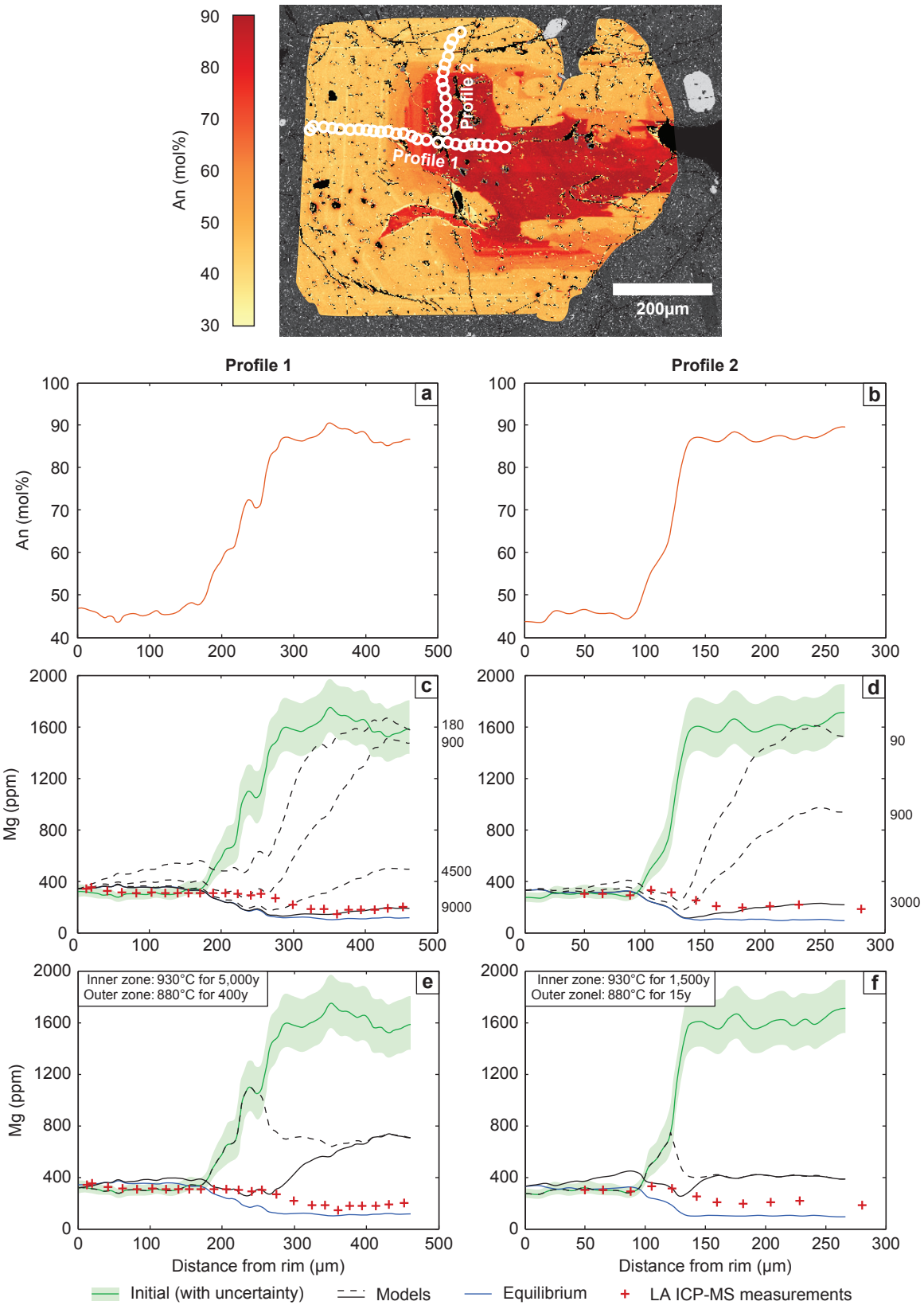

Figure E.2: GS10-14 XL66

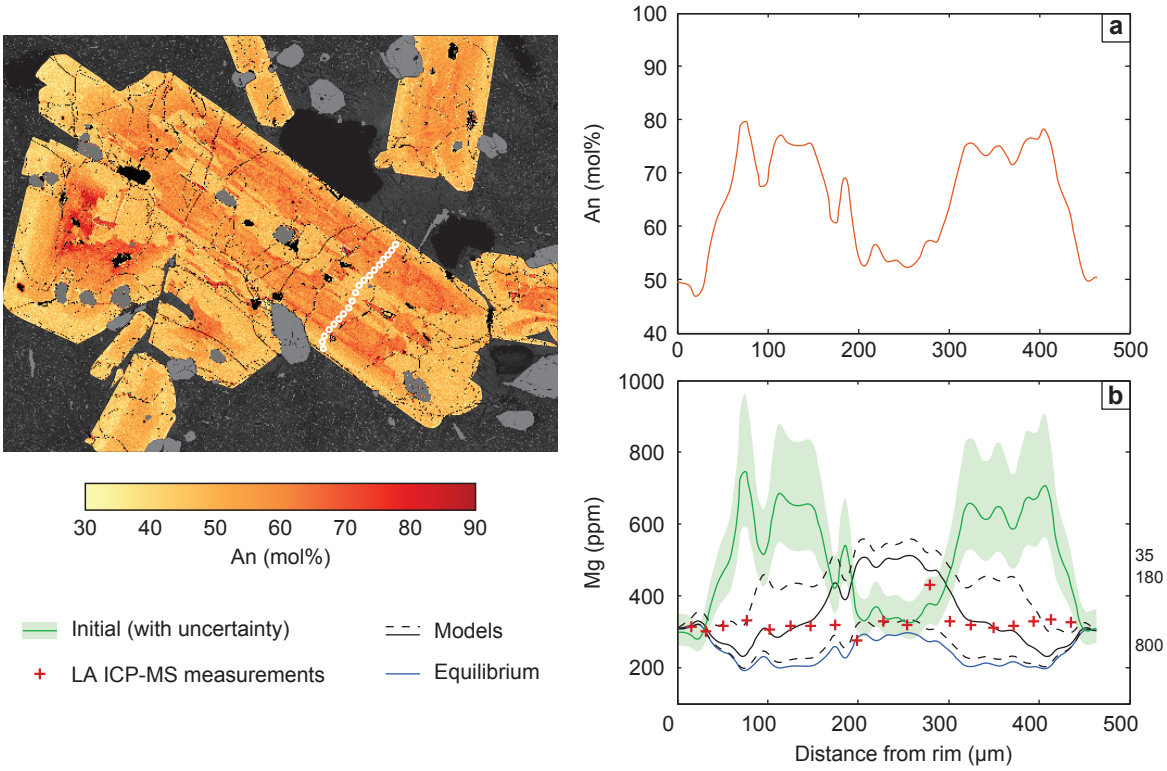

Figure E.3: GS10-16 XL148

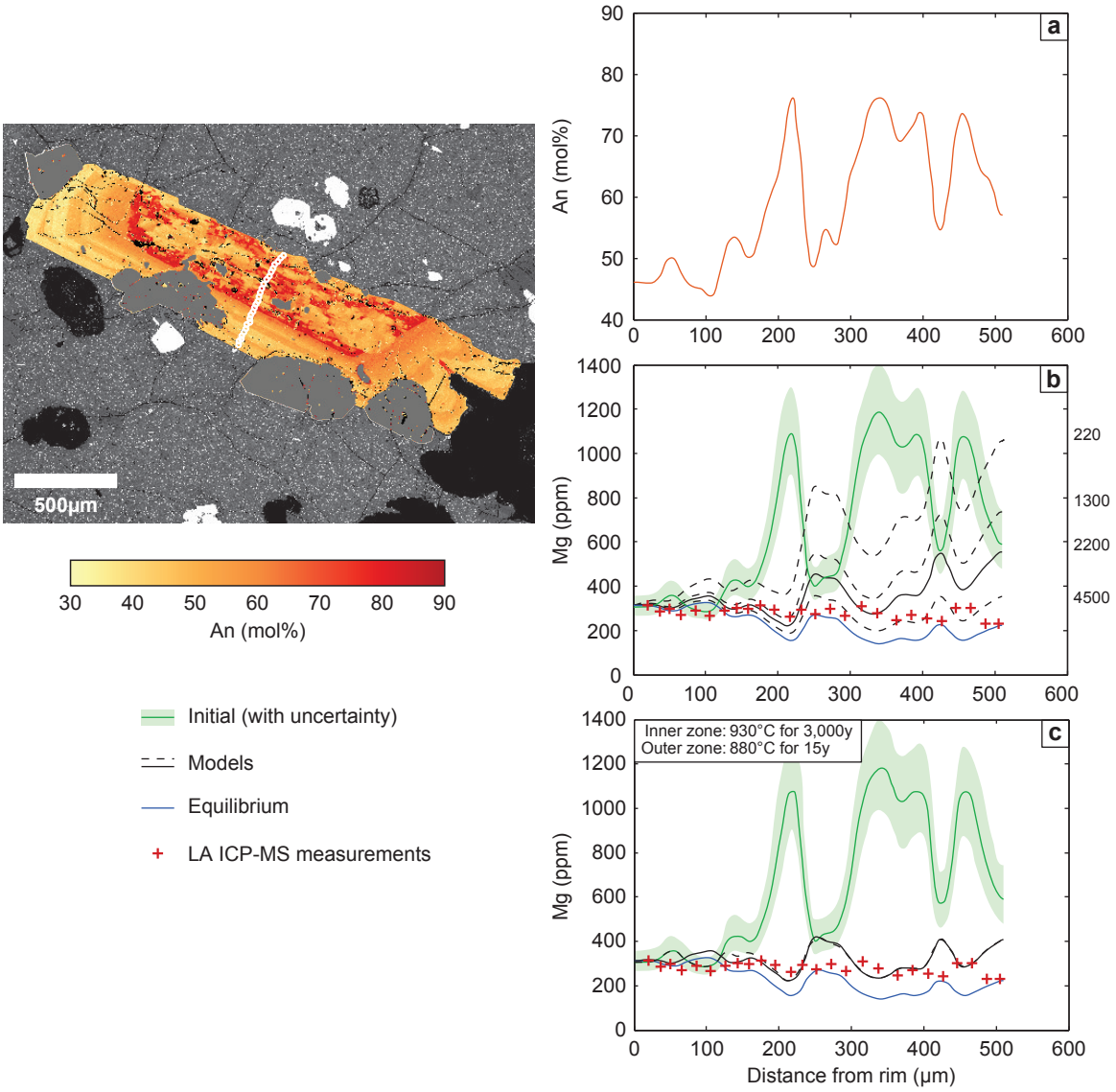

Figure E.4: GS10-17 XL60

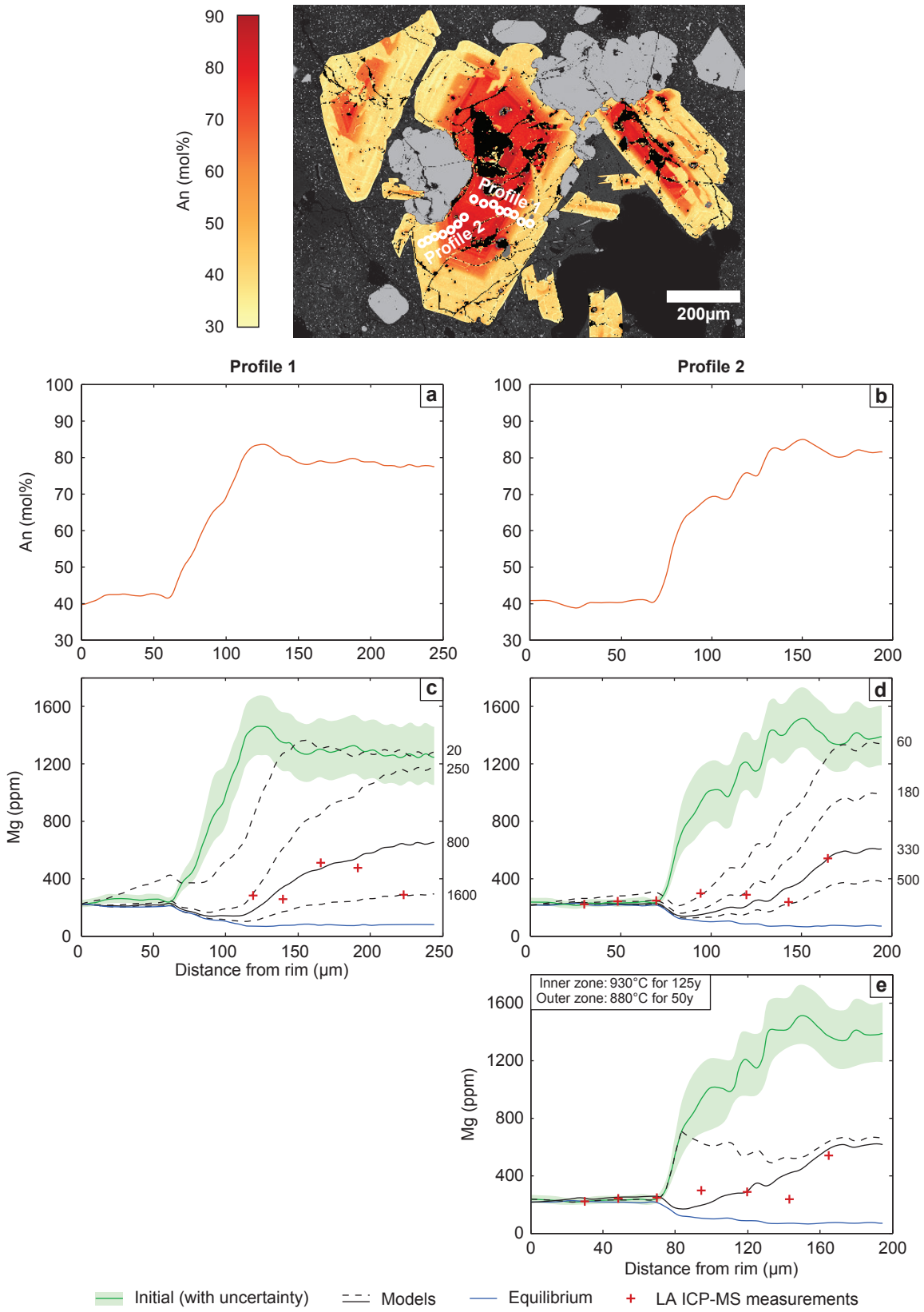

Figure E.5: GS10-17 XL71

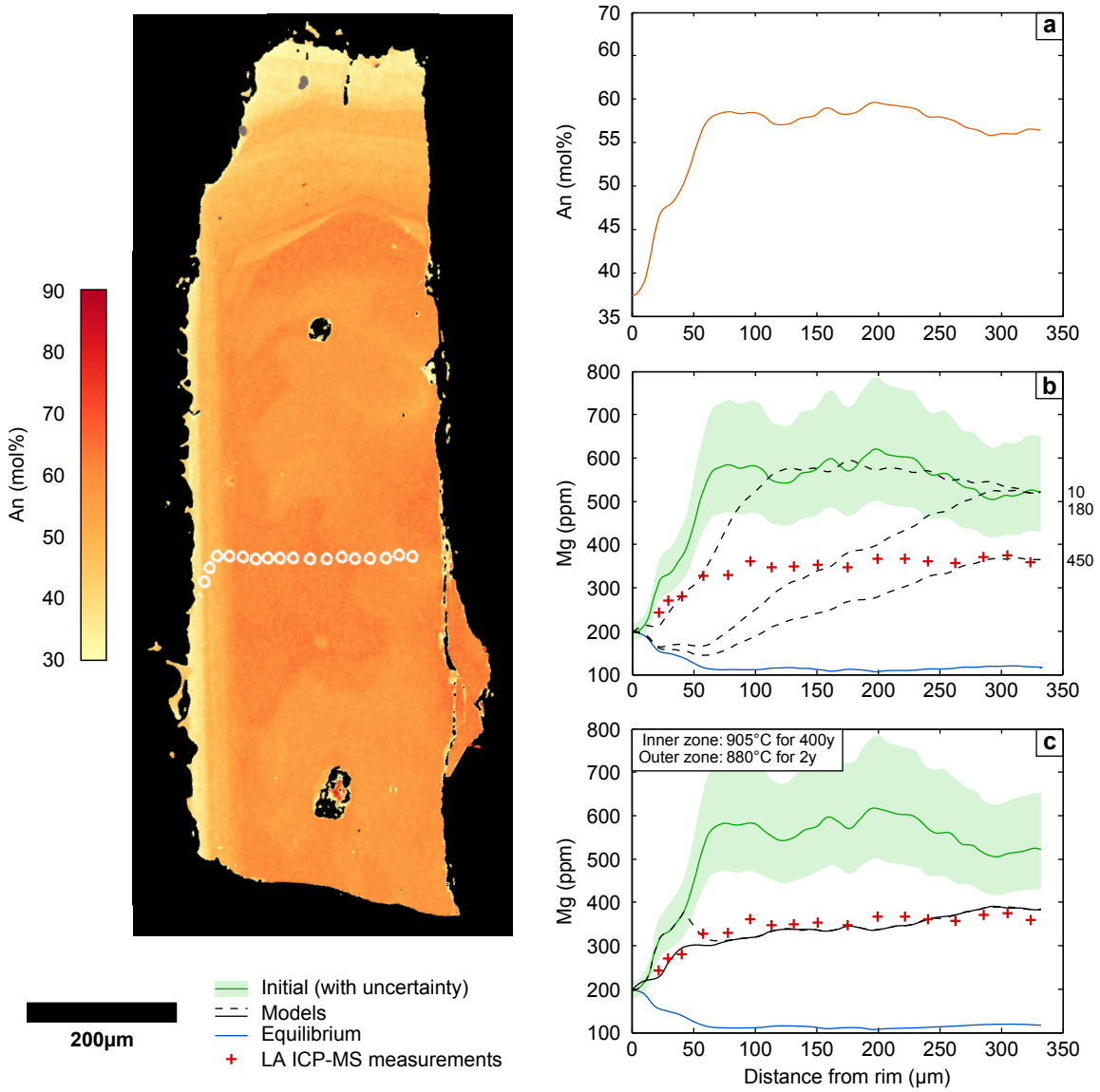

Figure E.6: GS11-30b XL15

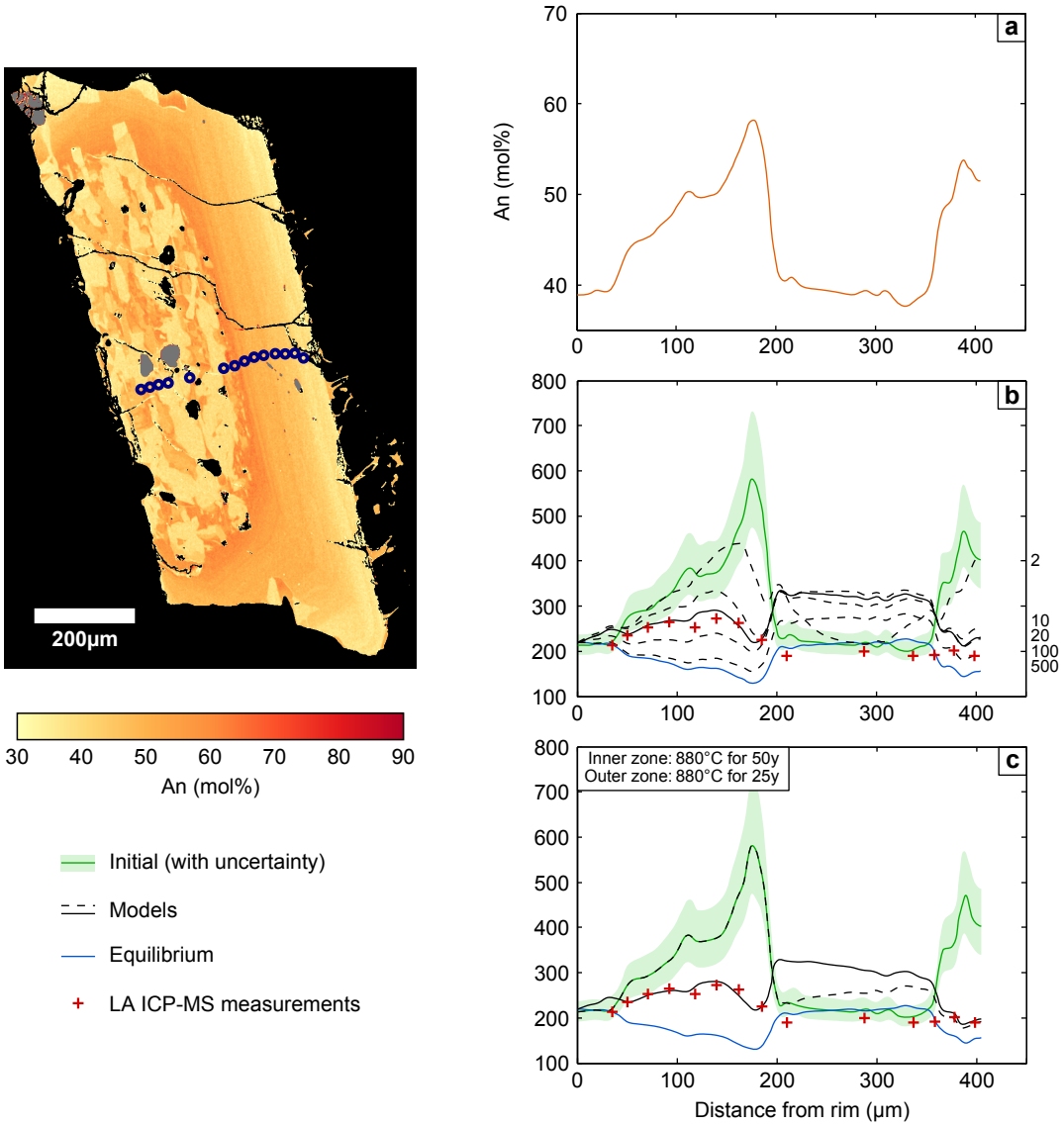

Figure E.7: GS11-30 XL18

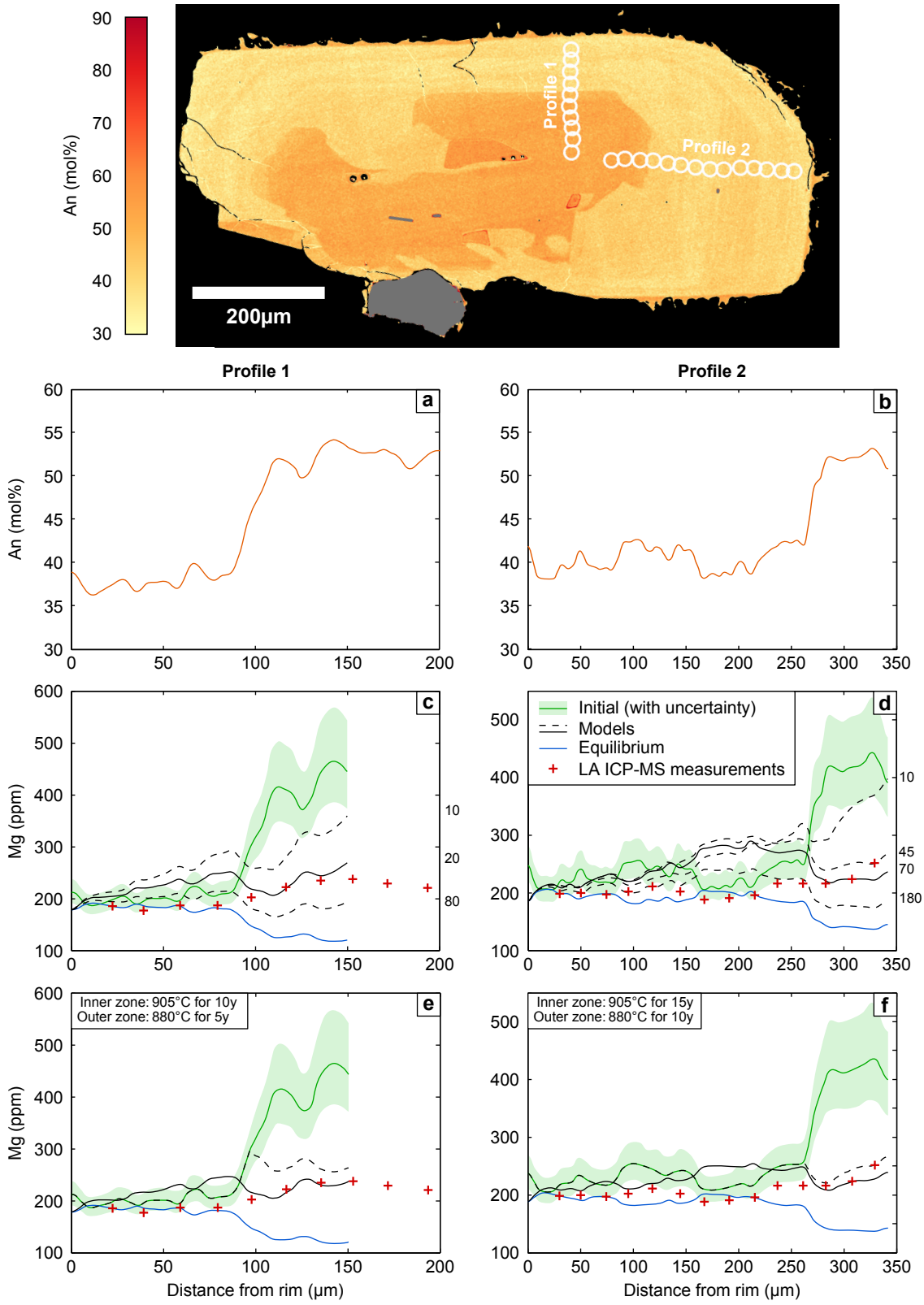

Figure E.8: GS11-34a XL09

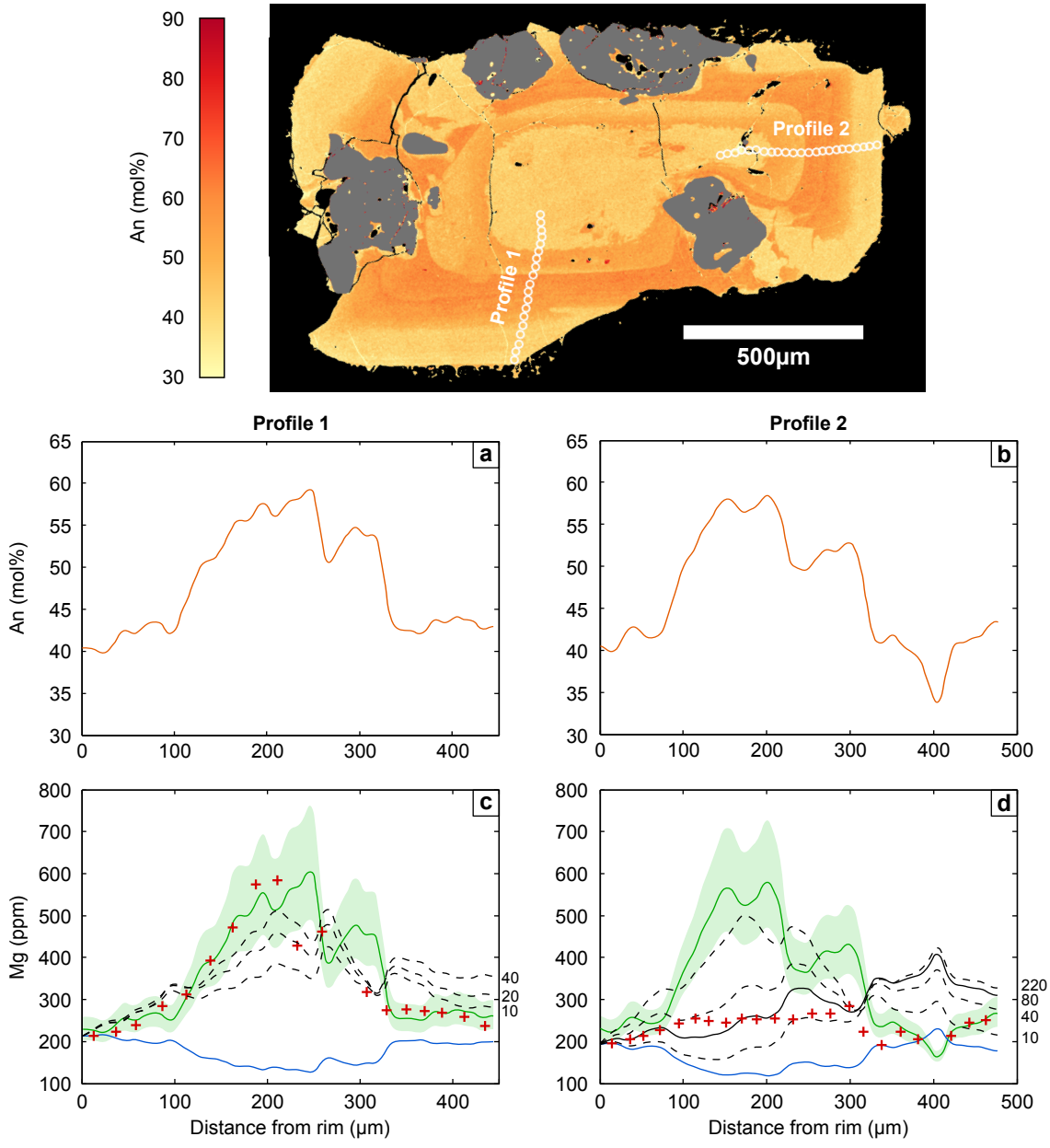

Figure E.9: GS11-34a-XL14

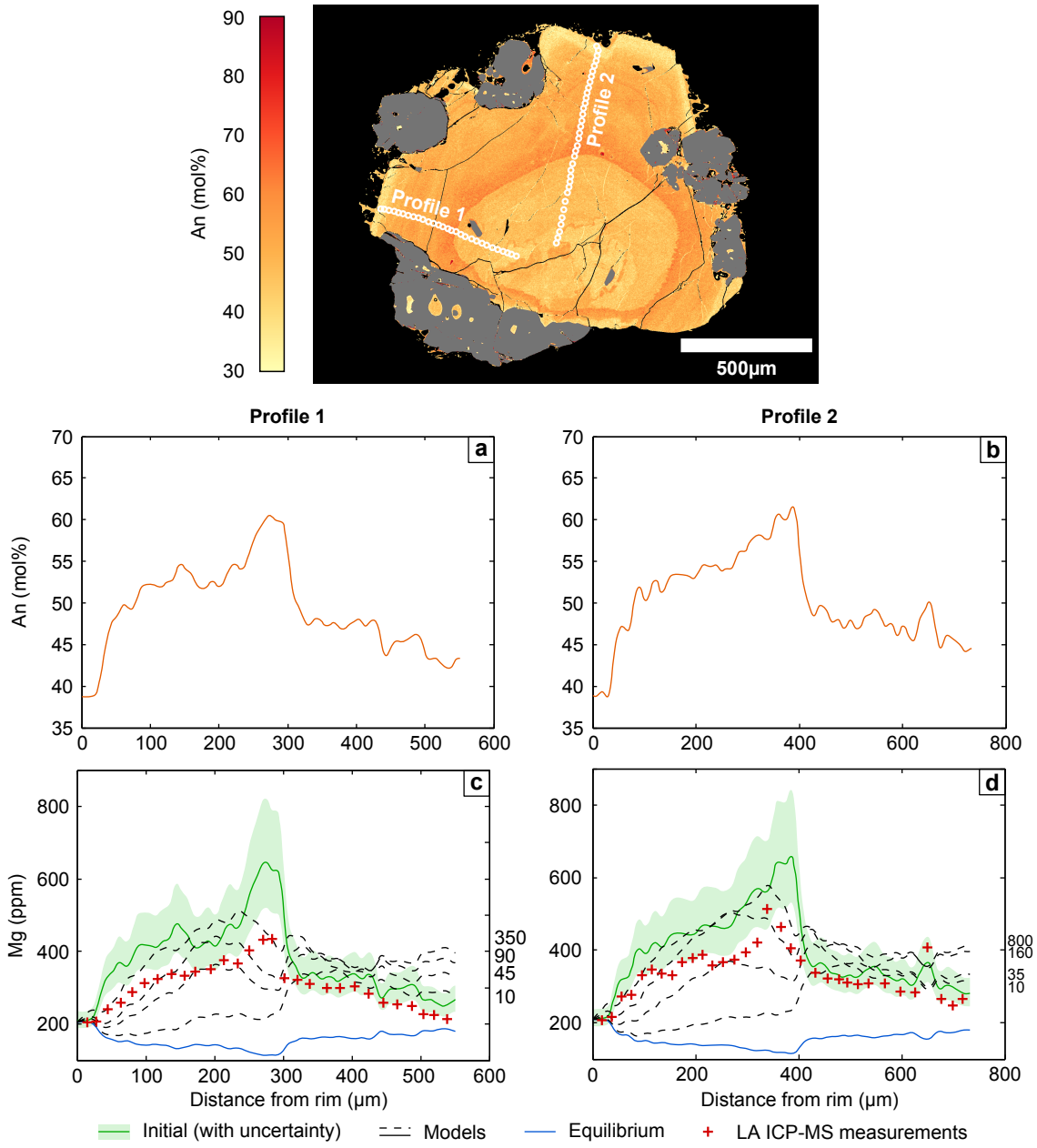

Figure E.10: GS11-34a XL23

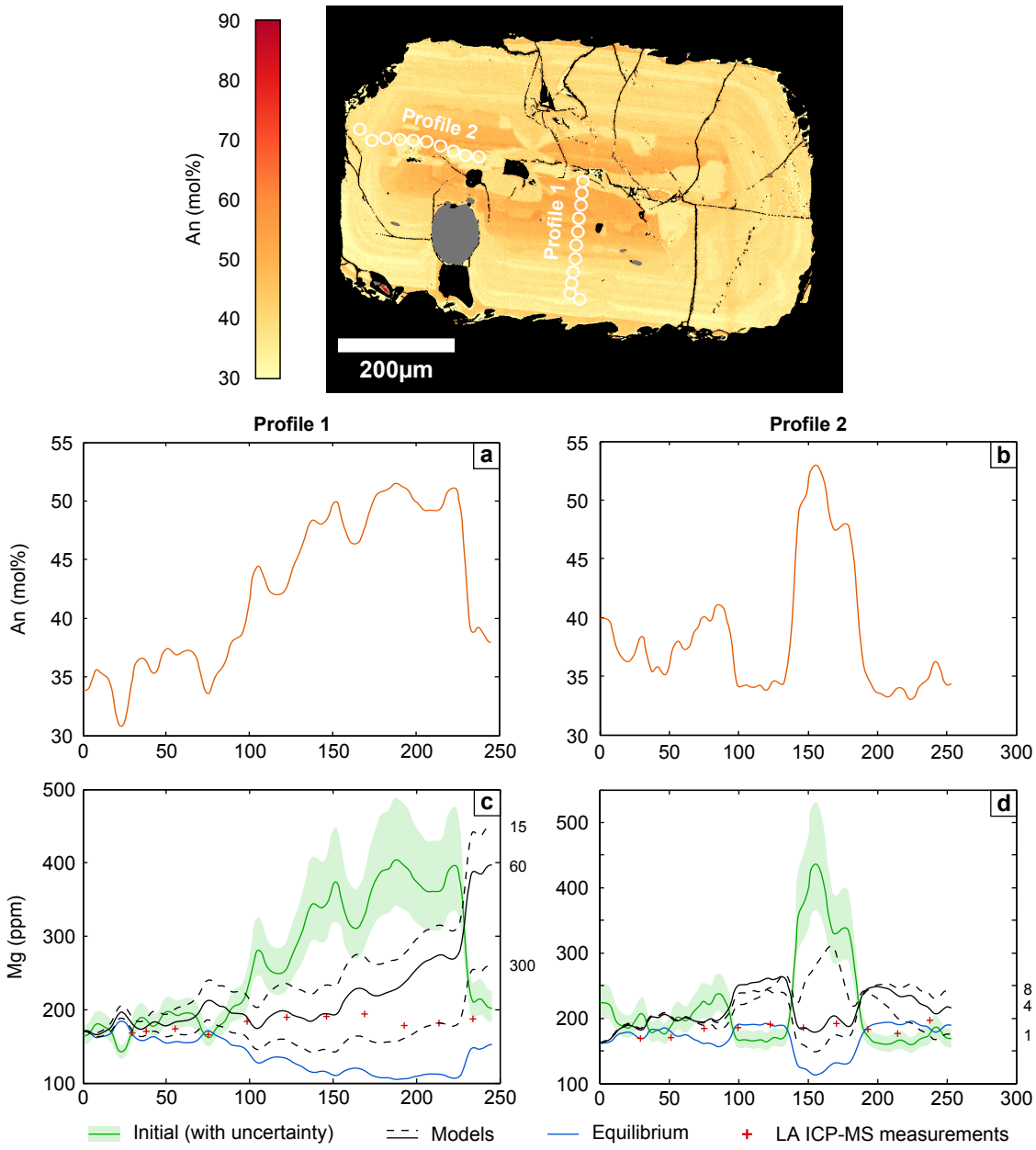

Figure E.11: GS11-39b XL29

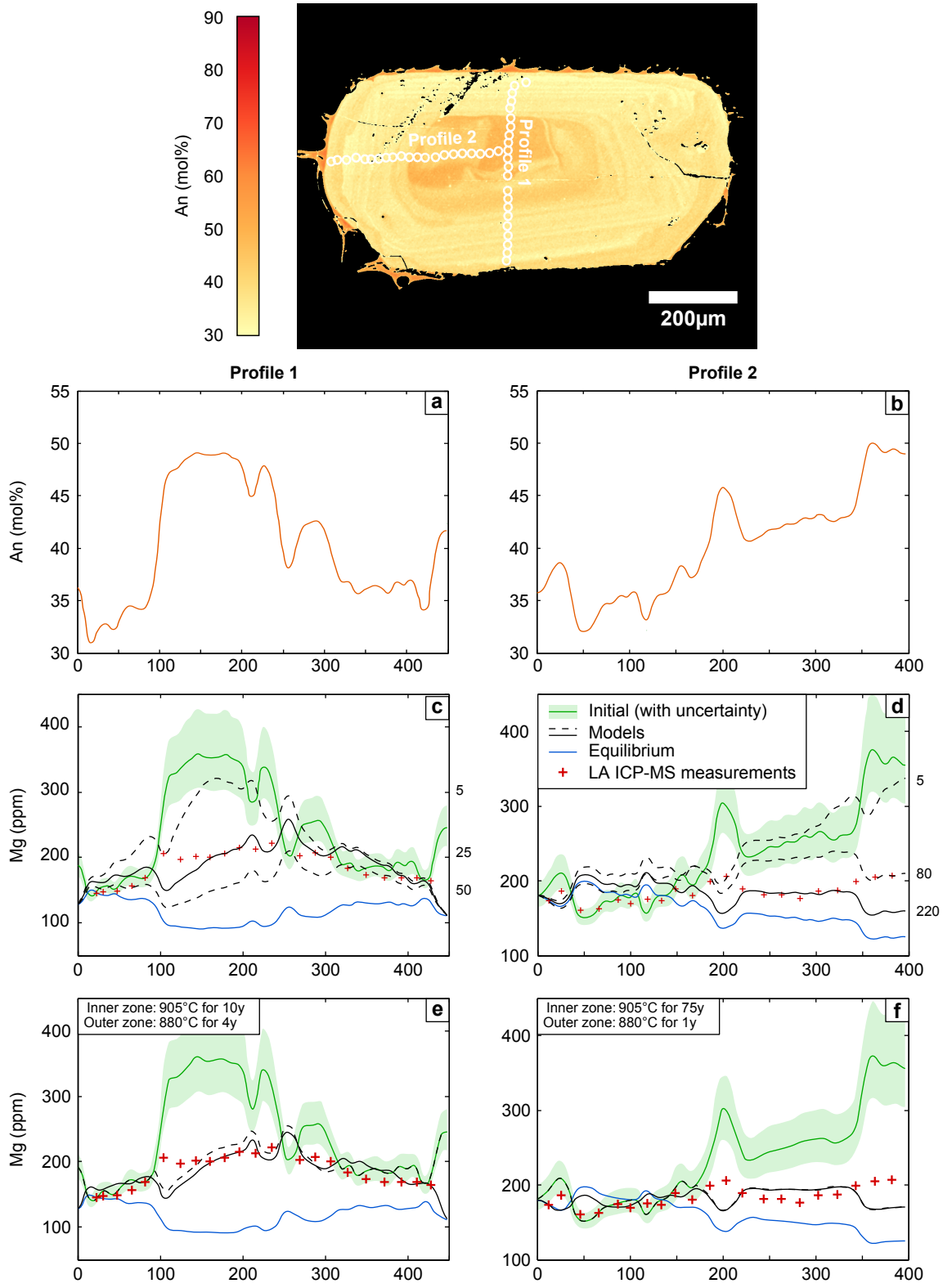

Figure E.12: S12-05 XL03

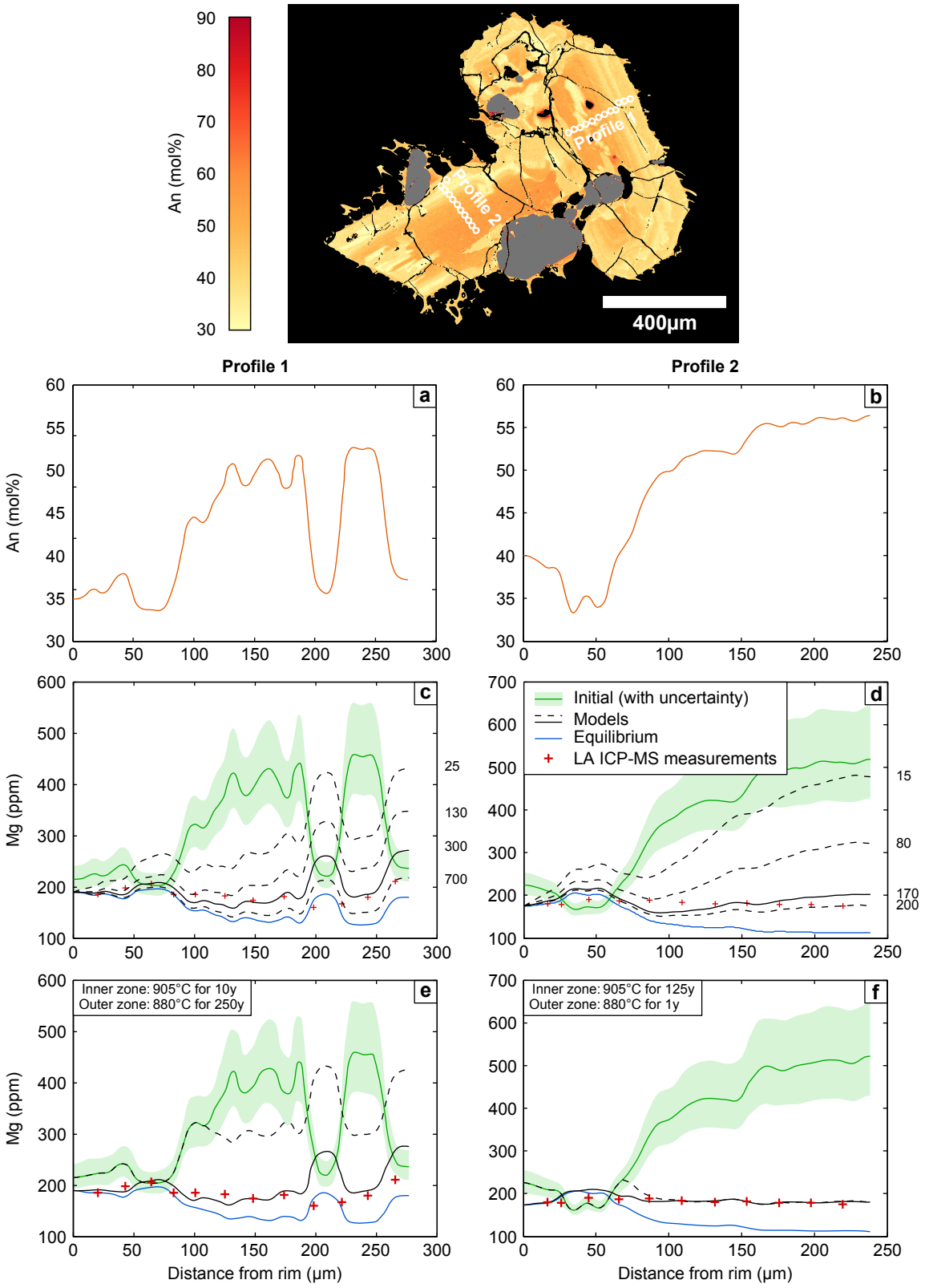

Figure E.13: S12-06 XL24

Appendix F

Orthopyroxene diffusion model results

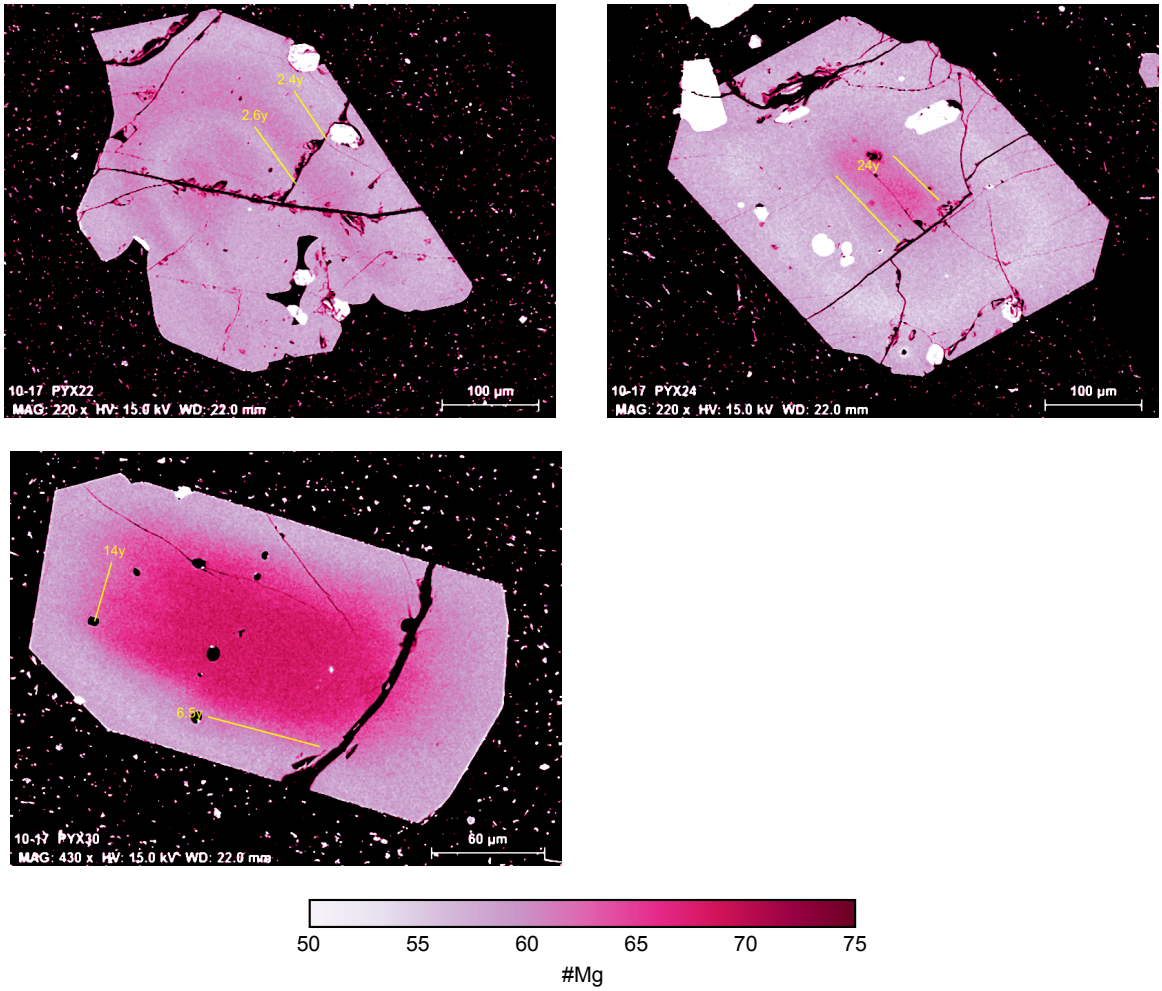

Figure F.1: Therasia dacite flow 5 (GS10-17)

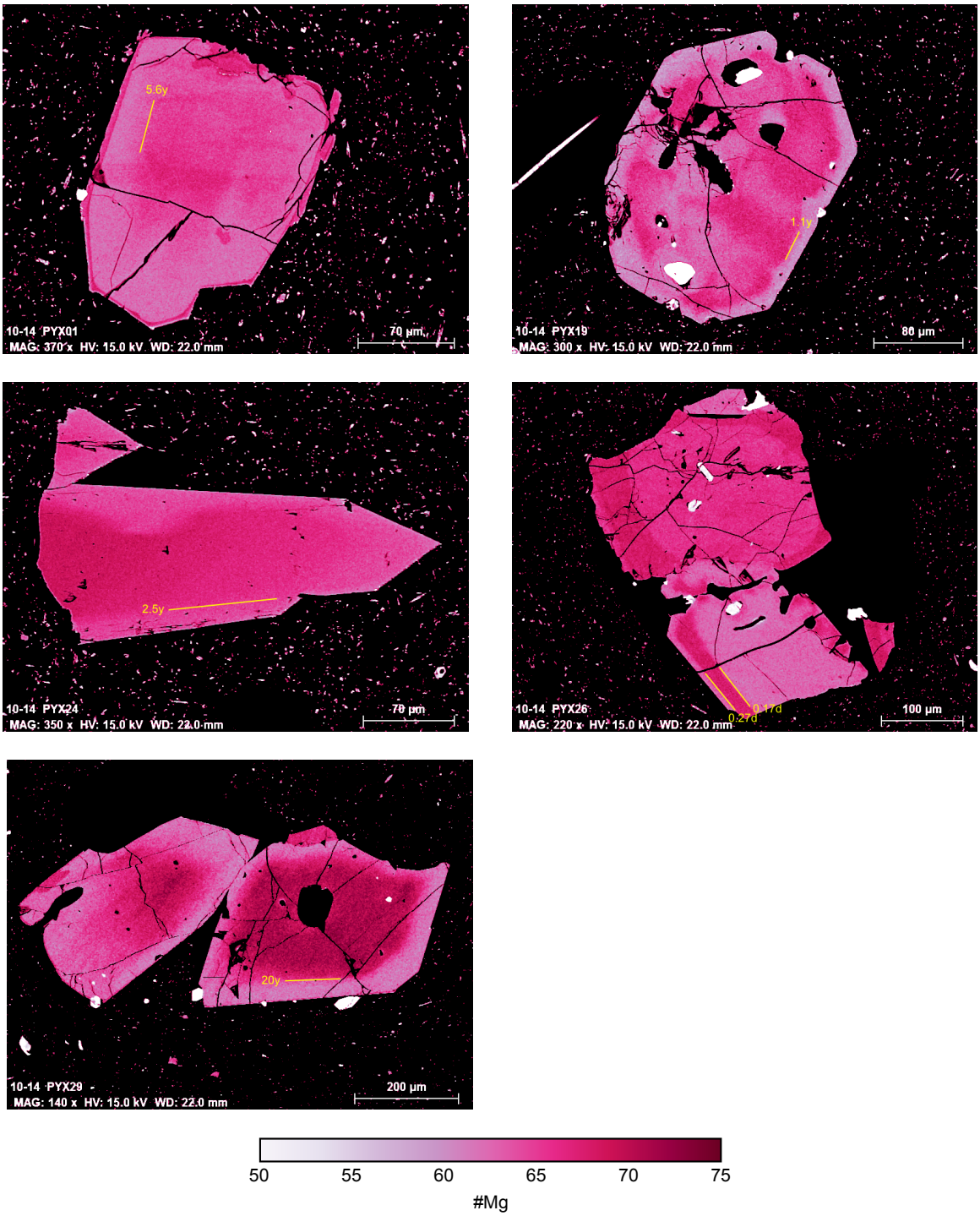

Figure F.2: Therasia dacite flow 8 (GS10-14)

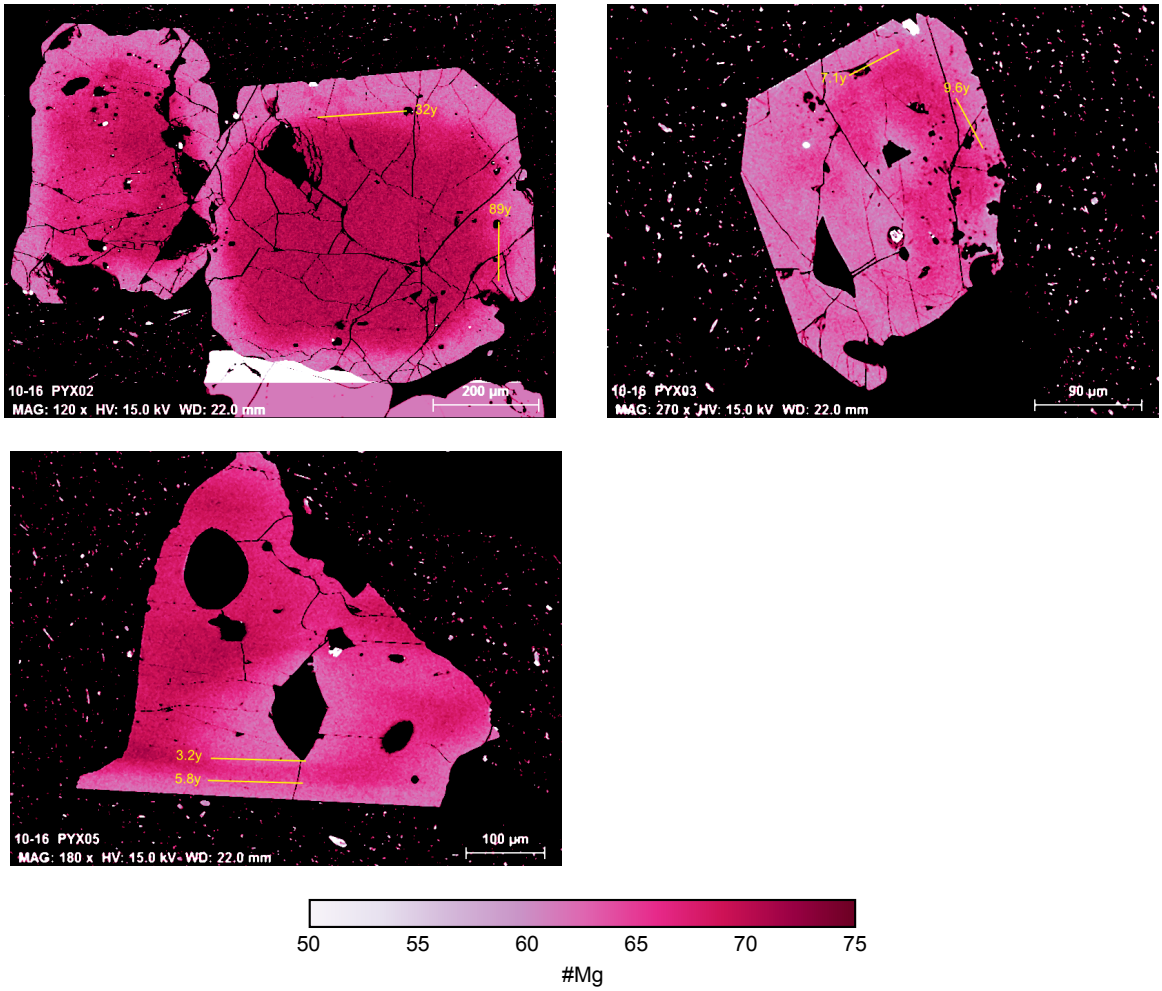

Figure F.3: Therasia dacite flow 9 (GS10-16)

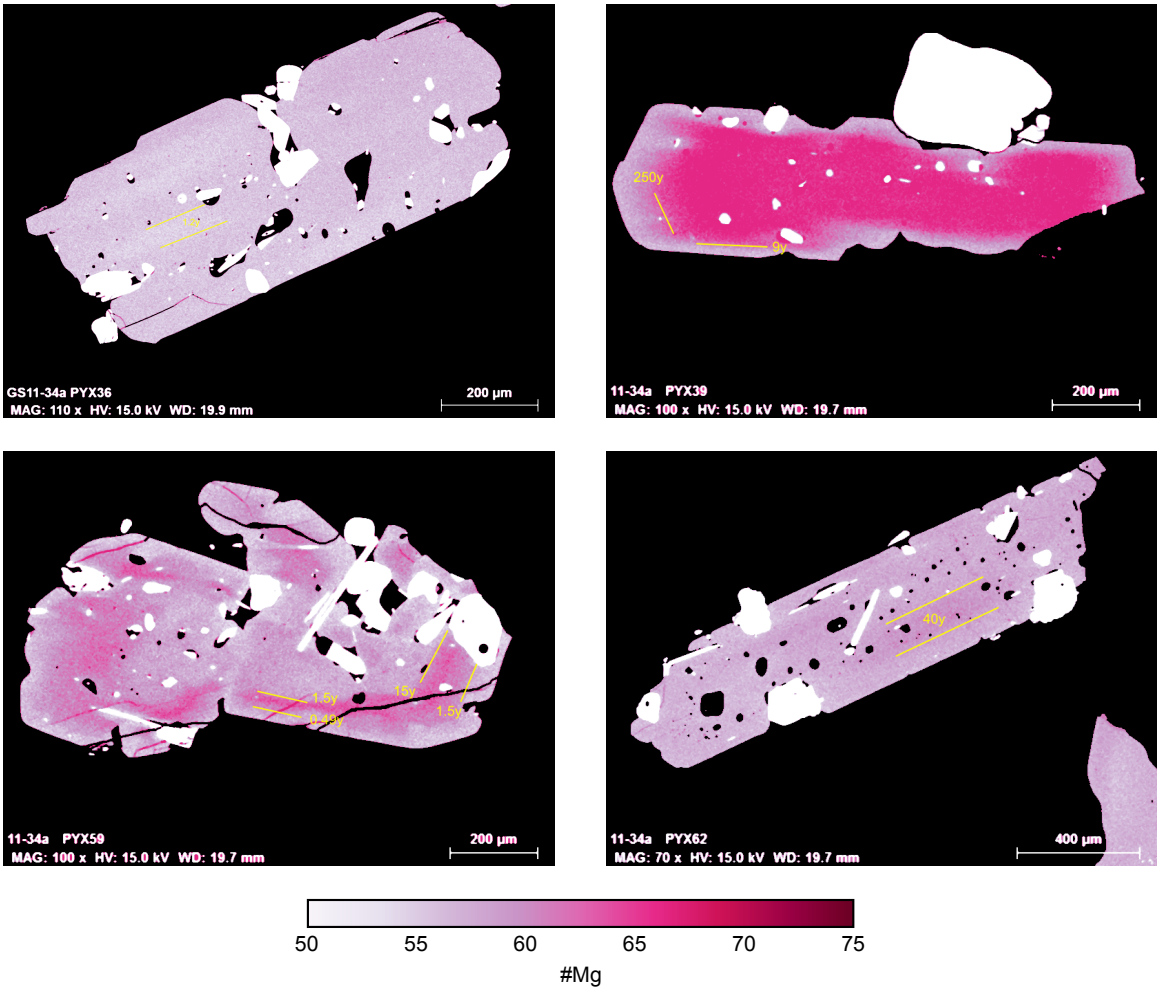

Figure F.4: Cape Riva A (GS11-34a)

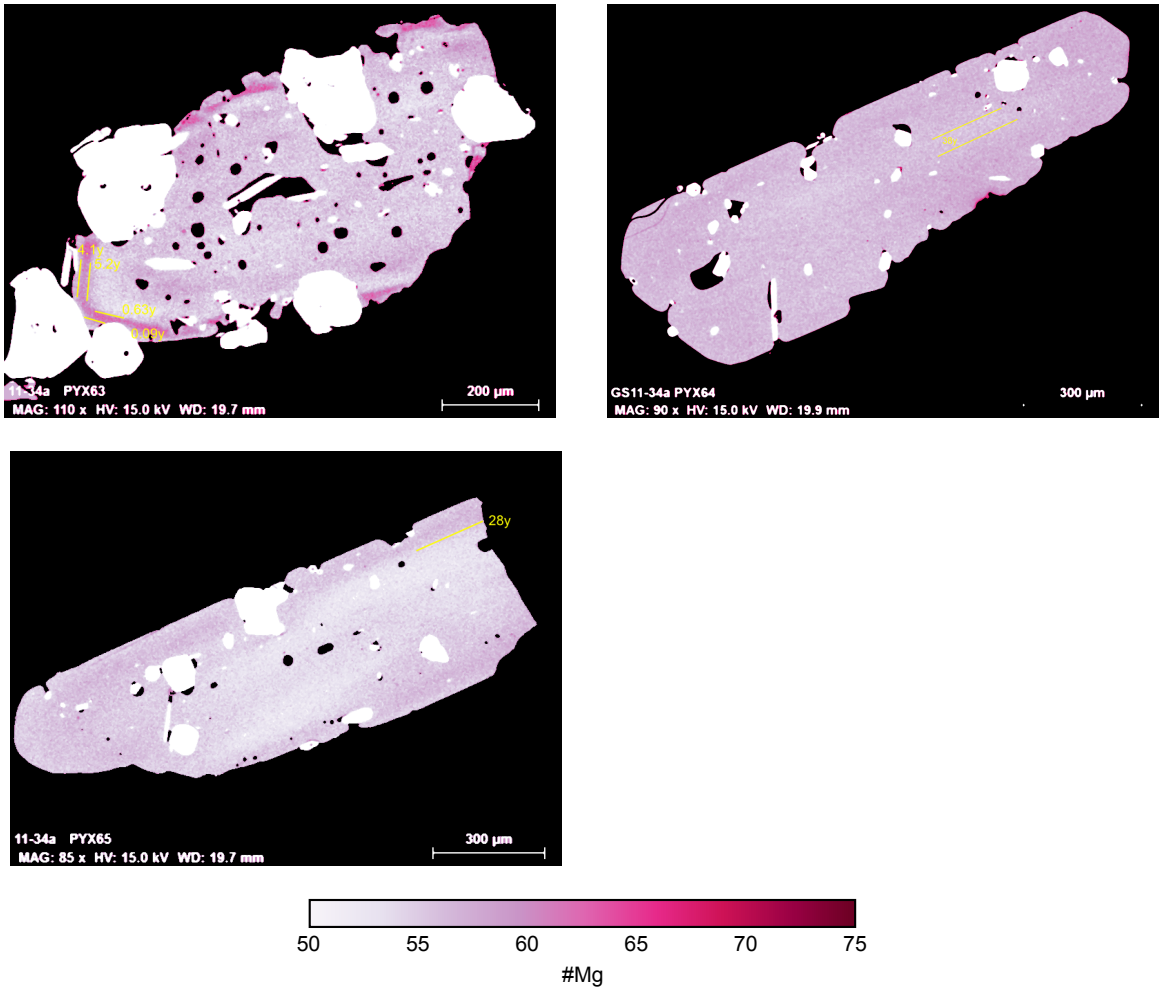

Figure F.4 continued: Cape Riva A (GS11-34a)

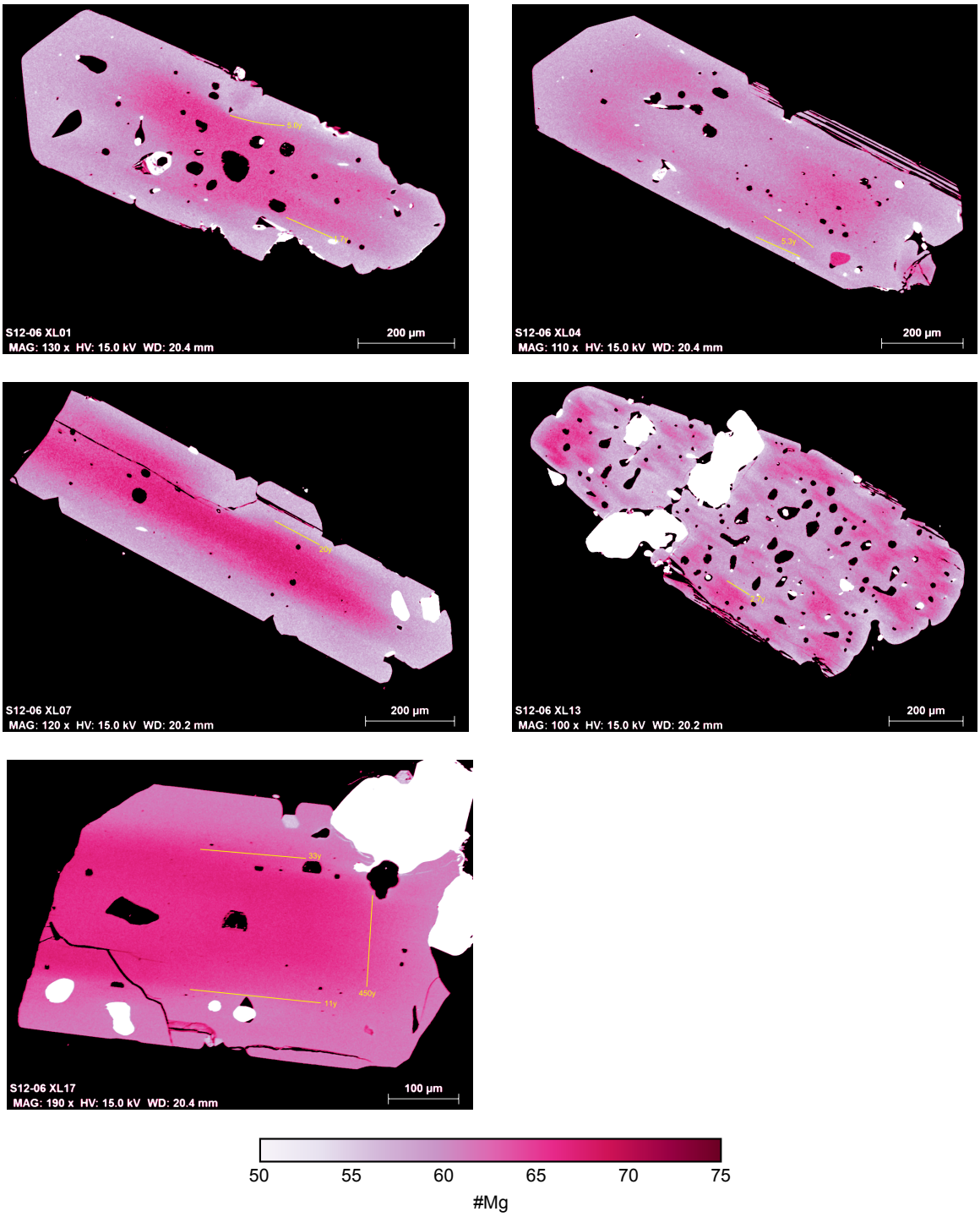

Figure F.5: Cape Riva B (S12-06)

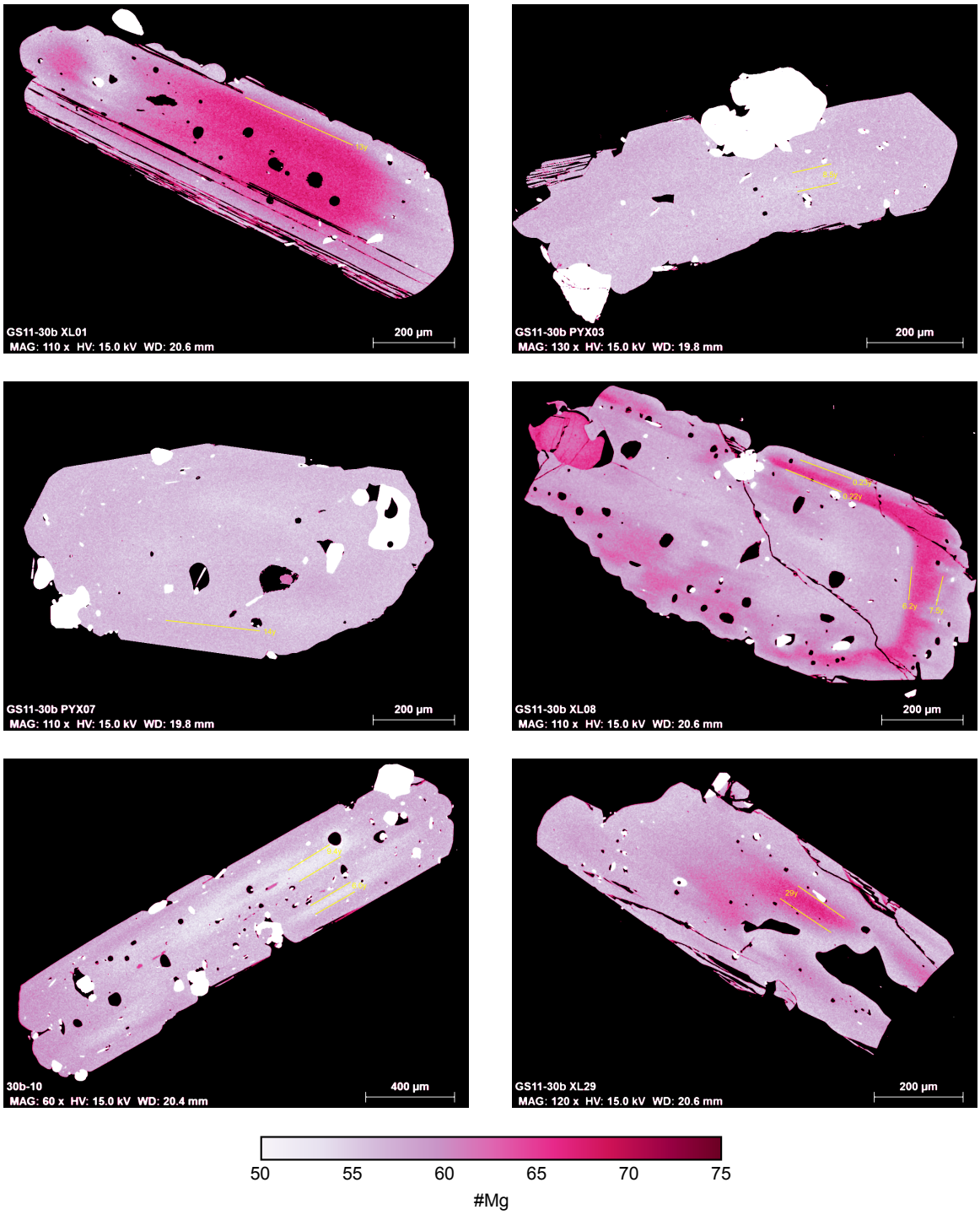

Figure F.6: Cape Riva C (GS11-30b)

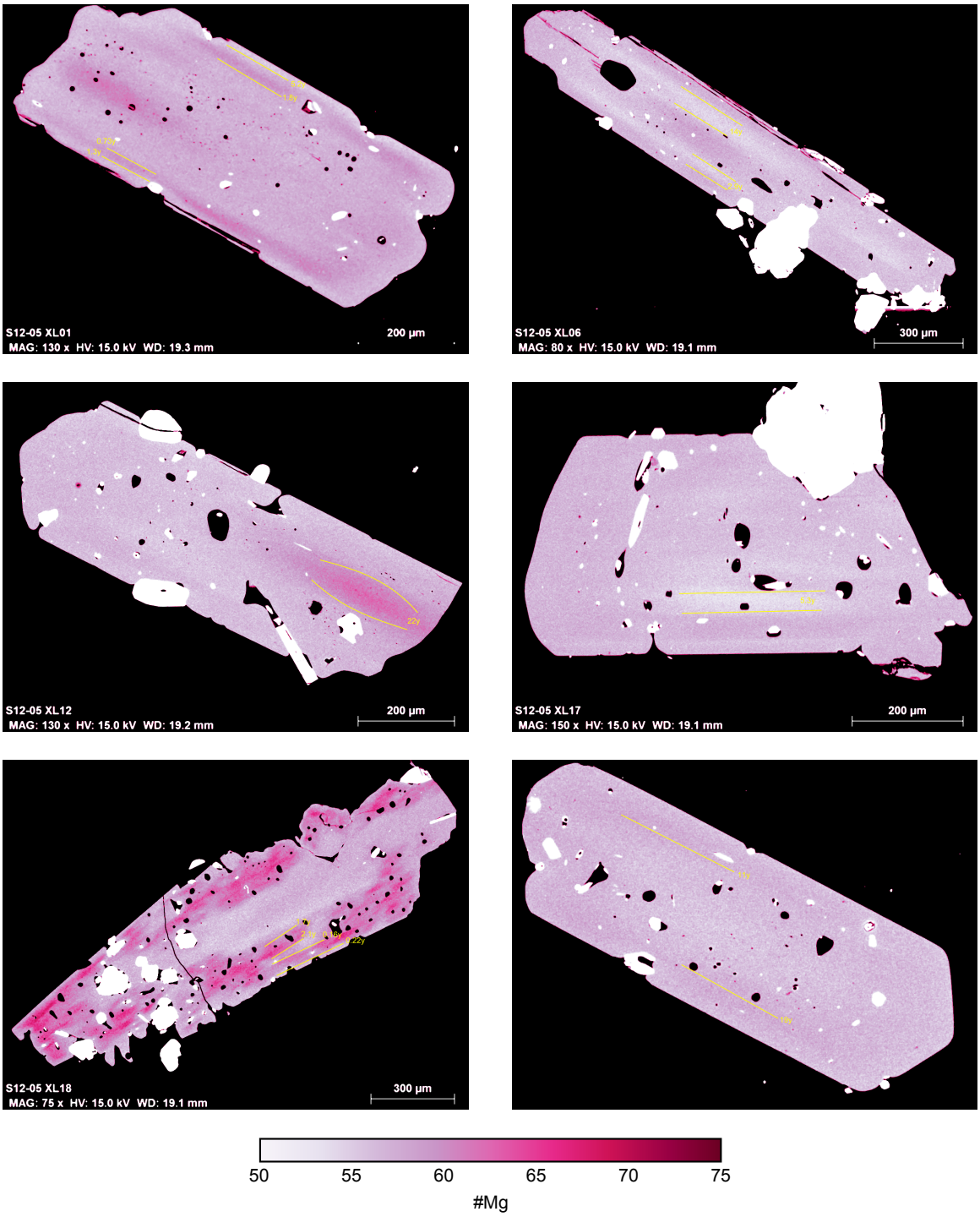

Figure F.7: Cape Riva C (S12-05)

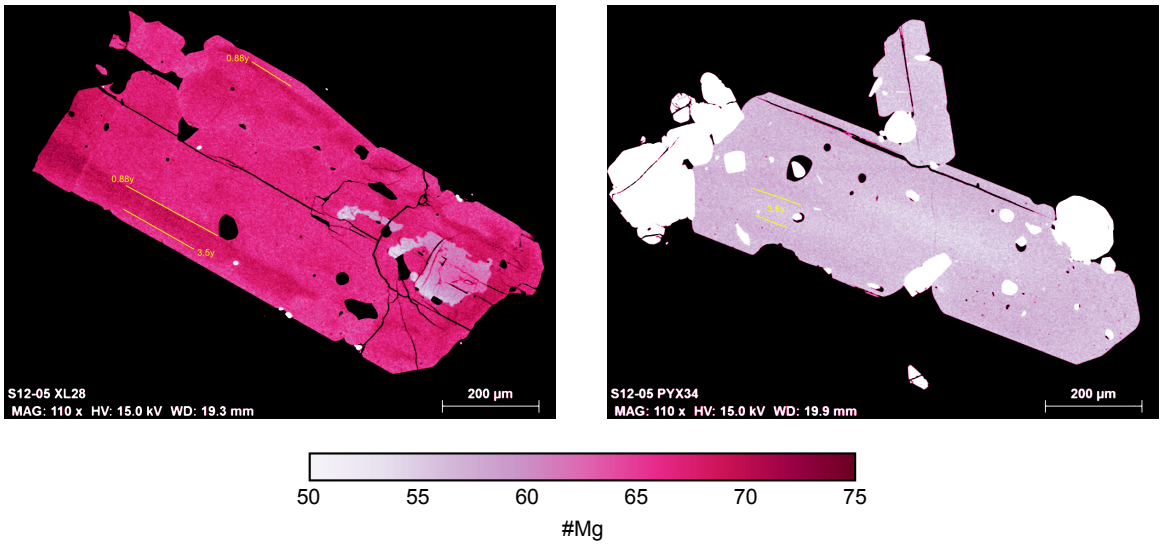

Figure F.7 continued: Cape Riva C (S12-05)

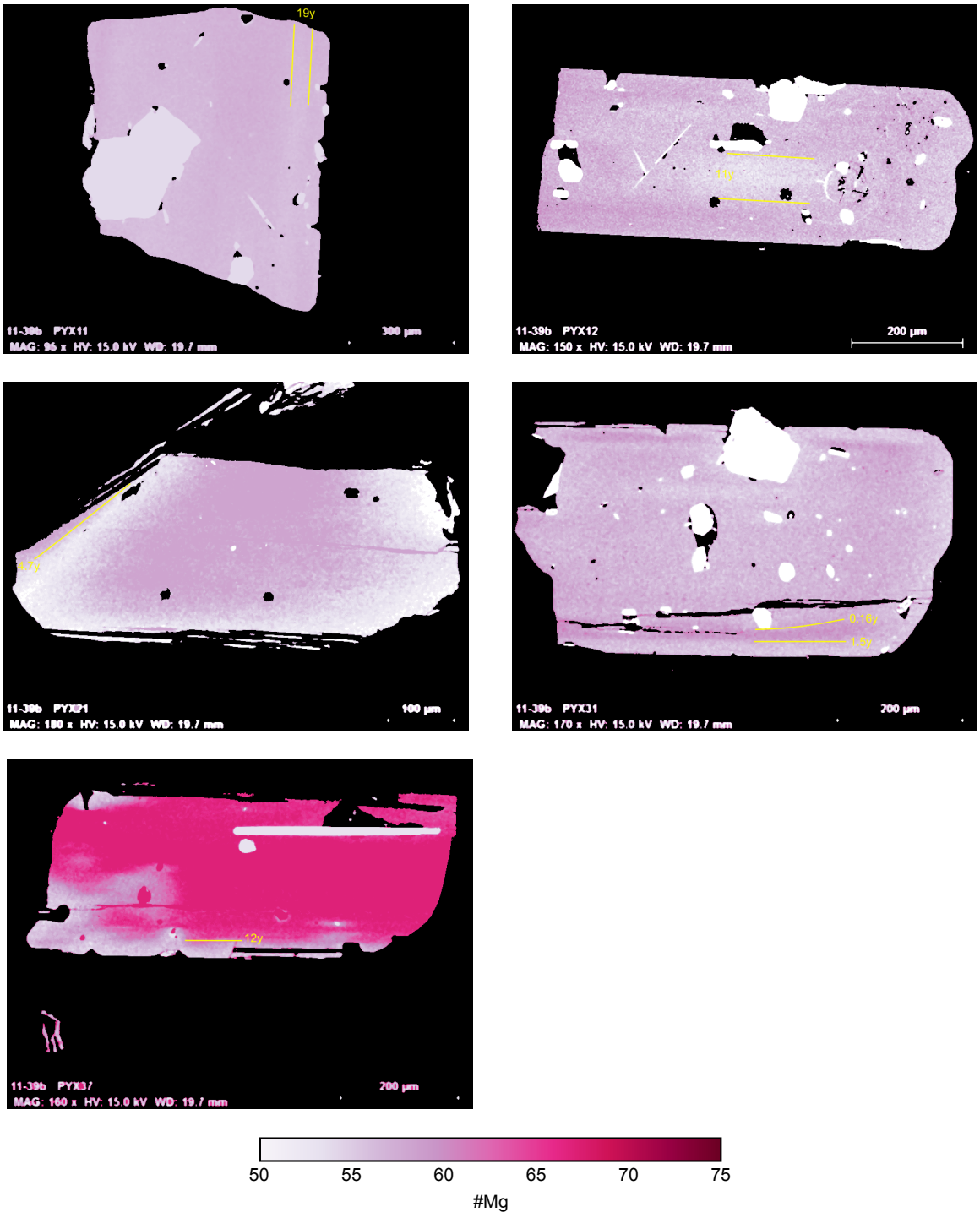

Figure F.7 continued: Cape Riva D (GS11-39b)

Appendix G

Evolution of the crustal magma plumbing system during the build-up to the 22 ka caldera-forming eruption of Santorini (Greece)

GN Fabbro[*a,b,c], TH Druitt[a,b,c], S Scaillet[d]

[a] Clermont Université, Université Blaise Pascal, Laboratoire Magmas et Volcans, BP 10448, F-63000 Clermont-Ferrand, France.

[b] CNRS, UMR 6524, LMV, F-63038 Clermont-Ferrand, France.

[c] IRD, R 163, LMV, F-63038 Clermont-Ferrand, France.

[d] Institut des Sciences de la Terre d'Orleans (ISTO), INSU-CNRS – Université d'Orleans, 1A rue de la Ferollerie, 45071 Orleans, France.

[*] Corresponding author:

Email: g.fabbro@opgc.univ-bpclermont.fr

Phone: +33 (0)6 47 17 60 58

Fax: +33 (0)4 73 34 67 44

Authors' accepted manuscript, published in the Bulletin of Volcanology, 75(12):1–21. The final publication is available at Springer via http://dx.doi.org/10.1007/s00445-013-0767-5

G.1 Abstract

The formation of caldera-sized reservoirs of crystal-poor silicic magma requires the generation of large volumes of silicic melt, followed by the segregation of that melt and its accumulation in the upper crust. The 21.8 ± 0.4 ka Cape Riva eruption of Santorini discharged $>10\,km^3$ of crystal-poor dacitic magma along with $\ll 1\,km^3$ of hybrid andesite, and collapsed a pre-existing lava shield. We have carried out a field, petrological, chemical and high-resolution $^{40}Ar/^{39}Ar$ chronological study of a sequence of lavas discharged prior to the Cape Riva eruption in order to constrain the crustal residence time of the Cape Riva magma reservoir. The lavas were erupted between 39∼and 25 ka, forming a $\sim 2\,km^3$ complex of dacitic flows, coulées and domes up to 200 m thick (Therasia dome complex). The Therasia dacites show little chemical variation with time, suggesting derivation from one or more thermally buffered reservoirs. Minor pyroclastic layers occur intercalated within the lava succession, particularly near the top. A prominent pumice fall deposit probably correlates with the 26-ka Y-4 ash layer found in deep-sea sediments SE of Santorini. One of the last Therasia lavas to be discharged was a hybrid andesite formed by the mixing of dacite and basalt. The Cape Riva eruption occurred no more than $2{,}800 \pm 1{,}400$ y after the final Therasia activity. The Cape Riva dacite is similar in major element composition to the Therasia dacites, but is poorer in K and most incompatible trace elements (e.g. Rb, Zr, LREE). The same chemical differences are observed between the Cape Riva and Therasia hybrid andesites, and between the calculated basaltic mixing endmembers of each series. The Therasia and Cape Riva dacites are distinct silicic magma batches and are not related by shallow processes of crystal fractionation or assimilation. The Therasia lavas were

therefore not simply precursory leaks from the growing Cape Riva magma reservoir. The change 21.8 ky ago from a magma series richer in incompatible elements to one poorer in those elements is one step in the well documented decrease with time of incompatibles in Santorini magmas over the last 530 ky. The two dacitic magma batches are interpreted to have been emplaced sequentially into the upper crust beneath the summit of the volcano, the first (Therasia) then being partially, or wholly, flushed out by the arrival of the second (Cape Riva). This constrains the crustal residence time of the Cape Riva reservoir to less than $2{,}800 \pm 1{,}400$ years, and the associated time-averaged magma accumulation rate to $>0.004\,\mathrm{km^3\,y^{-1}}$. Rapid ascent and accumulation of the Cape Riva dacite may have been caused by an increased flux of mantle-derived basalt into the crust, explaining the occurrence of hybrid andesites (formed by the mixing of olivine basalt and dacite in approximately equal proportions) in the Cape Riva and late Therasia products. Pressurization of the upper crustal plumbing system by sustained, high-flux injection of dacite and basalt may have triggered the transition from prolonged, largely effusive activity to explosive eruption and caldera collapse.

Keywords: Santorini, magma reservoirs, melt accumulation, residence timescales, calderas

G.2 Introduction

Caldera-forming ignimbrite eruptions discharge large volumes (1-$10^3\,\mathrm{km^3}$) of silicic magma from shallow reservoirs (Mason et al., 2004; Miller and Wark, 2008; Smith, 1979). The processes that generate such reservoirs, and the timescales on which those processes operate, are not completely understood (e.g. Bachmann and Bergantz, 2008a;

Costa, 2008; Gelman et al., 2013). This is particularly true of caldera systems such as Santorini that erupt crystal-poor silicic magmas (Allan et al., 2013; Bachmann and Bergantz, 2004; Druitt et al., 2012; Gualda et al., 2012b; Hildreth and Wilson, 2007; Wilson and Charlier, 2009).

The formation of caldera-sized reservoirs of crystal-poor silicic magma requires the generation of large volumes of silicic melt, followed by the segregation of that melt and its accumulation in the upper crust (Bachmann and Bergantz, 2004, 2008a; Lindsay et al., 2001). Large volumes of silicic melt are generated in crustal hot zones by fractional crystallization of mantle-derived basalt, partial melting of crustal rocks, defrosting of incompletely crystallized plutons (Annen et al., 2006; Hildreth, 1981; Hildreth and Moorbath, 1988; Solano et al., 2012). Fractional crystallization is driven by outgassing and cooling of magma during ascent (Blundy and Cashman, 2008). Partial melting of crustal rocks and pre-existing plutons is driven by heat advected by mantle-derived magma and magmatic volatiles (Bachmann and Bergantz, 2006; Hildreth, 1981; Huber et al., 2011). Silicic melt generation can occur over timescales of 10^5 to 10^1 years (Bachmann and Bergantz, 2006; Brown and Fletcher, 1999; Burgisser and Bergantz, 2011; Charlier et al., 2005; Huber et al., 2011; Klemetti et al., 2011). Magmatic crystal mushes generated by these processes may remain at depth, or may erupt en masse to form crystal-rich ignimbrites (the monotonous intermediates of Hildreth, 1981).

The formation of reservoirs of crystal-poor silicic magma requires the separation of melt from residual mush crystals, and the accumulation of that melt at a particular crustal level—either in situ within the mush (e.g. Bachmann and Bergantz, 2004), or at higher levels in the plumbing system (e.g. Allan et al., 2013). The rate at which

silicic melt can separate from crystals is limited by its high viscosity (Bachmann and Bergantz, 2008b; McKenzie, 1985). Possible mechanisms include gravitational separation through hindered settling of individual crystals, or compaction of a porous crystal network (Bachmann and Bergantz, 2004). Melt migration driven by shear or gas filter pressing may generate small, local segregations (Brown and Solar, 1998; Sisson and Bacon, 1999; Stevenson, 1989) that are subsequently concentrated into large melt lenses. Runaway reservoir growth requires rates of heat (and hence magma) input high enough to limit crystallisation and avoid plutonic death (Annen, 2009; Gelman et al., 2013; Schöpa and Annen, 2013).

Estimates of melt accumulation timescales for crystal-poor silicic magmas vary widely. Assembly of the rhyolitic magma reservoir that discharged the 600-650 km^3 Bishop Tuff has been estimated as $\sim 10^5$ y, based on zircon ages and on the chemical similarity between the Bishop magma and earlier rhyolites (Hildreth and Wilson, 2007). However, element diffusion profiles and melt inclusion faceting in Bishop quartz crystals yield much shorter timescales (10^3–10^2 y; Gualda et al., 2012b; Wark et al., 2007). The reservoir that fed the 530 km^3 Oruanui Ignimbrite at Taupo was assembled over 1600 years (Allan et al., 2013; Wilson and Charlier, 2009), and that of the $\sim$35 km^3 post-Oruanui 'Y' eruption was assembled over <1000 years (Sutton et al., 2000). The magma reservoir of the 30-60 km^3 Minoan eruption at Santorini underwent a spurt of rapid growth in the centuries preceding venting (Druitt et al., 2012). Ascent of silicic melt into shallow reservoirs can occur in pulses with durations that are short compared to the repose period between eruptions (Druitt et al., 2012; Parks et al., 2012).

In this paper we study a sequence of silicic and intermediate lavas at Santorini

that were discharged prior to a $\geq$10 km^3 caldera-forming eruption of crystal-poor silicic magma (the 22-ka Cape Riva eruption). The lavas record the development of the crustal plumbing system over many thousands of years preceding the Cape Riva eruption. We present field, petrological and chemical data for these lavas, along with new, high-precision 40Ar/39Ar ages. The results enable us to place constraints on the residence timescale of the Cape Riva magma reservoir in the upper crust.

G.3 Geological Setting

Santorini Volcano lies on the Hellenic volcanic arc, which stretches between Greece and Turkey through the Aegean Sea, and owes its origin to the subduction of the African plate beneath the Eurasian plate (Le Pichon and Angelier, 1979; Nocquet, 2012; Papazachos et al., 2000). Santorini lies on continental crust about 23 km thick (Karagianni et al., 2005; Tirel et al., 2004). The boundary between the upper crust and lower crust lies at about 15 km depth (Konstantinou, 2010).

The volcanic history of Santorini has been described by Druitt et al. (1999). Volcanism commenced about 650 ka (Figure G.1). From about 360 ka onwards, activity consisted of multiple large (>1 km^3) explosive eruptions alternating with periods of lava extrusion and minor explosive events. The last major eruption (Minoan eruption) occurred about 1639–1616 BCE (Manning et al., 2006) and discharged 30-60 km^3 of magma (Pyle, 1990; Sigurdsson et al., 2006). Since the Minoan eruption there have been at least ten dacitic effusive eruptions, building up the Kameni intra-caldera volcano (Pyle and Elliott, 2006).

Santorini magmas are calc-alkaline to mildly tholeiitic, and range from basalt to

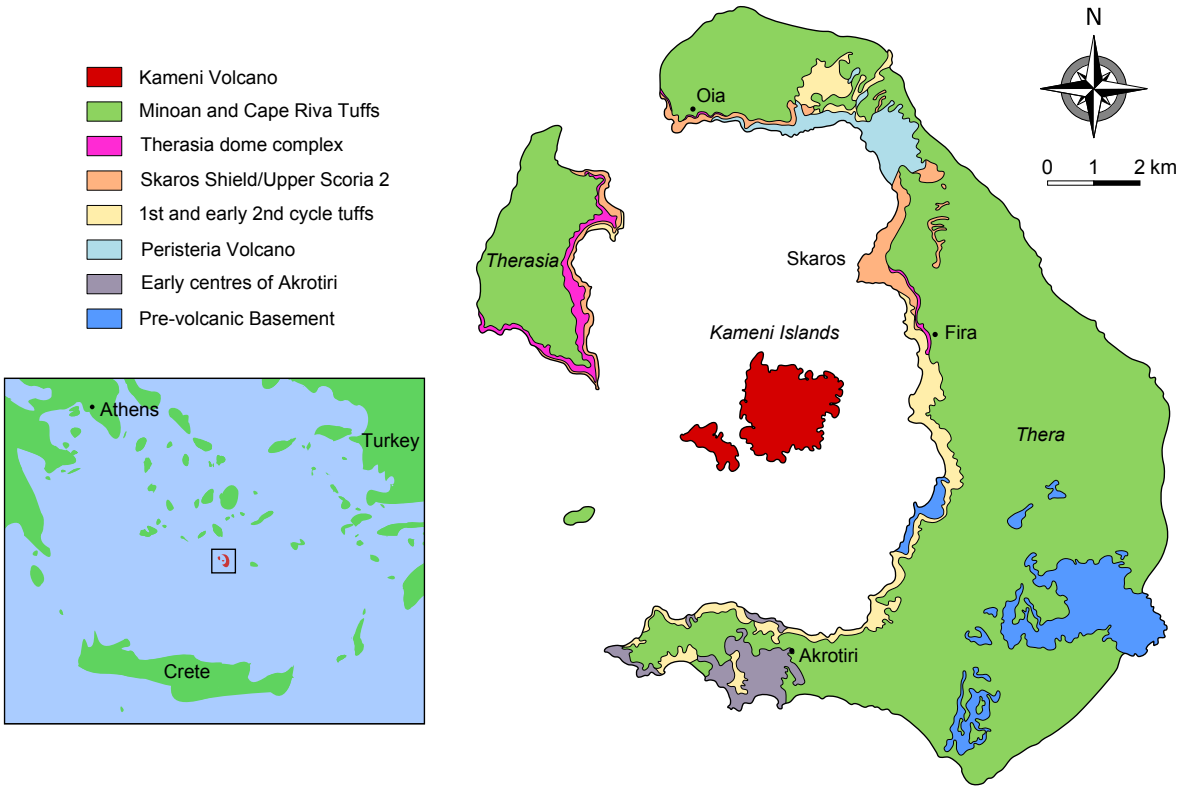

Figure G.1: Simplified geological map of Santorini, adapted from Druitt et al. (1999). Inset is a map of the Aegean region, with Santorini marked with a box

rhyodacite in composition (Druitt et al., 1999). The silicic magmas are generally poor in phenocrysts (<5–20 vol% on a vesicle-free basis). Phase-equilibria experiments (Andújar et al., 2010) have shown that mantle-derived basalt ascending beneath Santorini stagnates and fractionates to basaltic andesite at about 4 kb (∼15 km, assuming a mean upper crustal density of 2640 kg m^{-3}; Konstantinou, 2010), near the boundary between the upper and lower crust. The silicic magmas discharged during large eruptions are stored in the upper crust at 2 ± 0.5 kb (∼8 km) immediately prior to eruption (Cadoux et al., 2013).

Our study focuses on the products of the volcano from the period between 70 and 22 ka (Figure G.2). About 70 ky ago a caldera formed in the northern half of the volcanic field, probably as a result of one or more explosive eruptions (Druitt et al.,

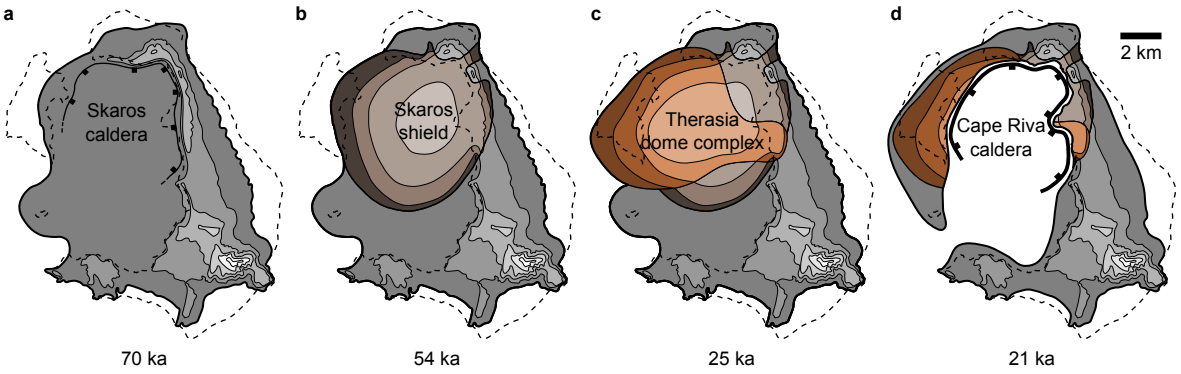

Figure G.2: Morphological evolution of Santorini between 70 ka and 21 ka, after Druitt et al. (1999). The dashed line is the present-day outline of the islands. Contours are at 100 m intervals (a) The volcano after collapse of the Skaros caldera, which happened some time before the first Skaros lava was erupted at 69 ± 7 ka (b) The maximum extent of the Skaros shield, which culminated with the 54 ± 3 ka Upper Scoria 2 eruption (c) The maximum extent of Therasia dome complex at ∼25 ka (d) The island shortly after the ∼22 ka Cape Riva eruption

1999). Eruption of basaltic to andesitic lavas then built up a lava shield within this caldera (Skaros lava shield; 70–54 ka). The shield grew to over 350 m above present-day sea level, filling and partly overspilling the caldera (Druitt et al., 1999; Huijsmans, 1985; Huijsmans and Barton, 1989). The volume of the shield has been estimated at about 12 km^3 from reconstructions based on lavas exposed in the caldera cliffs (Druitt et al., 1999). Construction of the shield culminated 54 ky ago with an explosive eruption called Upper Scoria 2, which generated a rhyodacitic Plinian fall deposit overlain by voluminous andesitic scoria flows (Mellors and Sparks, 1991). Following Upper Scoria 2, about 2 km^3 of silicic lavas were extruded across the summit and western flank of Skaros to form the Therasia dome complex.

At ∼22 ka, a large silicic explosive eruption (the Cape Riva eruption) collapsed the Skaros-Therasia edifice (Druitt and Francaviglia, 1992). The eruption had an initial Plinian phase from a vent located somewhere in the northern part of the volcanic field. This was followed by the discharge of pyroclastic flows that laid down welded

ignimbrite, non-welded ignimbrite and lithic-rich lag deposits up to 25 m thick all over the islands (Druitt and Sparks, 1982). The volume of magma discharged during the Cape Riva eruption is poorly constrained, since most of the ignimbrite lies under the sea. However distal tephra from the eruption, recognised as the Y-2 marine ash bed, is found over a very wide area of the eastern Mediterranean and as far north as the Island of Lesvos and the Sea of Marmara (Asku et al., 2008; Federman and Carey, 1980; Keller et al., 1978; Margari et al., 2007; Thunell et al., 1979; Wulf et al., 2002). The dispersal area and thickness of the Y-2 ash are similar to those of the Z-2 ash from the Minoan eruption, suggesting that the Cape Riva and Minoan eruptions were of comparable magnitude (Asku et al., 2008; Narcisi and Vezzoli, 1999). Graphical integration of Y-2 ash thicknesses recorded by the above authors yields a minimum volume of $\sim$10 km^3. Since distal ashes commonly have comparable volumes to the parent ignimbrite (e.g. Pyle, 1990), we very approximately infer a volume of $>$20 km^3 for the Cape Riva products, equivalent to $>$10 km^3 of magma.

Remnants of the Skaros and Therasia lavas are widely exposed in the northern half of the present day complex. The Skaros lavas are thickest (up to 300 m) on Thera, and the Therasia lavas are thickest (up to 200 m) on Therasia. The products of the Therasia and Cape Riva eruptions are the focus of the present paper.

G.4 Methodology

Lavas of the Therasia dome complex cropping out in the caldera cliffs were photographed from a boat, and the photos were merged using computer software and interpreted to produce synthetic sections detailing the relationships and lateral extents of

individual lavas. Correlations were checked by onland observations, and stratigraphic relationships were mapped out. Pumice layers and palaeosols between the lavas were also mapped. Lavas from four key stratigraphic levels were dated using the 40Ar/39Ar technique. The groundmass of each sample was separated, hand-picked, and cleaned in an ultrasonic bath of dilute nitric acid prior to irradiation in the Cd-lined fast neutron slot β1 of the Osiris reactor (CEA, Saclay) with sanidine ACR (1.206 ± 0.002 Ma, Renne et al., 2011, 2010). Upon receipt from the nuclear reactor, the samples were analysed by multiple laser fusion using a high-sensitivity mm5400 mass spectrometer operated in pulse-counting mode following the experimental and correction procedures of Scaillet et al. (2011, 2008). More than 25 individual ages were extracted from each sample via a two-step fusion of ∼10 mg of groundmass replicates (see procedural details in Scaillet et al., 2011).

Representative samples of lava and pumice from the Therasia complex, and pumice and scoria from the Cape Riva deposits, were collected for chemical analysis. All samples were chosen to be as fresh and glassy as possible. Groundmass separates of selected lavas were obtained in order to analyse the compositions of the melt phases of the magmas. This was done using a magnetic separator, and interstitial glasses of pumice samples were concentrated by flotation in water. Remaining crystals were then removed by hand picking under an optical microscope. Major elements were analysed using inductively coupled plasma atomic emission spectroscopy (ICP AES) at the Laboratoire Magmas et Volcans, Université Blaise Pascal, Clermont-Ferrand. Measurements were calibrated using three standards: a blank (LiBO2), basalt (BR) and granite (GH). The DR-N and BHVO-2 standards were then passed as unknowns.

Trace elements were analysed using inductively coupled plasma mass spectroscopy (ICP MS) at the Institut des Sciences de la Terre, Université de Grenoble. The ICP MS analyses were calibrated using the BR standard, and the BVHO-2 and AGV-1 standards were passed as unknowns. Some previous Cape Riva samples of Druitt et al. (1999) were re-analysed for comparison with the data of those authors. These comparisons showed good agreement between the two datasets for the elements used in the present paper.

Phenocryst contents were calculated by mass balance from Zr concentrations in whole rock and groundmass analyses of individual samples, by assuming that the crystals contain no Zr. Zirconium behaves incompatibly in all magmas younger than 530 ka at Santorini (Druitt et al., 1999; Huijsmans, 1985), and zircon has never been observed as a mineral phase in those magmas. Proportions of the different phenocryst phases were estimated by image analysis of thin sections using the ImageJ software package (Rasband, 2012). Mineral compositions were analysed using the Cameca SX 100 electron microprobe at the Laboratoire Magmas et Volcans, Université Blaise Pascal, Clermont-Ferrand, using a beam current of 15 nA. Glasses were analysed with a beam current of 4 nA and a defocussed beam (10-15 µm) in order to limit Na loss. Fe–Ti oxide compositions were analysed either in touching pairs or in pairs (that would have been in contact with the same melt) adhering to the outside of the same pyroxene crystal. Magmatic temperatures and oxygen fugacities were calculated with the ILMAT software package (Lepage, 2003) using the formulation of Andersen and Lindsley (1985) and Stormer (1983). This formulation has been found to give good agreement with data from phase-equilibria experiments within the 850-950 °C temperature range (Blundy

and Cashman, 2008; Cottrell et al., 1999). Values we obtained using the formulation of Ghiorso and Evans (2008) are 10–20 °C and 0.2–0.4 fO_2 log units higher than those obtained using Andersen and Lindsley (1985), for the temperature range in question.

G.5 Results

G.5.1 Field and stratigraphic relationships

Photographs and sketches of the Therasia cliffs are shown in Figure G.3; schematic diagrams summarising the architecture of the lavas are shown in Figure G.4 (with individual lavas numbered for reference). Lavas of the Therasia dome complex overlie Upper Scoria 2, separated by a palaeosol. They make up much of the present-day cliffs of Therasia (flows 1–24), and one lava crops out at the top of the caldera wall north of Fira town (flow 25). Thin lava flows occupying the same stratigraphic position (between Upper Scoria and Cape Riva) occur beneath the town of Oia (flow 26; Andesite of Oia of Druitt et al., 1999).

The lava succession on Therasia consists of many individual lava flows, coulées and domes (termed flows for short). Individual flows range in thickness up to 60 m (Figure G.5a); thin flows tend to be dark grey and glassy, whereas thicker ones are pale grey and de-vitrified. Many exhibit flow banding that is most evident in the thicker, de-vitrified flows. The greatest accumulated thicknesses occur near Cape Tripiti (∼150 m) and Mount Viglos (∼200 m), where, at each location, nine flows are stacked. Correlations of individual flows between the Tripiti and Viglos sections is difficult, as only two flows (3 and 4) are continuous between them. Flows 1 and 24 are compositionally

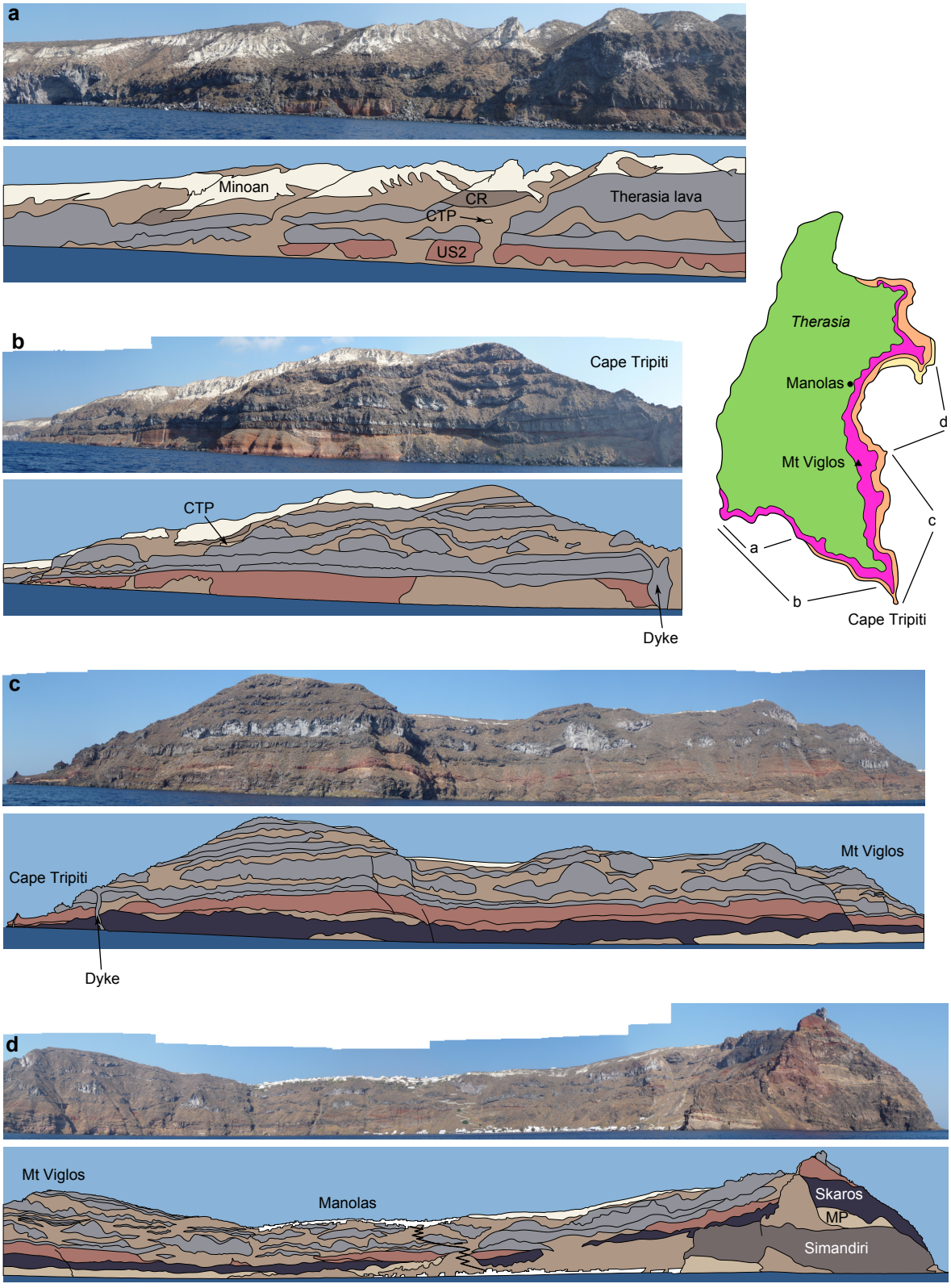

Figure G.3: Photos of the cliffs of Therasia, and the sketches drawn from them. Inset is a map of Therasia, showing where the photos of the cliffs were taken from. CR = Cape Riva, CTP = Cape Tripiti Pumice, US2 = Upper Scoria 2, MP = Middle Pumice

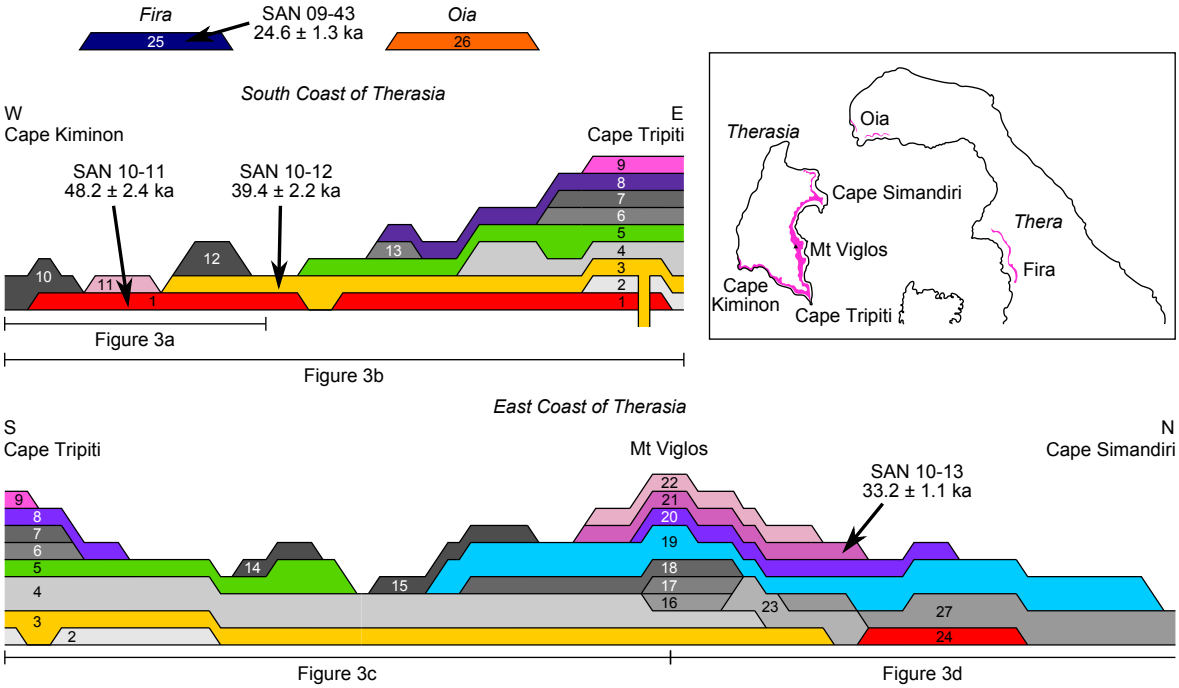

Figure G.4: Schematic representation of the different lava flows from the Therasia dome complex. Individual flow numbers are referred to in the text. Flows that were sampled and analysed are coloured, while unsampled flows are in grey. Where a correlation of two flows is made based on their chemistry, they are drawn in the same colour. Flows that have been $^{40}Ar/^{39}Ar$ dated are labelled with arrows; $^{40}Ar/^{39}Ar$ ages are weighted mean ages. The inset map has outcrops of the Therasia dome complex in pink

very similar, and are probably the same flow. This is also true of flows 11 and 22.

Most of the lava flows on Therasia are dacitic to rhyodacitic, with two exceptions. First, the basal flows 1 and 24 are andesitic, and we refer to them jointly as the lower Therasia andesite. Second, the topmost flow on Mount Viglos (flow 22) is also andesitic, and we refer to this (and the compositionally similar flow 11) as the upper Therasia andesite. Enclaves of quenched basaltic magma with crenulated margins occur in some of the lowest lavas (flows 1 and 3) and towards the top of the succession (flows 22 and 25); rare gabbroic enclaves also occur. The widespread distribution of the Therasia lavas show that they were fed from vents extending from the summit to the western flank of the Skaros shield (Figure G.2). The feeder dyke of flow 3 is preserved at Cape Tripiti (Figure G.3b,c). The dyke is oriented NE–SW, parallel to the main

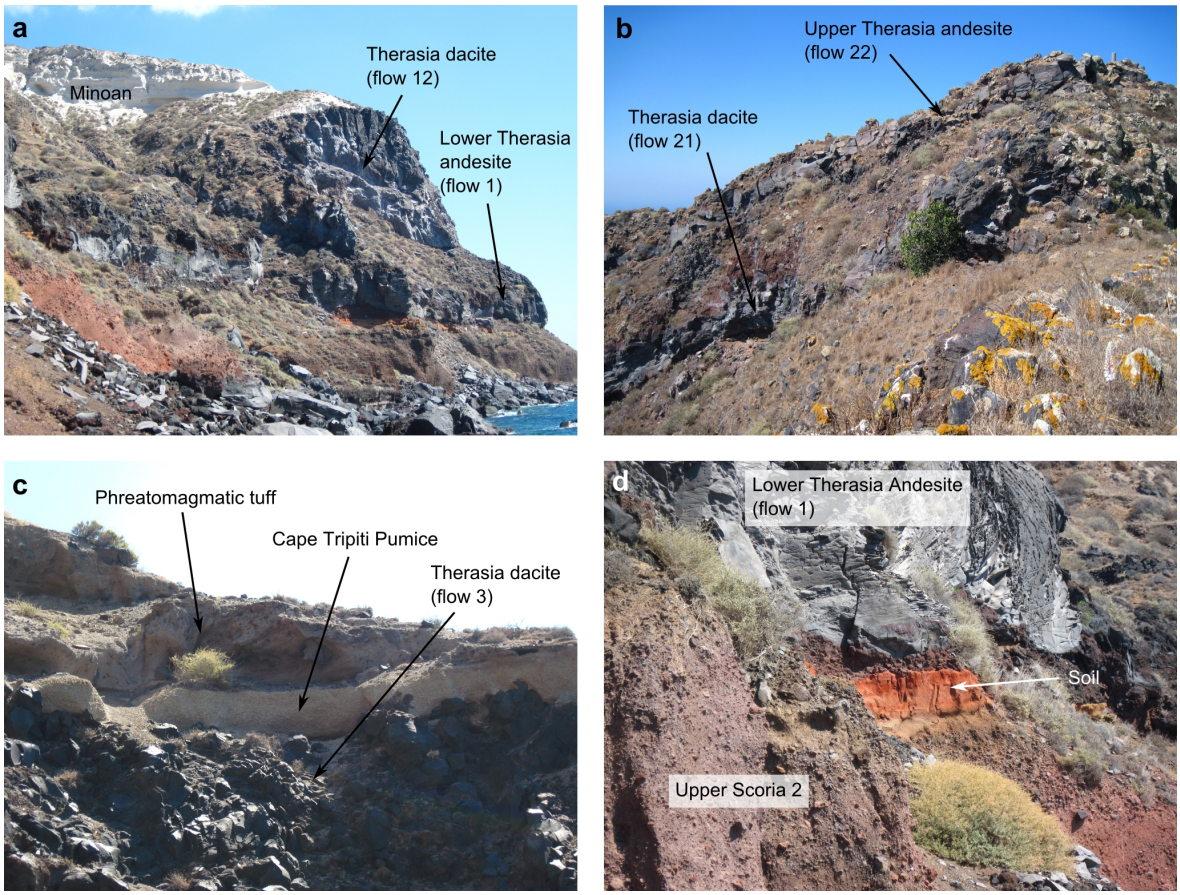

Figure G.5: Photos of the Therasia dome complex. (a) A thick dacitic dome above the lower Therasia andesite (b) The upper Therasia andesite on top of Mt Viglos (c) The Cape Tripiti pumice fall and an overlying phreatomagmatic tuff above lava flow 3 on the south coast of Therasia (d) The thick, orange soil between Upper Scoria 2 and the lower Therasia andesite

dyke trend in northern Thera and the alignment of the recent vents on the Kameni Islands (Druitt et al., 1999; Heiken and McCoy, 1984).

At least four dacitic pumice fall units and a phreatomagmatic tuff occur intercalated within the Therasia succession (Figure G.5c). The pyroclastic units are concentrated towards the top of the succession (younger than flow 7 at Tripti, and younger than flow 20 at Viglos), showing an increasing tendency for explosive activity with time during eruption of the Therasia dome complex. A single pumice fall deposit crops out between flows 24 and 27 below Manolas. The most prominent fall deposit is up

to a metre thick and widespread in the cliffs of southern Therasia (Figure G.5c). It occurs stratigraphically between lava flows 7 and 8, and is the product of a Plinian not recognized in previous studies. We name this unit the Cape Tripiti pumice fall deposit.

Palaeosols occur at several levels in the Therasia succession. A thick one separates the entire Therasia succession from Upper Scoria 2 (Figure G.5d). Another separates the lower Therasia andesite from overlying dacitic flows, showing that eruption of the lower Therasia andesite was both preceded, and followed, by significant time breaks. Local palaeosols also occur between some of the pyroclastic layers.

The andesite of Oia is both underlain and overlain by thick palaeosols. Long periods therefore separated its eruption from both the preceding Upper Scoria 2 eruption and the subsequent Cape Riva eruption. Four thin pumice fall layers (5–25 cm thick) occur within the palaeosol overlying the lava (sequence M11 of Vespa et al., 2006); they may correlate with the pumice layers intercalated within the lavas on Therasia, but this has not been checked chemically.

Products of the Cape Riva eruption are observed to overlie all lavas of the Therasia dome complex. They have been described in detail by (Druitt and Sparks, 1982), (Druitt, 1985), and (Druitt et al., 1999). The products of the eruption are predominantly dacitic, but minor amounts of andesitic scoria were erupted during the initial Plinian phase.

Table G.1: New $^{40}Ar/^{39}Ar$ ages for the Therasia dacites

Sample	Unit	Gauss-plot age (ka)	Weighted mean age (ka)
SAN 09-43	Flow 25	25.3 ± 1.4	24.6 ± 1.3
SAN 10-13	Flow 21	33.1 ± 1.1	33.2 ± 1.1
SAN 10-12	Flow 3	40.1 ± 2.2	39.4 ± 2.2
SAN 10-11	Flow 1	49.4 ± 2.5	48.2 ± 2.4

G.5.2 Age constraints

Radiometric dating of the Therasia lavas

The ages of flows 1, 3, 21 and 25 are reported as probability density plots in Figure G.6, along with the corresponding Gauss plots that reflect the statistical distribution of individual ages for each sample. Complete 40Ar/39Ar analytical data are reported in Supplementary Table S1 and are summarized in Table G.1, along with 2σ errors. All four samples exhibit relatively well behaved 40Ar/39Ar systematics in the form of unimodal density plots, with no (or only slightly) pronounced tails on either side of the mode. The homogeneity of the samples is reflected by the linear arrays formed by individual ages on the Gauss plots, indicating that they follow the distribution expected from the propagated Gaussian experimental errors. One exception is flow 3, which exhibits an age spread in excess of the variance expected from the analytical errors (i.e. excess-error scatter). This sample is, along with flow 1, the least glassy of the four, and both are characterized by slightly higher errors and some excess-error scatter. This suggests that flows 1 and 3 may have been affected by post-cooling alteration close to sea level near the base of the sequence, resulting in higher apparent ages (presumably due to K loss). In contrast, flows 21 and 25 are very glassy and pristine, with unusually tight error bars; especially flow 21.

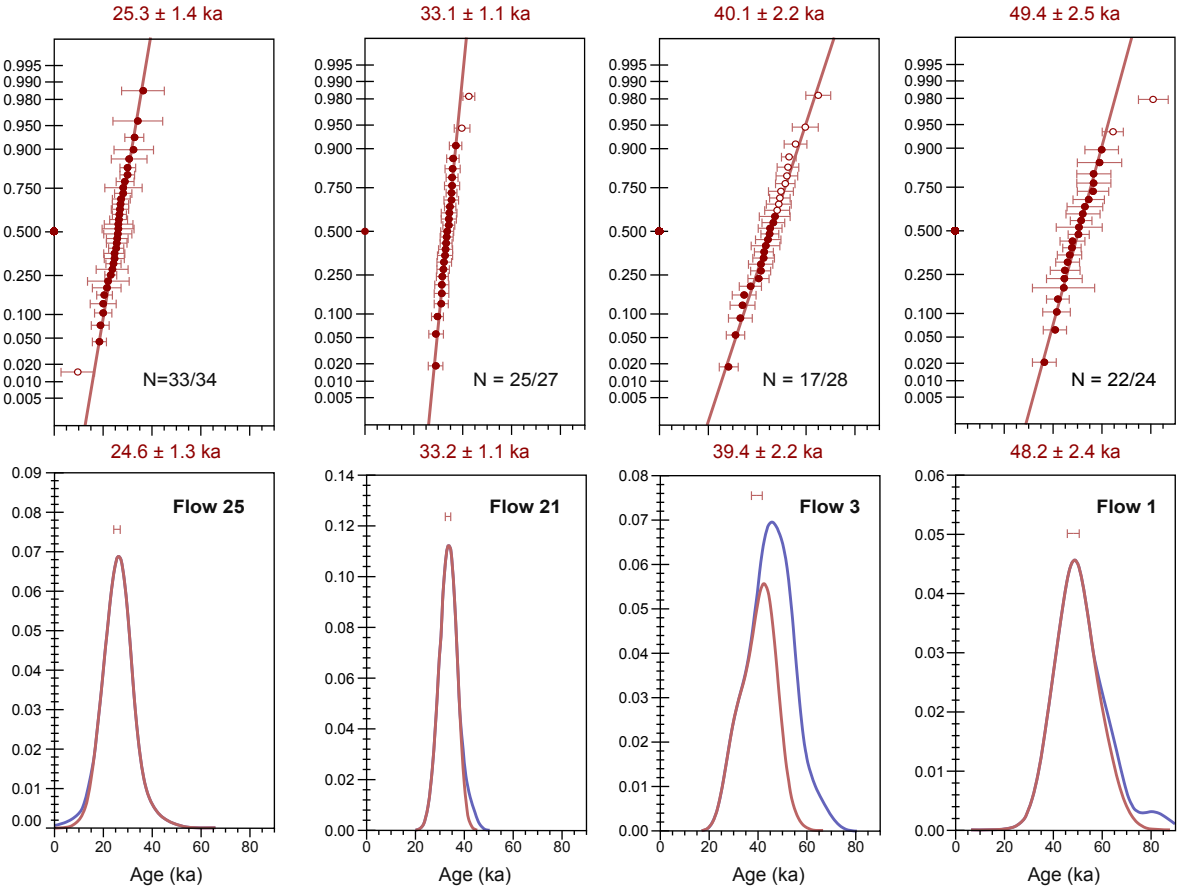

Figure G.6: Probability density plots (below) and Gauss plots (above) of $^{40}Ar/^{39}Ar$ data obtained on four lava flows dated in the Therasia sequence. Ages reported above each plot are $\pm 2\sigma$ and represent inverse variance weighted mean ages (density plots) or best-fit apparent ages through the linear array (Gauss-plot). Empty symbols on Gauss-plots: data excluded from the fit. Red curve on density plots: density distribution with outlier removed; blue curve: density distribution of complete dataset. N: number of data points included in the fit over total number of runs for each sample.

To account for secondary alteration effects, the data from flows 1 and 3 were statistically screened by computing a weighted mean age using a MSWD cut-off value. This includes only the youngest sub-population conforming to a Gaussian distribution within each sample (see procedure in Gansecki et al., 1996; Scaillet et al., 2011). In every instance, the weighted mean age agrees with the age derived from the best-fit line through the corresponding Gauss-plot array (Figure G.6). In what follows we cite the weighted mean ages.

The ages all are consistent with observed field stratigraphic constraints, as sum-

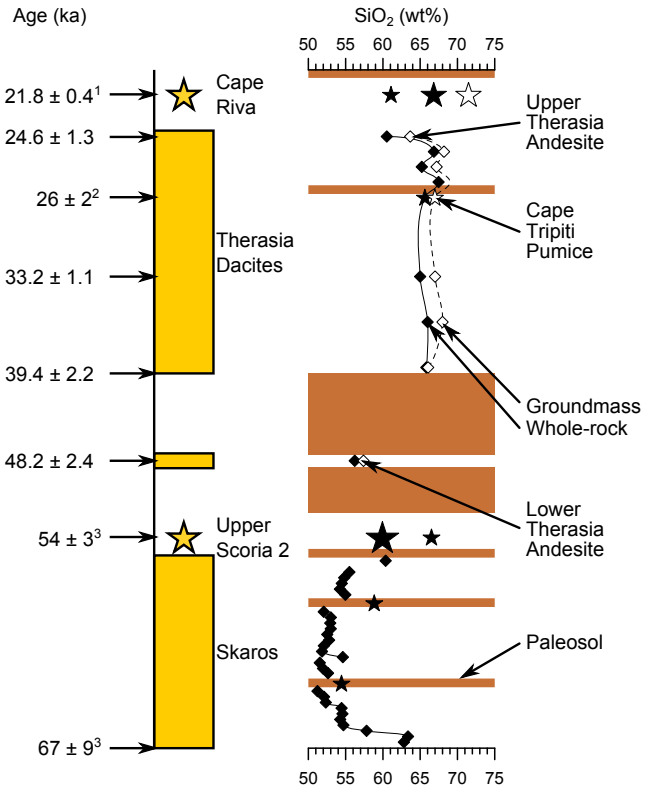

Figure G.7: Summary of magma compositions and ages between 70 and 20 ka. Major explosive eruptions are represented by stars, with periods of edifice construction coloured in yellow. Periods of little or no preserved eruptive activity are left blank. The SiO_2 content of the eruptive products is shown on the right. Black symbols are whole rock compositions, and white symbols are groundmass composition. Skaros data is taken from Huijsmans (1985) [1] Data and citations in Table G.2, [2] date taken from Schwarz (2000) [3] date taken from Druitt et al. (1999)

marized in Figure G.7. The age of the basal flow (flow 1; 48.2 ± 2.4 ka) is consistent with the presence of a palaeosol separating it from the underlying Upper Scoria 2 (previously dated by 40Ar/39Ar at 54 ± 3 ka by Druitt et al. (1999), and with another palaeosol separating it from the overlying flow 3 (39.4 ± 2.2 ka). Flow 21 yields an age of 33.2 ± 1.1 ka, and flow 25 (at Fira) gives an age of 24.6 ± 1.3 ka. Taken as a whole, our 40Ar/39Ar data between the base (48.2 ka) and the top (24.6 ka) of the lava sequence define a ~24 ky duration for the construction of the Therasia dome complex.

Correlation of the Cape Tripiti Pumice with the Y-4 deep-sea ash layer

The Cape Tripiti pumice is the most prominent pyroclastic layer in the Therasia sequence, and we have explored the possibility that, like most Plinian eruptions of Santorini, (Asku et al., 2008; Federman and Carey, 1980; Keller et al., 1978; Schwarz, 2000; Vinci, 1985; Wulf et al., 2002), the Cape Tripiti eruption left a recognisable ash layer in deep-sea sediments of the Aegean area. Previous studies have recognized a 2–7 cm-thick ash layer (Y-4 ash) preserved to the SE of Santorini; this ash lies stratigraphically beneath the Cape Riva Y-2 ash layer, and has an age of 25.8 ka estimated by interpolation in the sedimentary sequence of one core (Schwarz, 2000). The uncertainty on this age could be ±2 ka (J Keller, pers. comm). The mineralogy of the Y-4 ash (plag, opx, cpx) pinpoints its source to Santorini (Vinci, 1985). Schwarz (2000) explored the possibility that the Y-4 correlates with the rhyodacitic Plinian phase of Upper Scoria 2; however, the 40Ar/39Ar age data described above rule out this correlation, and show that the Y-4 lies chronologically in the period of the Therasia dome complex. We have analysed the interstitial glass of three pumice lumps from the Cape Tripiti deposit, and find excellent agreement with glass composition of the Y-4 (Figure G.8, Supplementary Table S2). A 26 ka age for the Cape Tripiti is consistent with all other age constraints (Figure G.7).

Synthesis of published dates for the Cape Riva eruption

The Cape Riva eruption has been dated previously by radiocarbon on charcoal from beneath the ignimbrite and via $\delta^{18}O$ wiggle matching in deep-sea sequences hosting the distal equivalent Y-2 tephra layer (data and sources in Table G.2). Calibration of

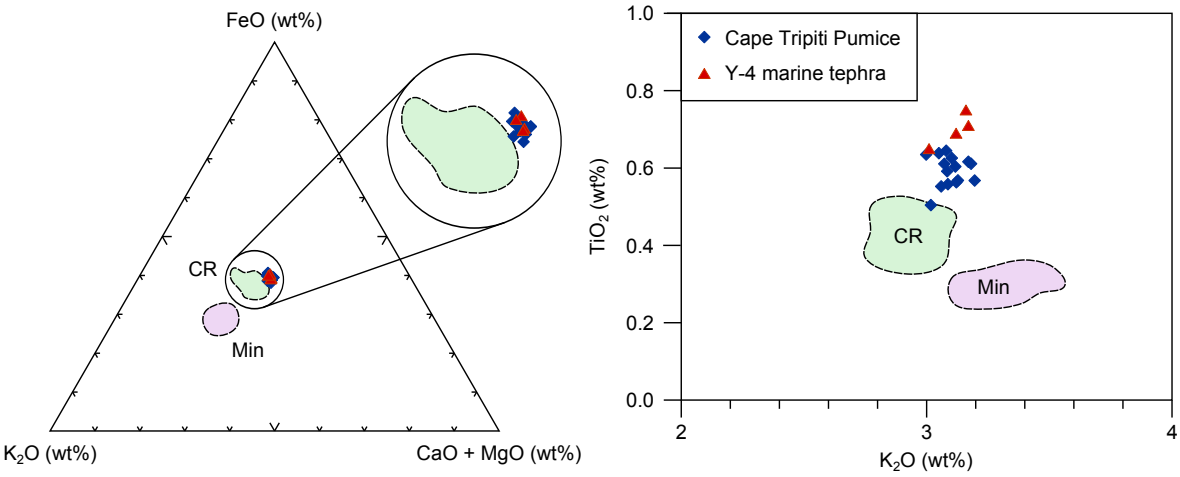

Figure G.8: Chemical discrimination plots for the Cape Tripiti pumice and Y-4 ash layer, after Wulf et al. (2002). The Y-4 data is taken from Vinci (1985) and Schwarz (2000)

the raw radiocarbon data against the curve of Fairbanks et al. (2005) returns a mean age of 21.8 ± 0.4 ka for Cape Riva (Table G.2). This yields an interval of $2{,}800 \pm 1{,}400$ (2σ) y between the youngest dated Therasia lava (flow 25) and the Cape Riva eruption. This is a maximum estimate for the interval separating the Cape Riva eruption from the Therasia lavas, since some of the undated flows on Therasia may be younger than flow 25, or a younger flow could have been erupted and not preserved.

G.5.3 Mineral chemistry and assemblages

In this section we present the petrology and chemistry of Therasia lavas and pumices younger than ~39 ka (i.e. flow 3), as well as the products of the Cape Riva eruption (Fig. 9). We exclude the lower Therasia andesite, which is significantly older, as well as the andesite of Oia. In so doing we focus on the effusive leaks of dacite during the build-up to the Cape Riva eruption.

Table G.2: Published ages for the Cape Riva eruption. The average of these ages is 21.8 ± 0.4 ka (2σ)

Uncalibrated ^{14}C age (ka)[a]	Calibrated age (ka)	Method	Sample dated	Reference
18.05 ± 0.34	21.46 ± 0.49[b]	^{14}C	Charred trees from ignimbrite	Pichler and Friedrich (1976)
18.17 ± 0.21	21.63 ± 0.33[b]			
18.05 ± 0.34	22.47 ± 0.24[b]			
18.15 ± 0.20	21.60 ± 0.32[b]	^{14}C	Charcoal from ignimbrite	Eriksen et al. (1990)
17.38 ± 0.23	20.53 ± 0.26[b]	^{14}C	Peat below Y-2 tephra, Philippi basin, Greece	St Seymour et al. (2004)
18.53 ± 0.15	21.75 ± 0.24[b]			
18.24 ± 0.14	22.14 ± 0.17[b]			
–	21.62	Interpolation between sapropels dated using ^{14}C		Asku et al. (2008)
–	19[c]	Interpolation between isotopic stages dated by ^{231}Pa/^{230}Th		Thunell et al. (1979)

[a] Published uncalibrated ^{14}C age
[b] Calibrated using the curve of Fairbanks et al. (2005)
[c] Not included in the average

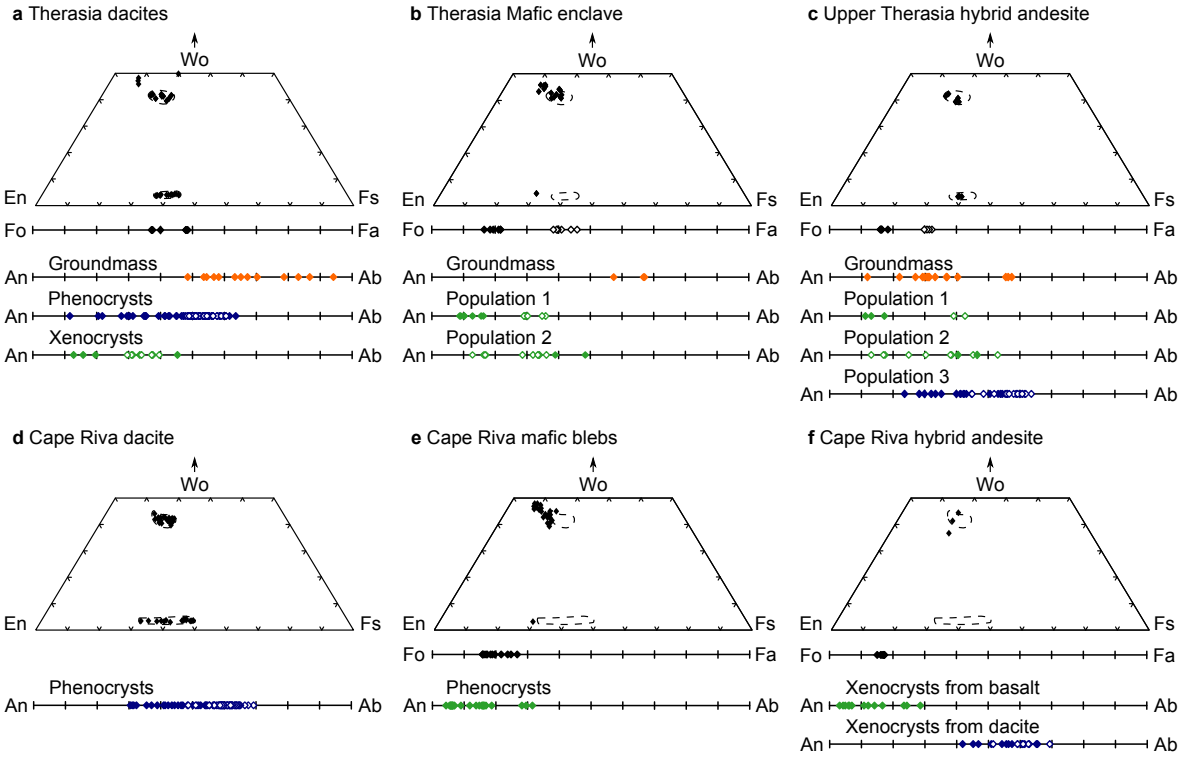

Figure G.9: Mineral compositions from the different rock units. Filled symbols are crystal cores or undifferentiated measurements, open symbols are crystal rims. Plagioclase populations are coloured according to their origin: orange symbols are groundmass crystals, blue symbols are populations that originated in a silicic magma and green symbols are populations that originated in a mafic magma. Some Cape Riva data taken from Druitt (1983). The fields of pyroxene compositions in the dacites (a, d) are shown on the other figures, for comparison.

Therasia products

Therasia dacites. The Therasia dacites have whole rock SiO_2 contents of 64.6–68.7 wt% and MgO contents of 0.7–1.5 wt%, with groundmass (i.e. melt) SiO_2 contents of 64.7-69.1 wt%. No systematic evolution of either whole rock or groundmass composition is observed with height in the lava succession (Figure G.7). The dacites contain 1-17 wt% of phenocrysts (with a smallest dimension >0.5 mm) of plagioclase (75-85 vol%), 2 pyroxenes (10-20 %, with opx > cpx), Fe–Ti oxides (5–8 %) and trace amounts of olivine. Apatite occurs as inclusions in orthopyroxene crystals. The glassy groundmass contains microlites of feldspar and Fe–Ti oxides. Plagioclase phenocrysts

are normally zoned, with cores of An_{38-89} and rims of An_{39-51}, and commonly contain multiple internal dissolution surfaces and sawtooth zoning. The rims are euhedral, and are compositionally similar to plagioclase microlites in the groundmass (An_{30-51}). Orthopyroxene phenocrysts are euhedral and unzoned, and have compositions of $Wo_{3-4}En_{54-60}Fs_{36-42}$. Clinopyroxenes are also euhedral and unzoned, and their compositions are $Wo_{39-42}En_{36-43}Fs_{15-22}$. Some phenocrysts occur as aggregates of multiple euhedral crystals with brown interstitial glass. Xenocrysts of calcic plagioclase (An_{60-89}) occur frequently in the dacites, along with more calcic clinopyroxenes ($Wo_{47-50}En_{30-44}Fs_{8-20}$). There are also fragments of sub-solidus olivine-bearing gabbro, with some olivines that have broken down to form pyroxene-magnetite symplectites. Fe–Ti oxides from three different dacitic pumice fall deposits within the Therasia sequence record magmatic temperatures of $875 \pm 5\,^{\circ}C$ at an fO_2 of 13.4 ± 0.1, $896 \pm 12\,^{\circ}C$ at an fO_2 of 12.7 ± 0.3, and $926 \pm 9\,^{\circ}C$ at an fO_2 of 11.4 ± 0.2 (2σ, where σ is the standard error of the mean, Supplementary Table S3).

The similarity between phenocryst rims and groundmass microlite compositions suggests an equilibrium phenocryst rim assemblage in these lavas. Sawtooth zoning of plagioclase is interpreted as recording repeated recharge of the magmas by hotter magma during phenocryst growth. Glass-bearing phenocryst clusters were probably derived from crystal mush of the reservoir margins.

Therasia mafic enclaves. Quenched basaltic (49.6–51.8 wt% SiO_2; 5.4–8.6 wt% MgO) enclaves 1–10 cm in diameter are found in flows 3 and 11, where they make up <1% of the erupted volume. They contain phenocrysts of plagioclase (∼55 vol%), pyroxenes (∼35 vol%, with cpx ≫ opx) and olivine (∼10 vol%) set in a glassy, diktytax-

itic groundmass. Two populations of plagioclase phenocrysts with different core compositions, but similar rim compositions, are observed: (1) normally zoned crystals with cores of An_{83-91} and rims of An_{64-71}; (2) reversely zoned crystals with cores of An_{51-61}, separated by a sieve-textured zone from rims normally zoned from An_{82-86} to An_{64-71}. Plagioclase in the groundmass is An_{32-42}. Olivines are normally zoned from cores of Fo_{77-82} to rims of Fo_{53-60}. Two clinopyroxene populations are found, although their textural relationships with the plagioclase populations are ambiguous. Both cpx populations are euhedral and unzoned, with compositions of (1) $Wo_{43-46}En_{42-46}Fs_{10-12}$ and (2) $Wo_{41-44}En_{39-43}Fs_{15-20}$. Rare orthopyroxenes with compositions of $Wo_3En_{67}Fs_{30}$ also occur.

The occurrence of two plagioclase populations with different core compositions, but similar, intermediate rim compositions is indicative of magma mixing. Plagioclases of population 1 are interpreted as derived from a basaltic melt, and those of population 2 from a more evolved melt. The cores of olivine crystals (molar Mg/Fe = 3.37–4.64) are in equilibrium with the whole rock (i.e. basaltic) composition (Mg/Fe = 1.20), assuming a crystal-melt partition coefficient of between 0.26 and 0.36 (Roeder and Emslie, 1970). The composition of population-2 clinopyroxenes is similar to that of the clinopyroxene phenocrysts in the dacite. The enclaves are interpreted as having formed by the inmixing of a small proportion of more evolved magma (possibly dacitic, containing population-2 plagioclase cores + population-2 cpx) into a basalt (containing population-1 plagioclase cores + olivine + population-1 cpx; Figure G.10). Mixing occurred long enough prior to eruption for plagioclase from the evolved component to partially melt (generating sieve texture), followed by overgrowth of equilibrium rim

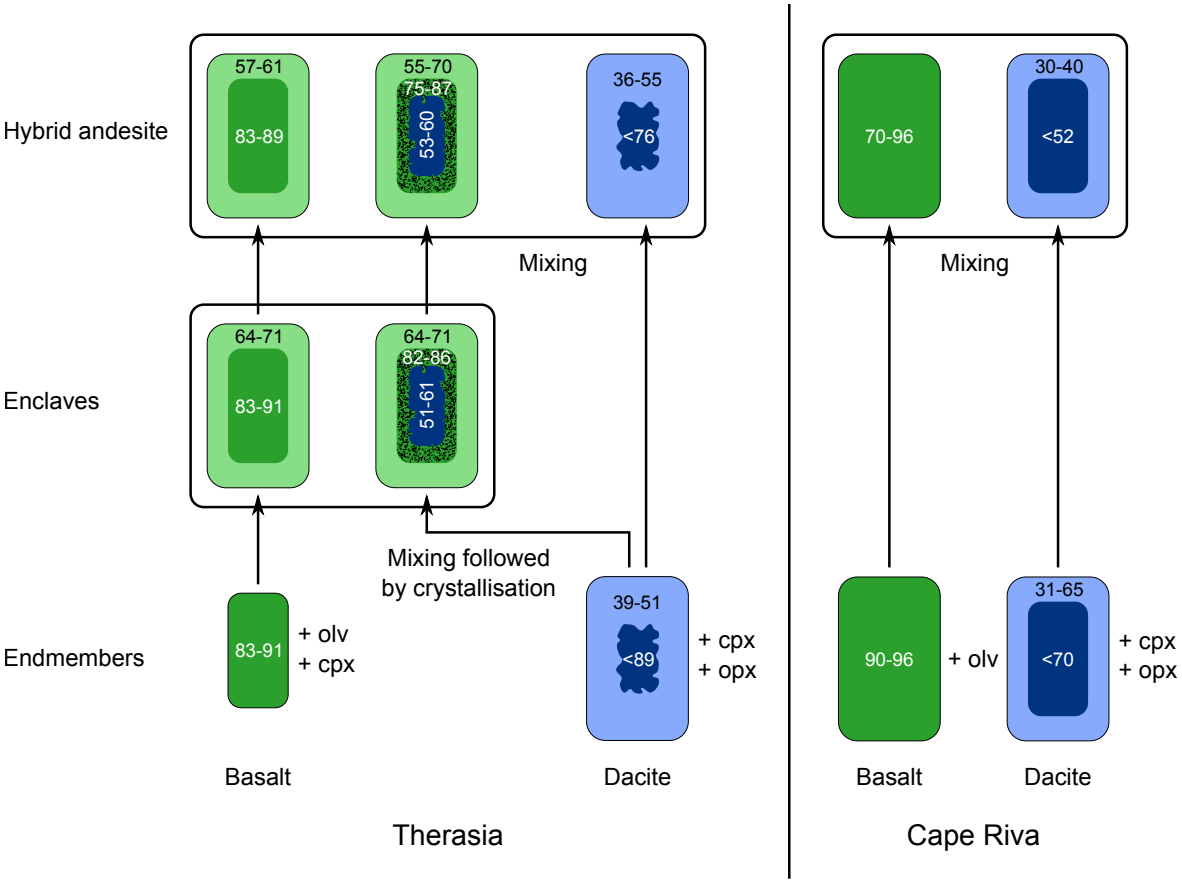

Figure G.10: Summary of plagioclase populations in the Cape Riva and Therasia rocks. The numbers are values of molar % anorthite content of plagioclase

compositions on plagioclases from both populations.

Upper Therasia andesite. The upper Therasia andesite (60.5 wt% SiO_2, 2.6 wt% MgO) contains 26 wt% of macroscopic crystals: plagioclase (75 vol%), pyroxenes (20 %, with opx ≈ cpx), Fe–Ti oxides (5 %) and trace amounts of olivine set in a glassy, 64 wt% SiO_2 groundmass containing microlites of plagioclase and magnetite. Three distinct populations of plagioclase are observed: (1) normally zoned crystals with cores of An_{83-89}, and euhedral rims of An_{57-61}; (2) crystals with cores of An_{53-60} separated by a sieve-textured zone from rims normally zoned from An_{75-87} to An_{55-70}; (3) normally zoned crystals with cores as calcic as An_{76} and rims of An_{36-55}. Rare olivines have cores of Fo_{80-83}, and rims of Fo_{67-69}. Orthopyroxenes have compositions of

$Wo_3En_{57-59}Fs_{38-39}$, and clinopyroxenes have compositions of $Wo_{39-42}En_{40-43}Fs_{15-20}$.

Plagioclase populations 1 and 2 texturally and compositionally resemble plagioclase populations 1 and 2 (respectively) in the basaltic enclaves; population 3 resembles plagioclase phenocrysts in the dacites. The olivine rims have a molar Mg/Fe ratio of 1.99–2.22, which is in, or close to, equilibrium with the groundmass (Mg/Fe = 0.76), assuming a partition coefficient of between 0.26 and 0.36 (Roeder and Emslie, 1970); the cores have an Mg/Fe ratio of 4.11–4.81 and grew in equilibrium with a basaltic melt. The two pyroxenes are indistinguishable from the same phases in the dacites. The upper Therasia andesite is interpreted as a hybrid magma formed by the mixing of the basalt (containing plagioclase of populations 1 and 2 + olivine) represented by the enclaves, with typical Therasia dacite (containing population-3 plagioclase + opx + cpx). Mixing occurred long enough prior to eruption to permit physical homogenization of the resulting hybrid melt, but not long enough for crystals to grow rims in equilibrium with that melt, or for those from the dacite to be resorbed.

Cape Riva products

Cape Riva Dacite. Dacitic pumices of the Cape Riva eruption have whole rock compositions of 64–67 wt% SiO_2 and 1.0–1.9 wt% MgO, and interstitial glasses with 70–72 wt% SiO_2. Phenocryst phases and proportions are the same as in the Therasia dacites, with total contents ranging from 15 to 20 wt%. Plagioclase phenocrysts are euhedral, with rims of An_{31-65}, and cores as calcic as An_{70}. As in the Therasia dacites, plagioclase phenocrysts in the Cape Riva dacite contain complex dissolution surfaces and saw tooth zoning. Rare xenocrysts of $An70-96$ also occur. Orthopyroxene phenocrysts have compositions of $Wo_3En_{52-68}Fs_{45-29}$, and clinopyroxenes from $Wo_{44}En_{41}Fs_{15}$

to $Wo_{40}En_{36}Fs_{24}$. Touching Fe–Ti oxide pairs give temperatures of 879 ± 15 °C and fO_2 of -12.9 ± 0.4 (Cadoux et al., 2013).

Cape Riva mafic enclaves. Millimetre-sized quenched blebs of basaltic magma occur dispersed ($\ll$1 %) through the Cape Riva dacite, and in banded pumices containing the dacite and andesite mingled together. They contain An_{90-96} plagioclase, Fo_{72-84} olivine, $Wo_{41-44}En_{36-41}Fs_{15-23}$ cpx and rare $Wo_3En_{68}Fs_{29}$ opx. The enclaves have microcrenulated surface textures, and many have a single crystal or xenocrystic fragment at their centres. They are interpreted as small fragments of chilled basaltic magma.

Cape Riva andesite. The Cape Riva andesitic scoria has 60–62 wt% SiO_2 and 3.2–2.5 wt% MgO; it contains ~12 wt% macroscopic crystals of plagioclase, olivine, clinopyroxene and magnetite set in brown dacitic glass with 63.5 wt% SiO_2. The pure andesitic component (free of any in-mingled streaks of dacite) contains two populations of plagioclase: (1) a calcic population of An_{70-96}, with a discrete population of euhedral, unzoned grains of An_{90-96}, and (2) a less abundant population with cores up to An_{52} and rims of An_{30-40}. Olivines are compositionally uniform (Fo_{84}). Augites occur sparsely as microphenocrysts of $Wo_{40-41}En_{41-43}Fs_{19}$. No orthopyroxene has been observed.

The olivines and population-1 plagioclases in the andesite resemble phenocrysts present in the basaltic enclaves, whereas population-2 plagioclase resembles phenocrysts in the dacites. Genesis of the Cape Riva andesite is inferred to have involved the mixing of basaltic and dacitic magmas. Eruption occurred long after mixing for the hybrid glass to become homogeneous at the scale of the electron beam (~10 µm).

G.5.4 Whole rock chemistry and mixing systematics

Representative samples of each unit are shown in Table G.3, and the complete dataset is presented in Supplementary Table S4. We have used a series of variation diagrams showing the whole rock compositions of the Therasia and Cape Riva magmas, plus those of the lavas of the Skaros shield (from Huijsmans, 1985) to gain insight into the petrogenesis of the different magmas (Figs 11 and 12). Typical fractionation trends for Santorini magmas are also shown (Druitt et al., 1999; Huijsmans, 1985; Mann, 1983).

Figure G.11 shows the variations of five key major oxides (CaO, MgO, FeO, TiO_2, P_2O_5) and two strongly compatible trace elements (Cr and Ni). On the plots of CaO and MgO (also Na_2O, Al_2O_3, V and Sc) on which typical fractionation trends are weakly curved, all the Therasia and Cape Riva magmas fall on, or close to, the fractionation trend. However, on the plots of FeO, TiO_2, P_2O_5, Cr and Ni, on which the fractionation trends are strongly curved, the Cape Riva hybrid andesite falls systematically off the fractionation trend. This is what we would expect to see if it was generated by the mixing of mafic and silicic end-members. The upper Therasia hybrid andesite also falls off the fractionation trend on plots of FeO and TiO_2, (it does not on the other plots because mixing occurred along the fractionation trend, not across it).

Mixing models using the 'PetroGraph' software (Petrelli et al., 2005) successfully reproduce the compositions of the upper Therasia and Cape Riva hybrid andesites (Table G.5). In the case of the upper Therasia andesite, low Cr and Ni require the mafic end-member to also have low Cr and Ni. The relatively high P_2O_5, close to the fractionation trend, requires the silicic end-member to have a high P_2O_5 content, limiting it to a silica content of 64–67 wt%. The upper Therasia andesite can be

Table G.3: Representative whole rock and groundmass analyses of the Therasia and Cape Riva products

	Therasia mafic enclave	Upper Therasia andesite	Therasia dacite	Cape Riva andesite	Cape Riva dacite
Sample	GS10-43	GS10-22	GS10-17	S09-41	S09-40
Unit	Flow 22	Flow 22	Flow 5	Cape Riva A	Cape Riva A
Major elements (ICP-AES, wt% dry)					
SiO_2	51.87	60.26	66.00	60.19	65.84
Al_2O_3	19.07	17.16	15.38	16.43	15.40
TiO_2	0.89	0.86	0.75	0.88	0.76
FeO_T[1]	8.08	6.05	4.66	6.58	4.88
MgO	5.44	2.66	1.08	3.17	1.16
CaO	10.16	5.98	3.15	6.20	3.28
Na_2O	3.30	4.52	5.48	4.63	5.84
K_2O	0.90	2.18	3.19	1.56	2.45
MnO	0.16	0.14	0.13	0.16	0.16
P_2O_5	0.14	0.19	0.18	0.19	0.22
Trace elements (ICP-MS, ppm)					
Li	16.2	18.1	25.5	16.4	17.4
Sc	25.9	17.4	13.9	23.4	13.8
V	193.0	109.0	30.1	139.0	30.2
Cr	31.30	9.52	1.17	27.10	0.60
Ni	15.80	5.65	0.86	14.20	2.57
Rb	25.8	68.1	104.0	50.0	71.7
Sr	323	231	133	185	127
Y	23.8	37.9	50.8	38.5	45.9
Zr	108	200	321	175	250
Nb	4.71	9.47	12.90	7.12	9.44
Ba	251	391	513	297	375
La	11.9	23.5	32.2	19.0	23.7
Ce	26.9	49.5	66.5	40.7	50.5
Pr	3.37	5.93	7.70	4.98	6.09
Nd	14.2	23.4	30.1	20.4	24.6
Sm	3.43	5.40	6.91	5.14	5.77
Eu	0.97	1.29	1.43	1.29	1.34
Gd	3.67	5.57	7.14	5.56	6.44
Tb	0.62	0.92	1.20	0.95	1.07
Dy	3.92	5.96	7.94	6.16	7.06
Ho	0.84	1.27	1.68	1.33	1.54
Er	2.53	3.89	5.20	4.11	4.77
Yb	2.42	3.94	5.30	4.08	4.92
Lu	0.37	0.59	0.81	0.62	0.75
Hf	2.78	5.27	7.51	4.69	6.22
Ta	0.29	0.63	0.92	0.50	0.64

[1] FeO_T is the total FeO and Fe_2O_3 content calculated as FeO

Table G.4 continued: Representative whole rock and groundmass analyses of the Therasia and Cape Riva products

	Upper Therasia andesite	Therasia dacite	Cape Riva andesite	Cape Riva dacite
Sample	GS10-22	GS10-17	S09-41	S09-40
Unit	Flow 22	Flow 5	Cape Riva A	Cape Riva A
Major elements (ICP-AES, wt% dry)				
SiO_2	63.67	67.99	61.53	69.88
Al_2O_3	15.44	14.70	16.98	15.05
TiO_2	0.79	0.63	0.74	0.48
FeO_T[1]	5.60	4.03	5.96	3.31
MgO	2.39	0.85	2.62	0.53
CaO	4.62	2.34	5.86	2.14
Na_2O	4.55	5.91	4.92	5.86
K_2O	2.60	3.25	1.82	2.95
MnO	0.14	0.12	0.15	0.12
P_2O_5	0.20	0.19	0.17	0.16
Trace elements (ICP-MS, ppm)				
Li	20.3	26.9	17.7	20.4
Sc	18.5	14.2	24.6	14.8
V	80.8	14.5	126.0	8.3
Cr	8.41	0.76	21.20	4.33
Ni	4.62	0.75	14.60	5.48
Rb	89.0	105.0	60.2	101.0
Sr	176	108	197	105
Y	44.9	53.6	44.2	61.1
Zr	271	334	214	341
Nb	11.40	13.30	7.58	11.60
Ba	455	542	323	460
La	27.9	33.9	20.5	28.9
Ce	63.2	70.2	43.6	61.6
Pr	7.07	8.22	5.41	7.40
Nd	27.9	31.9	21.6	29.5
Sm	6.31	7.16	5.28	7.09
Eu	1.20	1.33	1.27	1.28
Gd	6.40	7.35	5.68	7.50
Tb	1.09	1.27	0.97	1.29
Dy	7.12	8.43	6.58	8.58
Ho	1.51	1.80	1.41	1.87
Er	4.64	5.53	4.32	5.81
Yb	4.69	5.74	4.37	6.09
Lu	0.72	0.87	0.66	0.94
Hf	6.73	8.38	5.14	8.07
Ta	0.81	0.98	0.52	0.82

[1] FeO_T is the total FeO and Fe_2O_3 content calculated as FeO

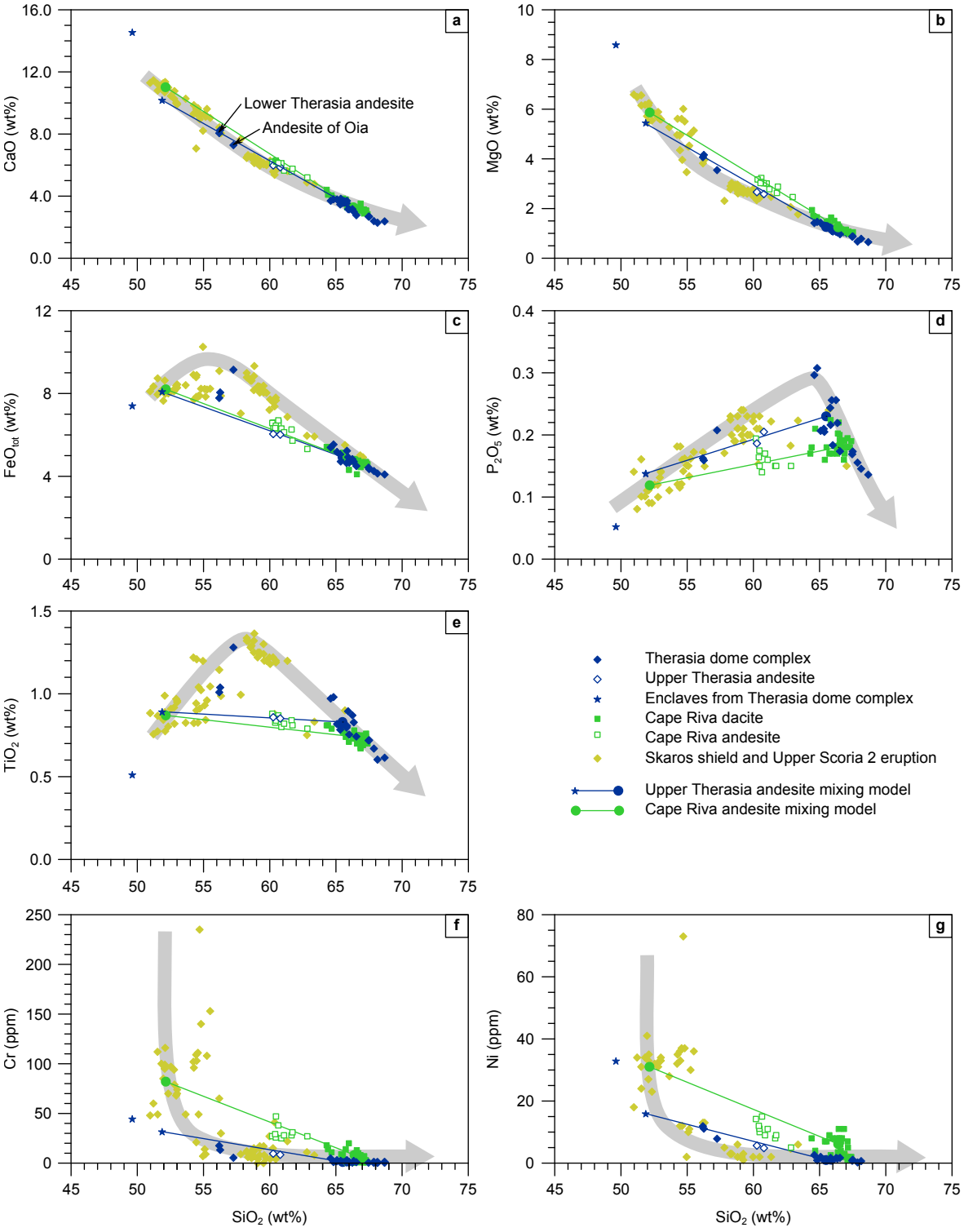

Figure G.11: Variation diagrams of major elements and selected highly compatible trace elements. Mixing models for the upper Therasia andesite and the Cape Riva andesite are shown as blue and green lines, respectively. The mixing calculations are presented in Table G.5. The typical fractionation trend for Santorini magmas discussed by Nicholls (1971), Mann (1983) and Druitt et al. (1999) is shown on the diagrams as a grey arrow. Composition of the Skaros lavas are also plotted for reference (Huijsmans, 1985), as are scoria from the Upper Scoria 2 eruption (Druitt et al., 1999)

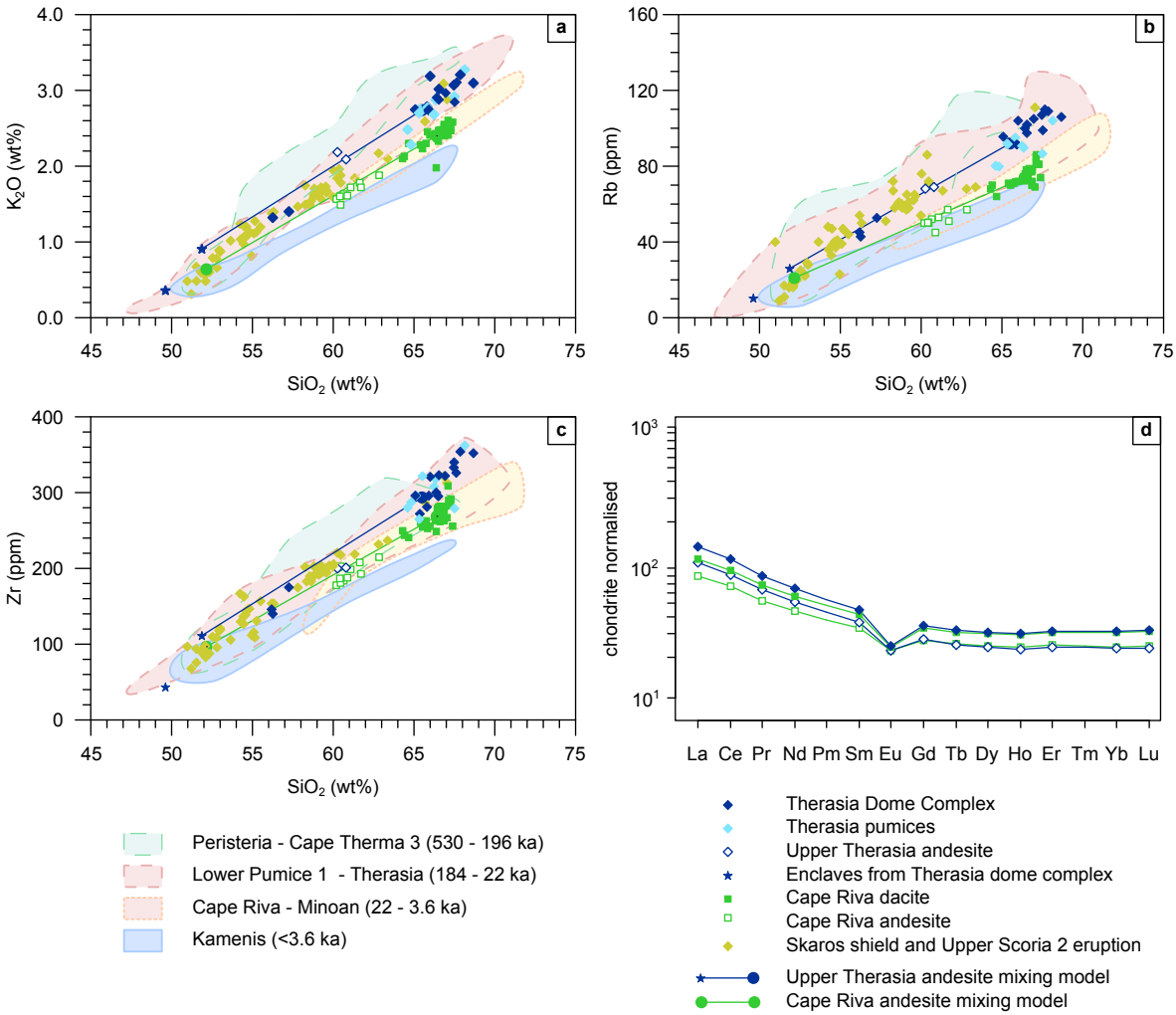

Figure G.12: Incompatible element variation diagrams. (a-c) Therasia and Cape Riva data are plotted as points, along with the Skaros data of Huijsmans (1985) and Upper Scoria 2 data of Druitt et al. (1999). Mixing models for the upper Therasia andesite and the Cape Riva andesite are plotted, as in Figure G.11. Fields of Santorini magma during the volcanic history since 530 ka are plotted, showing the long-term decrease in incompatible elements at Santorini (Druitt et al., 1999; Huijsmans, 1985; Martin, 2005). (d) REE diagram showing the Therasia and Cape Riva magmas. The Therasia dacite is an average of 14 flows with 65–68 wt% SiO_2, and the Cape Riva dacite is an average of four analyses with SiO_2 contents of 66–67 wt% (average: 66.5 wt%). The upper Therasia andesite is an average of flows 11 and 22 (average SiO_2: 60.5 wt%), and the Cape Riva andesite is an average of three analyses with SiO_2 contents between 60.2–60.4 wt% (average: 60.4 wt%).

successfully reproduced by mixing ∼60 wt% of a typical Therasia dacite with ∼40 wt% of mafic magma with the same composition as a basaltic enclave (GS10-43) collected from the same flow (sum of the squares of the residuals of 0.16). The Cape Riva andesite has higher Cr and Ni than the upper Therasia andesite, requiring that the mafic end-member also has higher contents of these elements. The composition of the Cape Riva andesite can be modelled by mixing ∼60 wt% of Cape Riva dacite with ∼40 wt% of an average Skaros basalt (sum of the squares of the residuals of 0.14). However, the calculated Ni content is higher than that measured in the Cape Riva andesite, suggesting that the mafic endmember had lower Ni than the average Skaros basalt.

Despite their broadly similar compositions in terms of silica content and many other major and trace elements, most of the Therasia dacites are enriched in incompatible elements such as K, Rb and Zr (also Nb, Ta, Th, Hf and LREE) compared to the Cape Riva dacite (Figure G.12). LREE are also more enriched in the Therasia dacites relative to the HREE. For example, the Therasia dacites have an average La/Yb ratio of 5.91 ± 0.16 (2σ), while the Cape Riva dacite has a ratio of 4.85 ± 0.04. Amongst the HFSE, Nb and Ta are more enriched than Zr and Hf. The 23 analysed samples of Cape Riva pumice form a tight linear cluster on Figure G.12, showing that the magma was well mixed. All of the 11 analysed Therasia lavas younger than ∼39 ka, and most of the intercalated pumice horizons, similarly form a tight linear cluster (at higher incompatible contents than the Cape Riva, for a given SiO_2 content). However, some of the Therasia pumices overlap with the Cape Riva field for some elements. Most prominent of these is the Cape Tripiti pumice (Fig. 5c), which lies in, or close to, the Cape Riva

Table G.5: Calculation for the mixing of (1) Therasia dacite plus Therasia basalt (mafic enclave) to produce the upper Therasia hybrid andesite, and (2) Cape Riva dacite plus Skaros basalt to produce the Cape Riva hybrid andesite.

			Upper Therasia Hybrid Andesite					Cape Riva Hybrid Andesite		
	Mean Therasia Dacite	Mafic Enclave (GS10-43)	Calculated	Measured (GS10-22)	Residual	Mean Cape Riva Dacite	Mean Skaros Basalt	Calculated	Mean Measured	Residual
Major Elements (wt%)										
SiO_2	65.50	51.86	60.28	60.26	0.02	66.41	52.16	61.22	61.14	0.08
TiO_2	0.83	0.89	0.85	0.86	−0.01	0.74	0.87	0.79	0.83	−0.04
Al_2O_3	15.51	19.07	16.87	17.16	−0.29	15.46	18.38	16.52	16.39	0.13
FeO_T[1]	4.93	8.08	6.13	6.05	0.08	4.75	8.20	6.01	6.27	−0.26
MnO	0.14	0.16	0.15	0.14	0.01	0.15	0.17	0.16	0.15	0.01
MgO	1.21	5.44	2.83	2.66	0.17	1.23	5.96	2.95	2.93	0.02
CaO	3.41	10.16	5.99	5.98	0.01	3.35	10.78	6.06	5.92	0.14
Na_2O	5.50	3.30	4.66	4.52	0.14	5.33	2.72	4.38	4.53	−0.15
K_2O	2.74	0.90	2.04	2.18	−0.14	2.40	0.64	1.76	1.68	0.08
P_2O_5	0.23	0.14	0.2	0.19	0.01	0.18	0.12	0.16	0.15	0.01
Total	100.00	100.00	100.00	100.00	0.00	100.00	100.00	100.01	99.99	0.02
			Sum of the Squares:		0.16			**Sum of the Squares:**		0.14
Trace Elements (ppm)										
Cr	2	31	13	10	3	8	82	35	33	2
Ni	1	16	7	6	1	6	31	15	10	5
Nb	12	5	9	9	0	10	4	8	8	0
Rb	92	26	66	68	−2	74	21	55	51	4
Zr	291	108	221	200	21	266	94	203	193	10
Sr	155	323	219	231	−12	143	226	173	179	−6

For the upper Therasia andesite, the mixing proportions are 38:62 mafic:silicic. For the Cape Riva andesite, the proportions are 36:64. Calculated using the PetroGraph software of Petrelli et al. (2005).

[1] FeO_T is the total FeO and Fe_2O_3 content calculated as FeO

field for most incompatible elements except K, suggesting that the magma that fed the Cape Tripiti eruption had some chemical characteristics intermediate between the two groups of dacite. The differences between the Therasia and Cape Riva dacites are also seen between the corresponding hybrid andesites of these two series. Despite having a similar SiO_2 content, the upper Therasia hybrid andesite is enriched in incompatible elements compared to the Cape Riva hybrid andesite (e.g. 2.1 wt% K_2O compared to 1.7 wt%, respectively). Like the Therasia dacites, the Therasia andesite is also enriched in LREE relative to HREE, and enriched in Nb and Ta relative to Zr and Hf compared top the Cape Riva andesite. This is also reflected in the calculated mafic mixing end-members of the two hybrid andesites shown on Figure G.12, although the difference is subtle.

G.6 Discussion

G.6.1 Origin of the magma series

The Therasia and Cape Riva dacites have similar whole rock major element compositions (for all major elements except K), phenocryst assemblages, phenocryst rim compositions and Fe-Ti oxide temperatures, although the Cape Riva dacite has slightly more evolved interstitial melt. The main difference between the two magmas is that the Cape Riva dacite is depleted in incompatible elements compared to the Therasia dacite. The Cape Riva hybrid andesite is also incompatible-depleted relative to the upper Therasia hybrid andesite, and there are indications that the basaltic mixing end-members were similarly different.

Since the Therasia and Cape Riva magma series form parallel trends on incompatible element variation diagrams (Figure G.12), and have different LREE/HREE ratios, they cannot be related to each other simply by closed-system crystal fractionation schemes like those explored in previously published papers (Druitt et al., 1999; Mann, 1983; Nicholls, 1971). Neither can the Cape Riva dacite be generated by simple back-mixing of Therasia dacite with an incompatible-depleted basalt, since mixing would displace the silicic compositions almost parallel to the compositional trends rather than perpendicular to them. Crustal contamination of Therasia dacite to produce Cape Riva dacite is also unlikely, as this would be expected to increase incompatible element concentrations, not decrease them (Barton et al., 1983; Druitt et al., 1999). Moreover, the two dacite types have very similar whole-rock $^{87}Sr/^{86}Sr$ ratios (0.7050 and 0.7049 respectively; Briqueu et al., 1986; Druitt et al., 1999; Zellmer et al., 2000), ruling out a significant difference in the extent of upper crustal contamination. The Therasia and Cape Riva magma series (basalt, dacite and hybrid andesite in each case) represent two fundamentally distinct magma batches that cannot be related to each other in any simple way by shallow-level processes.

This conclusion is supported by comparison of the two magma series with longer-term geochemical trends at Santorini (Druitt et al., 1999; Huijsmans, 1985; Huijsmans et al., 1988). The same incompatible elements have decreased progressively in Santorini magmas over the last 530 ka, such that the lavas of the historical Kameni Volcano are the most incompatible-depleted (Figure G.12). The difference between the (older) Therasia and (younger) Cape Riva series represents one step in this longer-term evolution. The magnitude of the decrease is similar for most incompatible elements, so that

the ratios between them (e.g. K/Zr, Rb/Zr, Rb/La) have remained approximately constant with time. However, the LREE have become depleted relative to HREE, a change that is also apparent between Cape Riva and Therasia (Figure G.12d). Similar changes also occur between different high field strength elements: Nb and Ta concentrations drop faster than those of Zr and Hf. Progressive depletion in K and other incompatible elements with time has also occurred at other centres in the Aegean region (Francalanci et al., 2005). A decrease in the extent of crustal contamination with time, as might be expected from the progressive sealing-off of ascending magmas from the crust, is not tenable; there is no evidence for a decrease in the $^{87}Sr/^{86}Sr$ ratio with time at Santorini. Isotopic signatures fluctuate with time (Barton et al., 1983; Briqueu et al., 1986; Druitt et al., 1999; Martin et al., 2010), and some young melts are amongst the most radiogenic in the history of the volcano (Martin et al., 2010; Vaggelli et al., 2009). Incompatible trace element contents and isotopic signatures at Santorini are decoupled, ruling out a simple common origin. A more likely explanation for the observed trends lies in the nature of the mantle sources of the parental basalts feeding the volcanic system. Possibilities include an increase with time in the degree of source depletion, an increase of source melt fraction, or a decrease in degree of source metasomatism by slab-derived fluids or melts. All of these mechanisms could potentially account for basaltic parents with decreasing incompatible element contents with time (Bailey et al., 2009; Clift and Blusztajn, 1999; Francalanci et al., 2005; Huijsmans et al., 1988; Zellmer et al., 2000). A mantle origin is supported by the recent discovery at Santorini of multiple co-existing basalt types with different trace element and isotopic signatures (Bailey et al., 2009; Vaggelli et al., 2009). Changing proportions of different parental basalts

that ascend into the crust, where they mix and differentiate at between 4 and 2 kb to intermediate and silicic compositions (Andújar et al., 2010; Cadoux et al., 2013), may account for the observed temporal variations of trace element chemistry. Irrespective of the exact explanation, our results demonstrate the availability of chemically distinct batches of silicic magma within the crustal plumbing system beneath Santorini, as has been demonstrated previously for basalts (Bailey et al., 2009).

G.6.2 Reconstruction of events leading up to the Cape Riva eruption

Construction of the ~12 km^3 basaltic-to-andesitic Skaros shield between 67 and 54 ka represented a period where the eruption rate was close to the average for Santorini (~1 $km^3\,ky^{-1}$; Druitt et al., 1999). The Skaros period culminated at 54 ka in the Upper Scoria 2 explosive eruption. Following Upper Scoria 2, the system stagnated and entered a ~15 ky-long period of near-repose until effusive activity resumed at about 39 ka. Only two lava flows are preserved in the cliffs of Therasia from this period: the ~48 ka lower Therasia andesite (flows 1 and 24) and an inaccessible flow (flow 2) immediately above it. The andesite of Oia could also belong to this period; it is chemically very similar to Upper Scoria 2 and could be residual magma from that eruption. This period of reduced activity, during which the apparent eruption rate based on preserved products was very low (<0.1 $km^3\,ky^{-1}$), is marked by the development of thick palaeosols.

Any mantle-derived basalt injected into the crust during this period must have been trapped at depth, perhaps due to the stress imposed by the high Skaros edi-

fice (Pinel and Jaupart, 2000). Accumulation of heat from prolonged, deep intrusion probably generated silicic melt by a combination of fractional crystallization, partial melting of crustal rocks and defrosting of extant mushy intrusions (Barton et al., 1983; Druitt et al., 1999; Huijsmans, 1985; Huijsmans and Barton, 1989; Mann, 1983). Then, between 39 and 25 ka, a chemically and thermally (895-925 °C) monotonous series of dacites (the Therasia dome complex) was extruded from the summit of Skaros and from dykes on its western flank. The lack of any systematic variation of whole rock or groundmass (i.e. melt) composition with time during this period (Figure G.7) suggests thermal buffering of the crustal storage region by an approximate balance of heat input, heat output and latent heat of crystallisation. The mean eruption rate during construction of the Therasia dome complex was very approximately 0.1–0.2 $km^3\,ky^{-1}$: lower than the long-term average on Santorini ($\sim$1 $km^3\,ky^{-1}$), but higher than that during the preceding repose period. Towards the end of the Therasia activity, lava extrusion became increasingly punctuated by explosive activity. Throughout most of this 15 ky period, the eruptions tapped typical Therasia-type dacite. However, the 26 ka Cape Tripiti eruption tapped dacite with some incompatible trace element contents intermediate between those of Therasia and Cape Riva. Any basaltic magma intruded beneath the summit region over the 15 ky was unable to reach the surface, except as rare quenched enclaves of dacite-contaminated olivine basalt. Towards the end of the period, basalt mixed with dacite in approximately equal proportions, forming the upper Therasia hybrid andesite.

Following extrusion of the last Therasia lava, no more than 2,800 $\pm$ 1,400 years elapsed before the 21.8 $\pm$ 0.4 ka Cape Riva eruption took place. At least 10 km^3 of

880 °C Cape Riva dacite, poorer in incompatible elements, was then erupted as Plinian fallout and pyroclastic flows. The eruption also discharged a small quantity ($\ll$1 km^3) of hybrid andesite formed by the mixing of olivine basalt and incompatible-depleted dacite in sub-equal proportions, and the Skaros-Therasia edifice collapsed (Druitt et al., 1999).

G.6.3 Constraints on magma reservoir development

The Therasia dacites have been previously interpreted as 'precursory leaks' from the growing Cape Riva magma body (Bacon, 1985; Druitt, 1985). Precursory leaks of silicic magma from diffuse vents prior to caldera-forming eruptions are believed to record the prolonged, incremental growth of large crustal magma reservoirs (Bacon, 1985). For example, leaks of rhyodacite at Mount Mazama (Crater Lake, Oregon) bear witness to the progressive growth, over about 20,000 years, of the magma body that was discharged 6,850 years ago (Bacon, 1985; Bacon and Lanphere, 2006). However, the Therasia lavas cannot simply be leaks from a single, growing Cape Riva reservoir, because they represent a chemically different magma batch.

One possibility is that the two dacite types were stored in separate, long-lived reservoirs that coexisted in the upper crust, perhaps for much of the 30 ky since Upper Scoria 2. The Therasia eruptions would have been fed from one or more small reservoir(s), and the Cape Riva eruption from another, larger reservoir. The Cape Tripiti pumice, with its intermediate chemical character, might have resulted from a temporary connection between the two reservoirs. However, field and phase equilibria data provide quite stringent constraints on the possible locations of the two reser-

voirs in such a model. First, the vents that fed the Therasia lavas lay within the area that subsequently collapsed to form the Cape Riva caldera (Druitt, 1985, 2014; Druitt and Francaviglia, 1992), showing that the reservoirs were geographically coincident. Second, the similarities in whole rock major element composition, phenocryst assemblage, phenocryst rim compositions and Fe–Ti oxide temperatures, show that the Therasia dacites must have been stored immediately prior to eruption at a pressure (2 ± 0.5 kb, equivalent to 8 ± 2 km) similar to that determined experimentally for the Cape Riva dacite by Cadoux et al. (2013). The two reservoirs must therefore have been situated within the ~4 km vertical distance represented by the ±0.5 kb uncertainty on the pressure. Moreover, this uncertainty is on the absolute pressure, not on the relative pressure difference between the two dacite types. It is difficult to see how two magma reservoirs within this confined space could remain largely isolated over many thousands of years. We cannot rule out this model, but it raises problems that are hard to surmount. Our preferred interpretation is that the Therasia and Cape Riva magma batches were emplaced sequentially into the upper crust beneath the summit of the volcano, the first then being partially, or wholly, flushed out by the arrival of the second. In this model the 15 ky of Therasia activity was fed either from a single long-lived, melt-dominated reservoir or by the ascent, partial eruption and rapid freezing of multiple melt packets (e.g. Zellmer et al., 2003). At 26 ka the system may have been replenished by incompatible-depleted dacite, which mixed with Therasia dacite and was discharged as the Cape Tripiti Pumice. The subsequent return to eruption of 'pure' Therasia dacite suggests that if a discrete Cape Riva reservoir already existed below the summit at this time, it had probably not yet reached its full size. Following

extrusion of the last Therasia lava flow, the input of incompatible-depleted dacite continued, and perhaps accelerated, during the $<2{,}800 \pm 1{,}400$ y preceding the Cape Riva eruption. The new input magma mixed with any remaining Therasia magma to generate the dacite that subsequently discharged during the Cape Riva eruption. This may have had the composition of pure Cape Riva dacite, or may have been a dacite even poorer in incompatibles (e.g. Kameni-like dacite; Figure G.12). Amalgamation and homogenization of the different magma batches resulted in the formation of a single, contiguous reservoir.

Assuming injection of most of the $>10\,\mathrm{km}^3$ of Cape Riva magma in <2800 y yields a time-averaged supply rate of $> 0.004 \pm 0.002\,\mathrm{km}^3\,\mathrm{y}^{-1}$, although the peak value may have been much higher. For comparison, the mean accumulation rate estimated over the 1600 y to prior the Oruanui eruption has been estimated as $>0.33\,\mathrm{km}^3\,\mathrm{y}^{-1}$, culminating in values of $\sim 1\,\mathrm{km}^3\,\mathrm{y}^{-1}$ (Allan et al., 2013; Wilson and Charlier, 2009). A late-stage growth spurt of the Minoan magma reservoir has been estimated as $>0.05\,\mathrm{km}^3\,\mathrm{y}^{-1}$ (Druitt et al., 2012). Intrusion rates comparable to, or higher than, that estimated for the Cape Riva are implied by measured deformation rates at silicic volcanoes such as Uturuncu ($\sim 0.01\,\mathrm{km}^3\,\mathrm{y}^{-1}$; Pritchard and Simons, 2004; Sparks et al., 2008), Kameni ($\sim 0.01\,\mathrm{km}^3\,\mathrm{y}^{-1}$; Parks et al., 2012), Yellowstone ($0.1\,\mathrm{km}^3\,\mathrm{y}^{-1}$; Chang et al., 2010), and Lazufre ($\sim 0.01\,\mathrm{km}^3\,\mathrm{y}^{-1}$; Froger et al., 2007; Ruch et al., 2009).

Rapid intrusion of the Cape Riva dacite into the upper crust would have favoured runaway growth of a melt-dominated magma reservoir (Annen, 2009; Gelman et al., 2013; Schöpa and Annen, 2013). Driving mechanisms for magma ascent may have included increased basaltic flux from the mantle, tectonic forces, or gravitational in-

stability of crustal magma storage regions. Possible evidence of increased basaltic flux is provided by the production of hybrid andesites (formed by mixing of basalt and dacite in approximately equal proportions) in the few thousand years prior to the Cape Riva eruption, as well as in the Cape Riva reservoir itself. Pressurization of the upper crustal plumbing system by sustained, high-flux injection of dacite and basalt may have triggered the transition from prolonged, largely effusive activity to catastrophic explosive eruption and caldera collapse.

G.7 Conclusions

We have combined field, high-resolution radiometric, petrological and geochemical approaches in a study of the evolution of the crustal magma plumbing system of Santorini prior to a silicic caldera-forming eruption. The main conclusions are listed below.

1. Between 39 ka and 25 ka, a sequence of compositionally (65-68 wt% SiO_2) and thermally (895-925 °C) monotonous dacitic lavas leaked out to form the $\sim$2 km^3 Therasia dome complex across the summit and western flank of the high, extant Skaros lava shield. Pyroclastic units interbedded with the lavas towards the top of the sequence record increasing explosivity of the system towards the end of this period. One prominent pumice fall deposit within the Therasia complex probably correlates with the 26 ka Y-4 ash layer observed in deep-sea sediments SE of Santorini. Following a pause in activity no longer than $2{,}800 \pm 1{,}400$ ky, the 21.8 ± 0.4 ka Cape Riva explosive eruption discharged >10 km^3 of 880 °C dacite, and collapsed the Skaros shield.

2. The Therasia and Cape Riva dacites are similar in most major elements, but the Cape Riva dacite has lower contents of K and incompatible trace elements (e.g., Rb, Zr, Th, LREE) than the Therasia dacites at a given silica content. This decrease in incompatibles that took place at 21.8 ka is one step in the well-documented longer-term decrease in incompatible elements with time observed at Santorini over the last 530 ka. The Therasia and Cape Riva dacites represent distinct magma batches that are unrelated by shallow-level processes.

3. Given that the source vents for the Therasia and Cape Riva dacites were geographically coincident, and that the reservoir depths estimated from phase equilibria were similar, accumulation of most of the Cape Riva magma in the upper crust probably took place within the $2{,}800 \pm 1{,}400$ y period between the last Therasia eruption and the Cape Riva. This would have required a time-averaged magma accumulation rate in excess of $0.004 \pm 0.002\,\mathrm{km^3\,y^{-1}}$.

4. Discharge of basaltic magma during this time period is limited to $\ll$1 % quenched enclaves of olivine basalt in some Therasia lavas and in Cape Riva pumice. However, hybrid andesite magmas formed by the mixing of olivine basalt and dacite in approximately equal proportions were erupted as lava towards the end of the Therasia, and as scoria in the Cape Riva eruption. These hybrids may record an increased influx of basalt into the upper crust over the several thousands of years leading up to the Cape Riva eruption. Increased basaltic flux may have played a role in the rapid accumulation of incompatible-depleted Cape Riva magma beneath the summit of Skaros Volcano prior to its 21.8 ka eruption.

5. Pressurization of the upper crustal plumbing system by sustained, high-flux in-

jection of dacite and basalt may have triggered the transition from prolonged, largely effusive activity (Therasia) to catastrophic explosive eruption and caldera collapse (Cape Riva).

Acknowledgments

We thank M Benbakkar and C Chauvel for providing major element and trace element analyses, respectively, and J-L Devidal for help with the electron microprobe. J Keller kindly drew our attention to the Y-4 deep-sea ash layer. E Klemetti, D Morgan and G Zellmer provided helpful reviews, and F Costa commented on an earlier version of the manuscript. The work was carried out in the framework of the project 'Storage and Mixing at Santorini' financed by the French Agence National de Recherche [ANR-08-BLAN-0249-01]. GN Fabbro was funded by the Région d'Auvergne. This is Laboratory of Excellence ClerVolc contribution number 76.